



THÈSE

En vue de l'obtention du

DOCTORAT DE L'UNIVERSITÉ DE TOULOUSE

Délivré par :

Institut Supérieur de l'Aéronautique et de l'Espace

Présentée et soutenue par :
Christopher WINGEL

le vendredi 8 septembre 2023

Titre :

Investigation of the RANS approach for the prediction of cooled turbine stage flows submitted to swirled hot streaks

Évaluation de l'approche RANS pour l'étude des écoulements avec points chauds dans les turbines refroidies

École doctorale et discipline ou spécialité :

ED MEGeP : Dynamique des fluides

Unité de recherche :

Équipe d'accueil ISAE-ONERA EDyF

Directeur(s) de Thèse :

M. Nicolas BINDER (directeur de thèse)
M. Yannick BOUSQUET (co-directeur de thèse)

Jury :

M. Sofiane KHELLADI Professeur Arts et Métiers ParisTech - Président, Examineur
M. Stéphane AUBERT Professeur Université de Lyon - Rapporteur
M. Nicolas BINDER Professeur ISAE-SUPAERO - Directeur de thèse
M. Yannick BOUSQUET Professeur associé ISAE-SUPAERO - Co-directeur de thèse
M. Jean-François BOUSSUGE Ingénieur CERFACS - Co-encadrant de thèse
M. Sébastien LE GUYADER Ingénieur Safran Helicopter Engines - Examineur
M. Julien MARTY Ingénieur de recherche ONERA - Examineur
M. Tom VERSTRAETE Professeur Von Karman Institute for Fluid Dynamics - Rapporteur

Remerciements

“ *Les performances individuelles, ce n'est pas le plus important. On gagne et on perd en équipe.* ”

Zinédine Zidane

La thèse est loin d'être un long fleuve tranquille. Elle s'apparente à un match décisif de football, avec ses temps forts, ses temps faibles et son fort enjeu. Je vous propose à travers ces lignes de retracer le match de ma thèse, en remerciant les nombreux acteurs qui y ont contribué.

Un match de football ne pourrait se dérouler sans la présence d'un corps arbitral, assurant le respect des règles du jeu et l'impartialité. Ainsi, je souhaiterais avant tout remercier les membres du jury pour l'arbitrage du manuscrit, les retours constructifs ainsi que les nombreux échanges lors de la soutenance de thèse : Pr. Stéphane Aubert, Pr. Sofiane Khelladi, Dr. Julien Marty et Pr. Tom Verstraete.

L'échauffement n'est souvent que la partie immergée de l'iceberg, mais il est pourtant ô combien capital dans le succès d'une rencontre sportive. J'ai eu la chance d'avoir les meilleurs préparateurs et coach possibles. Jeff, ton franc-parler peut déstabiliser au premier abord, mais il forge le caractère et permet de surmonter les temps faibles pour en ressortir plus fort. Merci pour ton œil aiguisé sur la simulation numérique, pour tes avis sur la qualité du manuscrit ou des papiers, et pour toute la confiance et la liberté que tu as pu me donner. Yannick (Whybe pour les intimes), tu as su me préparer de la meilleure des façons pour ce match, avec ton expertise et ton sens critique que peu de personnes ne peuvent égaler. Tu pourrais largement postuler à une place de préparateur auprès des plus grands au PSG. Merci pour toutes les discussions extra-thèse dans ton bureau ou en salle de pause (elles étaient nombreuses, régulières et bruyantes !). Enfin Nico, mon coach. Tu es le Pep Guardiola de la turbomachine, tout le monde te veut dans son équipe car tu es pétri de talent. Ta rigueur sur le terrain est indéniable avec une méthode propre à toi (mises sous pression avec la clé rouge¹, les « c'est naze » ou « c'est long » à répétition), mais tu sais être à l'écoute de tes joueurs. Ainsi, je t'exprime toute ma gratitude, car tu m'as permis de prendre confiance en moi, accompagné dans les bons moments mais surtout dans les moments plus compliqués.

¹Objet décrit comme une clé à molette, rouge, d'un mètre de long, pouvant être observé sur l'épaule de son propriétaire dans les couloirs du DAEP.

De nos jours, il n'y a pas de grand match sans un grand investissement préalable. Ainsi, ce match n'aurait pas pu voir le jour sans le financement de Safran Helicopter Engines. Mes remerciements se tournent en particulier vers Nicolas et Sébastien. Nicolas, tu m'as élevé du rang de stagiaire en m'accueillant dans ton équipe à l'aube de 2018 à celui de doctorant fin 2019 et enfin à celui de docteur. Que de chemin parcouru ! Merci pour ta disponibilité et ta réactivité qui ont fait que j'ai pu avancer agréablement au quotidien. Je te souhaite le meilleur pour la suite de ta carrière. Sébastien, tu es la force tranquille, toujours pourvu de précieux conseils et d'une expérience industrielle incontestable qui ont fortement aidé à ma réussite. Je n'oublie pas aussi ceux qui ont contribué de près ou de loin à cette thèse et dont je suis redevable : Emma, Nicolas, André, Charlie et Jacques. Le succès d'une thèse CIFRE se retrouve dans les nombreux échanges entre la partie industrielle et la partie académique, et dans les directions proposées par cette dernière. Je me souviens de la réunion de lancement durant laquelle nous étions encore sceptiques quant à la possibilité du RANS à prédire le transport de température. J'espère ainsi vous avoir convaincu que la méthode n'était pas encore à jeter² !

Historiquement, j'ai commencé ma carrière de joueur au CERFACS, dont le dernier rempart depuis plus de 30 ans se prénomme Chantal. Merci pour ton rire communicatif et l'attention que tu as au quotidien avec les petits jeunes. Je remercie également toute la ligne défensive composée de l'équipe administrative : Marie, Jade, Michèle, Lydia, Dominique et Brigitte. Un peu plus haut sur le terrain, que ferions-nous sans un milieu de terrain composé par CSG ? Vous alimentez notre attaque en faisant un boulot remarquable et en étant présents au moindre souci informatique. Pour tout cela, merci à Isabelle, Fred, Fabrice, Gérard, Patrick et Nicolas. Enfin, il y a toute cette attaque, composée en majeure partie de doctorants et post-doctorants. En presque 5 années au CERFACS, j'ai vu cette ligne offensive se renouveler constamment. Tout d'abord constituée de joueurs professionnels de l'En Avant Cerfacs, l'EAC, dont j'ai la double casquette joueur-président, elle a rapidement intégré des joueurs amateurs plus enclins à la LBM³ ou le kitesurf⁴. Ainsi je remercie Adèle, Thomas A., Kelu, Florian, Gauthier, Minh, Bastien, Thomas G., à qui j'associe également Adèle, Mai et Octavie, pour les multiples rigolades, soirées ou les nombreux voyages autour du Monde. Merci aussi à Catchi qui a, le temps d'un instant, troqué ta casquette d'Alpine pour rechausser les crampons afin d'assister à ma soutenance. Tu me feras toujours autant rire avec tes stratégies et ton trading sur MPG. Finalement, il n'y a pas de bonne équipe sans un ou plusieurs meneurs de jeu : Paulo et Marchal, merci pour votre soutien indéfectible, les soirées au Café Oz (Café quoi ?), les sorties vélo et bien d'autres. Dave et Laurent, vous vous êtes exilés hors de la ville rose mais vous n'en restez pas moins importants à mes yeux.

Pour qu'un match devienne légendaire, il faut une deuxième équipe de qualité sur le terrain. C'est le cas de l'équipe du DAEP, où j'ai été définitivement transféré début 2023. L'ambiance qui règne au sein de cette équipe est tout à fait remarquable. Pour cela, je tenais à remercier notre chef de département, Xavier, qui fait en sorte qu'il y ait une belle cohésion entre les acteurs du jeu, permanents et non-permanents. Évidemment, je ne peux pas oublier de remercier Hélène pour la préparation administrative de ma soutenance. Je te souhaite le meilleur pour ta retraite

²Et de l'utilité des modèles anisotropes ou de l'importance de la représentativité de la condition d'entrée.

³Lattice Boltzmann Method : méthode de calcul étant 10 fois plus rapide que n'importe quelle autre méthode.

⁴J'en profite pour vous remercier pour l'anémomètre : plus d'excuses pour ne plus kiter car il n'y a apparemment pas assez de vent, mais ça permettra par la même occasion de sauver mes doigts par fortes conditions.

bien méritée. Maxou, continue de nous sustenter avec tes pâtisseries, ça nous évite un coup de mou sur le terrain ! J'ai été accueilli au centre d'entraînement « 38.128 », communément appelé bureau des « TàRé⁵ », où j'ai pu peaufiner mon jeu. J'y ai rencontré mes coéquipiers émérites Dr. Alessio, Dr. Maxime et Dr. Massyl (Dr. Benichou je te rajoute), puis mes coéquipiers en formation tout comme moi : Greta, Dr. Julien, Dr. Sam, Dridri, Thibaut, Ian, Benoit et Jean. Merci à tous pour la superbe ambiance quotidienne et la cohésion de groupe. Après jumelage avec d'autres centres, l'équipe s'est renforcée autour de joueurs de qualité. Je remercie donc Xaxa, Dr. Ludo, Romain, Vincent, Juan, Anaïs, Julien, Flo⁶, Thomas, Pierre⁷ pour tous les moments de partage ainsi que Tiphaine pour le repos accordé sur le banc de touche quand j'en avais besoin. Bon courage pour vos futures soutenances !

Enfin, un match sans public n'aurait pas la même saveur. J'ai eu la chance de pouvoir communier avec le 12ème homme. Merci aux amis de l'INSA Adrien, Batou, Baba, Ben, Clément, Quentin et Vinssou, ainsi qu'aux +1. On s'est perdu de vue au cours de ce match, mais promis ça n'était que temporaire ! Merci aussi à toi Romain d'avoir fait le déplacement depuis Pau. La famille était également présente en tribunes : merci à mes tantes, tontons, cousines et grands-mères. On ne se voit pas souvent mais c'est toujours un plaisir de se voir ! J'ai au moment d'écrire ces lignes une pensée émue pour ceux qui ne sont plus là et qui auraient été fiers de cet aboutissement. Finalement, mes supporters depuis la première heure : mon frère et mes parents. Vous m'avez toujours encouragé et fait confiance dans mes choix, alors merci à vous.

Malgré l'importance de ce match, il aurait été impossible de départager les deux équipes dont j'ai à un moment fait partie et qui ont forcément chacune une place particulière dans mon cœur.

La victoire est tellement plus belle quand elle est collective.

Merci.

Christopher aka Krikri,
Toulouse, le 22 septembre 2023.

⁵Turbomoteurs à Réaction.

⁶Le FC Constantinople peut être fier de toi.

⁷Tout comme Dembélé qui ne sait pas s'il est droitier ou gaucher, Pierre ne sait pas s'il a les pieds carrés ou triangulaires.

Résumé

Pour atteindre l'Accord de Paris sur le climat, tous les acteurs du Monde sont appelés à limiter et à réduire de façon drastique leurs émissions de gaz à effet de serre. Parmi ces acteurs, ceux du secteur aérien, comme Safran Helicopter Engines qui est à l'origine de cette thèse, s'inscrivent dans cette démarche environnementale en proposant de nouvelles technologies de combustion visant à réduire les émissions de NO_x : les combustions à mélange pauvre. Néanmoins, ce genre de technologie conduit à un écoulement complexe en entrée de turbine haute-pression, caractérisé par des forts niveaux de turbulence et des points chauds swirlés. Ce type d'écoulement impacte l'aérodynamique et l'aérothermique de l'étage de turbine, qui peut, dans le pire des cas, causer des dommages irréversibles. La prédiction fiable de cet écoulement de point chaud swirlé doit donc se faire en amont avec des simulations numériques.

Dans ce travail de thèse, l'approche RANS est évaluée sur la configuration du projet FACTOR, où des données LES et expérimentales sont disponibles. Un premier état des lieux sur cette géométrie de turbine haute-pression avec des simulations stationnaires et instationnaires, et avec prise en compte ou non du refroidissement confirme un écoulement complexe à prédire, particulièrement du point de vue de la turbulence. Une configuration simplifiée est donc déclinée pour l'analyse d'un point chaud swirlé turbulent grâce à des LES et pour la calibration de simulations RANS. Cette étude révèle que la diffusion joue un rôle important dans le transport d'un point chaud dans un canal courbé, la diffusion étant pilotée par l'échelle de dissipation de la turbulence, qui est évaluée au travers d'une échelle intégrale. Un bilan d'énergie cinétique turbulente permet de décrire les mécanismes principaux qui gouvernent l'écoulement. Des études complémentaires basées sur l'analyse de Lumley montrent une forte anisotropie de la turbulence qui ne peut pas être correctement capturée par les modèles de turbulence RANS suivant l'hypothèse de Boussinesq. Ainsi, les modèles EARSM et RSM sont prometteurs, car ils permettent de retrouver la sensibilité à la courbure et à la rotation.

Avec l'expérience acquise grâce à cette étude académique, la configuration FACTOR est de nouveau traitée. Les modèles de turbulence anisotropes sont évalués, mais les résultats manquent de prédictibilité quand ils sont comparés aux essais. Deux problèmes sont mis en avant au niveau de la condition aux limites : des erreurs de mesure au plan d'entrée de la turbine haute-pression (P40) en raison des forts niveaux de giration, et une nature instationnaire du P40 en raison de la présence d'une instabilité hydrodynamique. Les analyses montrent que le premier point est d'une importance capitale, alors que le second améliore les résultats dans une moindre mesure.

Mots-clés : RANS, LES, turbulence, turbine haute-pression, point chaud.

Abstract

To fulfil Paris Agreement on climate change, a drastic decrease of CO₂ and non-CO₂ emissions must be done from all sectors in every part of the world. Particularly, the aeronautical sector cannot get away with it, and Safran Helicopter Engines, which is at the origin of this thesis, is enrolled in this process, by proposing new technologies of engine combustion that reduce NO_x emissions (lean burn combustion). While having a beneficial impact on NO_x emissions, such technologies lead to a highly complex flow at the inlet of the high-pressure turbine, characterised by high levels of turbulence, swirling motion and hot streaks. Even if it can cause irreversible damages in the worst case, such flow impacts the aerodynamics and aerothermal of the whole high-pressure turbine, and the reliable prediction of this type of flow must be performed with numerical simulations.

In this work, the RANS method is evaluated on the FACTOR project, where LES and experimental results are available. A first inventory on this high-pressure turbine geometry with steady and unsteady simulations, and by considering or not cooling confirms a complex flow to predict, especially in terms of turbulence. A simplified configuration is therefore studied for the analysis of a highly turbulent swirled hot streak flow by means of LES and the calibration of the RANS method. It reveals that diffusion plays a major role in the transport of hot streak in a bent channel, diffusion being piloted by the dissipation scale of turbulence, which is evaluated in this work through an integral length scale. A turbulent kinetic energy budget applied to the channel delineates the main mechanisms that govern the flow. Further studies using Lumley's theory also show a strong anisotropy of turbulence developing inside the channel, that cannot be correctly captured with classical RANS turbulence models following Boussinesq's hypothesis. In that sense, EARSM and RSM turbulence models seem a promising solution, as they enable to retrieve the effects of curvature and rotation.

Following the experience gained from this academic study, the FACTOR configuration is tackled again. Anisotropic turbulence models are applied, but still suffer from a lack of predictability when looking at temperature profiles. Two problems are put forward: measurement errors at the inlet of the high-pressure turbine (P40) because of the high levels of swirl, and an unsteady nature of P40 due to the presence of a Precessing Vortex Core. Investigations show that the first point is of major importance, while the second improves the results to a lesser extent.

Keywords: RANS, LES, turbulence, high-pressure turbine, hot streak.

Table of Contents

	Page
Remerciements	iii
Résumé	vii
Abstract	ix
Nomenclature	xvii
Introduction	1
Towards a greener aviation industry	1
Turboshaft engines	2
Industrial and scientific issues	3
Organisation of the manuscript	5
<hr/>	
Part I – Highlight of the difficulties to capture both the aerodynamics and aerothermal in a high-pressure turbine stage	9
<hr/>	
Chapter 1 Generalities on axial flow turbines and associated numerics	11
1.1 Aerodynamic and aerothermal phenomena in axial high-pressure turbines	12
1.1.1 Classification of unsteady phenomena	12
1.1.2 Vane/blade interactions	13
1.1.3 Combustion chamber/turbine interactions	15
1.1.4 Secondary flows	18
1.1.5 Technological effects	19
1.2 Numerical methods for the resolution of turbulent flows	22
1.2.1 The Navier-Stokes equations	22
1.2.2 The closure problem	23
1.2.3 Turbulence modelling approaches	24
1.2.4 RANS turbulence modelling	30
1.3 Modelling strategies of turbomachinery components	36
1.3.1 Steady simulations: the mixing-plane approach	36
1.3.2 Unsteady simulations	36
1.4 Conclusion	38

Chapter 2	Preliminary study on the FACTOR configuration	41
2.1	Presentation of the FACTOR project	43
2.1.1	Motivations	43
2.1.2	Test rigs and operating conditions	44
2.1.3	The use of CFD in the scope of FACTOR	45
2.1.4	Experimental data	51
2.2	Numerical set-up	54
2.2.1	Numerical domain	54
2.2.2	Angular adjustment of the profiles	54
2.2.3	Boundary conditions	55
2.2.4	Meshing strategy	58
2.2.5	Numerical parameters	60
2.3	Convergence and computational cost	62
2.3.1	Steady simulations	62
2.3.2	Unsteady simulations	63
2.3.3	Computational cost	66
2.4	Scope of investigation for the prediction of the hot streak transport	66
2.4.1	Impact of the clocking position on the hot streak migration and wall surface temperature	66
2.4.2	Variability of the operating point	69
2.4.3	Influence of unsteady simulations	72
2.4.4	Effect of the cooling	73
2.5	Conclusion	76

Part II – The sources of errors in the prediction of a swirled hot streak flow in a high-pressure turbine stage **81**

Chapter 3	Effect of turbulence levels and scales on the diffusion of hot streaks	83
3.1	Introduction	85
3.2	Description of the configuration and the numerical set-up	85
3.2.1	Geometry	85
3.2.2	LES and RANS meshes	85
3.2.3	LES boundary conditions	88
3.2.4	RANS boundary conditions	91
3.2.5	Numerical parameters	92
3.2.6	Post-processing	93
3.3	Convergence study	93
3.3.1	Mesh and statistical convergence of the LES	93
3.3.2	Numerical convergence	97
3.4	Analysis of the LES to study the topology of the swirled flow	98
3.4.1	Effect of swirl on the hot streak migration	98
3.4.2	Turbulent kinetic energy budget	100
3.4.3	Evaluation of an integral scale of turbulence	104
3.4.4	Effect of the turbulent length scale on the hot streak redistribution	106
3.4.5	Stability of the swirling jet	110

3.5	Evaluation of RANS against LES: sensitivity study to physical and numerical parameters	112
3.5.1	Prescription of the turbulent map obtained from the LES at the inlet boundary condition	114
3.5.2	Influence of the turbulent Reynolds number	116
3.5.3	Turbulent kinetic energy budget comparisons between diffusive and transport RANS turbulence set-ups	120
3.5.4	Brief discussion of the stability issue	121
3.6	Conclusion	122
Chapter 4	Anisotropy analysis of a swirled hot streak	127
4.1	Introduction	128
4.2	Evaluation of the validity of Boussinesq's constitutive relation	129
4.2.1	Schmitt's criterion	129
4.2.2	Alignment analysis	129
4.3	Characterisation of anisotropy in a turbulent flow	131
4.3.1	Lumley's theory	131
4.3.2	Application on a swirling hot streak	133
4.4	Dealing with anisotropy of turbulence in RANS modelling	137
4.4.1	Quadratic constitutive relation correction	137
4.4.2	EARSM/RSM turbulence models	137
4.5	Conclusion	146
<hr/>		
Part III	– Back to the industrial problematic and configuration	149
<hr/>		
Chapter 5	Predominant mechanisms of FACTOR	151
5.1	Introduction	152
5.2	Application of the results from the academic study on the high-pressure turbine configuration of FACTOR	152
5.2.1	Impact of the turbulent Reynolds number	152
5.2.2	Effect of the turbulence model	154
5.2.3	Accounting for the anisotropy of turbulence	155
5.3	Conclusion	158
Chapter 6	Towards realistic high-pressure turbine inlet boundary conditions	161
6.1	Introduction	163
6.2	Status of measurements at P40	165
6.2.1	Measurement difficulties	165
6.2.2	Differences at P40 between the experiments and the LES	166
6.3	Hypothesis 1: correction of type 'c' errors	168
6.3.1	LES database	168
6.3.2	Sensitivity to the inlet flow variables: test cases matrix	170
6.4	Hypothesis 2: investigation of type 'a' errors	171
6.4.1	Modification of the geometry	171
6.4.2	Boundary layer thickness	171
6.4.3	Impact of the modification of the map close the hub and shroud	172
6.5	Hypothesis 3: generation of an unsteady boundary condition	176

6.5.1	Emergence and signature of the PVC	176
6.5.2	Spectral Proper Orthogonal Decomposition method	176
6.5.3	Application on FACTOR’s configuration	178
6.6	Comparisons with steady experimental data	191
6.6.1	Radial distributions from the 5HP measurements	191
6.6.2	Isentropic Mach number distribution on the vane surface	194
6.6.3	Hub and shroud static pressure taps	194
6.7	Unsteady pressure measurements	195
6.7.1	Time-averaged pressure field at P40	196
6.7.2	PSD pressure amplitude at P40	196
6.7.3	Phase-locked average at P42	198
6.7.4	PSD pressure amplitude at P42	199
6.8	Conclusion	200
<hr/>		
Conclusion		205
	Reminder of the context and objectives	205
	Main findings	206
	Perspectives	208
<hr/>		
Part IV – Appendices		211
<hr/>		
Appendix A Complementary elements on the academic study		213
A.1	Influence of the turbulent Prandtl number	214
A.2	Slight modification of the turbulent Reynolds number	217
A.3	Effect of the mesh	218
Appendix B Complementary analyses of FACTOR’s configuration		221
B.1	y^+ distributions on the walls	222
B.2	Mesh refinement effect	223
B.3	Effect of the wall boundary condition for the specific turbulence dissipation rate	224
B.4	Zheng limiter	226
B.5	Influence of the SST correction	227
B.6	Imposition of the turbulent kinetic energy from a LES	229
B.7	Radial distributions of the sensitivity study for errors of type ‘c’	230
B.8	Radial distributions with the SST $k - \omega$ turbulence model and the inlet map from the LES	234
List of Figures		235
List of Tables		245
Bibliography		248

Nomenclature

Acronyms

5HP	5 Holes pressure Probe
AIM	Anisotropy Invariant Map
BPF	Blade-Passing Frequency
BPP	Blade-Passing Period
CDF	Cumulative Density Function
CFD	Computational Fluid Dynamics
CFL	Courant Friedrichs Lewy
CPU	Central Processing Unit
CT	Convective Time
CV	Cooled Vein
DLR	Deutsches zentrum für Luft-und Raumfahrt
DNS	Direct Numerical Simulation
DR	Degree of Reaction
EARSM	Explicit Algebraic Reynolds Stress Model
FACTOR	Full Aero-thermal Combustor-Turbine interactiOn Research
FFT	Fast Fourier Transform
FRAP	Fast-Response Aerodynamic Probe
HIT	Homogeneous Isotropic Turbulence
HP	High-Pressure
HWA	Hot Wire Anemometry
HS	Hot Streak
LE	Leading-Edge
LEC	Leading-Edge Clocking
LES	Large-Eddy Simulation
NGV	Nozzle Guide Vane
OP	Operating Point
OPR	Overall Pressure Ratio
P40	Plane 40
P41	Plane 41

P42	Plane 42
PAC	PASSage Clocking
PDF	Probability Density Function
PLA	Phase-Locked Average
PS	Pressure Side
PSD	Power Spectral Density
PTKE	Production of Turbulence Kinetic Energy
PVC	Precessing Vortex Core
QCR	Quadratic Constitutive Relation
RANS	Reynolds-Averaged Navier-Stokes
RMS	Root Mean Square
RSM	Reynolds Stress Model
RSN	Reduced Sector Number
SPOD	Spectral Proper Orthogonal Decomposition
SS	Suction Side
SST	Shear Stress Transport
SV	Smooth Vein
TE	Trailing-Edge
TIT	Turbine Inlet Temperature
TKE	Turbulence Kinetic Energy
UNIFI	Università degli Studi di Firenze
URANS	Unsteady Reynolds-Averaged Navier-Stokes

Latin letters

a_{ij}	Components of the anisotropy tensor	$[\text{m}^2 \cdot \text{s}^{-2}]$
$a_{ij}^{(ex)}$	Components of the modelled anisotropy tensor	$[\text{m}^2 \cdot \text{s}^{-2}]$
b_{ij}	Components of the normalised anisotropy tensor	$[-]$
A	Area	$[\text{m}^2]$
c_p	Constant pressure specific heat capacity	$[\text{J} \cdot \text{kg}^{-1} \cdot \text{K}^{-1}]$
c_v	Constant volume specific heat capacity	$[\text{J} \cdot \text{kg}^{-1} \cdot \text{K}^{-1}]$
Ca_x	Axial chord	$[\text{m}]$
E	Energy	$[\text{kg} \cdot \text{m}^2 \cdot \text{s}^{-2}]$
f	Frequency	$[\text{Hz}]$
\hat{f}	Reduced frequency	$[-]$
\mathbf{F}	Body force	$[\text{kg} \cdot \text{m} \cdot \text{s}^{-2}]$
h/H	Coordinate reduced height	$[-]$
k	Turbulence kinetic energy	$[\text{m}^2 \cdot \text{s}^{-1}]$
l_T	Turbulence length scale	$[\text{m}]$
$l_{T,i}$	Turbulence length scale in direction i	$[\text{m}]$
l_η	Kolmogorov scale	$[\text{m}]$
l_λ	Taylor scale	$[\text{m}]$
\dot{m}	Massflow rate	$[\text{kg} \cdot \text{s}^{-1}]$
m^*	Non-dimensional meridional coordinate	$[-]$
M	Mach number	$[-]$

M_{is}	Isentropic Mach number	[-]
\mathcal{M}	Pope's criterion	[-]
N	Rotational speed	[rpm]
N_S	Number of stator vanes	[-]
N_R	Number of rotor blades	[-]
P	Pressure	[Pa]
Pr	Prandtl number	[-]
Pr_T	Turbulent Prandtl number	[-]
\mathbf{q}	Heat flux vector	[kg.s ⁻³]
r	Specific gas constant	[J.kg ⁻¹ .K ⁻¹]
$R_{v_i v_i}$	Autocorrelation coefficient	[-]
$\overline{\mathbf{R}}$	Reynolds stress tensor	[m ² .s ⁻²]
Re	Reynolds number	[-]
Re_T	Turbulent Reynolds number	[-]
S_N	Swirl number	[-]
$\overline{\mathbf{S}}$	Velocity strain rate tensor	[s ⁻¹]
t	Time	[s]
T	Temperature	[K]
T_u	Turbulence intensity	[-]
v_x, v_y, v_z	Components of absolute velocity in the Cartesian frame	[m.s ⁻¹]
v_x, v_r, v_θ	Components of absolute velocity in the cylindrical frame	[m.s ⁻¹]
\mathbf{x}	Cartesian coordinates vector	[m]
x^*, y^*, z^*	Normalised coordinates	[-]
y^+	Non-dimensional wall distance	[-]
$\overline{\mathbf{Z}}$	Eigenvectors tensor of the normalised anisotropy tensor	[-]

Greek letters

α	Swirl angle	[°]
γ	Ratio of specific heat capacity	[-]
δ	Velocity boundary layer thickness	[m]
δ_t	Thermal boundary layer thickness	[m]
δ_{ij}	Kronecker symbol	[-]
Δ	Cell size	[m]
ϵ	Turbulence dissipation rate	[m ² .s ⁻³]
η	Third anisotropy invariant	[-]
θ	Azimuthal position	[°]
κ	Wavenumber	[m]
λ	Thermal conductivity	[W.m ⁻¹ .K ⁻¹]
$\overline{\mathbf{\Lambda}}$	Eigenvalues tensor of the normalised anisotropy tensor	[-]
μ	Dynamic viscosity	[kg.m ⁻¹ .s ⁻¹]
μ_T	Eddy (or turbulent) viscosity	[kg.m ⁻¹ .s ⁻¹]
ξ	Second anisotropy invariant	[-]
$\Pi_{t \rightarrow s}$	Total-to-static expansion ratio	[-]
$\Pi_{t \rightarrow t}$	Total-to-total expansion ratio	[-]

ρ	Density	$[\text{kg}\cdot\text{m}^{-3}]$
ρ_{RS}	Schmitt's criterion	$[-]$
τ	Time-lag	$[\text{s}]$
$\overline{\tau}$	Viscous stress tensor	$[\text{kg}\cdot\text{m}^{-1}\cdot\text{s}^{-2}]$
$\overline{\tau}^R$	Reynolds stress tensor	$[\text{kg}\cdot\text{m}^{-1}\cdot\text{s}^{-2}]$
$\overline{\tau}^{SGS}$	Subgrid-scale stress tensor	$[\text{kg}\cdot\text{m}^{-1}\cdot\text{s}^{-2}]$
ϕ	Pitch angle	$[\circ]$
ω	Specific turbulence dissipation rate	$[\text{s}^{-1}]$
Ω	Angular velocity	$[\text{rad}\cdot\text{s}^{-1}]$
$\overline{\overline{\Omega}}$	Vorticity tensor	$[\text{s}^{-1}]$

Subscripts and superscripts

∞	Freestream condition
0	Refers to inlet plane
$P40$	Plane at the combustor/turbine interface
$P41$	Plane downstream of the NGV
$P42$	Plane downstream of the rotor blade
red	Reduced quantity
ref	Reference state
R	Relative to rotor
RES	Refers to resolved
s	Static value
S	Relative to stator
SGS	Refers to subgrid-scale
t	Total value
\cdot^*	Quantity in terms of distortions
\cdot	Time-averaged quantity, Reynolds average
$\tilde{\cdot}$	Favre averaged quantity
\cdot'	Reynolds fluctuation
\cdot''	Favre fluctuation
$\overline{[\cdot]}$	Favre ensemble averaging
$\langle \cdot \rangle$	Statistical averaging
$\langle \cdot \rangle_\theta$	Azimuthally averaged quantity
$\langle \cdot \rangle_m$	Spatially mass-flow averaged quantity
$\langle \cdot \rangle_S$	Spatially area averaged quantity

Introduction

“ Once you have tasted flight, you will forever walk the earth with your eyes turned skyward, for there you have been, and there you will always long to return. ”

Leonardo da Vinci

Towards a greener aviation industry	1
Turboshaft engines	2
Industrial and scientific issues	3
Organisation of the manuscript	5

Towards a greener aviation industry⁸

Research in the aeronautics industry carried out over the past years with the use of experiments alongside Computational Fluids Dynamics (CFD) has led to encouraging results: efficiency has increased while noise or pollutant emissions have decreased, as a consequence of environmental regulations of the European Aviation Safety Agency (EASA) covering noise, NO_x or CO. As an example, the LEAP engine is 16% kerosene consumption and 10% carbon dioxide emissions lower compared to its predecessor, the CFM56 engine. However, the way towards the objectives of Paris Agreement adopted in 2015 is still long [51]. The initial objective to limit the rise in the mean global temperature below +2°, and preferably to +1.5° above pre-industrial levels at the end of the current century, seems totally unrealistic today with an exponential growth of the temperature. In fact, greenhouse gases emissions, CO₂ and non-CO₂ (*e.g.* contrails) emissions, are still increasing, for a part because of aviation with a continuous rise of air traffic (+225% of passengers between 2004 and 2019)⁹. To name but one, commercial aviation was responsible for 2.6% of the world’s CO₂ emissions in 2018 (see Figure 1) and more than 5% of effective radiative forcing over the period 2000-2018.

⁸See the thorough literature review of Delbecq *et al.* [24] from ISAE-SUPAERO for more details.

⁹Data of June 2022 from the International Civil Aviation Organization (ICAO).

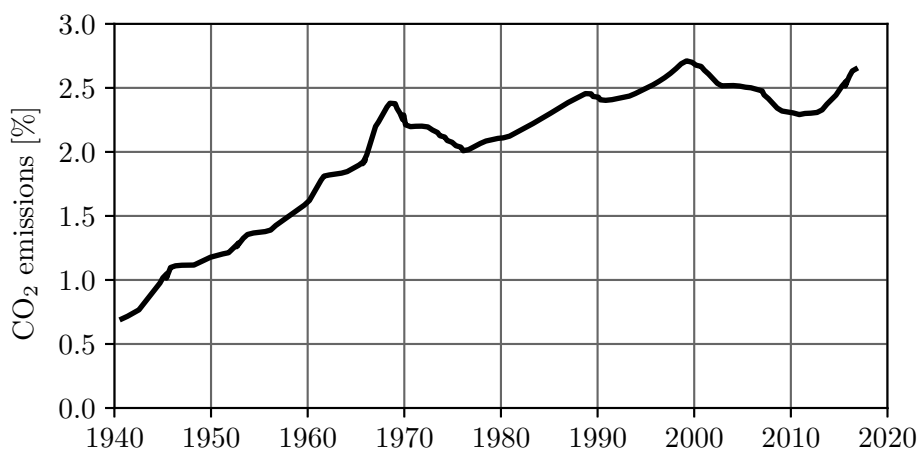


Figure 1 – Aviation CO₂ emissions from 1940 to 2018 expressed as a fraction of the total anthropogenic CO₂ emissions. Adapted from Lee *et al.* [67].

All the stakeholders of the aviation community agree that several levers exist to make aviation greener [106]:

- **Decarbonisation:** technological rupture towards zero carbon emitting aircraft fueled with hydrogen (such as the ZEROe Airbus aircraft). As it will take time to develop, certify and fly such aircrafts (≈ 2035), short-term technologies must be used. Batteries for tourism's short-range aircrafts and Sustainable Aviation Fuels (SAF) for mid-range aircrafts are a first step towards carbon neutrality;
- **Sobriety:** limit aircraft use, take the train when possible (a train emits nearly 20 times less CO₂ per capita and kilometre than a plane), etc.;
- **Increase efficiency:** optimise the components of the engines. As an example, for a typical modern turbofan engine, an increase of 1.2% of high-pressure turbine efficiency leads to a decrease of 1% of specific fuel consumption¹⁰.

This PhD work focuses on the last point, by studying a turbomachine component, but it remains clear that the final goal is decarbonisation.

Turboshaft engines

Considering its Latin etymology *turbo*, *turbinis*, that means circular motion, a turbomachine is a device in the mechanical term in which an energy exchange takes place between a moving part and a fluid: this is the concept of work in thermodynamics. Turbomachines have applications in different sectors but what remains clear is that their most important use is encountered in aeronautics: turbofan, turboprop or turboshaft. The distinction between the three designations either relies on the type of aircraft (fighter aircraft, civil aircraft, military transport aircraft, helicopter, etc.), on the desired cruise speed (subsonic, supersonic) or on the power-to-weight ratio. Nonetheless, their goal is common: generate a propulsive power in order to drive the

¹⁰It is the amount of fuel consumed per each unit of thrust produced. The SFC is a measure of the efficiency of the engine, as it inversely scales with the definition of the overall efficiency.

aircraft on which the turbomachine is placed. This power is produced either by the expansion of burnt gases or by the rotation of rotor blades.

In the specific case of this PhD thesis dealing with helicopters, the turboshaft engine is the element that generates the power necessary for the rotation of the rotor blades. As for turbojet or turboprop engines, it is composed of a gas turbine which is connected to a low-pressure turbine that generates the power. The working principle of a gas turbine is described in a (T, s) diagram by the real Joule-Brayton cycle (Figure 2a) where all the losses, *i.e.* entropy, are considered. Looking at the cycle, two important quantities emerge: the compression pressure ratio or Overall Pressure Ratio (OPR) and the Turbine Inlet Temperature (TIT), often referred as T_{t4} . The modification of these values has a strong impact on the turboshaft engine performance, and especially on the thermal efficiency η_{th} which qualifies the conversion of heat into useful work. The thermal efficiency should be the highest possible. In the case of the ideal Brayton cycle, η_{th} is independent of T_{t4} and only depends on the atmospheric temperature and OPR. When considering irreversibilities, which are marked by entropy production Δs_p , the evolution of the thermal efficiency is modified, as shown in Figure 2b: for a given TIT, η_{th} has an optimum at a certain OPR and then it decreases. For a given OPR, the thermal efficiency increases with the TIT, which can be illustrated with Figure 2a: the ratio of entropy exchange over entropy production is increasing alongside the TIT, getting closer to the ideal cycle (Figure 2b). The final engine performance is often a consequence of the reachable values for the OPR and the TIT which are limited by the capacity and integrity of the materials. For instance, a too-high value of TIT can lead to creeping in the high-pressure turbine.

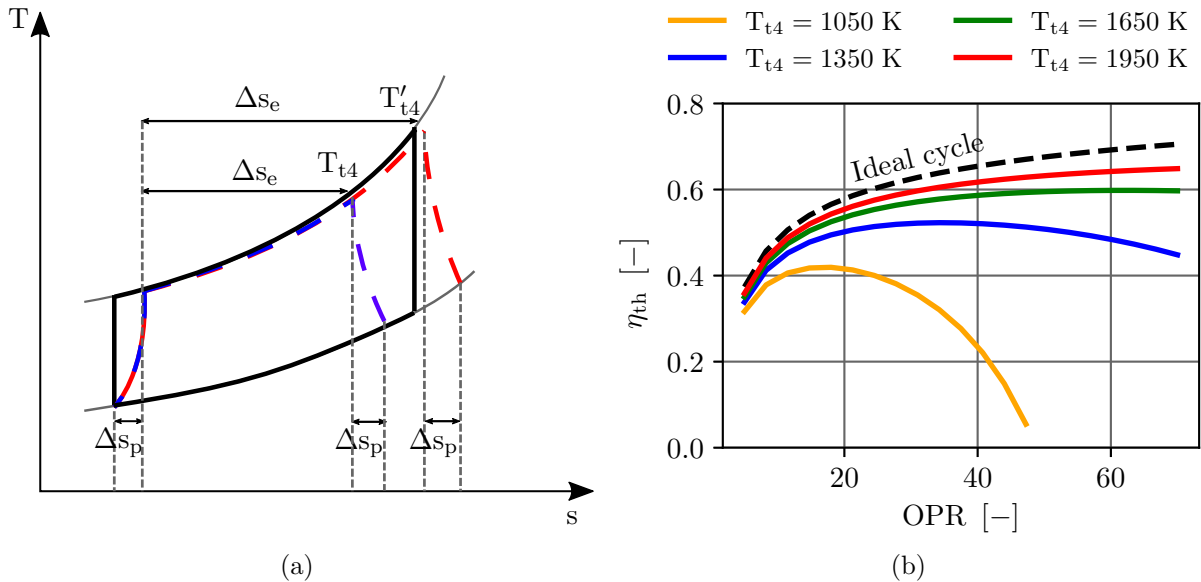


Figure 2 – Theoretical (black) and real (blue, red) Brayton cycle (a) and evolution of the thermal efficiency with the overall pressure ratio for different values of turbine inlet temperature (b).

Industrial and scientific issues

Safran Helicopter Engines, which is involved in this PhD thesis, is a French helicopter engine manufacturer that equips numerous helicopters on the market and that continually looks for

improving its future engines to address the market needs and environmental constraints, as for instance those presented in the first paragraph. Predicting and understanding the physics more accurately in the high-pressure turbine is obvious to reach the proper accuracy in the range of a few kelvins since a deviation of 10 K in the prediction can damage the system. Technologically speaking, lean burn combustion technology [38, 87] seems a promising way to achieve lower emissions, but leads to the presence of radial and azimuthal temperature and velocities distortions, also known as hot streaks, at the inlet of the high-pressure turbine. Their temperatures have gradually increased over the past decades, which is not a consequence of an increase in the flame temperature but a consequence of the modification of the equilibrium between cooling and burnt gases in the combustion chamber. Hot streaks must be studied thoroughly, as they interact with all the classical known phenomena in the high-pressure turbine that makes this component complex: unsteady interactions at the vane/blade interface such as segregation effects, cooling to prevent the materials from melting, combustor/turbine instabilities and turbulence to mention just a few as shown in Figure 3. As one may expect, there is a strong coupling between the components of an engine, especially between the combustion chamber and the turbine where hot streaks and turbulence interact for instance. The aerodynamic and aerothermal behaviour of the flow is thus challenging to predict and analyse, as reported by the literature and the experience of Safran Helicopter Engines. These high-pressure turbines must be studied carefully during the R&D step with the use of reliable and predictive numerical simulations.

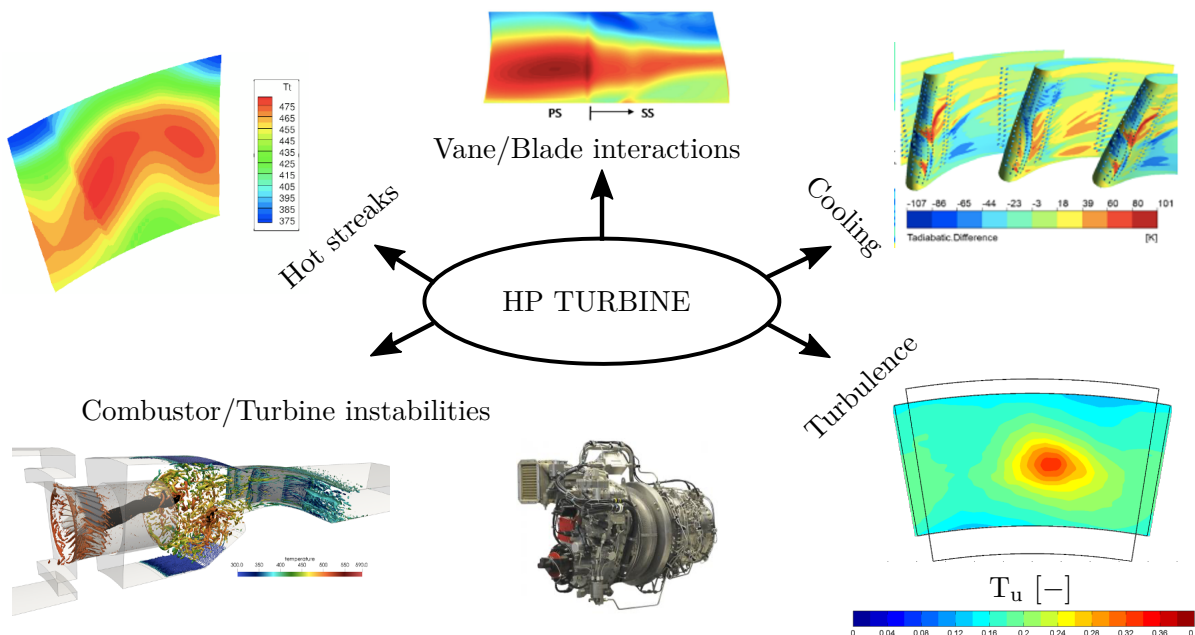


Figure 3 – The high-pressure turbine is a component of complex physics.

Over the last decades, Computational Fluid Dynamics has emerged to be a powerful tool to predict flows in many fluid dynamics problems, such as those encountered in aeronautics and more precisely in axial turbines which is the scope of this PhD thesis. From the first simulations in the 1960s using linear potential equations to the resolution of fully turbulent three-dimensional unsteady flows, CFD has improved the understanding and design of many

aeronautical components (see Figure 4). Although absolutely awesome since it enables to compute complex situations and have access to local quantities while offering a relatively low return time, CFD is not a perfect tool as it requires some modelling and relies on hypotheses. In that sense, numerical tools used during the design must gain in precision. The RANS method is still used in an industrial context, as this kind of modelling proposes a short return time, but it can occult part of the flow physics.

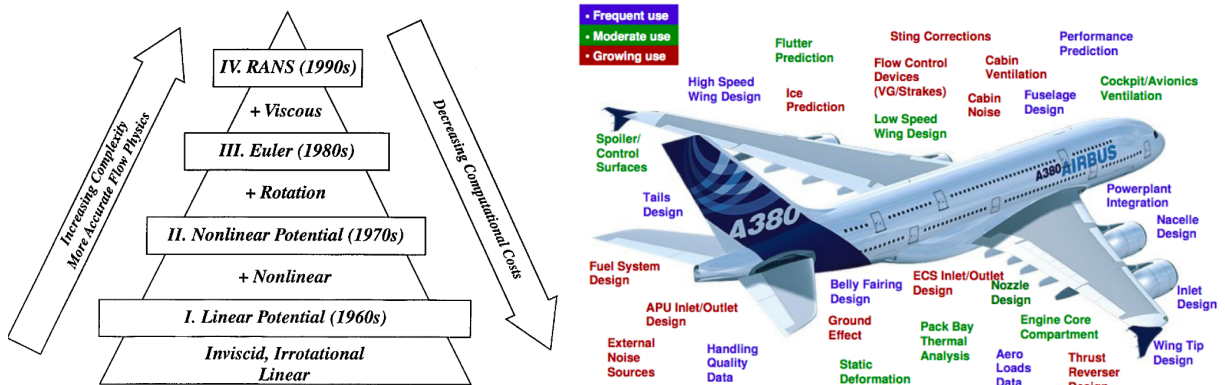


Figure 4 – Hierarchy of governing equations along the years (left) and CFD contribution of the Airbus A380 (right). From Jameson [53].

This PhD work aims to investigate the ability of the RANS method and check if it can meet the exigent level of accuracy expected, for both aerodynamic and aerothermal behaviours, while applied to the complex environment of cooled turbine stage flows submitted to swirled hot streaks.

The purpose here is to evaluate the impact of the modelling on the aerodynamic and aerothermal performances of an industrial turbine stage, through a detailed analysis of the flow, and to define a modelling methodology offering the best compromise between cost and precision. Different questions are raised: the first one deals with the RANS turbulence modelling for swirling flows, which are known to fault the classical RANS turbulence models. **What are the characteristics of turbulence associated with swirling flows and what are the approaches to model them?** The second one is related to the representativity of the high-pressure turbine inlet boundary conditions, with high levels of swirl and an unsteady nature in some cases. **Should it be steady or unsteady and should it come from the experiments or from a high-fidelity LES?** These two questions are addressed within the manuscript.

Organisation of the manuscript

In order to present the work performed during those past three years, this PhD work is decomposed into three main parts:

- **Part I: Highlight of the difficulties to capture both the aerodynamics and aerothermal in a high-pressure turbine stage.**

This first introductory part presents from a general point of view the nature of the flow in an axial high-pressure turbine stage, in terms of aerodynamics and aerothermal. In

view of the complexity of the flow, numerical methods have been developed to simulate it. These methods for solving turbomachinery flows are presented, with a focus on turbulence modelling and domain reduction techniques (Chapter 1). In Chapter 2, the high-pressure turbine configuration (FACTOR) studied in this PhD thesis is presented, together with a literature review of simulations previously performed by the scientific community. Other simulations are carried out to assess the difficulties of predicting correctly the dynamics of the flow;

- **Part II: The sources of errors in the prediction of a swirled hot streak flow in a high-pressure turbine stage.**

With the second part, a simplified bent channel configuration is created. LES are performed to study the hot streak redistribution under high-turbulence levels. The principle mechanisms linked with turbulence are highlighted and RANS is positioned against LES (Chapter 3). Then, Chapter 4 is dedicated to the anisotropy of turbulence, as it is suspected to explain the failure of classical RANS turbulence models based on Boussinesq's hypothesis;

- **Part III: Back to the industrial problematic and configuration.**

The final part of the manuscript focuses again on the high-pressure turbine configuration, where RANS anisotropic turbulence models are applied (Chapter 5). However, the results are still not satisfactory, and problems with the inlet boundary conditions are put forward and evaluated in Chapter 6. Data from unsteady pressure measurements are also post-processed.

This PhD has been co-financed by Safran Helicopter Engines and ANRT through a CIFRE grant (2019/0903).

Part I

Highlight of the difficulties to capture both the aerodynamics and aerothermal in a high-pressure turbine stage

The first part of this manuscript proposes a literature review on the axial high-pressure turbine and focuses on the flow features developing in this component. Numerical methods to solve flows in turbomachines are also presented (Chapter 1). This chapter is voluntarily exhaustive, from general elements to more specific ones, in order to give a wide coverage of the field. A first study on an industrial configuration is presented to highlight the difficulties of predicting faithfully the flow in such a component (Chapter 2).

Generalities on axial flow turbines and associated numerics

“ The ultimate test of your knowledge is your capacity to convey it to another. ”

Richard Feynman

Abstract

Axial high-pressure turbine flows are complex because of the positioning of the high-pressure turbine downstream of the combustion chamber. The flow features exhibit residual swirl and high-temperature distortions that must be taken into account in the early development of high-pressure turbines, either experimentally or numerically with high-fidelity simulations. This first chapter introduces the high-pressure turbine from a local view with specific physical phenomena. Then, the numerical methods for resolving such a complex flow are presented as well as the methods for turbomachinery flows.

1.1	Aerodynamic and aerothermal phenomena in axial high-pressure turbines	12
1.1.1	Classification of unsteady phenomena	12
1.1.2	Vane/blade interactions	13
1.1.3	Combustion chamber/turbine interactions	15
1.1.4	Secondary flows	18
1.1.5	Technological effects	19
1.2	Numerical methods for the resolution of turbulent flows	22
1.2.1	The Navier-Stokes equations	22
1.2.2	The closure problem	23
1.2.3	Turbulence modelling approaches	24
1.2.4	RANS turbulence modelling	30
1.3	Modelling strategies of turbomachinery components	36
1.3.1	Steady simulations: the mixing-plane approach	36
1.3.2	Unsteady simulations	36
1.4	Conclusion	38

1.1 Aerodynamic and aerothermal phenomena in axial high-pressure turbines

In a turbine stage, the aerodynamics and aerothermal are strongly impacted by different factors, either geometrical, structural or physical, although interconnected, that have an impact on the turbine stage efficiency. It is proposed here to perform a review of the most predominant factors. Note that shock/boundary layer interaction is not tackled, as no configuration with this phenomenon is studied in this PhD thesis. A first general overview of the unsteady phenomena is given in the following.

1.1.1 Classification of unsteady phenomena

Flows in turbomachines are inherently unsteady and complex. Different ways to classify the unsteadiness exist. One way for instance relies on a length-scale/frequency classification, proposed by Lagraff [63] and which is represented in Figure 1.1. It reveals a large range of sizes and characteristic times which makes unsteady phenomena important to study physically and capture numerically to correctly predict the flow fields and the losses, but also the heat transfers. Another classification based on the periodicity of the phenomena is presented in Figure 1.2. The unsteady phenomena can be classified into two main categories:

- **Non-periodic:** this is the case of transient (engine start/off) or chaotic phenomena (boundary layers, wakes, jets, etc.);
- **Periodic:** they can be uncorrelated with the rotational speed of the machine (Von Kármán vortex street, fluttering, surge) or correlated. Among the stable correlated phenomena, which are of interest in this PhD thesis, one can cite the so-called vane/blade interactions which are due to the relative motion of the blade rows and which are correlated to the blade-passing frequency (BPF) and its harmonics.

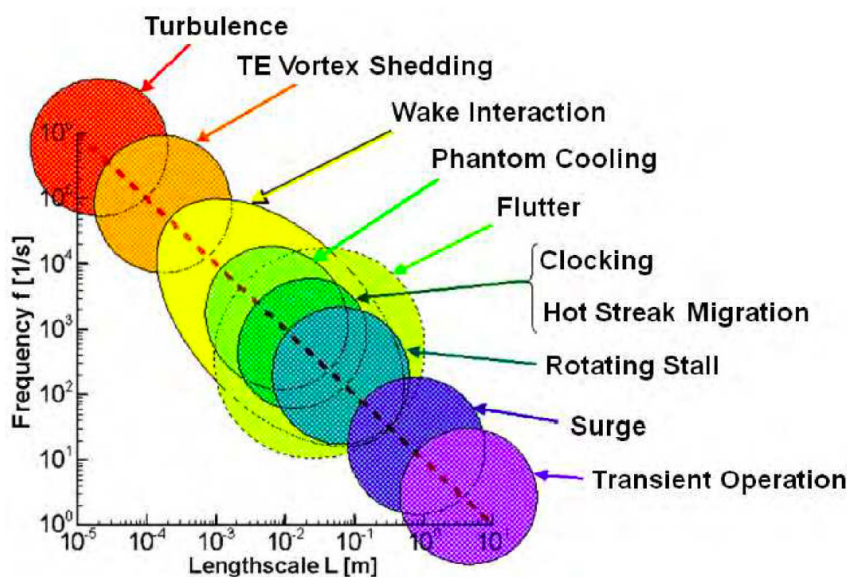


Figure 1.1 – Unsteady flow structures with a variation of five or six orders of magnitude in space and time [63].

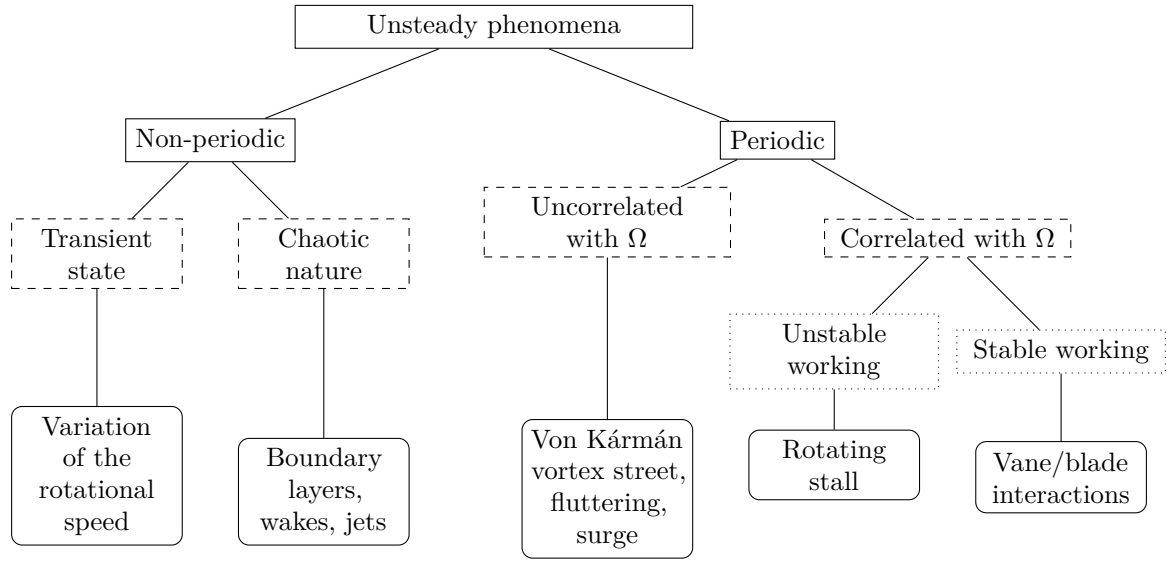


Figure 1.2 – Unsteady phenomena in turbomachines - Adapted from Callot [17].

In the case of vane/blade interactions, the flow unsteadiness can be evaluated with the reduced frequency \hat{f} defined by Tucker [126]:

$$\hat{f} = \frac{f_w}{f_c} = \frac{t_c}{t_w} \quad (1.1)$$

Where $t_c = Ca_x/w_x$ is the time required for a fluid particle to travel through a blade passage and $t_w = 2\pi/\Omega N$ is the time-scale related to the BPF of the opposite row. The value of \hat{f} is a measure of the degree of unsteadiness compared to quasi-steady effects. If $\hat{f} \rightarrow 0$, the flow is quasi-steady and can be described as a succession of steady states. Unsteady effects become important when $\hat{f} \approx 1$ and dominate at $\hat{f} > 1$. For instance, for a vane/blade configuration, if $\hat{f} = 10$, it means that there is an average of 10 stator wakes in the rotor passage. Typical values for compressors are $0.8 < \hat{f} < 1.2$, $0.3 < \hat{f} < 1$ for low-pressure turbines and about 0.3-0.4 for high-pressure turbines [126].

1.1.2 Vane/blade interactions

In the stable working of a turbomachine component, most of the unsteadiness is induced by the interactions between static and moving rows. These interactions are periodic in time and are related to the BPF of the opposite row.

1.1.2.1 Segregation effect

In a high-pressure turbine, thermal interactions at the vane/blade interface lead to a preferential migration of the flow towards the pressure side or suction side of the blade. They are correlated with the number of injectors in the upstream combustion chamber. These interactions are explained by the segregation of the hot and cold flows with a modification of the relative incidence angle at the inlet of the blade row. The segregation effect has been observed experimentally by Butler and Sharma [15] or numerically by Dorney *et al.* [27], Prasad and Hendricks [94] and Takahashi and Ni [116]. If the velocity composition is performed in the frame of the vane row with the blade velocity, it is shown that the hot flow (hot streak), with a relative Mach

number higher at the inlet of the blade row compared to the cold flow, migrates towards the pressure side of the blade. Inversely, the cold flow migrates towards the suction side: the blade thermal loading is therefore not uniform on both sides of the blade, as evidenced by Figure 1.3, where also secondary flows account for the temperature non-uniformities. From a numerical point of view, both steady and unsteady simulations capture the relative velocity of the hot and cold flows with respect to the mean flow. However, the mixing-plane involved in steady simulation azimuthally smooths the information, which is lost when incoming into the rotor domain. Unsteady simulations are preferred, since they preserve the wealth of information.

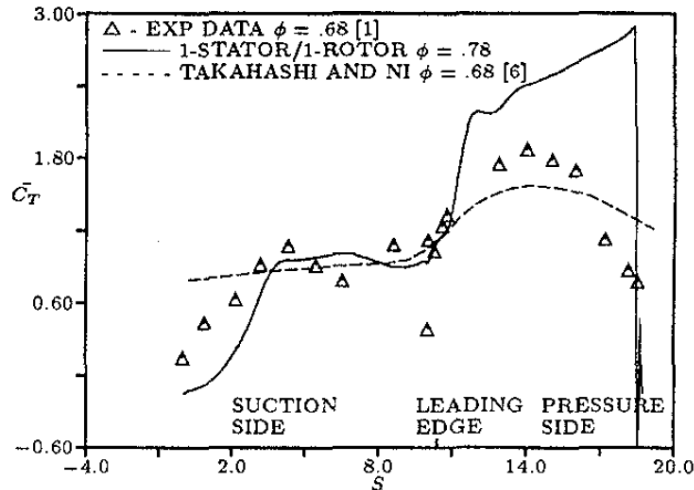


Figure 1.3 – Time-averaged surface temperature for a rotor mid-span section - Dorney *et al.* [27].

1.1.2.2 Potential effects

Potential effects originate from the presence of an obstacle in the flow, which are vanes and blades for a turbomachinery component. Because of the relative motion of the stator vanes and rotor blades, the potential effect is evidenced by the presence of an unsteady flow field and pressure waves in the downstream (with a competition with viscous effects) but also upstream direction (it is present even if viscosity is not considered). Parker and Watson [88] were one of the first to derive an expression making possible to characterise the decay of the potential effect as a function of the axial distance from the obstacle with an exponential law:

$$P_s \approx \exp \left[-2\pi \sqrt{1 - M_\Omega^2} \frac{x}{p} \right] \quad (1.2)$$

Where p is the blade pitch and x the distance from the obstacle. The decay with the distance strongly depends on the pitch, *i.e.* the geometry of the turbine, but also on the relative Mach number of propagation (with the blade velocity), so the operating point. Parker and Watson [88] suggested that above 30% of axial chord, the potential effect becomes negligible compared to the wake effect (see 1.1.2.3). Koupper [61] showed in its PhD thesis work that the potential effect of the stator vanes on the combustion chamber was not negligible: radial and azimuthal redistributions of massflow are observed until $0.25 \cdot C a_x$ upstream the LE of the stator vanes, and then decrease according to Parker's law. They also must be taken into account with unsteady simulations.

1.1.2.3 Wake effect

Because of the viscosity in the boundary layers around the blades, wakes are formed at the TE. The wakes are characterised by a decrease of total pressure and velocity (10% to 30%), but above all by an increase of entropy and turbulent activity (turbulent kinetic energy and turbulent viscosity) with the formation of vorticity from the TE. The wake transport mechanism is an unsteady phenomenon that only affects the downstream flow [88] and that is function of the rotational speed and the number of blades of the row. The dissipation of the wakes depends on the local viscosity of the fluid and is smaller than the dissipation of the potential effect. However, since the wakes are hotter, their trajectory is different from the undisturbed flow: the phenomenon is similar to the segregation effect at the vane/blade interface (see 1.1.2.1). The wakes produced by the upstream row are hatched when passing through the moving row with a curvature, stretching, slimming of the wakes in the blade passage and a displacement of the wakes towards the suction side close to the TE of the blade (Figure 1.4). The wake transport mechanism must be taken into account with unsteady simulations with sectorial or chorochronic methods.

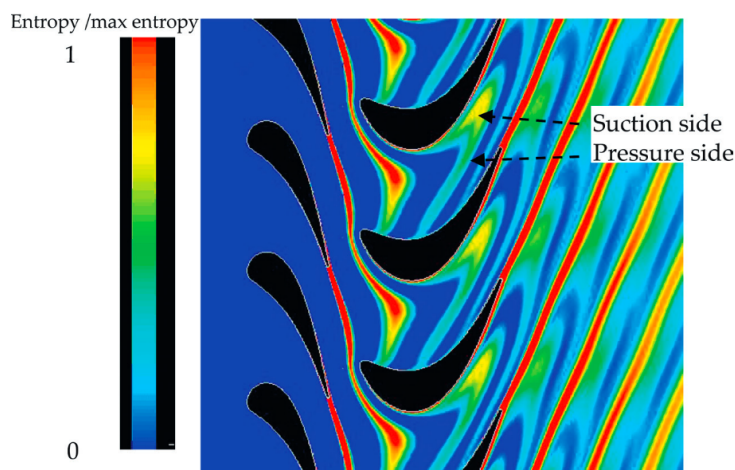


Figure 1.4 – Wake transport mechanism in a high-pressure turbine stage evidenced by the entropy field - From Gaetani [39].

1.1.3 Combustion chamber/turbine interactions

Combustion chamber/turbine interactions are reciprocal: the combustion chamber has an impact on the turbine because of the non-uniformities of the flow but the presence of the stator vanes modifies the flow fields in the downstream part of the combustion chamber. Here, the stress is laid on the interactions in the main flow direction, *i.e.* from the combustion chamber towards the high-pressure turbine.

1.1.3.1 Hot streak

The imperfect dilution of the swirling flow from the combustion chamber leads to the persistence of vortical structures at high temperatures at the inlet of the high-pressure turbine, as shown in Figure 1.5: these distortions are called *hot streaks*. One of the key problems of the high-pressure turbine is its capacity to resist to these high temperatures, which have gradually

increased over the last decades to improve the thermal efficiency of the turbine engine up to 30 – 35%. Temperatures can reach between 1100 and 1500 K at the inlet of the high-pressure turbine of a modern turboshaft engine [100]. The understanding of the dynamics of the hot streak is a challenge since temperature peaks are generally greater than the melting temperature of the materials composing the NGVs: the total temperature ratio between the hot streak and the surrounding flow can vary between 1.1 to 2 [15, 92].

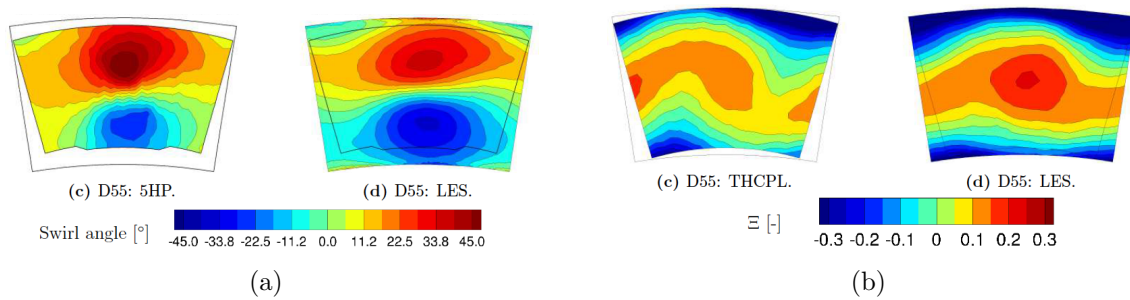


Figure 1.5 – Experimental and LES comparisons of swirl (a) and temperature fields (b) - From Koupper [60].

The study of the hot streak transport and its associated mechanisms (distortion, diffusion) covers a wide period, ranging from the 1950s to the present day, on both theoretical, experimental or numerical fields, or combining them [15, 27, 82, 85, 86, 94, 116].

In the passage of the vane, even if a total temperature gradient exists, there is very little or no radial or azimuthal redistribution of the hot streak provided total pressure is uniform and constant (no boundary layers) at the turbine inlet: Munk and Prim [82] already theoretically demonstrated this behaviour in 1947 by explaining that the total pressure uniformity at the inlet ensured no additional vorticity creation, under the hypothesis of isentropic steady flow. Thus, the transport in the vane passage is minimised. The possible distortions of the hot streak at the outlet of the NGV passage are the consequence of:

- The diffusive mixing, increased by turbulence (which plays a major role if total pressure is uniform), that promotes a spatial spreading of the hot streak [15];
- The effects of total pressure gradients at the inlet.

The effects of total pressure gradients have been investigated numerically by Ong and Miller [85, 86]. They reproduced the experiment of Praisner [92] for the purpose of studying the transport of a hot streak as well as the turbulent mixing in a bent duct representative of a NGV passage. They imposed both uniform and distorted inlet total pressure and observed that the distortion of the hot streak at the outlet was a consequence of the pressure gradients inside the channel and not the temperature gradient itself. In addition to the spatial spreading of the hot streak, a temperature peak decrease is observed, since it is the result of molecular and turbulent diffusion. Butler and Sharma [15] were one of the first to study this experimentally by seeding air with CO₂ at the inlet of the turbine and by tracking its concentration inside the turbine (Figure 1.6). They highlighted the diminution of CO₂, so the diminution of maximum temperature through the passage. This diminution is attributed to the intense mixing provoked by the inlet turbulence and depending on its characteristics (level and length scale). Jenny *et al.* [55]

noted a decrease of the temperature peak of about 30%. The same phenomena are observed in the blade passage, but the physics is more complex due to the rotation. The unsteadiness due to the relative motion of the blade row with respect to the stator row must be considered: thermal interactions combined with vane/blade interactions that lead to a hot streak having an impact on the development of secondary flows and the thermal loading of the blades.

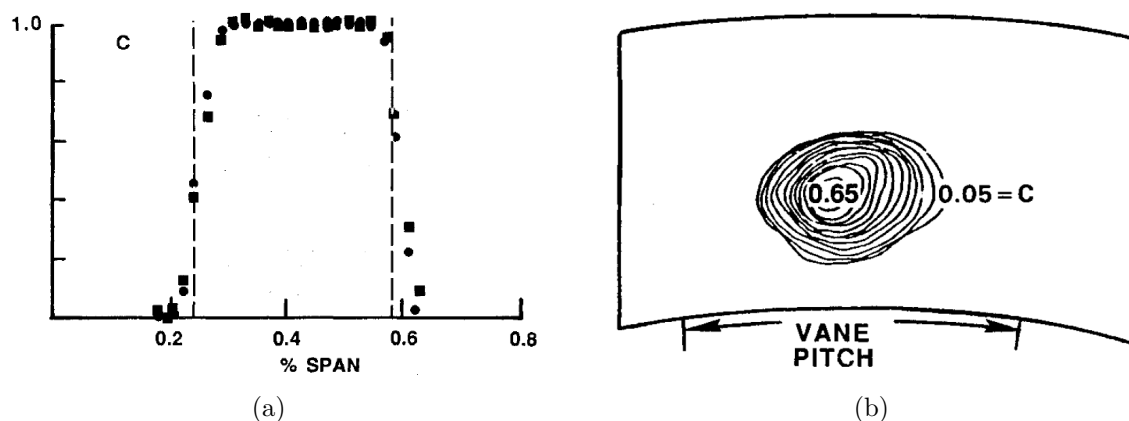


Figure 1.6 – CO₂ concentration at the inlet (a) and outlet (b) of the NGV passage - From Butler and Sharma [15].

1.1.3.2 Clocking

The azimuthal relative position of the hot streak with the NGVs is called *clocking*. It strongly impacts the thermal loading of the vanes downstream of the combustion chamber or the rotor blades. When dealing with high-pressure turbines, two clockings are generally considered: a *leading-edge clocking* (LEC) where the hot streak is aligned with the LE of a NGV and a *passage clocking* (PAC) where the hot streak is aligned with the center of the passage of two NGVs. Numerically, Dorney and Gundy-Burlet [28] and Koupper [60] showed that the clocking had a large contribution to the transport of a hot streak in a stator vane passage: it is more coherent in the case of a PAC and does not impact the suction side whereas it wraps around the NGVs' walls in the LEC case. In most cases, there is one hot streak for two NGVs, leading to important wall temperature differences between two consecutive NGVs. In the rotor row, aligning the hot streak with the passage increases the mean temperatures on the pressure side while the opposite is observed for a LEC. It must be underlined that, in the rotor row, the impact of the clocking is combined with other aforementioned interactions: potential effect, wake effect and segregation effect. However, Dorney and Gundy-Burlet [28] showed that a good strategy to reduce the blade wall temperature was to have a LEC since in this case, the hot streak mixed with the colder wake of the NGV. It is clearly noticeable in Figure 1.7 that aligning the hot streak with the LE of the NGV leads to a more important diffusion of the hot streak, limiting therefore the temperature gradients in the rotor row, but in return, the heat transfers are higher on the NGVs' walls.

1.1.3.3 Turbulence

Turbulence is a chaotic phenomenon that plays a significant role in the redistribution of a hot streak since its intensity is relatively high downstream of the combustion chamber: the thermal mixing is enhanced depending on the turbulence characteristics (level and length scale)

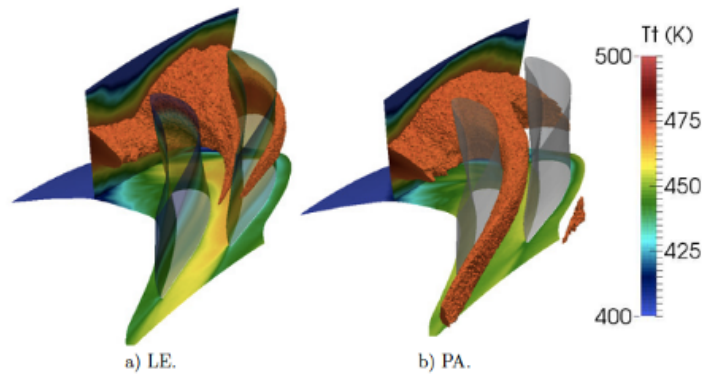


Figure 1.7 – Iso-contour of total temperature at 470 K for two clockings [60].

and orientation of turbulent structures (anisotropy). From a numerical point of view, turbulence modelling is an important topic as it impacts the main flow dynamics. For instance, in a RANS simulation, if the inlet turbulence is dissipated in the first cells, the hot streak at the outlet of the NGV will be too much coherent, leading to a wrong estimation of the temperature fields. More information on turbulence modelling can be found in the manuscript in 1.2.3, and on the coupling between turbulence and hot streak diffusion in Chapter 3 and Chapter 4.

As already mentioned, turbulence levels are quite important. Peaks around 20 – 30% can be observed (Figure 1.8a). Radomsky and Thole [95] showed that characteristic lengths associated with these intensities, in that case, were of the order of 5 – 7 mm. Such turbulence length scales increase the heat transfers at the walls and promote the boundary layer transition. Wang *et al.* [133] have demonstrated that increasing the turbulence intensity led to a uniform value of temperature at the NGVs' walls. However, such conclusions can not be extrapolated to the blade walls, since the segregation effect and the secondary flows combine. As evidenced by the work of Ong and Miller [85], the level of turbulence impacts the temperature peak at the NGV outlet: the higher this level is, the more turbulence mixing occurs. Thus, it decreases the temperature peak (see Figure 1.8b). However, the turbulence intensity naturally decreases in the NGV passage since an acceleration occurs in the mean flow [133]. In the blade row, the effect of turbulence both comes from the residual turbulence generated upstream by the mean flow, and also from the turbulence created in the wake of the blade. Thus, the intensity of a possible hot streak at the outlet of the turbine stage depends on turbulence's initial state, evolution and history inside the stage, where multiple physical phenomena have occurred.

1.1.4 Secondary flows

Secondary flows can be defined by the presence of a non-zero velocity component normal to the direction of the mean flow and are characterised by an important streamwise vorticity component with a highly tridimensional nature. Secondary flows are caused by the interaction between the boundary layer and the static pressure gradient normal to the walls. They are more complex than in compressors, because of the large flow-turning and the presence of a thick leading-edge. A detailed review of the secondary flow structures in axial turbines has been presented by Langston [65]. Many authors have contributed to the exact definition of the secondary flows, with detailed experimental studies led by Goldstein and Spores [44] for instance. From Figure 1.9, close to the endwalls, the boundary layer separates as it approaches

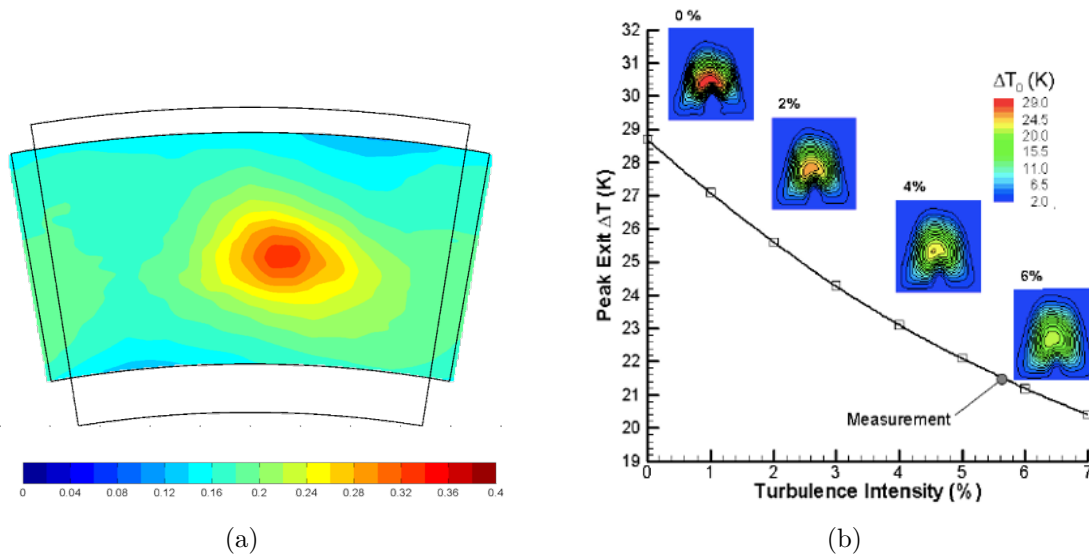


Figure 1.8 – Typical turbulence field at the inlet of a high-pressure turbine (a) and effect of the turbulence intensity on the temperature peak (b).

the stagnation point because of the low momentum in the boundary layer, and forms a horseshoe vortex with two distinct legs: the pressure side leg vortex (1) is convected towards the inter-blade passage due to the pressure difference between pressure and suction sides. As it crosses the passage, it combines with the passage pressure-to-suction side endwall flow to form the passage vortex (3). The suction side leg vortex (2) remains close to the suction side of the blade and has an opposite sense of rotation than the passage vortex: this counter vortex can wrap around the passage vortex as proposed by Sharma and Butler [104]. Goldstein and Spores [44] also noted the presence of a small and intense vortex: the leading edge corner vortex (6-7). Two additional vortices are created further downstream at the pressure and suction sides (4-5). Secondary flows stand for losses: Sharma and Bultler [104] showed that secondary flows losses accounted for 30 – 50% of total losses in a turbine stage since the kinetic energy contained in the secondary flow structures are dissipated by viscous effects. In the same way, a loss of lift or turbine work is observed. Their prediction is thus essential, with the use of complex 3D simulations or semi-empirical models [104].

1.1.5 Technological effects

1.1.5.1 Blade tip gap

The blade tip gap is inherent to the relative movement of the blade row with the shroud. A small gap is necessary to enable the rotation without damaging the casing. It creates an additional process known as tip clearance leakage flow (Figure 1.10). Because of the pressure gradient between the pressure side and the suction side, some flow moves through the gap from the pressure to suction side. The interaction between the leakage flow and the main flow leads to another vortex called the tip leakage vortex. The vortex can detach from the blade from the second half of the axial chord [77]. In the tip region, velocity and pressure are strongly modified, and high levels of turbulence are encountered. The production and dissipation of turbulent kinetic energy are sources of losses. In that sense, Bindon [10] showed that nearly 50% of the losses in the tip were attributed to the mixing between the tip leakage flow and the

main flow. Numerous correlations to account for tip gap losses have been derived: for instance, Lakshminarayana [64] expressed the decrease in stage efficiency as a function of the ratio tip gap height/blade span. He showed that a tip gap of 1% of blade span decreased by 3% the stage efficiency.

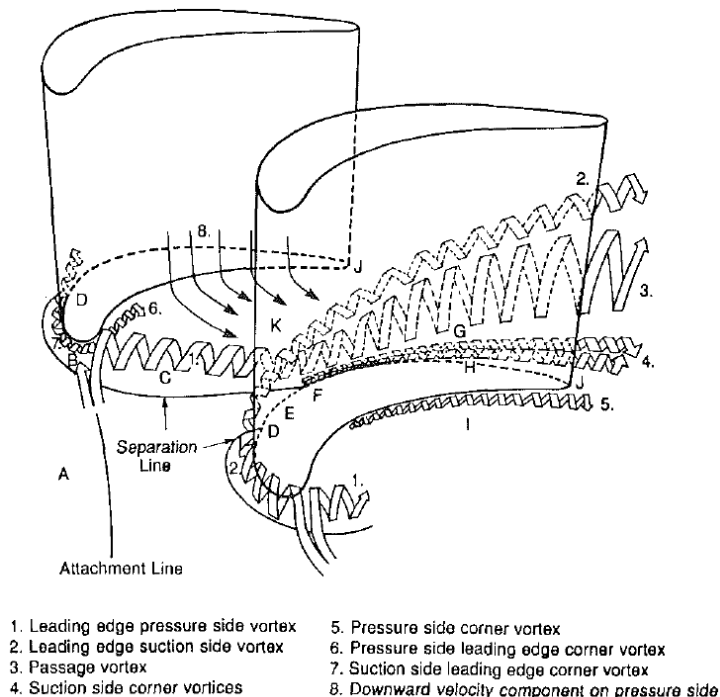


Figure 1.9 – Schematic view of the secondary flow structures in axial turbines [44].

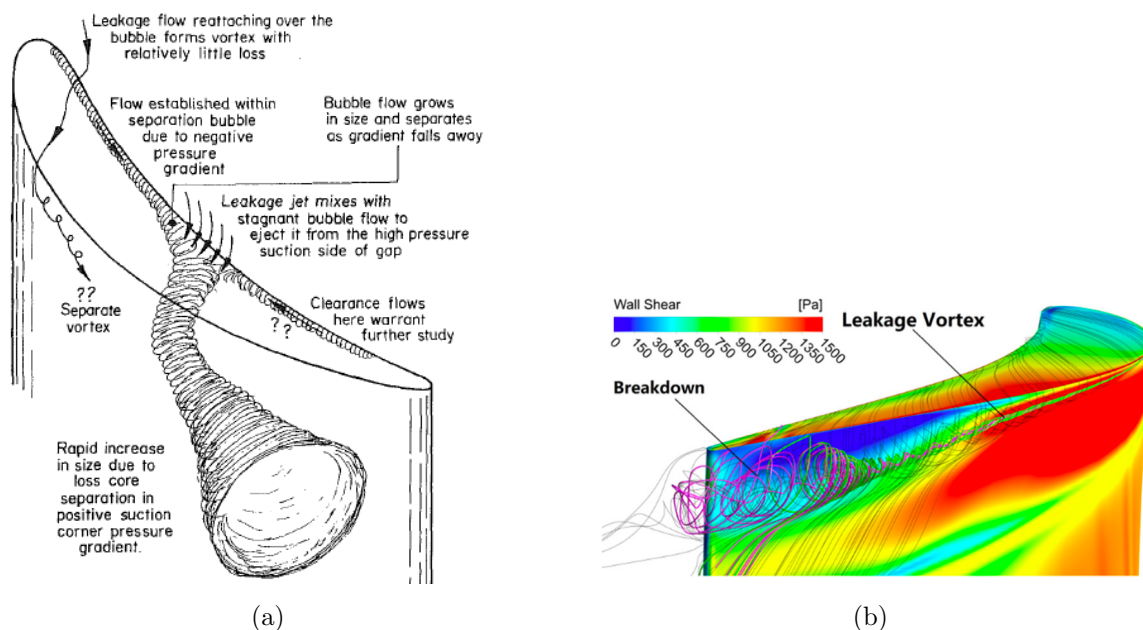


Figure 1.10 – Schematic view of a tip leakage vortex (a) and numerical simulation for a tip gap height of 1% of span (b) [10, 134].

1.1.5.2 Vane cooling

Vane cooling should not be neglected. As highlighted in 1.1.3.1, the hot streak core temperature is usually higher than the melting temperature of the materials composing the vane. Cooling strategies must be implemented. One of the possibilities is to cool down by *film cooling* (the reader can refer to the thorough review of Lakshminarayana [64] for a more exhaustive list of cooling techniques): cold flow is removed from the compressor (at 600 – 800 K) in order to feed cooling channels that results in holes on the NGV's walls (see Figure 1.11). The film at the vane surface enables to preserve the lifetime of the materials and is only efficient by playing on two parameters: the inclination angle of the holes and the massflow [20]. Two zones are mainly targeted for the cooling where the thermal stresses are the most important: at the leading-edge because of the stagnation point and at the trailing-edge where the thickness is the lowest [64]. As explained by Wilcock *et al.* [135], a compromise on the cooling flow rate must be found in order not to penalise the thermal efficiency and therefore the overall efficiency of the thermodynamic cycle. In fact, bleeding air from the compressor means delivering less power to the fluid when compressing. The retrieved power by the turbine is thus impacted. Finally, the cooling flow interacts with the main flow in a mixing zone: turbulence is modified with a dissipation of kinetic energy and losses arise because of thermal mixing. The flow is also unsteady. Jenkins *et al.* [54] experimentally confirmed that the combination of high levels of turbulence with film cooling significantly attenuated the hot streak, about 70%.

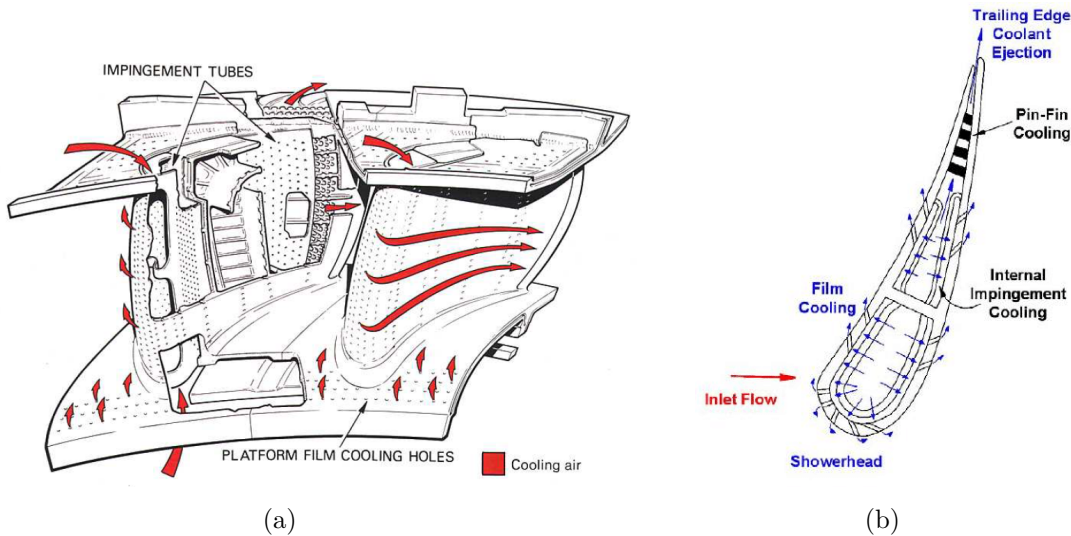


Figure 1.11 – Cooling architecture of a high-pressure turbine NGV [46, 118].

1.1.5.3 Cavity purge flows

Through the secondary air system, it is also possible to bleed air from the compressor and inject it at the hub of the turbine to cool down the rotor disks (Figure 1.12). This injection is necessary to prevent overheating and potential damages to rotor disks due to the centrifugal forces and is called *inter-disk cavity cooling*. However, because of the spacing at the hub due to the static and moving row, part of the cooling flow leaks towards the main vein, generating losses by mixing. This cooling leakage flow accounts for 1 – 2% of the main vein flow [34]. The phenomenon is unsteady, since the cooling leakage flow depends on

parameters such as the pressure in the vein and in the cavity, that vary both in space and time because of the wakes of the NGVs or the potential effect of the blades, but also because of turbulence. To limit the losses, rim seals are used at the hub of the vane/blade interface for which the shape is optimised (technologies are presented in [118]).

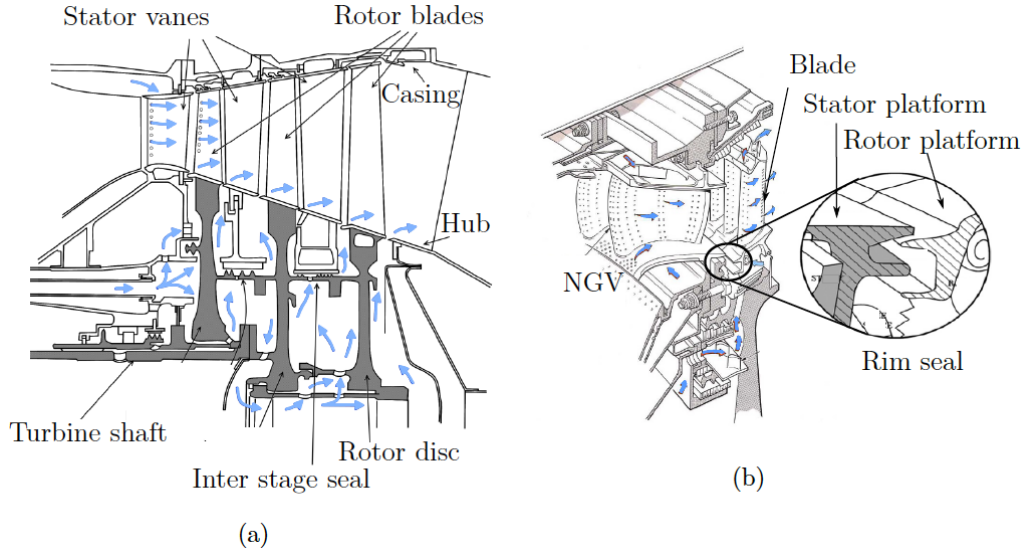


Figure 1.12 – Secondary air system in a turbine (a) and rim seal interface (b) - From the *Jet Engine* [118].

The bibliography study on high-pressure axial turbines revealed a very complex physics with unsteady phenomena that interact with each other and generate losses. Predicting numerically the flow in such a component is therefore not trivial. Numerical methods must cope correctly with this complex physics to be able to design efficiently the components of a gas turbine engine, and especially the high-pressure turbine. The Navier-Stokes equations are the basis of all existing numerical methods.

1.2 Numerical methods for the resolution of turbulent flows

1.2.1 The Navier-Stokes equations

A turbulent flow, characterised by velocity fluctuations and eddies of different sizes, compressible, viscous, monoatomic and non-reactive, is described by the compressible Navier-Stokes equations (1845) that reflect the mass conservation (one equation), the momentum balance (three equations) and the energy balance (one equation). Using Einstein's summation rule, it can be written with the following conservative form:

$$\frac{\partial \rho}{\partial t} + \frac{\partial}{\partial x_j} (\rho v_j) = 0 \quad (1.3)$$

$$\frac{\partial}{\partial t} (\rho v_i) + \frac{\partial}{\partial x_j} (\rho v_i v_j + P_s \delta_{ij} - \tau_{ij}) = \rho F_i \quad i = 1, 2, 3 \quad (1.4)$$

$$\frac{\partial}{\partial t} (\rho E_t) + \frac{\partial}{\partial x_j} (\rho E_t v_j + P_s v_j + q_j - v_i \tau_{ij}) = \rho v_j F_j \quad (1.5)$$

Where \mathbf{v} is the velocity vector, ρ the density of the fluid, t the time, \mathbf{x} the Cartesian coordinates vector, P_s the static pressure, δ_{ij} the Kronecker symbol, $\overline{\boldsymbol{\tau}}$ the viscous stress tensor, E_t the total energy and \mathbf{q} the heat flux vector. \mathbf{F} represents any external body force such as gravity or magnetic fields.

1.2.2 The closure problem

Since the system described by Equations 1.3, 1.4 and 1.5 is composed of eight unknown for five equations, it needs to be closed using three additional equations to give values for pressure, viscous stress tensor and heat flux.

The first equation is given by the ideal gas law that relates pressure, density and temperature:

$$P_s = \rho r T_s \quad (1.6)$$

Where r is the specific gas constant which is equal to $287.04 \text{ J.kg}^{-1}.\text{K}^{-1}$ for air. Then, for a Newtonian fluid and under Stokes' hypothesis, the viscous stress tensor is isotropically and linearly related to the strain rate tensor by the following relation:

$$\tau_{ij} = -\frac{2}{3}\mu \frac{\partial v_k}{\partial x_k} \delta_{ij} + 2\mu S_{ij} \quad (1.7)$$

Where μ is the molecular viscosity of the fluid and $S_{ij} = \frac{1}{2} \left(\frac{\partial v_i}{\partial x_j} + \frac{\partial v_j}{\partial x_i} \right)$ the mean velocity strain rate tensor, *i.e.* the symmetric part of the velocity gradient. Assumptions are made on the molecular viscosity of the fluid which is obtained with different empirical laws:

- **Sutherland's law:**

$$\mu(T_s) = \mu_{ref} \left(\frac{T_s}{T_{s,ref}} \right)^{\frac{3}{2}} \frac{T_{s,ref} + S}{T_s + S} \quad (1.8)$$

Where $\mu_{ref} = \mu_{ref}(T_s, S)$ is the molecular viscosity at the reference temperature $T_{s,ref}$ and S the Sutherland temperature. For air, one considers the following values: $\mu_{ref} = 1.717 \cdot 10^{-5} \text{ Pa.s}$, $T_{s,ref} = 273 \text{ K}$ et $S = 110.4 \text{ K}$. This law is used in *elsA*.

- **Power law:**

$$\mu(T_s) = \mu_{ref} \left(\frac{T_s}{T_{s,ref}} \right)^n \quad (1.9)$$

Where $\mu_{ref} = 1.717 \cdot 10^{-5} \text{ Pa.s}$, $T_{s,ref} = 300 \text{ K}$ et $n = 0.76$. This law is used in *IC3*.

Trends between 200 and 1500 K are depicted in Figure 1.13. In the scope of this PhD thesis, each law is used in a different code and may add some uncertainties when comparing the solutions. However, the impact of using two different laws is not evaluated in the following.

Finally, the heat flux is obtained using an isotropic and linear relationship with the static temperature gradient given by Fourier's law:

$$q_j = -\lambda \frac{\partial T}{\partial x_j} \quad (1.10)$$

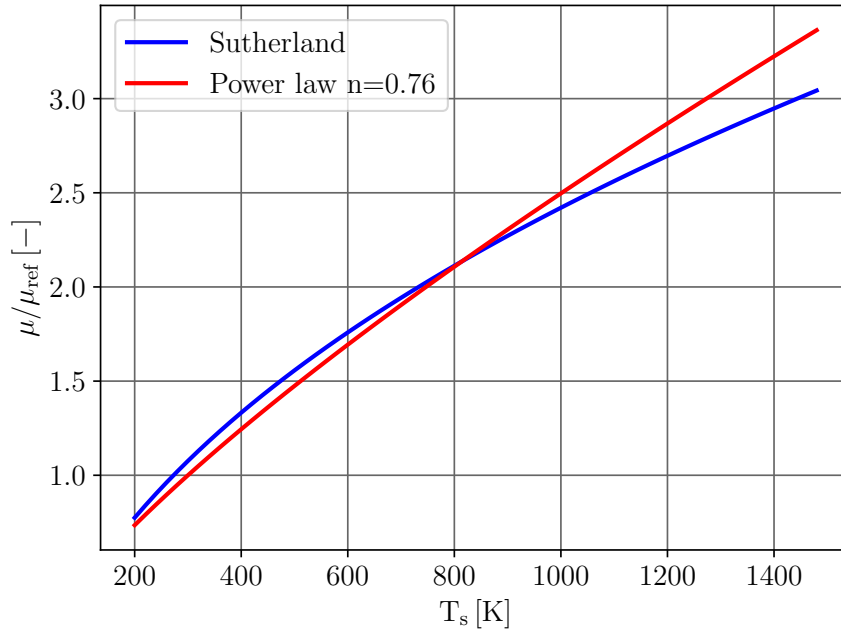


Figure 1.13 – Comparison of the viscosity laws.

Where the thermal conductivity only depends on the molecular viscosity and is given by $Pr = \mu c_p / \lambda$. Pr is the laminar Prandtl number ($= 0.7$) and c_p is the constant pressure specific heat capacity.

1.2.3 Turbulence modelling approaches

Beyond a certain critical Reynolds number, the flow described by the Navier-Stokes equations is no more deterministic and is characterised by stochastic fluctuations of the physical quantities. In a turbomachine, because of the numerous flow transformations and complex geometries (fillet, cavity, tip gap, etc.), turbulence is generated and is predominant in the whole machine. Tucker [128] made a thorough review of the turbulence treatments in CFD applied to turbomachinery. The author showed a wide range of high-Reynolds numbers that compels to use proper turbulence modelling in order to obtain a reliable description of the flow. As depicted in Figure 1.14, the Reynolds number in a turbomachine is of the order of $10^5 - 10^6$, which would lead to dramatically dense meshes if all the scales of turbulence were resolved. These values of Reynolds numbers are encountered in the configurations of this PhD thesis.

The random fluctuations of the turbulent flow are represented by eddies of different sizes that carry energy. Figure 1.15 shows the energy spectrum for homogeneous turbulence where the spectral density of turbulent energy $E(\kappa, t)$ is plotted against the wavenumber κ . This spectrum implies structures of different sizes, known as scales of turbulence [91, 136]. Richardson [97] firstly described and Kolmogorov [59] later on quantified a theory on the energy transfer between the different turbulent structures which is known as the *energy cascade*: turbulence consists of a continuous spectrum of scales ranging from largest to smallest in which the biggest structures

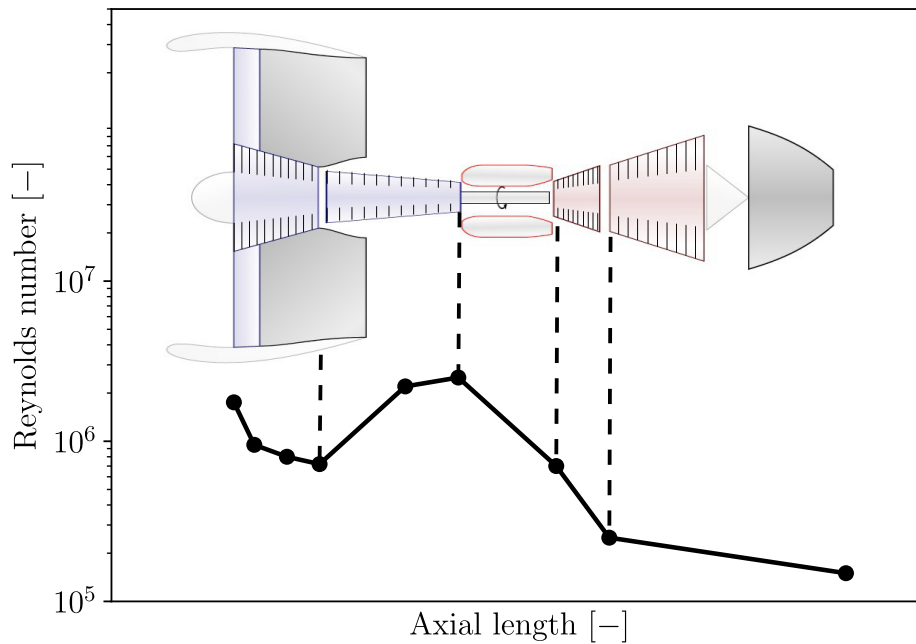


Figure 1.14 – Reynolds number evolution in a medium-sized gas turbine engine. Adapted from Mayle [76].

or integral length scale (at small wavenumber κ_{l_T}) that contains the energy and that are fully anisotropic split into smaller and smaller structures (at high wavenumber κ_{l_η}) *via* vortex stretching till a scale l_η called Kolmogorov scale for which the viscous effects prevail on the inertial effects ($Re = 1$). At this scale, turbulence is universal and isotropic (Kolmogorov’s hypothesis of local isotropy) and the kinetic energy contained in the eddies dissipates into heat through the action of molecular viscosity. These transfers occur through the non-linear terms of the Navier-Stokes equations $\nabla \cdot (\rho \mathbf{v} \otimes \mathbf{v})$ which lead to interactions between fluctuations of different wavenumbers and directions. In between the large and small eddies is the Taylor microscale l_λ with wavenumber κ_{l_λ} which corresponds to the scales of turbulence affected by viscosity leading to the dissipation of fluctuating kinetic energy into heat.

Based on these characteristic scales, the turbulence spectrum can be split into three regions:

- An energy production zone which is responsible for the enhanced diffusivity and stresses. Scales are dependant on the geometry and the statistics of the flow;
- An inertial subrange between integral scale and Kolmogorov scale where the scales have a universal form that is uniquely determined by the dissipation of turbulence ϵ , *i.e.* the rate at which turbulent kinetic energy is converted into thermal energy, independently of the kinematic viscosity ν . This is known as Kolmogorov’s second similarity hypothesis ($E \sim \epsilon^{2/3} \kappa^{-5/3}$);
- A dissipation region where the small-scale motions have a universal form that is uniquely determined by ν and ϵ .

From a numerical point of view, when the Reynolds number is sufficiently high, the Navier-Stokes equations can not be solved analytically due to the non-linear and stochastic turbulence

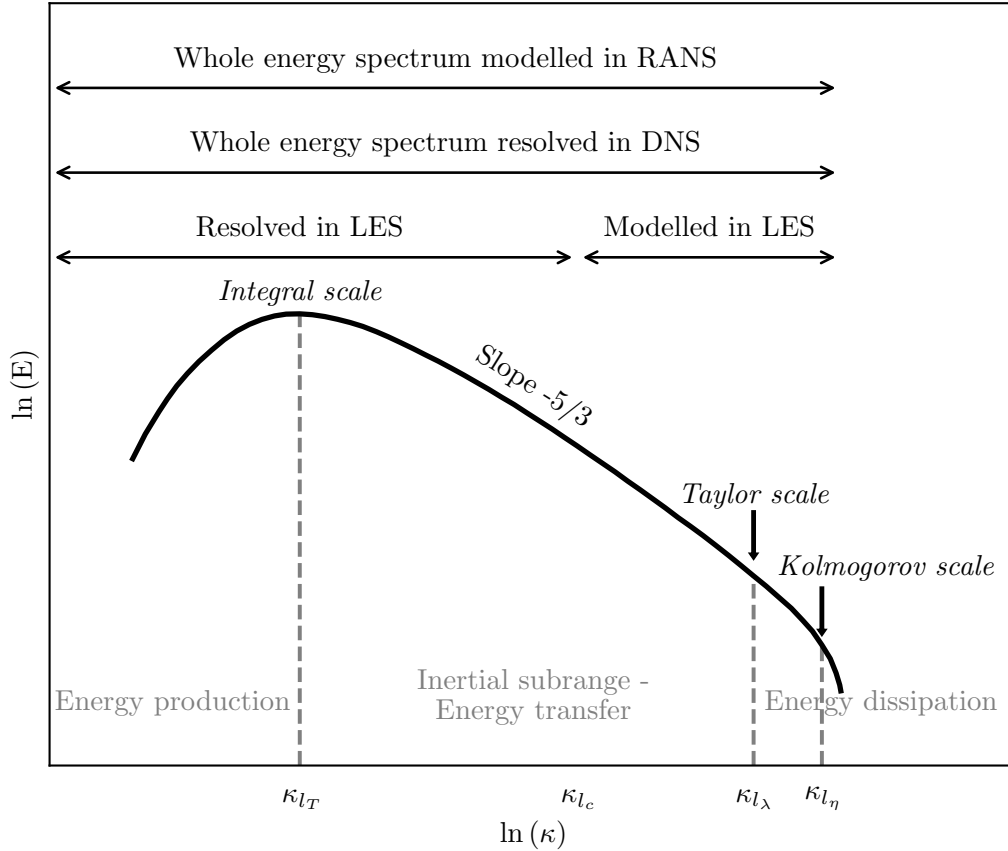


Figure 1.15 – Turbulence energy spectrum and energy cascade together with the different levels of modelling.

dynamics, as already exposed. Numerical methods have thus been developed to solve these equations by discretising them both in space and time. Depending on the amount of energy that is resolved by the numerical simulation, *i.e.* depending on the value of the cut-off frequency κ_{l_c} on the spectrum, different methods are defined. In Direct Numerical Simulation (DNS), the whole energy spectrum is solved, there is no modelling of turbulence ($\kappa_{l_c} = \kappa_{l_\eta}$). Since all the characteristic scales of the flow must be solved, the size of the mesh cells has to be of the order of magnitude of the smallest dissipative scales of turbulence and the computational effort is about $Re_T^{11/4}$ for a three-dimension domain, combining both the spatial and temporal resolution. Only a few academic studies or canonical flows at low Reynolds numbers can be simulated by DNS, making it possible to better understand turbulent flows or to validate other numerical approaches. To overcome the major limitation of DNS which is the computational cost, LES and RANS methods have been developed.

1.2.3.1 Large-Eddy Simulation

LES is an alternative to DNS that solves the large energy-containing scales (about 80%) and models the small scales. This modelling is based on the idea that the small scales are less affected by the boundary conditions and are more isotropic and universal, and therefore are more simple to model contrary to the large scales that are dependant on the problem to solve. The transition

between the resolved part and the modelled part is done at the spatial cut-off frequency κ_{lc} which is directly linked to the Nyquist frequency and the cell size of the mesh: $\kappa_{lc} = \pi/\Delta$ where Δ is close to the cubic root of the cell volume (see Figure 1.16). The mesh acts as a low-pass filter by filtering high frequencies. The scale separation involves a spatial filtering, either explicit using a subgrid-scale model or implicit with the numerical dissipation of the schemes.

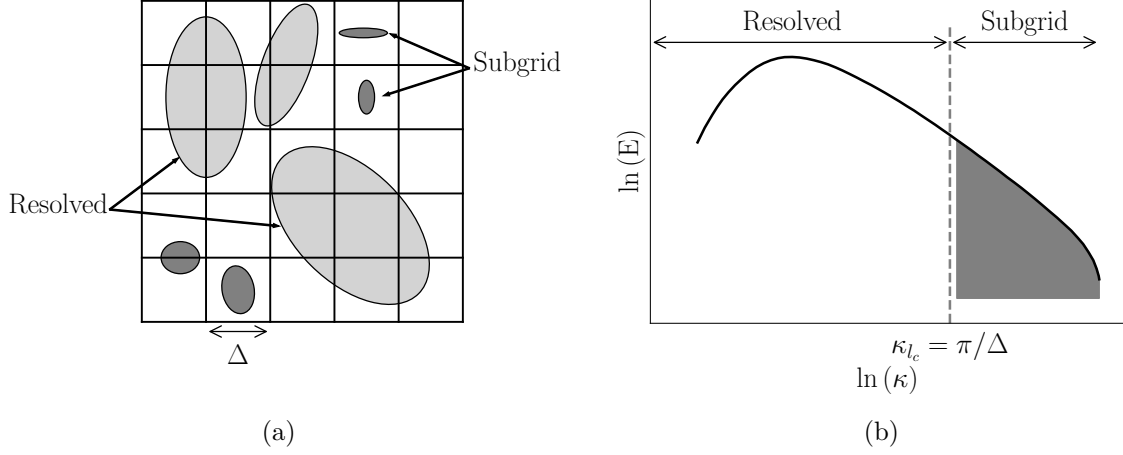


Figure 1.16 – Scale separation by the mesh in physical (a) and spectral (b) domains. Adapted from Sagaut [98].

Filtering of the Navier-Stokes equations

LES equations are obtained by filtering (in the physical or spectral domain) the Navier-Stokes equations. Using a Favre operation to take into account variable density flows $\tilde{\phi} = \overline{\rho\phi}/\bar{\rho}$, any quantity ϕ is decomposed as the sum of a filtered part and a modelled part:

$$\phi = \tilde{\phi} + \phi'' \quad (1.11)$$

The filtered quantity $\tilde{\phi}$ is solved whereas the quantity $\phi'' = \phi - \tilde{\phi}$ is modelled. Note that this decomposition does not satisfy the properties of the Reynolds decomposition: $\tilde{\phi}'' \neq 0$. The filtered compressible LES equations yields to (see Garnier *et al.* [41]):

$$\frac{\partial \bar{\rho}}{\partial t} + \frac{\partial}{\partial x_j} (\bar{\rho} \tilde{v}_j) = 0 \quad (1.12)$$

$$\frac{\partial}{\partial t} (\bar{\rho} \tilde{u}_i) + \frac{\partial}{\partial x_j} (\bar{\rho} \tilde{v}_i \tilde{v}_j + \bar{P} \delta_{ij} - \bar{\tau}_{ij} - \tau_{ij}^{SGS}) = \bar{\rho} F_i \quad (1.13)$$

$$\frac{\partial}{\partial t} (\bar{\rho} \tilde{E}_t) + \frac{\partial}{\partial x_j} [\bar{\rho} \tilde{E}_t \tilde{v}_j + \bar{P} \tilde{v}_i + \bar{q}_j + q_j^{SGS} - \tilde{v}_i (\bar{\tau}_{ij} + \tau_{ij}^{SGS})] = \bar{\rho} \tilde{v}_j F_j \quad (1.14)$$

The filtering implies in Equations 1.13 and 1.14 two unknowns:

- The subgrid-scale tensor $\tau_{ij}^{SGS} = -\bar{\rho} (\tilde{v}_i \tilde{v}_j - \tilde{v}_i \tilde{v}_j)$
- The subgrid-scale heat flux $q_j^{SGS} = \bar{\rho} (\tilde{v}_j \tilde{E}_t - \tilde{v}_j \tilde{E})$

In the LES formalism, these two terms are modelled to take into account the effect of the smallest eddies using either an explicit or implicit LES approach.

Subgrid-scale modelling for compressible flows

There are two ways of modelling the effects of the unresolved eddies in LES. The first one is called implicit LES (ILES). No explicit modelling is used and it is assumed that the action of the subgrid scales on the resolved scales is equivalent to a strictly dissipative action [98]. In other words, the dissipation of the smallest eddies is done by the numerical schemes. While providing good results on turbomachinery applications [50, 79], results are highly dependant on the numerical schemes used. The other method is called explicit LES, where τ_{ij}^{SGS} and q_j^{SGS} are explicitly solved using the concept of turbulent viscosity μ_{SGS} :

$$\tau_{ij}^{SGS} = 2\mu_{SGS} \left(\widetilde{S}_{ij} - \frac{1}{3} \frac{\partial \widetilde{v}_k}{\partial x_k} \delta_{ij} \right) \quad (1.15)$$

$$q_j^{SGS} = -\frac{\bar{\rho} \mu_{SGS} c_p}{Pr_{SGS}} \frac{\partial \widetilde{T}}{\partial x_j} \quad (1.16)$$

The objective of explicit subgrid-scale models is to give values for μ_{SGS} . The Smagorinsky model [42, 109] is considered the pioneer subgrid-scale model for LES. In this PhD thesis, the Vreman model [131] is used. Its advantage is to have a relatively small dissipation in transitional and near-wall regions, which is an improvement compared to the Smagorinsky model. Equations of the models are voluntarily not presented, but can be found in the above-mentioned references.

Turbulence injection

The flow exiting the combustion chamber and thus entering the high-pressure turbine can exhibit high levels of turbulence. In that sense in CFD, the knowledge of instantaneous turbulent fields and its associated space-time modes at the inlet of the computational domain is essential. However, as these quantities are hardly accessible, it is common to approximate the turbulent fields. Turbulence injection consists of superimposing fluctuations (of velocity and temperature) to the mean quantities. Different methods of turbulence injection, aiming at replicating the turbulence cascade spectrum (both in intensity and length scale) and depending on the application, exist:

- **Precursor method:** a DNS precursor simulation is performed in which the upstream flow is considered. The extraction plane in the precursor simulation, for which turbulence is fully developed, corresponds to the inlet of the domain of the main simulation. Even if highly reliable, this kind of method is very costly since all the statistics and scales of turbulence must be stored [83]. It has the main drawback to be applicable to simple generic flows;
- **Recycling-rescaling methods:** turbulence statistics are extracted at a plane in the domain where it is fully developed and established. A rescaling of the quantities, especially of the boundary layer thickness and its velocity profiles, is performed and the information is then prescribed at the inlet [140];
- **Synthetic turbulence methods:** a random field with statistical features is prescribed to generate the fluctuations at the inlet. These methods (spectral, digital filter, vortex, etc.) need an establishment length for the turbulence to become physical but they have the advantage to be less costly [58].

Note that this list is not exhaustive (a complete review is performed by Dhamankar *et al.* [26]). The first two classes of methods are very satisfying from the physical point of view but are in general not practicable. The last class is used in the LES solver *IC3* used in this PhD thesis.

Despite the strong emergence of LES in turbomachinery applications [127, 144], it remains costly in the industry as it scales at around $Re_T^{2.5}$, especially because of the near-wall treatment. The RANS approach remains the basis in an industrial context, as it gives very short return times.

1.2.3.2 Reynolds-Averaged Navier-Stokes simulation

To reduce even more the computational costs, the whole spectrum of energy can be modelled by performing a time-averaging or ensemble-averaging of the Navier-Stokes equations. This is called the Reynolds-Averaged Navier-Stokes (RANS) method. It has been first introduced by Reynolds in 1895 who decomposed each instantaneous variable of the flow as the sum of a mean part and a fluctuating part with the relation $\phi = \bar{\phi} + \phi'$ [96]. Since the compressible Navier-Stokes equations are considered in this manuscript, the Favre averaging [33], which is a density average, is used with $\phi = \tilde{\phi} + \phi''$ and the Favre averaged quantity $\tilde{\phi}$ writes $\tilde{\phi} = \overline{\rho\phi}/\bar{\rho}$. In this averaging, the random fluctuations are entirely modelled whereas the mean value $\bar{\phi}$ is obtained using a set average on a large number N of independent realisations of the same hypothetical simulation:

$$\bar{\rho}\tilde{\phi} = \lim_{N \rightarrow \infty} \frac{1}{N} \sum_{i=1}^N \rho\phi_i \quad (1.17)$$

By applying the Favre decomposition for the velocity, total energy and enthalpy¹, the URANS equations read:

$$\frac{\partial \bar{\rho}}{\partial t} + \frac{\partial}{\partial x_j} (\bar{\rho}\tilde{v}_j) = 0 \quad (1.18)$$

$$\frac{\partial}{\partial t} (\bar{\rho}\tilde{v}_i) + \frac{\partial}{\partial x_j} (\bar{\rho}\tilde{v}_i\tilde{v}_j + \bar{P}\delta_{ij} - \bar{\tau}_{ij} - \tau_{ij}^R) = \bar{\rho}F_i \quad (1.19)$$

$$\frac{\partial}{\partial t} [\bar{\rho}(\tilde{E}_t + k)] + \frac{\partial}{\partial x_j} [\bar{\rho}(\tilde{E}_t + k)\tilde{v}_j + \bar{P}\tilde{v}_i + \bar{q}_j + q_j^T - \tilde{v}_i(\bar{\tau}_{ij} + \tau_{ij}^R)] = \bar{\rho}\tilde{v}_j F_j \quad (1.20)$$

Where $\tilde{E}_t = \tilde{e} + \frac{\tilde{v}_i\tilde{v}_i}{2}$ and $\bar{P} = \bar{\rho}r\tilde{T}$. As for the LES, the viscous stress tensor τ_{ij} and the molecular heat flux q_j are given by the behaviour laws described in 1.2.2. When unsteady flows are considered (such as stator/rotor interactions - see Figure 1.17a), a phase averaging is used and the derivative of $\bar{\phi}$ with respect to time is not equal to zero. This is the so-called unsteady-RANS approach (URANS). As mentioned by Tucker [128], in order for URANS to be valid, since the unsteady temporal information is a combination of a periodic movement and turbulent fluctuations, a spectral gap must exist, *i.e.* the characteristic time of the deterministic fluctuations must be much larger than the characteristic time of turbulence. However, a clear separation is rarely observed or unknown *a priori*. Note that URANS will also capture non-deterministic unsteadiness (*e.g.* vortex shedding) provided a relatively small timestep is used

¹Note that for density and pressure, the Reynolds decomposition is used and that the correlation of fluctuating quantities are eliminated.

to capture the associated frequencies. Otherwise, for stationary turbulent flows ($\bar{\phi} = \text{cst}$ - see Figure 1.17b), the time derivative terms vanish and the steady solution is obtained by replacing the statistical average with a time average on an interval of time T larger than the time scale of the fluctuations.

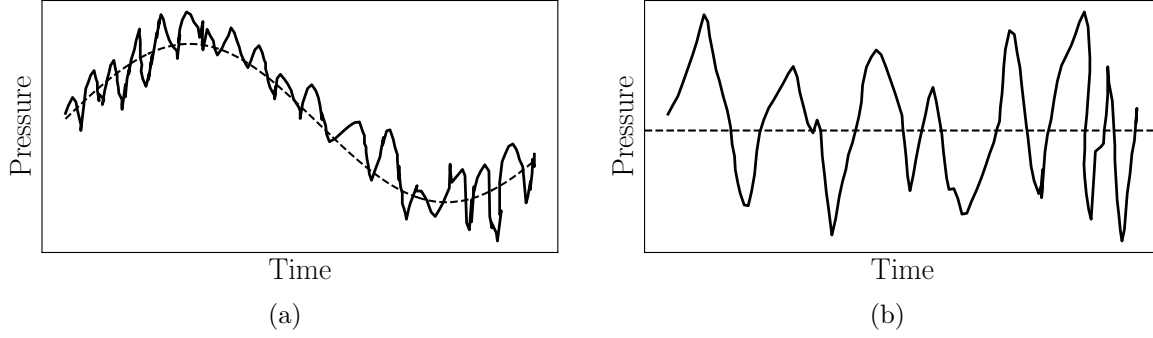


Figure 1.17 – Difference between an unsteady turbulent flow (a) and a steady turbulent flow (b) for a pressure probe signal.

The URANS set of equations defined by Equations 1.18, 1.19 and 1.20 leads to new unknown quantities:

- The Reynolds tensor $\tau_{ij}^R = -\overline{\rho v_i'' u_j''}$
- The turbulent kinetic energy $k = \frac{1}{2} \frac{\overline{\rho v_i'' v_i''}}{\bar{\rho}} = -\frac{\text{Tr}(\tau^R)}{2}$
- The turbulent heat flux $q_j^T = \overline{\rho v_i'' h''}$

To close the system of equations, turbulence must be modelled, *i.e.* expressions must be given for k , τ_R and q_T .

1.2.4 RANS turbulence modelling

RANS turbulence modelling relies either on the use Boussinesq's hypothesis (linear and non-linear) or on the resolution of the transport equations for the Reynolds stresses.

1.2.4.1 Linear eddy-viscosity turbulence models

According to Boussinesq's hypothesis (1877), the Reynolds stress tensor is linearly linked to the mean velocity strain rate tensor through an isotropic turbulent viscosity such as:

$$\tau_{ij}^R = 2\mu_T \left(\widetilde{S}_{ij} - \frac{1}{3} \frac{\partial \widetilde{v}_k}{\partial x_k} \delta_{ij} \right) - \frac{2}{3} \bar{\rho} k \delta_{ij} \quad (1.21)$$

Where $k = 0.5 \overline{v_i'' v_i''}$. The last term of Equation 1.21 guarantees that the trace of τ_{ij}^R is $-2\bar{\rho}k$. Equations 1.19 and 1.21 also show that only the deviatoric part of the Reynolds stress tensor is responsible for the transport of momentum, as the isotropic part is added to the pressure term [91]. Likewise, by analogy with Fourier's law, the turbulent heat flux is expressed as:

$$q_j^T = -\frac{\mu_T c_p}{Pr_T} \frac{\partial \widetilde{T}}{\partial x_j} \quad (1.22)$$

Where Pr_T is the constant turbulent Prandtl number set to 0.9. The turbulent kinetic energy k is computed from the Reynolds stress tensor. By looking at the two equations, the influence of turbulence is now only dependant on the turbulent kinetic energy k and on the turbulent viscosity μ_T , which is not a property of the fluid but that depends on the flow. With this definition, the turbulent structures are seen by the rest of the flow as an excess of viscosity. The objective of the turbulence models is to give a value for those two characteristic quantities. Different models have been derived over the past decades: algebraic or zero-equation models (*e.g.* Baldwin and Lomax [5]), one-equation models (*e.g.* Spalart-Allmaras [112]) and two-equations models. As two-equation turbulence models are extensively used in the scope of this PhD thesis through the *elsA* CFD solver, they are now presented.

Two-equation turbulence models have been developed to correct the major drawbacks of algebraic and one-equation models which are the non-local, turbulence history effects and the coupling between the velocity and length scales not being considered. Two-equation models give a transport equation for the turbulent kinetic energy (*i.e.* the velocity scale v^*) where the various terms appearing represent physical processes occurring as the turbulence moves through a given flow. The second equation is set for the length scale of turbulence l^* which is expressed either as the turbulence dissipation rate ϵ , specific turbulence dissipation rate $\omega = \epsilon/k$ or turbulence length scale l_T . All models are based on an equilibrium between the transient term, mean flow convection, production, diffusion, dissipation and source term. The models employed in the present work are now presented.

Launder-Sharma $k - \epsilon$ model

One of the most popular models is the low-Reynolds $k - \epsilon$ turbulence model developed by Launder and Sharma in 1974 [66] where one equation for the turbulent energy k and one for the modified turbulence dissipation rate $\hat{\epsilon} = \epsilon - D/\bar{\rho}$ are solved:

$$\begin{array}{c}
 \underbrace{\frac{\partial \bar{\rho} k}{\partial t}}_{\text{Transient term}} + \underbrace{\frac{\partial}{\partial x_j} (\bar{\rho} \tilde{v}_j k)}_{\text{Convection}} = \underbrace{\frac{\partial}{\partial x_j} \left[\left(\mu + \frac{\mu_T}{\sigma_k} \right) \frac{\partial k}{\partial x_j} \right]}_{\text{Diffusion}} + \underbrace{P_k}_{\text{Production}} - \underbrace{\bar{\rho} \hat{\epsilon}}_{\text{Dissipation}} - \underbrace{D}_{\text{Source term}} \quad (1.23)
 \end{array}$$

$$\begin{array}{c}
 \underbrace{\frac{\partial \bar{\rho} \hat{\epsilon}}{\partial t}}_{\text{Transient term}} + \underbrace{\frac{\partial}{\partial x_j} (\bar{\rho} \tilde{v}_j \hat{\epsilon})}_{\text{Convection}} = \underbrace{\frac{\partial}{\partial x_j} \left[\left(\mu + \frac{\mu_T}{\sigma_\epsilon} \right) \frac{\partial \hat{\epsilon}}{\partial x_j} \right]}_{\text{Diffusion}} + \underbrace{C_{\epsilon 1} f_1 \frac{\hat{\epsilon}}{k} P_k}_{\text{Production}} - \underbrace{C_{\epsilon 2} f_2 \bar{\rho} \frac{\hat{\epsilon}^2}{k}}_{\text{Dissipation}} + \underbrace{E}_{\text{Source term}} \quad (1.24)
 \end{array}$$

The turbulent viscosity is given by:

$$\mu_T = C_\mu f_\mu \bar{\rho} \frac{k^2}{\hat{\epsilon}} \quad (1.25)$$

Where C_μ , $C_{\epsilon 1}$, $C_{\epsilon 2}$, σ_k and σ_ϵ are constant of the model (see [66]), f_μ , f_1 and f_2 are damping functions that are removed when wall functions are used (high-Reynolds formulation) and $D = 2\nu \left(\partial \sqrt{k} / \partial n \right)^2$ and $E = 2\nu \nu_T \left(\partial^2 v / \partial y^2 \right)$ are low-Reynolds correction terms to take into account the effects of the walls. Note that k and $\hat{\epsilon}$ are equal to 0 at the walls. This model is well-suited for external flow interactions with complex geometries but lacks of precision close to the walls and for strong curvature into flows and jet flows.

Wilcox $k - \omega$ model

The original $k - \omega$ turbulence model has been developed by Wilcox in 1988 [137]. It is based on the transport of the turbulent kinetic energy k and the specific turbulence dissipation rate ω which can be seen as a frequency at which the dissipation of turbulence energy occurs:

$$\boxed{\begin{array}{l} \underbrace{\frac{\partial \bar{\rho} k}{\partial t}}_{\text{Transient term}} + \underbrace{\frac{\partial}{\partial x_j} (\bar{\rho} \tilde{v}_j k)}_{\text{Convection}} = \underbrace{\frac{\partial}{\partial x_j} \left[\left(\mu + \sigma_k \frac{\bar{\rho} k}{\omega} \right) \frac{\partial k}{\partial x_j} \right]}_{\text{Diffusion}} \underbrace{+ P_k}_{\text{Production}} \underbrace{- \beta^* \bar{\rho} \omega k}_{\text{Dissipation}} \end{array}} \quad (1.26)$$

$$\boxed{\begin{array}{l} \underbrace{\frac{\partial \bar{\rho} \omega}{\partial t}}_{\text{Transient term}} + \underbrace{\frac{\partial}{\partial x_j} (\bar{\rho} \tilde{v}_j \omega)}_{\text{Convection}} = \underbrace{\frac{\partial}{\partial x_j} \left[\left(\mu + \sigma_\omega \frac{\bar{\rho} k}{\omega} \right) \frac{\partial \omega}{\partial x_j} \right]}_{\text{Diffusion}} \underbrace{+ \frac{\gamma \omega}{k} P_k}_{\text{Production}} \underbrace{- \beta \bar{\rho} \omega^2}_{\text{Dissipation}} \end{array}} \quad (1.27)$$

The turbulent viscosity is given by:

$$\mu_T = \frac{\bar{\rho} k}{\omega} \quad (1.28)$$

Where β^* , β , γ , σ_k and σ_ω are constants of the model (see [137]). Note that since ω tends to infinity at the walls, its value should be imposed. The model correctly captures the behaviour of the flow in the boundary layer under adverse pressure gradients. The accuracy is also improved for curvatures, separated flows and jets. However, the model is very sensitive to the freestream boundary condition on ω .

Smith $k - l$ model

The Smith $k - l$ model [110], established in 1994, is a very popular turbulence model for turbomachinery applications and relies on the transport of the turbulent kinetic energy k and on the characteristic length of the large scales of turbulence l :

$$\boxed{\begin{array}{l} \underbrace{\frac{\partial \bar{\rho} k}{\partial t}}_{\text{Transient term}} + \underbrace{\frac{\partial}{\partial x_j} (\bar{\rho} \tilde{v}_j k)}_{\text{Convection}} = \underbrace{\frac{\partial}{\partial x_j} \left[\left(\mu + \frac{\mu_T}{\sigma_k} \right) \frac{\partial k}{\partial x_j} \right]}_{\text{Diffusion}} \underbrace{+ P_k}_{\text{Production}} \underbrace{- \frac{\bar{\rho} (2k)^{3/2}}{B_1 l}}_{\text{Dissipation}} \underbrace{- \bar{\rho} D}_{\text{Source term}} \end{array}} \quad (1.29)$$

$$\boxed{\begin{array}{l} \underbrace{\frac{\partial \bar{\rho} l}{\partial t}}_{\text{Transient term}} + \underbrace{\frac{\partial}{\partial x_j} (\bar{\rho} \tilde{v}_j l)}_{\text{Convection}} = \underbrace{\frac{\partial}{\partial x_j} \left[\left(\mu + \frac{\mu_T}{\sigma_\epsilon} \right) \frac{\partial l}{\partial x_j} \right]}_{\text{Diffusion}} + (2 - E_2) \frac{\bar{\rho} \sqrt{2k}}{B_1} \left[1 - \left(\frac{l}{K\eta} \right)^2 \right] \\ + \bar{\rho} l \frac{\partial \tilde{v}_k}{x_k} - \frac{\mu_T}{\sigma_l} \frac{1}{l} \left(\frac{\partial l}{\partial x_j} \right)^2 \left(\frac{l}{K\eta} \right)^2 + 2 \frac{\mu_T}{\sigma_l} \frac{1}{k} \frac{\partial l}{\partial x_j} \frac{\partial k}{\partial x_j} \end{array}} \quad (1.30)$$

The turbulent viscosity is given by:

$$\mu_T = \frac{\rho \sqrt{2k} l f_\mu}{B_1^{1/3}} \quad (1.31)$$

Where B_1 , E_2 , σ_k , σ_l and K are constants of the model (see [110]), f_μ is the wall damping function and η is the distance to the wall. Its popularity can be explained by its low sensitivity to the distribution of grid points close to the wall because of the linear turbulent length scale profile and its ability to better account for the compressibility effects. The value of the turbulent length scale to impose can easily be measured by experiments, contrary to the dissipation.

1.2.4.2 Non-linear eddy-viscosity turbulence models

Linear eddy-viscosity turbulence models based on Boussinesq's hypothesis rely on the alignment of the Reynolds stress tensor with the mean strain-rate tensor at all points of a turbulent flow. In general, this proportionality is no more valid for flows with sudden changes in mean strain rate, curvature, rotating structures or stratification. Explicit Algebraic Reynolds Stress Models (EARSM) are based on an altered definition of Boussinesq's constitutive relation to correct these deficiencies as well as to take into account the anisotropic behaviour of turbulence by making the assumption of a local equilibrium of the turbulence. The definition of τ_{ij}^R is modified in a non-linear way to determine explicitly each component of the Reynolds stress tensor such as:

$$\tau_{ij}^R = 2\mu_T \left(\widetilde{S}_{ij} - \frac{1}{3} \frac{\partial \widetilde{v}_k}{\partial x_k} \delta_{ij} \right) - \frac{2}{3} \bar{\rho} k \delta_{ij} - \underbrace{a_{ij}^{(ex)} \bar{\rho} k}_{\text{anisotropy}} \quad (1.32)$$

Where $a_{ij}^{(ex)}$ is the modelled anisotropy tensor that takes into account the effects of stress and rotation of the fluid with high-order tensor products of the mean strain-rate and vorticity tensors. The model developed by Hellsten, Wallin, and Johansson (2005) is used in this PhD thesis where two turbulent variables are still transported, k and ω [48]. The turbulent viscosity reads:

$$\mu_T = \rho C_\mu^* \frac{k}{\omega} \quad (1.33)$$

Where the variable C_μ^* depends on the velocity gradients, as opposed to a constant value for models based on Boussinesq's hypothesis. The anisotropy tensor is expressed as follows:

$$a_{ij}^{(ex)} = \sum_{k=1}^9 \beta_k M_{ij,k} \quad (1.34)$$

Where the M_k are high-order products of two non-dimensional tensors $S_{ij}^* = \frac{S_{ij}}{\omega}$ and $\Omega_{ij}^* = \frac{\Omega_{ij}}{\omega}$ and β_k are constants of the model. The exact definition of M_k and β_k is available in the original papers of the model [48, 132]. Damping functions are used at the wall to give a physical behaviour of the components of $a_{ij}^{(ex)}$.

Note that in the previous transport equations for linear and non-linear models, turbulent diffusion and pressure diffusion are modelled through the turbulent viscosity and the spatial gradient of the transported quantity and are added to viscous diffusion.

1.2.4.3 Second-order turbulence models

The last category of RANS turbulence models deals with second-order turbulence models or Reynolds Stress Models (RSM). They are based on the computation of each Reynolds stress tensor component $\bar{\rho} \widetilde{R}_{ij} = -\tau_{ij}^R = \overline{\rho v_i'' u_j''}$ independently (6 transport equations since the tensor is symmetric) plus the transport of a length-scale determining variable (1 equation). The notion of turbulent viscosity is no more used. For the SSG/LRR- ω developed by Cécora *et al.* in 2015 [19],

the six Reynolds stress equations and the length scale are given by:

$$\frac{\partial \overline{\rho R_{ij}}}{\partial t} + \frac{\overline{\rho v_k R_{ij}}}{\partial x_k} = \overline{\rho P_{ij}} - \overline{\rho \epsilon_{ij}} + \overline{\rho \Pi_{ij}} + \overline{\rho D_{ij}} \quad (1.35)$$

$$\frac{\partial \overline{\rho \omega}}{\partial t} + \frac{\partial}{\partial x_j} \left[\overline{\rho \tilde{v}_j k} - \left(\mu + \sigma_\omega \frac{\overline{\rho k}}{\omega} \right) \frac{\partial \omega}{\partial x_j} \right] = \frac{\gamma \omega}{k} P_k - \beta \overline{\rho \omega^2} \quad (1.36)$$

- The production term is exact:

$$\overline{\rho P_{ij}} = -\overline{\rho R_{ik}} \frac{\partial \tilde{v}_j}{\partial x_k} - \overline{\rho R_{jk}} \frac{\partial \tilde{v}_i}{\partial x_k} \quad (1.37)$$

All other terms on the right-hand side of Equation 1.35 need to be modelled:

- The pressure-strain correlation, which is responsible for the redistribution of the turbulent kinetic energy among the different components of the velocity fluctuations, is expressed as:

$$\overline{\rho \Pi_{ij}} = P'_s \left(\frac{\partial v''_i}{\partial x_j} + \frac{\partial v''_j}{\partial x_i} \right) \quad (1.38)$$

- The dissipation term (dissipation of turbulent structures under the action of molecular viscosity) reads:

$$\overline{\rho \epsilon_{ij}} = \overline{\tau'_{ik} \frac{\partial v''_j}{\partial x_k}} + \overline{\tau'_{jk} \frac{\partial v''_i}{\partial x_k}} \quad (1.39)$$

- The diffusion term is decomposed as the sum of a turbulent diffusion (diffusion of turbulent stresses by the turbulent fluctuations), viscous diffusion and pressure diffusion:

$$\overline{\rho D_{ij}} = \underbrace{-\frac{\partial}{\partial x_k} \left[\overline{\rho u''_i u''_j u''_k} \right]}_{\text{Turbulent diffusion}} + \underbrace{\frac{\partial}{\partial x_k} \left[\overline{\tau'_{ik} u''_j} + \overline{\tau'_{jk} u''_i} \right]}_{\text{Viscous diffusion}} - \underbrace{\frac{\partial}{\partial x_k} \left[\overline{P'_s u''_i} \delta_{jk} + \overline{P'_s u''_j} \delta_{ik} \right]}_{\text{Pressure diffusion}} \quad (1.40)$$

Cécora *et al.* proposed a closure for the pressure-strain correlation, the dissipation term and the diffusion terms. Details of the models can be found in [19]. The reader must keep in mind that the isotropic dissipation is retained: $\overline{\rho \epsilon_{ij}} = \frac{2}{3} \overline{\rho} \delta_{ij} \epsilon$ where the dissipation rate is given by the transport equation on ω .

1.2.4.4 Limitations of RANS turbulence models

Turbulent flows simulated with the RANS approach may suffer from deficiencies in specific parts of the numerical domain where the physics is complex, because of the hypotheses behind the models. In all the above-mentioned linear and non-linear eddy-viscosity turbulence models, the production term $P_k = \tau_{ij}^R \partial \tilde{v}_i / \partial x_j$ is never solved and is approximated. The way the approximation is performed impacts the dynamics of the flow, especially in flows with high levels of turbulence, rotation and curvature. Two ways of computing P_k are considered:

- From the mean velocity strain rate tensor:

$$P_k = \mu_T S^2 \quad (1.41)$$

$$S = \sqrt{2\widetilde{S}_{ij}\widetilde{S}_{ij}} \text{ and } \widetilde{S}_{ij} = \frac{1}{2} \left[\frac{\partial \widetilde{v}_i}{\partial x_j} + \frac{\partial \widetilde{v}_j}{\partial x_i} \right] \quad (1.42)$$

- From the vorticity tensor:

$$P_k = \mu_T \Omega^2 \quad (1.43)$$

$$\Omega = \sqrt{2\widetilde{\Omega}_{ij}\widetilde{\Omega}_{ij}} \text{ and } \widetilde{\Omega}_{ij} = \frac{1}{2} \left[\frac{\partial \widetilde{v}_i}{\partial x_j} - \frac{\partial \widetilde{v}_j}{\partial x_i} \right] \quad (1.44)$$

To better understand the issue with P_k , let us refer to a simple case where a longitudinal velocity gradient (acceleration or deceleration) is observed. In that case, $\partial \widetilde{v}_x / \partial x = -\partial \widetilde{v}_x / \partial y \neq 0$ and the exact production reads $P_k = -\bar{\rho} (\overline{v_x'^2} - \overline{v_y'^2}) \approx 0$. Modelling the production from the mean velocity strain rate tensor gives $P_k = 4\mu_T (\partial \widetilde{v}_x)^2 \gg 0$. Over-prediction of k is observed. This problem is known as the *stagnation point anomaly* [30] which can lead to significant errors in the turbomachinery field since too much turbulence is predicted. Computing the production for the vorticity tensor vanishes P_k . Other techniques exist, such as the Kato-Launder one, where the production term is computed as $P_k = \mu_T S \Omega$. Instead of modifying the computation of the production, it is also possible to have limiters and realisability constraints² (see Appendix B). The evaluation of both approximations for the production term is presented in Chapter 3.

Another limitation comes with the linear eddy-viscosity models that are inaccurate for flows with sudden changes in mean strain rate: flows with strong curvature or flows in rotating fluids for instance. They also fail when dealing with anisotropy of the normal Reynolds stress because of the isotropic turbulent viscosity assumption. Linear eddy-viscosity models can not predict any effect of streamline curvature that must appear in the production term [136]. As presented previously, non-linear eddy-viscosity models are tuned to recover the curvature effect, while RSM models capture it by definition since the production is exact. They are tackled in Chapter 4 and Chapter 5.

A wide range of RANS turbulence models have been developed over the past decades. Most of them are based on Boussinesq's hypothesis, which assumes a linear relationship between the so-called Reynolds stress tensor and the viscous stresses. Algebraic models were the first implemented, because of their simplicity, but they could not take into account any effect of turbulence history. This problem was corrected with one and two-equation linear turbulence models which are still extensively used in the industry nowadays. However, in complex flow situations (curvature, swirling flows, anisotropic turbulent flows), they lead to a loss of accuracy. To avoid the use of hybrid RANS-LES or simply LES, more sophisticated RANS turbulence models have been developed: the EARSM models, where a modelled anisotropy tensor is added to Boussinesq's relative constitution. The RSM models are the most complex RANS turbulence models, where each Reynolds stress tensor component is solved by a transport equation. This makes it possible to suppress the local relationship between the Reynolds stresses and the mean flow. However, they are not widely used in an industrial context because of their mesh sensitivity and computational cost.

²For a model to be realisable the normal Reynolds stresses must be non-negative and the Schwarz' inequality must be satisfied between fluctuating quantities.

1.3 Modelling strategies of turbomachinery components

As seen in Figure 1.2, the flow in a turbomachine is *a priori* unsteady. Different techniques for the simulation of a turbomachinery component exist. The choice is always a compromise between the available computational resources (because of the high Reynolds numbers) and the phenomena that the user needs to simulate. Full 360° simulations are required when the working of the turbomachinery is not stable and whose periodicity is not known or non-existent (rotating stall), but the computational time is quite important. However, for unsteadiness which is only due to the relative motion of two rows (the vane/blade interactions), numerous techniques have emerged to reduce the computational domain under certain hypotheses on the flow: steady methods and unsteady methods that have both their pros and cons. It is proposed here to present the techniques used in this PhD thesis.

1.3.1 Steady simulations: the mixing-plane approach

For steady simulations, the so-called *mixing-plane* technique proposed by Denton [25] is used for the treatment of the vane/blade interface. It relies on the hypothesis that only the radial heterogeneities of the flow have an impact from one row to another. Quantities such as the Riemann invariants are azimuthally averaged before being transmitted between rows. A consequence is that the wakes do not cross the interface. The flow is therefore considered to be identical in each passage of a row, reducing the number of passages to be simulated to only one blade-to-blade passage, and spatial periodic boundary conditions are applied in the azimuthal direction. In general, the mixing-plane is placed midway between the TE of the upstream row and the LE of the downstream row. This method is still commonly used in industry as the return time is short while predicting correctly the overall performance of the stage but part of the physics is biased since the vane/blade interactions, *i.e.* the unsteady mechanisms, are not taken into account.

1.3.2 Unsteady simulations

To improve the predictability and the quality of the numerical simulations, it is possible to account for the unsteady interactions between rows that generate a flow which is periodic in time in the frame of the row and depends only on the rotation velocities and the number of blades of the different rows.

1.3.2.1 Blade number reduction method

When a spatial periodicity exists, it is possible to reduce the number of channels for each row. A simple condition of space periodicity is applied at the azimuthal boundaries of each group of channels and a condition of axial-radial continuity is applied at the interface between two rows. The unsteady interactions between rows are well captured with a precision similar to a 360° simulation. If a geometrical periodicity does not exist (which is often the case for structural reasons), it is possible to either perform a contraction/dilatation at the interface, or to modify the geometry of one or more rows to retrieve a natural periodicity. Yet, by doing so, the physics is modified (modification of the frequency of the unsteady phenomena for instance).

1.3.2.2 Phase-lagged or chorochronic approach

The phase-lagged, or chorochronic approach, proposed by Erdos and Alzner [31] consists in reducing the computational domain to a single blade passage for each row and to take into account the unsteadiness due to the blade passing period (or blade passing frequency) of the opposite row defined for a vane/blade configuration as:

$$T_R = \frac{2\pi}{\Omega N_S} \quad T_S = \frac{2\pi}{\Omega N_R} \quad (1.45)$$

Because of this time periodicity of the flow, a time lag between the inter-blade passages of a row exists. From Figure 1.18, the passage of a row sees the same flow as the adjacent passage but with a time delay known as the chorochronic period which corresponds to the time δt required so that the flow in a passage at time t is equal to the one of the adjacent channel at time $t + \delta t$ (space-time periodicity):

$$\delta t = \left| \frac{2\pi(N_R - N_S)}{\Omega N_R N_S} \right| \quad (1.46)$$

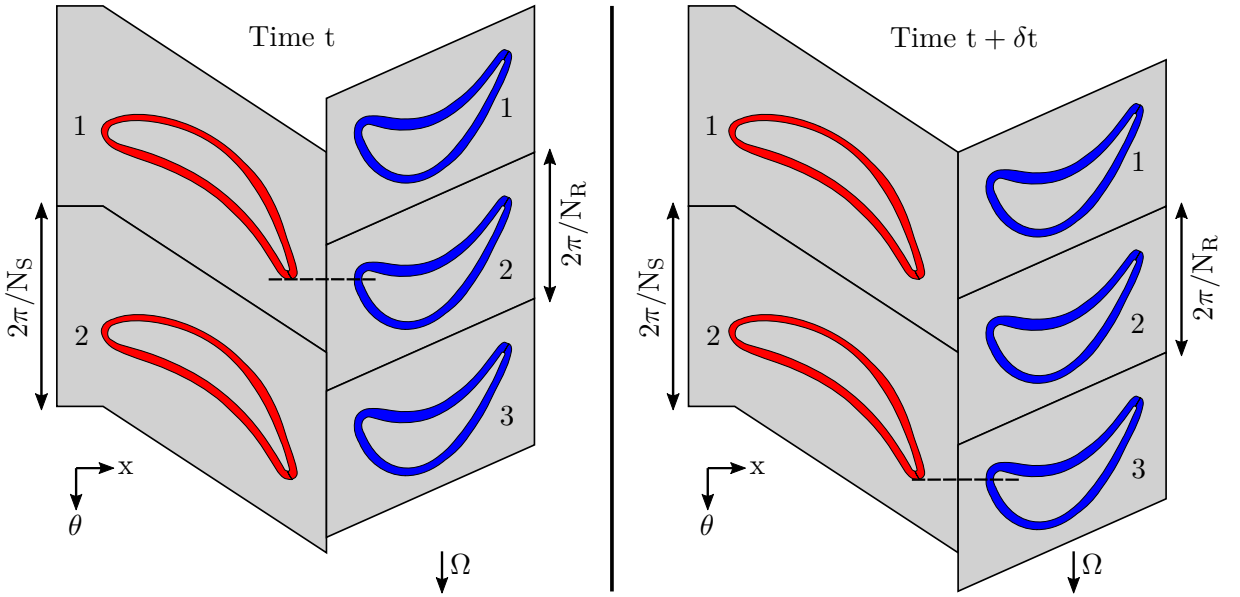


Figure 1.18 – Schematic view of the space-time periodicity of the flow.

Under the assumption of chorochronicity, Gerolymos *et al.* [43] showed that any quantity Φ in the passage of a row was equal to the one of its neighbour with a time delay:

$$\Phi(x, r, \theta, t) = \Phi \left(x, r, \theta - \frac{2\pi}{N_{S,R}}, t - \delta t \right) \quad (1.47)$$

$$= \Phi \left(x, r, \theta + \frac{2\pi}{N_{S,R}}, t + \delta t \right) \quad (1.48)$$

In this case, as the periodicity of the flow exceeds the extension of the channel, it is necessary to implement phase-lagged and space conditions, which are delayed conditions in space and time on the azimuthal boundaries to match the fields of the upper boundary with the one of the lower boundary delayed with δt and at the interface between two rows. To avoid storing all the fields

at the boundaries during a blade passing period as initially performed by Erdos and Alzner [31], He [47] proposed to decompose the fields as Fourier series at the chorochronic boundaries where only the Fourier coefficients are computed and stored over one period. These coefficients are refreshed while the periodic state is not reached. This procedure is used in the scope of this PhD thesis.

This method is not valid for unsteady flow configurations including frequencies which are uncorrelated with the blade passing frequency (or its multiple), as the spectrum is locked both in space and time.

1.4 Conclusion

In Chapter 1, a general overview of the flow in an axial high-pressure turbine has been presented. Because of its positioning downstream of the combustion chamber, the flow at the inlet of the high-pressure turbine presents all the features and the history of the flow that passed through the combustor: residual swirl, temperature non-uniformities and high levels of turbulence. That being said, the flow in a turbomachinery component is naturally complex and unsteady because of the curvatures and the shapes of the geometries and the presence of boundary layers that make three-dimensional effects playing a major role. The rotation of a row with respect to another also strongly impacts the flow in the turbine stage as well as technological effects that are present for structural reasons. All this makes the high-pressure turbine a complex environment where multiple physical phenomena occur and interact between themselves. Numerical methods have been developed to deal with complex flows. They are all based on the discretisation on a grid and the resolution of the Navier-Stokes equations. The methods mainly differ in the way turbulence is solved. DNS is the most precise but most costly method, as all the scales of turbulence are solved. An intermediate level consists in solving the largest scales of turbulence and in modelling the small isotropic turbulence structures (LES). The backbone of the resolution of the Navier-Stokes equations is the RANS approach where all the turbulence is modelled. Its wide use in industry is due to its low computational cost and good turbomachinery overall performance predictions. However, with this modelling, since the flow is fully turbulent, the laminar-turbulent transition must be modelled as well. The URANS approach is used when solving the mean flow and a low-frequency phenomenon, related to the BPF of a turbomachinery component. To even reduce the computational cost when simulating turbomachinery components with the URANS, reduction techniques have been implemented. They enable to capture phenomena that are correlated with the BPF and its harmonics. Otherwise, a full annular simulation must be performed, with increased computational costs.

Dans le Chapitre 1, une présentation global de l'écoulement dans les turbines haute-pression a été réalisée. Puisque ce composant est situé juste en aval de la chambre de combustion, l'écoulement à l'entrée de la turbine présente toutes les caractéristiques

et historique de l'écoulement qui est passé dans la chambre de combustion : giration résiduelle, non-uniformités de température et hauts niveaux de turbulence. Cela étant dit, l'écoulement dans un composant de turbomachine est naturellement complexe et instationnaire à cause de la courbure et de la forme des géométries, mais aussi en raison de la présence des couches limite qui font des effets tridimensionnels un acteur majeur. La rotation d'une roue par rapport à une autre impacte également fortement l'écoulement dans l'étage de turbine ainsi que les effets technologiques qui sont présents pour des raisons structurelles. Tout cela fait de la turbine haute pression un environnement complexe où de multiples phénomènes physiques se produisent et interagissent entre eux. Des méthodes numériques ont été développées pour traiter les écoulements complexes. Elles sont toutes basées sur la discrétisation des équations de Navier-Stokes sur une grille et leur résolution. Les méthodes diffèrent principalement par la façon dont la turbulence est résolue. La DNS est la méthode la plus précise mais la plus coûteuse, car toutes les échelles de la turbulence sont résolues. Un niveau intermédiaire consiste à résoudre les plus grandes échelles de turbulence et à modéliser les petites structures de turbulence isotropes (LES). Le pilier de la résolution des équations de Navier-Stokes est l'approche RANS où toute la turbulence est modélisée. Sa large utilisation dans l'industrie est due à son faible coût de calcul et aux bonnes prédictions des performances globales des turbomachines. Cependant, avec cette modélisation, puisque l'écoulement est entièrement turbulent, la transition laminaire-turbulent doit également être modélisée. L'approche URANS est utilisée pour résoudre l'écoulement moyen et un phénomène à basse fréquence, lié à la BPF d'un composant de turbomachine. Afin de réduire le coût de calcul lors de la simulation de composants de turbomachines avec l'approche URANS, des techniques de réduction ont été mises en œuvre. Elles permettent de capturer les phénomènes qui sont corrélés avec la BPF et ses harmoniques. Dans le cas contraire, une simulation annulaire complète doit être effectuée, avec des coûts de calcul accrus.

Preliminary study on the FACTOR configuration

“ *Of all the fluid-dynamic devices invented by the human race, axial-flow turbomachines are probably the most complicated.* ”

Peter Bradshaw

Abstract

This chapter focuses on the numerical simulations of a high-pressure low-speed turbine fed by a modern lean combustion chamber including the presence of hot streaks at the combustor/turbine interface. The project itself is firstly described along with the geometry, operating conditions and available experimental data. Previous simulations are also presented. Before presenting preliminary results to assess the difficulty of correctly predicting the dynamics of the flow on this configuration with different approaches (steady mixing-plane, phase-lagged, sliding mesh, without and with cooling holes and cavity purge flows), the numerical set-up and convergence study are given.

2.1	Presentation of the FACTOR project	43
2.1.1	Motivations	43
2.1.2	Test rigs and operating conditions	44
2.1.3	The use of CFD in the scope of FACTOR	45
2.1.4	Experimental data	51
2.2	Numerical set-up	54
2.2.1	Numerical domain	54
2.2.2	Angular adjustment of the profiles	54
2.2.3	Boundary conditions	55
2.2.4	Meshing strategy	58
2.2.5	Numerical parameters	60
2.3	Convergence and computational cost	62
2.3.1	Steady simulations	62
2.3.2	Unsteady simulations	63
2.3.3	Computational cost	66
2.4	Scope of investigation for the prediction of the hot streak transport	66

2.4.1	Impact of the clocking position on the hot streak migration and wall surface temperature	66
2.4.2	Variability of the operating point	69
2.4.3	Influence of unsteady simulations	72
2.4.4	Effect of the cooling	73
2.5	Conclusion	76

2.1 Presentation of the FACTOR project

2.1.1 Motivations

Most of the simulations presented in this PhD thesis are linked to the configuration of the FACTOR (Full Aero-thermal Combustor-Turbine interactiOn Research) project. The funder of this PhD thesis, Safran Helicopter Engines, was strongly involved in the project, as evidenced by the works of Koupper [60] and Thomas [119]. This project was launched in 2010 (and finished in 2017) with three main objectives:

1. Keep **competitiveness** in turbine stage design (increase materials lifetime, decrease specific fuel consumption - SFC);
2. Improve numerically the **combustor/turbine interface** treatment;
3. Develop and validate **high-fidelity numerical tools**.

Competitiveness because of the development of next-generation lean combustion chambers that must reduce CO_2/NO_x emissions. In classical Rich burn - Quick quench - Lean burn (RQL) combustion chambers, NO_x are massively created near stoichiometry during the quenching phase where most of the air is injected through dilution holes. Lean Partially Premixed (LPP) combustion only operates with an excess of air and cooling flow is injected through effusion cooling holes to shield the walls. The flame temperature is reduced, as a consequence leading to a net decrease of NO_x emissions (Figure 2.1). More details on the technologies can be found in [38, 87].

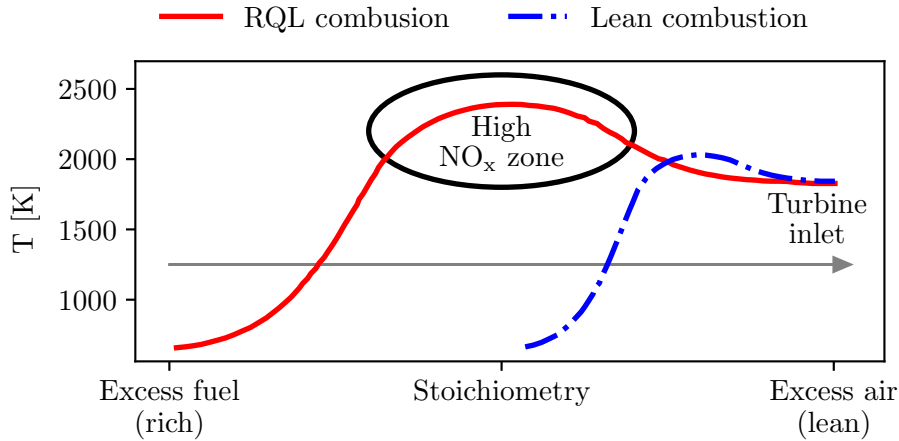


Figure 2.1 – NO_x are produced at high temperature close to stoichiometry. Adapted from Foust *et al.* [38].

Since less air is used (less mixing) and because of the compactness of the combustion chamber (shorter residence times), hot spots are expected to reach the high-pressure turbine with higher intensities. The high levels of swirl that are used to stabilise the flame affect the dynamics of the flow and the thermal stresses in the high-pressure turbine. Thus, the combustor and the turbine must be considered as a whole when dealing with numerical simulations of combustor/turbine interactions. Two options exist: either simulating the ensemble or better understanding and improving the **combustor/turbine interface**, for example imposing realistic turbine inlet boundary

conditions for an isolated turbine simulation, in which the hot streak migration remains realistic. Taking into account the coupling between the combustion chamber and the high-pressure turbine also involves unsteady phenomena: classical RANS mixing-plane simulations can not cope with combustion instabilities, cooling systems and purge cavities, heat transfer predictions, or vane/blade interactions. In that sense, the use of **high-fidelity numerical tools** is necessary (LES, URANS, solid-fluid coupling) and new turbine simulation methodologies should be developed.

Overall, «*the FACTOR objective is to optimise the combustor/turbine interactions design to develop low-cost turbines and reduce SFC by 2%, HPT weight by 1.5% and accordingly engine cost by 3% compared to the results from the TATEF2 and AITEB2 projects*».¹

2.1.2 Test rigs and operating conditions

In order to study the interactions between the combustion chamber and the high-pressure turbine, the geometry has been designed from scratch. It comprises a non-reacting combustion chamber simulator with effusion cooling holes, 20 axial swirlers, 40 film-cooled NGVs, 60 rotor blades with purge flow cavities, and 20 struts (see Figure 2.2). Different alignment of the swirlers with respect to the NGVs can be obtained by rotation of the combustion chamber: leading-edge clocking (LEC) where the swirler is aligned with the leading-edge of a NGV and passage clocking (PAC) where the swirler is aligned with the inter-NGV passage. The angular difference between the two clockings is less than half a NGV pitch (3.5° vs. 4.5°). Note also that the geometry has been designed to be *CFD-friendly* with a $1/20$ or 18° periodicity, leading to one swirler, two NGVs, three rotor blades, and one strut.

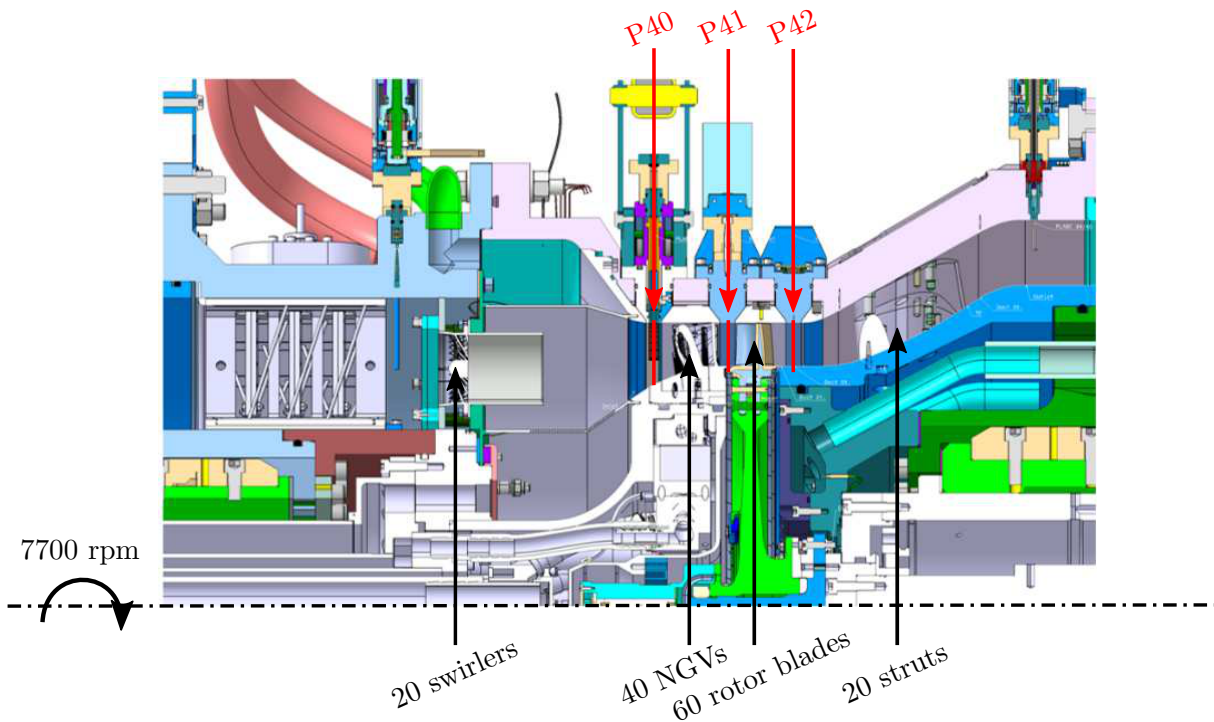


Figure 2.2 – Meridional view of the full-annular FACTOR configuration with the positioning of the measurement planes of interest.

¹From <https://cordis.europa.eu/project/id/265985/fr>.

Based on this geometry, two test facilities have been developed: in chronological order, a fixed trisector configuration at UNIFI (Università degli Studi di Firenze) in Florence [4] and then a full-annular 360° configuration installed at NG-Turb rig from DLR (Deutsches Zentrum für Luft-und Raumfahrt) in Göttingen [62]. The trisector rig features 54° of the full-annular rig with two possible configurations: one which features only the combustor, and another that has both the combustor and the NGVs. They have been used to validate the full 360° rig as well as to allow deep investigations inside the chamber without NGVs and the potential effect with NGVs either numerically or experimentally [4, 60, 61].

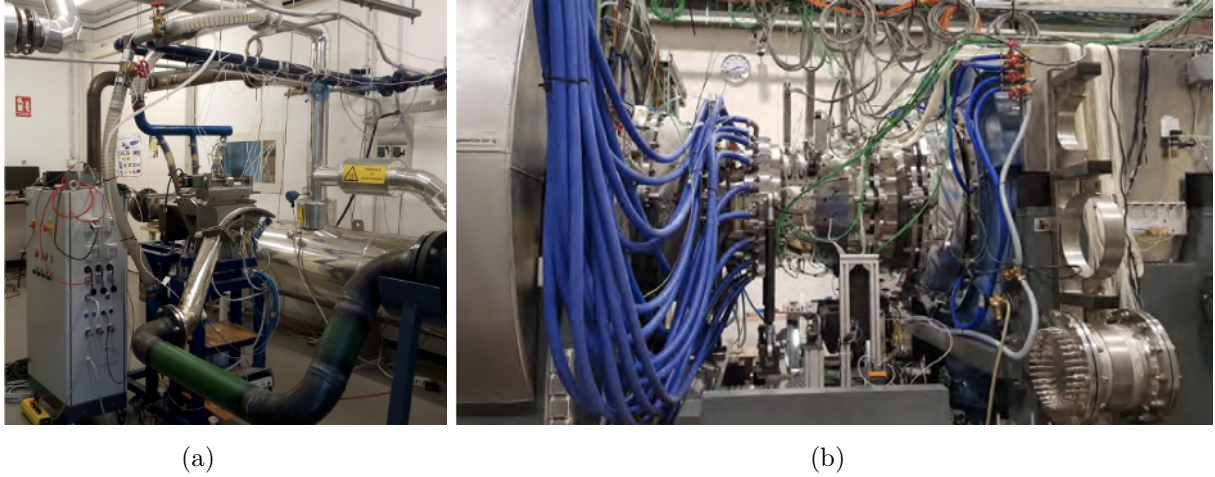


Figure 2.3 – Trisector (a) and full-annular (b) test rigs respectively installed at UNIFI and DLR.

The full-annular rig at DLR will only be focused on since it is the one used in all numerical simulations. Air is heated up to 513 K in a plenum before passing through the swirler and a 55 mm long cylinder to preserve the swirler velocity profiles and other flow characteristics [60] with high levels of turbulence (up to 30 %). Cold air at 300 K is injected through the effusion cooling holes at the inner and outer walls. Film cooling is present at the NGVs’ surfaces as well as cavity purge flows upstream and downstream of the rotor blades. The absolute Mach number is close to 0.13 at P40 (combustor/turbine plane), about 0.9 at P41 (NGV outlet plane) and 0.4 at P42 (rotor blade outlet plane). The vane inlet Reynolds number based on the NGV axial chord is about $1.1 \cdot 10^5$. Details of the operating point (OP) conditions are presented in Table 2.1.

2.1.3 The use of CFD in the scope of FACTOR

Since its launch in 2010, the number of publications in the field of combustor/turbine interactions, combustor exit, or hot streak has greatly increased. Especially, as it will be seen later on, with this particular non-reacting set-up, hydrodynamic instabilities can appear and have been widely tackled in the literature. On FACTOR, this vortex or Precessing Vortex Core (PVC) oscillates at 500 Hz. In the work of Thomas *et al.* [121], the authors characterised this PVC by performing a Proper Orthogonal Decomposition (POD). They showed that only the first energetic modes were required to characterise the PVC since they were associated with the biggest structures of the flow with a long characteristic time. Martin *et al.* [75] have drawn similar conclusions with the use of Spectral Proper Orthogonal Decomposition (SPOD). Such instability has a strong influence on the dynamics of the flow in the high-pressure turbine, particularly on the transport of hot streaks, as it can reach P40 and still exist at the outlet of the NGV.

Parameter description	Value	Unit
Inlet pressure (static \approx total)	143	kPa
Outlet static pressure	53.7	kPa
Pressure ratio (total-to-static)	2.7	-
Swirler massflow	3.09	kg.s ⁻¹
Combustor coolant feed total	1.88	kg.s ⁻¹
Combustor outer coolant massflow	0.95	kg.s ⁻¹
Combustor inner coolant massflow	0.67	kg.s ⁻¹
Rotor front cavity coolant massflow	0.072	kg.s ⁻¹
Rotor back cavity coolant massflow	0.072	kg.s ⁻¹
NGV cold coolant feed massflow	0.36	kg.s ⁻¹
Swirler air temperature	513	K
Coolant temperature	300	K
Turbine rotor RPM	7700	rpm
Turbine rotor power	395	kW
Turbine rotor torque	490	Nm

Table 2.1 – Operating point for the full-annular test rig at DLR (LEC).

Numerous numerical studies (LES, URANS and RANS) have compared whether or not to take into account this instability through:

- Coupled combustor/turbine simulations;
- Isolated turbine simulations;
- Steady simulations;
- Unsteady simulations.

The instability at the turbine inlet is the result of a coupling between swirl, temperature distortions and turbulence intensity. What is its impact on the dynamics of the flow in the high-pressure turbine, especially on the transport of hot streaks and how to model it?

2.1.3.1 Coupled vs. Isolated

Choosing between a coupled or an isolated simulation is often a question of available resources, since computational costs are high: performing a coupled simulation means taking into account the combustion chamber in which phenomena have a long characteristic time and low Mach number but also where multi-perforations must be either resolved (with very fine meshes) or modelled. Industrials preferably perform isolated simulations in which only the turbine stage is considered and boundary conditions are applied at the inlet of the turbine. It is proposed here to discuss the differences between coupled and isolated simulations from an aerodynamic and aerothermal point of view.

Coupled combustor/turbine simulations of the FACTOR configuration showed an important activity of the PVC. By performing LES, Thomas *et al.* [120] highlighted strong pressure fluctuations at the frequency of the PVC on the NGVs' walls as well as temperature fluctuations

at P41 driven by the presence of the PVC. Martin *et al.* [75] and Thomas *et al.* [121] also compared coupled simulations with isolated turbine simulations in which different energetic modes decomposed with SPOD or POD were imposed at P40: they showed that if the energetic selection did not take into account the PVC, the thermal mixing was under-estimated and temperature gradients at P41 were more intense than in the coupled simulations of reference. This can be explained by the fact that imposing the PVC enables to consider the biggest structures that dissipate less, so that their kinetic energy is more important. The same approach has been conducted with (U)RANS simulations: Andreini *et al.* [2] and Cubeda *et al.* [22, 23] studied the standalone combustor: they showed that the RANS over-predicts the temperature at P40 since the PVC was not captured. They also showed that a SAS-SST² simulation led to a relevant distribution at P40 compared to the experiments (Figure 2.4).

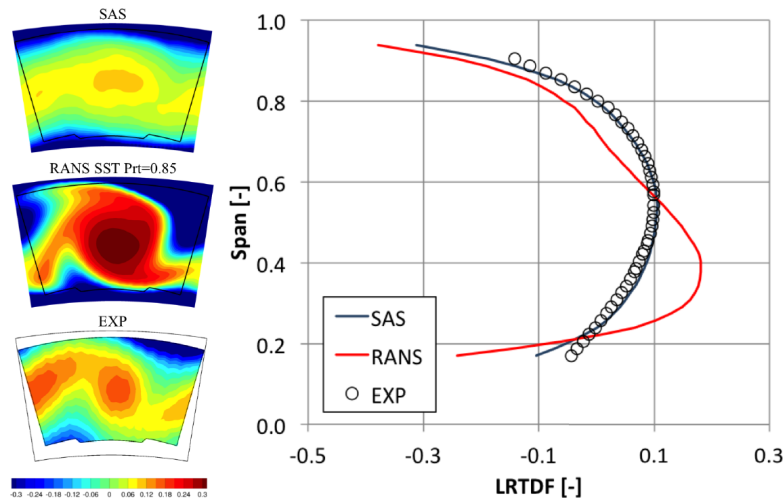


Figure 2.4 – Comparison of the normalised temperature distributions at P40 between experiments and standalone combustor simulations [22].

When taking into account the turbine stage downstream P40, the authors agreed that:

- A RANS isolated simulation with steady inlet boundary conditions coming from a SAS-SST simulation (so boundary conditions close to an experiment) would not promote correctly the mixing: the thermal loading of the vanes is higher [22, 49] (Figure 2.5), secondary flows are more important (which leads to a more important transport of cold flow toward the center of the NGV) but the aerodynamics seems well captured;
- Performing a coupled simulation was not the only requirement to reproduce the mixing: numerically, turbulence must be properly set. In that sense, Cottier *et al.* [21] showed that a coupled simulation with a SST $k - \omega$ turbulence model did not allow a correct transport of temperature. The transition to a SAS-SST model corrected that former problem so that the flow was mixed properly. They also showed that the hot streak redistribution mainly occurred in the NGV and to a lesser extent in the rotor.

Thus, a coupled simulation with a SST-SAS method enables to reproduce the impact of the unsteady fluctuations on the turbulence mixing and to have a better interaction between cold and hot flows. Temperature distributions on the NGVs' walls are more uniform.

²SAS: Scale-Adaptive Simulation, is an unsteady method coupling URANS in stable regions and LES in unstable regions of the flow.

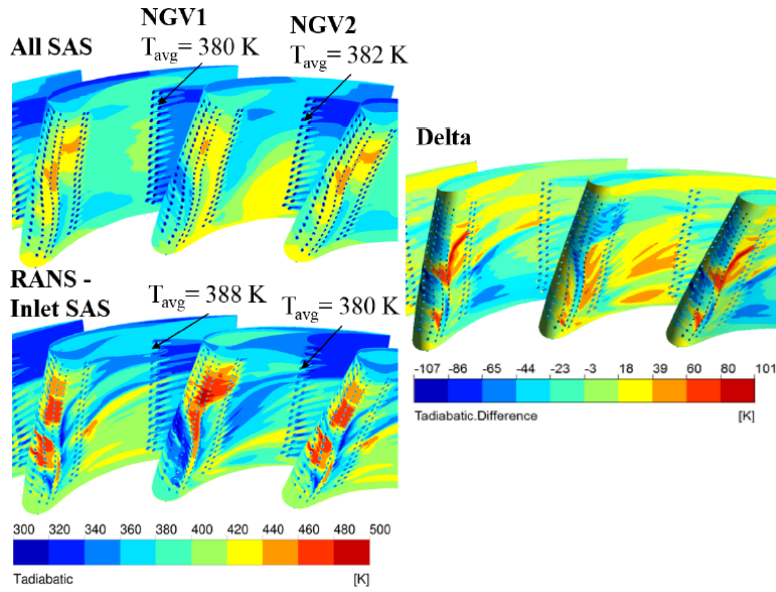


Figure 2.5 – NGVs’ adiabatic wall temperature - Comparisons between a full SAS-SST combustor/turbine simulation and an isolated RANS simulation with the inlet boundary condition from a SAS-SST simulation [22].

2.1.3.2 Steady vs. Unsteady

With an isolated simulation, the questioning of the inlet boundary condition is essential: should it be steady or unsteady? First indications have already been given implicitly in the previous paragraph. In their modal decomposition, Martin *et al.* [75] and Thomas *et al.* [121] reproduced a steady boundary condition at P40: in this case, they showed that the mixing was poor with secondary flows that were too important (since the unsteady oscillation is not present to break them) which provoked a too important migration of the cold flow toward the center of the NGV’s height that affected the local static temperature distribution on the walls (Figure 2.6).

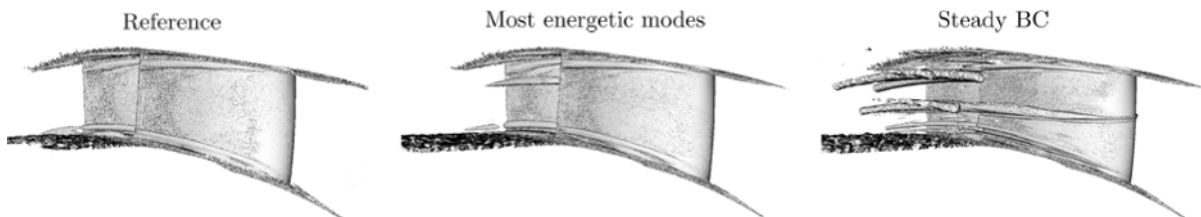


Figure 2.6 – Visualization of vortex structures in the NGV passage using an isosurface of Q-criterion (10^8) on solutions averaged over 40 ms [121].

On the contrary, they indicated that for an isolated turbine unsteady simulation where the energetic modes representative of the PVC were selected, temperature fields at P41 were correct since the velocity and temperature fluctuations were imposed properly.

In the steady case with RANS, Vagnoli *et al.* [129] overestimated the temperature levels at P41 and P42 as well as on the NGVs’ walls. They pointed out the fact that turbulence behaved differently between RANS simulations and LES and that it impacted the mixing (with

a strong coupling with the PVC), by its chaotic anisotropic nature amplified by the presence of vorticity. From a numerical point of view, the questioning of turbulence in (U)RANS method is fundamental, as it is fully modelled and that its behaviour varies from one model to another. Vagnoli *et al.* [129] widely analysed this issue with the imposition of the turbulent inlet boundary conditions. They concluded that it was necessary to use a SST $k - \omega$ model and to calibrate the dissipation, expressed in terms of μ_T/μ , at the inlet in order to best fit the total temperature radial distributions at the outlet of the NGV. While obtaining the correct turbulent kinetic energy evolution upstream of the NGV (see Figure 2.7), they showed an overestimation of the total temperature distribution at the outlet of the NGV compared to a reference LES, possibly because of the instability of the PVC or a lack of turbulent information. The use of non-linear eddy-viscosity turbulence models might be a solution to deal with anisotropy. In their paper, Cottier *et al.* [21] concluded that unsteady boundary conditions at P40 would enable to reproduce the low frequencies generated by the combustion chamber (swirl, mixing and hot streak). To the author's knowledge, this procedure has never been done in the context of FACTOR with the URANS method and is performed in Chapter 6.

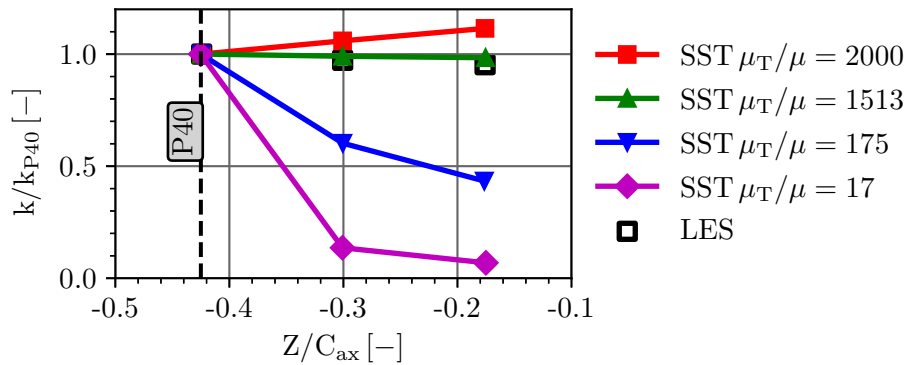


Figure 2.7 – Evolution of the turbulent kinetic energy upstream of the NGV of FACTOR for different values of dissipation. Reproduced from Vagnoli *et al.* [129].

The literature review applied to FACTOR showed the difficulties to predict both the aerodynamic and aerothermal behaviour of the flow in the turbine stage, due to the unsteady nature of the flow at the turbine inlet, but also due to the limitations of the numerical methods employed. Table 2.2 sums-up the main simulations performed in the scope of the FACTOR configuration.

Authors	Year	Institution	Solver	Method	Geometry	References
Koupper <i>et al.</i>	2015	CERFACS	ABVP	LES	CC + NGVs	[60, 61]
Andreini <i>et al.</i>	2015	UNIFI	CFX, Fluent	(U)RANS, SAS-SST	CC	[2]
Vagnoli <i>et al.</i>	2016	VKI	FINE/Turbo	RANS	Isolated NGVs	[129]
Duchaine <i>et al.</i>	2017	CERFACS	AVBP	LES	CC + NGVs, Isolated NGVs	[29]
Barhaghi and Hedlund	2018	Siemens	CFX	(U)RANS, SAS-SST, LES	CC	[6]
Thomas <i>et al.</i>	2018, 2019	CERFACS	AVBP	LES	CC + NGVs, CC + NGVs + Blades, Isolated NGVs	[120, 121]
Cubeda <i>et al.</i>	2018, 2019	UNIFI	Fluent	(U)RANS, SAS-SST	CC + NGVs, Isolated NGVs	[22, 23]
Cottier <i>et al.</i>	2019	MTU	CFX	(U)RANS, SAS-SST	CC + NGVs, Isolated NGVs	[21]
Gövert <i>et al.</i>	2019	DLR	TRACE	RANS	CC + NGVs	[45]
Luquet <i>et al.</i>	2019	Safran	elsA	(U)RANS	NGVs + Blades + Strut	[71]
Martin	2021	CERFACS	AVBP	LES	CC + NGVs, CC + NGVs + Blades + Strut, Isolated NGVs	[73]

Table 2.2 – Main numerical simulations realised in the scope of the FACTOR project - CC and NGV respectively stands for combustion chamber and nozzle guide vane.

2.1.4 Experimental data

2.1.4.1 Available data

Through the FACTOR project, a large experimental database has been generated on both test facilities, making possible direct comparisons with the numerical simulations. Bacci [4] and Koupper [60] made a detailed review of the instrumentation used for the UNIFI trisector rig. The same type of instrumentation has been used for the full-annular rig at DLR [62]. Among all the data obtained with intrusive and semi-intrusive techniques for both clocking positions, exploited data in this PhD thesis are:

- **Steady five-hole probes (5HP)** measurements at P40, P41 and P42, where the reference planes are displayed in Figure 2.2. Data were obtained with a cobra probe equipped with a thermocouple mounted on an automatic $r - \theta$ traverse system where P_t , T_t , M and flow angles were measured over a sector covering at least 18° . For every evenly distributed single measurement point, because of the strong flow gradients, the probes were pre-aligned to face the local tangential direction of the flow. Missing measurement zones in the core of the flow were filled with the method proposed by Garcia [40] leading to the current data. Note that due to the head size of the probe, the radial extension of the measurements could not cover the whole vein height. Table 2.3 presents some elements of the measurement campaign;

Plane	Angular extend [$^\circ$]	Radial extension [% h/H]	Measured surface [% sector]	Nb. radial points	Nb. azimuthal points	Total points
P40 - LEC	20.25	6.7 – 96.3	90.7	41	42	1722
P40 - PAC	20.5	7.1 – 98.0	91.1	31	28	868
P41 - LEC	19.95	10.2 – 98.5	88.8	29	58	1682
P41 - PAC	21	10.2 – 98.5	88.8	29	61	1769
P42 - LEC	19.95	10.2 – 98.5	88.8	29	43	1682
P42 - PAC	26.95	10.2 – 98.5	88.8	29	50	1450

Table 2.3 – Coverage of the measurements with the traverse system at P40, P41 and P42 for LEC and PAC.

- **Steady wall static pressure** measurements at about 50% NGV’s height. Signals were recorded during 3 – 5 hours at 20 different positions (10 on the PS of one NGV and 10 on the SS of an adjacent NGV);
- **Steady hub and shroud static pressure taps** at P40, P41 and P42, with 3 to 5 hours of measurement when the steady regime was reached;
- **Unsteady pressure measurements obtained with fast-response aerodynamic probes (FRAP)** at P40 and P42 where data were sampled at 500 kHz filtered at 125 kHz, leading to 16 points per blade passage. As for the 5HP measurements, a yaw angle is imposed to align the FRAP with the flow direction.

Experimentally, Bacci [4] showed on the trisector rig the presence of the PVC at P40 that remained present at P41. Power spectral densities (PSD) of turbulent kinetic measurements obtained with hot-wire anemometry (HWA) showed that the PVC accounts for 4% to 7% of the

turbulent kinetic energy at P40 (Figure 2.8) and 2.5% to 5% at P41. It strongly evidences the unsteady behaviour of the flow due to the presence of the vortex.

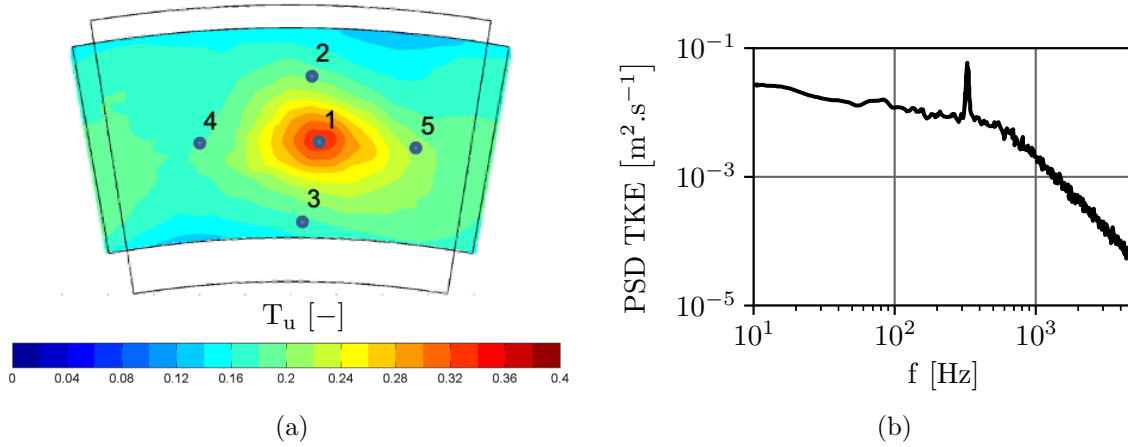


Figure 2.8 – Turbulence intensity on P40 (a) and PSD of turbulent kinetic energy at point 1 (b).

2.1.4.2 Post-processing of the data

Data from the 5HP are post-processed with in-house Safran Helicopter Engines scripts used to analyse CFD and thermodynamic averages based on *Antares* [3] developed at CERFACS to enable a fair and direct comparison with the results of the numerical simulations. Zones obtained by extrapolation at the hub and shroud are marked with gray zones. Specific post-processing of the FRAP is presented in Chapter 6. Other data are raw compared with the simulations.

2.1.4.3 Missing data at P40 and uncertainties

Data from the 5HP at P40 are used as inlet boundary conditions for the simulations of FACTOR. When using a 5HP, the measurement is possible within a certain range of flow direction which is obtained from the probe calibration. In general, the probe is pre-aligned in the mean direction of the flow to keep measurement errors as low as possible. For example, if the measurement is performed at the outlet of the NGV, it is fair enough to say that the mean flow follows the deviation of the vane at the TE.

Nevertheless, in the specific case of P40, because of the flow history coming from the combustion chamber, and especially the strong radial and azimuthal velocities distortions, the pre-alignment was not possible during FACTOR’s measurement campaign. Krumme *et al.* [62] revealed numerous difficulties at P40 using 5HP, as shown in Figure 2.9a. Missing data labelled ‘a’ and ‘b’ are due to the geometry of the probe and problems in the traverse system, and huge blank spaces ‘c’ are a consequence of the probe calibration that did not yield results from the existing raw probe pressure data. The latter is explained by the high values of flow angles at P40, that lead to blank spaces for angles greater than $\pm 30^\circ$, as represented in Figure 2.9a. Here, the focus lies on P40, which is of interest as it is used for the inlet boundary conditions, but note that blanks of type ‘c’ are not observed at P41 and P42. The interpolation method named INPAINTN and developed by Rolls-Royce Deutschland is then used to fill ‘a’, ‘b’ and ‘c’ zones, leading for instance to the result depicted in Figure 2.9b. One of the first questions that arise with this kind of post-processing is: how reliable is this method at P40, since the plane is then used as

inlet boundary conditions? This question is addressed in Chapter 6. Figure 2.9b clearly shows that the zone of high temperature is the zone of high flow angles which was not measured, and accounts for about 40% of the surface area. Thinking also in terms of CFD and total temperature transport inside FACTOR’s configuration, the literature review presented in 2.1.3 revealed a lack of predictability of temperature distributions at the outlet of the NGV. In that sense, this interpolation process at P40 may be questionable.

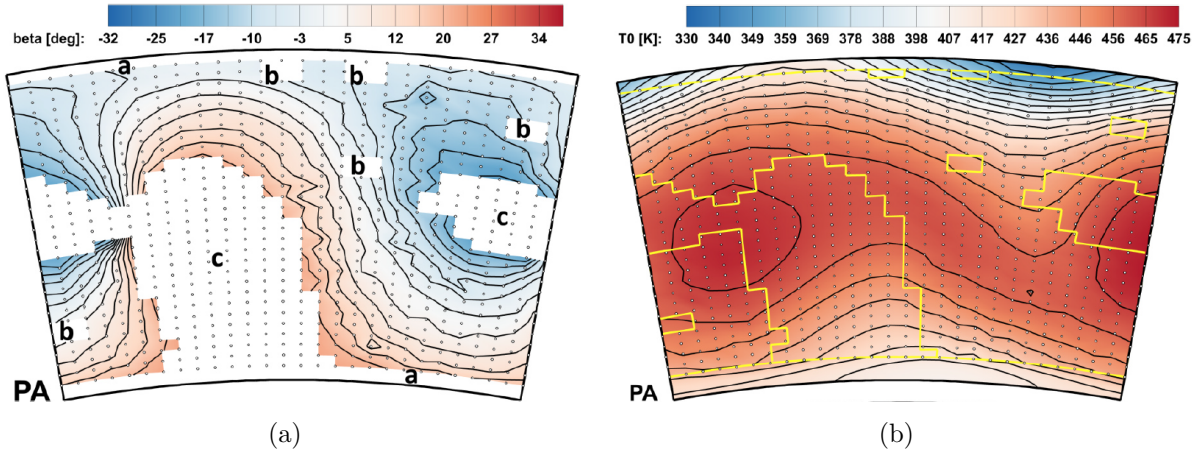


Figure 2.9 – 5HP results obtained for the pitch angle (a) and results of INPAINTN interpolation for the total temperature at P40 (b). Yellow lines delineate measured and interpolated zones [62].

In terms of uncertainties, some errors only for the 5HP are available and are plotted in Figure 2.10: within the range of Mach numbers encountered (0.1-0.95), the errors on the swirl angle and the Mach number are kept low, less than 0.3° for the swirl angle and less than 0.005 for the Mach number.

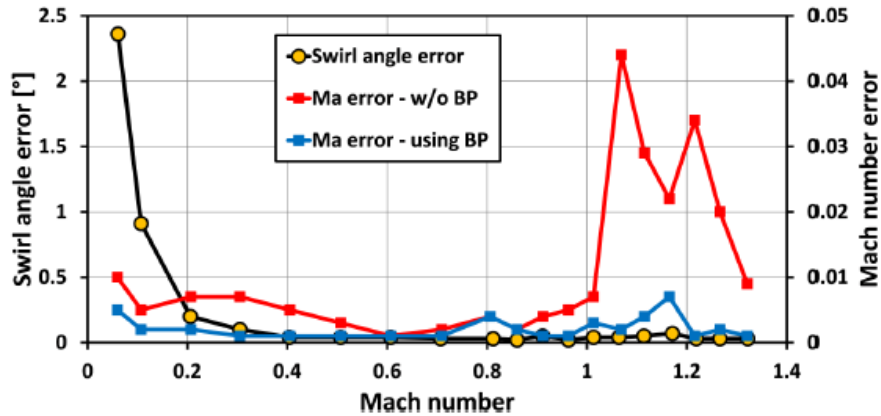


Figure 2.10 – Errors on the Mach number and swirl angle for the 5HP [62].

2.1.4.4 Use of the data within the manuscript

Experimental data are used as a basis for comparison with the numerical simulations. CFD results are systematically compared to the 5HP, either with plane-to-plane or radial distribution comparisons. Comparisons are extended with static pressure taps and FRAP in Chapter 6. A summary of the use of experimental data is done in Table 2.4.

Experimental data	Chapter
Five-hole probes	Chapter 2, Chapter 5, Chapter 6
Wall NGV static pressure	Chapter 6
Hub and shroud static pressure	Chapter 6
FRAP	Chapter 6

Table 2.4 – Summary of the use of available experimental data in the manuscript.

2.2 Numerical set-up

2.2.1 Numerical domain

For the present studies, the simulation domain is composed of the high-pressure turbine stage with two NGVs and either one or three rotor blades depending on the type of (U)RANS simulation:

- One rotor blade: mixing-plane and chorochronic simulations (blue domain of Figure 2.11 on the left);
- Three rotor blades: reduced sector number (RSN) simulations based on the natural periodicity of the configuration (blue+red domain of Figure 2.11 on the left).

A blade tip gap of 0.48 mm is imposed (1.2% of the vein height). The inlet of the domain is the combustor/turbine interface P40, which is located $0.425 \cdot Ca_{x,S}$ upstream of the NGV LE, where $Ca_{x,S}$ is the axial chord of the NGV and measures 40 mm. P41 is positioned $0.2 \cdot Ca_{x,S}$ downstream the TE of the NGV and the interface 0.4 mm downstream P41. P42 and the outlet are respectively $0.625 \cdot Ca_{x,R}$ and $0.875 \cdot Ca_{x,R}$ downstream the TE of the rotor blade where $Ca_{x,R}$ is the axial chord of the rotor blade. The vein has a convergent shape from the inlet to the TE of the NGV where the vein height is $Ca_{x,S}$. Note that normally, for mono-passage simulation methods (mixing-plane and phase-lagged), only one NGV is sufficient. But since there is one swirler for two NGVs on the FACTOR's configuration, two NGVs are considered to preserve the effect of the clocking. Note also that in the scope of this PhD thesis, the fillets are not taken into account. Previous simulations at Safran Helicopter Engines have shown a negligible effect of the fillets on the redistribution of a hot spot. Finally, the squealer tip, which would have been taken into account using a Chimera method [7], is not regarded. Some differences are thus expected near the shroud of the rotor blade when compared to the experiments or other numerical simulations containing the squealer tip. However, the focus of this PhD thesis is on the HS.

2.2.2 Angular adjustment of the profiles

To have a quick overview of the behaviour of the flow in the configuration, first simulations are performed without considering cooling holes or purge cavities. They are called «*smooth vein simulations*» (SV) throughout this manuscript (as opposed to «*cooled vein simulations*» - CV - when cooling is taken into account). By doing so, the work extracted by the rotor, or simply the degree of reaction (DR), is modified. To avoid that, the NGV and rotor blade profiles are opened or closed, which corresponds to a modification of the stagger angle. In the present simulations, the modification consists of the opening or closing of the NGV and rotor blade profiles by a few tens of degrees for both clocking positions.

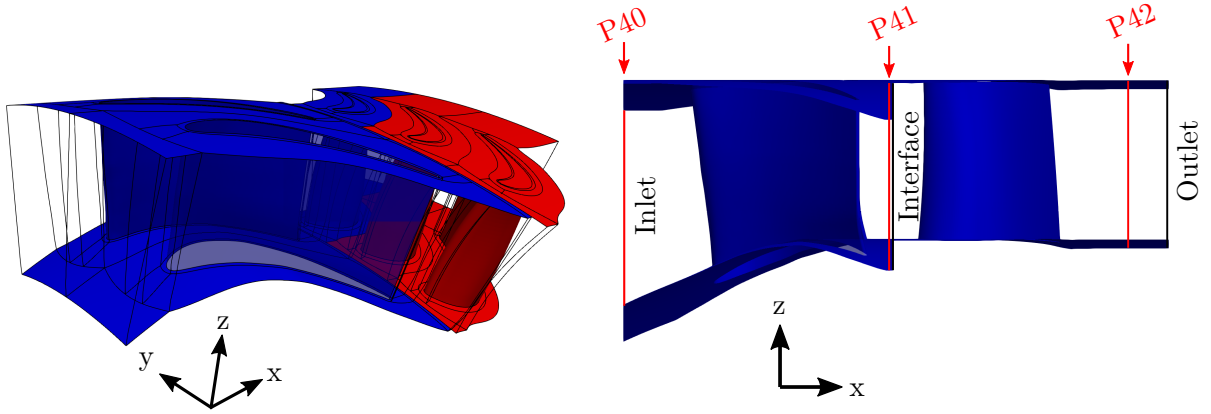


Figure 2.11 – 3D view of the numerical domain on the left: blue for mixing-plane and phase-lagged simulations; blue+red for reduced section number simulations - Meridional view of the domain on the right.

2.2.3 Boundary conditions

2.2.3.1 Inlet

The inlet conditions are subsonic inlet boundary conditions. 2D steady maps obtained from the 5HP and the INPAINTN interpolation are imposed at the inlet of the domain in terms of total temperature T_t , total pressure P_t and flow angles α and ϕ by clipping the data on a periodic sector and duplicating them to cover the entire inlet plane. 1D distribution of turbulence obtained with HWA at UNIFI or the equivalent 0D values for k and l_T are also imposed (where a scaling on k is applied to convert isothermal conditions to nominal conditions). When dealing with the SV simulations, a scaling-shifting on the values of P_t and T_t is applied to reproduce a hypothetical cooling in the NGVs' domain by targeting dimensionless quantities: reduced massflow \dot{m}_{red} and reduced rotational speed N_{red} at the LE of the rotor. Table 2.5 sums up the averaged values and Figure 2.12 shows the inlet aerodynamic fields for the cooled simulations.

Simulations type	$\langle \overline{P_t} \rangle_S$ [kPa]	$\langle \overline{T_t} \rangle_S$ [K]	$\langle \overline{k} \rangle_S$ [$\text{m}^2 \cdot \text{s}^{-2}$]	$\langle \overline{l_T} \rangle_S$ [mm]
Smooth vein LEC	142.3	429.6	168	9
Cooled vein LEC	142.4	441.4	168	9

Table 2.5 – Averaged values at the inlet boundary conditions for the smooth vein and cooled vein simulations.

2.2.3.2 Outlet

Static pressure P_s of 56 kPa with a radial equilibrium condition and a pivot position at $h/H = 0.5$ is applied at the outlet:

$$\frac{\partial P_s}{\partial r} = \rho \frac{v_\theta^2}{R} \quad (2.1)$$

Its value can vary slightly to match the dimensionless quantities \dot{m}_{red} and N_{red} .

2.2.3.3 Solid walls

The size of the first cell at the wall allows to reach a y^+ value smaller than 1 (Figure 2.17) and a no-slip boundary condition with adiabatic walls is used.

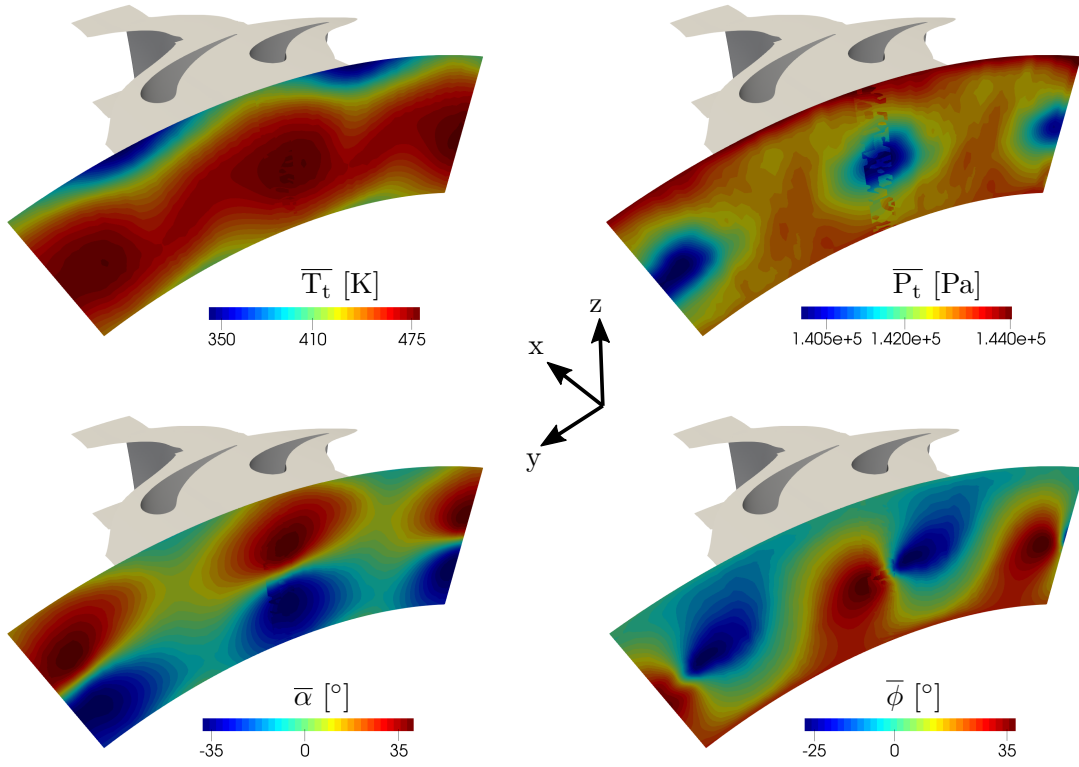


Figure 2.12 – Steady aerodynamic maps applied as inlet boundary conditions for the cooled vein simulations for the LEC configuration.

2.2.3.4 Azimuthal walls

For steady simulations and unsteady reduced sector number method simulations, matching periodicity is applied. A chorochronic condition is applied when dealing with phase-lagged simulations with 16 harmonics that are actualised at every iteration. The number of harmonics can be checked *a posteriori* when the solution is periodic. The last harmonics must be nearly equal to zero. Let us consider the field Φ at a given position of the boundary. The field can be decomposed with Fourier series such as:

$$\Phi(t) \approx a_0 + \underbrace{\sum_{n=1}^N a_n \cos\left(\frac{2\pi nt}{T}\right) + b_n \sin\left(\frac{2\pi nt}{T}\right)}_{n^{th} \text{ harmonic}} \quad (2.2)$$

Where T is the period of the stator T_S or the rotor T_R and a_n and b_n are the Fourier coefficients given by:

$$a_0 = \frac{1}{T} \int_{t_0}^{t_0+T} \Phi(t) dt \quad (2.3)$$

$$a_n = \frac{2}{T} \int_{t_0}^{t_0+T} \Phi(t) \cos\left(\frac{2\pi nt}{T}\right) dt \quad n \geq 1 \quad (2.4)$$

$$b_n = \frac{2}{T} \int_{t_0}^{t_0+T} \Phi(t) \sin\left(\frac{2\pi nt}{T}\right) dt \quad n \geq 1 \quad (2.5)$$

Figure 2.13 shows the Fourier coefficients for the 7 first harmonics for the density field at a

fixed position of the azimuthal boundary of the rotor row. It clearly shows that from the 5th harmonic, the Fourier coefficients are close to zero so that the original signal is well decomposed.

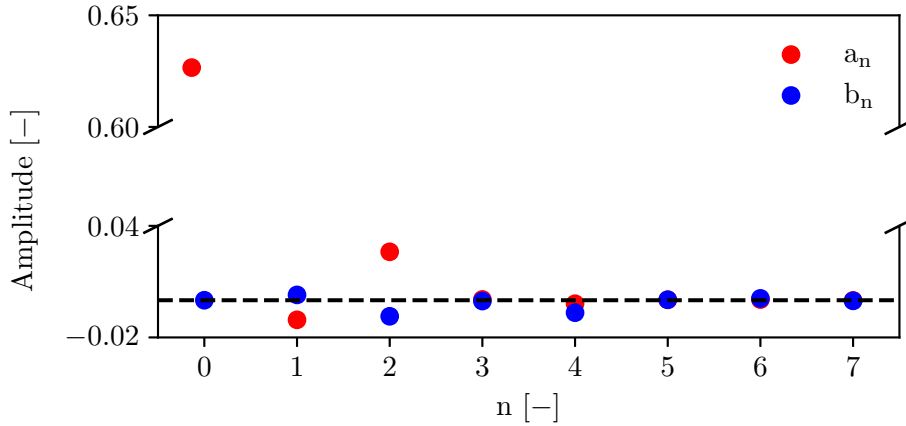


Figure 2.13 – Fourier coefficients of the density field at a fixed position of the rotor azimuthal boundary for a converged chorochronic simulation.

2.2.3.5 Cooling holes and purge cavities

Similarly to a real high-pressure turbine, the FACTOR’s configuration is fitted with a cooling system. It includes 171 holes grouped into 8 film rows on the NGV’s surface fed by two ducts and two purge flow cavities upstream and downstream of the rotor blade with a complex secondary air system. The diameter of the holes ranges from 0.5 mm to 0.8 mm. Each line of holes has a relative angle to the surface to best mix the cold flow with the mainstream flow. The cooling flow in the holes is $7.5\% \cdot \dot{m}_{P40}$ and $1.5\% \cdot \dot{m}_{P40}$ in each purge cavity, where \dot{m}_{P40} is the massflow at P40 comprising both the swirler massflow and the inner/out coolant massflow. The exact values can be found in Table 2.1 on page 46. To save computational time, cooling holes and purge cavities are not meshed. The 171 holes are replaced by 5 patches on the NGV’s walls (Figure 2.14) as well as the purge cavities that are replaced by 2 patches at the rotor hub. Massflow, enthalpy and flow angles are specified at each patch³ where the flow is set to quasi-laminar.

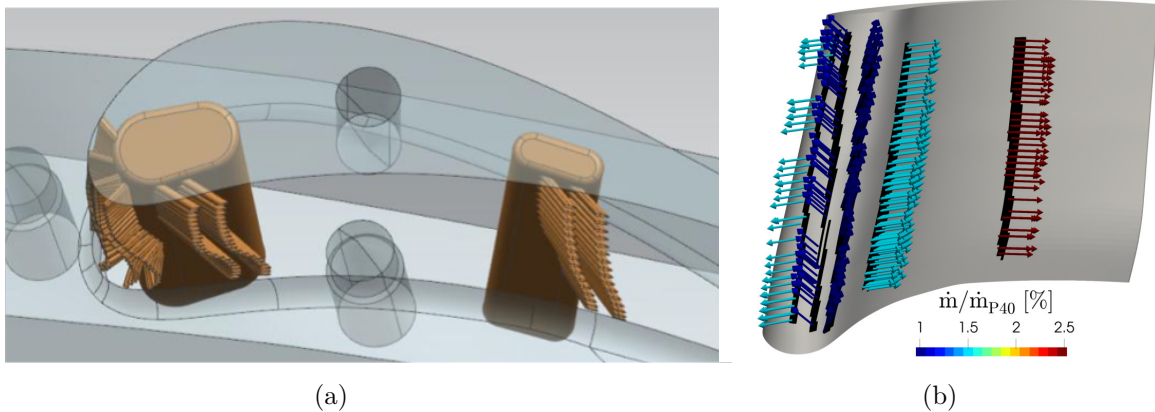


Figure 2.14 – Real cooling holes system with the plenum (a) - View of the patches that replace the cooling holes with unit normal vectors coloured by massflow (b).

³For the NGV’s cooling, the value of the cooling massflow presented in Table 2.1 is distributed over the patches knowing the initial number of holes in a given patch. The flow angles are the geometrical angles of the holes.

2.2.4 Meshing strategy

Meshes have been performed following a structured multi-blocks approach, which is suitable for configurations where very few technological effects are taken into account. Using the software *Autogrid5* developed by *Cadence*, a O-6H topology with periodic coincident joins has been used for both the vanes and blades, where the O-block around the solid body enables to capture correctly the boundary layer with a fine mesh while minimizing orthogonality errors. The remaining H-blocks are used to discretise the rest of the row. To avoid interpolation errors, all the blocks are joined with coincident boundaries. The only no-match join is located at the vane/blade interface. Figure 2.15 presents the blocking for the blade of FACTOR.

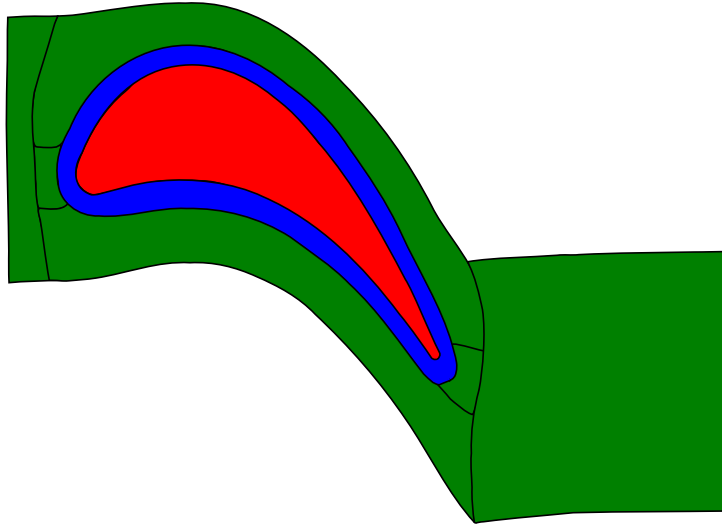


Figure 2.15 – Structured multi-blocks O-6H topology of FACTOR’s blade. H-blocks in green, O-block in blue and solid body in red. The boundaries of the blocks are displayed in solid black lines.

In terms of meshing, the following criteria have been used: around 100 layers are used to discretise the span, the cell size normal to the walls is $1\ \mu\text{m}$ and 37 cells are used to discretise the tip blade gap. In order to discretise the passage in the vane row and in the blade row, 68 cells and 48 cells are respectively used in the azimuthal direction. The mesh is refined at the LE and TE of the vane and the blade. Surface mesh can be visualised in Figure 2.16. In the entire domain, the expansion ratio⁴ is kept below 2 (except for the tip gap where a value of 3 is encountered), the orthogonality⁵ is greater than 18° and the maximum aspect ratio⁶ is 1330. Close to the walls, these criteria are stricter and are respectively smaller than 1.2, greater than 80° and below 500. All these metrics guarantee a good mesh quality. Preliminary internal studies on mesh convergence revealed that the current mesh is sufficient (see Appendix B - section B.2). The mesh size close to the walls ensures to reach the quality requirements for a wall-resolved simulation with $y^+ = 1$ and for which the first cell is in the viscous sub-layer of the boundary layer. Figure 2.17 shows the distribution of y^+ around the vane obtained for a RANS mixing-plane simulation. y^+ remains below unity for the surfaces. This behaviour is also observed for the blade, as well as for the hub and shroud surfaces (see Appendix B - section B.1).

⁴Ratio of the edge length between two successive cells.

⁵Angle between two contiguous faces of a cell.

⁶Ratio between the longer and shorter edge of a cell.

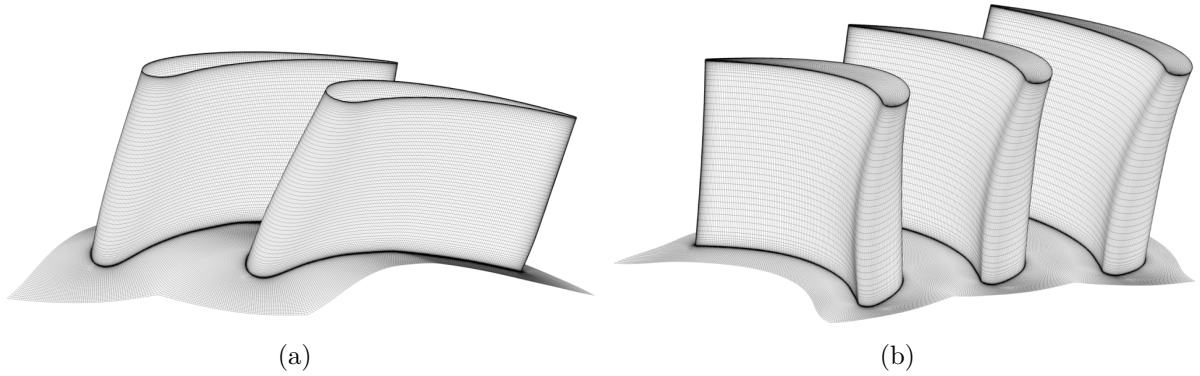


Figure 2.16 – View from upstream to downstream of the surface mesh on the vanes (a) and blades (b). Shroud walls have been voluntarily removed for sake of clarity.

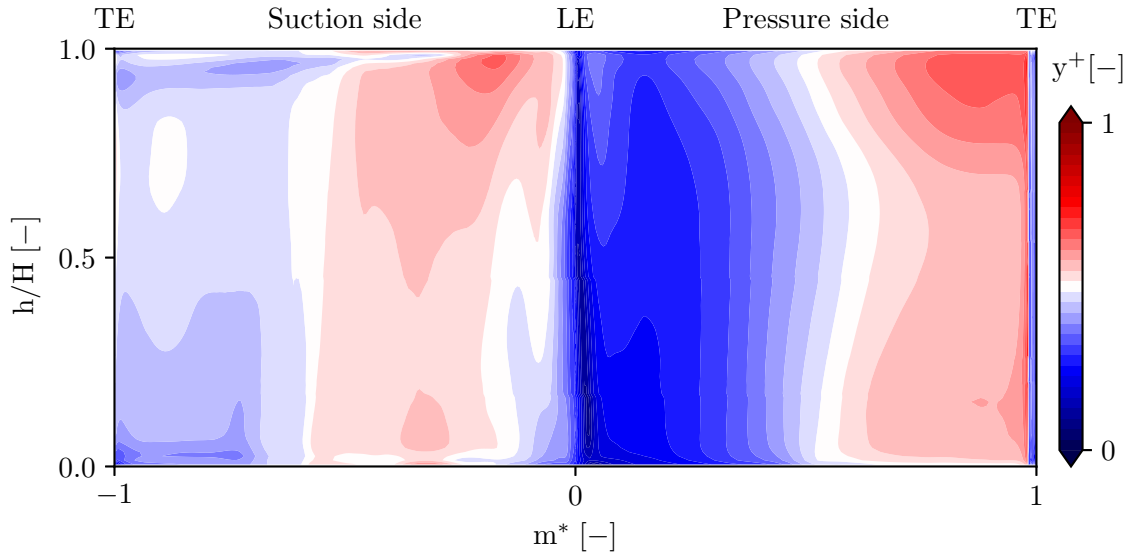


Figure 2.17 – y^+ distribution on the unwrapped NGV of FACTOR.

Overall, one single blade passage is composed of $3.3 \cdot 10^6$ cells in the vane row and $2.6 \cdot 10^6$ cells in the blade row. Table 2.6 sums-up the mesh sizes in the stator and the rotor after replication of the mesh for the mixing-plane, chorochronic and RSN simulations with the most important quality metrics.

Domain	Nb. cells (10^6) 2 vanes/1 blade	Nb. cells (10^6) 2 vanes/3 blades	Min. ortho- gonality	Max. expansion ratio	Max. aspect ratio
Stator	6.6	6.6	40.8	1.46	1099
Rotor	2.6	7.8	18.2	3.2	1330
Total	9.2	14.4	18.2	3.2	1330

Table 2.6 – Main features of the meshes used for both steady and unsteady simulations.

2.2.5 Numerical parameters

The starting point for the numerical parameters is chosen from the feedback and methodology of Fiquet [35].

2.2.5.1 Tools

Sirah

To ease the pre/post-processing and the simulations, *Sirah* has been used. *Sirah* (SIMulations aéRodynamiques elsA Hybride) is a software developed at Safran Helicopter Engines which aims at setting up and realising numerical simulations with the *elsA* CFD software from ONERA [90] and launching post-processings with the tool *AntS* based on *Antares* developed at CERFACS [3]. Structured, unstructured and hybrid meshes are accepted by the software. Basically, *Sirah* is an ensemble of Python scripts that generate an input card (where all the numerical parameters are stored) and a CGNS-based mesh required by the numerical solver *elsA*. Through this PhD thesis, new functions dealing with turbulence models have been implemented in *Sirah*, allowing the use of a multitude of classical turbulence models based on Boussinesq's hypothesis but also more advanced turbulence models (non-linear first-order turbulence models).

elsA

As above-mentioned, RANS and URANS simulations have been performed using the ONERA multi-physics *elsA* software [18], which is a multi-blocks cell-centred implicit solver that solves the compressible 3D Navier-Stokes equations on hexahedral meshes based on the following semi-discretised finite volume approach where the time-space integration is decoupled:

$$\frac{d}{dt} \mathbf{W}_\Omega = -\frac{1}{\mathcal{V}(\Omega)} \left[\sum_{i=1}^6 \mathbf{F}_\Omega \cdot \mathbf{N}_{\Sigma_i} - \mathcal{V}(\Omega) \mathbf{S}_\Omega \right] = -\frac{1}{\mathcal{V}(\Omega)} \mathbf{R}_\Omega \quad (2.6)$$

Where Ω is a control volume, \mathcal{V}_Ω the volume of the control volume, \mathbf{W}_Ω is a numerical approximation of the vector of the transported quantities, \mathbf{F}_Ω is the numerical flux (convective + diffusive), \mathbf{S}_Ω is an approximation of the source term which is equal to zero when Equation 2.6 is applied to the N-S equations. Finally, \mathbf{R}_Ω is called the numerical modelling residual. Space discretisation schemes include classical second order centred or upwind schemes. Pseudo-time integration can be performed using a backward Euler technique or using a 4-steps Runge-Kutta (RK4) scheme for steady simulations. However, the RK4 technique, which is explicit, requires very refined time resolution for stability reasons and will not be used in the following studies. The Gear method is used for unsteady simulations.

2.2.5.2 Steady simulations

For steady simulations, the backward Euler technique with the LU-SSOR decomposition [142] allows the use of a high CFL (Courant–Friedrichs–Lewy) number with a local time-stepping approach. The physical time t is replaced by a pseudo-time t^* that has no physical meaning. The convergence is reached when the derivative term on the pseudo-time goes to 0. In all the simulations, the CFL varies between 10 and 30. The convective fluxes are discretised using an upwind Roe scheme. The most important parameters used for the steady simulations are presented in Table 2.7.

Parameter	Value
Convective fluxes	2 nd order Roe scheme (minmod limiter)
Diffusive fluxes	Centred 5 points discretisation (2 nd order)
Time integration	Backward Euler (1 st order)
Implicit phase	LU-SSOR
CFL	10-30
Turbulence model	Smith $k - l$

Table 2.7 – Numerical set-up for the steady simulations of FACTOR.

2.2.5.3 Unsteady simulations

For unsteady simulations, the advance in time has a physical meaning and the time-step can not be different from one cell to another. It must be chosen carefully to capture the unsteady phenomena which are related to the BPF of an adjacent row. Let us consider the vane/blade configuration of FACTOR. By defining the parameter:

$$n_{qo} = \max(\min_{niter}/N_S, \min_{niter}/N_R) \quad (2.7)$$

Which facilitates the post-processing by dividing the characteristic periods into an entire number of time-steps. The global time-step of the simulation is therefore given by:

$$dt = \frac{2\pi}{n_{qo} N N_S N_R} \quad (2.8)$$

Typical values of $\mathcal{O}(10^2)$ for the number of iterations per period lead to values of $\mathcal{O}(10^5)$ for one wheel rotation, which is suitable for unsteady simulations. The time-step allows about 200 points per blade passage. A convergence study on the time-step is performed in 2.3. In the following unsteady simulations, the 2nd order time accurate Gear scheme with sub-iterations is used. The number of sub-iterations is fixed to 12. Other numerical parameters are summed-up in Table 2.8.

Parameter	Value
Convective fluxes	2 nd order Roe scheme (minmod limiter)
Diffusive fluxes	Centred 5 points discretisation (2 nd order)
Time integration	Gear (2 nd order)
Number of sub-iterations	12
Time-step	$6.49 \cdot 10^{-7}$ s
Implicit phase	LU-SSOR
Turbulence model	Smith $k - l$

Table 2.8 – Numerical set-up for the unsteady simulations of FACTOR.

2.2.5.4 The treatment of turbulence in the solver elsA

In Chapter 1, the general formulation of the most classical turbulence models have been presented. By performing a dimensional analysis, one can relate the turbulent quantities k , ϵ , ω and l_T by $\omega \propto k^{1/2}/l_T$ and $\epsilon \propto k^{3/2}/l_T$. Depending on how the models are implemented in the solver, *i.e.* how the constants are embedded, the proportionality coefficients can differ. It is

proposed here to give the proportionality for two distinct situations: when the turbulent length scale l_T is known and when the turbulent Reynolds number $Re_T = \mu_T/\mu$ is known. Note that the wall damping functions are neglected and that the turbulent kinetic energy k is an input, as it can be easily measured by experiments or by a high-fidelity simulation.

When the turbulent length scale l_T is provided, the dissipation and specific dissipation of turbulence read:

$$\epsilon = \frac{C_\mu B_1^{1/3} k^{3/2}}{\sqrt{2} l_T} \quad (2.9)$$

$$\omega = \frac{B_1^{1/3} k^{1/2}}{\sqrt{2} l_T} \quad (2.10)$$

However, this turbulent length scale is not always known. To overcome this problem, it is possible to specify the turbulent Reynolds number and the proportionality is given by:

$$Re_T = \frac{\rho\sqrt{2k}l_T}{\mu B_1^{1/3}} = \frac{\rho k}{\mu\omega} = C_\mu \frac{\rho k^2}{\mu\epsilon} \quad (2.11)$$

Where $B_1 = 18$ and $C_\mu = 0.09$. The switch from one turbulence model to another is now straightforward, as it will be done further in the manuscript. As also mentioned in Chapter 1, the production of k must be modelled. The term is either computed from the mean velocity strain rate tensor or from the vorticity tensor. For the present study, the computation from the vorticity tensor is retained.

2.3 Convergence and computational cost

2.3.1 Steady simulations

RANS simulations are based on the hypothesis that the flow variables do not vary with time which numerically means that they do not evolve from one iteration to another. All steady RANS simulations are converged when the following criteria are reached:

- Decrease of three orders of magnitude and stabilisation of the residuals;
- Difference between the inlet and outlet massflow rate lower than 0.1% and stabilisation.

Since numerous RANS simulations are performed in this chapter, only one is assessed for the convergence in the following. Note that similar behaviours are observed for the rest of the simulations. Figure 2.18 shows the evolution of the dimensionless massflow rate at the inlet and outlet of the domain. It reveals that a short time is needed for the stabilization of the massflow rates where the plateau is obtained after approximately 2000 iterations. The difference between the inlet and outlet massflow rate is also lower than 0.1%. In terms of residuals, Figure 2.19 presents the evolution of the residuals for several quantities. All residuals have decreased by three orders of magnitude and reached a plateau after around 20000 iterations. RANS has thus reached a converged state.

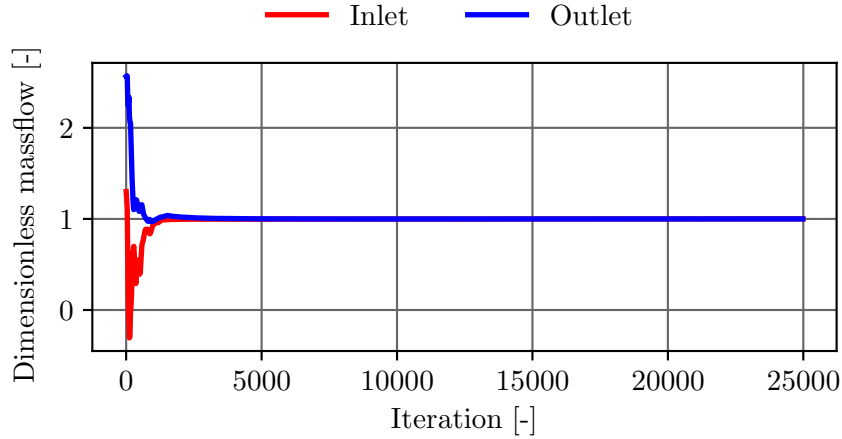


Figure 2.18 – Evolution of the massflow rate at the inlet and outlet of the domain for a RANS simulation.

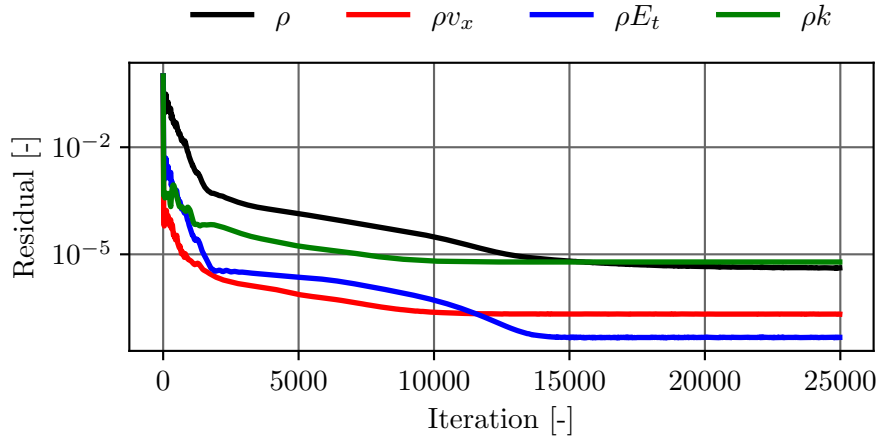


Figure 2.19 – Convergence of continuum, axial momentum, total energy and turbulent residuals for a RANS simulation.

2.3.2 Unsteady simulations

For unsteady simulations (URANS), a preliminary time-step convergence is performed. As mentioned in 2.2.5.3, the time-step can be *a priori* determined knowing the BPF of the adjacent rows. Based on this Δt (200 iterations per period), it is decided to evaluate the convergence with $2\Delta t$ (100 iterations per period) and $\Delta t/2$ (400 iterations per period). Different probes are placed within the computational domain: probe 1 in the stator, in the freestream and at mid-span, probe 2 at mid-span in the freestream at the inlet of the rotor and probe 3 at the stator outlet close to the shroud. Pressure fluctuations evolutions and FFT of the signals for the different probes are displayed in Figure 2.20. It shows that the unsteady phenomena are only related to the BPF for probe 1 and probe 2. The time-step has not a strong impact either on the pressure amplitude or frequency content. In the case of probe 3, the unsteady activity is more important (with a stochastic content) because of the presence of the boundary layer which leads to a relative dependency on the time-step. However, even if the case $2\Delta t$ seems enough for the present simulated case, the discretisation of 200 iterations per period is retained, as it also enables to have enough snapshots for the reconstruction of the unsteady flow.

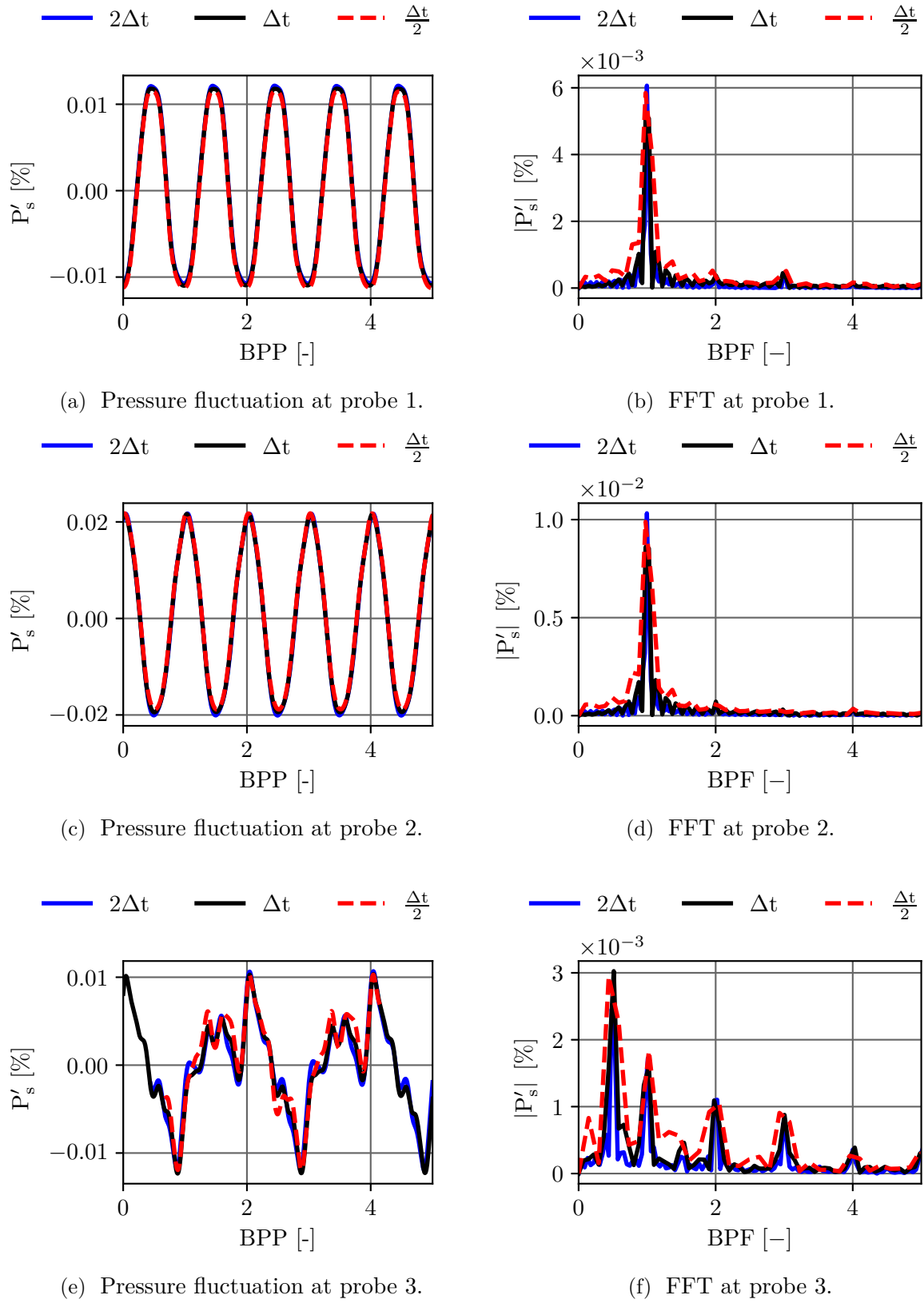


Figure 2.20 – Pressure fluctuation evolution (left column) and FFT of the pressure signal (right column) for different probe locations and time-steps.

Considering the time-step Δt , the convergence of an unsteady simulation is evaluated by means of moving averages of massflow rates and spectrograms at the vane/blade interface where the periodic state is targeted. Note that all unsteady simulations are initialised from a steady simulation and that 12000 time-steps are necessary for a wheel turn. The convergence is shown here for a chorochronic simulation, where 2 vanes and 1 blade are considered. Figure 2.21 presents the evolution of the massflow rates averaged on windows equalled to the BPP. The stabilization is well evidenced and the discrepancy between inlet and outlet massflow rates is less than 0.1%. To better qualify the convergence, a frequency analysis can be performed. As shown in Figure 2.22, by performing a FFT, the temporal evolution of the amplitude of the massflow rate signals enables to check the stabilization of the frequencies, expressed as multiples of the BPP. The periodic behaviour of the flow for this specific operating point is thus reached.

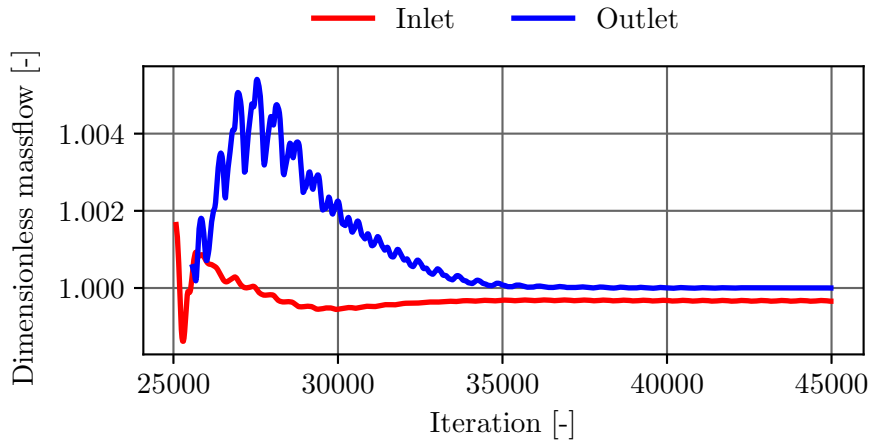


Figure 2.21 – Temporal evolution of the moving averaged massflow rates at the inlet and outlet of the domain.

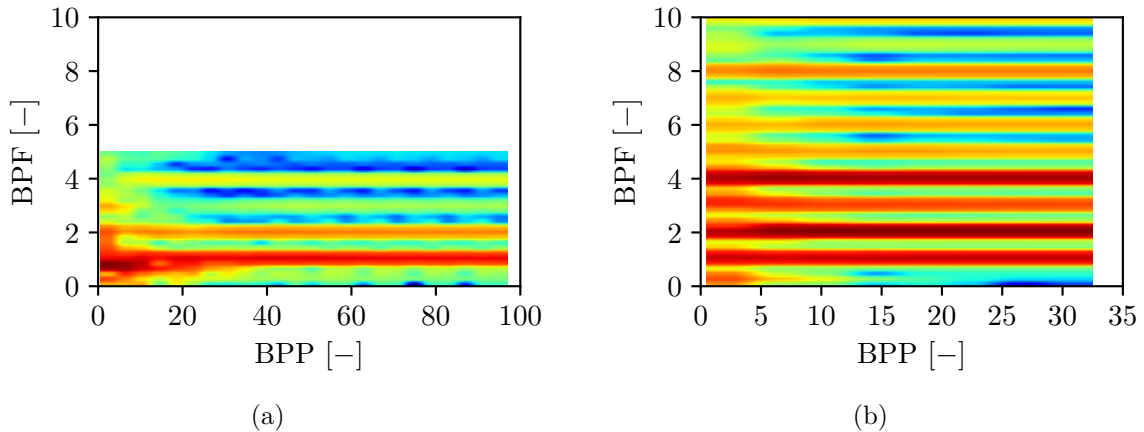


Figure 2.22 – Temporal evolution of the frequency spectrum of the massflow rate signals at the stator outlet (a) and at the rotor inlet (b).

2.3.3 Computational cost

The computational cost is evaluated for different types of simulations:

- Steady smooth vein (SV) mixing-plane simulations (1);
- Steady cooled vein (CV) mixing-plane simulations (2);
- Unsteady reduced sector number SV simulation (3);
- Unsteady chorochronic SV simulation (4).

All simulations are performed on the Topaze supercomputer at Centre de Calcul Recherche et Technologie (CCRT) using AMD Epyc 7763 nodes. For unsteady simulations, the CPU time includes both the computational time and the extraction time of the snapshots required for the averaging and the reconstruction of the solution. The number of snapshots is defined as the maximum of the BPP of the rows. Table 2.9 sums up the CPU times. It should be noted that even if very slight differences are observed between a smooth vein and a cooled vein simulation, the pre-processing for the latter is more important, as the cooling patches must be generated. The CPU time for unsteady simulation is about 20 times more important than steady simulations, but this is not surprising. For chorochronic simulations, one-and-a-half wheel rotation is required for the transient part, whereas this time is reduced to only a few BPP for the blade number reduction method simulation. Overall, these simulations allow a return time of the order of magnitude of hours and in the worst case one day.

Simulation type	CPU time [h]
(1)	360
(2)	362
(3)	6300
(4)	7650

Table 2.9 – Comparison of CPU time for different FACTOR simulations.

2.4 Scope of investigation for the prediction of the hot streak transport

In this section, several points are addressed in order to restrict the field of investigation for the prediction of the HS transport in the rest of the manuscript. First of all, the effect of the clocking position is tackled, as well as the variability of the operating point. Then, unsteady simulations are considered before studying the impact of the cooling. When appropriate, a flow analysis is performed. All these analyses should provide a framework to classify the mechanisms affecting the HS transport and to assess whether an increase in complexity is necessary for its prediction.

2.4.1 Impact of the clocking position on the hot streak migration and wall surface temperature

In this subsection, both clocking LEC and PAC are considered, before putting aside the PAC for the rest of the manuscript. SV mixing-plane simulations are performed. The turbulence characteristics from Table 2.5 on page 55 are used with the $k - l$ turbulence model.

First of all, the influence of the clocking position on the dynamics of the mean flow in the stator is evaluated through the use of Figure 2.23 and Figure 2.24. The former displays an iso-contour of total temperature inside the NGVs passage and the latter represents the temperature distribution on the NGVs' PS and SS. For the LEC position, the HS is aligned with the LE of NGV2. Then, it wraps around the vane till the TE and migrates towards the shroud endwall where it is more intense on the PS. NGV1 also presents a small pattern of HS, which results from its 'S' shape at the inlet (Figure 2.24). The thermal loading of NGV2 is more important compared to NGV1. For the PAC position, the HS is injected between NGV1 and NGV2 (Figure 2.23). It remains close to the SS of NGV2 and radially migrates towards the hub endwall at the TE. The cold flow coming from the outer cavity of the combustion chamber is also impacted by the clocking position, as evidenced by Figure 2.24: it is more predominant for the PAC than the LEC, which could be explained by the cold flow being enrolled by the shroud passage vortex. A general observation is that the PS is always hotter than the SS, regardless of the clocking position and the NGV. For the LEC, NGV2 is 2.2% hotter than NGV1 in average, and is also 1.6% higher than total temperature at P40. Considering PAC, NGV1 is 4.2% hotter than NGV2, but less than 1% higher than total temperature at P40. The clocking position clearly impacts the thermal loading of the vanes, where the temperature difference between the vanes is more pronounced for the PAC.

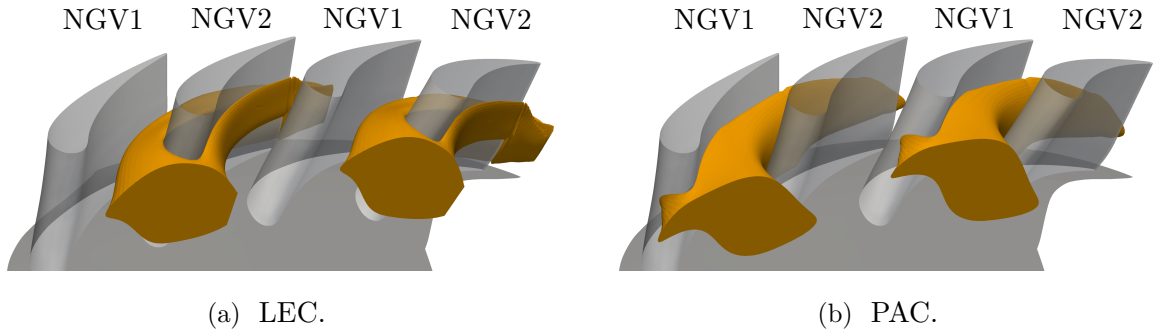


Figure 2.23 – Transport of the HS inside the NGVs evidenced by an iso-contour of total temperature at 450 K for both clocking positions.

In the moving part, in Figure 2.25, the differences in wall temperature are due to the DR that is different between the LEC and PAC (0.25 vs. 0.24) but also to the dynamics of the flow coming from the static row at the inlet of the moving row. Despite the presence of the mixing-plane at the vane/blade interface, the segregation effect described in Chapter 1 is observable: the hot flow accumulates on the PS of the rotor blade, while the SS sees an increase of cold flow in the outer part of the blade when moving towards the TE, independently of the clocking. The latter is explained by the presence of both the hub passage vortex and the tip leakage vortex. Moreover, the HS is impacting the blade at a higher span position for the LEC, which results from the flow dynamics evidenced by Figure 2.24. The blade temperature is about 380 K for LEC and PAC.

Finally, to better highlight the differences due to the clocking position, the transport of temperature is evaluated through the plot of radial total temperature distributions at P40, P41 and P42. Moreover, to account for the feeding differences for the two clocking positions in terms of total temperature (440.7 K for the LEC vs. 432.9 K), the plots are normalised by $\langle \overline{T}_t \rangle_{m,P40}$. It also enables to compare to the experimental data obtained with the 5HP, which takes into account the NGVs' cooling. Results are displayed in Figure 2.26. It reveals that most of the

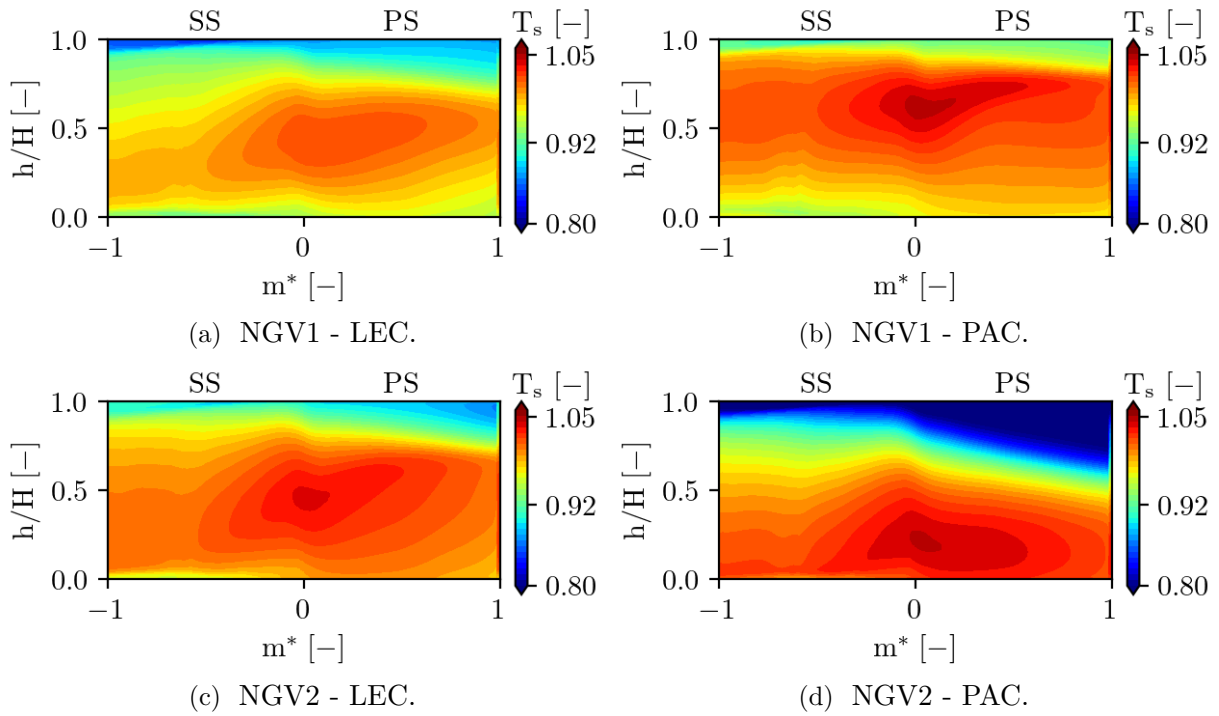


Figure 2.24 – Wall static temperature distribution on the two NGVs for LEC and PAC normalised by the inlet total temperature at P40.

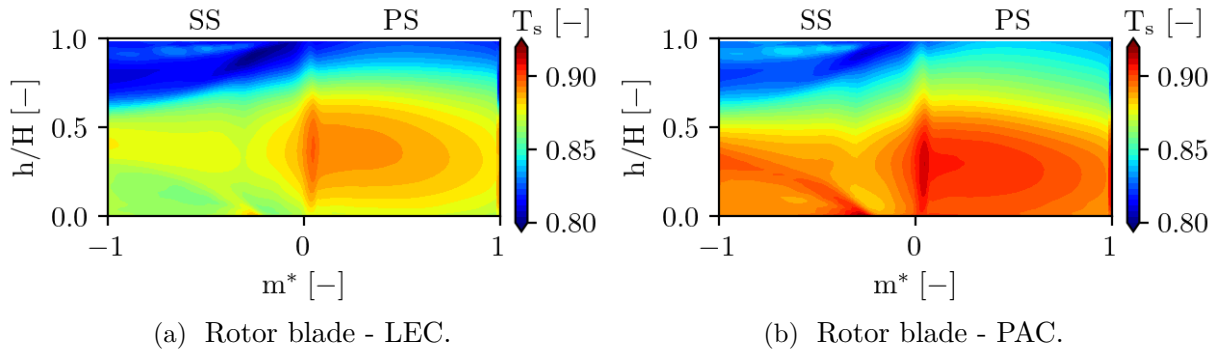


Figure 2.25 – Wall static temperature distribution on the rotor blade for LEC and PAC.

radial redistribution of temperature takes place in the NGV passage, and this independently of the clocking position. It also shows that the simulations do not promote the correct mixing in the NGV passage, as the distribution of \overline{T}_t is not spread enough in the radial direction. As it will be shown later on in this manuscript, adding the cooling on the NGV surface does not improve the results. Then, not surprisingly, the \overline{T}_t decrease occurs in the rotor, where the work is extracted (P42).

The dynamics of the flow is affected by the clocking position, as evidenced earlier by the wall static distribution. The HS migrates to a lower radial position with the PAC compared to the LEC, as shown at P41 in Figure 2.26. In the following of this PhD thesis, all the analyses are now performed on the LEC, since this study showed that the clocking position did not correct the misprediction of total temperature transport.

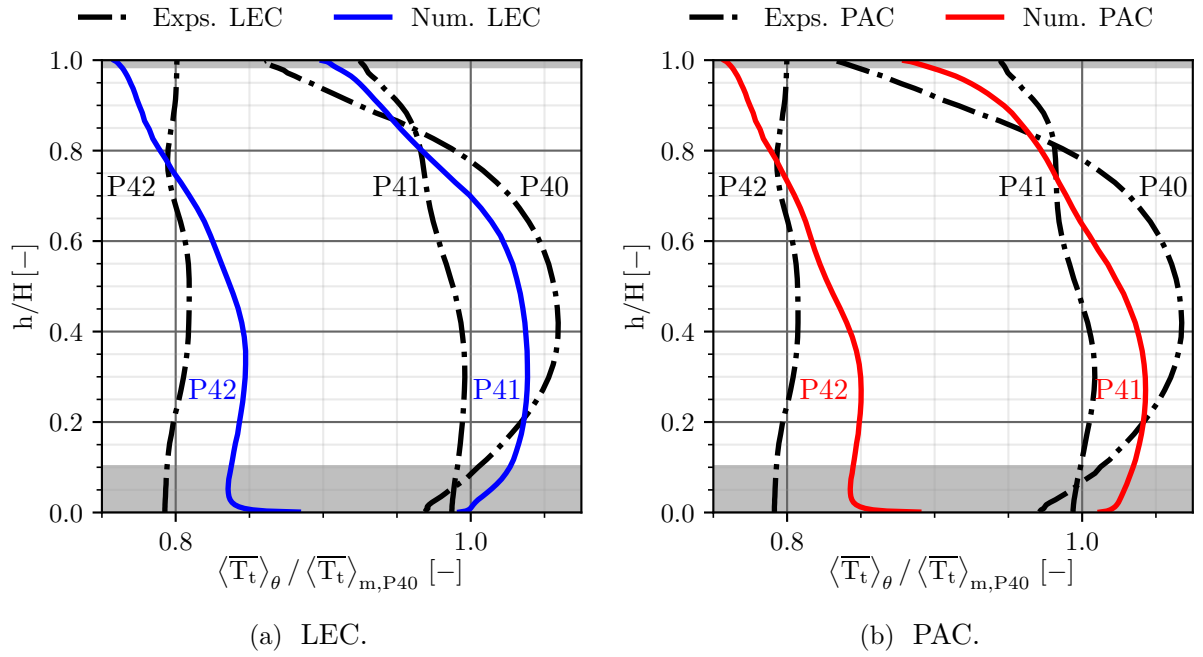


Figure 2.26 – Effect of the clocking position on the radial distributions of total temperature inside the high-pressure turbine.

2.4.2 Variability of the operating point

For the simulations of the FACTOR configuration, two global quantities are targeted to match the OP based on the experiments, namely the reduced massflow rate \dot{m}_{red} and the reduced rotational speed N_{red} at the LE of the rotor (whose plane is P41'). Those quantities are defined as follows:

$$\dot{m}_{red} = \frac{\dot{m}_{P41'} \sqrt{r T_{t,P41'}}}{AP_{t,P41}} ; N_{red} = \frac{ND}{\sqrt{r T_{t,P41'}}} \quad (2.12)$$

Since the gas and the geometry do not change, r , D and A vanish in the equations. Here, it is proposed to evaluate the impact of a slight modification of \dot{m}_{red} or N_{red} on the global performance of the stage and on the radial distributions. These modifications are respectively obtained by varying the outlet static pressure and the rotational speed. This study is necessary as:

- A modification of the turbulence model or turbulence characteristics at the inlet changes the OP, since the dynamics of the mean flow is impacted (see for instance Chapter 3 or Chapter 4);
- The feeding conditions of the simulations may differ. For example, between CV and SV simulations, a scaling-shifting is applied. In Chapter 6, maps are also applied from a LES.

The aim is to check if it is possible to get rid of a small deviation from the operating point in the analysis of the simulations. The configuration SV for the LEC is considered. \dot{m}_{red} is firstly tackled, where the reference value is 0.800. Figure 2.27 shows the radial distributions of $\bar{\alpha}$ and \bar{T}_t for different values of \dot{m}_{red} . Several comments can be done. First of all, both on the swirl angle or temperature distributions, the modification of \dot{m}_{red} does not impact the shape of the distributions at P40 and P41, since there is no work or heat exchange in the NGV row. Then, a modification of 1.4% on \dot{m}_{red} shifts the absolute level of swirl angle and temperature at P42,

i.e. at the rotor outlet. A shift of 20° for $\bar{\alpha}$ and 18 K for \bar{T}_t on the absolute level is observed. The higher the value of \dot{m}_{red} and the higher the values of DR and $\Pi_{t \rightarrow t}$ are, which means that the rotor is extracting more work. For example, between $\dot{m}_{red} = 0.793$ and $\dot{m}_{red} = 0.804$, DR varies from 0.24 to 0.28 (+17%) and $\Pi_{t \rightarrow t}$ changes from 2.06 to 2.54 (+24%). The values for the reference \dot{m}_{red} are respectively 0.25 and 2.29.

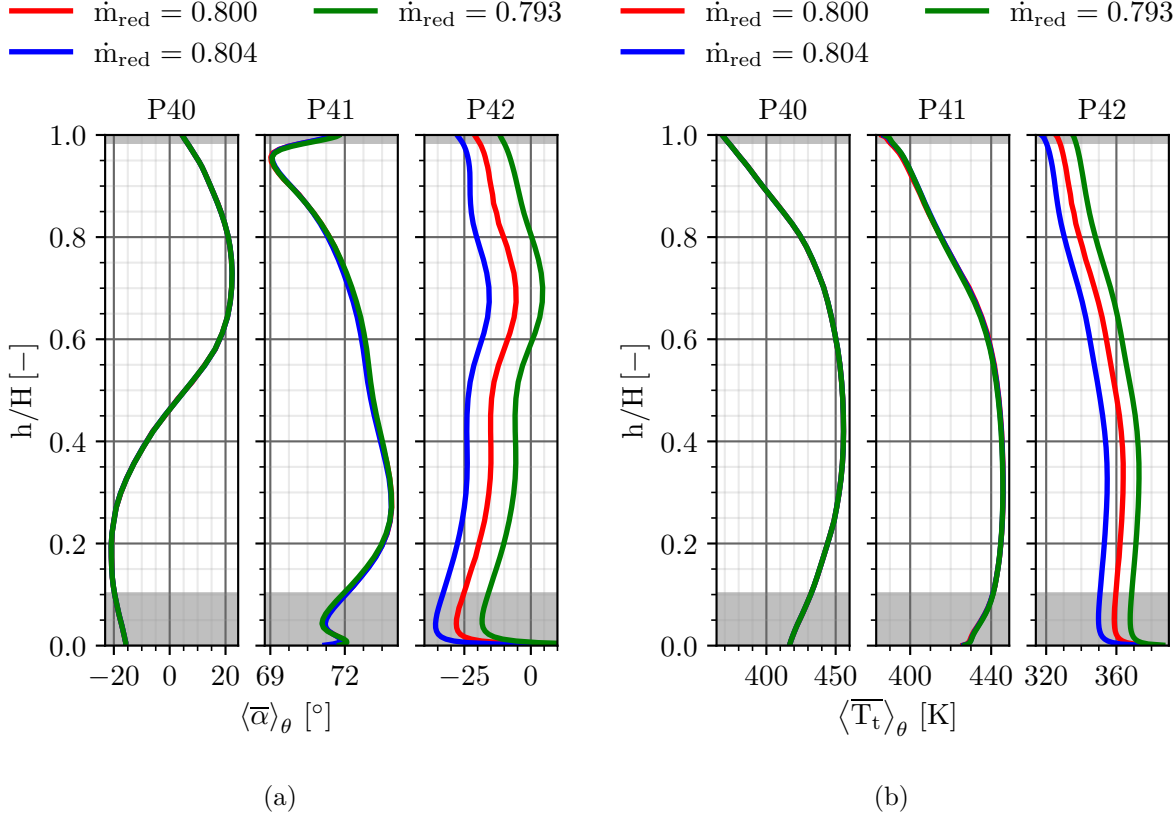


Figure 2.27 – Radial distributions of $\bar{\alpha}$ (a) and \bar{T}_t (b) for different values of \dot{m}_{red} .

To overcome operating point differences, it is possible to choose a proper normalisation of the radial distributions, in order to focus on the distortions and not on the values of the absolute level. At each plane, each distribution is normalised by its mean value at the given plane for the total quantity \bar{T}_t . Regarding the swirl and pitch angles, the mean value is subtracted. The resulting quantities are flagged with the exponent '*'. In Figure 2.28 are depicted the results of this normalisation in terms of distortions. The distortion of \bar{T}_t^* is not impacted by a modification of \dot{m}_{red} , while the one of $\bar{\alpha}^*$ is impacted to a lesser extent, especially in the blade tip region: the DR affects the nature of the tip gap flow (by incidence and ΔP effects) which, in turn, affects the swirl angle distribution. This result is satisfying in the scope of this PhD thesis, where the transport of temperature is mainly regarded.

The same analysis is performed for the impact of N_{red} , where the reference value is 371. For the sake of brevity, only \bar{T}_t is considered. Absolute and normalised distributions are plotted in Figure 2.29. A modification of 2% on N_{red} has no impact, either on the absolute level or on the distortions of \bar{T}_t , which can be explained by the proximity of the iso-rotational speed lines in the turbine performance map. It would be interesting to change even more N_{red} to see its impact, but within the range of 2%, the independence of the results on N_{red} is proven.

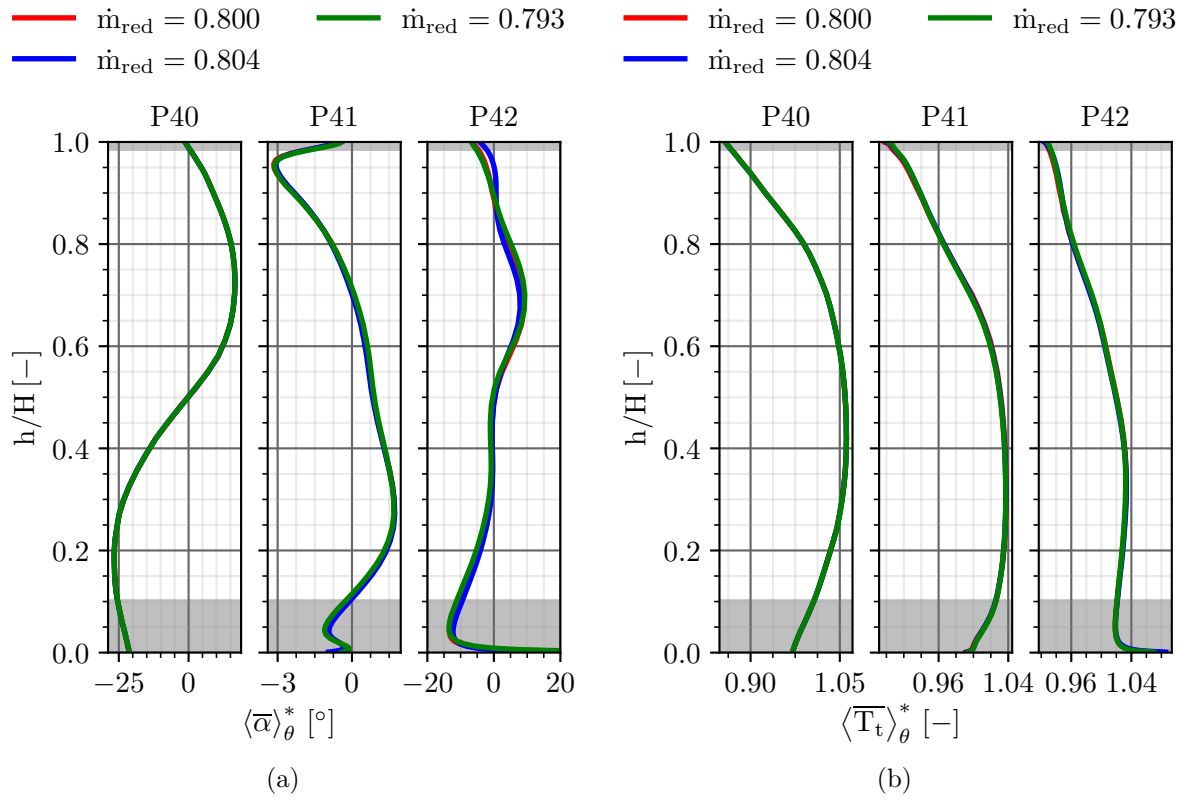


Figure 2.28 – Radial distributions of normalised $\bar{\alpha}$ (a) and \bar{T}_t (b) for different values of \dot{m}_{red} .

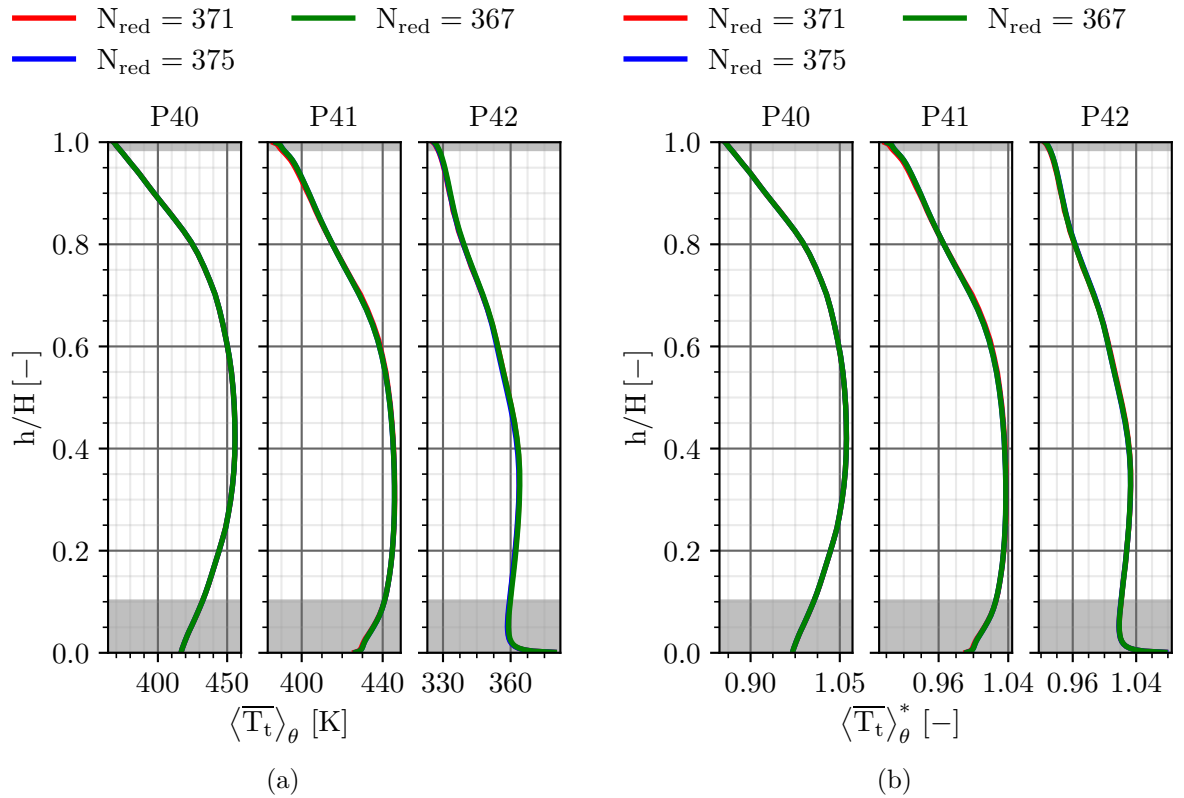


Figure 2.29 – Radial distributions of \bar{T}_t (a) and normalised \bar{T}_t (b) for different values of N_{red} .

While changing the OP by varying either \dot{m}_{red} or N_{red} , it is possible to get rid of its impact on the radial distributions by plotting them in terms of distortion. The conclusions of the comparisons with the experiments are not modified. Plots in terms of distortions are now performed for the rest of the analyses dealing with FACTOR's project in the manuscript. Moreover, this study also reveals that \dot{m}_{red} has more impact than N_{red} .

2.4.3 Influence of unsteady simulations

Unsteady simulations (SV reduced sector number and SV chorochronic) are now compared to the steady SV mixing-plane simulation on the LEC. Cooling is still not considered. For unsteady simulations, a time average is performed on the BPP of each row, and the snapshots are extracted at a frequency corresponding to 2.5% of the smallest BPP. For the present study, the reduced frequency is $\hat{f} \approx 0.9$, which signifies that unsteady effects due to the vane/blade interactions may have an impact on the flow field in the rotor. Figure 2.30 shows the radial distributions of \overline{T}_t and \overline{P}_t for both steady and unsteady simulations compared to the experiments.

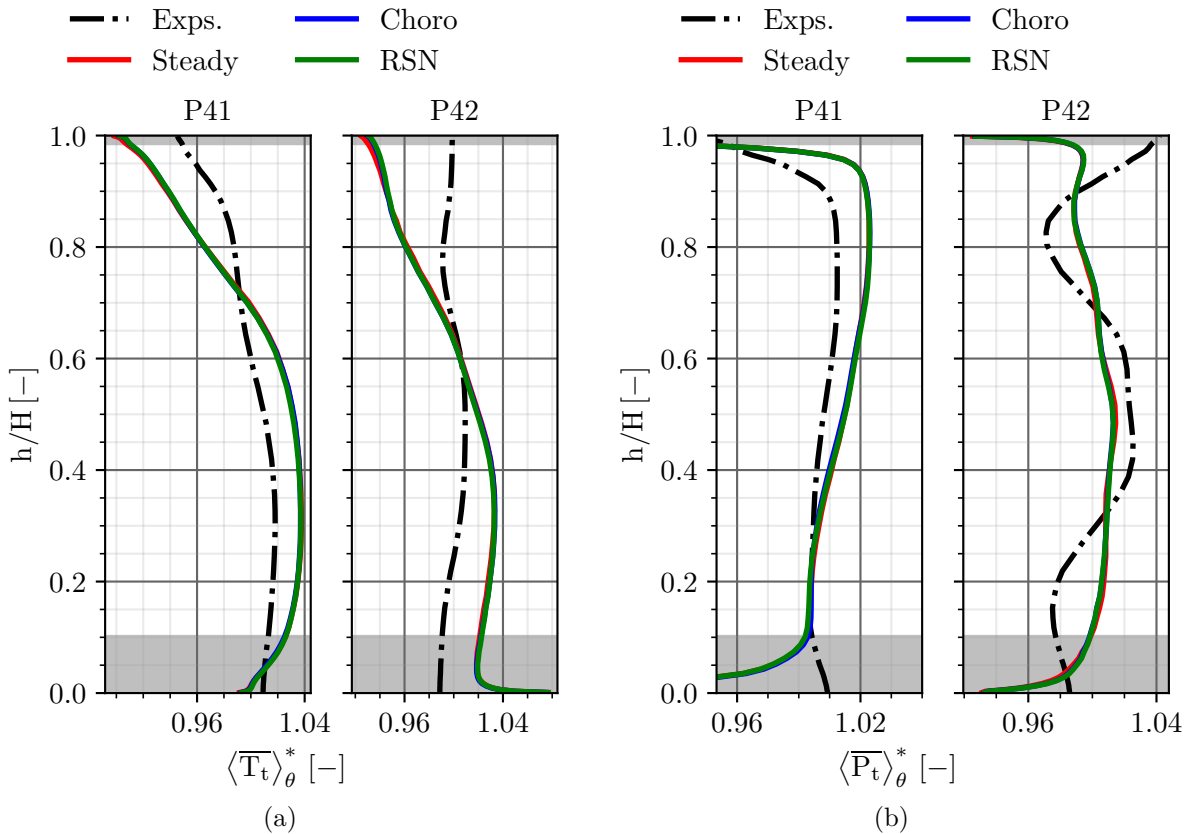


Figure 2.30 – Influence of unsteady simulations on the radial distributions of \overline{T}_t (a) and \overline{P}_t (b) for the SV simulations - RSN: reduced sector number - Choro: chorochronic. Distributions are plotted in distortion.

Radial distributions of \overline{T}_t and \overline{P}_t are not impacted by unsteady effects: the flow topology is not modified. The overestimation of \overline{T}_t does not vanish. Moreover, the shroud passage vortex is not reproduced with the numerical simulations, as evidenced by the radial distribution of \overline{P}_t . It is also the case for the hub passage vortex, but this is normal since the cavity purge flows are not considered for the moment.

Unsteady simulations do not enable to solve the problem of temperature transport in the high-pressure turbine. Therefore, RANS simulations are mostly employed in the rest of the manuscript (except at the end of Chapter 6 where an unsteady boundary condition is applied).

2.4.4 Effect of the cooling

Finally, cooling in the high-pressure turbine stage is considered, namely the film-cooling on the NGVs' walls and upstream and downstream rotor cavity purges. The vane and blade stagger angles are nominal. RANS simulations on the LEC are performed. First of all, the radial distributions depicted in Figure 2.31 and Figure 2.32 are commented. It shows that the swirl angle and total pressure distributions are not impacted by the cooling on the vane surfaces, while the total temperature sees a more important radial redistribution, which can be attributed to the stronger mixing between cold and hot flows. The total temperature distortions are better represented. Moreover, in the rotor blade passage, the presence of the cavity purges modifies the distributions at the hub, because of the secondary flows that enrol the upstream cavity purge flow. Both the swirl angle and total pressure distributions at P41 attest for that at the hub. However, at the shroud, the intensity of the shroud passage vortex is not reproduced, whether cooling is considered or not.

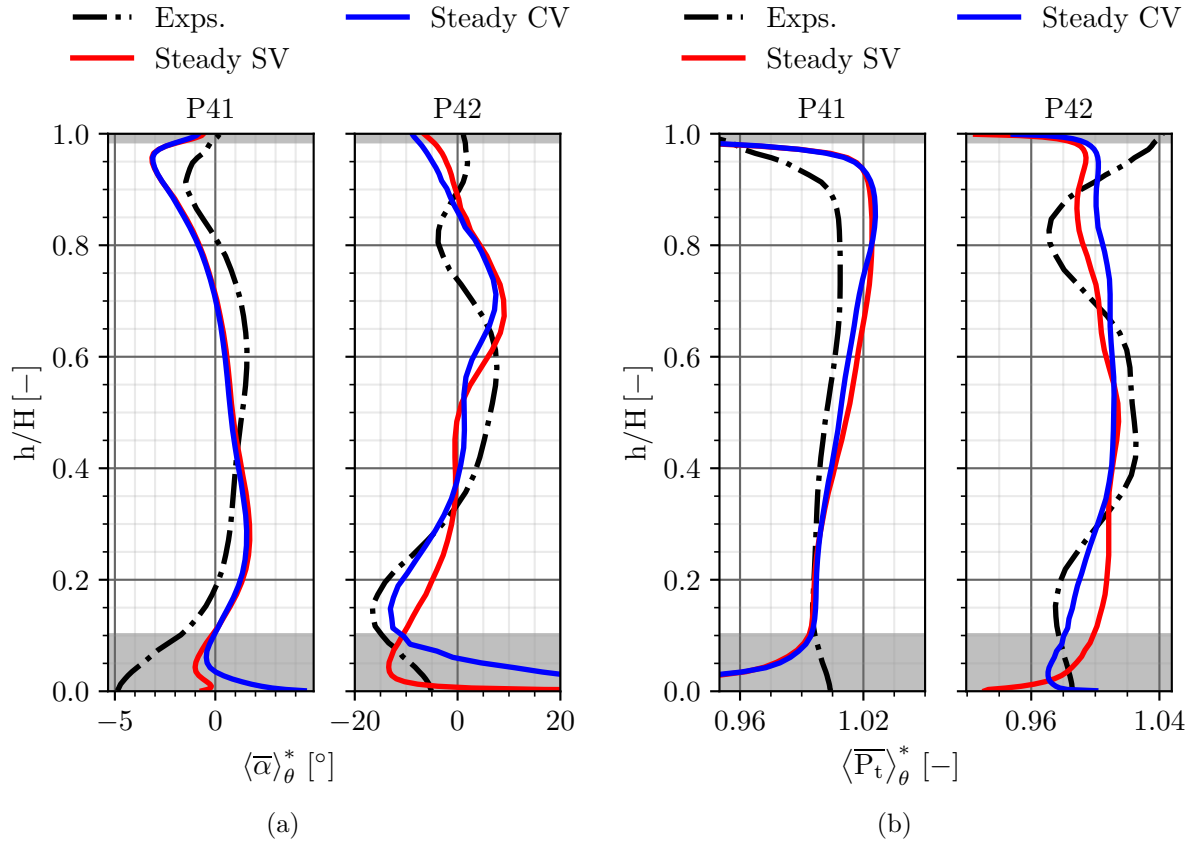


Figure 2.31 – Influence of the cooling on the radial distributions of $\bar{\alpha}$ (a) and \bar{P}_t (b). Distributions are plotted in distortion.

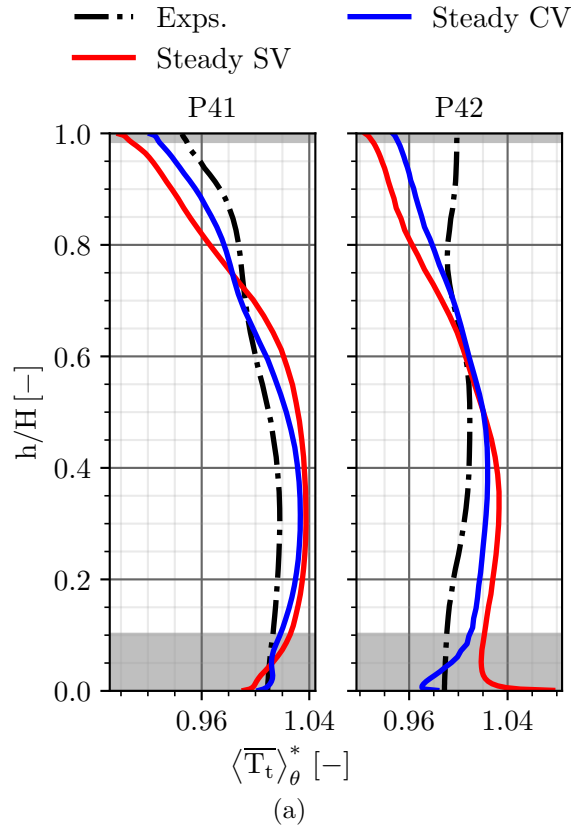


Figure 2.32 – Influence of the cooling on the radial distributions of \overline{T}_t . Distributions are plotted in distortion.

The presence of the cooling brings more physics in the high-pressure turbine. For instance, Figure 2.33 presents the total temperature fields at P41, *i.e.* at the NGVs' outlet plane for the SV and CV simulations. They are compared to the results post-processed from the 5HP measurements. These results clearly show the local overestimation of total temperature at the outlet of the NGVs, independently of considering or not the cooling, as discussed previously. However, the wake is more pronounced with the CV simulation, which is due to the presence of the cold film around the vanes.

This cooling flow on the vanes is evidenced by Figure 2.34. The surface temperature is highly reduced, compared to the SV simulation (Figure 2.24). For both NGVs, on the SS, the cooling flow migrates towards the hub and shroud endwalls, while it remains more uniform on the PS of NGV1. On the PS of NGV2, the mixing of the cold flow and hot flow modifies the temperature distribution in the radial direction, where the surface is cooling down when moving upwards. In the rotor blade, the presence of the upstream cavity purge flow strongly affects the wall temperature distribution. Despite being injected on a whole blade pitch, the cooling flow preferentially migrates towards the SS of the blade. This is explained by the presence of the secondary flows, represented in Figure 2.35. While both SV and CV simulations similarly reproduce the tip leakage vortex and the shroud passage vortex, the hub passage vortex is strongly affected by the presence of the cooling: the purge flow is enrolled by the hub passage vortex, which is therefore more intense and migrates higher in the span direction.

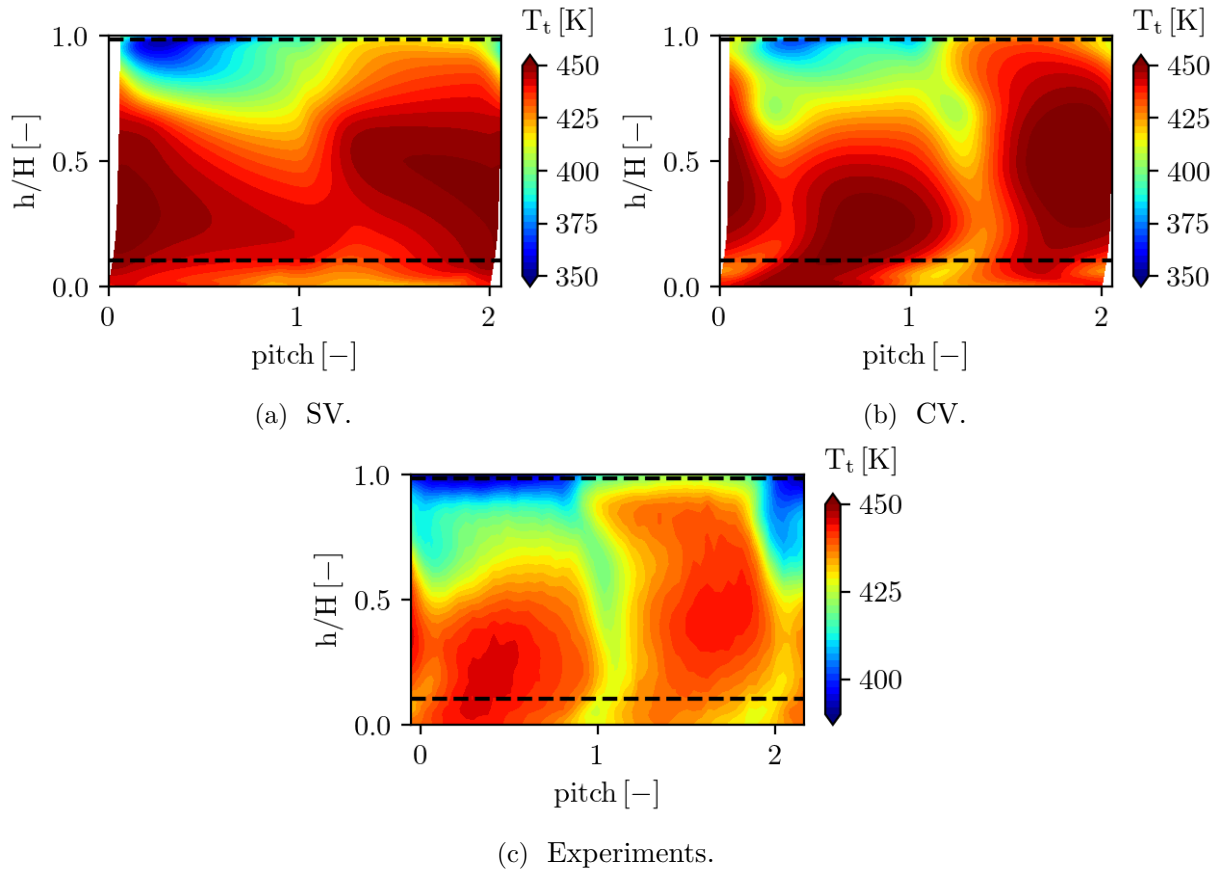


Figure 2.33 – Comparisons of \overline{T}_t fields at P41 between SV simulation (a), CV simulation (b) and experiments (c).

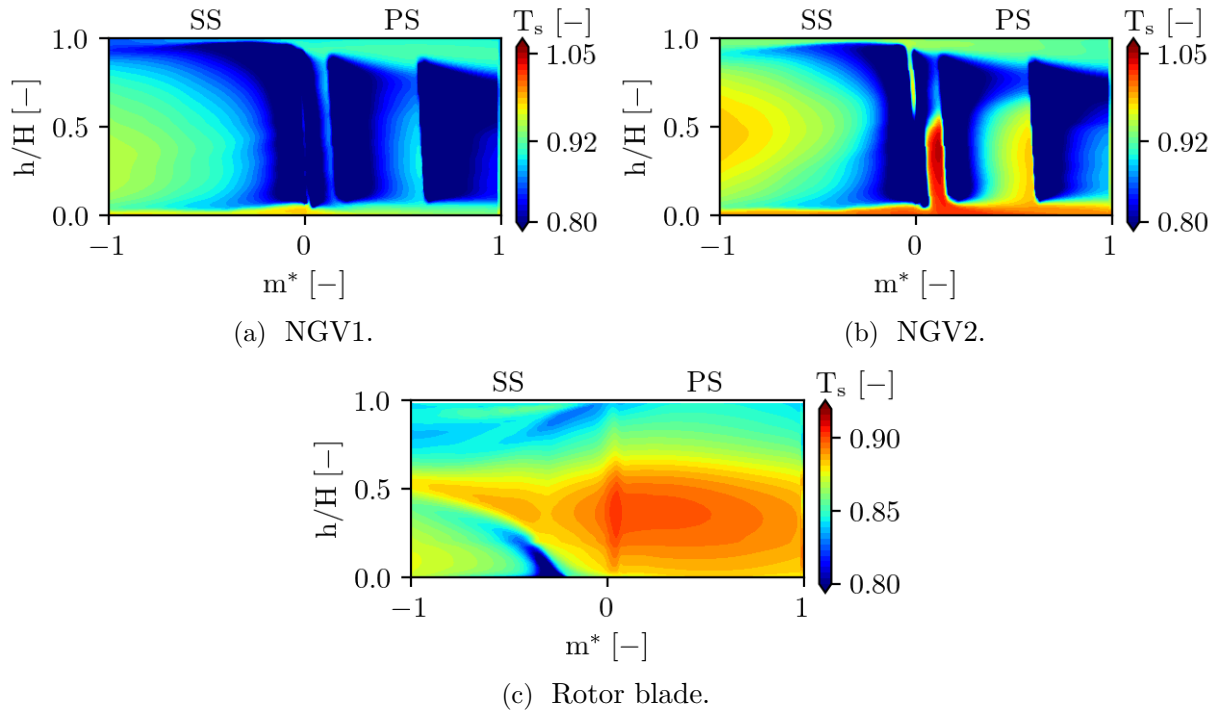


Figure 2.34 – Wall static temperature distribution on the two NGVs and the rotor blade normalised by the inlet total temperature at P40.

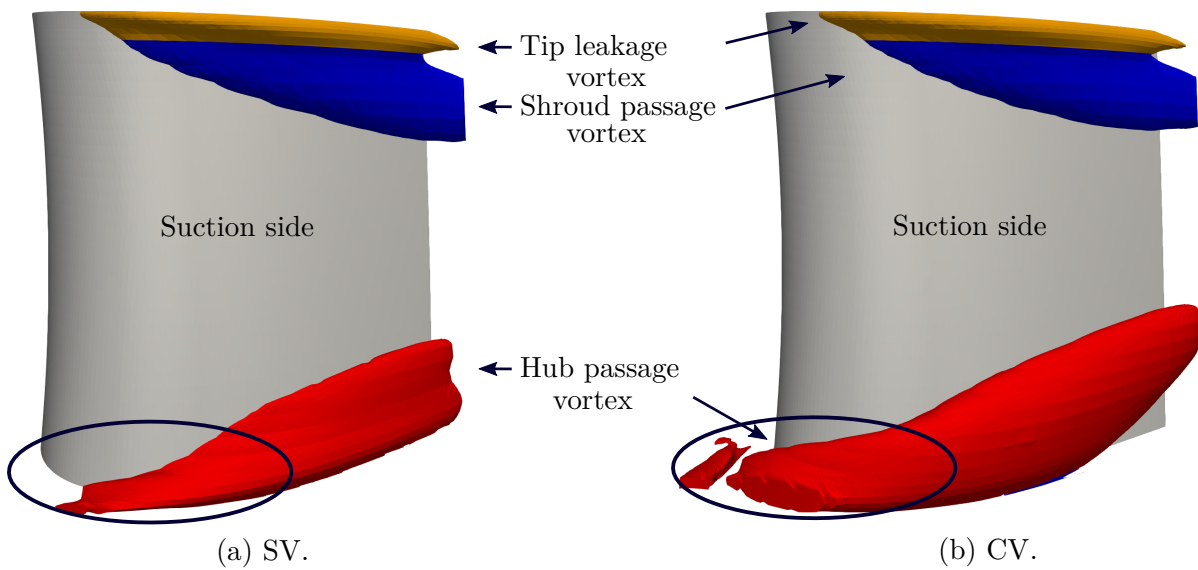


Figure 2.35 – Secondary flows on the suction side of the rotor blade evidenced by iso-surfaces of Q-criterion at $1 \cdot 10^8 \text{ s}^{-2}$ - Comparisons between SV (a) and CV (b).

Despite being simplified (holes replaced by patches on the NGVs' surfaces, and flow coming from the cavity purges without tangential velocity), the contribution of taking into account the cooling is no longer to be demonstrated. However, in spite of an improvement, temperature distributions are still far from the experimental ones at P41 and P42.

2.5 Conclusion

In Chapter 2, a wide coverage of the FACTOR project has been performed. The motivations of the project have been presented, as well as a literature review focused on the use of CFD in the scope of FACTOR. This literature review showed all the difficulties of this configuration, that fail most of the simulations in predicting correctly the aero-thermal in the high-pressure turbine stage, either using RANS simulations or URANS simulations. Then, the experimental data of the project have been summed-up. Because of the high swirling motion at the combustor outlet, the experiments could not be as precise as expected, and led to numerous missing areas, that might have an impact on the quality of the results of the simulations. Before presenting preliminary results, all the numerical set-up has been detailed, as well as the strategy to take into account the cooling on the vane surfaces and in the rotor blade row. Finally, in order to have a clear reading grid concerning the prediction of the temperature transport inside the high-pressure turbine of FACTOR, several simulations of different complexity have been performed. Results revealed a complex flow dynamics, which is influenced by the clocking position of the HS, and which lead to different thermal loadings of the vane and blade surfaces. Unsteady simulations did not improve the total temperature

distributions, while the use of the cooling did, with stronger secondary flows. However, despite all these attempts to correctly predict the total temperature evolution, none of them led to satisfactory results. The conclusions of this chapter allow us to draw up the scientific program that will be addressed in the rest of the manuscript:

- Despite an increase in the complexity of the simulations, it is necessary to go back to the basics of RANS modelling. A first way to overcome the temperature misprediction deals with the turbulence modelling in the RANS approach, which is studied in Chapter 3 and Chapter 4. Since the temperature misprediction already appeared in the NGV passage of FACTOR, a simplified configuration mimicking such a domain is used for this academic study. All kinds of turbulence models are tackled, ranging from first-order linear eddy-viscosity turbulence models to second-order turbulence models;
- The results from the academic case are then applied to FACTOR's configuration (Chapter 5);
- Finally, the measurements uncertainties being too important at P40 (which is employed as inlet boundary conditions), results from high-fidelity simulations are used to generate a new boundary condition, both steady and unsteady. Turbulence modelling is put aside. The new steady boundary condition must correct errors of type 'a' and type 'c' while the unsteady boundary condition must represent the PVC (Chapter 6).

Dans le Chapitre 2, une large présentation du projet FACTOR a été réalisée. Les motivations du projet ont été présentées, ainsi qu'une revue de la littérature centrée sur l'utilisation de la CFD dans le cadre de FACTOR. Cette revue de la littérature a montré toutes les difficultés de cette configuration, qui font échouer la plupart des simulations à prédire correctement l'aérothermique dans l'étage de turbine haute pression, que ce soit en utilisant des simulations RANS ou des simulations URANS. Ensuite, les données expérimentales du projet ont été résumées. En raison du fort mouvement de giration à la sortie de la chambre de combustion, les mesures expérimentales n'ont pas pu être aussi précises que prévu, et ont conduit à de nombreuses zones manquantes, qui pourraient avoir un impact sur la qualité des résultats des simulations. Avant de présenter les résultats préliminaires, tout le paramétrage numérique a été détaillé, ainsi que la stratégie pour prendre en compte le refroidissement sur les surfaces des aubes et dans la roue haute pression. Enfin, afin d'avoir une grille de lecture claire concernant la prédiction du transport de la température au sein de la turbine haute pression de FACTOR, plusieurs simulations de complexité différente ont été réalisées. Les résultats ont révélé une dynamique d'écoulement complexe, qui est influencée par la position du point chaud par rapport au distributeur, et qui conduit à des charges thermiques différentes sur les surfaces des aubes et des pales. Les simulations instationnaires n'ont pas amélioré les profils de température totale, alors que l'utilisation du refroidissement l'a fait, avec des écoulements secondaires plus marqués. Cependant, malgré toutes ces tentatives pour prédire correctement l'évolution de la température totale, aucune d'entre elles n'a abouti à des résultats satisfaisants. Les conclusions de ce chapitre

nous permettent de dresser le programme scientifique qui sera abordé dans la suite du manuscrit :

- Malgré une augmentation de la complexité des simulations, il est nécessaire de revenir aux bases de la modélisation RANS. Une première façon de traiter la mauvaise prédiction de température concerne la modélisation de la turbulence dans l'approche RANS, qui est étudiée dans le Chapitre 3 et le Chapitre 4. Puisque la mauvaise prédiction de température est déjà apparue dans le passage du distributeur, une configuration simplifiée reproduisant un tel domaine est utilisée pour cette étude académique. Tous les types de modèles de turbulence sont abordés, allant des modèles linéaires du premier ordre aux modèles de turbulence du second ordre;
- Les résultats du cas académique sont ensuite appliqués à la configuration FACTOR (Chapitre 5);
- Enfin, les incertitudes des mesures étant trop importantes au P40 (qui est utilisé comme condition limite d'entrée), des résultats de simulations haute-fidélité sont utilisés pour générer une nouvelle condition aux limites, à la fois stationnaire et instationnaire. La modélisation de la turbulence est mise de côté dans cette étude. La nouvelle condition aux limites stationnaire doit corriger les erreurs de type 'a' et de type 'c' tandis que la condition aux limites instationnaire doit représenter le PVC (Chapitre 6).

Part II

The sources of errors in the prediction of a swirled hot streak flow in a high-pressure turbine stage

The second part of this manuscript is dedicated to the numerical study of the swirled hot streak redistribution under high turbulence levels, by using high-fidelity simulations (LES) and RANS simulations. The physics of such a flow is tackled, as well as a methodology for RANS turbulence inlet set-ups (Chapter 3). The anisotropy of turbulence is then examined, as it is suspected to explain the failure of the usual RANS turbulence models (Chapter 4).

Effect of turbulence levels and scales on the diffusion of hot streaks

“ *Big whirls have little whirls, that feed on their velocity; And little whirls have lesser whirls, And so on to viscosity.* ”

Lewis Fry Richardson

Abstract

Preliminary simulations on the FACTOR configuration resulted in a poorly calibrated diffusion of the hot streak inside the high-pressure turbine stage. On the one hand, the reason for such deficiencies can rely on the RANS turbulence modelling for which imposing the proper turbulence at the inlet boundary condition is not trivial. These turbulence levels and scales are modelled by the ratio of turbulent viscosity to molecular viscosity μ_T/μ . On the other hand, physically, turbulence is known to have a substantial impact on the diffusion of hot streaks, as it enhances the heat transfers in the fluid as well as swirl that impacts momentum and modifies the aerodynamics. This chapter studies the redistribution of a highly turbulent swirled hot streak in the simplified case of a bent duct to highlight the first-order physics. The configuration together with the numerical set-up are firstly described. Then, the LES convergence, both in terms of mesh and statistics, is thoroughly reviewed, as the LES is used for the calibration of RANS simulations. Finally, the physical analysis of LES is done, to study the topology of the swirled flow, before making a sensitivity study to physical and numerical parameters to compare RANS and LES.

3.1	Introduction	85
3.2	Description of the configuration and the numerical set-up	85
3.2.1	Geometry	85
3.2.2	LES and RANS meshes	85
3.2.3	LES boundary conditions	88
3.2.4	RANS boundary conditions	91
3.2.5	Numerical parameters	92
3.2.6	Post-processing	93

3.3	Convergence study	93
3.3.1	Mesh and statistical convergence of the LES	93
3.3.2	Numerical convergence	97
3.4	Analysis of the LES to study the topology of the swirled flow	98
3.4.1	Effect of swirl on the hot streak migration	98
3.4.2	Turbulent kinetic energy budget	100
3.4.3	Evaluation of an integral scale of turbulence	104
3.4.4	Effect of the turbulent length scale on the hot streak redistribution	106
3.4.5	Stability of the swirling jet	110
3.5	Evaluation of RANS against LES: sensitivity study to physical and numerical parameters	112
3.5.1	Prescription of the turbulent map obtained from the LES at the inlet boundary condition	114
3.5.2	Influence of the turbulent Reynolds number	116
3.5.3	Turbulent kinetic energy budget comparisons between diffusive and transport RANS turbulence set-ups	120
3.5.4	Brief discussion of the stability issue	121
3.6	Conclusion	122

3.1 Introduction

The lack of predictability of the numerical simulations presented in Chapter 2 in the context of hot streaks in high-pressure turbines naturally led to the question of turbulence and its effect on the diffusion of those hot streaks. Especially with the strong hypothesis of RANS turbulence modelling (turbulent viscosity that does not change by rotation, Boussinesq’s hypothesis), the modification of the turbulent length scale modifies the dynamics of the mean flow: the turbulent viscosity, which is computed from the turbulence models, appears in the momentum and energy equations. Thus it must be imposed at the inlet with care to accurately reproduce the flow dynamics. In particular, Bode *et al.* [13] reported that for high turbulence intensities and moderate turbulence decay, the inlet should be modified to best fit the experiments, thus leading to harsh turbulence decay and small turbulent length scale to be imposed ($l_T \approx 1 \cdot 10^{-4}$ m). All those difficulties in predicting the turbulence decay or the temperature evolution are enhanced by the presence of vane thickness, boundary layers, twist of the vanes, swirl and vane/blade interactions, as already presented on FACTOR configuration. In the present study, a simplified NGV passage is considered to study the fundamental mechanisms of swirled hot streak redistribution due to turbulence and vorticity inside a bent channel in a sanitised environment, *i.e.* without considering any boundary layers.

The common thread of this chapter is taking into account the coupling effects between turbulence and temperature gradients in a stationary environment by performing LES and RANS simulations. The finality is to study the hot streak redistribution both in terms of phenomenology and methodology for turbulent inlet set-ups. For the latter, RANS numerical set-ups are compared to a reference high-fidelity LES.

3.2 Description of the configuration and the numerical set-up

3.2.1 Geometry

The geometry is representative of the NGV passage of a high-pressure turbine, as depicted in Figure 3.1. The configuration is voluntarily very simple, without boundary layers, in order to isolate the basic mechanisms. The axial chord Ca_x , which is used for the axial direction normalisation (denoted x^*), is equal to 40 mm. The angle at the TE ($x^* = 1$) is 75° , which is the value of FACTOR’s configuration. In the third direction, the geometry is extruded by one Ca_x . Two Ca_x are imposed upstream of the LE ($x^* = 0$) in order to correctly develop the turbulence fields. In the curved region, for $0 < x^* < 1$, the lateral walls represent respectively the pressure side and suction side of a skeletal NGV, which are computed with slip walls. The downstream domain is long enough to prevent reflections and backflows (two Ca_x). Finally, the position $x^* = -0.425$ is equivalent to P40, and referred as such.

3.2.2 LES and RANS meshes

3.2.2.1 Estimation of cell size for the generation of LES mesh

Generating correct meshes is essential for the quality of the results obtained, especially with a view to calibrate a method (RANS) against another (LES). The classical criteria on x^+ , y^+ or z^+ , which are generally set according to the turbulent boundary layer physics, are no more

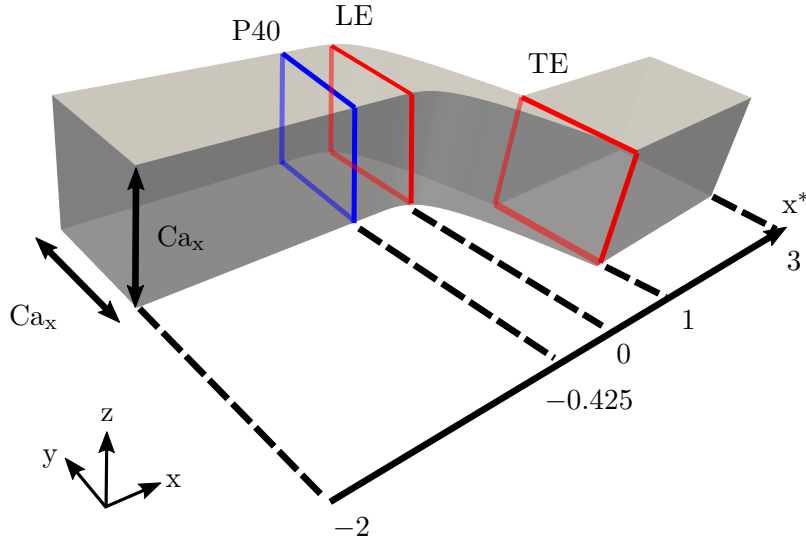


Figure 3.1 – Geometry of the bent duct with the dimensions normalised by the chord.

applicable [89, 98]. The estimation of the cell size is based on the Kolmogorov theory already described in 1.2.3. Values are *a priori* targeted at P40:

$\langle \overline{T_t} \rangle_S$ [K]	$\langle \overline{P_t} \rangle_S$ [kPa]	$\langle \overline{M} \rangle_S$ [-]	$\langle \overline{l_T} \rangle_S$ [mm]	$\langle \overline{v'_i} \rangle_S$ [m.s ⁻¹]	$\langle \overline{k} \rangle_S$ [m ² .s ⁻²]
435	141	0.18	7	9	120

Table 3.1 – Targeted values of the flow at plane 40.

For the present study, the biggest cell size is tuned on Taylor’s micro-scale, which is a common scale to characterise a turbulent flow. The estimation is based on the hypothesis of homogeneous isotropic turbulence (HIT) at the inlet. It is therefore possible to derive the Reynolds numbers associated with the different turbulent scales depicted in Figure 1.15 [91]:

- Based on the integral scale l_T :

$$Re_{l_T} = \frac{k^{1/2} l_T}{\nu} \quad (3.1)$$

- Based on the Taylor micro-scale l_λ :

$$Re_{l_\lambda} = \frac{v' l_\lambda}{\nu} = \left(\frac{20}{3} Re_{l_T} \right)^{1/2} \quad (3.2)$$

- Based on the Kolmogorov scale l_η :

$$Re_{l_\eta} = \frac{v_\eta l_\eta}{\nu} = 1 \quad (3.3)$$

The Kolmogorov scale is determined *a priori* through the following relationship:

$$l_\eta / l_T = Re_{l_T}^{-3/4} \quad (3.4)$$

The characteristic Reynolds numbers and turbulent scales associated with the flow are presented

in Table 3.2. The final retained cell size is $\Delta = 5 \cdot 10^{-4}$ m. By comparing the scale Δ and Kolmogorov's scale with a non-dimensional parameter Δi^+ , it leads to 44 for the biggest cells and 12 for the smallest cells in the curved part of the channel. The biggest cell size is also 14 times smaller than the reference integral scale of turbulence, which is in the recommended range of 10-15 cells across the integral length scale for LES. A mesh convergence based on this value of Δ is performed in 3.3.1.

Re_{l_T} [-]	Re_{l_λ} [-]	l_λ [m]	l_η [m]
$5.2 \cdot 10^3$	$1.9 \cdot 10^2$	$3.1 \cdot 10^{-4}$	$1.15 \cdot 10^{-5}$

Table 3.2 – Reynolds numbers and flow characteristic scales.

3.2.2.2 LES mesh quality criterion

In addition to the mesh convergence that will be presented later in this report, the quality of the LES mesh is evaluated through Pope's criterion [91]. The quality of the mesh must be checked, since on the one hand, the large eddies must be captured (the energy-containing scales) to have relevant statistics of turbulence, and on the other hand, the filter size must not be too big to minimise the influence of the modelled part. In the case of Pope's criterion, the metric \mathcal{M} is defined as:

$$\mathcal{M}(\mathbf{x}, t) = \frac{k_{SGS}(\mathbf{x}, t)}{k_{SGS}(\mathbf{x}, t) + k_{RES}(\mathbf{x}, t)} \quad (3.5)$$

Where $k_{RES} = 0.5 \cdot \overline{v'_i v'_i}$. Pope's criterion makes it possible to measure the fraction of turbulent kinetic energy resolved by the mesh. It is said in the community that an adequate LES must solve at least 80% of the turbulent kinetic energy, *i.e.* stay in the range of $\mathcal{M} < 0.2$. In the above formula, k_{SGS} is unknown and must be estimated through a subgrid-scale linked with the size of the modelled eddies. The following formulas are considered to compute this subgrid-scale turbulent kinetic energy:

$$k_{SGS} = \left(\frac{\mu_{SGS}}{\rho l_{SGS}} \right)^2 \quad (3.6)$$

$$l_{SGS} = C_S \times (\text{Cell volume})^{1/3} \quad (3.7)$$

Where $C_S < 1$ to ensure the turbulent length scale to be smaller than the cell size. This value depends on the subgrid-scale model used and is fixed to 0.07 for the Vreman subgrid-scale model.

3.2.2.3 Mesh generation

LES mesh is created following a multi-blocks approach with *ICEM-CFD* software. The maximum cell size is relevant with the estimation of the Taylor micro-scale ($\Delta = 5 \cdot 10^{-4}$ m). Convergence of the streamlines in the curved part due to the restriction of the cross-section area leads to a natural decrease of the cell size, ensuring it is always below Taylor's micro-scale in this particular region. It is then unstructured to match the requirements of the LES solver. RANS simulations are performed on the same mesh (with the sole difference that it is kept structured), in order to focus on turbulence modelling and not on the numerics (flux schemes, limiters, etc.). The baseline mesh contains 4.7 million hexahedra, which can seem low but the reader should

remind that no boundary layers are considered. Figure 3.2 shows the mesh in the most curved part of the channel where every two points are displayed for the sake of clarity.

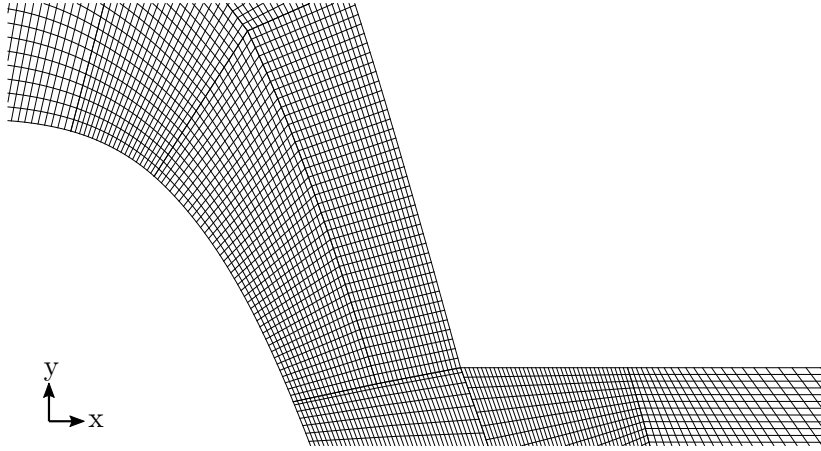


Figure 3.2 – Zoom of the mesh in the most curved part (every two points displayed).

3.2.3 LES boundary conditions

The boundary conditions for the LES are now described. They are quickly summarised in Figure 3.3. The inlet is a combination of a temperature Gaussian, a vortex and an injection of turbulence.

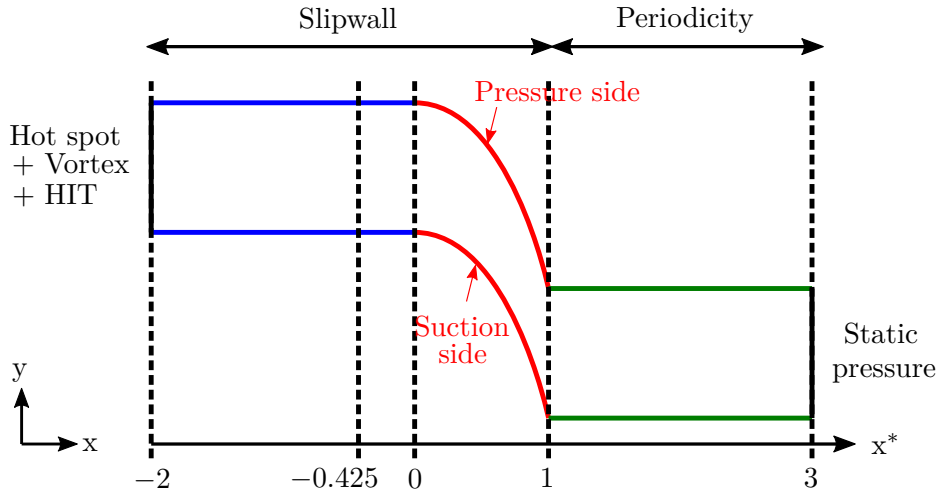


Figure 3.3 – Schematic view of the bent duct with the boundary conditions.

- **Inlet:** the hot streak is imposed at the inlet through static temperature distribution with a Gaussian function defined as follows:

$$T_s = T_{s,min} \left[1 + (R - 1) \cdot e^{-\left(\frac{(y-y_0)^2}{2\sigma_y^2} + \frac{(z-z_0)^2}{2\sigma_z^2} \right)} \right] \quad (3.8)$$

Where y_0 and z_0 are chosen to center the hot streak both in the pitchwise and spanwise directions. $\sigma_y = \sigma_z = 6.25 \cdot 10^{-2} \cdot Ca_x$. The value of $T_{s,min}$ is obtained by giving the

desired $\langle \overline{T_s} \rangle_S$ and $R = T_{s,max}/T_{s,min}$ ($= 3$), which, after integration over the inlet plane yields to:

$$T_{s,min} = \frac{\langle \overline{T_s} \rangle_S \times A}{C} \quad (3.9)$$

Where A is the inlet surface area and C the constant of integration.

A vortex is also imposed to create the swirl movement. A vortex is a rotating flow characterised in its center by a viscous region and then by a region that behaves like a potential flow. The passage from one region to another takes place at the core radius denoted r_c . The vortex is composed of axial, azimuthal and radial velocity perturbations, as well as static and total pressure perturbations. Among all the existing models of vortex generation described in [8] (Rankine, Kaufmann, Scully, Lamb-Oseen), the Vatistas model [78, 130] makes possible, under the hypothesis of an axisymmetric vortex and incompressible flow, to define in the polar reference frame the tangential velocity that depends on the radius from the center of the vortex:

$$v_\theta(r) = \frac{\Gamma_0}{2\pi} \left[\frac{r}{(r_c^{2n} + r^{2n})^{1/n}} \right] \quad (3.10)$$

Where Γ_0 is the circulation of the vortex, r_c the radius of the core and n an integer that depends on the type of application. If $n = 1$, the velocity distribution is the same as the Kaufman and Scully's one. Axial and radial velocities are obtained by linearising the Navier-Stokes equations and by injecting the Vatistas tangential velocity. This is well explained in [8] and leads to:

$$v_x(r, x) = v_\infty - \frac{\mathcal{A}}{x} \left[1 - \frac{r^2}{(r_c^{2n} + r^{2n})^{1/n}} \right] \quad (3.11)$$

$$v_r(r, x) = -\frac{\mathcal{A}r}{2x^2} \left[1 - \frac{r^2}{(r_c^{2n} + r^{2n})^{1/n}} \right] \quad (3.12)$$

With \mathcal{A} the deficit (+) or excess (-) of momentum, x the axial distance from the leading edge of a blade and v_∞ the axial free-stream velocity far from the vortex. The pressure field is derived from the radial equilibrium equation:

$$\frac{v_\theta^2}{r} = \frac{1}{\rho} \frac{\partial p}{\partial r} \quad (3.13)$$

After integrating, replacing the expression of the tangential velocity and supposing $n = 1$, the pressure field is given by:

$$P_s = P_\infty - \frac{\rho}{2} \left[\frac{\Gamma_0}{2\pi r_c} \right]^2 \left[\frac{r_c^2}{r_c^2 + r^2} \right] \quad (3.14)$$

The incompressibility hypothesis makes possible to obtain the total pressure field:

$$P_t = P_s + \frac{1}{2}\rho \left(v_\theta^2 + v_r^2 + v_x^2 \right) \quad (3.15)$$

By making the hypothesis of a vortex centred on the origin of the plane, the input parameters that should be given by the user are r_c , Γ_0 , P_∞ , v_∞ , ρ , A et x . The theoretical distributions of v_θ , v_r , v_x and P_s are depicted in Figure 3.4.

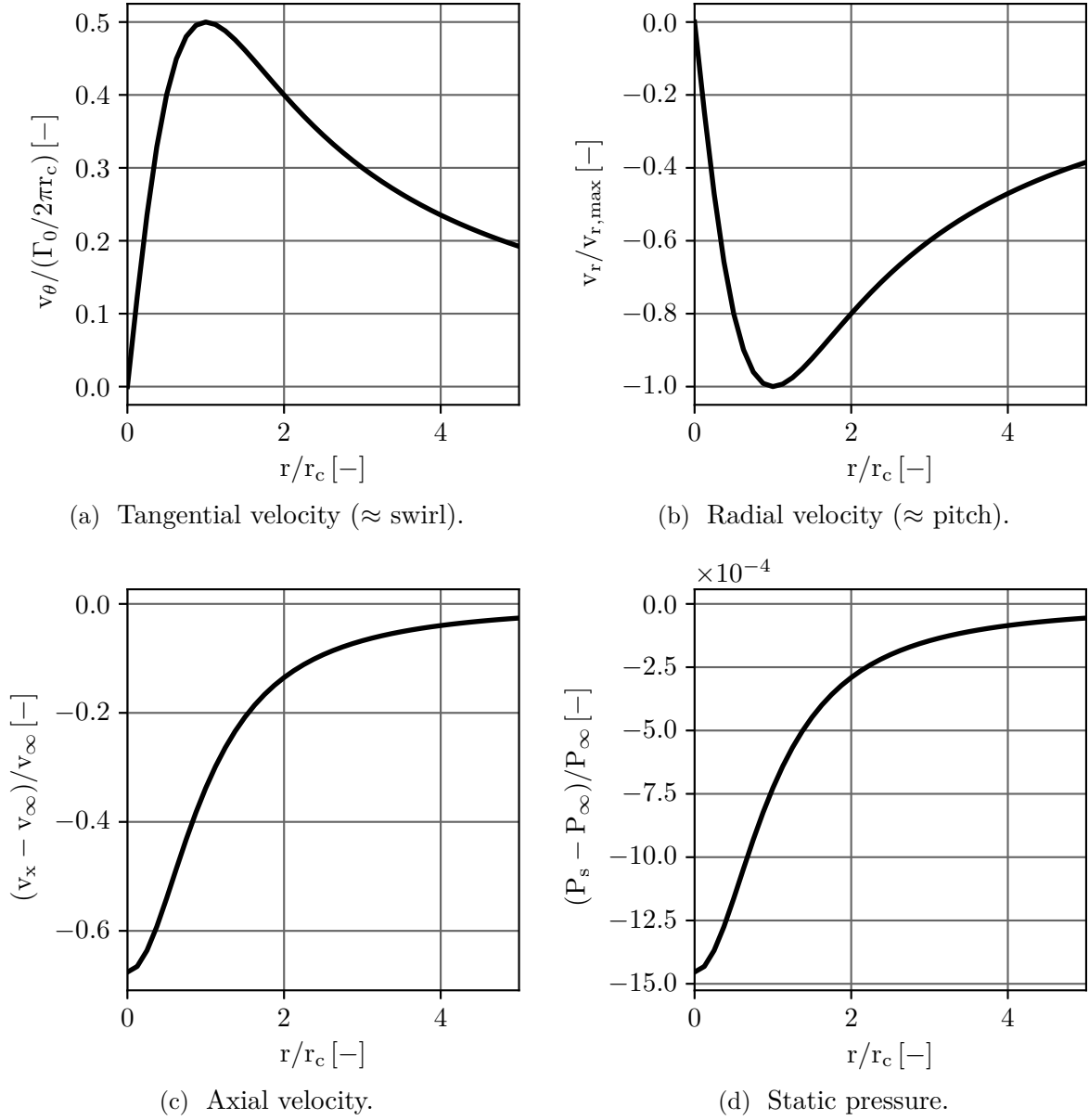


Figure 3.4 – Theoretical distributions of the normalised fields obtained from the Vatistas model for $n = 1$.

Velocities in the Cartesian reference frame $\mathbf{v}_{(x,y,z)}$ are obtained from the polar coordinates velocities $\mathbf{v}_{(x,r,\theta)}$ and the passage matrix \mathcal{P} :

$$\mathbf{v}_{(x,y,z)} = \mathcal{P}\mathbf{v}_{(x,r,\theta)} \quad (3.16)$$

$$\begin{pmatrix} v_x \\ v_y \\ v_z \end{pmatrix} = \begin{pmatrix} 1 & 0 & 0 \\ 0 & \cos \theta & -\sin \theta \\ 0 & \sin \theta & \cos \theta \end{pmatrix} \begin{pmatrix} v_x \\ v_r \\ v_\theta \end{pmatrix} \quad (3.17)$$

Based on the experimental data of the FACTOR project, it is possible to define all the input parameters and constants and to obtain the velocities and pressure fields in the Cartesian reference frame. Table 3.3 sums up the main characteristics of the vortex.

r_c [m]	Γ_0 [$\text{m}^2 \cdot \text{s}^{-1}$]	v_∞ [$\text{m} \cdot \text{s}^{-1}$]	P_∞ [kPa]	x [m]	\mathcal{A} [$\text{m}^2 \cdot \text{s}^{-1}$]	ρ_∞ [$\text{kg} \cdot \text{m}^{-3}$]
$5 \cdot 10^{-3}$	0.6	74	140	1	50	1.116

Table 3.3 – Characteristics of the vortex.

Finally, synthetic turbulence using a digital filter based on the work of Klein *et al.* [58] and the modifications of Touber and Sandham [123] and Xie and Castro [141] is imposed. It has the advantage to be adapted to compressible flow and not to introduce any non-physical low-frequency mode. With this method, the turbulent length scale is imposed as well as the Reynolds stresses. The turbulence imposed at the inlet is homogeneous isotropic turbulence (HIT) where the turbulent structures are the same in all directions ($l_{T,i} = 7$ mm) and the diagonal terms of the Reynolds stress tensor are set equally to target the turbulent kinetic energy ($R_{ii} = \overline{v'_i v'_i} = 80 \text{ m}^2 \cdot \text{s}^{-2}$). The extra-diagonal terms are set to zero;

- **Outlet:** static pressure of 85 kPa is specified at the outlet of the domain with a relaxation coefficient. To avoid any reflection, the outlet condition is far enough from the TE;
- **Lateral walls** $-2 < x^* < 1$: adiabatic slip condition;
- **Lateral walls** $1 < x^* < 3$: periodicity condition. Periodic boundary conditions are applied to guide properly the hot spot to the outlet of the domain and to avoid bouncing on the walls and the appearance of a possible back-flow. It also enables to keep the deviation as in a turbine. A possible instability at the junction between the slip wall condition and the periodic boundary condition has not been observed. Finally, no vortex pairing has been evidenced;
- **Top and down walls:** adiabatic slip condition.

3.2.4 RANS boundary conditions

Boundary conditions for the RANS simulations are the same as the LES except for the turbulent quantities and the value of pressure at the outlet which is adjusted to match LES radial Mach number distribution at the TE plane ($x^* = 1$). The inlet boundary conditions are mapped from the LES for which time-averaged conservative variables $\overline{\rho}$, $\overline{\rho v_x}$, $\overline{\rho v_y}$, $\overline{\rho v_z}$ and $\overline{\rho E_t}$ are extracted to obtain total quantities $\overline{P_t}$ and $\overline{T_t}$ and flow angles $\overline{\alpha}$ and $\overline{\phi}$. Overall, the inlet Mach number is 0.18 and the Reynolds number is $1.5 \cdot 10^5$. A particular focus on turbulent quantities to impose is done and is presented in section 3.5. The inlet map can be seen in Figure 3.5.

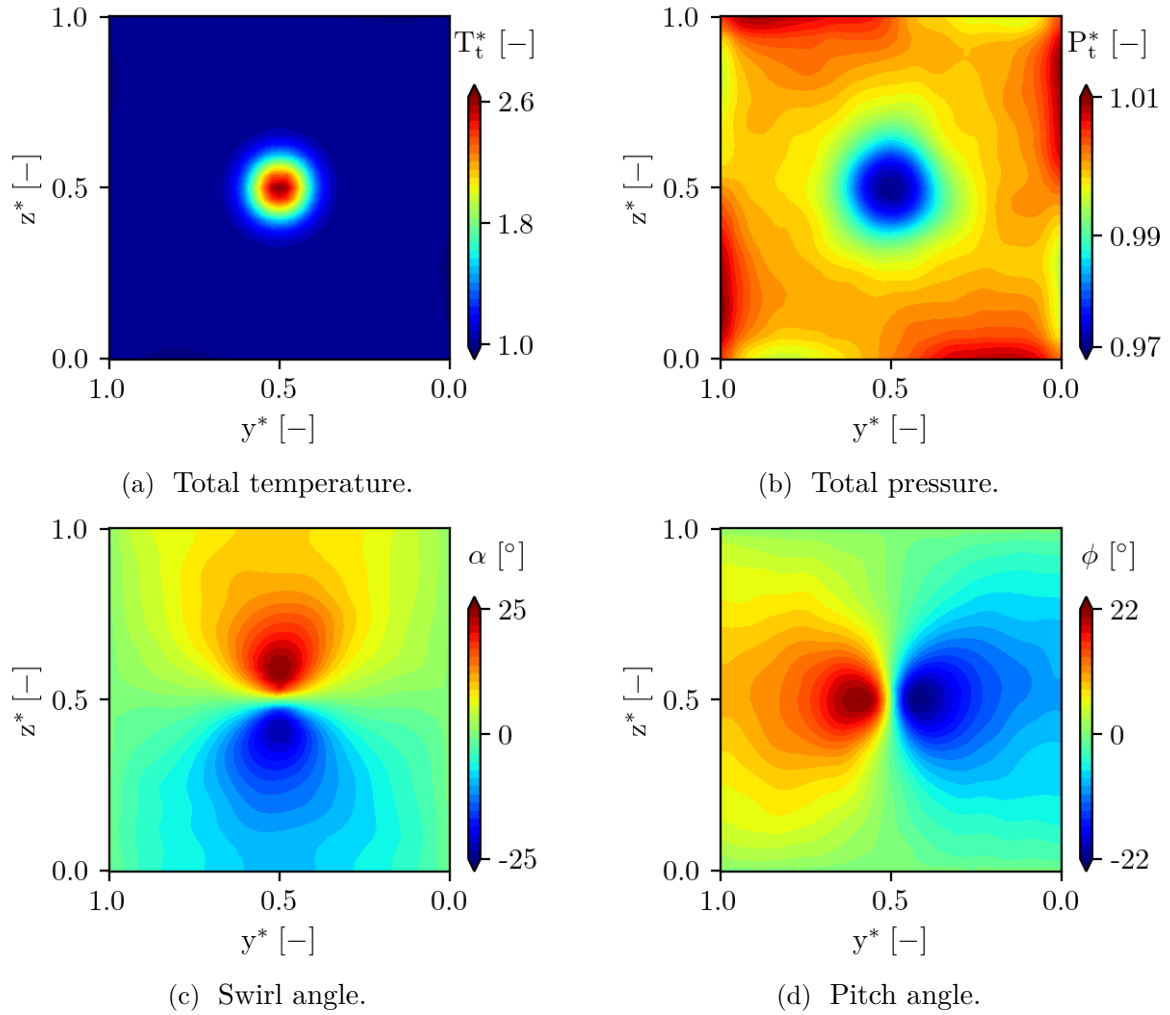


Figure 3.5 – Steady boundary conditions applied at the inlet of the duct for both LES and RANS simulations. Total temperature and total pressure are normalised by the mean value. The vortex is rotating in a clockwise direction looking downstream.

3.2.5 Numerical parameters

All RANS simulations are performed with the ONERA multi-physics *elsA* software, already described in Chapter 2 where an upwind Roe scheme with a minmod limiter is used for convective terms. Diffusive fluxes are computed with a second-order centred scheme. Different turbulence models are used: Smith $k-l$, Wilcox $k-\omega$ and Launder-Sharma $k-\epsilon$. Turbulence intensity or production of turbulence are punctually modified and will be presented in 3.5 in the sensitivity study.

LES are performed with *IC3* developed at Département d’Aérodynamique d’Énergétique et de Propulsion (DAEP) at ISAE-SUPAERO and forked from the *CharLES^X* solver [12, 99]. It is an unstructured explicit cell-centred density-based solver that solves the compressible formulation of the Navier-Stokes equations in their conservative form. Spatial convective fluxes are computed from interpolated values of ρ , v_i , and P_s at the barycentre of each control volume face. Hybridisation between a fourth-order non-dissipative centred scheme and a third-order dissipative but more stable upwind scheme obtained with the Harten, Lax and van Leer Contact

(HLLC) approximate Riemann solver [122] is used for the computation of a unique flux at each internal face [32, 57, 70]. The blending coefficient to switch from centred to upwind scheme and *vice versa* depends on the skewness of the mesh. In general, its value remains close to 0 so that the centred scheme is adopted. Time integration is done with an explicit third-order Runge-Kutta method, so that the time-step is limited by the CFL condition. Since the numerical dissipation is low (explicit LES), it is necessary to use a subgrid-scale model to take into account the effect of unresolved turbulence on the resolved flow. The smallest turbulent scales are therefore modelled with the Vreman subgrid-scale model [131], with the model constant $C_V = 0.07$. Finally, note that recent development performed in the scope of Sáez Mischlich's thesis [115] with the sliding mesh enables to run turbomachinery simulations. A high-order version of the code based on the spectral difference and flux reconstruction methods is also available [115].

Numerical approach	Spatial scheme	Temporal scheme	Turbulence model/SGS
RANS	Upwind (2 nd order)	Backward Euler	Smith $k-l$, Launder-Sharma $k-\epsilon$, Wilcox $k-\omega$
	Centred (2 nd order)	CFL = 10-30	
LES	Upwind (3 rd order)	Explicit RK3	Vreman
	Centred (4 th order)	CFL = 0.9 $\Delta t = 9 \cdot 10^{-8}$ s	

Table 3.4 – Numerical set-up for the Navier-Stokes numerical approaches.

3.2.6 Post-processing

Radial distributions are obtained using an in-house thermodynamic average based on the temporal-averaged conservatives. The azimuthal averaged quantity Φ is denoted by $\langle \overline{\Phi} \rangle_\theta$. The axial evolution of a quantity Φ is obtained by a mass-weighted average of the quantity Φ on surfaces perpendicular to the principle axis such as:

$$\langle \overline{\Phi} \rangle_m = \frac{\int_S \overline{\rho \vec{U} \Phi} \cdot \vec{n} dS}{\int_S \overline{\rho \vec{U}} \cdot \vec{n} dS} \quad (3.18)$$

Values are made non-dimensional by the inlet value $\langle \overline{\Phi} \rangle_{m,0}$. Note that the turbulence length scale is area-weighted averaged, with the naming $\langle \overline{\Phi} \rangle_S$. LES and RANS simulations are thus post-processed using the same procedure.

3.3 Convergence study

3.3.1 Mesh and statistical convergence of the LES

As already mentioned, convergence of the LES is relatively important in the study as the LES is used as a basis for the RANS calibration. In that sense, mesh and statistical convergence are performed.

For the mesh convergence, two additional meshes have been generated in addition to the baseline mesh: a coarser and more refined mesh. Characteristics of the meshes and associated

simulations are presented in Table 3.5. All the simulations are realised at iso-numerical parameters and iso-boundary conditions. Mesh convergence is also used to perform a time-step convergence since, at constant CFL, the time-step decreases as the cell volume decreases.

Mesh	Nb. cells (10^6)	CFL	Δt [s]	V_{\min} [m^3]	Δx_{\min} [m]	CPU time [-]
Baseline	4.8	0.9	$8.9 \cdot 10^{-8}$	$6.4 \cdot 10^{-11}$	$1.4 \cdot 10^{-4}$	1
Coarse	2.4	0.9	$1.1 \cdot 10^{-7}$	$2.4 \cdot 10^{-10}$	$1.7 \cdot 10^{-4}$	0.3
Fine	9.5	0.9	$7.2 \cdot 10^{-8}$	$2.1 \cdot 10^{-11}$	$1.1 \cdot 10^{-4}$	1.8

Table 3.5 – Meshes characteristics for the mesh convergence. The CPU time is normalised with respect the baseline mesh time necessary for the convergence of the statistics.

The first analysis of the mesh convergence is based on the LES criterion explained in 3.2.2.2: Pope’s criterion. Figure 3.6 shows instantaneous distributions of this criteria at mid-span of the channel. They are well respected for the baseline and fine meshes. For the coarse mesh, the value of Pope’s criterion is too high in the curved part, where the velocity gradients are stronger (Figure 3.6b). This mesh must be avoided. For the three meshes, values are out of the tolerated range downstream of the TE. This is normal since the mesh is voluntarily coarsened from that point.

A spatial probability density function of Pope’s criterion is then displayed in Figure 3.7. It is obtained using one snapshot of the volume clipped from the part downstream the TE. Cumulative distribution is used to better quantify the quality of the meshes as it tends to 1. Once again, most of the cells of the baseline and fine meshes are contained within the recommended range.

Finally, a temporal analysis is performed. The same histogram is plotted in Figure 3.8 only for the baseline mesh, which is obtained using 970 snapshots at a given position (at mid-length of the curved part centred on the HS position). The baseline mesh is well-resolved since the criterion is well respected.

Mesh convergence can also be checked by looking at radial distributions of some aerodynamic quantities: the swirl angle $\bar{\alpha}$ and the total temperature \bar{T}_t are studied at different axial positions

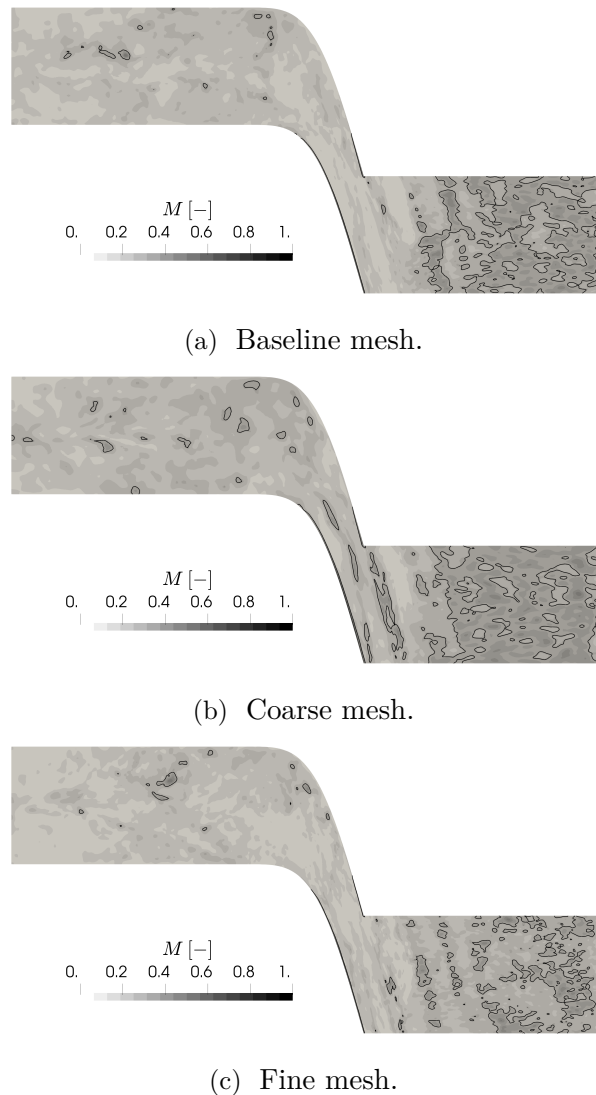


Figure 3.6 – Evolution of Pope’s criterion at mid-span of the channel - Contours at 0.2 displayed in black

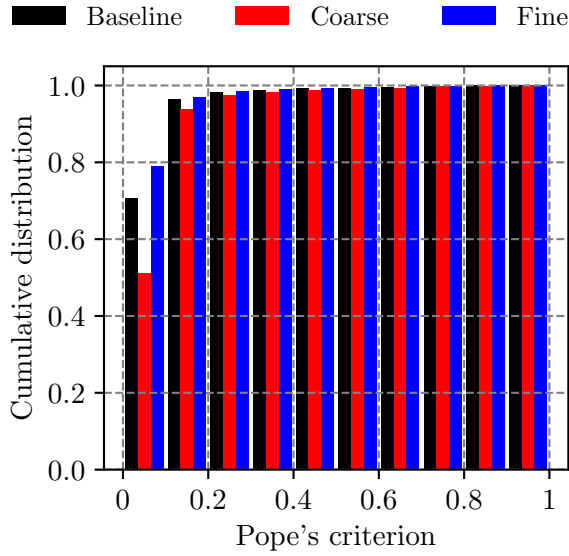


Figure 3.7 – Spatial PDF of Pope's criterion for the three meshes.

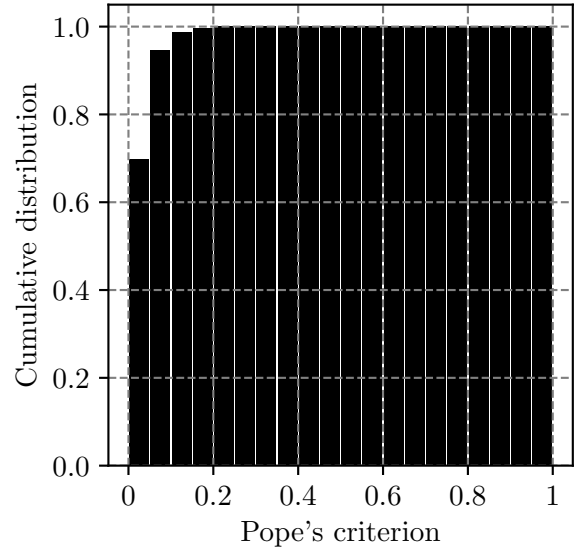


Figure 3.8 – Temporal PDF of Pope's criterion for the baseline mesh.

of the channel (Figure 3.9). The coarse mesh gives different results in the curved part compared to the baseline and fine meshes. In particular, looking at \overline{T}_t distribution, both the diffusion and the intensity are more important for the coarse mesh.

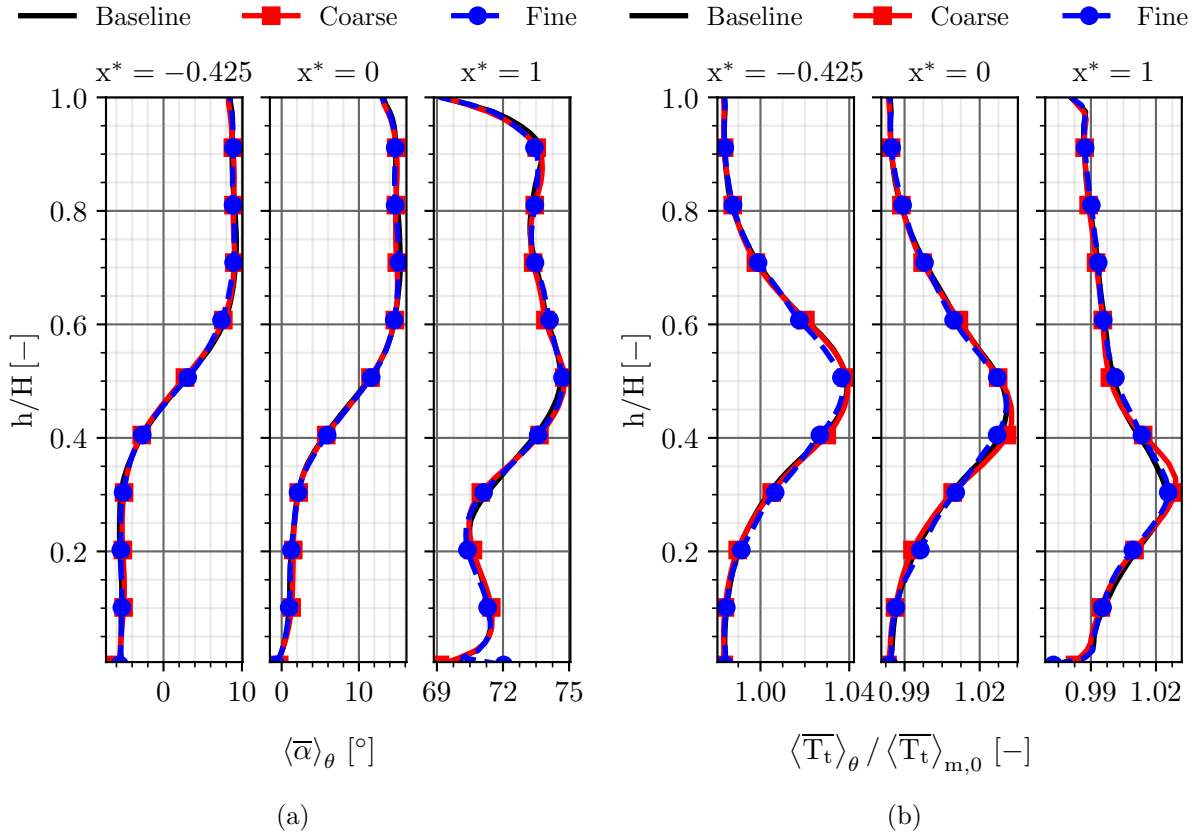


Figure 3.9 – Radial distributions of $\overline{\alpha}$ (a) and \overline{T}_t (b) for the different meshes.

As the turbulent kinetic energy from the LES is compared to the values obtained from the RANS simulations by considering only the resolved part ($k = 0.5 \cdot \overline{v'_i v'_i}$), the contribution of the modelled part must be evaluated. Figure 3.10 shows the axial evolution of the mass-weighted turbulent kinetic energy for different mesh resolutions. It clearly shows that refining the mesh does not modify the evolution of resolved turbulent kinetic energy, although there is less modelled turbulent kinetic energy. In that sense, for the LES/RANS simulations comparisons, only the resolved part of turbulent kinetic energy is considered.

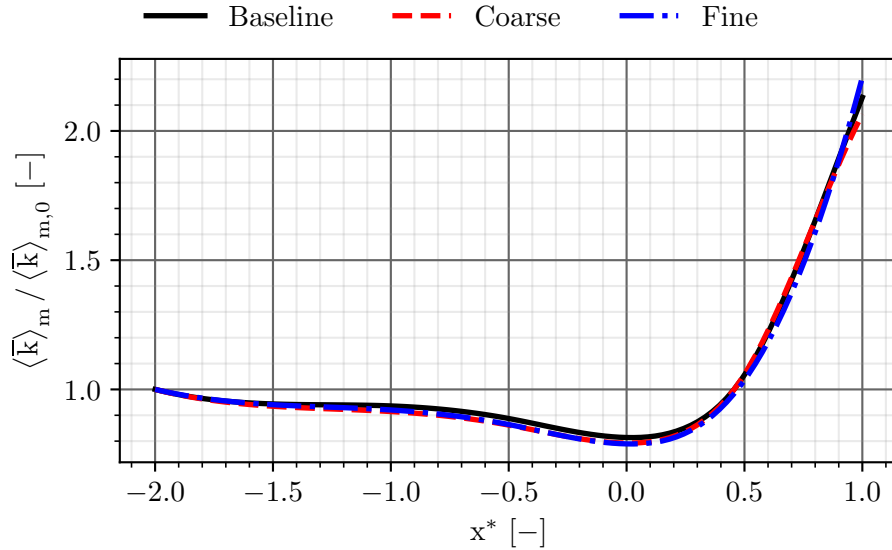


Figure 3.10 – Axial evolution of k_{RES} for different mesh resolutions.

Statistical convergence has been performed on the baseline mesh for different statistical windows based on a convective time (CT) defined as the time a particle travels between the inlet of the domain and the TE ($x^* = 1$) at the mid-span channel's velocity. 5, 10 and 15 CT have been studied (where about 20000 iterations are required for 1 CT). It reveals that 10 CT are required to reach independency of the statistical window.

Moreover, the dependence of k on the averaging time has also been quantified. Since the averaging procedure can hide statistical convergence issues, power spectral density of $v'_i = v_i - \overline{v_i}$ have been performed for the CT used for the statistical convergence, *i.e.* 5, 10 and 15 CT at different local positions. Probes have been placed on the averaged HS position, where turbulence activity is higher. In Figure 3.11 are depicted the PSD of the components of the fluctuating velocity at probe 5 (see definition in Figure 3.27) for a sampling frequency of 45 kHz obtained with the Welch method [125]. Low and high frequencies are well captured in the same way for 10 and 15 convective times.

Mesh and statistical convergence have been performed on the LES to ensure a good quality and reliability of the high-fidelity simulations. In that sense, the baseline mesh together with a statistical average on 10 convective times are required.

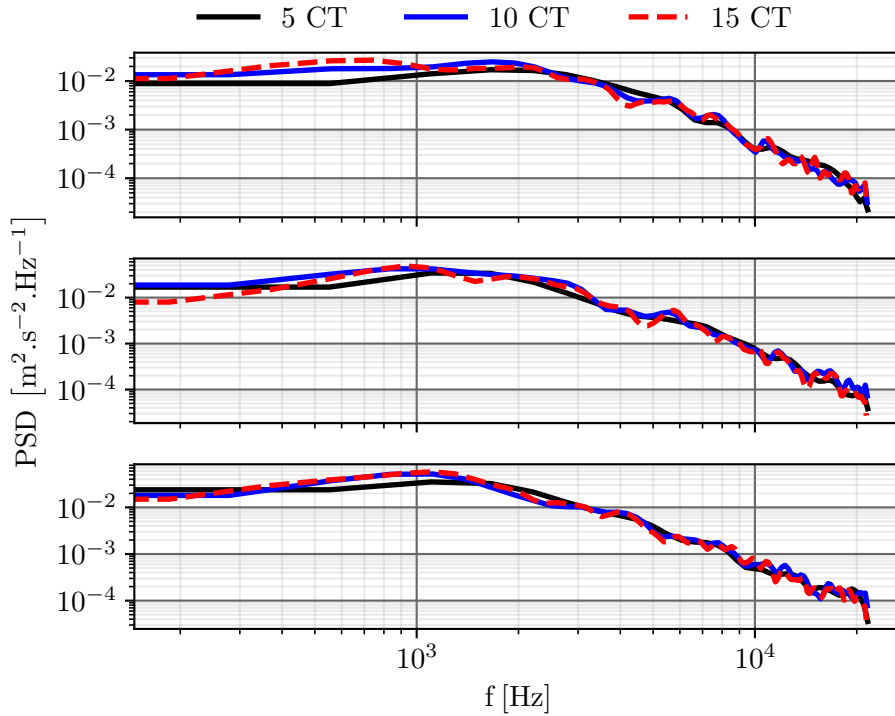


Figure 3.11 – PSD of fluctuating velocity at probe 5 for different convective times - Top: PSD of v'_x , middle: PSD of v'_y , bottom: PSD of v'_z . Sampling frequency is 45 kHz.

3.3.2 Numerical convergence

For the LES, the numerical convergence is also assessed with the evolution of the normalised massflow rate at the inlet and outlet of the domain as well as with the convergence of the statistics (mean, RMS and extra-diagonal Reynolds stress tensor values) by means of probes at different locations of the domain. The evolution of the massflow rate at the inlet and outlet of the domain is proposed in Figure 3.12a. The convergence is reached after very few convective times. In terms of statistics, Figure 3.12b presents the evolution of the RMS of the velocity components at the specific position $x^* = 0$ at mid-span of the channel. Once the statistics firstly reach a plateau (after 5 CT), they are reset for the acquisition of the averaged solution (10 CT).

Considering RANS simulations, the same criteria described in 2.3 are applied and are thus not depicted. Finally, Table 3.6 shows the overall CPU time for each type of simulation. Note that LES have been performed thanks to the HPC resources from CALMIP on the Olympe supercomputer using Intel Skylake 6140 nodes, which differs from the RANS simulations, as already discussed in 2.3.

Simulation type	Convective time	CPU time/ite [$\mu\text{s}/\text{nbCell}$]	CPU time [h]
LES	15	8.8	12000
RANS	-	6.5	250

Table 3.6 – Evaluation of the computational cost on the channel’s configuration.

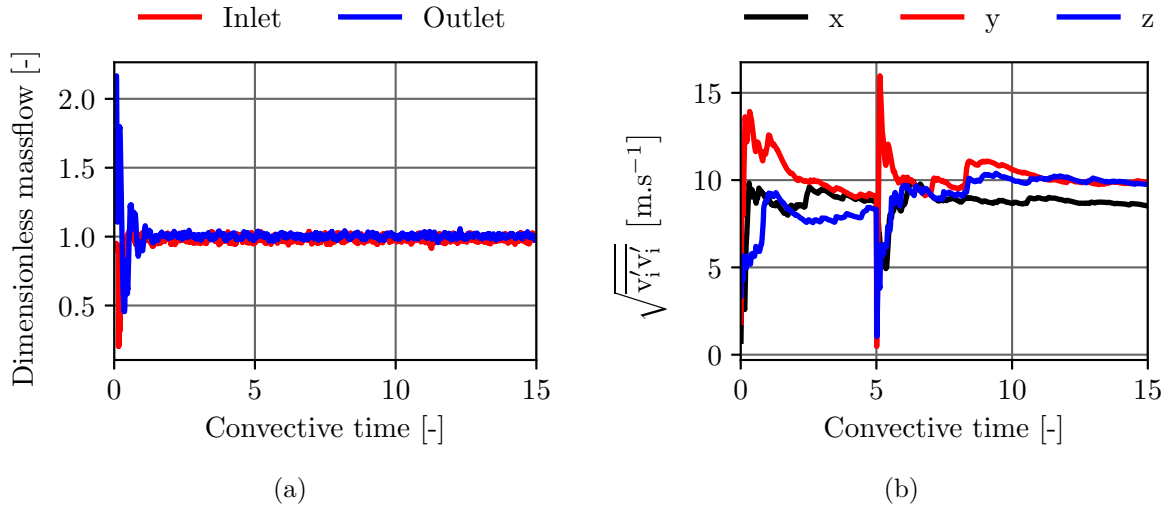


Figure 3.12 – Evolution of the massflow rate at the inlet and outlet of the domain (a) and convergence of the RMS of velocity (b) for the LES.

3.4 Analysis of the LES to study the topology of the swirled flow

This section focuses on the physics of the stratified flow to establish the general behaviour of this kind of flow that will serve as a reference for RANS simulations. To correctly capture the transport of a hot streak inside a turbine stage, both the migration and the diffusion must coexist. The competition between both of them depends on physical factors that are going to be described in this section.

The effect of the direction of the swirl’s rotation is firstly tackled. Then, a turbulent kinetic energy budget along the bent duct is performed, to highlight the most predominant terms that govern the turbulent flow motion. In a third part, the evaluation of an integral length scale is achieved. Finally, before dealing with the stability of the swirled flow, the integral length scale at the inlet, *i.e.* the dissipation scale, is modified to see its impact both on the migration and diffusion of the swirled hot streak.

3.4.1 Effect of swirl on the hot streak migration

The swirl intensity directly sets the trajectory of the HS, and needs to be correctly captured. In the following, three LES are considered: a first one denoted ‘SWIRL +’ in which the HS is rotating in a clockwise direction looking downstream, a second one ‘SWIRL -’ with counter-clockwise rotation. The third one is named ‘NO SWIRL’ and exhibits no swirl components at the inlet, *i.e.* a purely axial injection. Note that the swirl has the same absolute value for ‘SWIRL+’ and ‘SWIRL -’. Figure 3.13 shows an iso-coutour of \overline{T}_t at 460 K colored by $\overline{\phi}$ angle for ‘SWIRL +’, ‘SWIRL -’ and ‘NO SWIRL’ cases. \overline{T}_t fields at the LE and TE are also displayed. Without any swirl components at the inlet, no radial migration of the HS is observed. Then, the direction of rotation strongly impacts the way the HS radially migrates: a positive swirl implies a radial migration of the HS towards the shroud. The contrary is observed for the ‘SWIRL -’ case.

Without taking into account any boundary layers, only the effects of swirl components and curvature lead to a radial migration of the HS, that a simple radial equilibrium equation applied to the channel can explain:

$$\frac{\partial P_s}{\partial n} = \rho \frac{v_\theta^2}{R_c} \quad (3.19)$$

Where R_c is the radius of curvature, which is constant over the spanwise direction. v_θ can be decomposed as the sum of $v_{\theta,curvature}$ (that is radially constant) and $v_{\theta,swirl}$ where the value of $v_{\theta,swirl}$ depends on the case:

- SWIRL +: $v_{\theta,swirl}$ goes from negative to positive from the hub to the shroud of the channel.
- SWIRL -: $v_{\theta,swirl}$ goes from positive to negative from the hub to the shroud of the channel.
- NO SWIRL: $v_{\theta,swirl}$ remains constant over the spanwise direction.

Consequently, the pressure gradient normal to the curvature is modified in the spanwise direction and explains the migration of the HS. This is observed in Figure 3.14 where the transverse pressure gradient is plotted on a line passing through the HS. For the case, without swirl components at the inlet, $\partial P_s / \partial z$ remains close to zero as $v_{\theta,swirl}$ vanishes. It also shows that the redistribution is symmetrical with respect to the channel's height for 'SWIRL +' and 'SWIRL -' cases. Computations in a straight duct and a convergent duct with dimensions equivalent to the bent duct and injection of turbulence with positive swirl components at the inlet have been performed (but not presented here) and showed no radial migration of the HS.

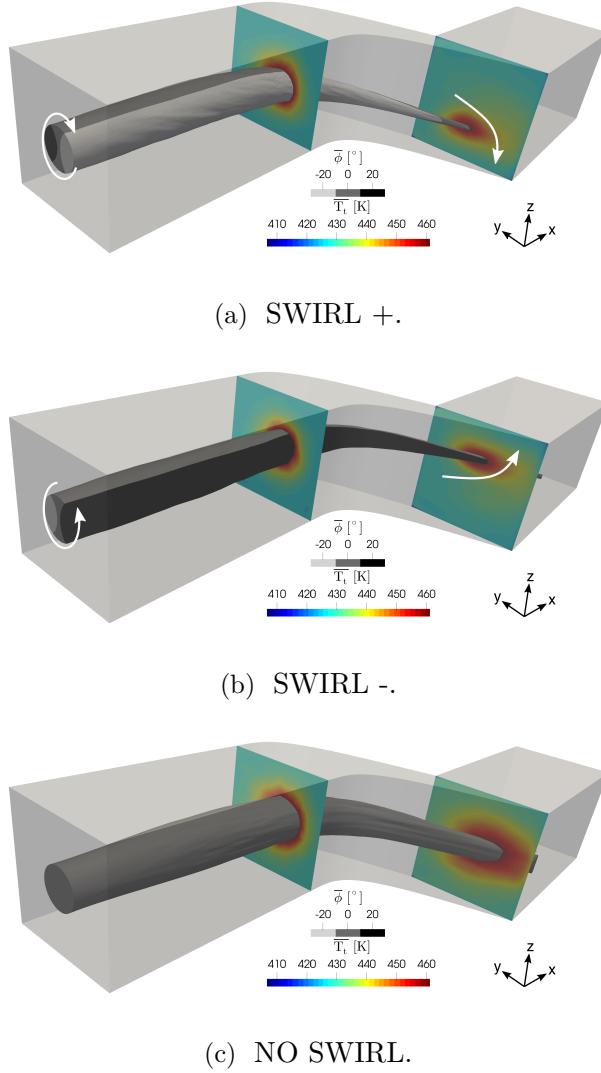


Figure 3.13 – Iso-contour at 460 K of time-averaged total temperature coloured by pitch angle.

The swirl intensity is thus of first importance in defining the HS trajectory. Such a sheared flow also activates turbulence production, which in turn promotes diffusion. A delicate mechanism is occurring, possibly out of the reach of the RANS approach, which models the production. In low curved geometries such as compressors, the redistribution will be small rather than in turbines where the curvature is more pronounced and where swirl predictability gaps will lead to a wrong prediction of the HS trajectory. From now on, one only considers the case representative of what is encountered in an axial high-pressure turbine, *i.e.* the 'SWIRL +' case.

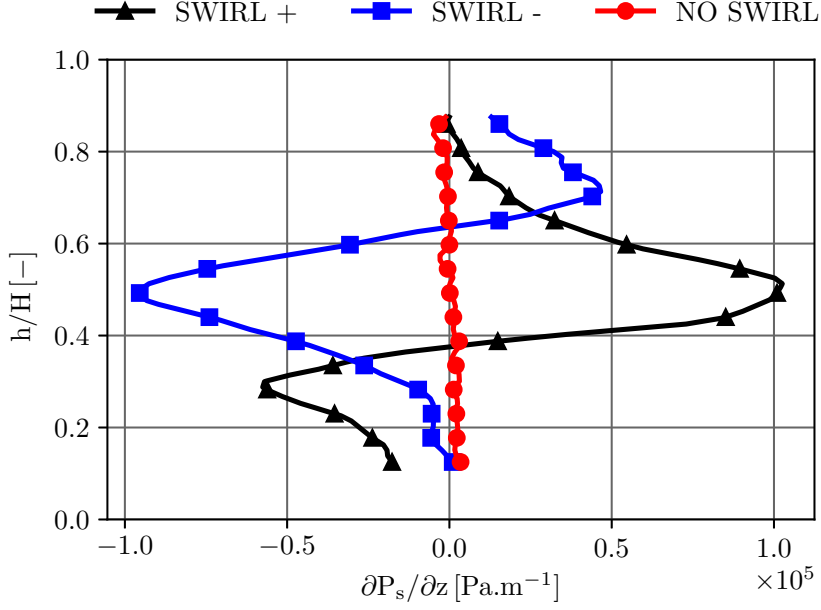


Figure 3.14 – Radial evolution of the transverse static pressure gradient at $x^* = 0.25$.

3.4.2 Turbulent kinetic energy budget

To better understand the dynamics of the flow and the turbulence energy transfers within the channel, it is necessary to place at the turbulent level and to perform a turbulent kinetic energy budget to emphasise the most predominant terms that govern the fluid motion. A turbulent kinetic energy budget is used when the relative contribution of production, dissipation and transport of turbulence must be evaluated. The weight of each term gives deep details on the flow stability. The flow's ability to destroy or produce turbulence can also be identified. In the literature, many TKE budgets have been performed. Jiménez *et al.* [56] performed a budget of a turbulent boundary layer simulation. In his PhD thesis, Monier [81] performed a TKE budget analysis of a corner separation and a tip-leakage flow and compared both LES and RANS simulations. Bhide and Abdallah [9] used LES to make a budget in compressible rectangular jets. The present TKE budget is based on the work of Bogey and Bailly who performed a TKE budget in a round jet by using LES and compared it to DNS data. More details and derivations can be found in [14]. The TKE budget equation is obtained from the transport equation of the Reynolds Stresses (see Equation 1.35 - terms related to the SGS must be added) where the sum of the three ensemble-averaged equations of the diagonal are added [136], leading to:

$$\begin{aligned}
 0 = & \underbrace{-\frac{\partial}{\partial x_j} \left(\frac{1}{2} \langle \bar{\rho} v_i''^2 \rangle [\tilde{v}_j] \right)}_{\text{Mean flow convection}} - \underbrace{\langle \bar{\rho} v_i'' v_j'' \rangle \frac{\partial [\tilde{v}_i]}{\partial x_j}}_{\text{Production}} - \underbrace{\frac{1}{2} \frac{\partial}{\partial x_j} \langle \bar{\rho} v_i''^2 v_j'' \rangle}_{\text{Turbulent diffusion}} \\
 & \underbrace{-\frac{\partial}{\partial x_i} \langle P_s' v_i'' \rangle}_{\text{Pressure diffusion}} + \underbrace{\left\langle P_s' \frac{\partial v_i''}{\partial x_i} \right\rangle}_{\text{Pressure-dilatation}} - \underbrace{\langle v_i'' \rangle \frac{\partial \langle \bar{P}_s \rangle}{\partial x_i}}_{\text{Pressure work}} \\
 & \underbrace{-\left\langle \bar{\tau}_{ij} \frac{\partial v_i''}{\partial x_j} \right\rangle}_{\text{Viscous dissipation}} + \underbrace{\frac{\partial}{\partial x_j} \langle \bar{\tau}_{ij} v_i'' \rangle}_{\text{Viscous diffusion}} - \underbrace{\left\langle \tau_{ij}^{SGS} \frac{\partial v_i''}{\partial x_j} \right\rangle}_{\text{SGS dissipation}} + \underbrace{\frac{\partial}{\partial x_j} \langle \tau_{ij}^{SGS} v_i'' \rangle}_{\text{SGS diffusion}}
 \end{aligned} \tag{3.20}$$

In this equation, statistical averaging of the variable ϕ is noted $\langle \phi \rangle$ and Favre ensemble averaging is given by $[\tilde{\phi}] = \langle \rho \phi \rangle / \langle \rho \rangle$. The filtered fluctuating part and the filtered Favre fluctuating part are respectively represented by $\phi' = \bar{\phi} - \langle \bar{\phi} \rangle$ and $\phi'' = \tilde{\phi} - [\tilde{\phi}]$. Note that the budget is exact for DNS, and that it may not be correctly balanced for LES so that a residual may be added to close the budget.

The extraction of the turbulent kinetic energy budget using LES is quite complex: it requires the computation of the gradients on-the-fly as well as the high-order statistics to build the temporal and Favre-averaged quantities. In the following, the solver *IC3* is used. Two post-processing are performed:

- Axial evolution of the TKE budget from $x^* = -2$ to $x^* = 1$ where Equation 3.20 is integrated over equally spaced blocks with a volume integration. The solution is firstly clipped using a threshold on total temperature to isolate the HS (as in Figure 3.13a) before performing the integration on this new domain to extract the TKE budget. 200 blocks are used;
- 2D maps of the TKE production term at different axial positions.

A global evolution of the TKE budget in the HS is plotted in Figure 3.15. Production, convection, turbulent diffusion, pressure diffusion, pressure-dilatation and dissipation (viscous + sub-grid scale) terms are considered for the analysis.

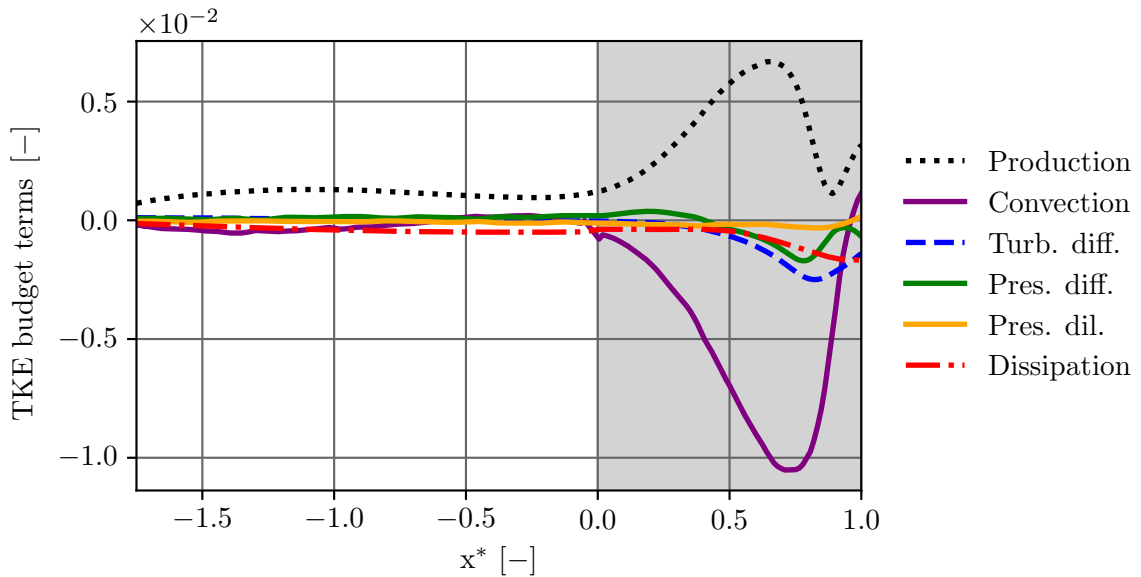


Figure 3.15 – Budget for the turbulent kinetic energy along x^* . Grey zone represents the curved part. Quantities are normalised by $(\rho_\infty v_\infty^3 r_c^2)$.

The TKE budget on the HS clearly reveals two different behaviours depending on the axial position:

- $-2 < x^* < 0$: it corresponds to the straight part of the channel. All the terms are close to 0, except a slight dissipation and production which is a little bit more important and that can be attributed to shear and vorticity. In that sense, Figure 3.16, which represents the PSD of the velocity components at different axial positions on the mean trajectory of the

HS, shows that turbulent kinetic energy increases in this part, evidenced by an increase of the PSD intensity for all velocity components between $x^* = -2$ and $x^* = 1$. Figure 3.17 reveals large coherent structures that are associated with the HS;

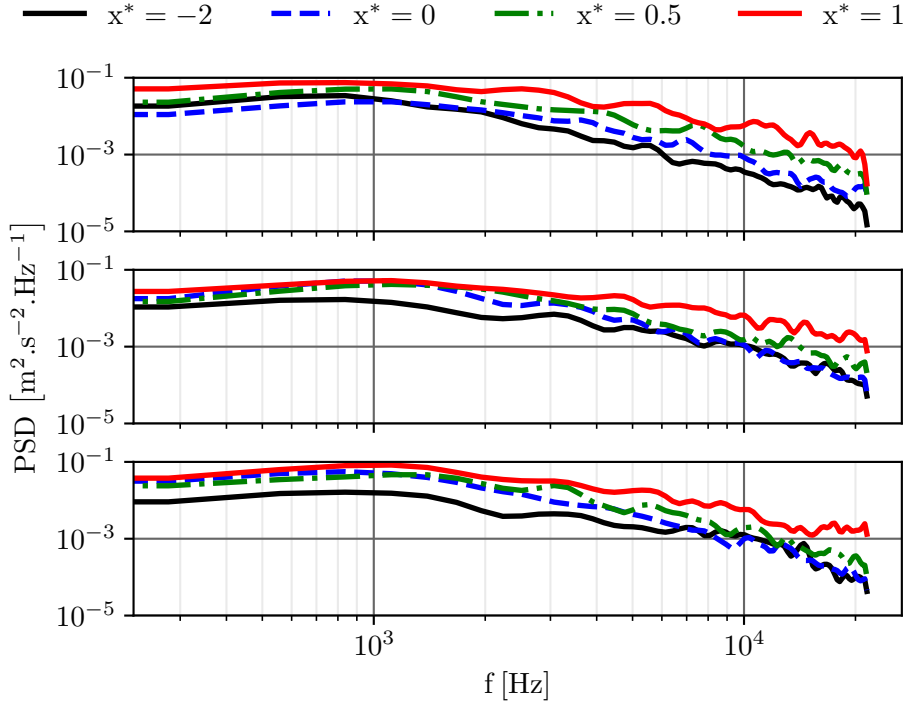


Figure 3.16 – PSD of fluctuating velocity for different axial positions on the mean position of the HS - Top: PSD of v'_x , middle: PSD of v'_y , bottom: PSD of v'_z . Sampling frequency is 45 kHz.

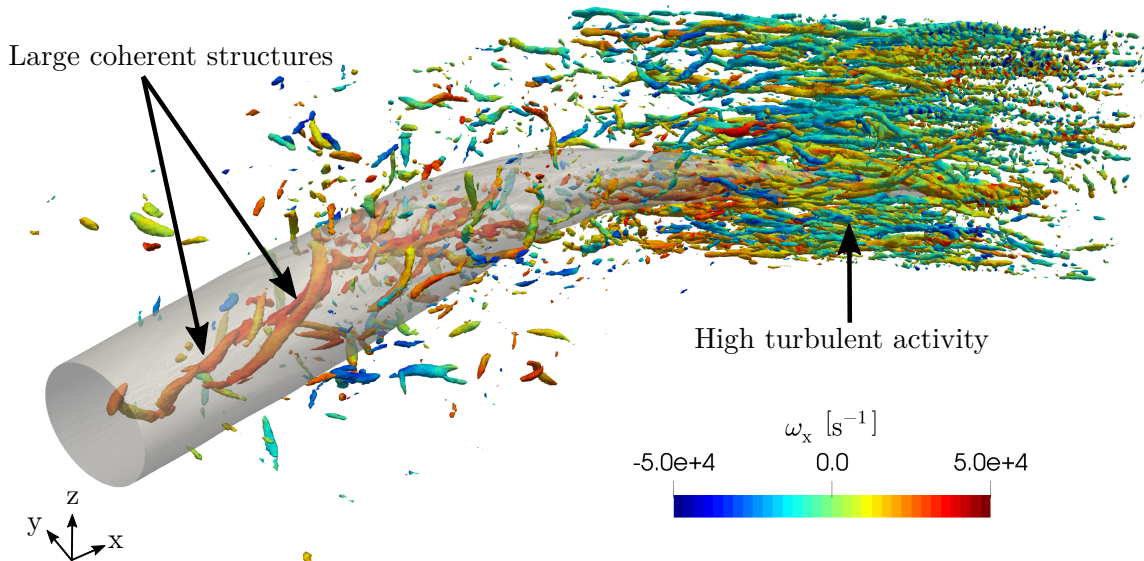


Figure 3.17 – Instantaneous iso-surfaces of Q -criterion at $2.2 \cdot 10^8 \text{ s}^{-2}$ coloured by axial vorticity. The mean position of the HS is represented in grey with an iso-contour at 440 K of time-averaged total temperature.

- $0 < x^* < 1$: in this case, the curvature and the shrinking of the cross-section area are considered, which means additional vorticity and acceleration. The pressure-dilatation term still does not play a major role. Production increases, with a maximum value close to $x^* = 0.7$, corresponding to the position of the throat, and is balanced by convection which is activated with the strong mean acceleration of the flow (from Mach 0.18 at $x^* = 0$ to Mach 0.9 at $x^* = 1$). Redistribution terms have their major contribution at $x^* = 0.8$, with a dominance of turbulence diffusion over pressure diffusion. Dissipation starts after the peak of production where turbulent kinetic energy is higher and eddies are smaller. Figure 3.17 shows that the large coherent structures of the straight part are split into smaller but more resistant structures in the curvature where additional vortices are also generated. These structures have a larger integral length scale (Figure 3.21). Overall, turbulent kinetic energy increases inside the curved part (by comparing blue and red curves of Figure 3.16).

The TKE budget on the HS evidenced two zones where turbulence behaves differently: in the straight part, production dominates whereas in the curved part, both production and mean flow convection are predominant in the budget, with a higher intensity than in the straight portion. This complex physics is expected to fail most turbulence models based on Boussinesq's hypothesis, for which the equilibrium may be substantially affected.

The minimum of production visible at $x^* \approx 0.8$ in Figure 3.15 suggests that backscatter of turbulence is locally present. This phenomenon is observed in Figure 3.18 for negative values of the production term where part of the energy is transferred from the fluctuating to the mean field [91]. Even if some backscatter is noticeable at the beginning of the curvature (Figure 3.18a), most of the energy transfer follows a forward-scatter path. The energy transfer inversion is however more important in the final part of the curvature (Figure 3.18b). This behaviour can be attributed to the close presence of the walls that leads to the anisotropy of turbulence, as explained later in Chapter 4.

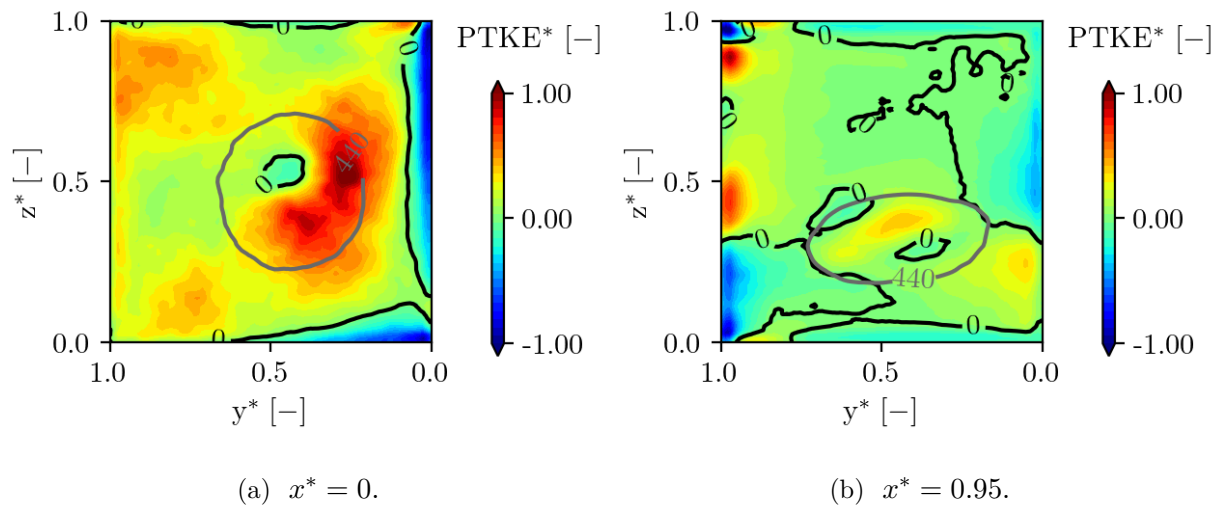


Figure 3.18 – Normalised fields of turbulent kinetic energy production at two axial positions. Iso-contour of $PTKE^* = 0$ in black and iso-contour of time-averaged total temperature at 440 K in grey.

3.4.3 Evaluation of an integral scale of turbulence

The evaluation of an integral scale of turbulence in many turbulent applications is challenging as it is a purely mathematical object based on a statistical approach that can not be directly obtained in a numerical simulation. Its dependency on many parameters and its numerous definitions may lead to different results [91]. According to Pope and Sagaut [91, 98], there exist a multitude of scales of turbulence that are distributed over the turbulence spectrum and that are associated with eddies, *i.e.* turbulent structures with a local swirling motion where vorticity is significant. In the following, the characteristic scale of turbulence related to the energy-containing eddies is considered. The objective is to check the turbulence injection and to look at the evolution of the integral length scale along the channel. The computation of the integral length scale is based on the autocorrelation (or the two-point correlations) of instantaneous velocity signals. The autocorrelation can be of two types: either spatial or temporal. In the first case, the integral length scale is obtained by integrating the autocorrelation function over a length over which the turbulent fluctuations are mutually correlated:

$$l_{T,i} = \int_0^{+\infty} R_{v_i v_i}(\xi) d\xi \approx \int_0^{\xi_0} R_{v_i v_i}(\xi) d\xi \quad (3.21)$$

$$R_{v_i v_i}(\xi) = \frac{E[v'_i(x_i, t)v'_i(x_i + \xi, t)]}{\sigma^2} \quad (3.22)$$

Where $E[\cdot]$ is the expectation operator and σ^2 is the variance. The integration to the first zero crossing ξ_0 gives the integral length scale in the direction i [91]. This method requires numerous equally displayed probes for the computation of the scale. The other technique is based on the temporal autocorrelation which can only be used assuming Taylor's frozen turbulence hypothesis. Turbulent eddies are transported by the mean velocity of the flow in a frozen way and the autocorrelation function provided in Equation 3.22 may be also calculated based on the time history at one point only [117]:

$$l_{T,i} = \int_0^{+\infty} R_{v_i v_i}(\tau) d\tau \cdot \bar{V} \approx \int_0^{\tau_0} R_{v_i v_i}(\tau) d\tau \cdot \bar{V} \quad (3.23)$$

$$R_{v_i v_i}(\tau) = \frac{E[v'_i(x_i, t)v'_i(x_i, t + \tau)]}{\sigma^2} \quad (3.24)$$

Where τ is the time-lag, *i.e.* the time necessary for no correlation and \bar{V} the mean velocity of the main flow at the given probe. For discrete signals, the autocorrelation function must be normalised by the number of samples N and reads:

$$R_{v_i v_i}(\tau) = \frac{\frac{1}{N} \sum_{j=1}^N (v'_{i,j} \cdot v'_{i,j+k})}{v_{i,RMS}^2} \quad (3.25)$$

Where $k = \tau/dt$ are all the discrete values for the time-lag based on the acquisition timestep $dt = 1/f_{acq}$. Integrating Equation 3.25 gives the turbulent timescale.

Equations 3.23 and 3.25 reveal that the turbulent length scale depends on the sampling frequency of the signal. This point is now tackled for the axial length scale. Probes of Figure 3.27 are used for the analysis. In Figure 3.19 is plotted the evolution of the autocorrelation coefficient

as a function of the time-lag for one probe. It shows that $R_{v_x v_x}$ starts at 1, decreases till a first zero crossing at $t = \tau_0$ and then oscillates around 0. The area under the curve to take for the integration can be questionable: even if the choice of the first zero crossing seems a logical choice, some may prefer to plot the turbulent time as a function of the phase-lag and to wait for a plateau, whereas others may eliminate the low-frequency noise by fitting the autocorrelation function [1, 16, 37]. However, the first method is kept, with the first zero crossing, as depicted in Figure 3.19. This method is often used in experiments.

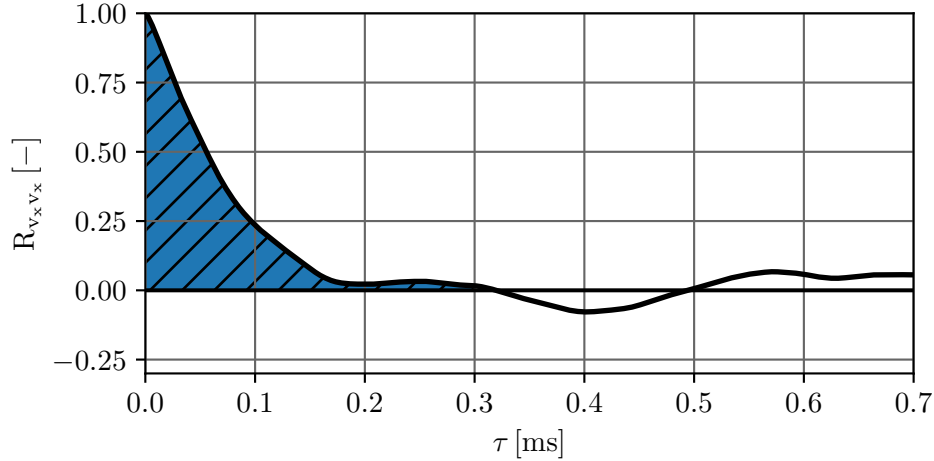


Figure 3.19 – Autocorrelation coefficient of the axial velocity for a random probe.

The acquisition frequency f_{acq} is firstly studied, as it impacts the possible values for the time-lag, and therefore the precision of the integration. Different frequencies are studied: $f_{acq} = 10$ kHz, $f_{acq} = 25$ kHz, $f_{acq} = 45$ kHz and $f_{acq} = 110$ kHz. For all the signals, the time duration is the same and is equivalent to 30 CT. Results are plotted in Figure 3.20 for the longitudinal integral length scale $l_{T,x}$. It clearly shows that a minimum sampling frequency of $f_{acq} = 45$ kHz is required for the convergence of the scale. It also appears that the value of 7 mm imposed at the inlet is not retrieved, with a value slightly smaller at $x^* = -2$. Apart from an increase at $x^* = -1.5$, the scale follows a plateau in the straight part of the channel. Things are different when the flow enters the curved part, where the length scale suddenly increases from 5 mm to 26 mm, as a consequence of the strong acceleration of the flow.

Having converged towards a sampling frequency of 45 kHz, different integral length scales are examined: longitudinal $l_{T,x}$, spanwise $l_{T,y}$, pitchwise $l_{T,z}$ and global l_T . The global integral length scale is obtained by performing the autocorrelation of the magnitude of the velocity. The other scales are recovered from each velocity component. The convection velocity, *i.e.* the mean magnitude of the velocity, is still used to convert from a two-point to one-point correlation. The scales plotted in Figure 3.21 give a very interesting insight into the weight of each directional length scale on the global length scale. It appears that, in the straight part, the major contributor of the global length scale is the longitudinal length scale, for which both scales follow the same evolution and values. In the same way, the transverse scales are equal, due to the symmetry of the vortex in the straight part. From $x^* = 0$, the behaviour is different: the global length scale is firstly and slightly affected by the spanwise length scale $l_{T,z}$ because of the radial redistribution of the flow as already shown in Figure 3.13. Then, the pitchwise scale $l_{T,y}$ has the major weight in the global scale as a consequence of the strong deviation of the flow.

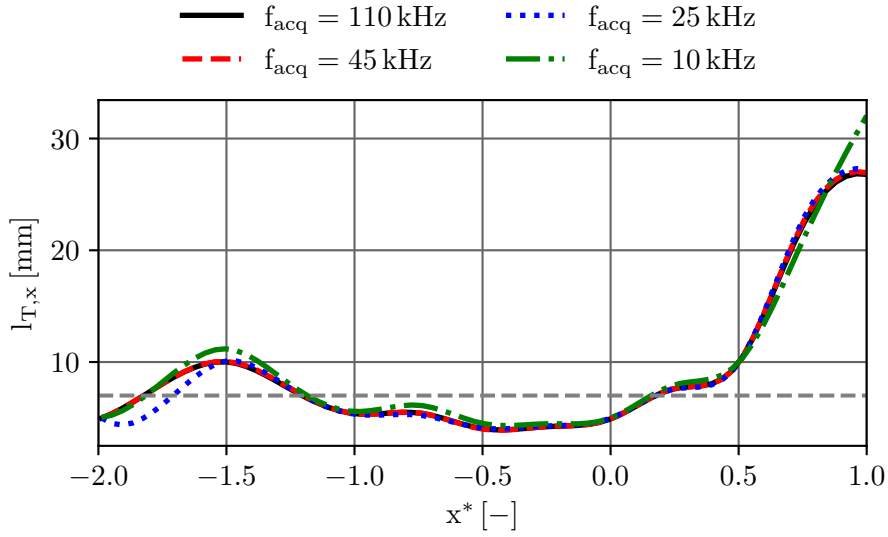


Figure 3.20 – Evolution of the longitudinal integral length scale for different frequency acquisitions along the mean position of the HS. The grey horizontal dashed line represents the turbulence injection scale.

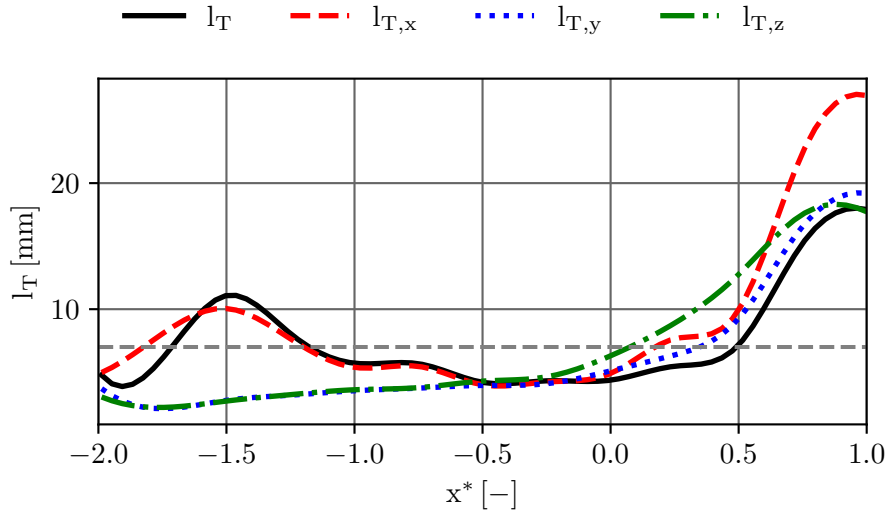


Figure 3.21 – Evolution of different integral length scales along the mean position of the HS. The grey horizontal dashed line represents the targeted turbulence injection scale.

3.4.4 Effect of the turbulent length scale on the hot streak redistribution

In this subsection, the effect of the size of the turbulent structures prescribed at the inlet through turbulence injection is examined. Modifying the turbulent length scale is known to modify the turbulent regime, which can switch from a transport regime to a dissipation regime. But the modification does not only have an impact on the turbulence characteristics. It also has a substantial impact on the aerodynamics and aerothermal. The previous simulation with turbulent length scale $\overline{l_T} = 7$ mm is completed with a second one with a turbulent length scale divided by a factor of 10 ($\overline{l_T} = 0.7$ mm). This present study on the turbulent length scale is not innocuous: the literature review on the FACTOR configuration showed that the prediction of the flow with

the RANS approach is strongly dependant on the value of μ_T/μ , *i.e.* the dissipation scale or turbulent length scale. In that sense, as already mentioned in Chapter 2, Vagnoli *et al.* [129] played with the value of μ_T/μ at the inlet of the domain with turbulence models based on Boussinesq's hypothesis. The aim was to fit the axial evolution of turbulent kinetic energy given by a LES upstream of the NGV of the turbine. By proceeding in this way, the equilibrium of turbulence may differ. Nonetheless, as a first approximation, considering only the turbulent kinetic energy as a metric for the correct imposition of the turbulence dissipation scale is a good candidate. This metric based on Vagnoli's work will be extensively used in Section 3.5.

Figure 3.22 and Figure 3.23 are now described. LES results with the initial length scale of 7 mm show a decrease of radial maximum total temperature combined with a spanwise diffusion: this is due to the effect of molecular diffusion but above all to turbulent diffusion that enhances the thermal mixing (Figure 3.22b). This is the first time that the mechanism involving both the location (radial position) and diffusion (intensity) of the HS is clearly evidenced. This mechanism is at the origin of the aerodynamics/thermal problematic of the high-pressure turbine stage, where both the position and intensity of the HS must be well predicted. In terms of turbulence, \bar{k} naturally decreases in the straight part of the channel ($-2 < x^* < 0$) before increasing as a consequence of the acceleration of the flow (Figure 3.23) [133]: turbulence is transported inside the channel.

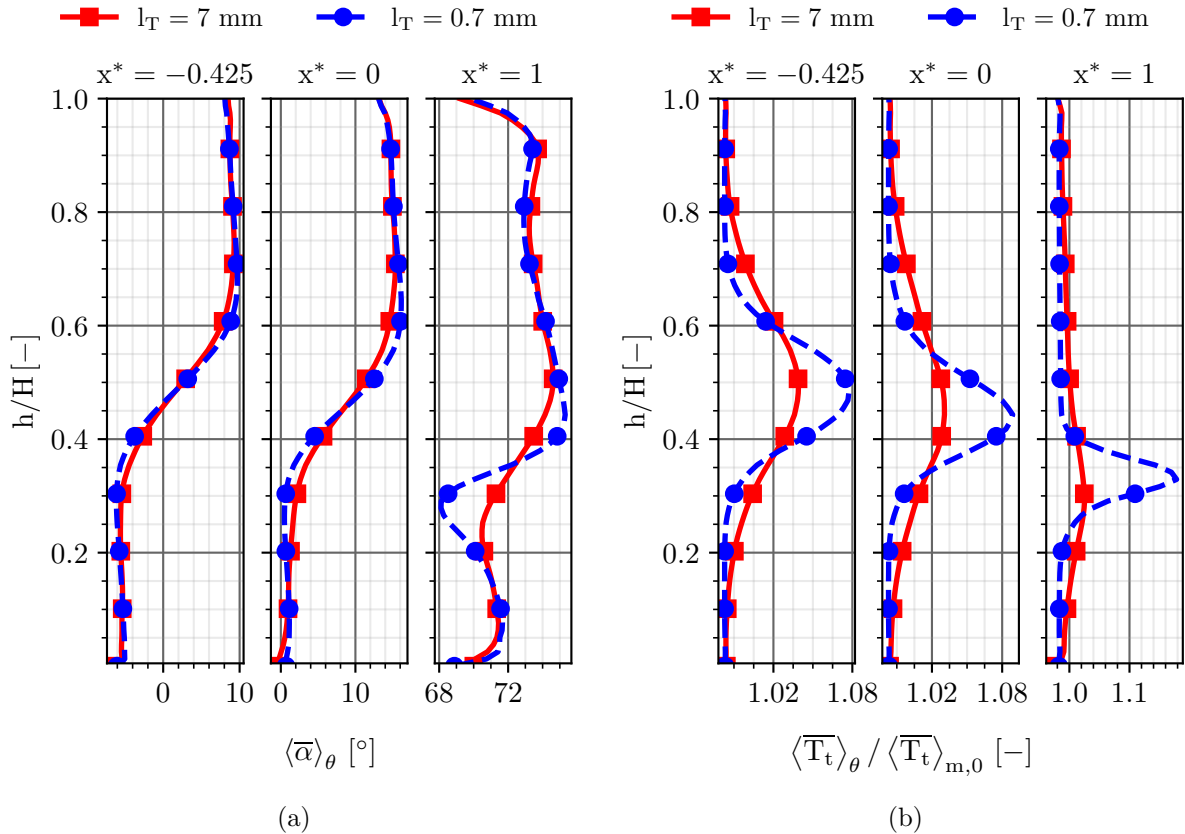


Figure 3.22 – Radial distributions of $\bar{\alpha}$ (a) and $\overline{T_t}$ (b) for the two inlet turbulent length scales.

When decreasing the turbulent length scale, dissipation occurs: \bar{k} strongly decreases in the straight part of the duct. It is divided at maximum by 4 (Figure 3.23). Turbulent structures are dissipated (which would have been highlighted by performing the same TKE budget as for

the nominal turbulent length scale), leading to more coherent aerodynamic structures (the swirl angle is better preserved as shown in Figure 3.22a) but also a too more coherent hot streak with a higher peak of \overline{T}_t (Figure 3.22b). Turbulent diffusion is less dominant compared with the viscosity of the fluid, which is at least one order of magnitude smaller than turbulent diffusion. The dissipation regime is well evidenced with small values of turbulent length scales that shift the spectrum towards the dissipative scales. Figure 3.23 shows that the slope of \overline{k} is higher for the smaller turbulent length scale, which can be explained by:

- A more important production of turbulent kinetic energy;
- Less dissipation in the curved part compared to the nominal case since turbulence already dissipated upstream the curvature.

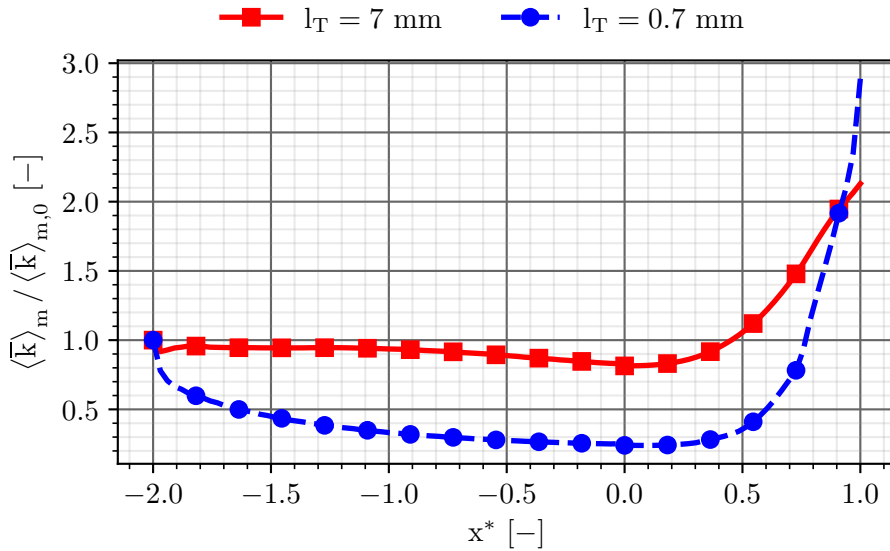


Figure 3.23 – Axial evolution of \overline{k} for different prescribed inlet integral length scale.

From an industrial point of view where the material must resist to high temperatures without melting, the maximum averaged total temperature is now considered. At different axial position x^* , the couple (y^*, z^*) of the maximum temperature $\overline{T}_{t,max}$ is noted, and the evolution of \overline{T}_t in the radial and azimuthal direction is plotted. It enables to track the evolution of the maximum total temperature, the displacement of the HS, and the spreading of the HS. Figure 3.24 and Figure 3.25 show respectively the evolution in the azimuthal and radial directions. First of all, it reveals that the maximum total temperature is different by a factor of 2 before the curvature ($x^* = -0.425$), where the value of maximum total temperature for a turbulent length scale of 0.7 mm is more important. This is the consequence of a higher dissipation of turbulence. This factor is preserved all along the curved part of the channel. In terms of position, the maximum total temperature is not influenced by the turbulent length scale either in the azimuthal direction or in the radial direction. This is clearly evidenced when looking at the different markers of Figure 3.24 and Figure 3.25. It shows that the dynamics of the HS is not influenced by the value of the turbulent length scale imposed at the inlet. However, the diffusion, or spreading of total temperature, is strongly impacted by the value of the turbulent length scale. The higher this value, and the higher the spreading of the Gaussian is. For both turbulent length scales, the spreading is more pronounced in the azimuthal direction than in the radial direction, due to the strong azimuthal deviation of the flow.

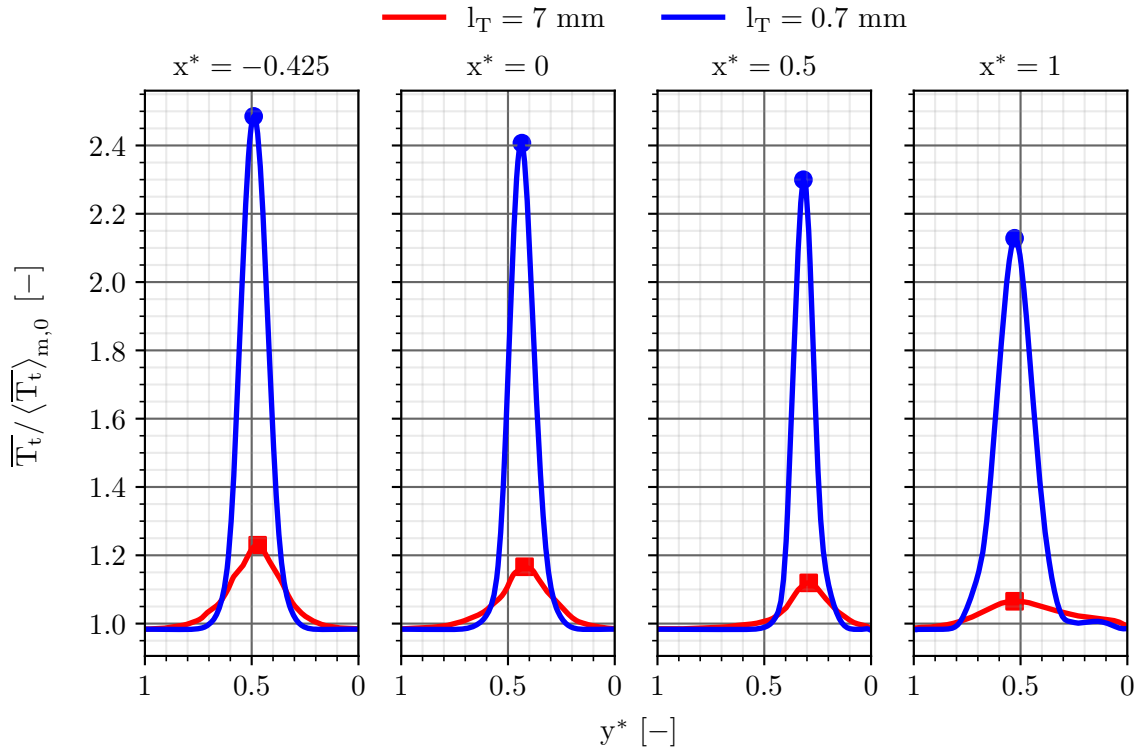


Figure 3.24 – Evolution of \overline{T}_t in the azimuthal direction at the $z_{T_t, max}^*$ position for different abscissa. The position of the maximum total temperature is localised with markers.

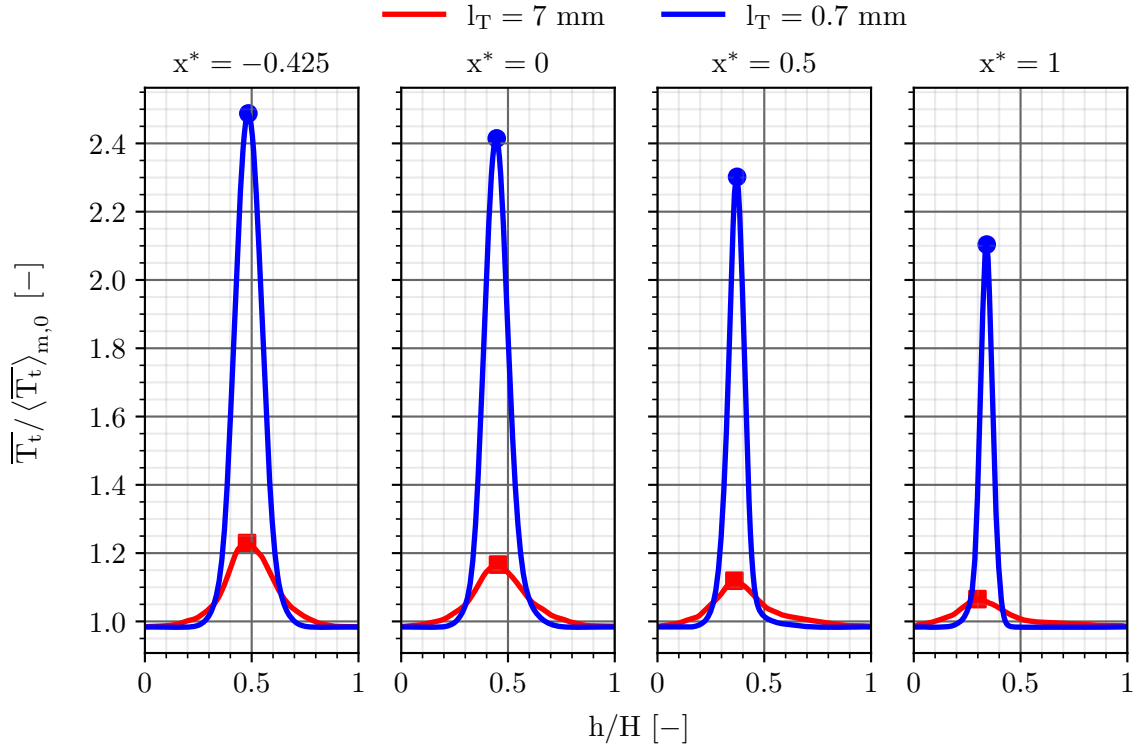


Figure 3.25 – Evolution of \overline{T}_t in the radial direction at the $y_{T_t, max}^*$ position for different abscissa. The position of the maximum total temperature is localised with markers.

To better quantify the intensity of the HS, the evolution of the maximum total temperature along x^* is also studied and is depicted in Figure 3.26 for both turbulent length scales. It shows that for the initial length scale of 7 mm, the diminution of $\overline{T}_{t,max}$ mainly occurs in the upstream domain ($-2 < x^* < -0.425$), with a decrease of 57%. On the contrary, the decrease is linear for the initial length scale of 0.7 mm, with the same value of 14% either in the straight part or in the curved part. Note also that the decrease of $\overline{T}_{t,max}$ in the curved part ($0 < x^* < 1$) does not depend on the turbulent length scale imposed at the inlet, *i.e.* on the turbulence characteristics at the inlet (the value of the turbulent kinetic energy is also not modified), with the same decrease for both turbulent length scales.

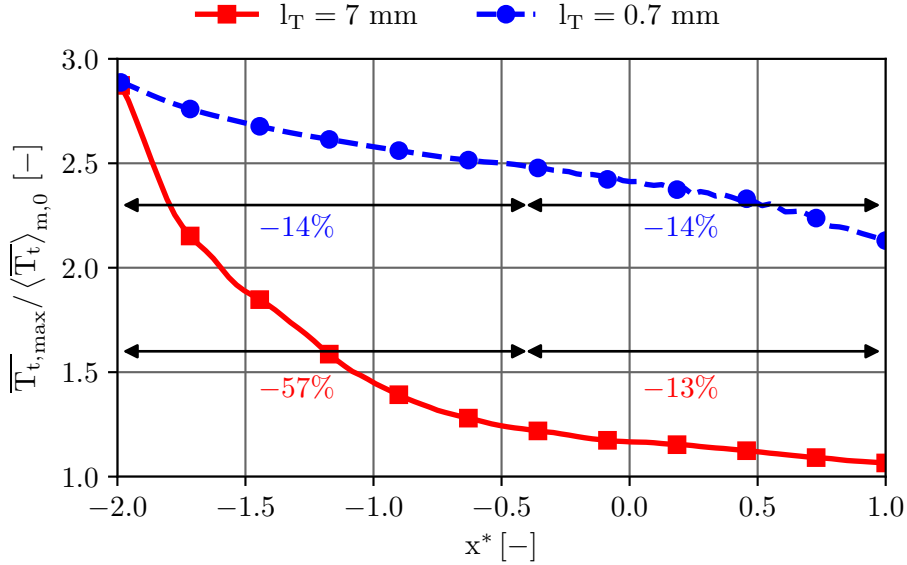


Figure 3.26 – Axial evolution of $\overline{T}_{t,max}$ for different prescribed inlet integral length scale.

3.4.5 Stability of the swirling jet

The stability of axisymmetric swirling flows at high Reynolds numbers has largely been tackled in the literature [52]. Swirling flows are mostly used to favour mixing, increase heat transfers in pipes, or to stabilise flames in combustion chambers by creating central reverse flows at a distance from the injector [52, 72, 114]. However, these recirculation zones can oscillate or precess, leading to the so-called Precessing Vortex Core (PVC). This topic will be largely tackled in Chapter 6 but one particular point to remember is that the PVC has a typical low-frequency signature and is linked to vortex breakdown, and that the precession depends on the type of combustion chamber, flow rate and on the swirl number. The level of swirl is guided by the swirl number which is defined as the ratio of angular momentum to axial momentum:

$$S_N = \frac{G_\theta}{R_{sw} G_x} = \frac{\int_0^{R_{sw}} \rho v_x v_\theta r^2 dr}{R_{sw} \int_0^{R_{sw}} \rho v_x^2 r dr} \quad (3.26)$$

Where v_x et v_θ are respectively the circumferentially-averaged axial and tangential velocity in the swirler frame of reference, R_{sw} the radius of the swirler and ρ the density. The value of the swirl number determines whether recirculation zones and PVC appear within the flow.

In the specific test case studied in this chapter, the radius of the swirler is taken as the

radius of the vortex core r_c and the axial and tangential velocities are taken from the Vatistas theory. By applying Equation 3.26, the swirl number of the 'SWIRL+' case computed at the inlet reads $S_N = 0.3$. There is no consensus in the scientific community for the lower limit of S_N responsible for the appearance of instabilities. For some authors, vortex breakdown may appear at 0.6, whereas it can emerge at higher (0.94) or lower (0.45) values [114]. Anyway, in this test case, there is no reason to believe that the vortex injected at the inlet is unstable. Nevertheless, its stability across the channel must be evaluated. In particular, it must be checked if low frequencies appear by the use of PSD at different probe locations on the mean trajectory of the hot streak. The mean trajectory of the hot streak is localised by tracking the maximum total temperature at different axial planes. Probes are equally spaced along the trajectory, as depicted in Figure 3.27; the numbering of the probes is also displayed. Probes 1 to 9 correspond to the straight part whereas probes 10 to 13 account for the curvature.

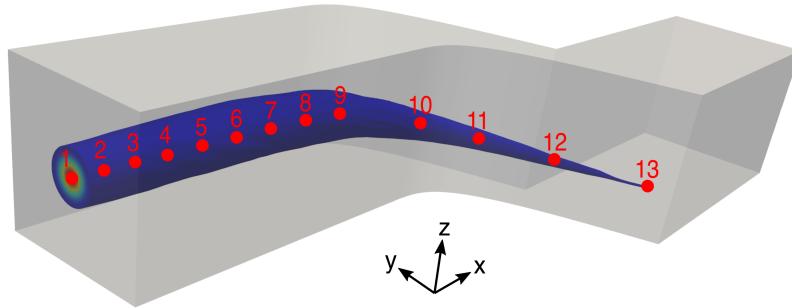


Figure 3.27 – Positioning of the probes on the mean trajectory of the hot streak.

Figure 3.28 shows the PSD of axial velocity at different probe locations for a sampling at 1100 kHz. At probe 1, the vortex is stable as no tonal sound is observable, which was desired by the author. Then, when moving across the channel, the same comments can be made, meaning that the vortex does not destabilise. This is in agreement with the swirl number chosen for the vortex. Turbulence is evidenced by a broadband noise over the spectrum with fluctuations of the PSD amplitude. Finally, with this sampling frequency, the mesh cut-off frequency is reached with a typical change of the PSD slope which basically depends on the mesh resolution and on the order of the numerical schemes. The cut-off frequency is evidenced with dashed red lines in Figure 3.28.

A destabilisation of the vortex would lead to a local increase of turbulence, *i.e.* a local increase of the turbulent viscosity μ_T in a RANS approach, which, in turn, would mean an intensification of momentum and energy. Diffusion of the HS would be enhanced, affecting both its trajectory and intensity.

The use of a high-fidelity simulation made it possible to evaluate different integral scales of turbulence, which are purely obtained with a statistical approach. The turbulent kinetic energy budget realised on the hot streak emphasised the most predominant terms that govern the motion of the turbulent flow which are production and mean flow

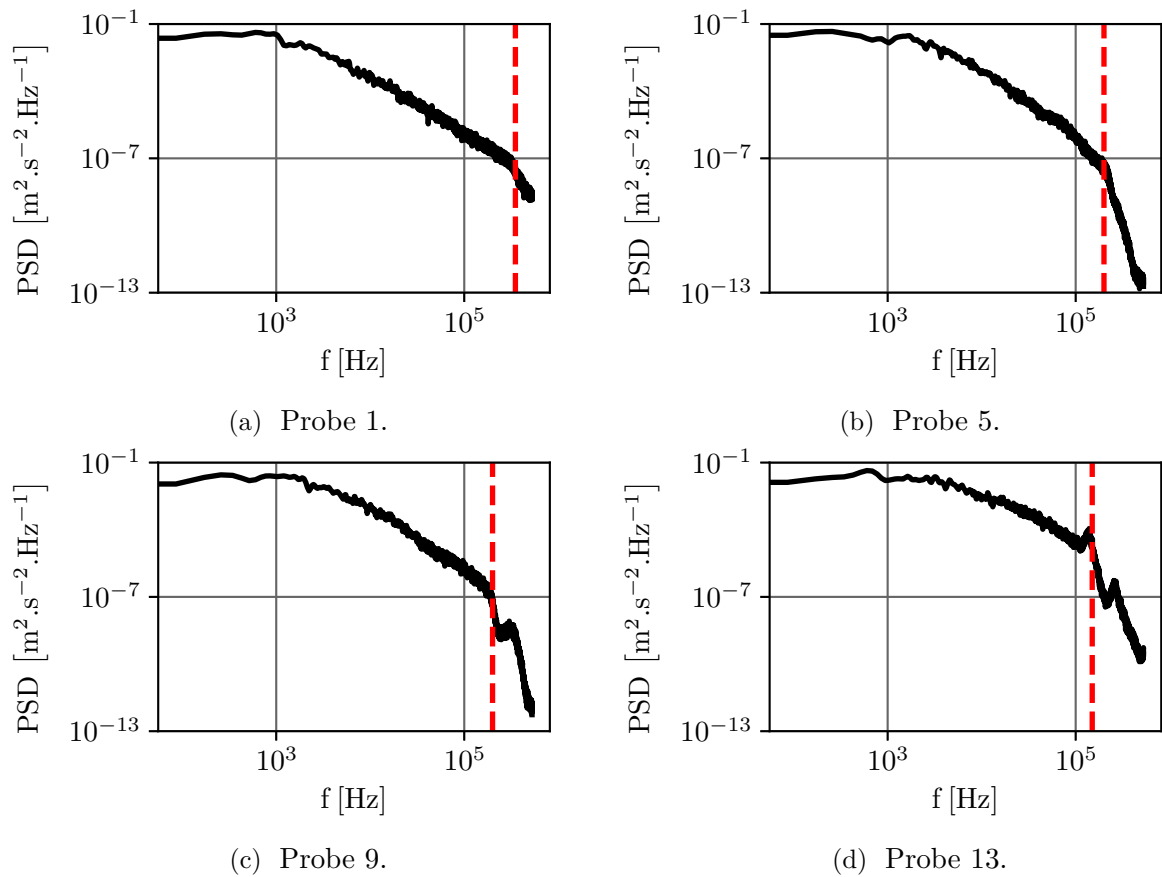


Figure 3.28 – PSD of axial velocity component at different locations. 20 blocks are used with 50% overlap and a Hann windowing.

convection. Both the computation of integral length scales and turbulent kinetic energy budget revealed two different behaviours, either considering the straight or curved part of the channel. Of course, it was predictable but it has been formalised. Finally, the effect of the turbulent length scale at the inlet showed that decreasing the turbulent length scale increased dissipation and therefore decreased diffusion. Thus the regime of turbulence is modified, from a transport regime for high values of turbulent length scales to a dissipation regime for small values. Both the spreading and intensity of the hot streak are modified, while the position of the maximum total temperature is not affected. This mechanism involving the position and intensity of the hot streak is the focus of high-pressure turbine designers, since the temperature strongly impacts the lifetime of turbine components.

3.5 Evaluation of RANS against LES: sensitivity study to physical and numerical parameters

In what follows, the capacity of RANS to correctly predict the transport of a swirled hot streak is checked. The LES analysis evidenced a strong sensitivity to diffusion, for which RANS needs calibration. A sensitivity analysis is performed on some numerical parameters, and mainly on the turbulent variables prescribed at the inlet. For the two-equation turbulence models used in this section, the choice is to specify the turbulent kinetic k which can be easily measured in

experiments (HWA) or obtained in LES. The second turbulent variable is expressed in terms of the ratio μ_T/μ as a common basis of comparison between the turbulence models (as shown in Equation 2.11). Other choices exist: for instance, Firrito *et al.* [36] decided to use the turbulence length scale l_T and the turbulence intensity T_u . In both cases, the biggest uncertainty lies with the definition of the turbulence length scale that depends on the turbulence models. For instance, in the Wilcox $k - \omega$ model [136, 137], the turbulence length scale is given by $l_T = k^{1/2}/\omega$, whereas for the Smith $k - l$ turbulence model [110], it leads to the definition given by Equation 2.10: $l_T = C_1 k^{1/2}/\omega$. The two length scales are different by a factor $C_1 = 1.85$. Such inconsistencies may lead to relatively soft or harsh turbulence decay that, in turn, modifies the dynamics of the main flow.

In the present study, more than 70 combinations of the different parameters have been tested but only the most relevant are detailed. Table 3.7 presents the different RANS set-ups used for the sensitivity study. The 'SWIRL+' case is considered as well as the Launder-Sharma $k - \epsilon$, Wilcox $k - \omega$ and Smith $k - l$ turbulence models. In all the following simulations, the turbulent BC at the inlet is applied as a 2D map, with different properties:

- **Mapped from the LES:** in this case, \bar{k} and \bar{l}_T are taken from the LES and imposed at the inlet of a $k - l$ simulation (Cases 1 and 2). The value of $\mu_T/\mu = 1750$ at the inlet is a consequence of the couple (k, l_T) (see Equation 2.11);
- **Mapped from a $k - l$ basis simulation with unchanged \bar{k} :** in this case, the user keeps \bar{k} unchanged from the LES and imposes a target value of μ_T/μ , leading to a variation of the second turbulent variable (Cases 4 to 7);
- **Mapped from a $k - l$ basis simulation with modified \bar{k} :** in this case, the user specifies target values for T_u and μ_T/μ , leading to new values for \bar{k} and the dissipation scale (Case 3).

When \bar{k} is taken from the LES, it is computed from the resolved part of the LES turbulent kinetic energy. This choice is justified by the fact that the fraction of modelled turbulent kinetic energy is negligible, as already discussed in Figure 3.10. RANS simulations are compared to the LES previously described and exhibit the same turbulence intensity at the inlet so that $\langle T_u \rangle_m = 11\%$, except for Case 3 where $\langle T_u \rangle_m = 4\%$. RANS simulations are performed at iso-total-to-static expansion ratio between the inlet and the outlet. Since analyses are performed till the TE plane, any modification of $\Pi_{t \rightarrow s}$ between the inlet and the TE is the result of the simulation and must be considered as such.

Case	Turbulence model	T_u	μ_T/μ	P_k	Pr_T
Case 1	Smith $k - l$	11%	1750	from_sij	0.9
Case 2	Smith $k - l$	11%	1750	from_vorticity	0.9
Case 3	Smith $k - l$	4%	1	from_sij	0.9
Case 4	Smith $k - l$	11%	1500	from_vorticity	0.9
Case 5	Smith $k - l$	11%	200	from_vorticity	0.9
Case 6	Launder-Sharma $k - \epsilon$	11%	200	from_vorticity	0.9
Case 7	Wilcox $k - \omega$	11%	200	from_vorticity	0.9

Table 3.7 – RANS test cases matrix for the sensitivity study. T_u and μ_T/μ are averaged values on the inlet plane.

With this test cases matrix, it is thus possible to compare the effect of the:

- Laminar/Turbulent inlet condition: Cases 1 and 3;
- Computation of P_k : Cases 1 and 2;
- Dissipation rate at iso-turbulence model: Cases 2, 4 and 5;
- Turbulence model: Cases 5, 6 and 7.

The two first points are tackled in 3.5.1, while the next two are discussed in 3.5.2. Finally, term-by-term TKE budget comparisons between RANS and LES are intended in 3.5.3. Additional studies on the effect of the turbulent Prandtl number or a slight modification of the turbulent Reynolds number around the optimal value are presented in Appendix A (sections A.1 and A.2). The application on a coarse mesh representative of a RANS mesh is also exposed in Appendix A (section A.3).

3.5.1 Prescription of the turbulent map obtained from the LES at the inlet boundary condition

The relevance of the imposition of the turbulence characteristics obtained from the LES (both \bar{k} and \bar{l}_T) is firstly assessed. For comparison purposes, the extreme case in terms of turbulence, *i.e.* a laminar flow at the inlet, is also considered. Case 1 and Case 3 are thus compared to the reference LES in terms of radial distributions of swirl angle $\bar{\alpha}$ and total temperature \bar{T}_t at different axial positions labelled in Figure 3.1. Axial evolution of mass-weighted averaged turbulent kinetic energy \bar{k} as well as area-weighted averaged turbulent length scale \bar{l}_T are also compared. Since \bar{k} is used for the validation of RANS simulations, error bars are added to measure the grid dependence of the turbulent kinetic energy in the LES. The LES turbulent length scale \bar{l}_T differs from what has been presented in 3.4.3 since it is now obtained by performing autocorrelation of velocity signals on planes and no longer on probes. Case 2 is also plotted to consider the method used for the modelled turbulence production term P_k . The following observations are made:

- On the one hand, when imposing the LES turbulence map (Case 1) at the inlet of the RANS simulation, *i.e.* the most straightforward approach is done, it provokes a flattening of the swirl and total temperature distributions and the trace of the HS is no more visible, which is a consequence of an important radial diffusion (Figure 3.29). This behaviour is attributed to the high value of μ_T/μ that overestimates the stresses and the turbulent heat flux. This case is a diffusion regime case;
- On the other hand, when imposing a quasi-laminar flow at the inlet ($\mu_T/\mu = 1$, $T_u = 4\%$), the swirl components are preserved (Figure 3.29a) and a radial migration of the HS is noted, as observed for the LES (Figure 3.29b). Nevertheless, the peak of \bar{T}_t is too high compared to the LES since in this case, turbulence is dissipated at the inlet and the production term P_k , however small it may be, takes over. Thinking in terms of turbulent length scale \bar{l}_T , Figure 3.30 reveals that when imposing the value of μ_T/μ from the LES, the evolution is quite similar between the LES, Case 1 and 2 whereas it is one order of magnitude smaller for Case 3 where the dissipation is relatively high. Thus, as already mentioned earlier, the value of \bar{l}_T to impose at the inlet does not seem to be the proper choice, since it does not lead to the correct aerothermal behaviour. Case 3 is a dissipative RANS turbulence inlet set-up case;

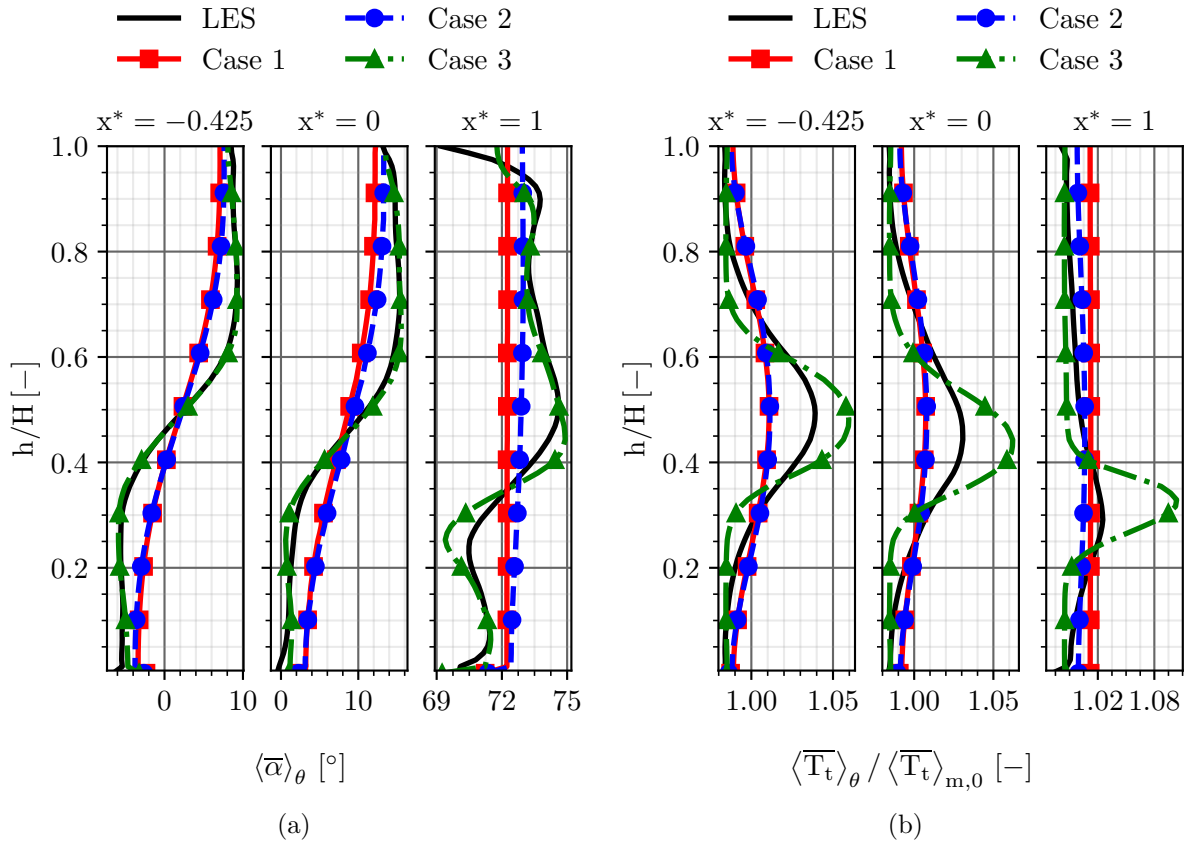


Figure 3.29 – Radial distributions of $\bar{\alpha}$ (a) and \bar{T}_t (b) for the laminar/turbulent inlet boundary condition comparisons.

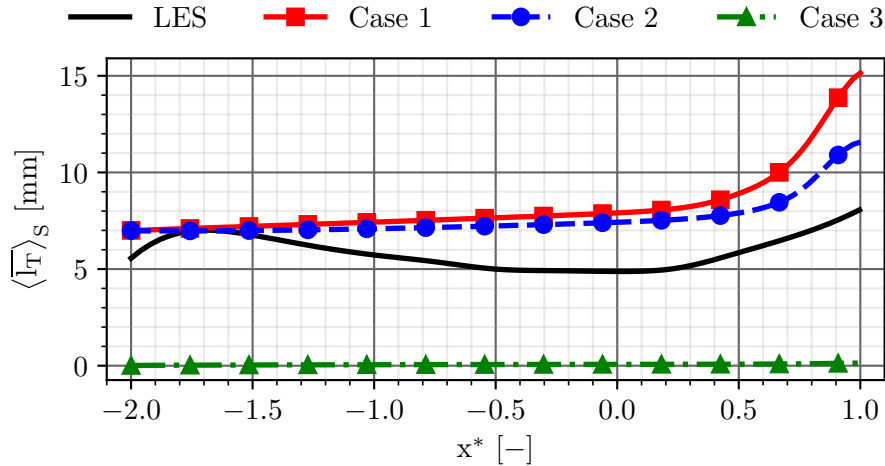


Figure 3.30 – Axial evolution of \bar{l}_T for the laminar/turbulent inlet boundary condition comparisons.

- Also, the way the production of turbulent kinetic energy P_k is computed impacts the history of \bar{k} inside the channel. If computed from the mean velocity strain rate tensor, one sees a dramatic increase of \bar{k} when the curvature is reached (Figure 3.31): this is expected in flows with strong acceleration zones or stagnation points [30]. This over-prediction of \bar{k} results from a very small value of the dissipation rate. It finally leads to an over-prediction of

μ_T/μ . Computing P_k from the vorticity tensor leads to more realistic values of \bar{k} inside the channel (Case 2 in Figure 3.31). In fact, the production is set to zero for irrotational flows, which is the case here outside the influence of the swirled HS, as well as the stagnation points. This is an interesting result in a methodology context, and the computation of production from the vorticity tensor is kept in the rest of the thesis. Other techniques exist for the management of the production term: limit the turbulent viscosity (Wilcox [136]), give a lower bound for the specific dissipation rate ω from the Schwartz inequality on the Reynolds stresses as derived by Zheng and Liu [143], or limit the ratio P_k/ϵ . These have been tested without improving the present results. From all the results presented, Case 2 is now the new reference for the RANS.

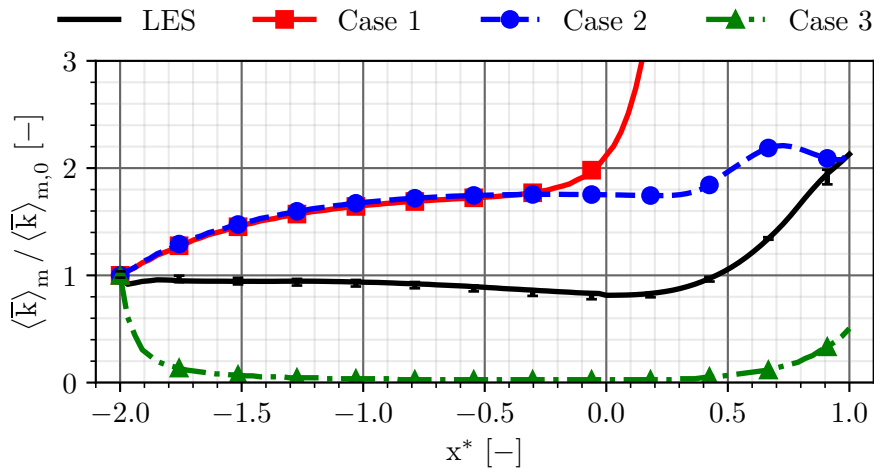


Figure 3.31 – Axial evolution of \bar{k} for the laminar/turbulent inlet boundary condition comparisons.

3.5.2 Influence of the turbulent Reynolds number

Results of Figures 3.32, 3.33, 3.34 are now exploited. The Smith $k-l$ turbulence model is considered. At iso- \bar{k} at the inlet and by varying the value of μ_T/μ , which corresponds to calibrating the dissipation from the turbulent length scale, the impact is not negligible. This approach is the one reported by Vagnoli *et al.* [129] and already described in 3.4.4. A compromise between the keeping of the swirl components (low μ_T/μ) and the correct diffusion (moderate μ_T/μ) should be found. It exists a certain range for the value of μ_T/μ (≈ 200 - Case 5) that preserves the swirl components (with the right slope breaks at 20% and 60% of h/H - Figure 3.32a) and that gives the correct total temperature diffusion (Figure 3.32b). At this range, a decrease of \bar{k} in the straight part of the channel is now observed (Figure 3.33). This is the best balance between swirl and diffusion. This is a transport regime case. This decrease of \bar{k} is a good indicator for the imposition of turbulent quantities at the inlet. Vagnoli *et al.* [129] drew the same conclusions on the FACTOR high-pressure turbine configuration, except for the value of μ_T/μ , which is discussed in 3.5.4. In terms of turbulent length scale \bar{l}_T , the averaged value for Case 5 at the inlet is $\bar{l}_T = 0.5$ mm, which is about $1/10^{\text{th}}$ of the LES value, as depicted in Figure 3.34. The value of μ_T/μ is one of the first-order parameters that pilots the evolution of the mean flow quantities. The higher the value is, the higher the temperature diffusion is, and the higher the swirl components vanish.

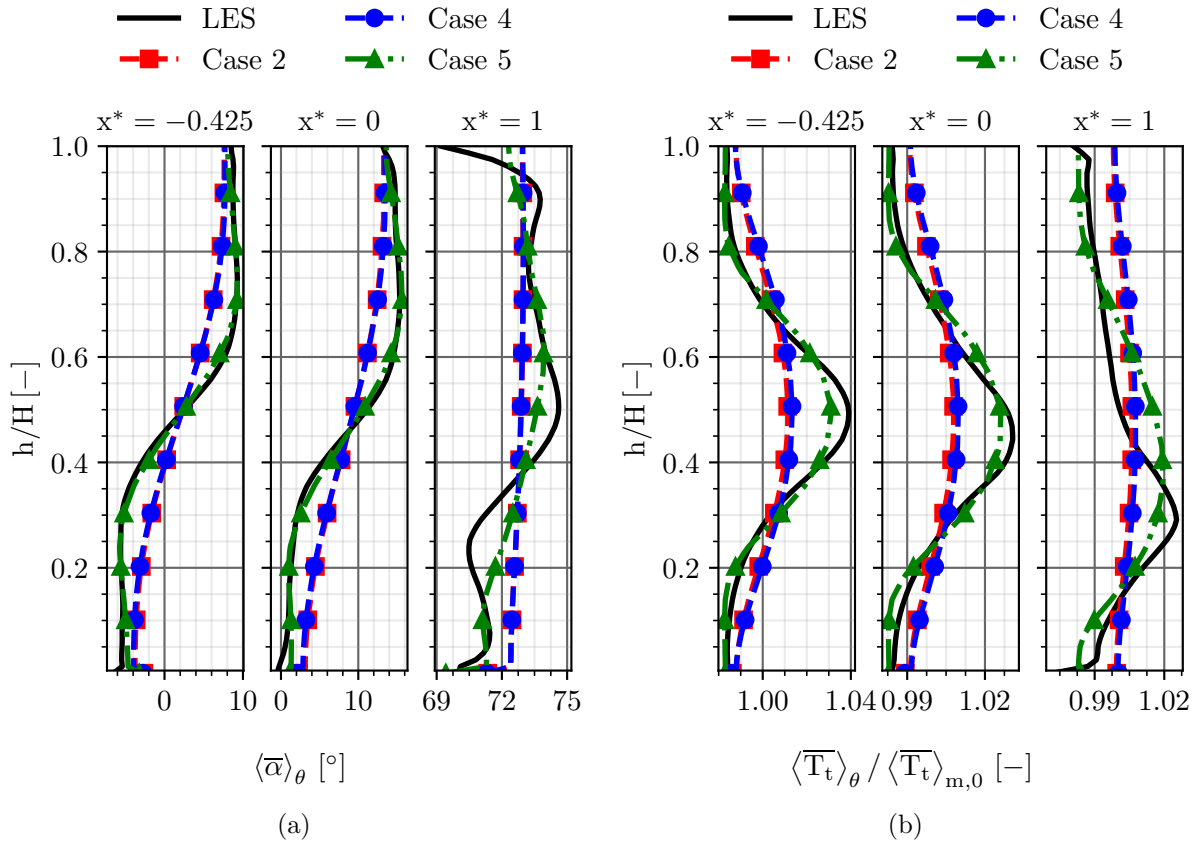


Figure 3.32 – Radial distributions of $\bar{\alpha}$ (a) and \bar{T}_t (b) for different values of turbulent Reynolds number.

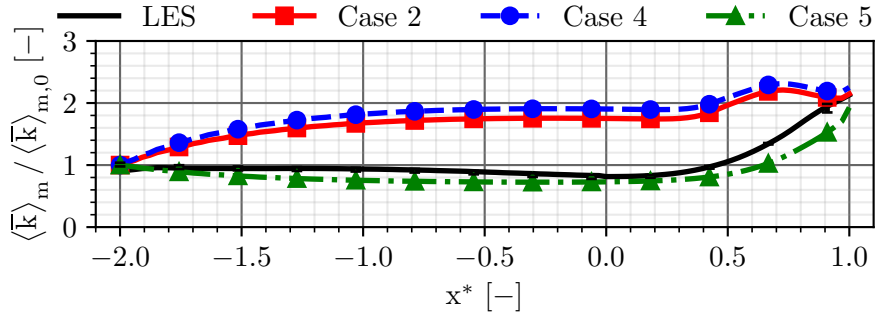


Figure 3.33 – Axial evolution of \bar{k} for different values of turbulent Reynolds number.

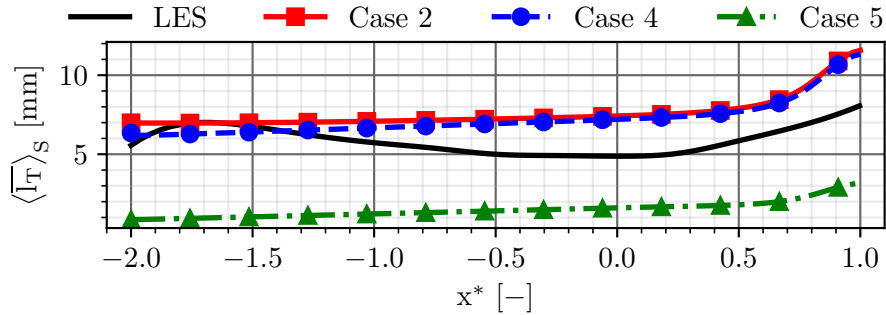


Figure 3.34 – Axial evolution of \bar{l}_T for different values of turbulent Reynolds number.

3.5. EVALUATION OF RANS AGAINST LES: SENSITIVITY STUDY TO PHYSICAL AND NUMERICAL PARAMETERS

The turbulence model is examined on the swirl angle and total temperature distributions of Figure 3.35 and on the turbulent kinetic energy evolution of Figure 3.36. The Launder-Sharma $k - \epsilon$ and the Wilcox $k - \omega$ models are added for the comparisons. It seems that the Wilcox $k - \omega$ turbulence model (Case 7) is the best compromise between the aerodynamics and turbulence, even if still no boundary layers are considered, so a firm conclusion is not possible.

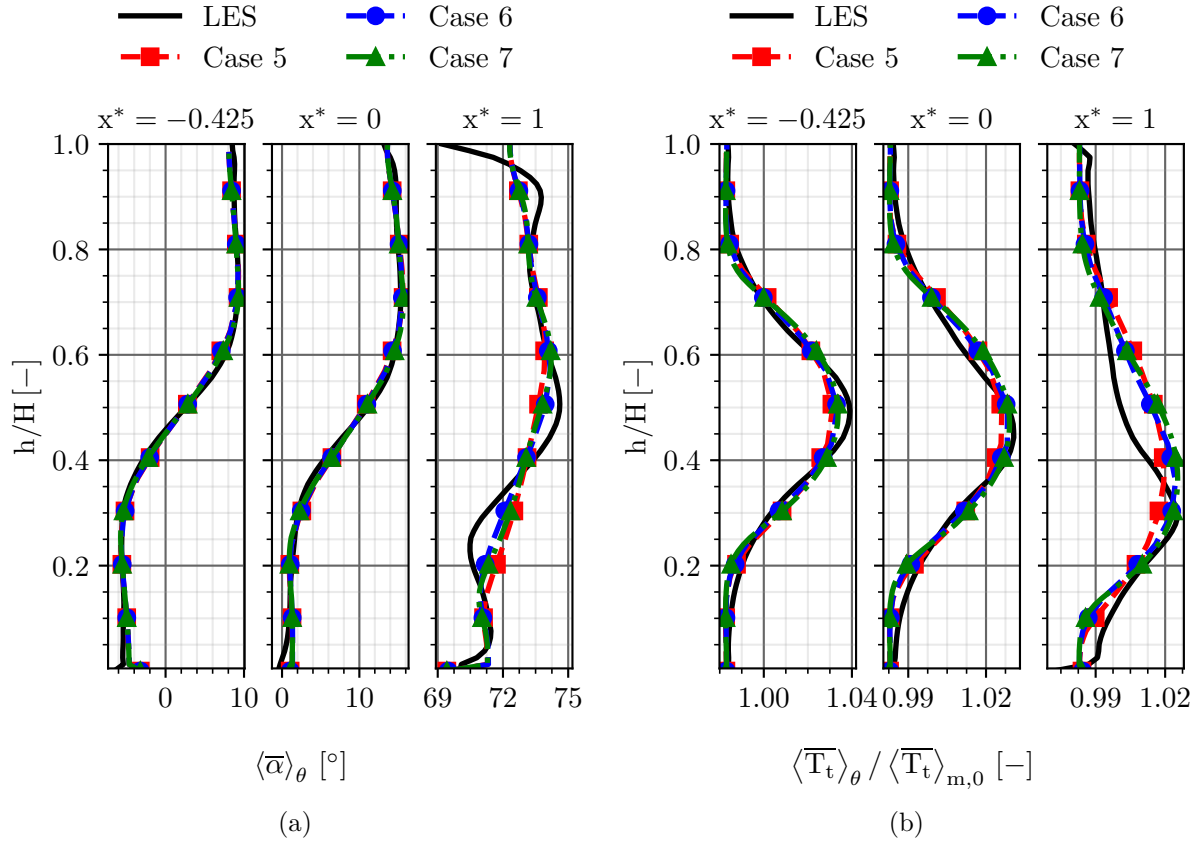


Figure 3.35 – Radial distributions of $\bar{\alpha}$ (a) and \bar{T}_t (b) for different turbulence models.

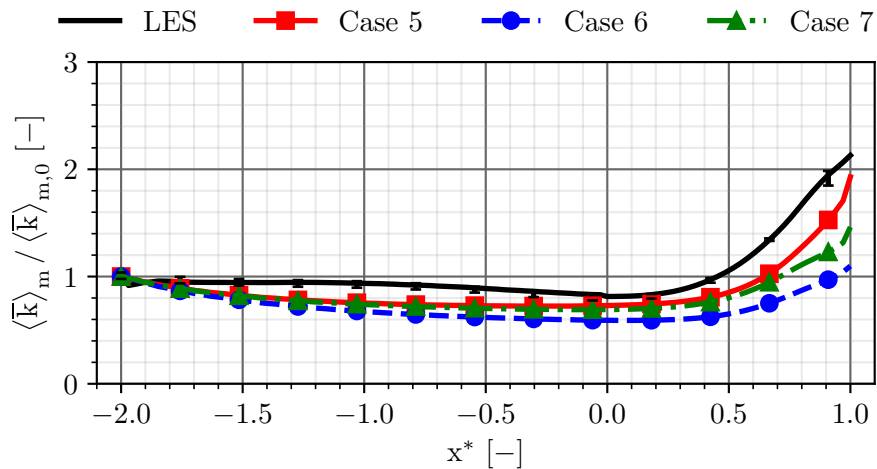


Figure 3.36 – Axial evolution of \bar{k} for different turbulence models.

A deeper investigation is performed with a TKE budget applied to Case 7 and compared to the reference LES. The TKE budget is performed on the mean HS trajectory depicted in Figure 3.37. For comparison purposes, the turbulent and pressure diffusion terms have been embedded together. Figure 3.38 presents the evolution of the different terms along x^* . While obtaining a relatively correct total temperature diffusion, a modification of the equilibrium is observed between RANS and LES. The production term is more important in RANS and is constant in the straight part of the channel. Its level is fixed by the swirl number and the plateau is a result of the vortex that is not affected by the curvature. In the straight part again, the dissipation term is more pronounced, due to the smaller value of μ_T/μ at the inlet, resulting in a higher dissipation. Other terms remain close to zero. In the curvature, the diffusion and the mean flow convection terms are well-captured, whereas the production term is over-estimated. However, it presents the same peak at $x^* = 0.75$. The trend for the dissipation is the same, with a shift resulting from the prescribed value of μ_T/μ at the inlet.

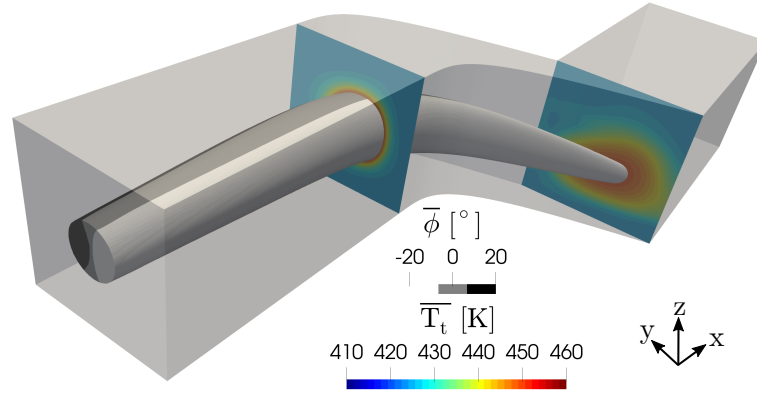


Figure 3.37 – Iso-contour at 450 K of total temperature coloured by pitch angle for Case 7. \bar{T}_t fields at the LE and TE are also displayed.

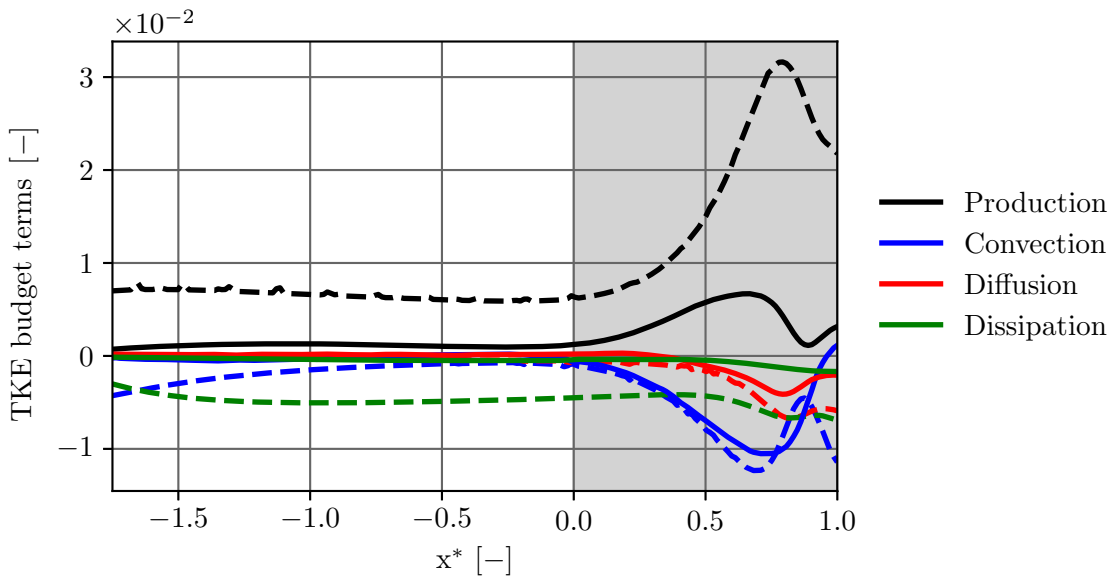


Figure 3.38 – Budget for the turbulent kinetic energy along x^* . Grey zone represents the curved part. Comparisons between LES (—) and Case 7 (---). Quantities are normalised by $(\rho_\infty v_\infty^3 r_c^2)$.

Finally, Gaussian evolutions at the couple (y^*, z^*) of the maximum temperature $\overline{T}_{t,max}$ are plotted for the transport regime case (Case 7). The evolution in the azimuthal direction is only considered here for compactness reasons. The dissipative (Case 3) and diffusive (Case 2) regime cases are also displayed. Results are shown in Figure 3.39. As already mentioned, the dissipation regime leads to very high values of maximum total temperature (Case 3) compared to the reference LES, while on the contrary the diffusion regime induces smaller values (Case 2). The transport regime enables to keep the total temperature peak relatively close to the one predicted by the LES. However, a common observation for RANS cases can be done: both the position and intensity are influenced by the turbulence characteristics imposed at the inlet, while only the intensity is affected for the different LES (see Figure 3.24 for example).

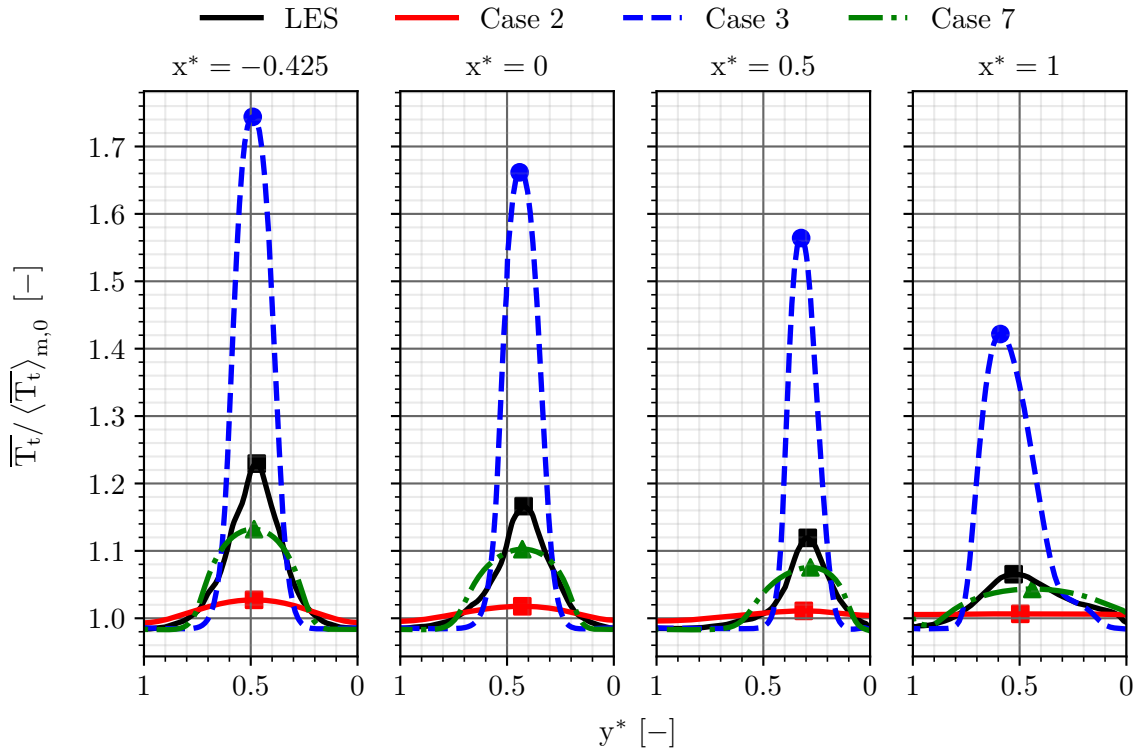


Figure 3.39 – Evolution of \overline{T}_t in the azimuthal direction at the $z_{T_t,max}^*$ position for different abscissa and different RANS turbulent inlet set-ups. The position of the maximum total temperature is localised with markers.

3.5.3 Turbulent kinetic energy budget comparisons between diffusive and transport RANS turbulence set-ups

In order to assess the impact of the value of μ_T/μ on the redistribution of a HS, the TKE budgets for the diffusive (Case 2) and transport (Case 7) set-ups are now compared term-by-term with the LES. For the diffusive case, all dash-dotted lines stop at $x^* \approx -0.5$, where the HS defined by the iso-contour is fully diffused. While following the same trend between LES and Case 7 regarding production, Case 2 evidences a dramatic decrease (Figure 3.40a) which is explained by the strong diffusion in the upstream part of the channel. The suspected overestimation of the turbulent heat flux for Case 2 is marked by an excess of diffusion at the very beginning of the channel, which is not present for the LES. This diffusion vanishes the $\partial \tilde{v}_j / \partial x_i$ terms for Case 2

whereas they are preserved for Case 7 (Figure 3.40b), as a result of a lower dissipation. This smaller dissipation was desired by the authors (Figure 3.40c). Convection is well represented for the transport case whereas it is overestimated for Case 2 (Figure 3.40d). Overall, diffusion and mean flow convection terms are enhanced compared to the LES for the diffusive case while production and dissipation terms are increased for the transport case. It clearly shows here that the equilibrium is modified between RANS and LES and that the value of μ_T/μ is of first importance. For a high value, a diffusion regime is observed, whereas for a moderate value, a transport regime is observed.

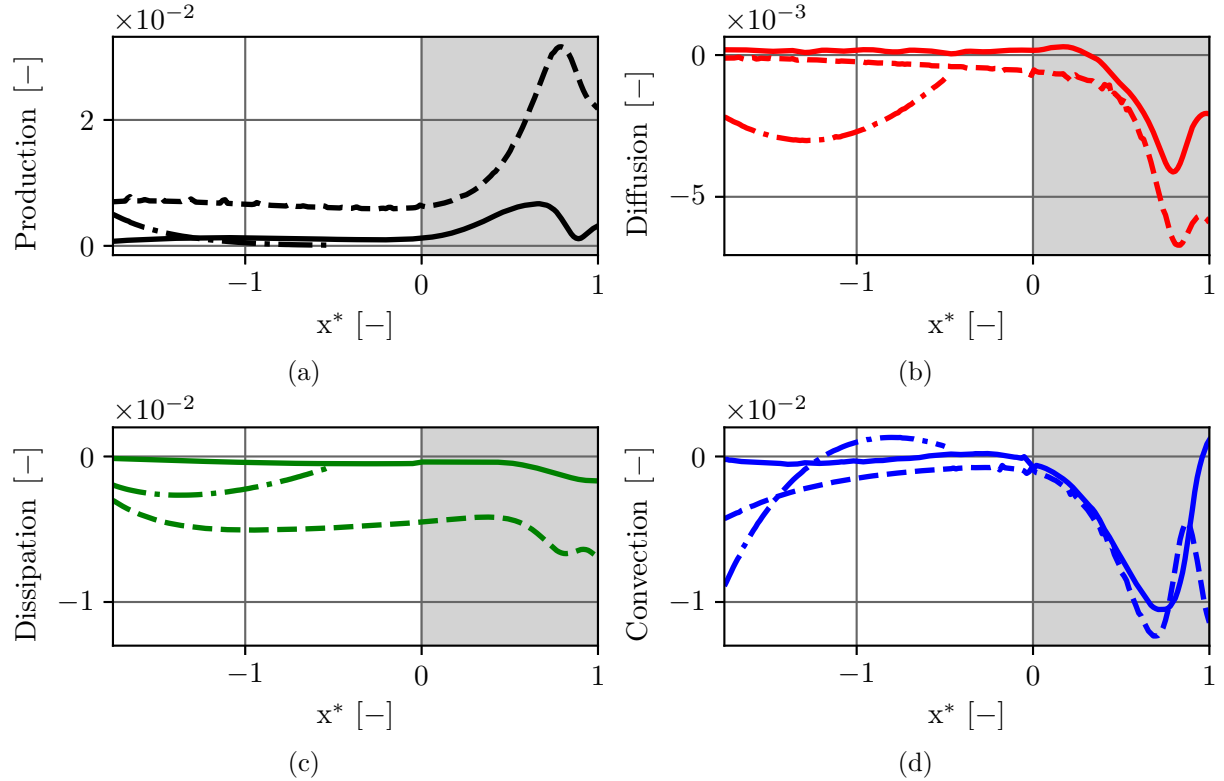


Figure 3.40 – Comparisons of production (a), diffusion (b), dissipation (c) and convection (d) terms between LES (—), Case 2 (---) and Case 7 (-.-). Grey zone represents the curved part. Quantities are normalised by $(\rho_\infty v_\infty^3 r_c^2)$.

3.5.4 Brief discussion of the stability issue

Results of the previous study showed that the optimal value of μ_T/μ found ranges around 200, which is one order of magnitude smaller than what has been found in the literature in an HP turbine stage configuration (≈ 1500 - Vagnoli *et al.* [129]). A RANS case has been conducted at this value of 1500, leading to a too high temperature diffusion (which results from the same conclusions as Case 2). These differences in the value of μ_T/μ can be explained by the fact that in [129], the authors take into account the energetic content of the instability (PVC) coming from the combustion chamber that is not present in the bent duct since the vortex is stable, as evidenced by the stability analysis. In that sense, we attempted to destabilise the swirled hot streak to mimic the presence of the PVC using LES, without success. A destabilisation of the vortex would lead to a local increase of turbulence, *i.e* a local increase of the turbulent viscosity μ_T in a RANS approach.

3.6 Conclusion

In Chapter 3, the effect of turbulence levels and scales on the diffusion of hot streaks has been tackled. The use of high-fidelity LES on an academic case made it possible to establish the general behaviour of highly turbulent swirling flows, as those encountered in real high-pressure turbines. Those preliminary results showed the impact of the direction of rotation of the swirl on the way the hot streak radially migrates, which can be simply explained with a radial equilibrium law. Thanks to the use of the highly time-resolved LES, turbulence has been examined in detail: integral length scales, obtained by temporal autocorrelations of velocity signals, reported preferential directions for the global integral length scale, driven by the axial direction in the straight part and by the transverse directions in the curved part. The turbulence activity is also different, as evidenced by the turbulent kinetic energy budget performed on the hot streak. The activity is impacted when reaching the curvature, where production and mean convection terms are predominant. Diffusion and dissipation terms exist, but to a lesser extent. Then, a stability analysis revealed that the vortex did not destabilise inside the channel, which was of first importance in order to only focus on RANS turbulence modelling thereafter. From these conclusions, a RANS sensitivity study to turbulence inlet set-ups and turbulence history has been performed to check if RANS was able to predict the correct redistribution of the hot streak inside the channel. It led to the following conclusions:

- Imposing the turbulent quantities from the LES caused immediate destruction of the swirl components and a too-high total temperature diffusion, which has been clearly evidenced by a turbulent kinetic energy budget;
- One solution to have both the aerodynamics and aerothermal is to fix k obtained from the experiments or from an LES and to vary μ_T/μ till an optimal range is obtained which means calibrating the dissipation from the turbulent length scale;
- The indicator that assesses for the optimal range of μ_T/μ is based on the decrease of k ;
- This range is case dependent: inlet flow conditions (aerodynamics and turbulence) and geometry, but ranges can be established in the way of common sense depending on the component of the gas turbine and the stability of the flow. For instance, low values of μ_T/μ close to a quasi-laminar flow are expected for a compressor with the axial and stable flow. Higher values of μ_T/μ are expected in a turbine because of its position downstream of the combustion chamber;
- Depending on the value of μ_T/μ , different regimes have been identified: dissipation regime (low μ_T/μ), transport regime (moderate μ_T/μ) and diffusion regime (high μ_T/μ);
- The turbulent kinetic energy budget for the transport regime case showed a different equilibrium compared to the LES, but trends are well represented;

- In a real HP turbine configuration, measuring k in the experiments for at least two axial positions upstream of the LE of an NGV could be a good idea to have the evolution of k , as one did by comparing RANS simulations and LES.

Dans le Chapitre 3, l'effet des niveaux et des échelles de turbulence sur la diffusion d'un point chaud a été abordé. L'utilisation de LES sur un cas académique a permis d'établir le comportement général des écoulements tourbillonnaires fortement turbulents, tels que ceux rencontrés dans les turbines haute pression. Ces résultats préliminaires ont montré l'impact du sens de rotation du tourbillon sur la façon dont le point chaud migre radialement, qui peut être expliqué simplement par un équilibre radial. Grâce à l'utilisation d'une LES hautement résolue temporellement, la turbulence a été examinée en détails : les échelles de longueur intégrale, obtenues par autocorrélations temporelles des signaux de vitesse, ont indiqué des directions préférentielles pour l'échelle de longueur intégrale globale, portée par la direction axiale dans la partie droite et par les directions transverses dans la partie courbe. L'activité de la turbulence est également différente, comme le montre le bilan d'énergie cinétique turbulente réalisé sur le point chaud. L'activité est impactée lorsque la courbure est atteinte, où les termes de production et de convection moyenne sont prédominants. Les termes de diffusion et de dissipation existent, mais dans une moindre mesure. Ensuite, une analyse de stabilité a révélé que le tourbillon ne se déstabilise pas à l'intérieur du canal, ce qui était de première importance pour ne se concentrer par la suite que sur la modélisation de la turbulence dans l'approche RANS. À partir de ces conclusions, une étude de sensibilité RANS aux conditions d'entrée de la turbulence et à l'historique de la turbulence a été réalisée pour vérifier si la RANS était capable de prédire correctement la redistribution du point chaud à l'intérieur du canal. Cette étude a conduit aux conclusions suivantes :

- L'imposition des grandeurs turbulentes à partir de la LES a causé la destruction immédiate des composantes du giration et une diffusion trop élevée de température totale, ce qui a été clairement mis en évidence par un bilan d'énergie cinétique turbulente;
- Une solution pour avoir à la fois l'aérodynamique et l'aérothermique est de fixer k obtenu à partir des essais ou d'une LES et de faire varier μ_T/μ jusqu'à ce qu'une plage optimale soit obtenue, ce qui signifie calibrer la dissipation à partir de l'échelle de longueur turbulente;
- Cet indicateur qui évalue la plage optimale de μ_T/μ est basé sur la diminution de k ;
- Cette plage dépend du cas d'étude : conditions de l'écoulement à l'entrée (aérodynamique et turbulence) et géométrie, mais des gammes peuvent être établies en fonction du composant de la turbine à gaz et de la stabilité de l'écoulement. Par exemple, de faibles valeurs de μ_T/μ proches d'un écoulement quasi-laminaire sont attendues pour un compresseur alimenté par un écoulement axial et stable. Des valeurs plus élevées de μ_T/μ sont attendues dans une turbine en raison de sa position en aval de la chambre de combustion;
- Le bilan d'énergie cinétique turbulente pour le cas du régime de transport a

montré un équilibre différent par rapport à la LES, mais les tendances sont bien représentées;

- Dans une configuration réelle de turbine HP, mesurer k dans les essais pour au moins deux positions axiales en amont du bord d'attaque d'un distributeur pourrait être une bonne idée pour avoir l'évolution de k , comme réalisé entre les simulations RANS et la LES.

Anisotropy analysis of a swirled hot streak

“ *Turbulence is the most unsolved problem of classical physics.* ”

Richard Feynman

Abstract

In the simulation of a highly turbulent swirling jet, the anisotropy of turbulence is suspected to fail the classical RANS turbulence models based on Boussinesq’s hypothesis. This chapter focuses on a criterion to check the validity of Boussinesq’s constitutive relation and a metric to measure the type and level of anisotropy of turbulence. Then, more advanced turbulence models applied to the swirled hot streak test case are used: non-linear eddy-viscosity turbulence models (EARSM) and Reynolds stress models (RSM). These models show improvements in the transport of a hot streak which are related to a better treatment of anisotropy of turbulence.

4.1	Introduction	128
4.2	Evaluation of the validity of Boussinesq’s constitutive relation	129
4.2.1	Schmitt’s criterion	129
4.2.2	Alignment analysis	129
4.3	Characterisation of anisotropy in a turbulent flow	131
4.3.1	Lumley’s theory	131
4.3.2	Application on a swirling hot streak	133
4.4	Dealing with anisotropy of turbulence in RANS modelling	137
4.4.1	Quadratic constitutive relation correction	137
4.4.2	EARSM/RSM turbulence models	137
4.5	Conclusion	146

4.1 Introduction

In Chapter 3, the axial evolution of turbulent kinetic energy for the best set-up of inlet turbulence using a turbulence model based on Boussinesq's hypothesis (Case 7 in Figure 3.36) showed a very similar trend with the LES. However, the bias induced by the azimuthal average vanishes strong discrepancies that can be observed in Figure 4.1 where \bar{k} field is represented at mid-span for the LES and Wilcox $k - \omega$ turbulence model. The Wilcox $k - \omega$ case presents very high values of \bar{k} in the region of the swirled HS, which can be attributed to the anisotropy not being correctly taken into account in the classical RANS turbulence models following Boussinesq's hypothesis.

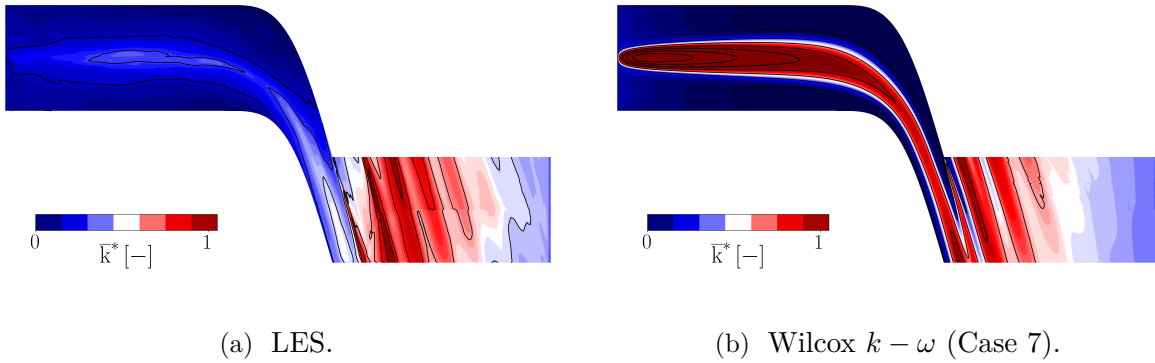


Figure 4.1 – Evolution of turbulent kinetic energy at mid-span of the channel (scaled from the LES values).

Anisotropy of turbulence is characterised by a flow where the fluctuating flow properties have some directional dependence. This phenomenon is observed in canonical configurations (turbulent boundary layer, mixing layer, swirling jet, axisymmetric contraction, etc.) because of the presence of wall curvature, rotation or shear. It is opposed to isotropic turbulence, in which the velocity fluctuations do not vary with rotation. In terms of Reynolds stresses, the normal components are thus the same. Issues related to the anisotropy of turbulence and its impact on the dynamics of a swirled flow are tackled in this chapter. The aim of studying the anisotropy of turbulence is to identify the limitations of the RANS approach which are suspected linked with this characteristic of turbulence. A first step is to detail LES results, and compare them to the classical RANS turbulence modelling following Boussinesq's approximation in which local anisotropy is neglected. The anisotropy is evaluated with the Reynolds stress anisotropy tensor defined as:

$$a_{ij} = \overline{v'_i v'_j} - \frac{2}{3} k \delta_{ij} \quad (4.1)$$

Which is nothing more than the traceless Reynolds stress tensor. In this formalism, Boussinesq's hypothesis is a strong one since it relates the anisotropic Reynolds stress tensor to the mean strain rate tensor through the turbulent eddy viscosity μ_T which is an isotropic scalar quantity. To go further, Pope [91] presents in his book the deficiencies of such a hypothesis in some simple canonical cases. The author divides the assumption into two parts:

- **The intrinsic assumption:** the anisotropic Reynolds stress tensor is determined by the local mean velocity gradients;
- **The specific assumption:** the two tensors are linearly related with the turbulent viscosity.

In general, these assumptions are not strictly true and some examples are described in section 10.1 of [91]. In the following, the turbulent fluctuations are considered, as all the anisotropy is confined to the energy-containing motions, and, in turn, all the production of turbulence.

4.2 Evaluation of the validity of Boussinesq's constitutive relation

4.2.1 Schmitt's criterion

Schmitt developed a criterion to check the validity of Boussinesq's hypothesis, *i.e.* the specific assumption [103]. It measures the degree of alignment between the traceless Reynolds stress tensor $\overline{\mathbf{R}}$ and the mean strain rate tensor $\overline{\mathbf{S}}$. In its original form, the metric ρ_{RS} reads:

$$\rho_{RS} = \frac{|\langle \overline{\mathbf{R}}, \overline{\mathbf{S}} \rangle_F|}{\|\overline{\mathbf{R}}\|_F \|\overline{\mathbf{S}}\|_F} \quad (4.2)$$

With this metric, the proportionality can be easily tested provided $\overline{\mathbf{R}}$ and $\overline{\mathbf{S}}$ are known independently, which is perfectly suited using LES or DNS results. However, in this form, negative values for ρ_{RS} , *i.e.* anti-aligned tensors, are not allowed. Monier [81] proposed a modification without the absolute value to account for negative values. The new criterion writes:

$$\rho_{RS} = \frac{\langle \overline{\mathbf{R}}, \overline{\mathbf{S}} \rangle_F}{\|\overline{\mathbf{R}}\|_F \|\overline{\mathbf{S}}\|_F} \quad (4.3)$$

This form is used in the alignment analysis for the swirling jet case. The Frobenius inner product between real matrices is defined as $\langle \overline{\mathbf{A}}, \overline{\mathbf{B}} \rangle_F = \text{Tr}(\overline{\mathbf{A}}^T \overline{\mathbf{B}})$ and $\|\overline{\mathbf{A}}\|_F = \sqrt{\langle \overline{\mathbf{A}}, \overline{\mathbf{A}} \rangle_F}$. The criterion given by Equation 4.3 is equivalent to the cosine of the angle between vectors. When $\rho_{RS} = 1$, the tensors are aligned and Boussinesq's hypothesis is valid. The closer this coefficient is to 0, and the lesser the hypothesis is valid. Negative values highlight non-physical results if Boussinesq's constitutive relation is used. Schmitt proposed to consider the alignment between the two tensors for an angle of $\pi/6$, *i.e.* $\rho_{RS} = 0.86$. From this value, the assumption is considered valid.

4.2.2 Alignment analysis

From Equation 4.3, the alignment analysis is studied on the configuration presented in Chapter 3, where the LES 'SWIRL +' case is still considered. First of all, to have a global overview of the validity of Boussinesq's assumption, Schmitt's criterion is plotted on the domain from the inlet to the TE (after this abscissa, the mesh is voluntarily coarsen so the evaluation does not make sense). Probability density function (PDF) and cumulative density function (CDF) of ρ_{RS} are plotted in Figure 4.2. The quantity of anti-aligned points remains small: less than 9% of the points are concerned, which is evidenced by the blue dashed lines of the CDF of Figure 4.2. Looking at the PDF, a gradual increase of ρ_{RS} is observed from 0 to 0.8 before decreasing. A more quantitative view of the validity of the constitutive relation is possible with the CDF. It reveals that nearly 80% of the points of the domain are not valid (70% if not considering the non-physical solutions), which is attested by the red dashed lines. By relying on

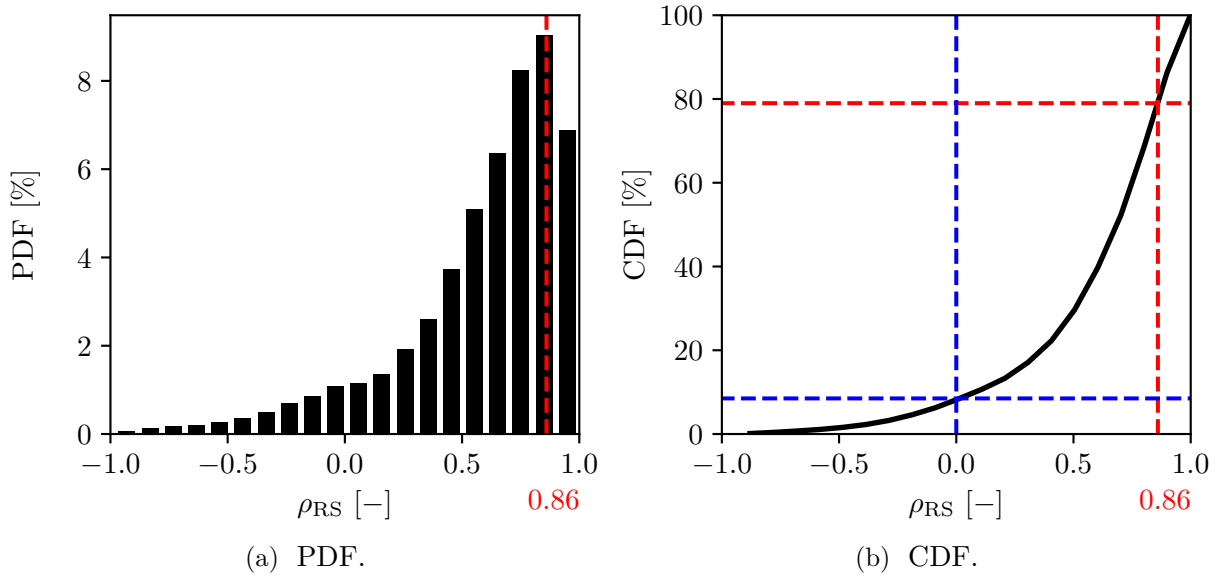


Figure 4.2 – Probability density function (a) and cumulative density function (b) of Schmitt’s criterion on the domain ranging from $x^* = -2$ to $x^* = 1$ computed from the LES ‘SWIRL +’ case.

Schmitt’s conclusions [103], depending on the configuration, the failure of the linear constitutive relation does not mean for sure a failure in the prediction of the mean flow properties. However, the second-order moments, which are linked to turbulence (Reynolds stresses, turbulent kinetic energy and dissipation) are not well predicted. For complex cases, both the first-order and second-order moments are missed. In this configuration, results of Chapter 3 with the best linear eddy-viscosity turbulence set-up are still not satisfactory, with a radial diffusion higher than what predicts the LES. This can be attributed to the delicate equilibrium of turbulence that is not correctly obtained with the turbulence model following Boussinesq’s hypothesis.

To better qualify where Boussinesq’s constitutive relation is not valid, axial and radial cuts of Schmitt’s criterion are represented in Figure 4.3 and Figure 4.4. It clearly reveals that the alignment is not valid in the straight part of the channel, which may be due to the presence of strong discrepancies in the velocity gradients (a consequence of the swirled HS). The curvature seems to realign slightly the tensors, since from Figure 4.3a ($x^* = 0$) to Figure 4.3b ($x^* = 0.75$), more values greater than $\rho_{RS} = 0.86$ are present. However, the realignment does not occur at the position of the HS, which is of interest to capture correctly the diffusion. The impact of the slip walls is also noted, where negative values of ρ_{RS} are highlighted, which can be explained by the generation of false anisotropy at the walls. This point is tackled in 4.3. With this simple analysis using Schmitt’s criterion, Boussinesq’s hypothesis is judged not valid in most of the domain, and also in the regions of the hot streak, where temperature and velocity gradients are more intense. The misalignment of the Reynolds stress tensor and the mean strain rate tensor may be due to the effects of curvature and rotation, that lead to anisotropy of turbulence. A simple correction can be added to Boussinesq’s hypothesis to realign the tensors: add to the zero-trace mean strain rate tensor a rotation term, which is the aim of the Quadratic Constitutive Relation (QCR) correction. Nevertheless, in highly swirling flows, this correction is not sufficient and more advanced turbulence models are used: the Explicit Algebraic Reynolds Stress Models (EARSM) or Reynolds Stress Models (RSM). These three points are tackled in 4.4.

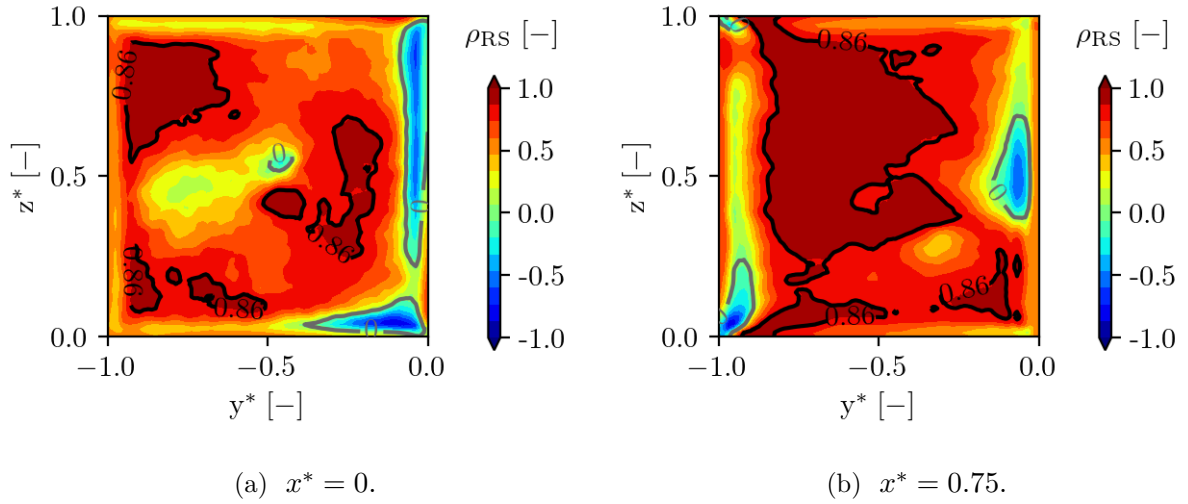


Figure 4.3 – 2D field of Schmitt’s criterion plotted at different axial positions. Iso-contour of $\rho_{RS} = 0$ and $\rho_{RS} = 0.86$ respectively in grey and black.

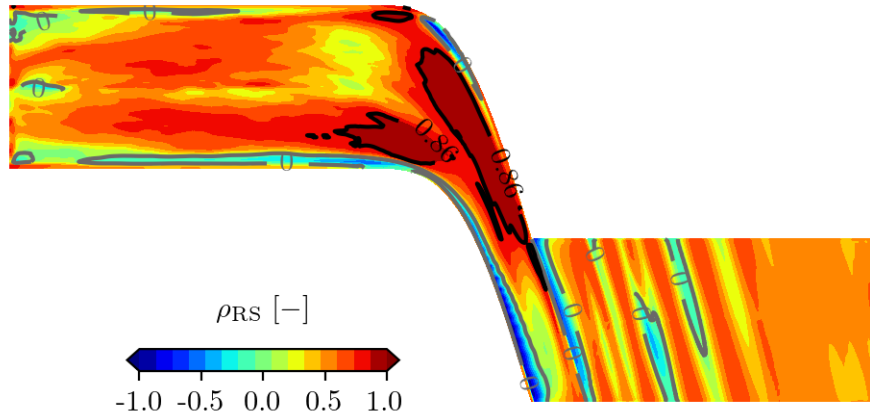


Figure 4.4 – 2D field of Schmitt’s criterion plotted at mid-span of the channel. Iso-contour of $\rho_{RS} = 0$ and $\rho_{RS} = 0.86$ respectively in grey and black.

4.3 Characterisation of anisotropy in a turbulent flow

4.3.1 Lumley’s theory

It is possible to characterise the anisotropy of turbulence using Lumley’s theory [69, 107]. This theory is based on the symmetric Reynolds stress tensor written as:

$$\tau_{ij} = \overline{v'_i v'_j} = \begin{bmatrix} \overline{v_x'^2} & \overline{v_x' v_y'} & \overline{v_x' v_z'} \\ \overline{v_y' v_x'} & \overline{v_y'^2} & \overline{v_y' v_z'} \\ \overline{v_z' v_x'} & \overline{v_z' v_y'} & \overline{v_z'^2} \end{bmatrix} \quad (4.4)$$

This tensor can be decomposed into the sum of a deviator and a spherical tensor, respectively traceless and isotropic tensors. In order to quantify the deviation from isotropy, it is convenient

to define the anisotropy tensor (see Equation 4.1), normalised by twice the turbulent kinetic energy, leading to:

$$b_{ij} = \frac{a_{ij}}{2k} = \frac{\overline{v'_i v'_j}}{\overline{v'_k v'_k}} - \frac{1}{3} \delta_{ij} \quad (4.5)$$

Where δ_{ij} is the Kronecker symbol. It has the following properties: zero trace and vanishes in the case of isotropy. Any deviation from $b_{ij} = 0$ means anisotropy of turbulence. However, under this form, the analysis of turbulence is not easy, because the normalised anisotropy tensor has 6 independent variables. Since this tensor is real and symmetric, it can be diagonalised by an orthogonal matrix giving three eigenvalues λ_1 , λ_2 , and λ_3 . Therefore, the Reynolds stress tensor can be written as:

$$\tau_{ij} = 2k \left(\frac{\delta_{ij}}{3} + b_{ij} \right) = 2k \left(\frac{\delta_{ij}}{3} + Z_{ij} \Lambda_i Z_{ij}^{-1} \right) \quad (4.6)$$

Where the isotropic part is equivalent to the turbulent kinetic energy and the deviatoric part accounts for transporting momentum with rotational components [91]. The eigenvector matrix components Z_{ij} give information on the orientation of the Reynolds stresses whereas λ_i inform on their shape, and therefore on the nature of turbulence. Both of them will be focused on in the following. Because the trace of the anisotropy tensor is zero¹, it has just two independent invariants η and ξ defined as:

$$\eta^2 = \frac{1}{3} \left(\lambda_1^2 + \lambda_1 \lambda_2 + \lambda_2^2 \right) \quad (4.7)$$

$$\xi^3 = -\frac{1}{2} \lambda_1 \lambda_2 (\lambda_1 + \lambda_2) \quad (4.8)$$

It is thus possible to reduce the space from six components (the b_{ij}) to only two components η and ξ . The spatial representation is performed in Lumley's triangle or AIM (Anisotropy Invariant Map) depicted in Figure 4.5 where ξ gives the kind of turbulence and η indicates the intensity of anisotropy. Every realisable turbulence must lie within this triangle which is bounded at its boundaries by typical turbulence states. Isotropic turbulence is found at the origin of the plot. $\eta = \xi = 1/3$ corresponds to a one-component turbulence, where two eigenvalues are equal to 0. The opposite case is found at $-\eta = \xi = -1/6$ for a two-dimensional turbulence where one eigenvalue is equal to 0 and the two others are equal. Red and blue dashed lines represent every turbulence where the three eigenvalues co-exist with always two eigenvalues equal (axisymmetric turbulence). Finally, the black dashed line shows a two-component turbulence where only two diagonal components exist and their sum is constant: this is typically encountered in boundary layers where the normal component vanishes. The eigenvalues are also interpreted as the spheroidal radii in the principle axis basis, so that it is possible to write the equation for a spheroid:

$$\left(\frac{\zeta_1}{\sigma_1} \right)^2 + \left(\frac{\zeta_2}{\sigma_2} \right)^2 + \left(\frac{\zeta_3}{\sigma_3} \right)^2 = 1 \quad (4.9)$$

Where σ_i are the eigenvalues of the Reynolds stress tensor and $\lambda_i = \frac{\sigma_i}{\tau_{kk}} - \frac{1}{3}$. It gives a relationship between the shapes of the Reynolds stresses in the principle axis basis of coordinates $(\zeta_1, \zeta_2, \zeta_3)$ and the invariants of the anisotropy tensor. For example, at isotropy, the ellipsoid is a sphere. It can be either a prolate or oblate spheroid for axisymmetric turbulence [107]. This is now illustrated on the swirled hot streak case.

¹In that case, $\lambda_3 = -(\lambda_1 + \lambda_2)$.

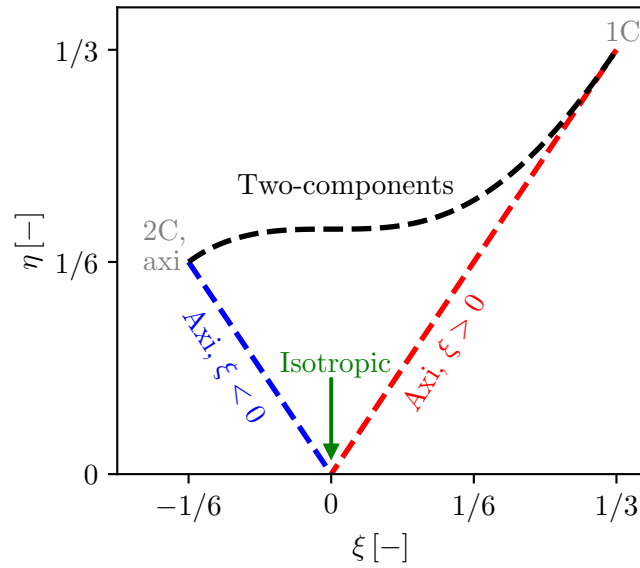


Figure 4.5 – Lumley’s triangle on the plane of the invariants η and ξ of the Reynolds stress anisotropy tensor. Adapted from Pope [91].

4.3.2 Application on a swirling hot streak

The anisotropy analysis is realised on the LES ‘SWIRL +’ case defined in Chapter 3. First of all, the impact of the walls on the development of turbulence anisotropy is evaluated in Figure 4.6. Using slip walls inevitably suppresses the development of isotropic turbulence, which is visible in Figure 4.6a. In this figure, the points remain close to the two-component turbulence, which is normal since the slip wall boundary condition is coded to vanish the normal velocity fluctuation. To check if this anisotropy impacts the HS, the normal stresses of the Reynolds stress tensor at the throat of the channel are plotted in Figure 4.6b together with the evolution of total temperature. For this particular plane, the b_{ij} are computed in the curvilinear reference frame (s, n, z) , so a passage matrix is applied. It reveals that the anisotropy developing at the walls does not interfere with the HS, as evidenced by the comparison of the plots of b_{zz} , b_{nn} (component normal to the walls at the throat) and total temperature.

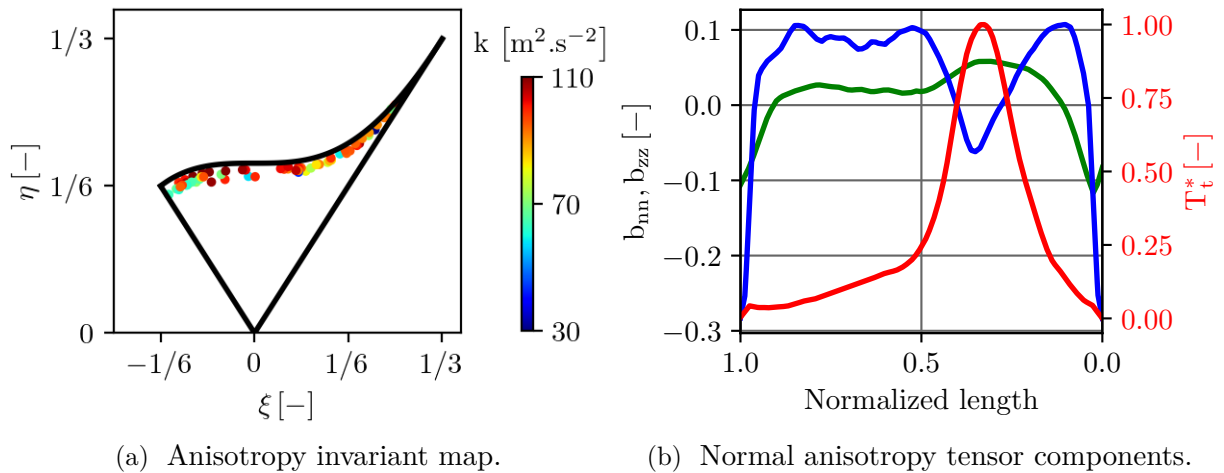


Figure 4.6 – Anisotropy invariant map applied close to the walls at $x^* = 0$ (a) and normal components b_{zz} (—) and b_{nn} (—) of the anisotropy tensor at the throat of the channel (b).

Lumley's triangle is now plotted on a line passing through the mean trajectory of the HS, where the probe numbering of Figure 4.7 is used. It enables to follow locally the behaviour of turbulence. Results are shown in Figure 4.8. The shapes of the Reynolds stresses defined by Equation 4.9 are also displayed at some specific locations.

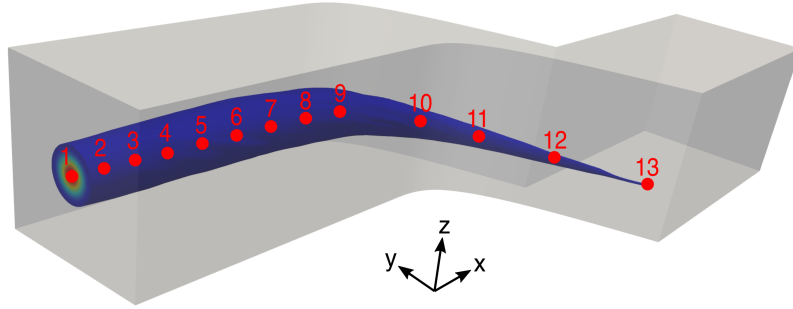


Figure 4.7 – Positioning of the probes on the mean trajectory of the hot streak.

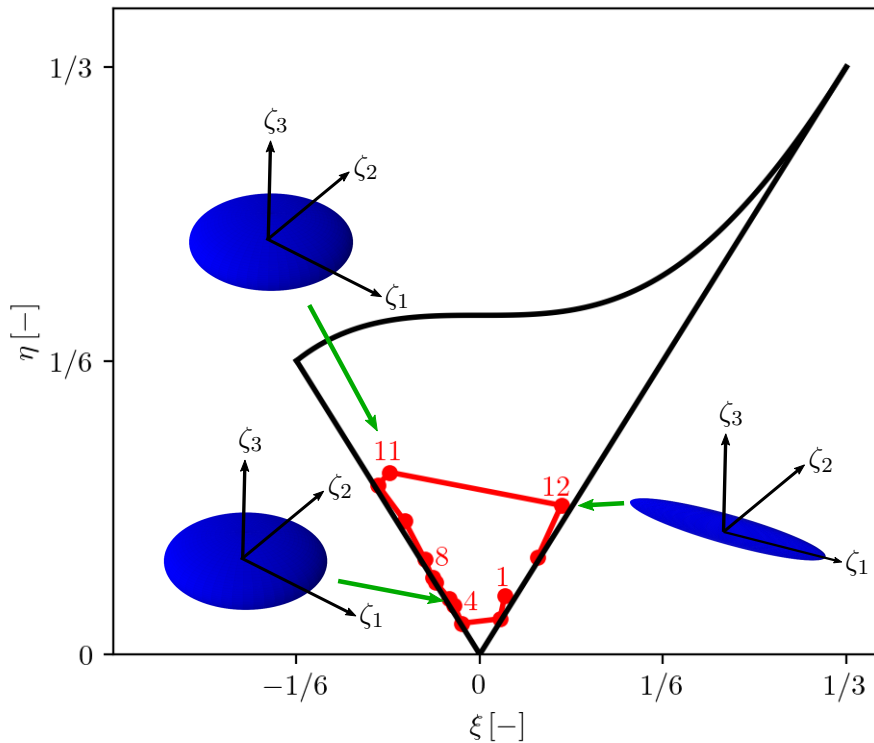


Figure 4.8 – Anisotropy invariant map applied to the 'SWIRL +' case.

When following the mean trajectory of the HS, it reveals that homogeneous isotropic turbulence is not fully reached at the inlet (probe 1) since the couple (η, ξ) does not go to $(0, 0)$, which could be explained by the strong gradients provoked by the swirling flow. Then, turbulence becomes axisymmetric from probe 4 since the trajectory follows the left-hand side straight curve. It corresponds to an axisymmetric contraction in which one eigenvalue is smaller than the two other ones. Between probe 11 and probe 12 is observed a change of branch, *i.e.* a change of type

of anisotropy, from a contraction to an axisymmetric expansion. It means that one eigenvalue is more significant than the two others, *i.e.* turbulence is predominant in one direction. This is due to the strong acceleration and curvature of the flow. Results are coherent as axisymmetric turbulence is commonly observed in round jets, circular disk wakes, or swirling jets. As said previously, the eigenvalues are also used to establish the shape of the Reynolds stress on the principal axis basis. To better understand the orientation of the stresses, the deviation of the eigenvectors $\mathbf{Z}_1, \mathbf{Z}_2, \mathbf{Z}_3$ with respect to the Cartesian basis vectors is evaluated at probes 4, 11 and 12 and is displayed in Figure 4.9:

- **Probe 4:** the eigenvectors are aligned with the Cartesian basis vectors since a maximum deviation angle of 10° is observed. The shape of the Reynolds stress is an oblate spheroid squashed in the spanwise direction (z direction), so that turbulence mainly occurs in (x, y) planes;
- **Probe 11:** the shape is still an oblate spheroid but the eigenvectors are no more aligned with the Cartesian basis: a deviation of 45° with the x -axis is observed. However, the radial deviation is still less than 10° ;
- **Probe 12:** the change in turbulence anisotropy also impacts the shape of the Reynolds stress, which is now a prolate spheroid. The deviation of the eigenvectors basis with respect to the Cartesian basis is about 72° , which is more or less the deviation imposed by the geometry (75° at the TE). The expansion is well occurring in the direction of the mean trajectory of the HS.

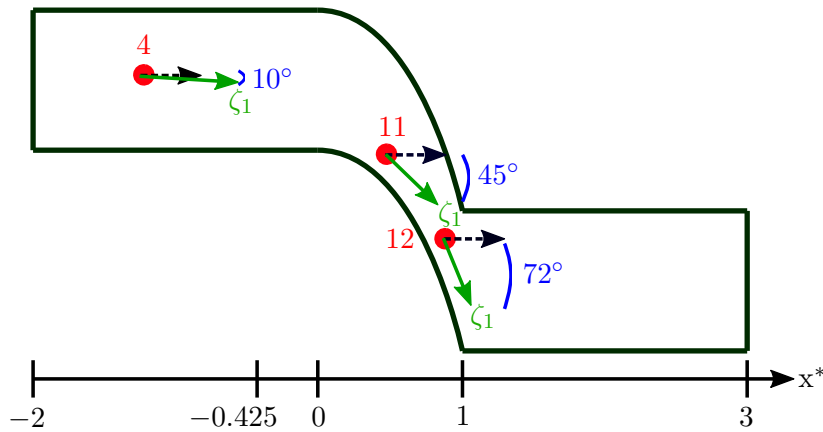


Figure 4.9 – Deviation of the eigenvectors of the anisotropy tensor with the Cartesian basis.

A more global view of turbulence anisotropy is presented in Figure 4.10. Turbulence triangles are plotted at different axial positions x^* for all the points contained within a threshold of total temperature at 450 K, which corresponds to a delimitation of the HS. Points are coloured by turbulence kinetic energy. Note that turbulence kinetic energy amplitude is different for each sub-plot in order not to saturate the colormap. As already mentioned, isotropy of turbulence is retrieved at the inlet of the domain (Figure 4.10a), where turbulent kinetic energy levels are roughly the same. This is a consequence of the turbulence injection method. Then, axisymmetric turbulence is evidenced in Figure 4.10b. Note that the more turbulence kinetic energy there

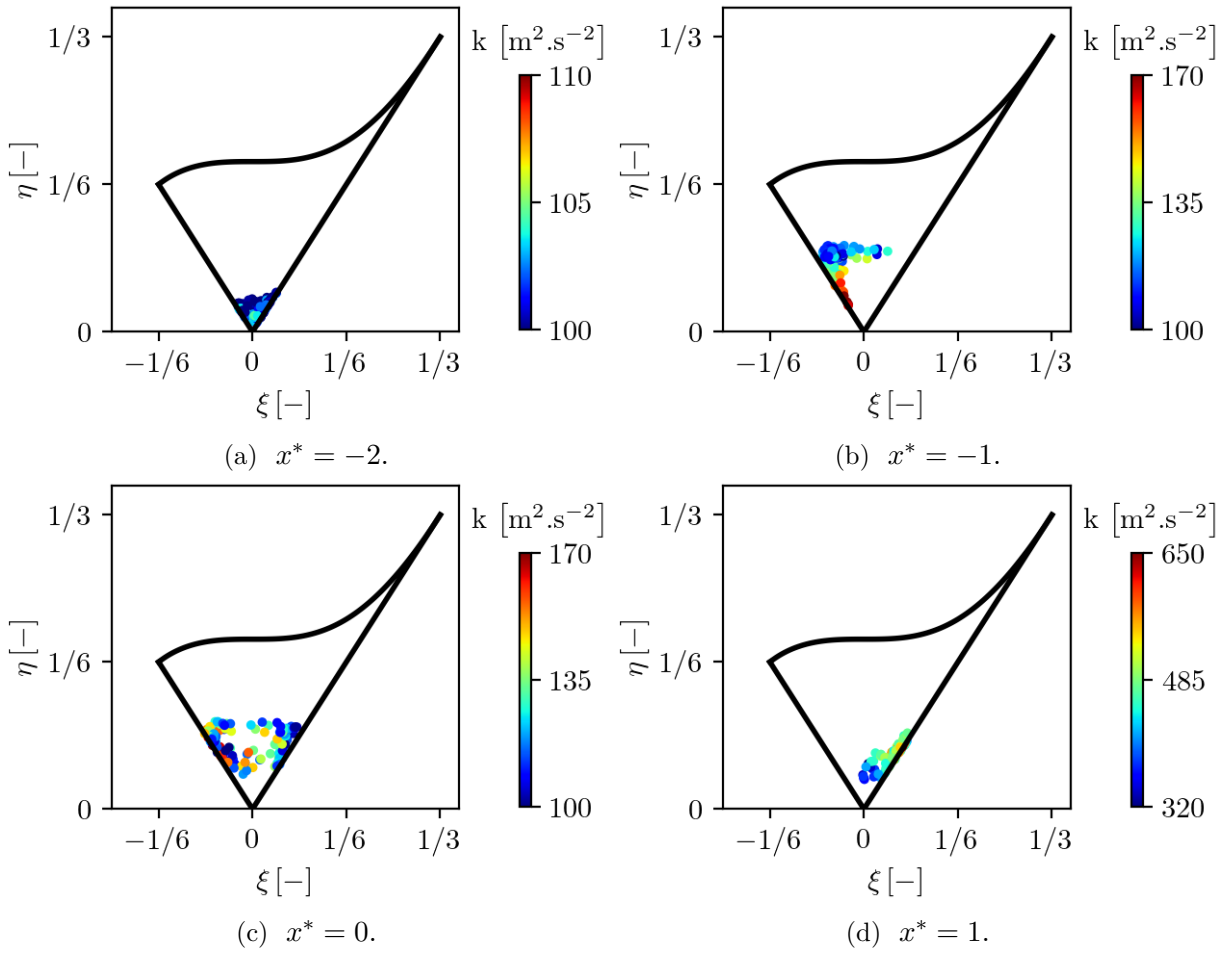


Figure 4.10 – Anisotropy invariant map applied on an iso-contour at 450 K of time-averaged total temperature at different axial positions. Points are coloured by turbulence kinetic energy.

is and the more resistant to anisotropy the points are. The change of anisotropy is seen in Figure 4.10c at the beginning of the curvature, where roughly half of the points are on the left branch, and half of the points on the right branch. Finally, at the outlet of the curvature in Figure 4.10d, all the points lie on the expansion branch with very high levels of turbulence kinetic energy. The contrary is observed for the levels of turbulence kinetic energy: there is a kind of delay for the return to isotropy, defined by Lumley [69], where the points with higher energy are more resistant.

Based on Schmitt’s criterion and Lumley’s analysis applied to the ‘SWIRL +’ case, the turbulence is clearly anisotropic, and one expects the RANS methods with classical Boussinesq’s hypothesis to badly predict the flow dynamics because of a lack of turbulence information. The following section investigates that point.

4.4 Dealing with anisotropy of turbulence in RANS modelling

In this section, corrections to take into account the anisotropy of turbulence are considered, either by adding a QCR correction to Boussinesq's hypothesis, or by using EARSM or RSM turbulence models. The post-processing which are presented in the following use the same methodology as the one presented in Chapter 3 for the radial distributions, axial evolutions or TKE budgets, and the one presented in Chapter 4 for Lumley's analysis.

4.4.1 Quadratic constitutive relation correction

The previous part has shown an important alignment default that fails most of the turbulence models based on Boussinesq's hypothesis, as seen in Chapter 3 with the results of Case 7. A first way to correct the misalignment is to add a rotation term to the zero-trace mean strain-rate tensor, which is called the quadratic constitutive relation (QCR) correction presented by Spalart in 2000 [111]:

$$\tau_{ij}^{QCR} = \tau_{ij}^R - C_{nl1} \left(O_{ik} \tau_{jk}^R + O_{jk} \tau_{ik}^R \right) \quad (4.10)$$

Where $C_{nl1} = 0.3$ is a constant and O_{ik} is an antisymmetric normalised rotation tensor defined by:

$$O_{ik} = \frac{2\Omega_{ik}}{\sqrt{\frac{\partial \tilde{v}_m}{\partial x_n} \frac{\partial \tilde{v}_m}{\partial x_n}}} \quad (4.11)$$

The QCR correction is applied on Case 7 presented previously with the Wilcox $k - \omega$ turbulence model. First of all, Figure 4.11 shows that this correction does not affect both the swirl angle and total temperature distributions. This may be explained by the fact that the flow is highly rotational, and the correction is not sufficient to counter-balance these high levels of vorticity. The turbulent kinetic energy budget applied on the HS is not affected. In fact, when comparing the two budgets of Figure 4.12 where the Wilcox $k - \omega$ case in solid lines is compared to the QCR correction case in dashed lines, differences are very slight. More important corrections must be taken into account, or the transport equation for each Reynolds stress must be considered.

4.4.2 EARSM/RSM turbulence models

Explicit Algebraic Reynolds Stress Models (EARSM) and Reynolds Stress Models (RSM) are used to correct the alignment between the Reynolds stress tensor and the mean strain-rate tensor. The models presented in Chapter 1 are considered, *i.e.* the EARSM model developed by Hellsten, Wallin and Johansson, and the SSG/LLR- ω RSM turbulence model. The dissipation scale is the specific turbulence dissipation rate ω . The value of μ_T/μ at the inlet is retained. For the RSM turbulence model, the diffusion term corresponds to a simplified isotropic form of the diffusion, the isotropic dissipation is retained and is obtained with a particular transport equation. Finally, the pressure-strain correlation is decomposed as the sum of different contributions presented in Cécora *et al.* in 2015 [19]. The RSM simulation is initialised from the EARSM simulation, where the extra-diagonal components of the Reynolds stress tensor are set to 0, and each component of the diagonal is fixed to $2/3 \cdot \bar{k}$. The dissipation scale computed by the EARSM model is also used.

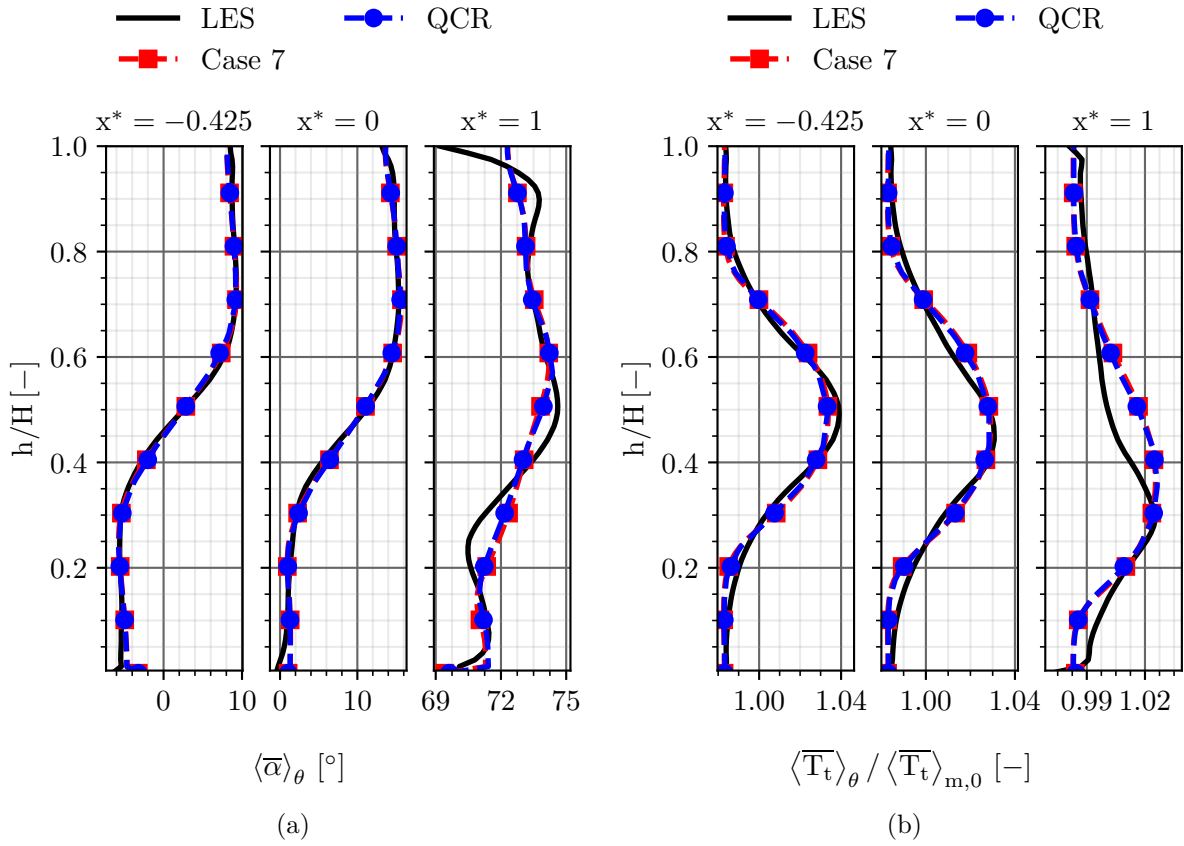


Figure 4.11 – Radial distributions of $\bar{\alpha}$ (a) and \bar{T}_t (b) using the QCR correction.

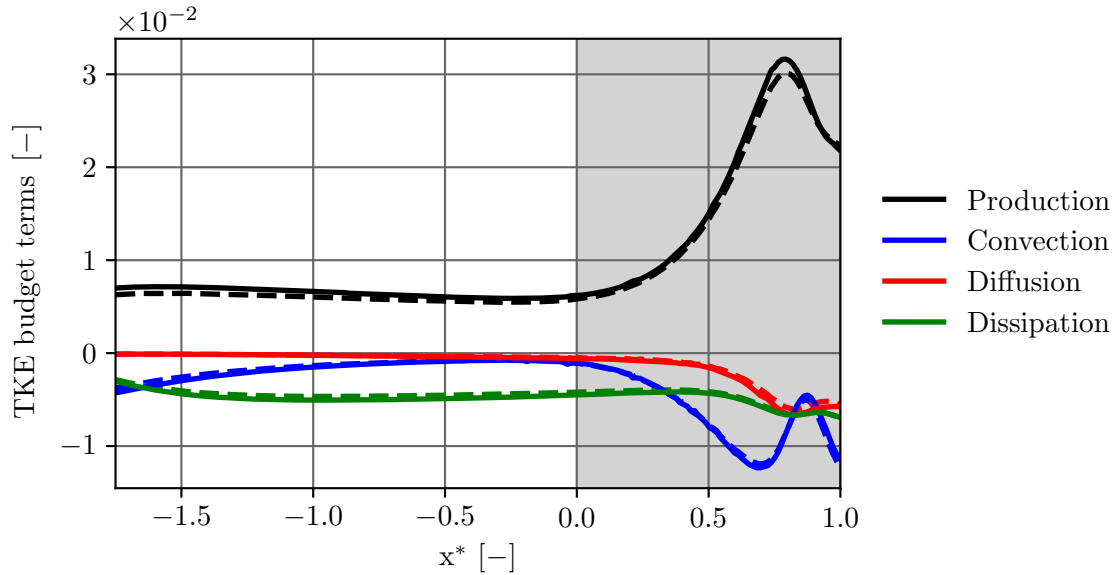


Figure 4.12 – Budget for the turbulent kinetic energy along x^* . Grey zone represents the curved part. Comparisons between Case 7 (—) and the QCR correction (---). Quantities are normalised by $(\rho_\infty v_\infty^3 r_c^2)$.

4.4.2.1 Aerothermal analysis

Results depicted in Figure 4.13 and Figure 4.14 show the importance of this kind of model for strongly curved and rotating flows. The EARSM model not only better preserves the swirl components (Figure 4.13a) but also allows a better temperature diffusion since the radial spreading is closer to the LES (Figure 4.13b). This last point is of interest in an industrial context and justifies the use of such turbulence model. The evolution of maximum total temperature presented in Figure 4.14 shows a strong improvement, where the decrease is well-captured for the EARSM model compared to Case 7. This is particularly true in the upstream part of the domain, where temperature gradients are more important. Then, maximum total temperature differences between linear and non-linear Boussinesq's turbulence models are reduced.

For the RSM model, looking at radial distributions of Figure 4.13, it seems that the swirl angle is better predicted compared to the EARSM or Wilcox $k - \omega$ models, with inflection points at 25% and 50% of channel's height that are close to the LES results. This can be explained by the fact that each component of the Reynolds stress tensor is transported independently. In the context of this work, the most important consideration is to correctly predict the temperature distributions (while keeping a relatively good agreement with the aerodynamics). In that sense, the RSM simulation presents a similar radial evolution of total temperature compared to the EARSM one, as evidenced by the plot of Figure 4.13b: the spreading and intensity at $x^* = 1$ are the same, and the RSM simulation even shows upstream improvements at $x^* = -0.425$ and $x^* = 0$. However, the evolution of maximum total temperature from $x^* = -2$ presented in Figure 4.14 shows some disagreements in the straight part of the channel, with a too important decrease in this specific region, which may be explained by: the inlet boundary conditions which are more sensitive since there is a multiplication of the variables to impose, or the modelled terms presented in Chapter 1, especially the diffusion term which is supposed isotropic. A way to improve the results would be to use a different formulation for the computation of the diffusion term. The generalised gradient diffusion hypothesis has been tested, but failed to converge. In the following, the analysis is deepened on the EARSM turbulence model case, since it reaches the criterion on the transport of temperature.

4.4.2.2 Turbulent kinetic energy budget

The turbulent kinetic energy budget with the simulation using the EARSM turbulence model is performed on the HS and is presented in Figure 4.15. It can be compared to the one presented in Figure 4.12. A dramatic improvement is observed, especially in the amplitude of the production term in the curved part, which has been reduced by a factor of 6, at iso-production limiter. This can be explained by the anisotropy in the production of turbulence. The evolution of the dissipation term also shows a strong change which is now comparable with the LES. Diffusion has been downgraded, but it has been previously shown that production and convection terms play the major role in the dynamics of the HS. This TKE budget confirms that the anisotropy of turbulence is well-captured, especially in the curved part of the domain ($0 < x^* < 1$).

This is validated by Figure 4.16 where the same field presented in Figure 4.1 is performed. It shows a better treatment of turbulence on the HS trajectory, where the evolution of \bar{k} is in better agreement with LES for the EARSM case compared to the Wilcox $k - \omega$ case that presents very high values of \bar{k} in the region of the swirled HS. In fact, turbulent flows are known

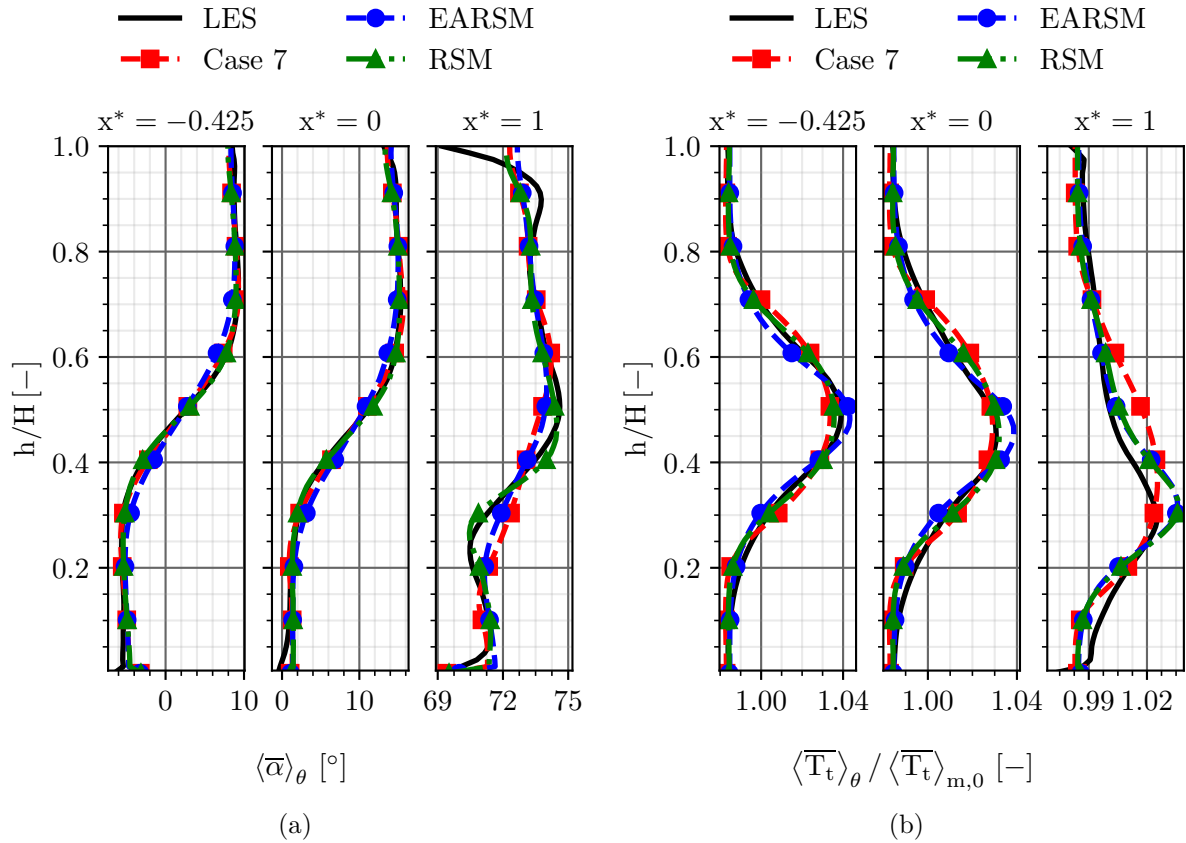


Figure 4.13 – Radial distributions of $\bar{\alpha}$ (a) and \bar{T}_t (b) for EARSM/RSM turbulence models.

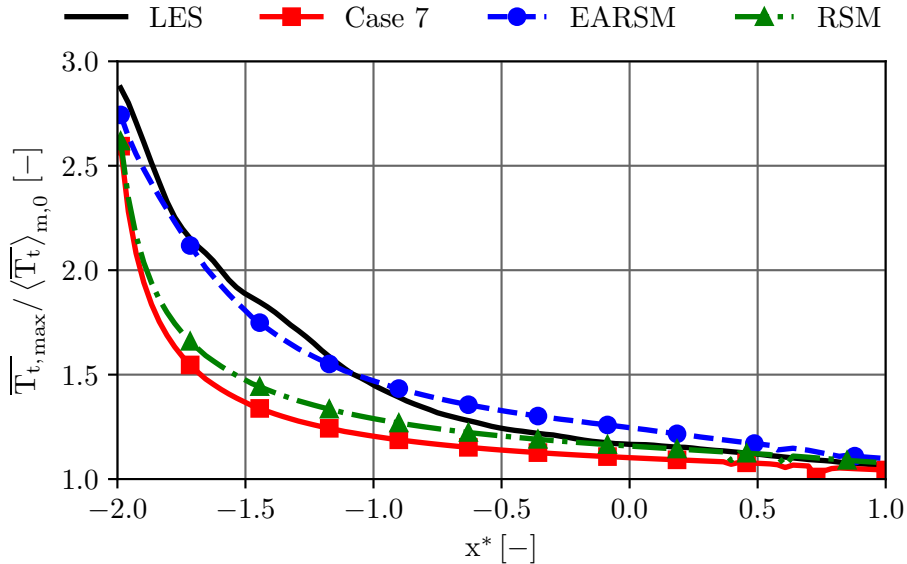


Figure 4.14 – Axial evolution of $\bar{T}_{t,max}$ for the EARSM/RSM turbulence models.

to be sensitive to streamline curvature. By their definition with Boussinesq's approximation, linear turbulence models are insensitive to the effects of streamline curvature. EARSM models retrieve part of this sensitivity with the quadratic terms (sensitivity to anisotropy) and cubic terms (sensitivity to streamline curvature). It leads to a better representation of the vorticity

inside the channel, especially the streamwise vorticity generated by the non-circular shape of the channel (stress-induced secondary flows), as discussed in [84, 113]. However, the present case is of higher complexity than what is presented in those two references because of the vorticity induced by the vortex that creates its own anisotropy.

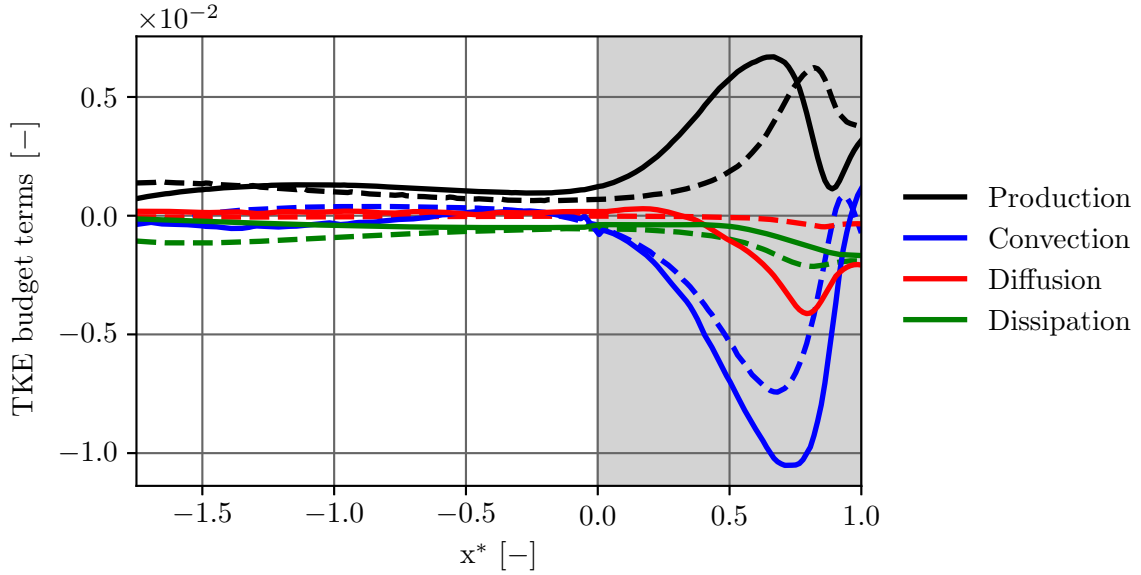


Figure 4.15 – Budget for the turbulent kinetic energy along x^* . Grey zone represents the curved part. Comparisons between LES (—) and EARSIM (---). Quantities are normalised by $(\rho_\infty v_\infty^3 r_c^2)$.

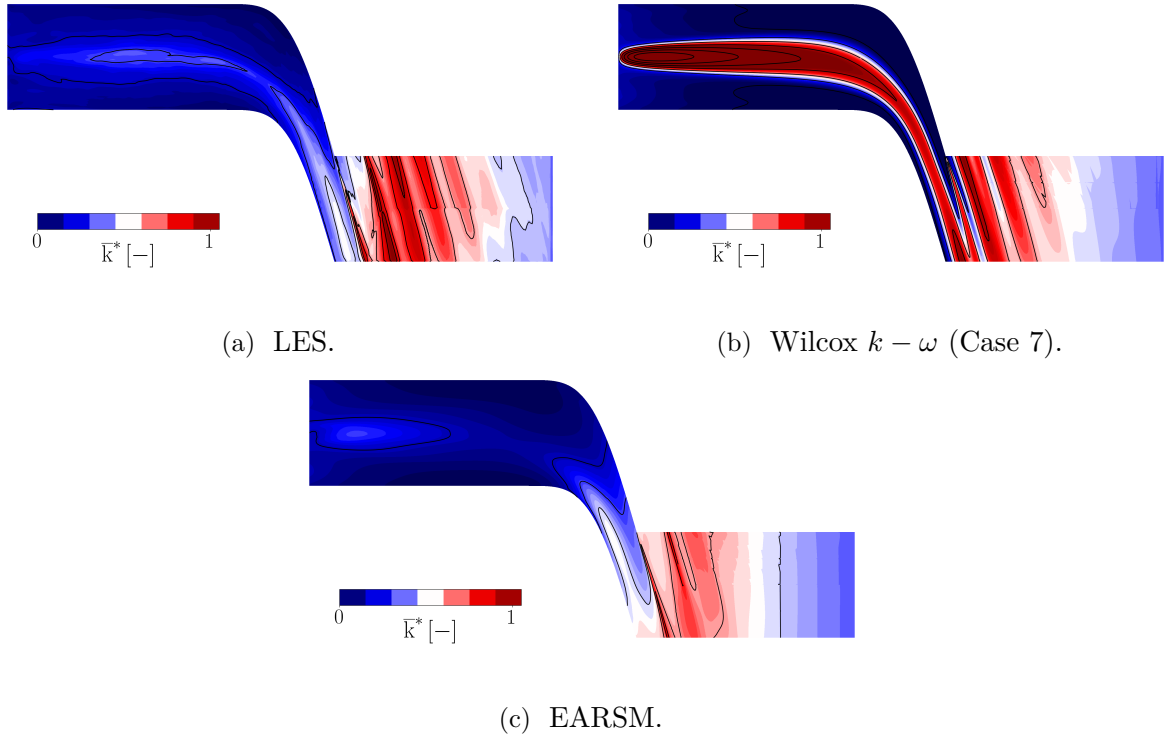


Figure 4.16 – Evolution of turbulent kinetic energy at mid-span of the channel using EARSIM and Wilcox $k - \omega$ turbulence models compared to the LES (scaled from the LES values).

4.4.2.3 Anisotropy invariant map

To better underline the differences due to the anisotropy of turbulence, Lumley's analysis is performed on Case 7 using the Wilcox $k - \omega$ turbulence model and on the case using the EARSM model. Before reducing the space with the invariants of the anisotropy tensor, 2D cuts of the normalised anisotropy tensor have been represented at mid-length of the straight duct ($x^* = -1$) for the LES, Wilcox $k - \omega$ and EARSM cases. Extra-diagonal component b_{xz} is depicted in Figure 4.17 whereas normal component b_{yy} is depicted in Figure 4.18. The Reynolds shear stress b_{xz} (Figure 4.17c) for the LES shows in the vortex core two regions of opposite sign stress. It changes sign at the vortex core center ($y^*, z^* = (-0.5, 0.5)$). Regarding the prediction by RANS, it seems that the intensity of the stress is correctly captured by the Wilcox $k - \omega$ model with values close to ± 0.08 near the boundaries of the vortex (Figure 4.17a). However, the dissymmetry of the distribution with respect to the $z^* = 0.5$ line is only represented by the EARSM model (Figure 4.17b), even if the intensity is higher than what is predicted by the LES, possibly arising from the lower values of \bar{k} as shown in Figure 4.16b. Regarding the Reynolds normal stress b_{yy} , only the EARSM turbulence model correctly captures the shape of the stress, especially in the vortex core region (Figure 4.18b). The behaviour of b_{yy} close to the wall for the LES case (Figure 4.18c) is attributed to the slip boundary condition that generates anisotropy.

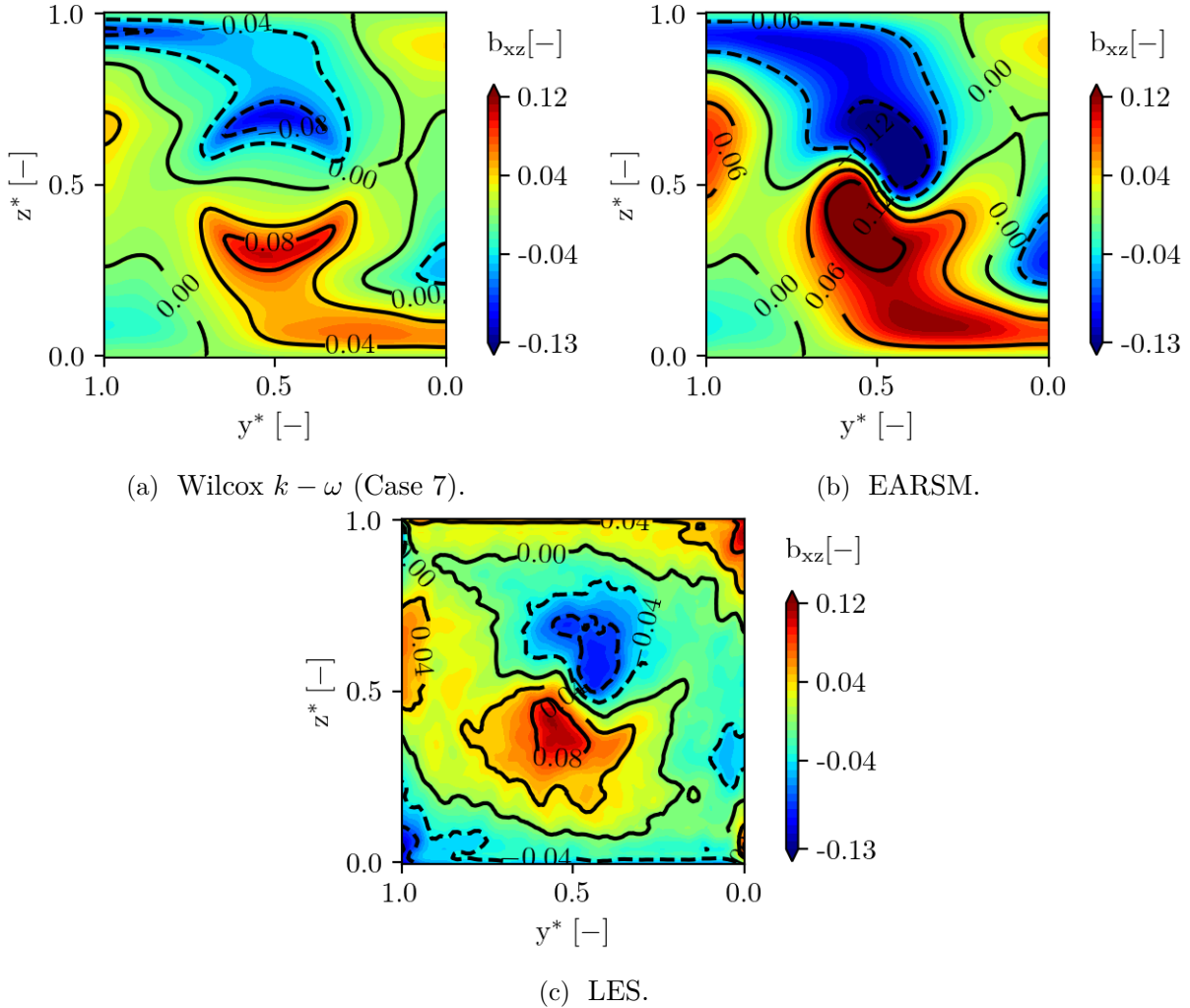


Figure 4.17 – b_{xz} component of the anisotropy tensor at $x^* = -1$. View from upstream to downstream.

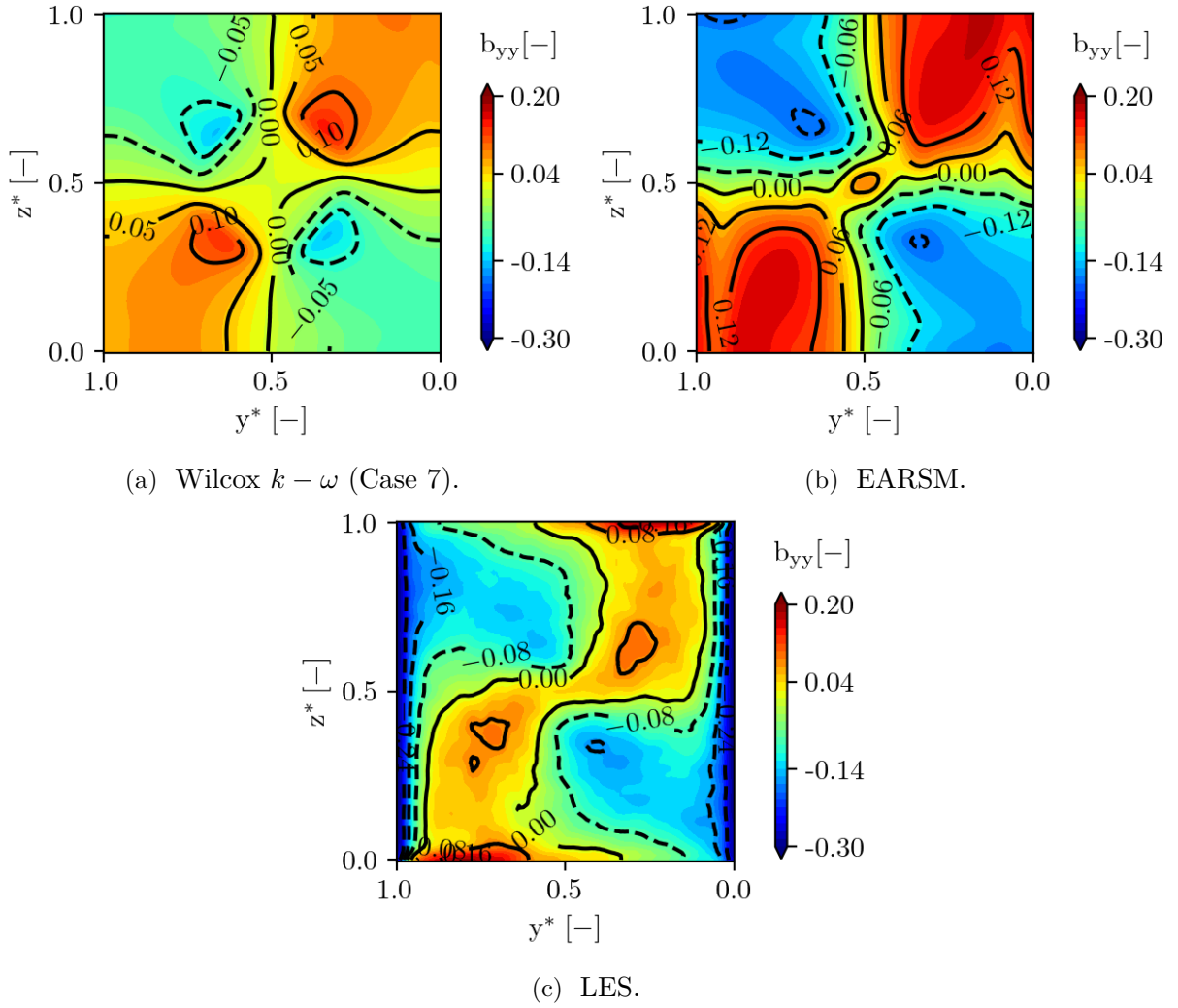


Figure 4.18 – b_{yy} component of the anisotropy tensor at $x^* = -1$. View from upstream to downstream.

Turbulence triangles are now plotted at different axial positions for the Wilcox $k - \omega$ turbulence model (Case 7), the EARSIM turbulence model and the LES, and are depicted in Figure 4.19 and Figure 4.20. They are obtained using a threshold of total temperature at 450 K delimiting the HS. Points are coloured by turbulent kinetic energy, scaled from the LES results. First of all, in Figure 4.19, *i.e.* in the straight part of the channel ($x^* = -1$), the axisymmetry of turbulence is better captured with the EARSIM turbulence model with the correct intensity of anisotropy marked by the value of η . The points are more random in terms of nature of turbulence ξ for the Wilcox $k - \omega$ model. The turbulent kinetic energy is also more relevant with the EARSIM model compared with the Wilcox $k - \omega$ model, where its value is over-predicted, as evidenced previously (Figure 4.1).

Figure 4.20 shows the turbulence triangles at the TE ($x^* = 1$). It reveals that for both linear and non-linear approaches, axisymmetric turbulence is not correctly captured in that case. However, once again, the turbulent kinetic energy level is more representative using the EARSIM turbulence model rather than using the Wilcox $k - \omega$ turbulence model, which has already been evidenced when comparing the production term of the TKE budget for both approaches.

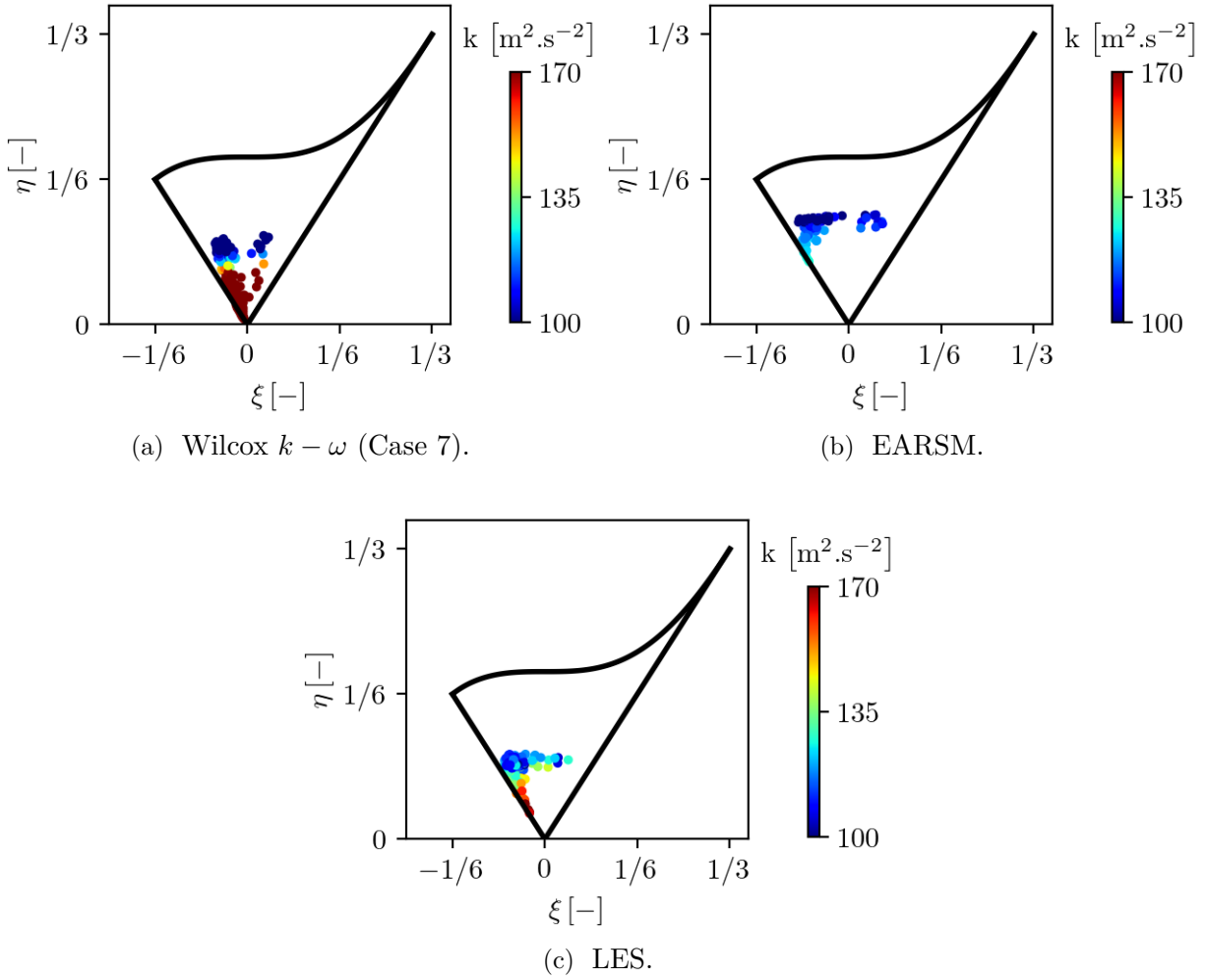


Figure 4.19 – Anisotropy invariant map at $x^* = -1$.

In reality, the Wilcox $k - \omega$ suffers from a lack of predictability of anisotropy of turbulence earlier in the channel, where the turning induced by the curvature is more pronounced. Figure 4.21 represents the turbulence triangles for both linear and non-linear approaches at $x^* = 0.5$, where the production term is nearly at its peak. Almost all the points for the Wilcox $k - \omega$ turbulence model are outside the triangle, whereas they are maintained inside the triangle with the correction of the EARSM turbulence model. Points that are outside the domain bounded by the triangle are defined as non-realizable turbulence (a non-physical turbulence). To be realizable, a turbulence must satisfy two conditions based on the Reynolds stresses:

- The energies are non-negative: $R_{\alpha\alpha} \geq 0$;
- The off-diagonal components must satisfy the Schwarz' inequality: $R_{\alpha\alpha} \cdot R_{\beta\beta} \geq R_{\alpha\beta}^2$.

Where there is no implied summation using the Greek indices α and β . These conditions have been tested *a posteriori* both on the linear and non-linear turbulence models simulations and on the LES. While the LES and EARSM simulation keep the realizability constraints, they are not satisfied when using the Wilcox $k - \omega$ turbulence model.

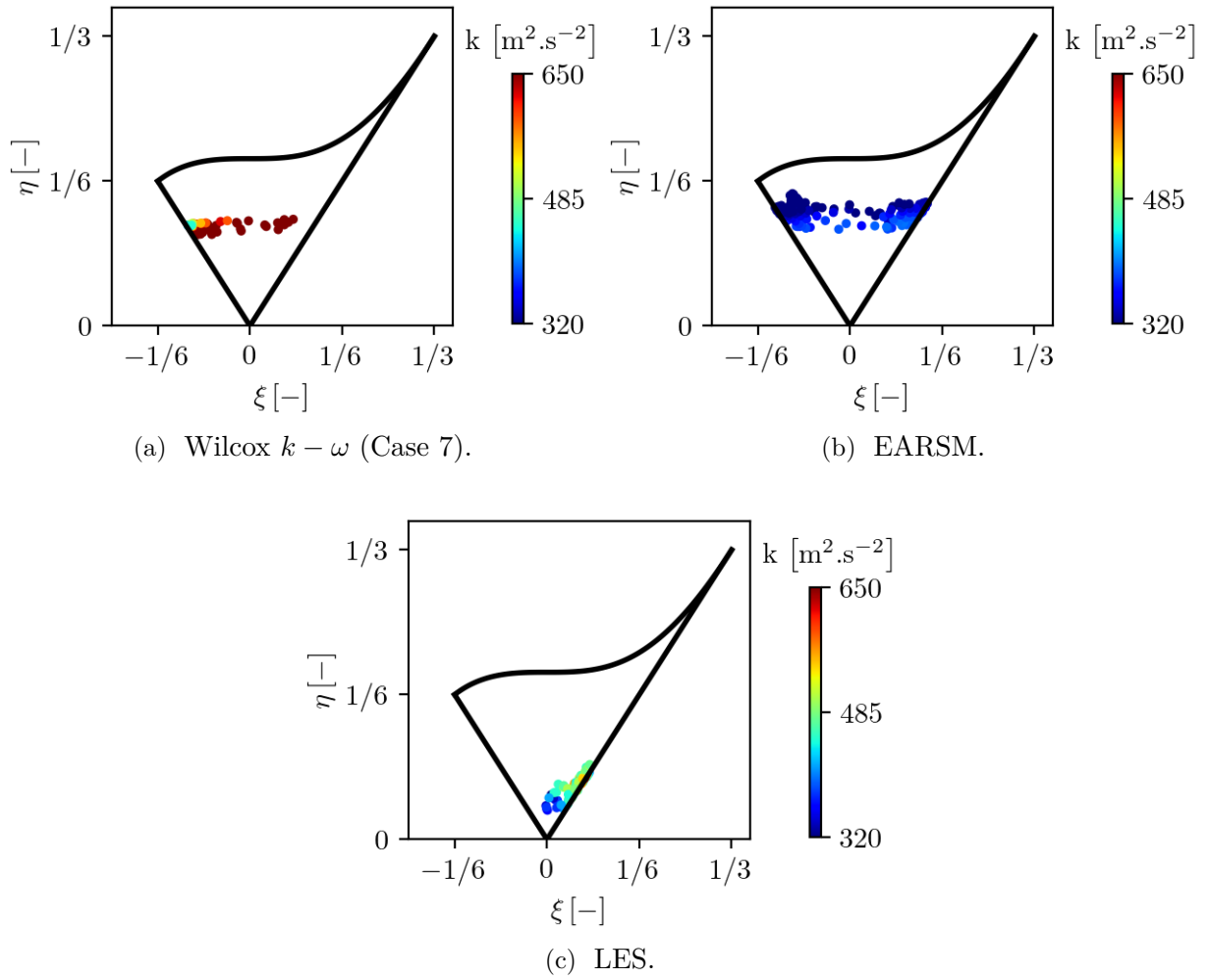


Figure 4.20 – Anisotropy invariant map at $x^* = 1$.

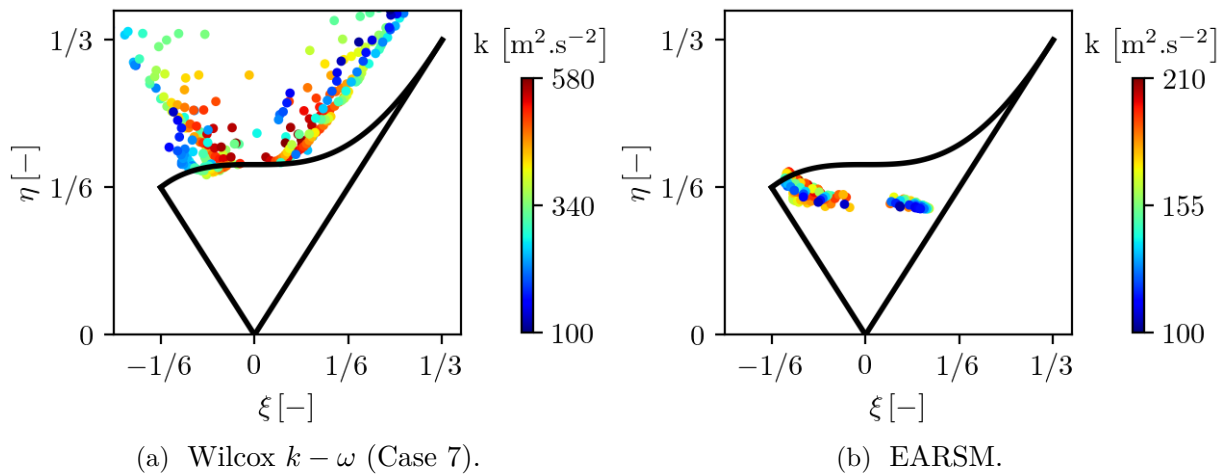


Figure 4.21 – Anisotropy invariant map at $x^* = 0.5$. Highlight of non-realisable turbulence for the Wilcox $k - \omega$ turbulence model.

4.5 Conclusion

In Chapter 4, the anisotropy of turbulence has been studied. Results of the LES based on two metrics revealed:

- A misalignment of the Reynolds stress tensor with the mean strain-rate tensor, which is the basis of all classical RANS turbulence models based on Boussinesq's hypothesis;
- A strong anisotropy of turbulence that is developing inside the channel.

These two points in particular explain the failure of classical RANS turbulence models such as the Wilcox $k - \omega$ model to predict highly turbulent swirling flows. Then, the anisotropy of turbulence has been tackled in the RANS approach by applying corrections of increasing order to correct the alignment of the tensors. The QCR correction is a simple one, but not efficient in our case because of the high vorticity. To correct even more the misalignment due to the anisotropy of turbulence, both the EARSM and RSM turbulence models have been tested successfully. They agree better with the LES since the anisotropy of turbulence is improved. In the TKE budget, the production term is well-computed using the EARSM model, resulting in a better evolution of turbulent kinetic energy inside the channel. This improvement can be explained by Lumley's analysis. While the linear turbulence model fails to predict realisable turbulence, the EARSM turbulence model keeps a physical turbulence. The anisotropy improves the transport inside the channel, but not the inlet boundary condition since the value of μ_T/μ to impose for the dissipation of turbulence must fall inside the optimal range discussed in Chapter 3.

Dans le Chapitre 4, l'anisotropie de la turbulence a été étudiée. Les résultats de la LES basés sur deux métriques ont révélé :

- Un désalignement du tenseur de Reynolds avec le tenseur des taux de déformation moyens, qui est la base de tous les modèles classiques de turbulence RANS basés sur l'hypothèse de Boussinesq;
- Une forte anisotropie de la turbulence qui se développe à l'intérieur du canal.

Ces deux points expliquent notamment l'échec des modèles de turbulence RANS classiques, tels que le modèle $k - \omega$ de Wilcox, à prédire les écoulements tourbillonnaires fortement turbulents. Ensuite, l'anisotropie de la turbulence a été abordée dans l'approche RANS en appliquant des corrections d'ordre croissant pour corriger l'alignement des tenseurs. La correction QCR est simple, mais n'est pas efficace dans notre cas en raison de la forte vorticité. Pour corriger encore plus le désalignement dû à l'anisotropie de la turbulence, les modèles de turbulence EARSM et RSM ont été testés avec succès. Ils concordent mieux avec la LES puisque l'anisotropie de la turbulence est mieux traitée. Dans le bilan TKE, le terme de production est bien calculé en utilisant le modèle EARSM, ce qui entraîne une meilleure évolution de l'énergie

cinétique turbulente à l'intérieur du canal. Cette amélioration peut être expliquée par l'analyse de Lumley. Alors que le modèle de turbulence linéaire ne parvient pas à prédire une turbulence réalisable, le modèle de turbulence EARSM conserve une turbulence physique. L'anisotropie améliore le transport à l'intérieur du canal, mais pas la condition aux limites d'entrée, puisque la valeur de μ_T/μ à imposer pour la dissipation de la turbulence doit se situer dans la plage optimale discutée dans le Chapitre 3.

Part III

Back to the industrial problematic and configuration

In the last part of the manuscript, a return to the industrial problematic and to the FACTOR configuration is performed. With the experience gained from the academic study, more advanced turbulence models are applied (Chapter 5). However, because of too many missing areas at P40 during the experimental campaign, the representativity of the inlet boundary condition can be questioned. To alleviate this, high-fidelity combustor/turbine simulations of the FACTOR project are used to generate both steady and unsteady boundary conditions at the inlet of the turbine (Chapter 6).

Predominant mechanisms of FACTOR

“ *Perhaps some day in the dim future it will be possible to advance the computations faster than the weather advances and at a cost less than the saving to mankind due to the information gained. But that is a dream.* ”

Lewis Fry Richardson

Abstract

In this transition chapter, the recommendations established through the academic study in terms of turbulence are applied to the high-pressure turbine of the FACTOR project: modification of the dissipation scale of turbulence and use of advanced turbulence models which deal with the anisotropy of turbulence.

5.1 Introduction	152
5.2 Application of the results from the academic study on the high-pressure turbine configuration of FACTOR	152
5.2.1 Impact of the turbulent Reynolds number	152
5.2.2 Effect of the turbulence model	154
5.2.3 Accounting for the anisotropy of turbulence	155
5.3 Conclusion	158

5.1 Introduction

The academic study presented in Chapter 3 and Chapter 4 exposed a strong dependency of the results, and especially the temperature distributions, on the inlet turbulence characteristics. Especially, in the RANS formalism, the ratio of turbulent viscosity over molecular viscosity, or simply μ_T/μ , is a first-order parameter that drives the evolution of the aerodynamic and aerothermal quantities. The smaller the value of this ratio, and the higher the dissipation of turbulence is, leading to good results in terms of aerodynamics, but too coherent temperature spots. This is not suitable in a high-pressure turbine where the temperature is a limiting factor in the design of the component. To overcome this problem, a compromise on the value of μ_T/μ has been found, based on the decrease of the turbulent kinetic energy. Moreover, the deepened turbulence analysis performed in Chapter 4 showed the importance of anisotropic turbulence models in swirling flows, that enable to capture the effects of curvature and rotation.

These two aspects as well as different linear eddy-viscosity turbulence models are tackled in this chapter, where they are applied to FACTOR's configuration, for which a first state-of-the-art performed in Chapter 2 revealed a major problem with the temperature transport in the turbine stage.

5.2 Application of the results from the academic study on the high-pressure turbine configuration of FACTOR

In order to decouple the effect of the cooling and turbulence modelling, only SV simulations are considered in this chapter. The inlet boundary conditions are those presented in Table 2.5 and in Figure 2.12 on pages 55/56.

5.2.1 Impact of the turbulent Reynolds number

For this first study, the turbulent Reynolds number at the inlet is modified through the value of the turbulent length scale l_T . The Smith $k-l$ model is still considered and the numerical radial distributions are compared to the experiments from the DLR already described. Results are presented in Figure 5.1 for the radial distributions, and in Figure 5.2 for the axial evolution of \bar{k} . Different turbulent length scales are used, for which a value of μ_T/μ around the HS peak position is associated:

- **$l_T = 9 \text{ mm}$** : this value is obtained from the experiments. It leads to a value $\mu_T/\mu \approx 3000$;
- **$l_T = 18 \text{ mm}$** : the initial value is multiplied by 2, leading to an averaged value $\mu_T/\mu \approx 6000$;
- **$l_T = 1.8 \text{ mm}$** : the initial value is divided by 5, leading to an averaged value $\mu_T/\mu \approx 600$;
- **$l_T = 0.015 \text{ mm}$** : for this last case, a laminar flow is targeted at the inlet. Both T_u ($= 4\%$) and μ_T/μ (≈ 1) are adjusted, having thus an impact on k and l_T .

By varying the turbulent Reynolds in that way, all the regimes presented in Chapter 3 (dissipation, transport and diffusion) are studied. Figure 5.1 clearly shows a negligible impact of the turbulent length scale on the distortions of total temperature. The only difference relies on the radial redistribution, which is more important when the turbulent length scale increases,

resulting in a higher diffusion. The total pressure distribution is more affected, resulting in a better-predicted shroud passage vortex for a small turbulent length scale, *i.e.* a higher dissipation of turbulence. Differences are more pronounced when looking at axial evolutions. It appears that the higher the turbulence length scale is, and the lesser differences between the two cases are (see $l_T = 9$ mm and $l_T = 18$ mm in Figure 5.2). This confirms that the diffusion regime is not affected by the value of the turbulent length scale above a certain threshold, as already shown by Firrito *et al.* [36].

The value of $l_T = 1.8$ mm, which corresponds to an intermediate μ_T/μ , enables a decrease of \bar{k} upstream the LE of the stator (Figure 5.2). This decrease was a recommendation established in Chapter 3 for the good setting of the turbulent quantities at the inlet. However, despite this decrease, the prediction of total temperature inside the high-pressure turbine stage is not in agreement with the experiments. The last value of l_T ($= 15$ μm) falls in the dissipation regime: the value of μ_T/μ remains close to 1, since all the turbulence dissipated. Overall, the evolution of \bar{k} is quite similar for the four cases: it remains stable in the NGV passage, and increases at the TE of the stator before reaching again a plateau. Finally, most of the increase occurs in the rotor, where the peak is reached at the TE.

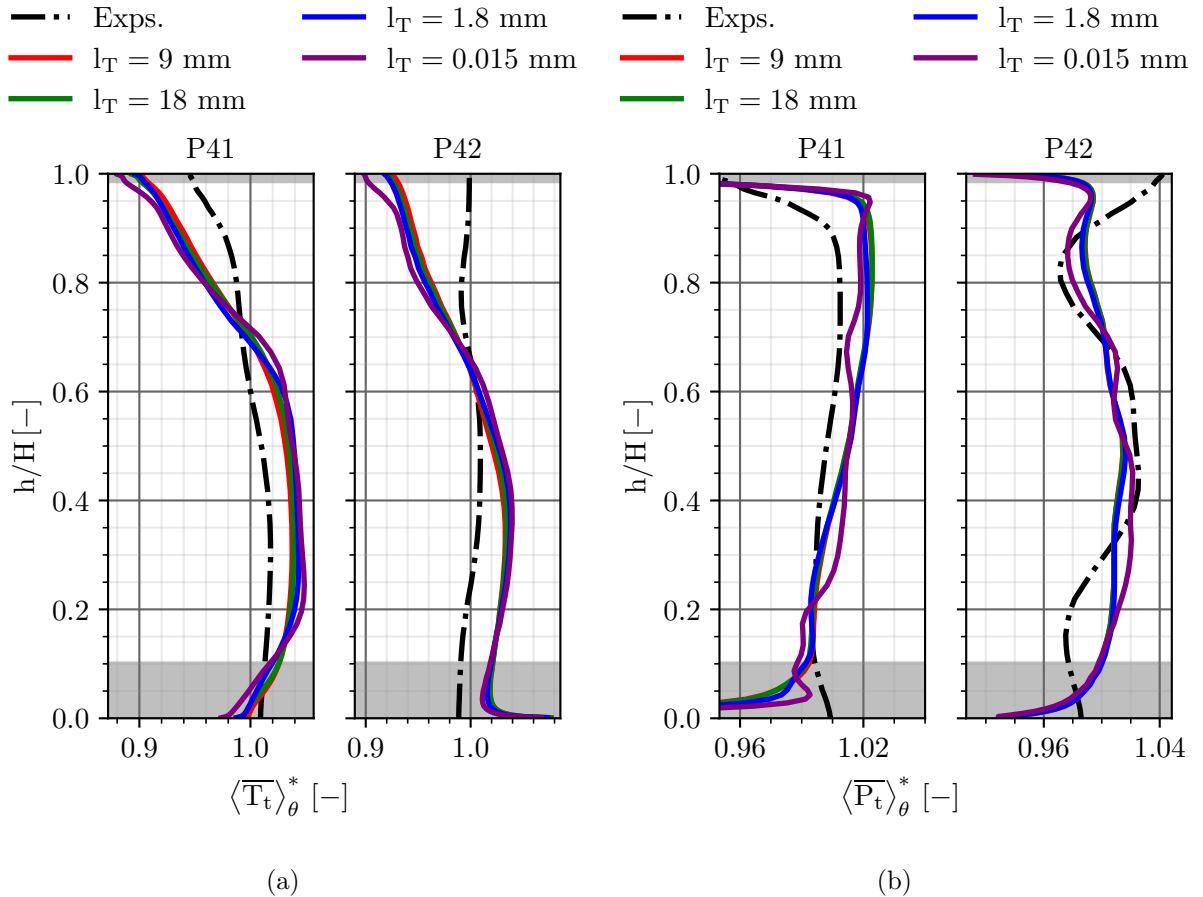


Figure 5.1 – Influence of the turbulent length scale on the radial distributions of \bar{T}_t (a) and \bar{P}_t (b) for steady SV simulations.

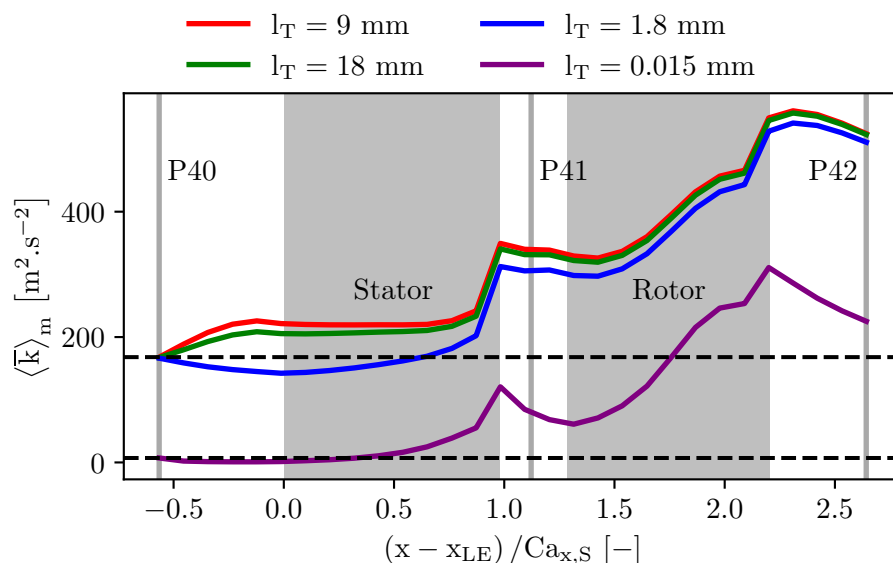


Figure 5.2 – Axial evolution of mass-weighted average turbulent kinetic energy for different values of turbulent length scale at the inlet. The position of the stator and rotor is represented with grey zones and the reference planes with grey vertical lines.

A first attempt in improving the transport of temperature in the high-pressure turbine stage has been performed, following the recommendations established in Chapter 3 based on the decrease of turbulent kinetic energy. Despite obtaining a decrease for a given value of turbulent length scale (or an equivalent value of turbulent viscosity ratio), the transport of temperature is not affected. A first hypothesis for such result may rely on the fact that the temperature ratio between the HS and the freestream is less important than in the academic study (1.1 vs. 2.8), so that the sensitivity to the inlet turbulence characteristics is less crucial.

5.2.2 Effect of the turbulence model

Other linear eddy-viscosity turbulence models are exploited. Especially, as for the academic study, a model with the specific turbulence dissipation rate ω is used (Wilcox $k - \omega$). The SST correction is also applied to limit the eddy viscosity in shear flows and strongly separating flows. The SST correction differs from the standard one presented by Menter [80] in order to be active both inside and outside the boundary layer, which makes this SST correction suitable for highly turbulent flows [138]. This model is often referred to as the Wilcox 2006 $k - \omega$ model. Since ω tends to infinity at the walls, its value is limited with a first-order extrapolation. Complementary studies on the wall condition for ω , turbulence limiters or the SST correction are presented in Appendix B (sections B.3, B.4 and B.5). Note that they do not modify the incoming conclusions. The nominal turbulence length scale from the experiments $l_T = 9\text{ mm}$ is retained, as well as its equivalent for ω at the inlet.

Results plotted in Figure 5.3 show an improvement in the total pressure distribution, where the shroud passage vortex is better predicted. The modification of the intensity of the shroud passage vortex is evidenced in Figure 5.4 with the visualisation of relative total pressure at the TE of the rotor blade. The turbulent kinetic energy behaves differently when using the SST $k - \omega$

turbulence model: it presents limited values compared to the reference $k-l$ turbulence model, as depicted in Figure 5.5. Especially, in the rotor part, strong discrepancies are observable. The stress-limiter modification plays a major role in the production of \bar{k} . However, despite all of this, the temperature transport inside the turbine stage is still not well-predicted. Anisotropic turbulence models are now used to enrich turbulence modelling.

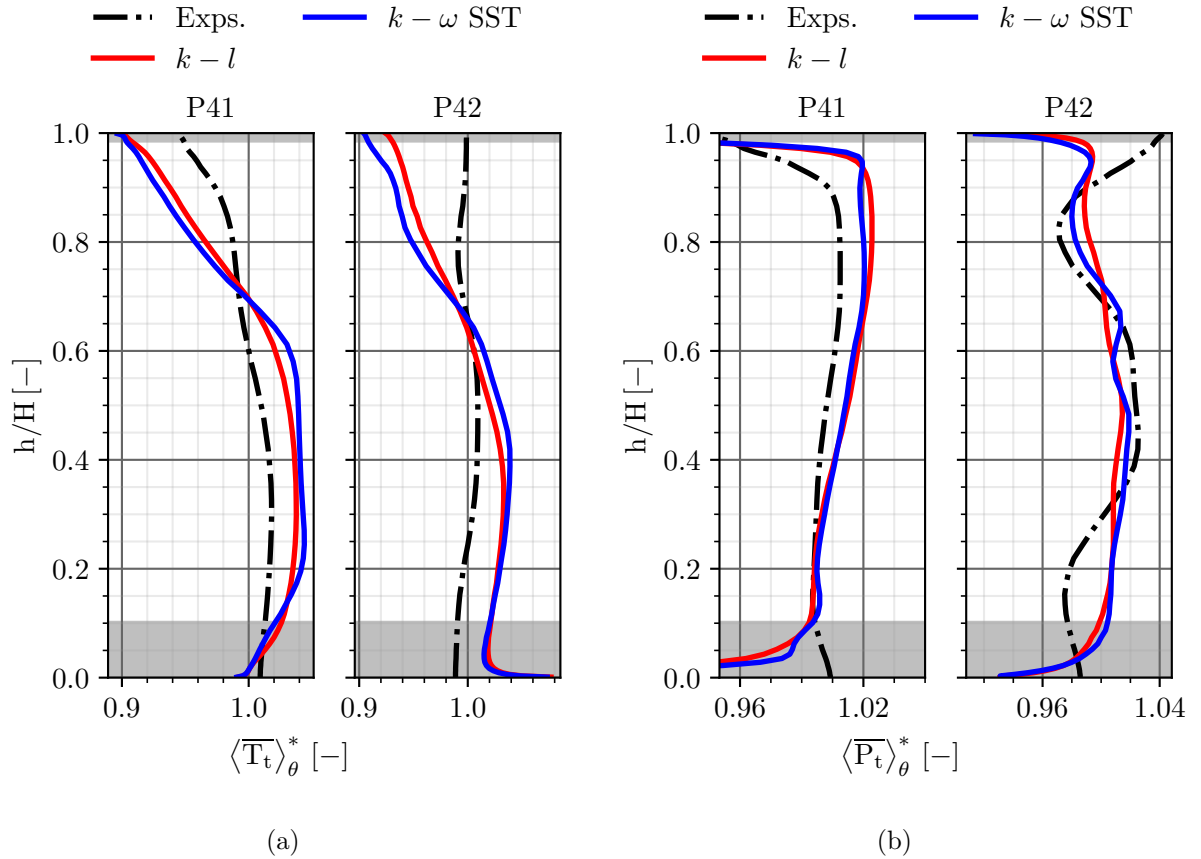


Figure 5.3 – Influence of linear-eddy viscosity turbulence models on the radial distributions of \overline{T}_t (a) and \overline{P}_t (b) for steady SV simulations.

5.2.3 Accounting for the anisotropy of turbulence

In this last subsection, anisotropic turbulence models are used: the EARSM turbulence model based on k and ω , and the RSM SSG/LRR- ω turbulence model. For the RSM turbulence model simulation, the procedure from Chapter 4 is used: it is initialised from the EARSM simulation, where the extra-diagonal components of the Reynolds stress tensor are set to 0, and each component of the diagonal is fixed to $2/3 \cdot \bar{k}$. The dissipation scale computed by the EARSM model is also used. Radial distributions are presented in Figure 5.6, while \bar{k} evolution is plotted in Figure 5.7. The improvement of anisotropic turbulence models presented in Chapter 4 is little noticeable on FACTOR. Temperature distributions are not affected, and there is still a lack of predictivity. However, pressure distributions show differences close to the shroud. In terms of \bar{k} , the EARSM turbulence model shows a dramatic increase through the turbine stage, while the RSM SSG/LRR- ω model keeps values comparable to the $k-l$ model. This difference of evolution

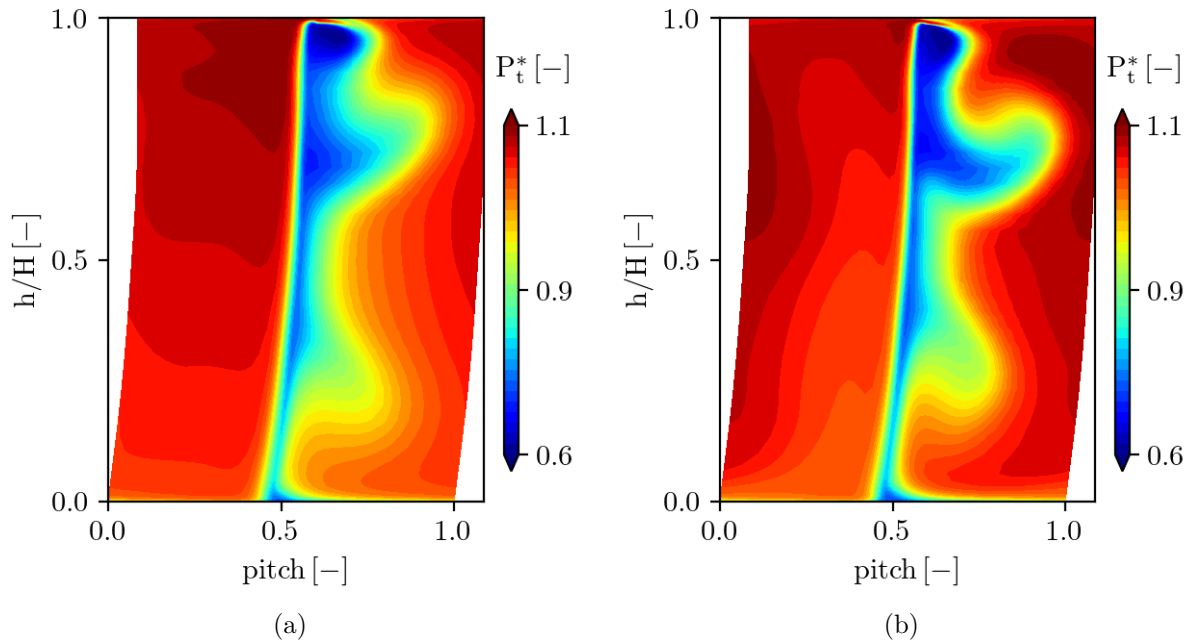


Figure 5.4 – 2D maps of relative total pressure plotted in terms of distortions at the TE of the rotor blade for the $k-l$ (a) and SST $k-\omega$ (b) turbulence models simulations.

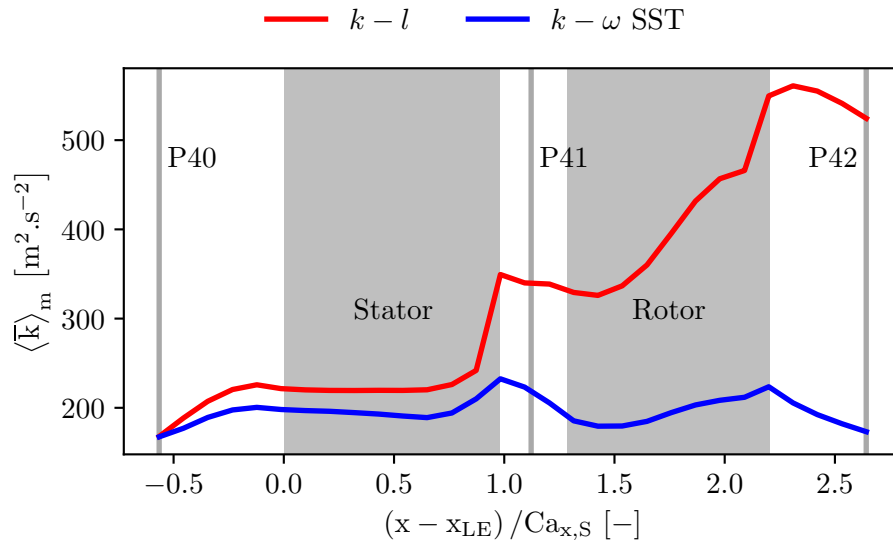


Figure 5.5 – Axial evolution of mass-weighted average turbulent kinetic energy depending on the turbulence model. The position of the stator and rotor is represented with grey zones and the reference planes with grey vertical lines.

for \bar{k} for the EARSM turbulence model can be explained by the SST correction that is not used (and which is at this time not developed in the *elsA* solver). This is in accordance with the observations of Vagnoli *et al.* [129] where the use of Wilcox $k-\omega$ turbulence model without any SST correction led to a dramatic increase of \bar{k} . Once again, despite these strong discrepancies in the evolution of \bar{k} , the predictivity of the temperature transport inside the high-pressure turbine is not acceptable from an industrial point of view, where errors in temperature prediction may lead to durability issues.

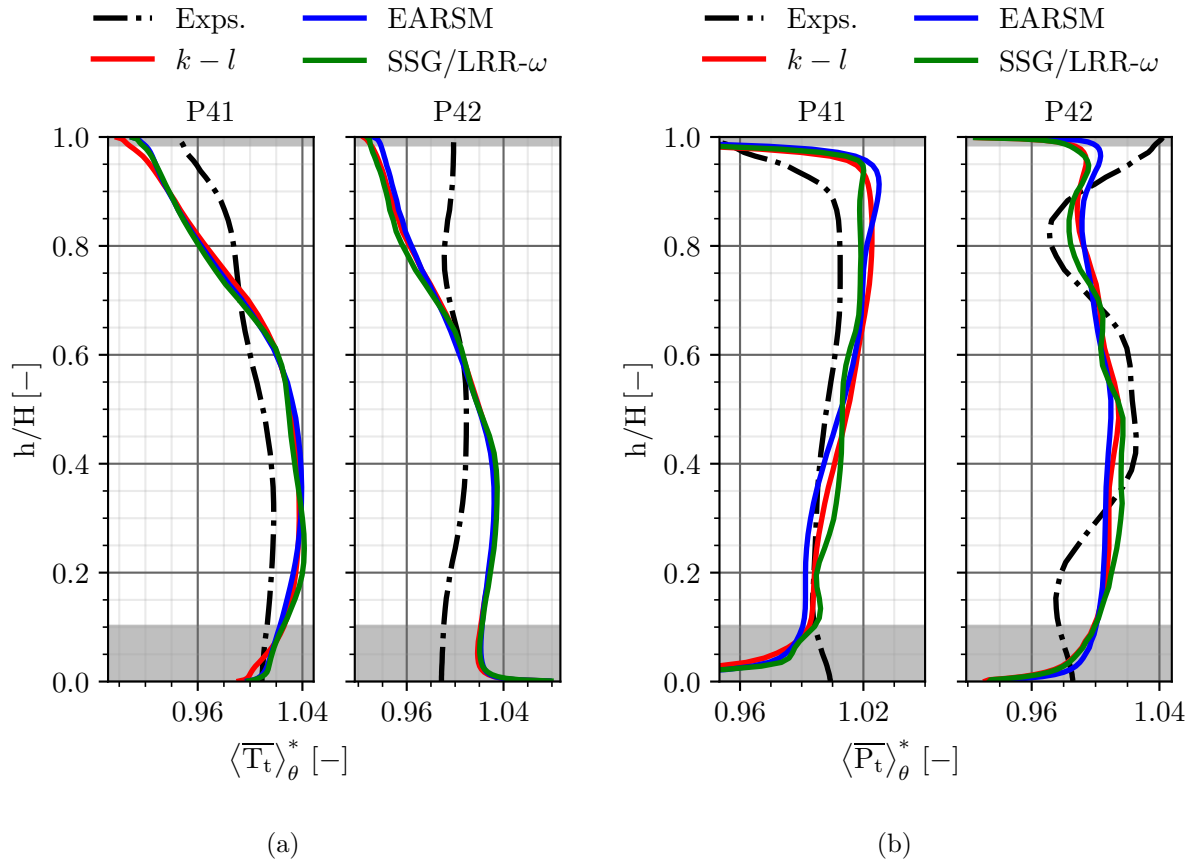


Figure 5.6 – Influence of anisotropic models on the radial distributions of \overline{T}_t (a) and \overline{P}_t (b) for steady SV simulations.

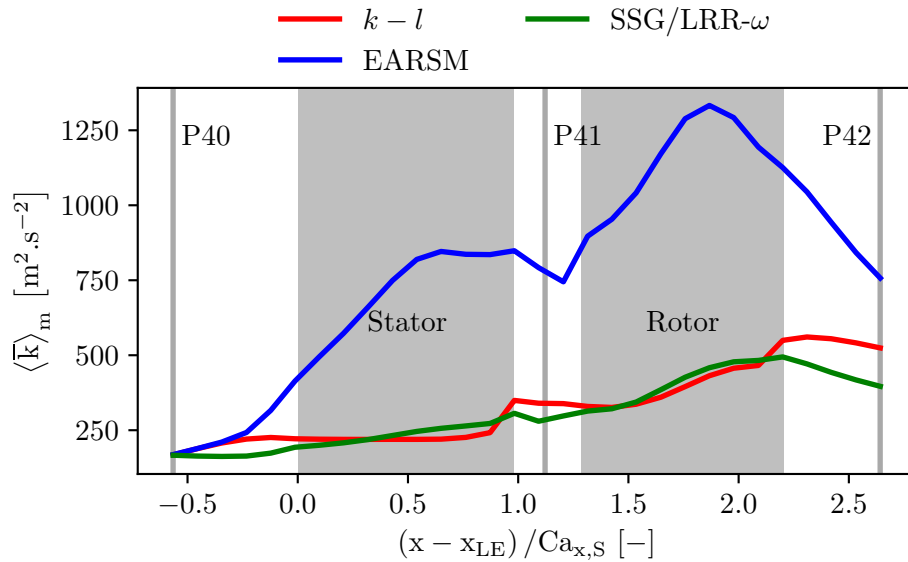


Figure 5.7 – Axial evolution of mass-weighted average turbulent kinetic energy with anisotropic turbulence models. The position of the stator and rotor is represented with grey zones and the reference planes with grey vertical lines.

5.3 Conclusion

Chapter 5 demonstrated all the difficulties in predicting correctly the temperature transport inside the high-pressure turbine of FACTOR. Thanks to Chapter 2, our field of study has been restricted to focus only on turbulence modelling, leading to the studies of Chapter 3 and Chapter 4. The recommendations established through the academic study have been applied to the configuration of FACTOR. However, none of them are suitable for the correct prediction of the temperature evolution inside the turbine, whether it is the impact of the turbulent Reynolds number, the effect of the turbulence model or taking into account anisotropy. It is therefore clear that the dominant mechanism responsible for the poor prediction of temperature transport is not related to turbulence modelling. It will be shown in Chapter 6 that the temperature transport is highly sensitive to the inlet boundary condition, imposed until now from the measurements of the 5HP, and for which the missing areas have been filled up with an interpolation.

Le Chapitre 5 a démontré toutes les difficultés à prédire correctement le transport de température à l'intérieur de la turbine haute pression de FACTOR. Grâce au Chapitre 2, notre champ d'étude a été restreint pour se concentrer uniquement sur la modélisation de la turbulence, ce qui a conduit aux études du Chapitre 3 et du Chapitre 4. Les recommandations établies durant l'étude académique ont été appliquées à la configuration FACTOR. Cependant, aucune d'entre elles ne permet de prédire correctement l'évolution de température à l'intérieur de la turbine, que ce soit l'impact du nombre de Reynolds turbulent, l'effet du modèle de turbulence ou la prise en compte de l'anisotropie. Il est donc clair que le mécanisme dominant responsable de la mauvaise prédiction du transport de température n'est pas lié à la modélisation de la turbulence. Il sera montré au Chapitre 6 que le transport de température est très sensible à la condition aux limites d'entrée, imposée jusqu'à présent à partir des mesures des sondes 5 trous, et pour lesquelles les zones manquantes ont été obtenues par interpolation.

Towards realistic high-pressure turbine inlet boundary conditions

“ *The important thing is not to stop questioning. Curiosity has its own reason for existing.* ”

Albert Einstein

Abstract

This last chapter deals with the inlet boundary conditions. Before presenting and studying different hypotheses that may explain the failure of temperature transport inside the high-pressure turbine, a reminder on the measurement difficulties at P40 is done. Then, each hypothesis is tackled: the impact of the errors in the core flow, the effect of the boundary layers and the influence of an instability at the inlet. Finally, comparisons with steady measurements and first post-processing dealing with unsteady pressure measurements are presented.

6.1	Introduction	163
6.2	Status of measurements at P40	165
6.2.1	Measurement difficulties	165
6.2.2	Differences at P40 between the experiments and the LES	166
6.3	Hypothesis 1: correction of type 'c' errors	168
6.3.1	LES database	168
6.3.2	Sensitivity to the inlet flow variables: test cases matrix	170
6.4	Hypothesis 2: investigation of type 'a' errors	171
6.4.1	Modification of the geometry	171
6.4.2	Boundary layer thickness	171
6.4.3	Impact of the modification of the map close the hub and shroud	172
6.5	Hypothesis 3: generation of an unsteady boundary condition	176
6.5.1	Emergence and signature of the PVC	176
6.5.2	Spectral Proper Orthogonal Decomposition method	176
6.5.3	Application on FACTOR's configuration	178

6.6	Comparisons with steady experimental data	191
6.6.1	Radial distributions from the 5HP measurements	191
6.6.2	Isentropic Mach number distribution on the vane surface	194
6.6.3	Hub and shroud static pressure taps	194
6.7	Unsteady pressure measurements	195
6.7.1	Time-averaged pressure field at P40	196
6.7.2	PSD pressure amplitude at P40	196
6.7.3	Phase-locked average at P42	198
6.7.4	PSD pressure amplitude at P42	199
6.8	Conclusion	200

6.1 Introduction

While in a compressor, the feeding conditions are uniform in most cases (for a machine running at the nominal point without sideslip angle for instance), this is never the case for a high-pressure turbine. This difference is due to the position of this element downstream of the combustion chamber, where a very complex physics involving chemical reactions takes place. The turbine is thus fed by a flow that keeps all the physics from the combustion chamber. Important levels of turbulence, swirling motions, hot streaks and hydrodynamic instabilities are present at the inlet of the turbine, and are amplified on modern engines due to their compactness, which leads to a high coupling between the components.

In the context of a numerical simulation, it is therefore crucial to accurately prescribe the inlet boundary condition which is at the interface between the combustion chamber and the high-pressure turbine, in order to reach an acceptable accuracy. This prescription is based on three criteria which are ranked in random order according to their level of importance:

- Turbulence characteristics;
- Aerodynamic fields;
- Unsteady phenomena.

The first two points can be converted easily into a numerical boundary condition, while the last one requires a highly resolved unsteady database, and an onerous pre-processing and computational effort. Turbulence characteristics are often obtained through the use of hot wire anemometry (HWA), which makes it possible to quantify turbulence levels and distribution over a given plan [61]. It is the case for FACTOR. Aerodynamic mean fields are acquired with steady five-hole probes (5HP) from a calibration map [62]. Unsteady motions at the combustor/turbine interface (P40) can be measured with fast-response aerodynamic probes (FRAP).

So far in this manuscript, the study of FACTOR's configuration has demonstrated all the complexity of correctly predicting the transport of temperature within the turbine stage. No matter how turbulence is modelled (turbulence model, turbulence characteristics), the distortions are not well captured. Unsteady simulations do not improve the transport. Cooled simulations allow more physical phenomena to be taken into account (with stronger secondary flows for example), but are still not satisfactory. These conclusions are supported by the state-of-the-art on this configuration which revealed a general failure in correctly predicting the temperature radial distributions at the outlet of the NGV passage (P41): those are overestimated [21, 45, 71, 129]. All these results were obtained while prescribing a steady boundary condition at P40, extracted from the experiments of the DLR, and with RANS simulations. However, on this configuration, Martin [73] matched the experiments at P41 by performing a LES, considering both the combustion chamber and the NGVs, which is depicted in Figure 6.1. The author avoided the question of the complex boundary condition at P40, by imposing a uniform field at the inlet of the combustion chamber, leaving the flow to develop, even the possible presence of instabilities (PVC as already mentioned in Chapter 2 - section 2.1.3).

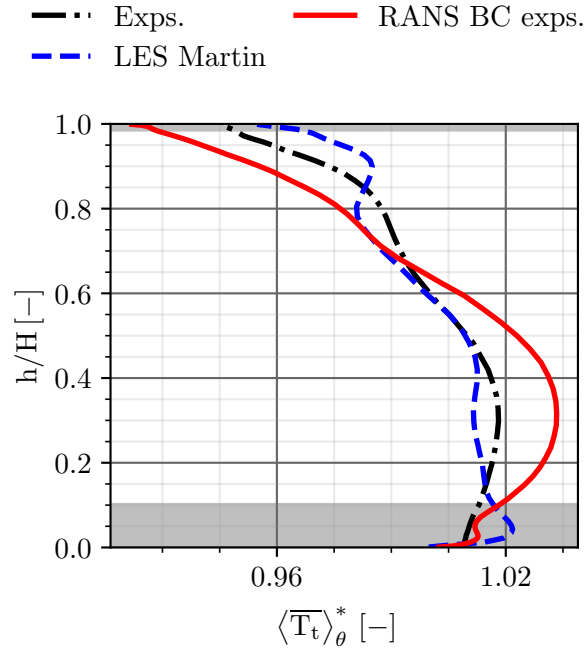


Figure 6.1 – Radial distributions of total temperature at P41. Comparisons between the experiments, the isolated turbine simulation of Chapter 2 with a steady boundary condition extracted from the experiments and the coupled combustion chamber/NGVs LES of Martin [73].

From all these observations, both the validity of the data measured in the experiments and the impact of an unsteadiness at P40 must be evaluated. This is the scope of Chapter 6. Different hypotheses for the inaccuracy of the boundary condition at P40, causing misprediction of the temperature transport, are put forward and studied:

- **Hypothesis 1: interpolation errors in the core of the flow measured on the test bench.** Due to the high values of flow angles at P40, huge blank spaces in the core of the flow are filled up with an interpolation process;
- **Hypothesis 2: the boundary layers are not correctly captured by the probing.** A percentage of the vein height close to the hub and the shroud is not measured because of the walls/probe interactions, and data are extrapolated;
- **Hypothesis 3: a PVC from the combustion chamber impacts the dynamics of the flow in the high-pressure turbine.** The experiments showed the presence of a hydrodynamic instability at the inlet of the turbine that still persists at the outlet of the NGVs. However, imposing a steady boundary condition filters the effect of the instability.

To check the aforementioned hypotheses, the thesis work and LES database of Martin [73] are used to generate new boundary conditions suitable for RANS simulations. This chapter is decomposed into six main parts. First, a status of the experimental campaign at P40 performed by the DLR is done. Then, each hypothesis is tackled. Finally, steady measurements and unsteady measurements obtained with FRAP are studied and compared to the numerical simulations. Turbulence modelling is put aside to focus only on the boundary condition in terms of aerodynamic quantities. The reader can refer to the studies from Chapter 2 to Chapter 5 for this particular question.

6.2 Status of measurements at P40

As already detailed in Chapter 2, the 5HP measurements at P40 suffered from different difficulties which are summed up in Figure 6.2. All the missing areas have been filled up by an interpolation process developed by Rolls-Royce Deutschland named INPAINNTN [40] which is purely a mathematical approach based on a penalised least-square method. This process may be questioned at some point, especially when no RANS modelling correctly predicts the temperature evolution.

6.2.1 Measurement difficulties

In this chapter, errors of type 'b' are not suspected to impact the quality of the numerical simulations. They are due to an error in traverse gear step motor control for which the radial axis punctually could not move the probe. In this PhD thesis, particular attention is focused on errors of type 'a' and 'c', which are respectively due to the probe head size, and flow angles too high to yield results from the probe calibration process. From a numerical point of view, since P40 is the inlet boundary condition, errors of type 'a' may signify that the boundary layers are not captured while errors of type 'c' may lead to a misprediction of the swirled HS, and therefore to a misprediction of the temperature transport inside the high-pressure turbine.

Krumme *et al.* [62] validated the INPAINNTN interpolation for errors of type 'c' at the NGV outlet (P41), as shown in Figure 6.3. This plane was chosen since the measurement points were in great majority inside the calibration range. A range of data such that $\beta > 3^\circ$ was removed, and a successful application of the interpolation was reported, with minor differences compared to the initial data. Applying the same technique at P40 is questionable, as the gradients and flow angles are much more intense, leading to more numerous and larger unmeasured zones. This concern is the heart of the present chapter, for which results of LES are used for the generation of new boundary conditions and compared to the INPAINNTN post-processing.

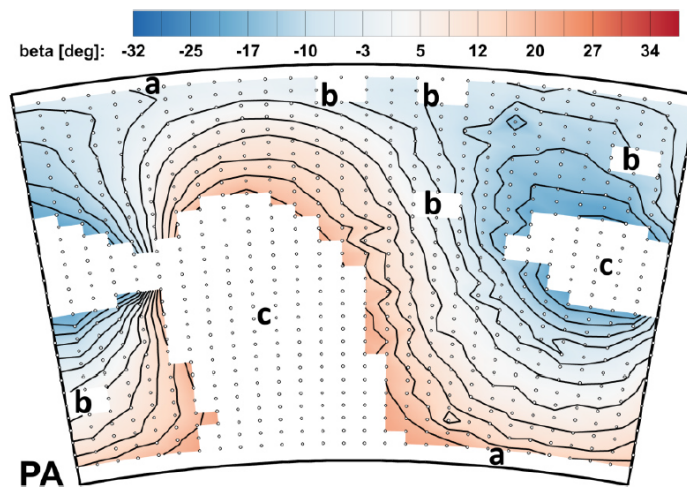


Figure 6.2 – 5HP results obtained for the pitch angle at P40. From Krumme *et al.* [62].

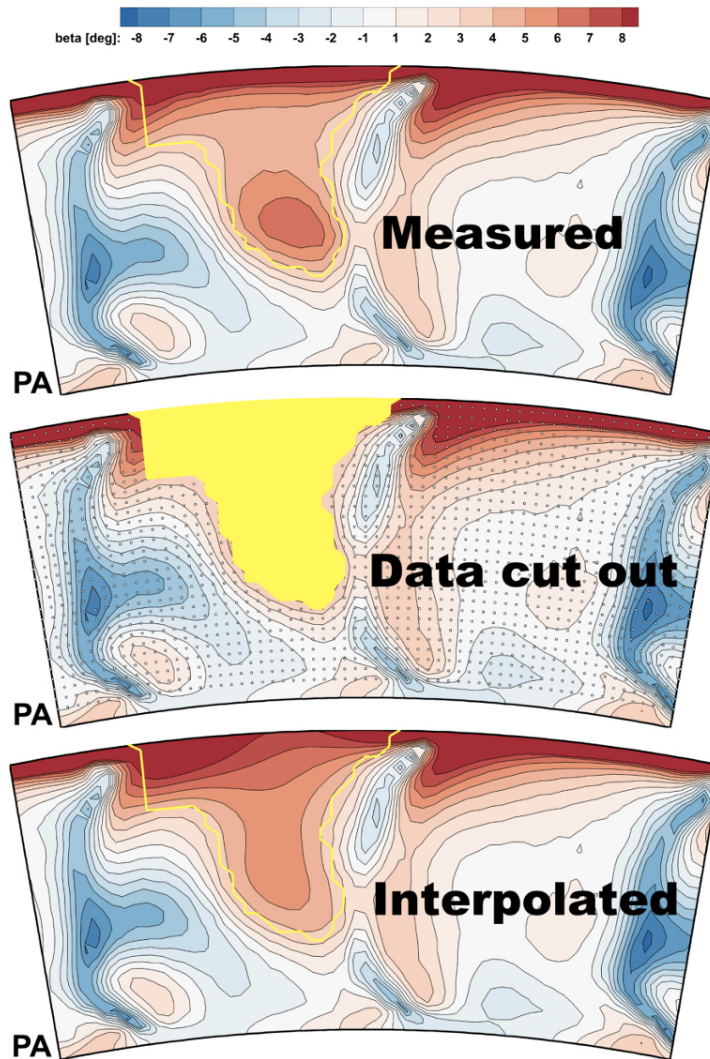


Figure 6.3 – Interpolation validation at P41. From Krumme *et al.* [62].

6.2.2 Differences at P40 between the experiments and the LES

Given the measurement difficulties at P40 during the experimental campaign, it is proposed here to compare total pressure, total temperature and flow angles fields of the experiments with the fields from the integrated combustion chamber/turbine simulation performed by Martin [73] and detailed hereafter in 6.3.1. Results are depicted from Figure 6.4 to Figure 6.7. Fields are not dimensionless. All the quantities studied vary between the experiments and the LES: in the LES, total temperature is lower close to the hub, which may result in an effect of the effusion cooling from the combustion chamber that is captured differently (Figure 6.4). Temperature is also higher in the upper part of the vein. The position and intensity of the HS is also different: it is predicted at a higher position using the LES as evidenced by the plots of total temperature and swirl angle (Figure 6.5). The pitch angle is also quite different, with higher positive values for the LES and smaller negative values for the experiments (Figure 6.6). Finally, total pressure distribution differs in the core, where the total pressure deficit is less pronounced when using the LES map (Figure 6.7). All these differences may be due to a lack of precision during the experimental campaign at P40, which required therefore a lot of interpolation.

In the following two sections, the impact of errors of type 'a' and errors of type 'c' on the transport of temperature inside the HP turbine stage of FACTOR is addressed, which corresponds to the first two hypotheses aforementioned. The aim is to highlight the most predominant interpolation error(s). Note that in all the following (U)RANS simulations, cooling is considered (CV) but is not suitable with EARSM turbulence models in the current version of the *elsA* solver. These anisotropic turbulence models could therefore not be tested.

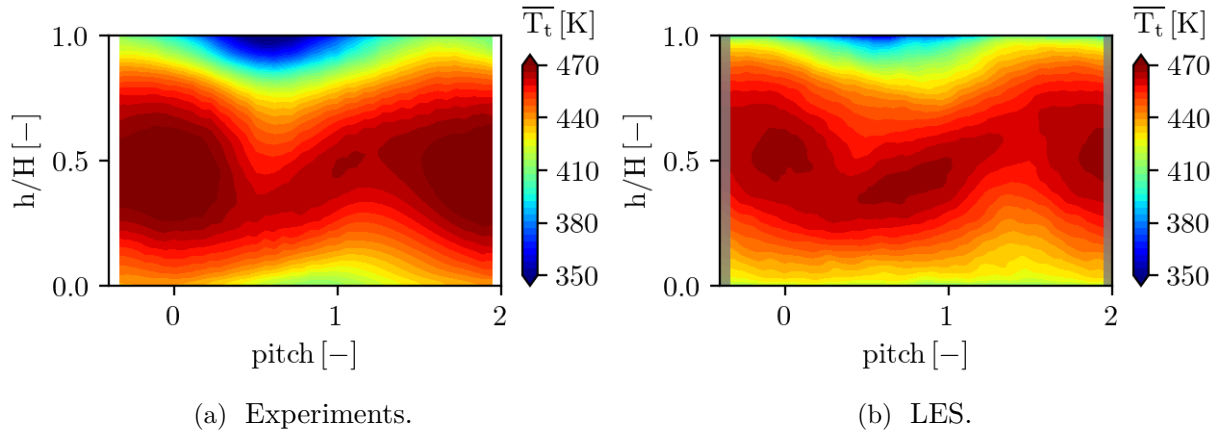


Figure 6.4 – \overline{T}_t field at P40 between the experiments and the LES.

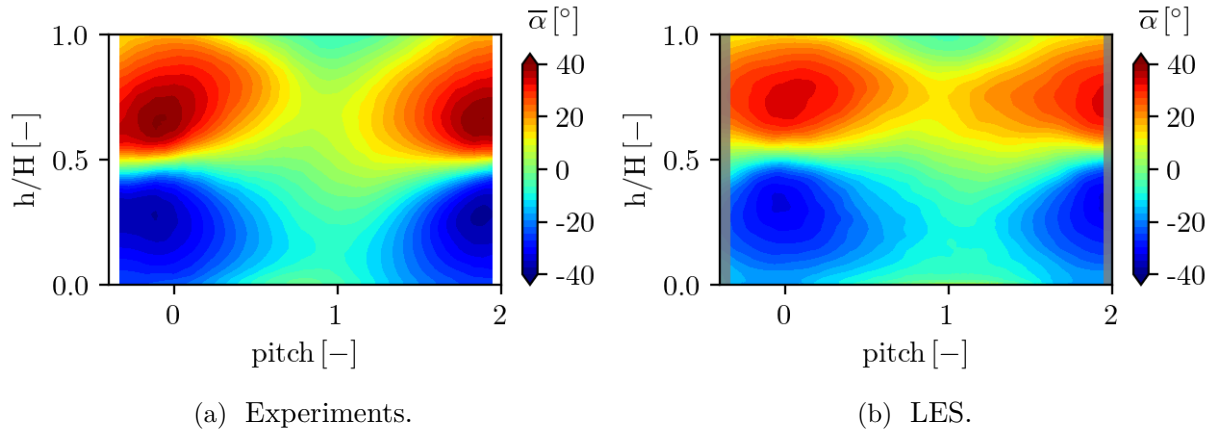


Figure 6.5 – $\overline{\alpha}$ field at P40 between the experiments and the LES.

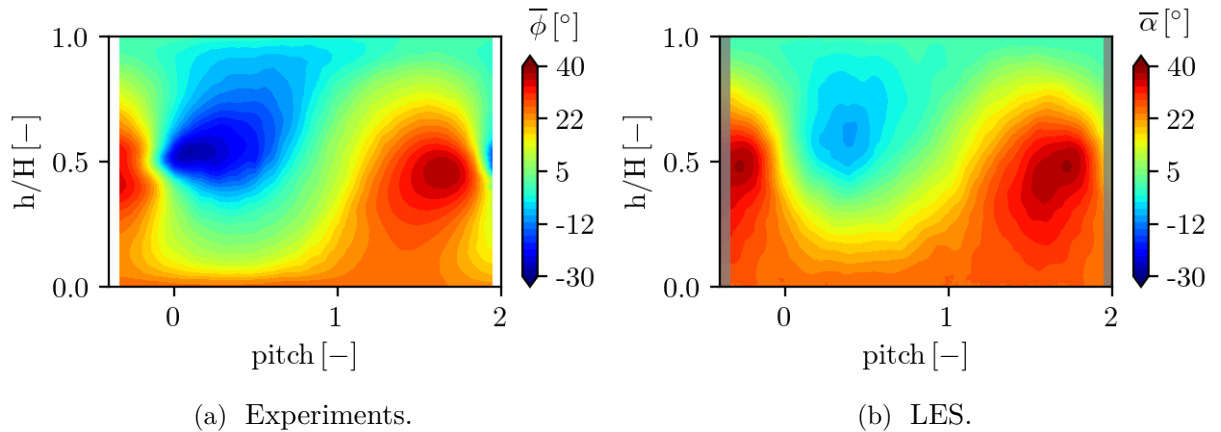


Figure 6.6 – $\overline{\phi}$ field at P40 between the experiments and the LES.

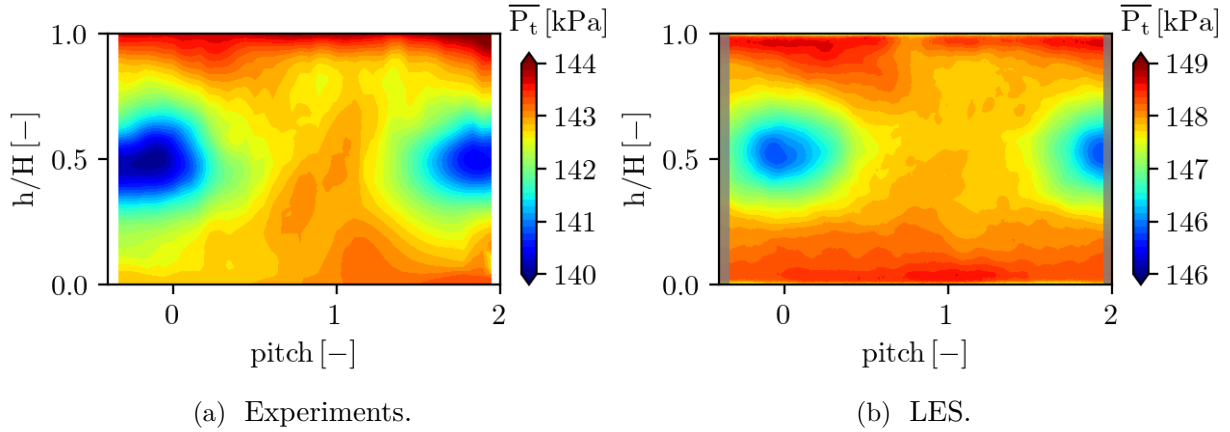


Figure 6.7 – \overline{P}_t field at P40 between the experiments and the LES.

6.3 Hypothesis 1: correction of type 'c' errors

First of all, since strong uncertainties are present in the core of the flow, the impact of the interpolation on errors of type 'c' is evaluated. The inlet boundary conditions imposed from the steady measurements are modified with data from a LES in order to find the origin of the differences with the experiments at P41 and P42 and thus establish the sensitivity to the inlet boundary conditions. This process of using LES data as inlet boundary conditions and comparing the result of the simulations to the experiments at P41 and P42 may seem paradoxical, but the measurements are much more reliable with fewer gradients of the flow variables that nearly all fall in the calibration range, as reported by Krumme *et al.* [62]. Before presenting a sensitivity study to the inlet flow variables, the LES database is presented.

6.3.1 LES database

From now on, the boundary condition at the inlet of the numerical domain for the RANS simulations is no more taken from the steady probing of FACTOR but from the LES performed by Martin [73, 74, 75]. The purpose of the work of Martin was to generate a realistic boundary condition at the inlet of the high-pressure turbine of FACTOR for an unsteady simulation of the isolated NGVs, and to compare the results with a simulation comprising both the combustion chamber and the NGVs. The realisation of the boundary condition is based on the Spectral Proper Orthogonal Decomposition (SPOD) algorithm at a given plane (represented in green in Figure 6.8), which enables to select certain modes and frequencies. By doing so, Martin could compare the reference coupled simulation to different simulations with both steady and unsteady boundary conditions at the inlet of the high-pressure turbine. This specific topic based on the SPOD is tackled in 6.5, for which an unsteady boundary condition is generated to check the influence of the unsteadiness (PVC). In the following, the reference coupled simulation is denoted '**LES A**'. The associated numerical domain is depicted in Figure 6.8. Martin also simulated the whole high-pressure turbine and the strut together with the combustion chamber (see Figure 6.9). This simulation is denoted '**LES B**'. Both simulations consider the hub stator vane and rotor blade fillets. Film cooling on the NGVs' surfaces is modelled using the heterogeneous injection model [11]. The cavity purge and the squealer tip of 0.5 mm for the rotor are considered in '**LES B**'. However, Martin used the cold tip clearance gap, which is 50% higher than the measured tip clearance used in all our simulations. This may lead to an overestimation of the secondary

flows. The time-averaged solutions of 'LES A' and 'LES B' are used for comparison purposes. More details on the set-ups can be found in the PhD thesis of Martin [73].

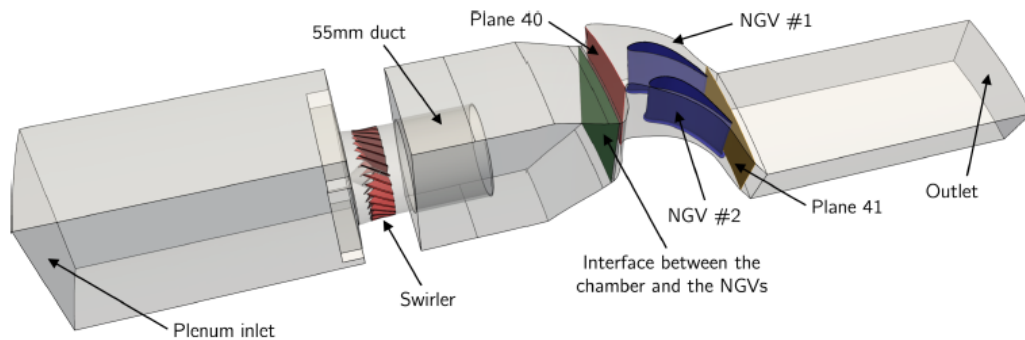


Figure 6.8 – Numerical domain of 'LES A'. Courtesy of Martin [73].

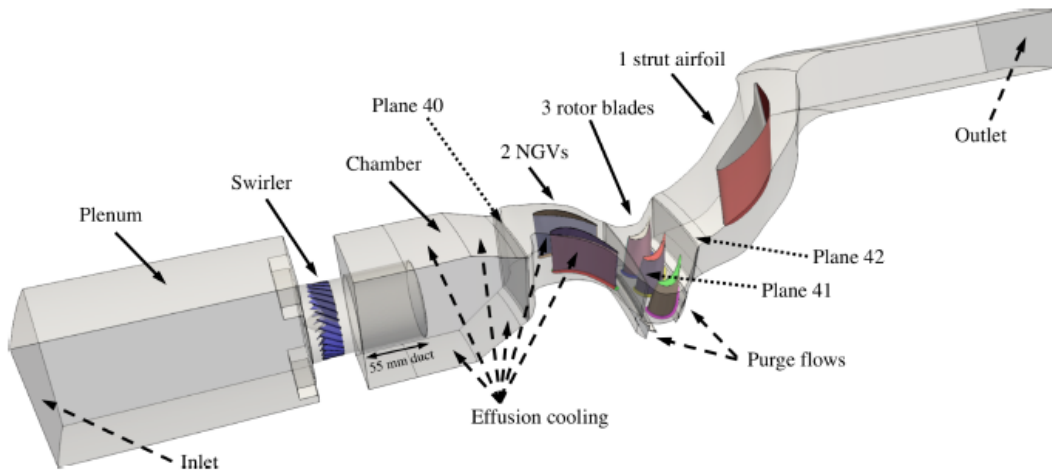


Figure 6.9 – Numerical domain of 'LES B'. Courtesy of Martin [73].

Table 6.1 highlights the main geometrical differences between the LES of Martin and the simulations performed during this PhD thesis.

Item	Wingel	LES A	LES B
Combustion chamber	✗	✓	✓
NGVs	✓	✓	✓
Rotor blades	✓	✗	✓
Strut	✗	✗	✓
Fillets	✗	✓	✓
Squealer tip	✗	✓	✓
Tip gap	✓	✓ (50% too high)	✓ (50% too high)

Table 6.1 – Geometrical differences between the simulations of this PhD thesis and the simulations of Martin.

6.3.2 Sensitivity to the inlet flow variables: test cases matrix

To study the impact of the differences in the core of the flow presented in 6.2.2 on the results at P41 and P42, a parametric study of all the possible combinations between the required quantities for the inlet boundary condition *i.e.* P_t, T_t, α, ϕ , is performed. The test cases matrix is composed of 2^n possible combinations, where n is the number of variables ($n = 4$). In Table 6.2, '0' refers to the quantity from the experiments and '1' to the quantity from 'LES A'. Thus, all quantities are taken either from the experiments or the LES at P40, which is the inlet of the numerical domain for the present study.

Case	P_t	T_t	α	ϕ
A	1	1	1	1
B	0	0	1	0
C	0	0	1	1
D	0	0	0	1
E	1	0	0	0
F	1	0	1	0
G	1	0	1	1
H	1	0	0	1
I	1	1	0	0
J	1	1	1	0
K	1	1	0	1
L	0	1	0	0
M	0	1	1	0
N	0	1	1	1
O	0	1	0	1
P	0	0	0	0

Table 6.2 – Test cases matrix for the impact of the inlet boundary condition at P40.

All the cases presented in Table 6.2 have been simulated with steady mixing-plane CV simulations. Only a few of them are necessary to classify the aerodynamic quantities by order of importance. These cases are highlighted in grey in Table 6.2. Note that this choice is not the unique one. The influence being limited on the radial distributions of $\bar{\alpha}$, $\bar{\phi}$ and \bar{P}_t , it is proposed to plot only $\bar{\alpha}$ together with \bar{T}_t . The Smith $k-l$ turbulence model is still considered. The conclusions of the study are presented below. The reader can find the corresponding radial distributions in Appendix B (section B.7).

As previously suspected, in the specific case of FACTOR, turbulence modelling is not the predominant mechanism that impacts the dynamics of the flow in the high-pressure turbine. Thanks to the use of data from a LES, this parametric study clearly revealed the sensitivity of the total temperature inlet map, *i.e.* only imposing temperature from the LES and keeping the other variables from the experiments, on the transport of temperature inside the high-pressure turbine. The combination of high flow angles at the inlet together with the presence of temperature distortion led to too important not measured zones that must have been filled with an interpolation (errors of type 'c'). Total temperature seems to be very sensitive to this interpolation. Then, in decreasing order, pitch angle, swirl angle and total pressure play to a lesser extent.

6.4 Hypothesis 2: investigation of type 'a' errors

In this section, the impact of the presence of the hub and shroud boundary layers at the inlet boundary condition on the transport of temperature is evaluated. As a reminder, the extrapolation process for type 'a' errors does not allow to recover a boundary layer profile. The notion of boundary layer was introduced by Prandtl in 1904 [93] and allows to characterise the near-wall region where viscous effects are preponderant. Outside the boundary layer, these effects can be considered negligible. The velocity gradually switches from 0 at the wall towards the freestream velocity outside the velocity boundary layer. In the same way as the dynamic boundary layer, a thermal boundary layer is also defined, where the temperature changes from T_0 at the wall to the freestream temperature. The boundary layer is the seat of important shear stresses and the consequences of neglecting it in the case of FACTOR's configuration could not be neutral for the dynamics of the flow.

6.4.1 Modification of the geometry

When comparing coupled and isolated simulations using the SPOD decomposition, Martin did not use P40 as inlet plane for the isolated simulations, but a plane which is placed $0.38 \cdot C a_{x,S}$ upstream P40 (green plane in Figure 6.8). In order to be consistent with this work, it was necessary to change the position of the inlet in the numerical simulations. From now on, the new inlet plane is identical to the green plane of Figure 6.8, and the domain has been extended upstream following the converging shape of the hub and shroud lines, leading to the red plane depicted in Figure 6.10a. This plane is referred to as P40*. Despite having the same azimuthal extension (18°), its azimuthal position differs from the LES, which is visible in Figure 6.10b. A consequence is that the conversion from the LES inlet map to the RANS inlet map requires a duplication of the green plane over a sector covering at least the numerical domain, before being able to interpolate the fields on the red plane of Figure 6.10.

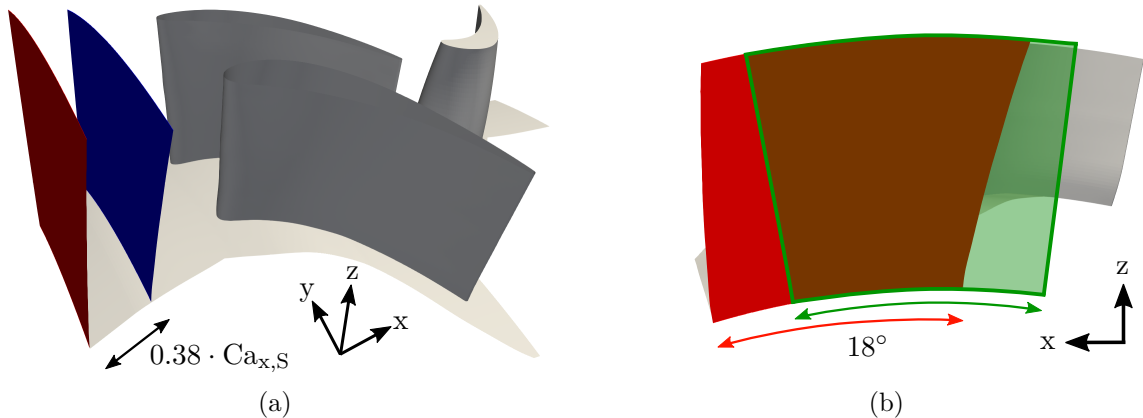


Figure 6.10 – Impact of the modification of the geometry on the position of the inlet plane (a) and difference of azimuthal position between LES inlet and RANS inlet (b).

6.4.2 Boundary layer thickness

Theoretically, the velocity (thermal) boundary layer thickness δ (δ_t) is defined as the distance from the wall for which the velocity (temperature) reaches 99% of the freestream velocity

(temperature). Its value depends on the Reynolds (Prandtl or Reynolds) number and the laminar or turbulent nature of the flow. For laminar flows over a flat plate, $\delta_t = \delta Pr^{-1/3}$, which means that the thermal boundary layer is thicker than the velocity boundary layer if $Pr < 1$, which is the case in the present configuration. For turbulent flows, the thermal boundary layer thickness depends on the Reynolds number and is approximately equal to the velocity boundary layer thickness $\delta_t \approx \delta$. To evaluate the thickness of the boundary layer, 'LES A' is used. The hub and shroud axial velocity profiles at the green (P40*) plane of Figure 6.8 are plotted at different azimuthal positions over two NGVs' pitches. Results are shown in Figure 6.11.

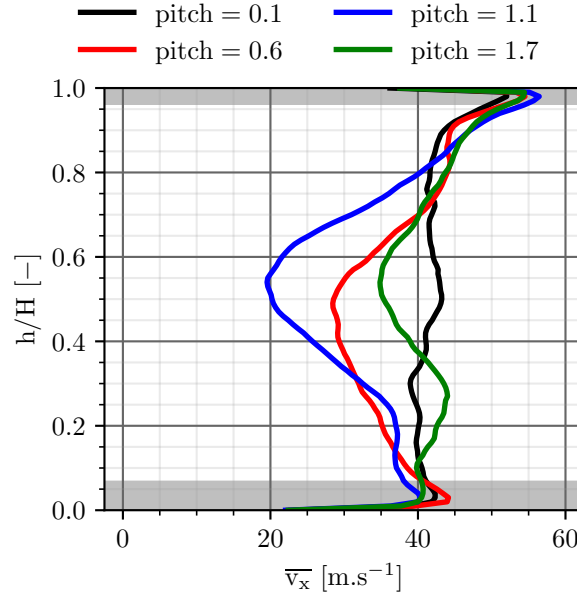


Figure 6.11 – Axial velocity profiles at P40* for different pitch positions.

A velocity boundary layer profile is clearly observable. This velocity profile is mainly comprised within the grey zones, which correspond to errors of type 'a' that have been corrected by extrapolation. A thermal boundary layer can not be plotted, as the LES solver uses a simple log law for the velocity only. To quantify the boundary layer thickness, it is however not possible to estimate it using 99% of the freestream velocity, because of the non-uniform fields coming from the combustion chamber. As a first approximation, the first inflection point is considered for the boundary layer thickness. The velocity boundary layer thickness is depicted in Figure 6.12. It shows a relative boundary layer thickness between 1% and 5% of vein height (between 0.7 mm and 3.5 mm). Moreover, the thickness falls within the range that is not measured in the experiments. As a consequence, all the boundary layer is missed since the extrapolation can not cope with a boundary layer closure close to the walls. The steady map from the experiments which is imposed in the simulations is not representative close to the walls. Such differences may have an impact on the dynamics of the flow that must be quantified.

6.4.3 Impact of the modification of the map close the hub and shroud

The presence of the boundary layer is now evaluated. The LES domain from P40* is considered. The steady map from 'LES A' is modified in such a way that the percentage corresponding to the grey zones, *i.e.* not measured zones leading to errors of type 'a', is removed. Missing data $\bar{\alpha}$, $\bar{\phi}$, \bar{P}_t and \bar{T}_t are then extrapolated on a new grid with size 100x100 using the inverse distance

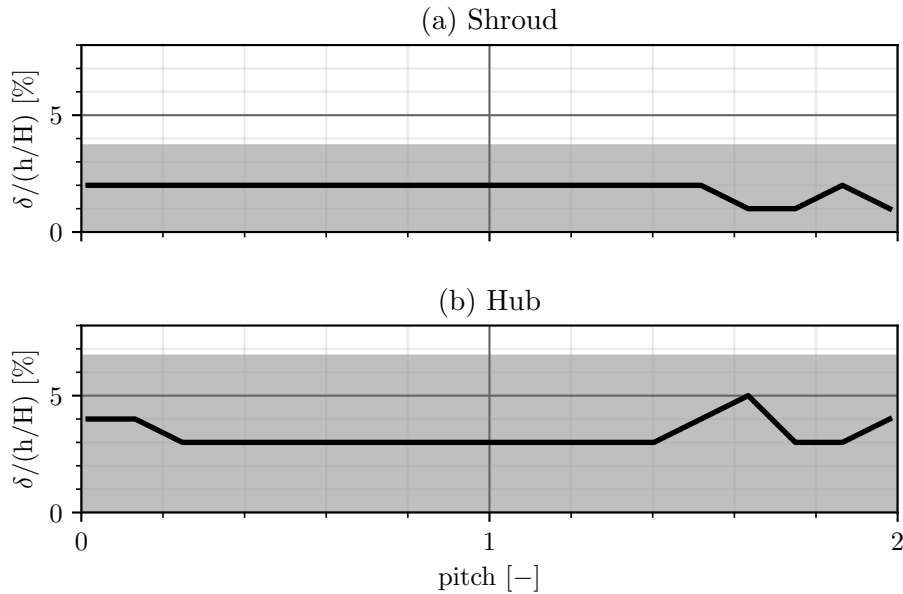


Figure 6.12 – Velocity boundary layer thickness at the shroud (a) and hub (b) of P40* (—) expressed at a percentage of vein height.

weighting with a power parameter of 3.5 [105]. First of all, the result of the inverse distance weighting is depicted in Figure 6.13 for total temperature and in Figure 6.14 for swirl angle. Iso-contours at $h/H = 0.067$ and $h/H = 0.963$, corresponding to the limits of errors of type 'a', are also displayed. These plots confirm the modification of the shape of the fields close to the hub and shroud, while the fields in the core of the flow are kept unchanged. Results of the simulations are shown in Figure 6.15 where the baseline inlet map with the velocity boundary layer in solid blue line is compared to the removed velocity boundary layer completed by inverse distance weighting in solid red line. Since the inlet position is shifted upstream, P40 is also added for comparison purposes. For the swirl angle and total pressure distributions (Figure 6.15a and Figure 6.15b), the differences are limited to the grey zones at P40, before vanishing at P41 and P42. Discrepancies are more pronounced for total temperature in Figure 6.15c and propagate outside the grey zones, meaning that the dynamics of the HS is influenced by all the radial evolution of the quantities. Temperature is more important close to the endwalls with the inverse distance weighting, as the cold flow of the effusion cooling in the combustion chamber is not correctly reproduced. However, despite these discrepancies, the global evolution of total temperature inside the HP turbine is affected to a lesser degree.

The impact of errors of type 'a' has been checked by removing part of the fields that were not measured with the 5HP, which includes the boundary layer. Missing data have been extrapolated with inverse distance weighting. Results of the simulations revealed a minor impact of the presence of the boundary layer on the dynamics of the mean flow, meaning that errors of type 'a' are negligible for the total temperature transport with respect to errors of type 'c' that have been tackled earlier.

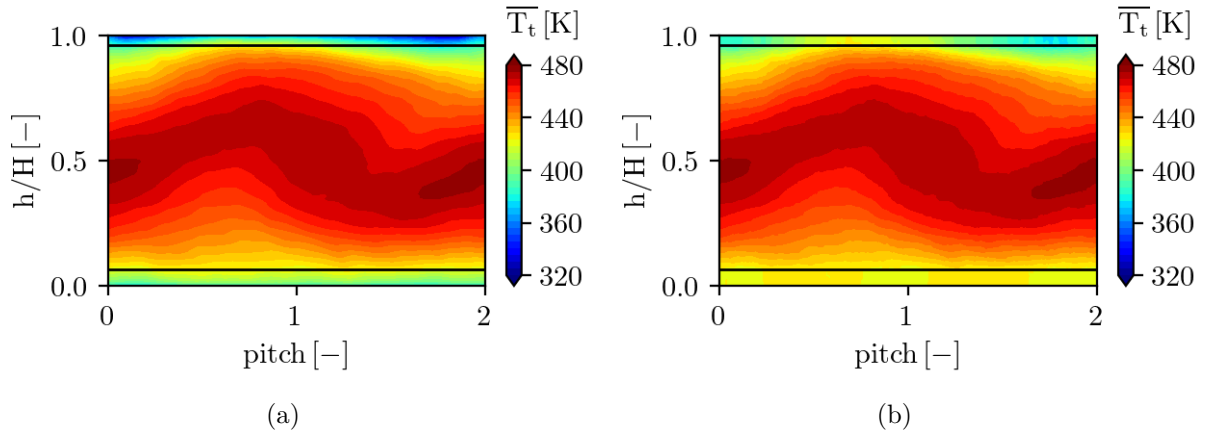


Figure 6.13 – \overline{T}_t field at P40* for the steady LES map (a) and the map obtained with inverse distance weighting (b).

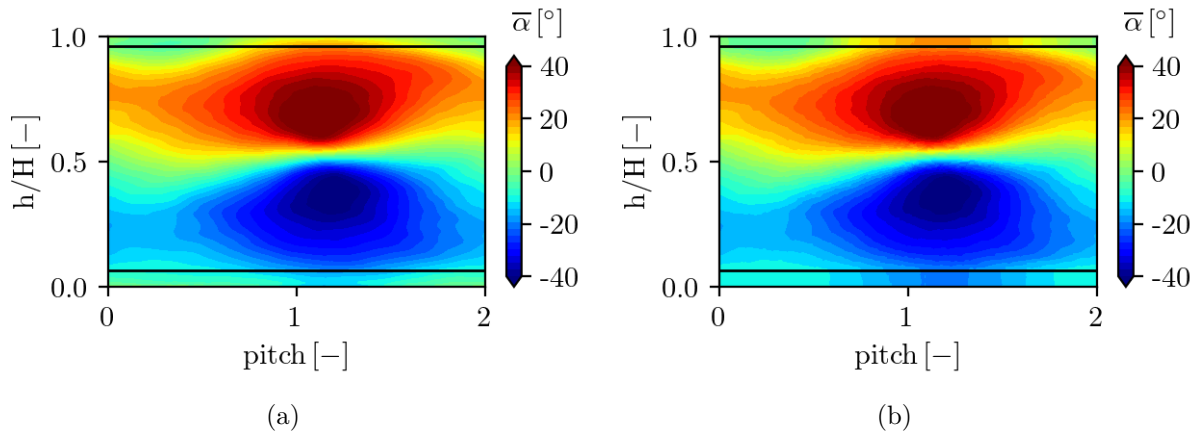


Figure 6.14 – $\overline{\alpha}$ field at P40* for the steady LES map (a) and the map obtained with inverse distance weighting (b).

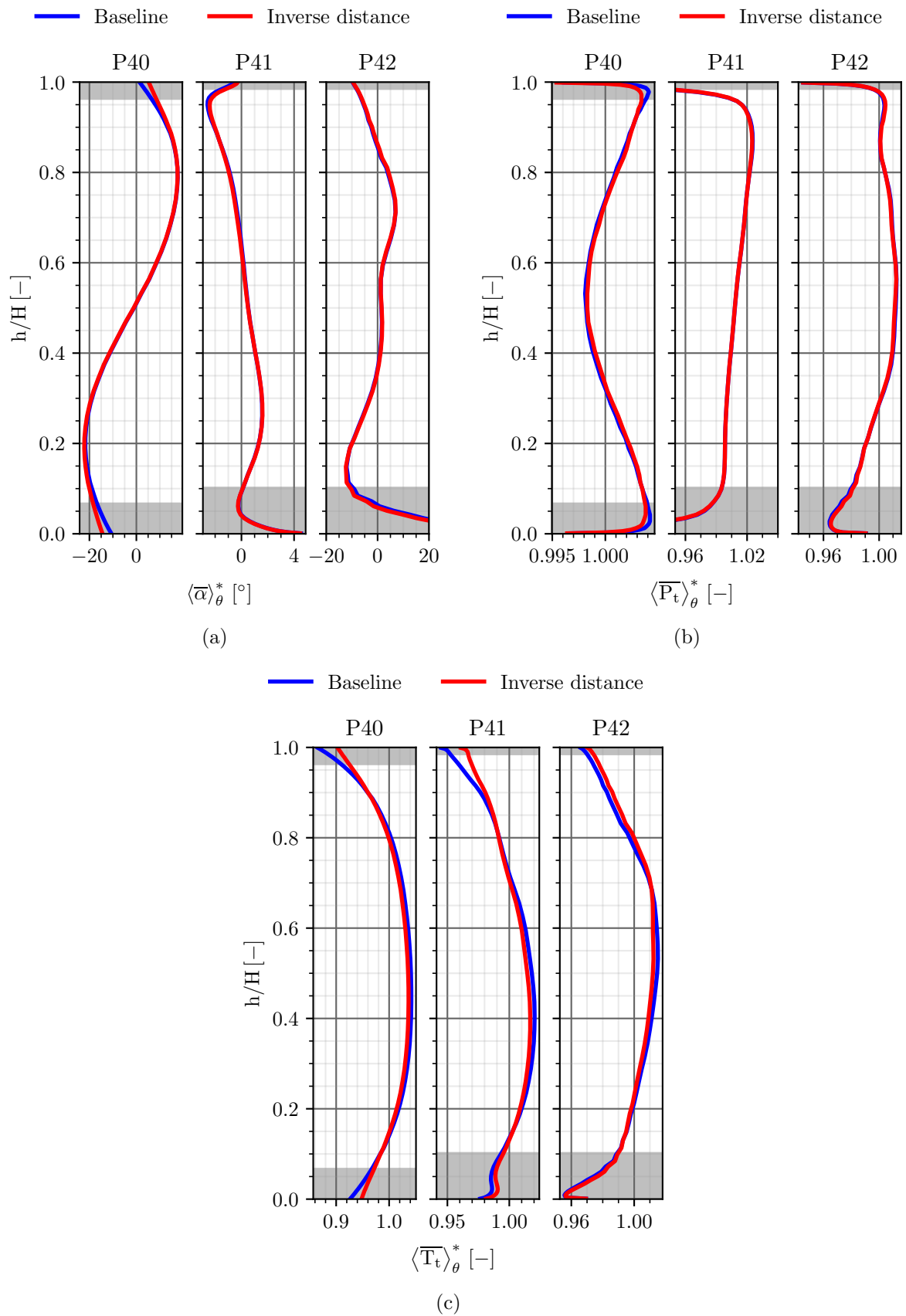


Figure 6.15 – Radial distributions of $\bar{\alpha}$ (a), \bar{P}_t (b) and \bar{T}_t (c) with and without velocity boundary layer.

6.5 Hypothesis 3: generation of an unsteady boundary condition

The final hypothesis deals with the impact of an instability, the so-called Precessing Vortex Core (PVC) coming from the combustion chamber, that is not considered when applying a steady boundary condition at the inlet of the domain. The work of Martin [73], based on the generation of an unsteady boundary condition for a LES with the use of the Spectral Proper Orthogonal Decomposition method, is largely employed in the present study, for which an equivalent approach to feed URANS is conducted. Martin showed that a fraction of the spectral content containing the PVC was sufficient to satisfactorily reproduce the flow dynamics in the turbine. The present study aims to isolate the flow associated with the PVC and convert it to an unsteady boundary condition. First of all, a reminder of the features of the PVC is performed. Then, the SPOD method is detailed. Finally, the results of the impact of the unsteady boundary condition are presented.

6.5.1 Emergence and signature of the PVC

In some combustor technologies, such as low NO_x combustion chambers, the outlet flow is characterised by hydrodynamic instabilities. The European project FACTOR, thanks to its experimental and numerical database, made it possible to analyse the plane at the combustor/turbine interface. In their experimental and numerical PhD theses, Bacci [4] and Koupper [60] revealed the presence of a vortex inside the combustion chamber with a low characteristic frequency. The rotation movement created by the swirlers plays a major role in a combustion chamber as it stabilises the flame while minimizing pressure losses: downstream the swirler is created a recirculation zone. Under certain conditions, the recirculation zone can oscillate in a hydrodynamic instability: the PVC. Because of this rotation movement, turbulence, swirl and distortion levels at the turbine inlet are quite important and the combustion chamber/turbine interface plane takes an unsteady form, which is further reinforced by the presence of effusion cooling. As a consequence, the prescription of the inlet boundary condition for an isolated turbine simulation with flow unsteadiness must be as accurate as possible.

Numerous studies on the PVC from the combustion point of view have been conducted (see the thorough review of Syred [114]). If its trace is not clear and systematic at P40 in reactive cases (dependence on the kind of fuel, the equivalence ratio and the confinement level), it is present in most non-reactive cases for swirl numbers around 0.6-0.7 and Strouhal numbers of about 0.5-0.6¹, which is the case for FACTOR's configuration [60]. Its frequency strongly depends on the operating point and few on the design of the swirler or the combustion chamber. Its value remains in low frequencies: about 500 Hz for the FACTOR configuration. It is up to the designers of combustion chambers to specify the frequency of the PVC to the turbine designers. An overview of the PVC on FACTOR's configuration is visible in Figure 6.16.

6.5.2 Spectral Proper Orthogonal Decomposition method

Like Proper Orthogonal Decomposition (POD) [68, 108] or Dynamic Mode Decomposition (DMD) [101], Spectral Proper Orthogonal Decomposition (SPOD) is a mode decomposition method that is used in complex flows to extract the spatial and temporal flow structures (*i.e.* the modes) from a large statistically stationary dataset. The mathematical basis of the method using

¹ $St = \frac{fD_{sw}}{v_{\theta sw}}$ where $v_{\theta sw}$ is the tangential velocity at the exit of the swirler.

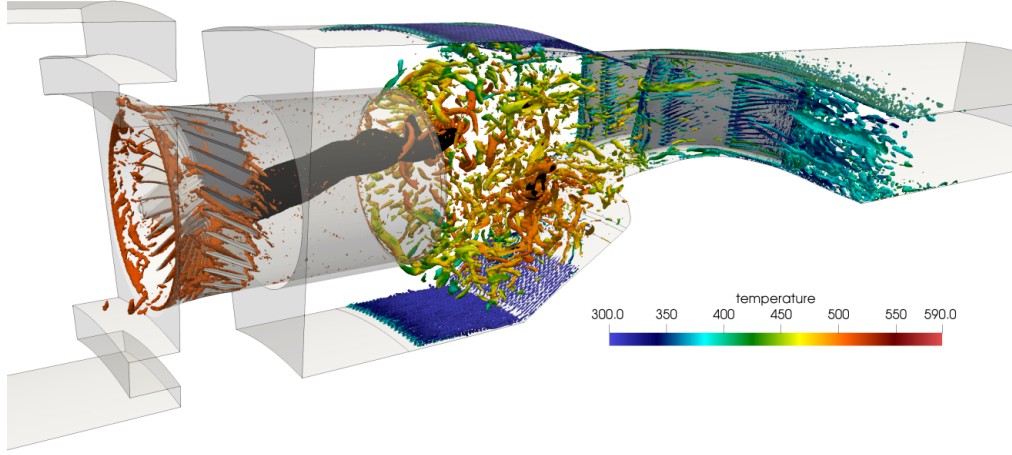


Figure 6.16 – Representation of the PVC with an iso-contour of low pressure in black. Turbulent structures are visible with an iso-contour of Q-criterion coloured by static temperature. Courtesy of Martin [73].

the Welch formulation has been introduced by Schmidt *et al.* [102] and Towne *et al.* [124]. It can be employed either for modes classification or data reduction. SPOD enables the identification of modes that vary both in space and time and are orthogonal under a space-time inner product, which makes its strength when dealing with multi-time scales complex turbulent flows. The algorithm finds a set of orthogonal modes that optimally captures the energy in the data, with each mode oscillating at one frequency at a time and being ranked by its modal energy. It thus combines the advantage of POD and DMD, respectively energy-ranked and frequency-resolved properties of the decompositions. The method is widely explained in [102, 124]. A global overview of the method is given in Figure 6.17, with the steps being described hereafter:

- Let us consider a data matrix:

$$\mathbf{Q} = [\mathbf{q}_1, \mathbf{q}_2, \dots, \mathbf{q}_{N_s-1}, \mathbf{q}_{N_s}] \in \mathbb{R}^{N \times N_s} \quad (6.1)$$

Which is a chronological collection of N_s equally spaced snapshots $\mathbf{q}_k \in \mathbb{R}^N$ at time t_k during a time t_s . The column vector \mathbf{q}_k represents any instantaneous zero-mean data of length $N = N_v \times N_p$ where N_v is the number of flow variables and N_p is the number of grid points;

- The matrix \mathbf{Q} is divided into N_b blocks, and each block can be regarded as a member of an ensemble realisation of the flow which contains N_f snapshots during t_f . The n_{th} block reads:

$$\mathbf{Q}^{(n)} = [\mathbf{q}_1^{(n)}, \mathbf{q}_2^{(n)}, \dots, \mathbf{q}_{N_f-1}^{(n)}, \mathbf{q}_{N_f}^{(n)}] \in \mathbb{R}^{N \times N_f} \quad (6.2)$$

The blocks are overlapping on N_o snapshots, so that the number of blocks is determined by $N_b = \lfloor (N_s - N_o) / (N_f - N_o) \rfloor$ where $\lfloor \cdot \rfloor$ is the floor operator. The Discrete Fourier Transform (DFT) is performed on each block to switch to the frequency domain. To reduce spectral leakage, a Hann window is used to limit the discontinuities with a hypothetical next period. The resulting matrix for the n_{th} block yields:

$$\hat{\mathbf{Q}}^{(n)} = [\hat{\mathbf{q}}_1^{(n)}, \hat{\mathbf{q}}_2^{(n)}, \dots, \hat{\mathbf{q}}_{N_f-1}^{(n)}, \hat{\mathbf{q}}_{N_f}^{(n)}] \in \mathbb{C}^{N \times N_f} \quad (6.3)$$

- New data matrices $\hat{\mathbf{Q}}'_{f_k} \in \mathbb{C}^{N \times N_b}$ are defined to collect all the Fourier realisations of the different blocks at the frequency f_k :

$$\hat{\mathbf{Q}}'_{f_k} = \sqrt{\kappa} \left[\hat{\mathbf{q}}_k^{(1)}, \hat{\mathbf{q}}_k^{(2)}, \dots, \hat{\mathbf{q}}_k^{(N_b-1)}, \hat{\mathbf{q}}_k^{(N_b)} \right] \quad (6.4)$$

Where κ accounts for the windowing function. The weighed cross-spectral density (CSD) tensor at frequency f_k is thus written:

$$\mathbf{R}_{f_k} = \hat{\mathbf{Q}}'_{f_k} \hat{\mathbf{Q}}'^*_{f_k} \in \mathbb{C}^{N \times N} \quad (6.5)$$

Where \cdot^* is the Hermitian transpose;

- The POD based on the singular value decomposition (SVD) is finally performed on the CSD matrix at each frequency f_k :

$$\mathbf{R}_{f_k} \mathbf{W} \Psi_{f_k} = \Psi_{f_k} \Lambda_{f_k} \quad (6.6)$$

With \mathbf{W} the weight matrix (*i.e.* the type of inner product) that depends on the studied data. The decomposition leads to the SPOD modes (eigenvectors) $\Psi_{f_k} \in \mathbb{C}^{N \times N_b}$ that are classified in descending order according to their modal energy (eigenvalues) $\Lambda_{f_k} \in \mathbb{R}^{N_b \times N_b}$.

In practice, the number of blocks N_b is much smaller than the problem size N and the method of snapshots is used, solving a $N_b \times N_b$ eigenvalue problem instead of a $N \times N$ one [108]. As already mentioned, SPOD is used to extract the spatial and temporal flow structures from a large dataset. It can also be used for data compression, or partial reconstruction of the initial database by selecting the desired modes and frequencies. For instance, Martin *et al.* [74] showed that the storage cost of the reconstruction relative to the initial database was only 6.5% for a reconstruction accounting for 99% of the total energy of the original signal. In the following, partial reconstruction is used for the generation of an unsteady boundary condition suitable for the URANS approach that accounts only for the mode and frequency associated with the PVC. Partial reconstruction requires the use of inverse POD and inverse DFT. More details on the method for partial reconstruction of the initial database can be found in the PhD thesis of Martin [73].

6.5.3 Application on FACTOR's configuration

SPOD analysis

In the work of Martin *et al.* [74], the authors used P40* depicted in green in Figure 6.8 for the collection of the snapshots. The flow variables ρ , v_x , v_y , v_z and T_s are considered for the SPOD. The inner product, *i.e.* the weight matrix \mathbf{W} , is based on the total compressible energy norm. The number of snapshots is $N_s = 20000$ ($t_s = 0.1$ s), divided into 7 blocks, so that $N_f = 3200$ and $N_o = 400$. A Hamming window is used. The choice of the parameters of the SPOD is a trade-off between frequency resolution and modes convergence. The time-step of the simulation is $\Delta t_{LES} = 5 \cdot 10^{-8}$ s, and the snapshots are extracted every 100 iterations, *i.e.* $\Delta t_s = 5 \cdot 10^{-6}$ s. The simulation is statistically converged. The main parameters for the SPOD are summed up in Table 6.3. Martin performed a deep analysis of the SPOD on FACTOR's configuration for the mode shapes and energies [73, 74, 75]. However, since this study is based on the reconstruction of the database at given modes and frequencies, the reader is referred to the aforementioned references for more details.

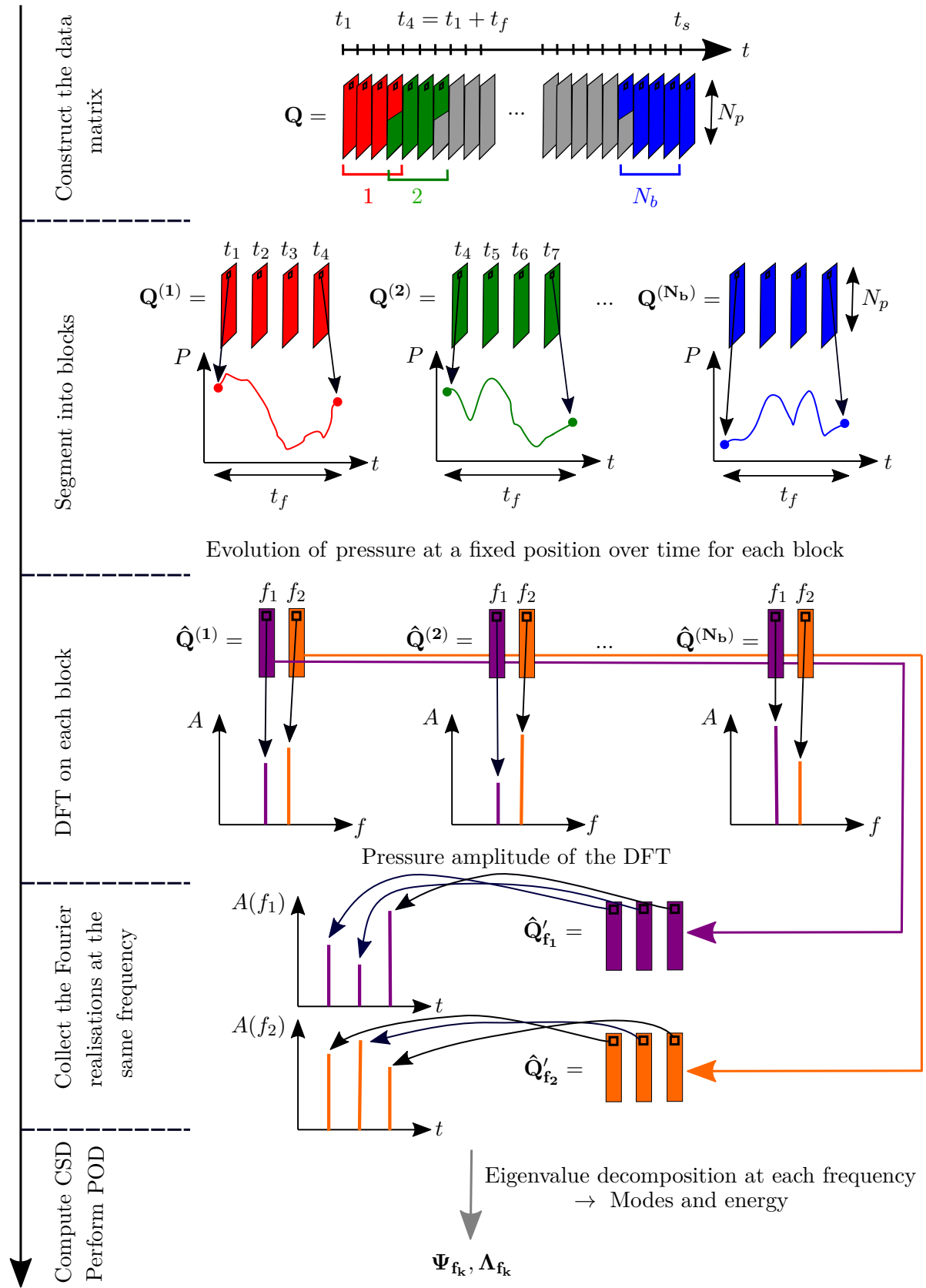
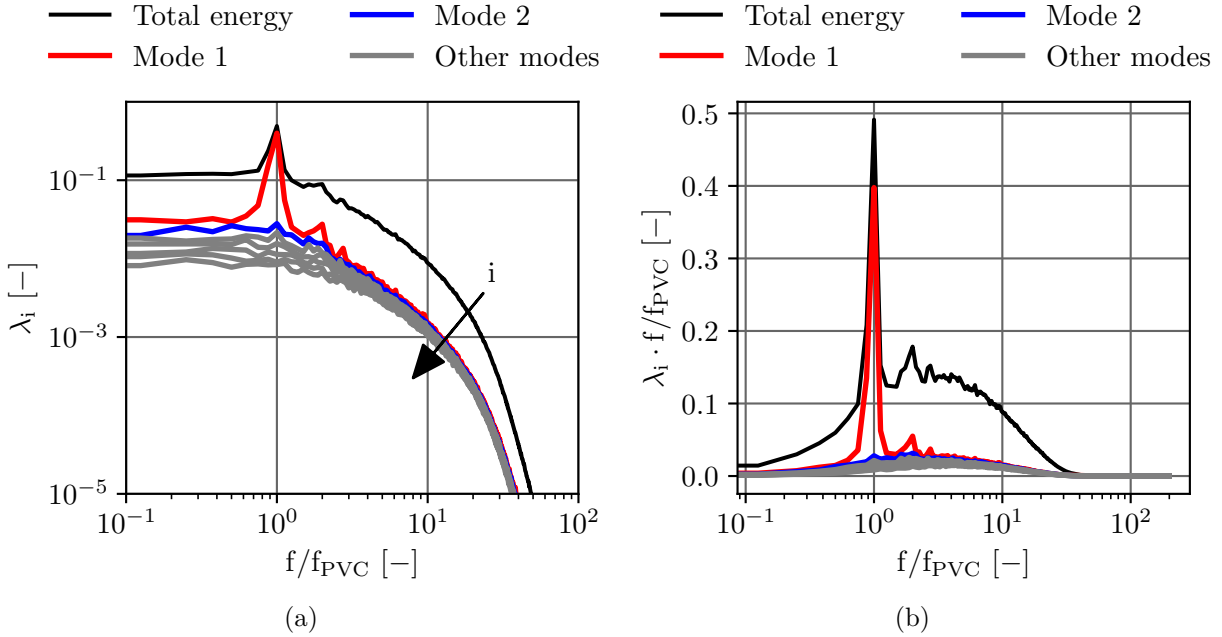


Figure 6.17 – Principle of the SPOD method. In this example, each snapshot is composed of $N_v = 1$ variable (P) of length N_p and each block contains $N_f = 4$ snapshots. The overlapping region is composed of $N_o = 1$ snapshot. The flow variable being real, half of the frequencies (positive) are kept ($N_f/2$). The phase is not illustrated but is an output of the treatment.

Database				SPOD			
Variable	N_v	N_p	N_s	N_b	N_f	N_o	Norm
ρ, v_x, v_y, v_z, T_s	5	59353	20000	7	3200	400	Total energy

Table 6.3 – Parameters of the database and of the SPOD analysis.

Based on the time-step of the snapshots and the Nyquist criterion, the maximum resolved frequency is $f_{max} = 100$ kHz and the frequency resolution is $\Delta f = 65.5$ Hz, leading to a total of 1601 frequencies. The SPOD modal energy spectrum at P40* is plotted in Figure 6.18a and represents the energy of the modes normalised by the total energy at a given frequency. The pre-multiplied energy spectrum is also represented in Figure 6.18b. The frequency axes are normalised by the frequency of the PVC $f_{PVC} = 500$ Hz. Black line corresponds to the total energy obtained by summing the energies of each mode for all the frequencies, while red line and blue line respectively account for mode 1 and mode 2. The plot of Figure 6.18a clearly evidences the dominance of mode 1 at the frequency of the PVC. Its first harmonic has also a contribution to the energy spectrum, but to a lower extent. Martin [73] showed in his PhD thesis that for the axial velocity, mode 1 at f_{PVC} had a two-arms shape with a $\pi/2$ phase shift, while mode 2 at $2 \cdot f_{PVC}$ had a four-arms shape. The pre-multiplied energy spectrum in Figure 6.18b represents the energy contained in each mode as the area under the curve of the mode. It illustrates the fact that the decomposition is low-rank, *i.e.* a dominant mechanism is present and can be characterised by the first mode. The contribution of the PVC is well-evidenced on a narrow frequency range. Most of the energy is contained within this low-frequency component of the flow, which may impact the dynamics of the flow in the high-pressure turbine. At f_{PVC} , mode 1 accounts for nearly 80% of the total energy at this frequency, and around 30% at $2 \cdot f_{PVC}$.


Figure 6.18 – SPOD mode energy spectrum (a) and pre-multiplied energy spectrum (b).

In order to estimate the contribution of each mode at each frequency, the cumulated mode energy fraction ι is defined. It represents the dimensionless cumulated amount of energy till the

k_{th} frequency and l_{th} mode and reads:

$$\iota = \frac{\sum_{f=1}^k \sum_{m=1}^l \lambda_m^{(f)}}{\sum_{f=1}^{\lfloor N_f/2 \rfloor + 1} \sum_{m=1}^{N_b} \lambda_m^{(f)}} \quad (6.7)$$

The spatial representation of the quantity ι is depicted in Figure 6.19a with a zoom close to the frequency of the PVC in Figure 6.19b. It confirms that at the frequency of the PVC, mode 1 accounts for most of the energy since the iso-10% is nearly vertical. This kind of plot is interesting in the context of a partial reconstruction of the database for the generation of an unsteady boundary condition as it reveals the number of modes and frequencies required for a given amount of energy. It shows that using only the dominant mode at the frequency of the PVC accounts for nearly 10% of the total energy of the initial database (the affirmation is true in the sense that the frequencies below f_{PVC} do not contribute in terms of energy, as evidenced with the plot of the premultiplied energy spectrum in Figure 6.18b). Moreover, the more you move to the top right part of Figure 6.19a, and the more total energy you get. This plot opens the discussion on partial reconstruction of the initial database to account for specific flow features.

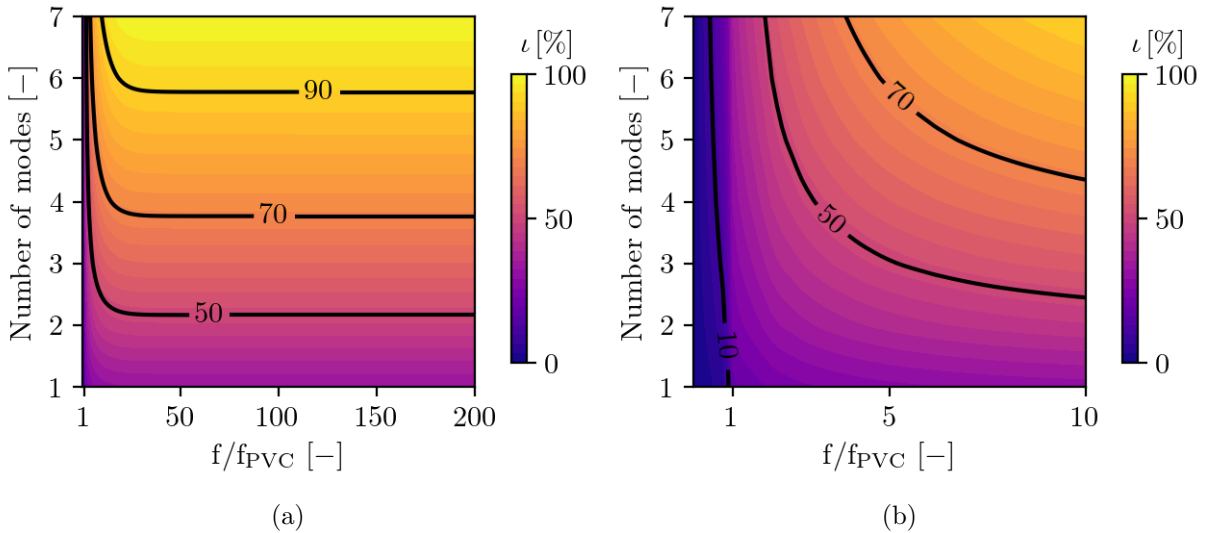


Figure 6.19 – Cumulated mode energy fraction of the SPOD (a) and zoom close to the frequency of the PVC (b).

Methodology for the partial reconstruction of the database for the generation of an unsteady boundary condition

To estimate the impact of an unsteady boundary condition in the URANS simulation of FACTOR's configuration, it is decided to perform the following reconstructions (see methodology in Martin [73]):

- **F10:** reconstruction using mode 1 at the frequency of the PVC f_{PVC} . The energy of the reconstruction contains 10% of the total energy of the initial database;
- **F20:** reconstruction using mode 1 with the frequencies around f_{PVC} and its first harmonic $2 \cdot f_{PVC}$. Overall, 10 frequencies are used and the energy of the reconstruction contains 20% of the total energy of the initial database.

This procedure has already been employed in the scope of the work of Martin. In the present work, the LES boundary condition must be converted into a URANS boundary condition, with a time-consuming procedure that requires both spatial and temporal interpolations, as well as the conversion from the SPOD variables to the quantities required for the boundary condition (P_t, T_t, α, ϕ) . Special attention is paid to the temporal interpolation: for the URANS, CV RSN simulations are performed with a time-step $\Delta t_{URANS} = 6.49 \cdot 10^{-7}$ s. Compared to the time-step of the LES and of the snapshots, one has $\Delta t_{URANS} = 7.7 \cdot \Delta t_{LES}$ and $\Delta t_{URANS} = 0.077 \Delta t_s$. This means that the temporal interpolation from the time-step of the snapshots towards the time-step of the URANS needs the creation of temporal information, which is simply done with a linear interpolation in the scope of this PhD thesis. To assess the precision of spatial and temporal interpolations, Figure 6.20 presents the temporal evolution of the surface-averaged total temperature on P40* after each step, where the characteristic time of the PVC $t_{PVC} = 1/f_{PVC}$ is used for the normalisation of the time axis. It shows that very few differences are induced by the spatial interpolation.

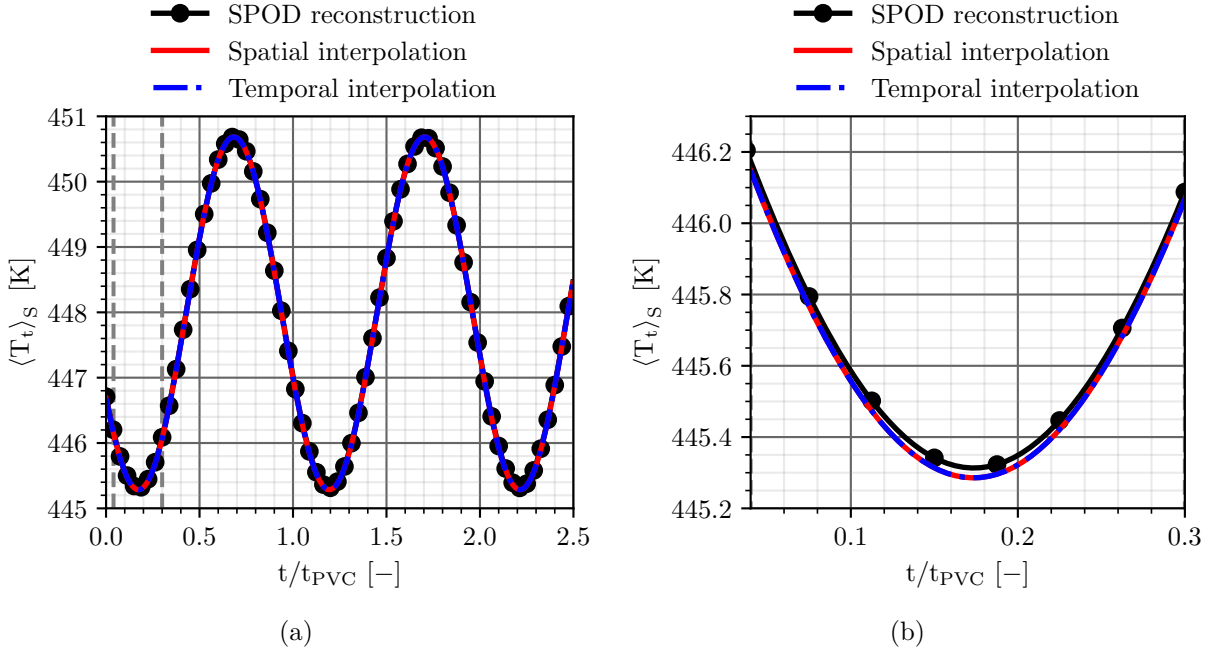


Figure 6.20 – Impact of the spatial and temporal interpolations on the time evolution of total temperature at P40* for the F10 reconstruction (a) and zoom on the part delimited by the vertical dashed gray lines (b).

The result of the temporal interpolation leads to 154000 snapshots ($\approx 50 \cdot t_{PVC}$), instead of the 20000 of the initial LES database. Then, for the imposition of the unsteady boundary condition, a code-coupling procedure with *elsA* written in Python has been developed, based on a CGNS tree approach which collects the snapshots in the form of arrays. The boundary condition is therefore modified at a given number of iterations defined by the user. In the scope of this PhD thesis, the boundary condition is modified at every iteration, *i.e.* every time-step². For case F10 only, to save memory, the boundary condition is periodised at the frequency of the PVC, reducing by 50 the number of snapshots. For case F20, a number of snapshots required for convergence and extraction of the snapshots is used (≈ 30000). F10 and F20 simulations

²A coupling has been tested every eight iterations. The simulation being only 8% quicker, it was decided to keep the coupling frequency at each iteration.

are performed based on the unsteady numerical set-up presented in Chapter 2 and turbulent quantities are taken from the LES ($\bar{k} = 328 \text{ m}^2 \cdot \text{s}^{-2}$ and $\bar{l}_T = 16 \text{ mm}$). The Smith $k-l$ turbulence model is used. Since a low-frequency phenomenon is injected, the convergence is evaluated by means of moving averages on windows equalled to the BPP and for which the periodic evolution due to the PVC is reached. The plots are depicted in Figure 6.21. It shows that after $6 \cdot t_{PVC}$, convergence is reached. Moreover, for the case F10 (Figure 6.21b), despite the moving average, the oscillation at the period of the PVC is clearly evidenced, both at the inlet of the stator and the outlet of the rotor.

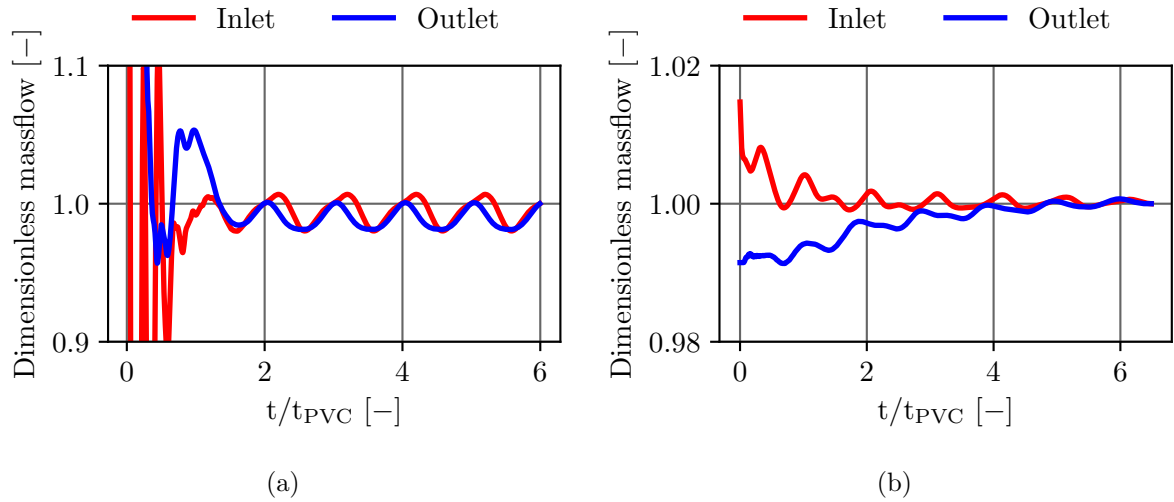


Figure 6.21 – Moving averages of inlet and outlet massflow for F10 (a) and F20 (b).

Finally, to confirm that the energetic selections imposed at the inlet of the numerical domain are consistent, FFT of instantaneous massflow at P40* for the simulations F10 (—) and F20 (—) are plotted and depicted in Figure 6.22. Both the selections F10 and F20 are well represented, with the peak at f_{PVC} for F10, and the first harmonic at $2 \cdot f_{PVC}$ for F20. More energy is contained in F20, which is in agreement with the observations of Martin [73].

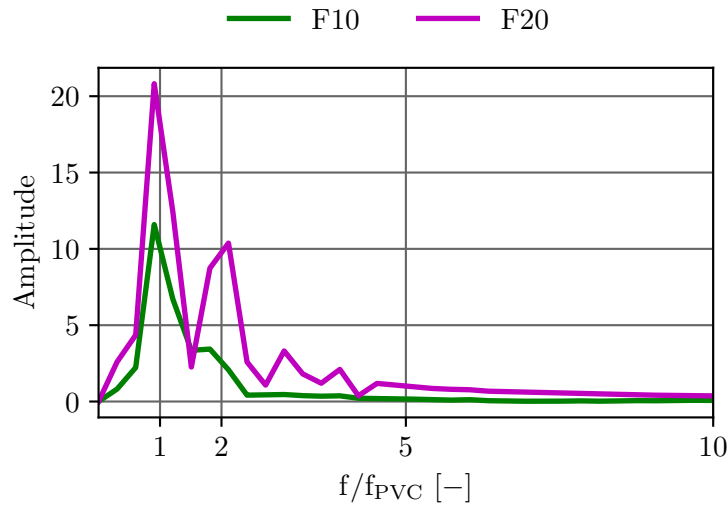


Figure 6.22 – FFT of instantaneous massflow at P40* for F10 and F20.

Results of case F10 and case F20

RSN CV simulations are performed and are preferred to chorochronic simulations since the latter restrict the frequencies at the BPF and its harmonics at the chorochronic boundaries. This approach is not suitable for a simulation with a low-frequency content that is not related to the BPF. For both F10 and F20 cases, the snapshots are extracted over a period of the PVC to perform the average. The snapshots are extracted every 5 iterations, *i.e.* at a frequency $f \approx 300$ kHz. A convergence has been performed on the radial distributions over multiples of the period of the PVC to confirm that one characteristic time of the PVC was sufficient. Since no differences are observed, this convergence is not represented. However, it is not possible to reduce the average to less than t_{PVC} , as classically done when studying vane/blade interactions where a period of the BPF or related to the periodicity of the simulation is retained to capture the flow physics. In the present case, the average over the characteristic time of the PVC covers 15.4 rotor blade passages, while the periodicity would lead to an average over only 3 rotor blade passages. The differences of such averages are depicted in Figure 6.23. It clearly shows that 15 BPP are necessary to converge properly the average, which is equivalent to an average over 5 periodic patterns. This is explained by the strong dependency of the evolution of total temperature over a period of the PVC. To assess this, the instantaneous evolution of total temperature in the wake of the rotor blade at mid-span of the vein is plotted in Figure 6.24. Coloured arrows in accordance with Figure 6.23 are also added. The normal averaging procedure based on 1 periodic pattern is clearly not suitable because of the strong variation of the dynamics involved by the presence of the PVC at the inlet of the domain. From now on, the averages are performed over a period of the PVC.

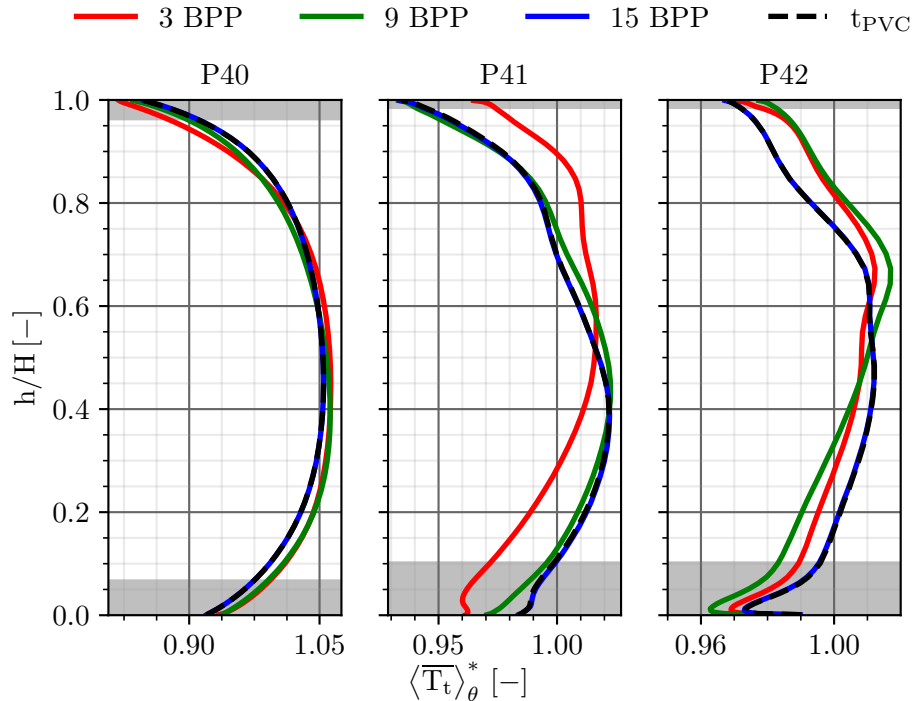


Figure 6.23 – Convergence of \overline{T}_t distributions over t_{PVC} .

Swirl angle, total pressure and total temperature radial distributions at P40, P41 and P42 are respectively plotted in Figure 6.25, Figure 6.26 and Figure 6.27. For the sake of clarity, F10 (—) and F20 (—) are represented on two different graphs for each quantity. They are

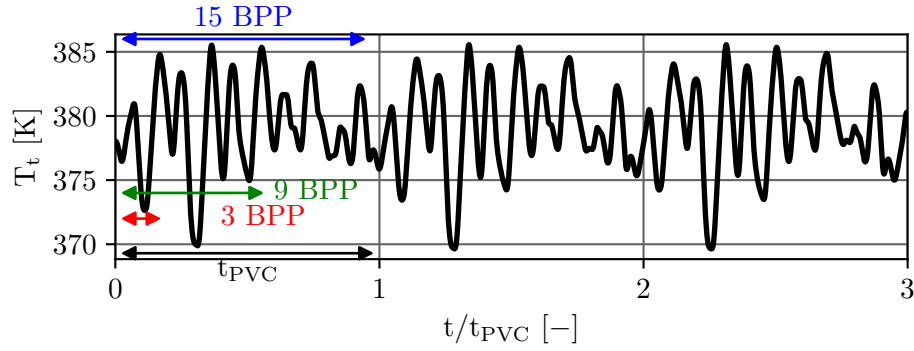


Figure 6.24 – Total temperature signal recorded by a probe in the wake of the rotor blade at mid-span. The lengths of the averages is evidenced by the arrows.

compared to the experiments and LES, as well as the steady mixing-plane simulation with the steady boundary condition from the LES presented in 6.3. The swirl angle in Figure 6.25 is not impacted by the unsteady condition (F10 or F20) compared to the steady boundary condition. The same comment is done for total pressure (Figure 6.26), where only a few differences are noticeable close to the hub at P42, possibly because of the interaction of the main flow with the cooling flow from the purge. This is once again the same for total temperature in Figure 6.27: the effect of the cooling from the purge modifies the distribution at the hub at P42. Then, the distortions seem better captured with case F10 and case F20 in the region between $h/H = 0.2$ and $h/H = 0.6$, which may be explained by the unsteady boundary condition that reproduces temperature fluctuations, thus promoting a better mixing. Overall, there are no differences between case F10 and case F20. For that reason, case F20 is put aside for the rest of the analyses.

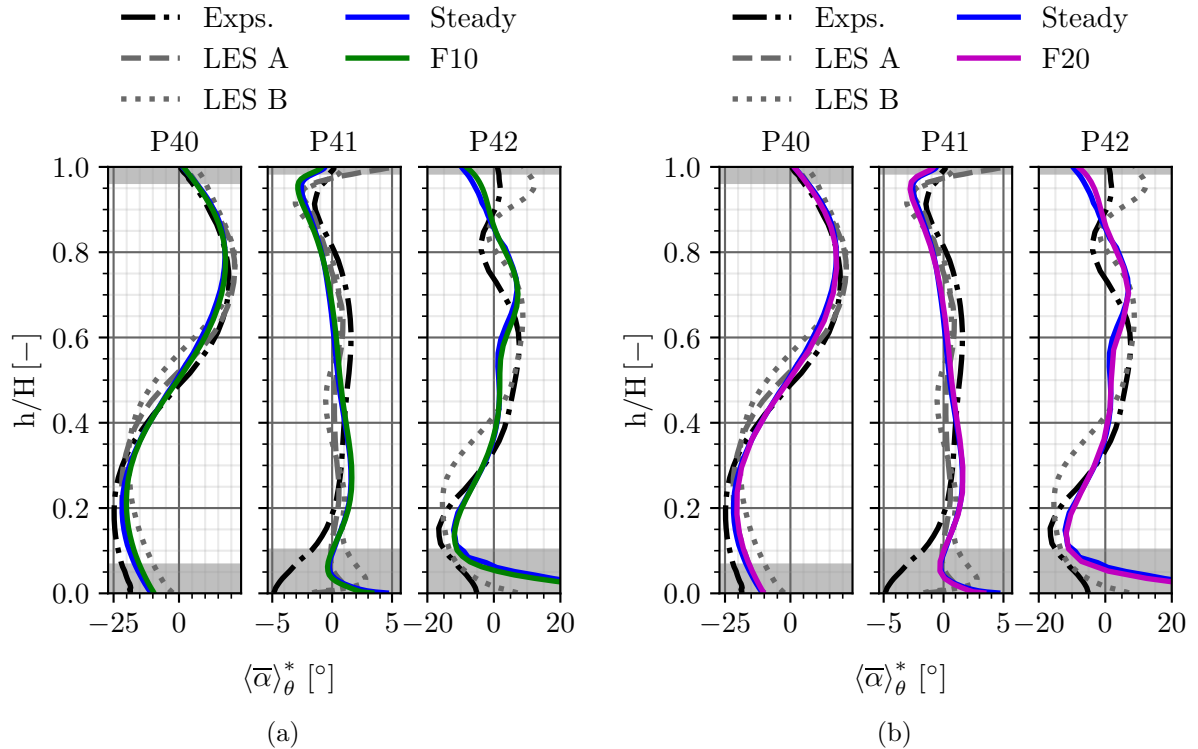


Figure 6.25 – Radial distributions of $\bar{\alpha}$ for case F10 (a) and case F20 (b) compared to the experiments and LES.

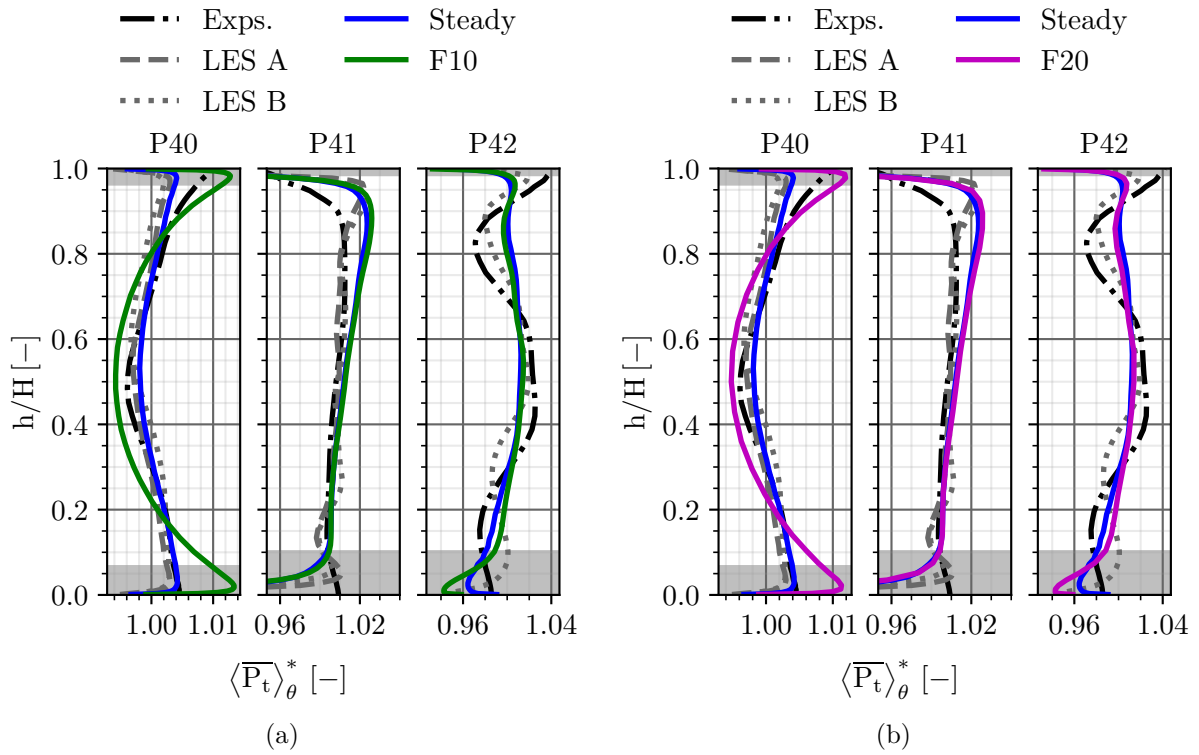


Figure 6.26 – Radial distributions of \bar{P}_t for case F10 (a) and case F20 (b) compared to the experiments and LES.

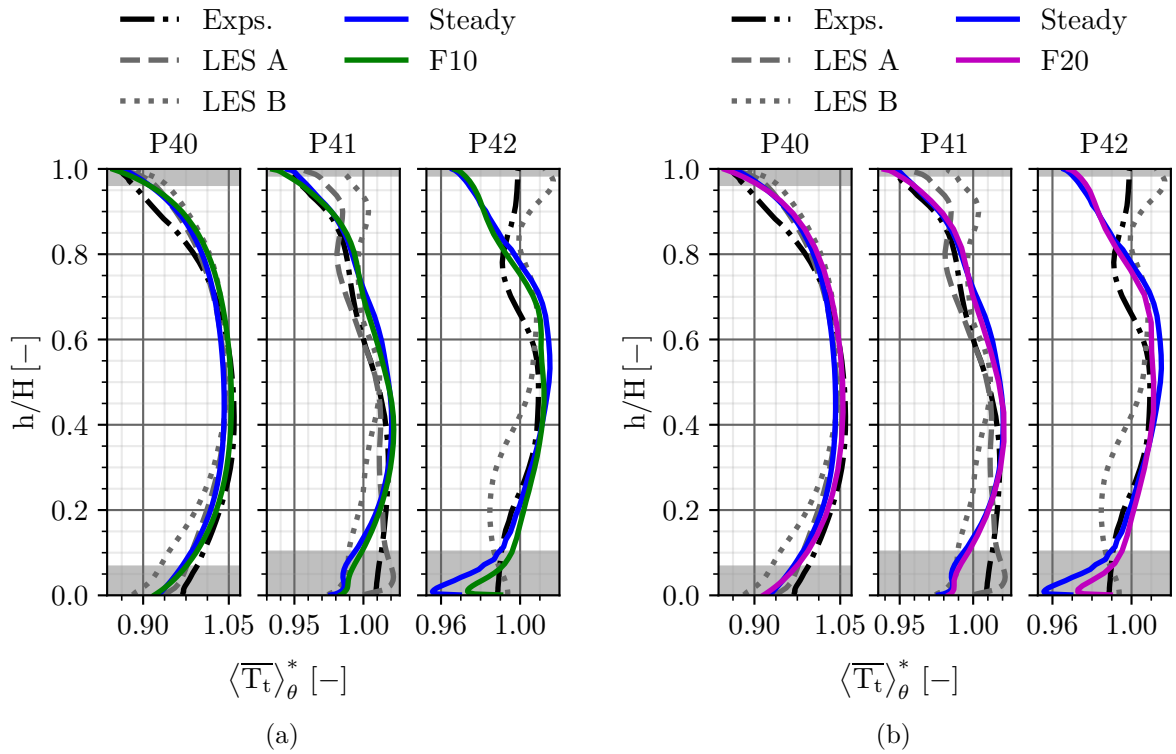


Figure 6.27 – Radial distributions of \bar{T}_t for case F10 (a) and case F20 (b) compared to the experiments and LES.

In order to have a more local view of the influence of the unsteady boundary condition, steady 2D maps at P41 and P42 are compared to the steady experimental maps from the DLR. Results of the steady simulation with the steady inlet boundary condition from the LES are also added at P41. Figure 6.28 shows the total temperature fields at P41. The improvement of case F10 compared to the case with the steady boundary conditions from the LES is quite marginal, where few differences are observable in regions of cold flow (in the wake of the NGV at a pitch position of 1 and close to the hub and shroud).

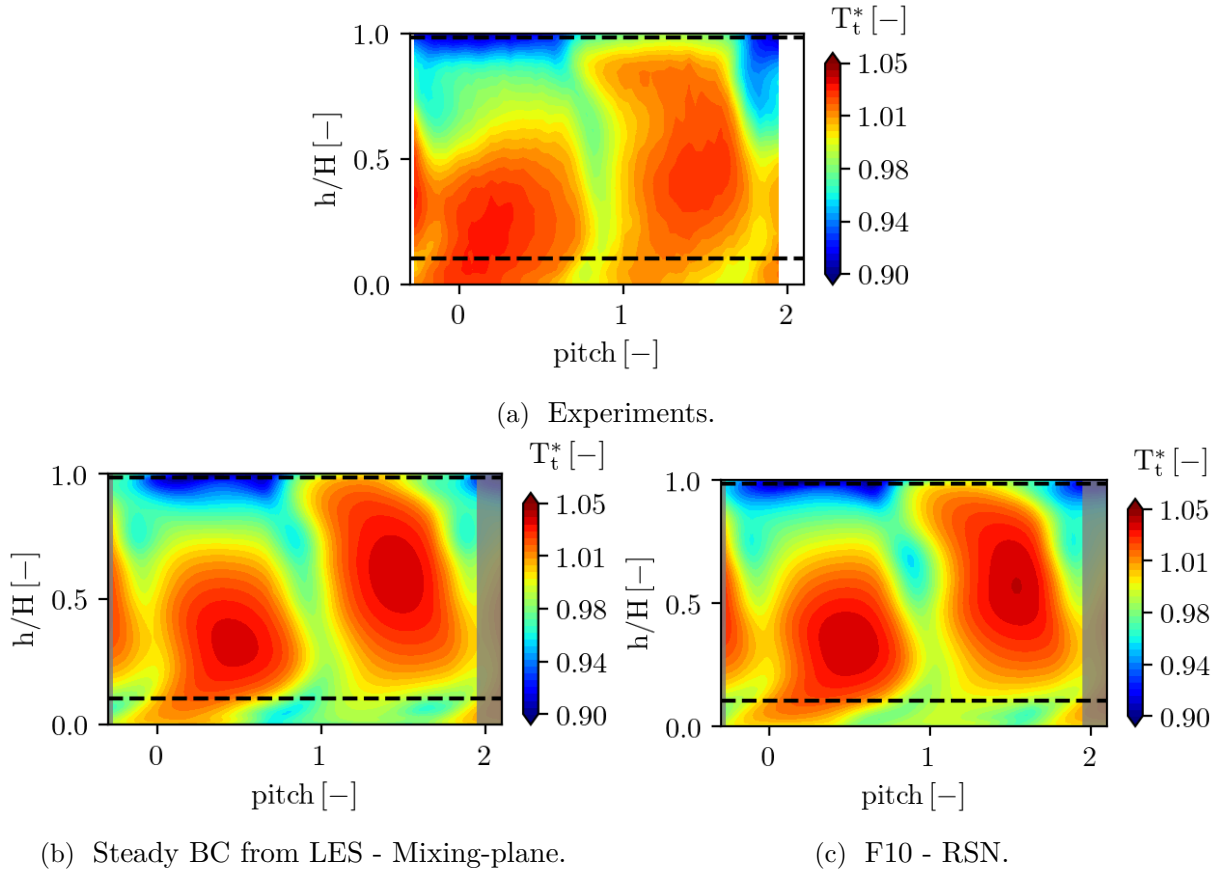


Figure 6.28 – Comparison of \overline{T}_t fields at P41 between the experiments and the simulation accounting for the PVC.

In terms of total pressure, the fields represented in Figure 6.29 confirm the evolution seen on the radial distributions (Figure 6.26a): the patterns induced by the NGVs are similar from one passage to another. Both simulations predict higher intensities of distortions (either minimum or maximum) and the wakes are thicker than the experiments. In addition, case F10 does not provide any additional information compared to the steady simulation with the steady boundary condition.

Moving to the rotor row and P42, the swirl angle is depicted in Figure 6.30. The effects of the rotor are azimuthally averaged and two similar patterns generated by the NGVs are observed. The region of maximum swirl angle is shifted from $h/H = 0.5$ for the experiments to $h/H = 0.7$ for case F10. This may be explained by the shroud passage vortex not being correctly taken into account. This is confirmed by looking at the fields of total pressure in Figure 6.31: both the deficit (intensity and position) of total pressure at the hub and shroud are not correctly predicted,

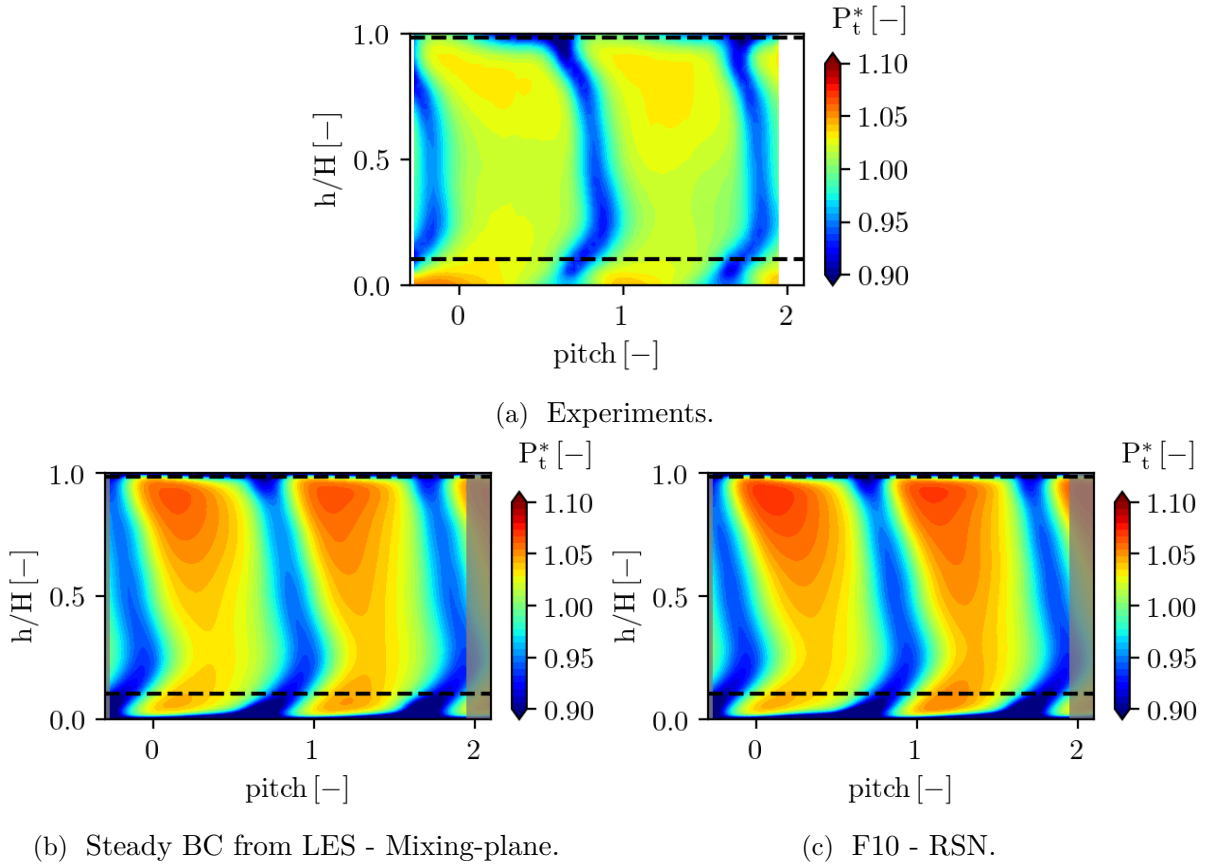


Figure 6.29 – Comparison of \overline{P}_t fields at P41 between the experiments and the simulations accounting for the PVC.

which was already visible on the total pressure radial distribution (Figure 6.26a). One of the explanations could be the poor prediction of secondary flows generated by technological effects (hub and shroud stator fillets, hub rotor fillet, rotor squealer tip) and cooling (purge cavity) and which are only partially modelled or not taken into account in the numerical simulation F10. Finally, total temperature is addressed in Figure 6.32. The quite good agreement of the radial distribution (Figure 6.27a) is also noticeable on the fields of Figure 6.32. The patterns are retrieved but are still shifted upwards for case F10 compared to the experiments. Once again, a deficiency in the correct prediction of the secondary flows is suggested. However, the improvement compared to the work of Cottier *et al.* is notable [21].

The instantaneous total temperature evolution depicted in Figure 6.33 shows a complex dynamics of the flow over a period of the PVC. The hottest flow appears in the first half of the period, while cooling flow pops up in the second half of the period close to the shroud.

CPU time

The computational cost is evaluated for the different types of simulations presented in Chapter 6 using both the steady and unsteady boundary conditions from the LES. Simulations are performed on the Topaze supercomputer at Centre de Calcul Recherche et Technologie (CCRT) using AMD Epyc 7763 nodes. For unsteady simulations, the CPU time includes both the computational time and the extraction time of the snapshots required for the averaging and the reconstruction

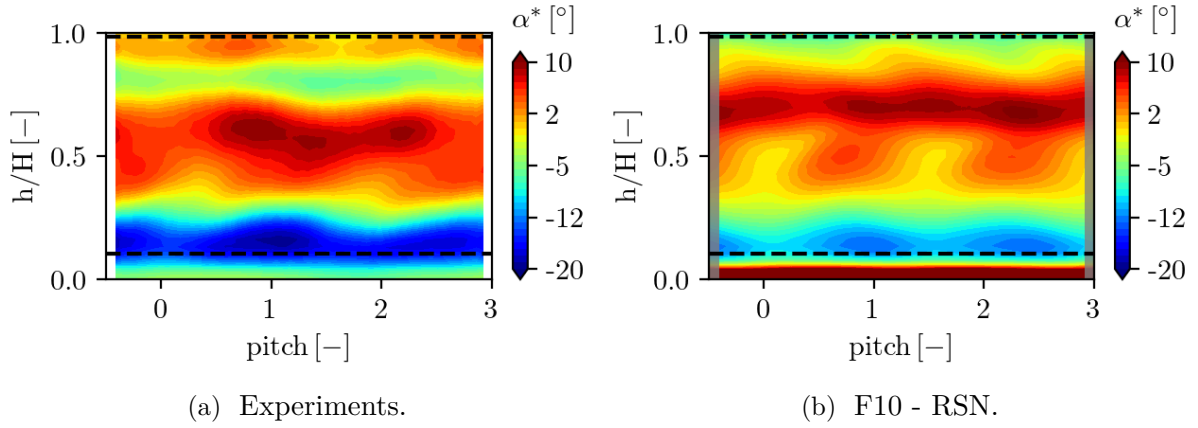


Figure 6.30 – Comparison of $\bar{\alpha}$ fields at P42 between the experiments and case F10.

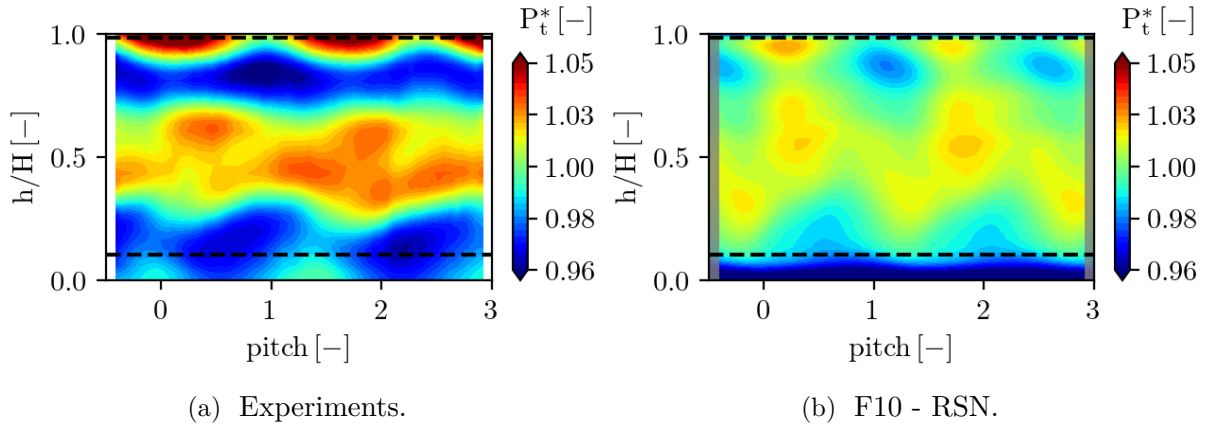


Figure 6.31 – Comparison of \bar{P}_t fields at P42 between the experiments and case F10.

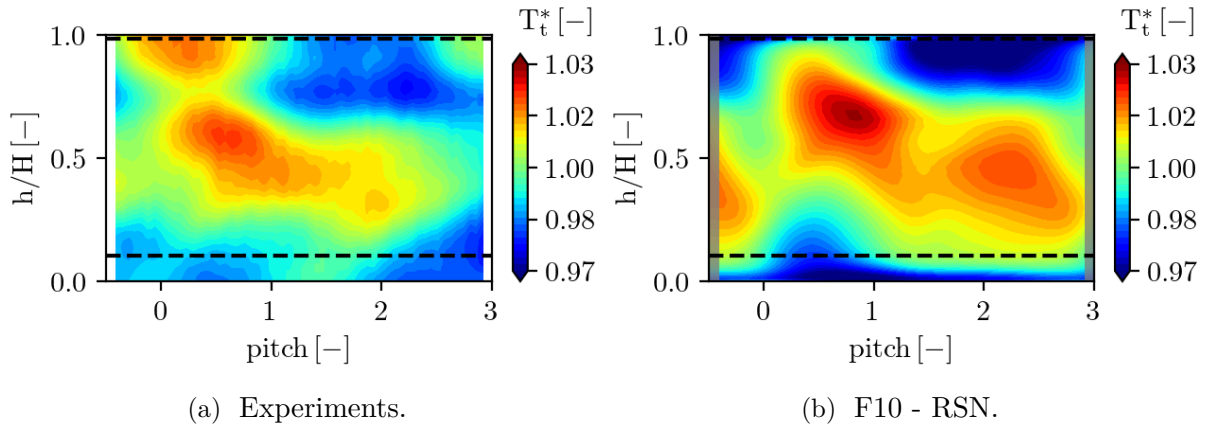


Figure 6.32 – Comparison of \bar{T}_t fields at P42 between the experiments and case F10.

of the solution. As mentioned earlier, the number of snapshots is defined as a multiple of the period of the PVC (t_{PVC} for F10 and $3 \cdot t_{PVC}$ for F20). Table 6.4 sums up the CPU times. Since the extraction is time-consuming, the last column account for this time. It should be noted the pre-processing for the unsteady boundary condition (in particular the generation of the coupling tree) is not considered but accounts for a lot. Between the steady and unsteady F10 simulations, a factor of 6 is noticed, while F20 needs 1.5 more CPU time compared to F10, since it is more

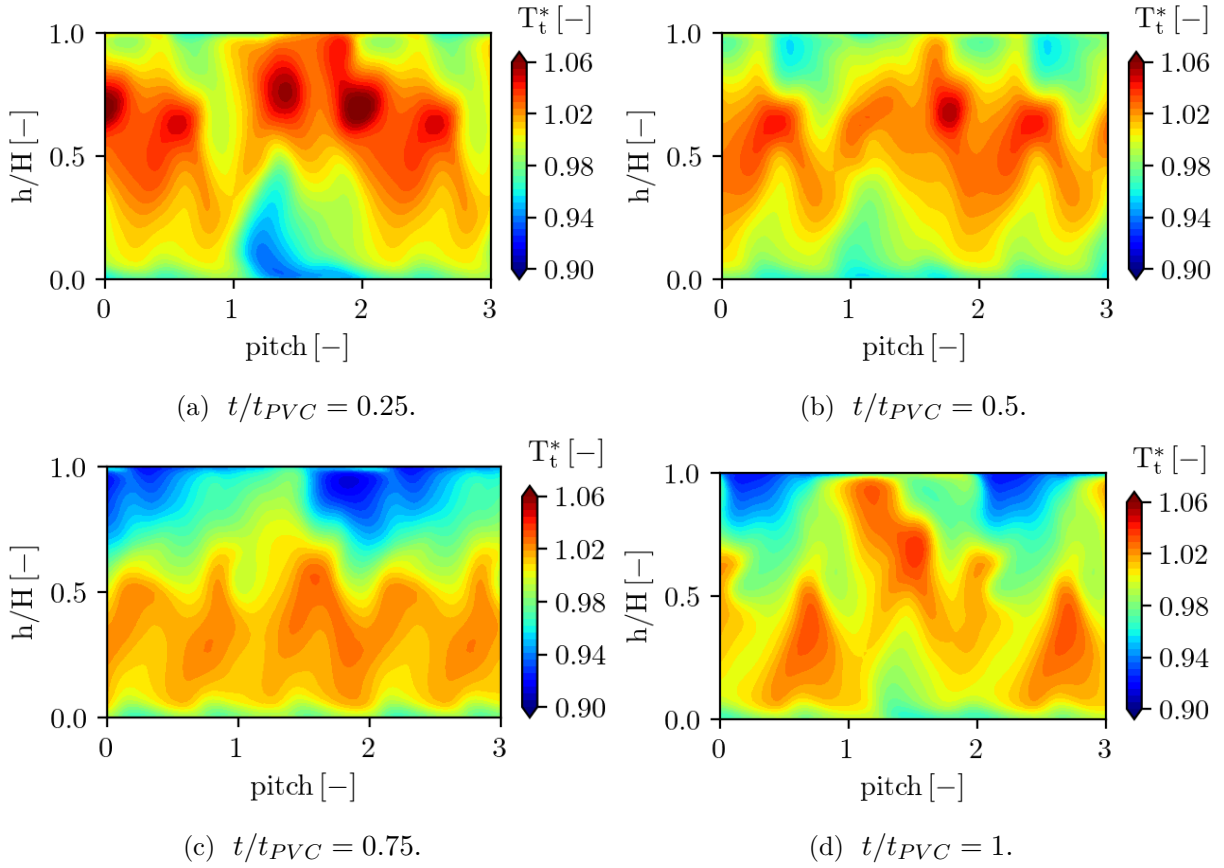


Figure 6.33 – Instantaneous total temperature field at P42 over a period of the PVC.

complex to convergence. The extraction of the snapshots accounts for 20% of the total CPU time for F10 and 30% for F20.

Simulation type	CPU time [h]	CPU time snapshots [h]
Steady cooled vein (CV) mixing-plane simulation	900	X
Unsteady RSN CV simulation F10	5300	900
Unsteady RSN CV simulation F20	8200	2700

Table 6.4 – Comparisons of CPU time for different FACTOR simulations with both steady and unsteady boundary condition from the LES.

The presence of the PVC at the inlet has been checked. By performing a SPOD analysis from a LES, it was possible to reconstruct a boundary condition accounting for the energetic content of the PVC. URANS simulations have been performed with the unsteady boundary condition: results showed a marginal impact of the unsteady boundary condition from the LES compared to a steady simulation with the steady boundary condition from the LES when looking at radial distributions. The unsteadiness due to the PVC does not seem to impact the results in the rotor row, for which the BPF must but prevail on the frequency of the PVC. To confirm that, it would be interesting to perform a RSN simulation with the steady boundary condition from the LES. The

CPU time associated with this unsteady boundary condition is not negligible, which opens the debate on the correct consideration of technological effects and cooling with a steady boundary condition, which might be less time-consuming. Once again, the choice of the boundary condition depends on the purpose of the simulation: steady or unsteady local analysis? radial distributions?

6.6 Comparisons with steady experimental data

The new steady inlet boundary condition having been set, results are now compared to various steady experimental data. To be the most representative of the isolated simulation of Martin, the new geometry with the modified inlet plane is considered. The steady fields from the LES are used and a CV simulation with the Smith $k-l$ turbulence model is performed. It is compared both to the experiments and to the Smith $k-l$ CV simulation with the steady inlet map from the experiments. When possible, the results of 'LES A' and 'LES B' are also added and are represented in grey lines. Results from Chapter 2 and Chapter 5 showed an insensitivity of the shape of the radial distributions to the numerical set-up. In that sense, a parametric study with the LES inlet map is not performed.

6.6.1 Radial distributions from the 5HP measurements

Radial distributions of $\bar{\alpha}$, \bar{P}_t and \bar{T}_t obtained from the measurements of the 5HP are compared to the CV numerical simulations, both with the inlet map from the experiments and from the LES. Results are depicted in Figure 6.34.

The swirl angle is not modified by the inlet boundary conditions map at P41, since the deviation is largely given by the deviation of the NGVs (Figure 6.34a). The distributions are in agreement with the LES, as well as with the experiments, except at the hub. Once again, at P42, no differences between the two types of inlet maps are observed. The position of the hub passage vortex is correctly predicted with the RANS, while the LES overestimates its radial position. However, strong discrepancies between the LES and the experiments are visible close to the shroud, where the tip passage vortex and shroud passage vortex interact. Surprisingly, the LES captures the swirl angle and total pressure deficit close to the shroud, although the tip gap is 50% higher than in the experiments (Figure 6.34a and Figure 6.34b). The secondary structures are dissipated at the shroud with the RANS (improvements are nevertheless observed when using a SST Wilcox $k-\omega$ turbulence model - see section B.8 in Appendix B).

Looking at total temperature distributions in Figure 6.34c, the improvement is remarkable when using the boundary condition from the LES, where the temperature distortion agrees with the experiments between $h/H = 0.2$ and $h/H = 1$ at P41. The differences at the hub may be explained by the way cooling is taken into account, which can still be improved. This improvement is clearly observable on the 2D fields depicted in Figure 6.35, where the experiment is compared to the simulations with the boundary condition from the experiments and from the LES. At P42, except close to the shroud where the distortion is not predicted by the RANS as discussed earlier with the pressure distribution, a very good agreement with the experiments is reached when the boundary condition from the LES is applied. Once again, these observations confirm the fact that the measurements at the inlet of the HP turbine must be accurate to correctly predict the dynamics of the flow, especially for the temperature field.

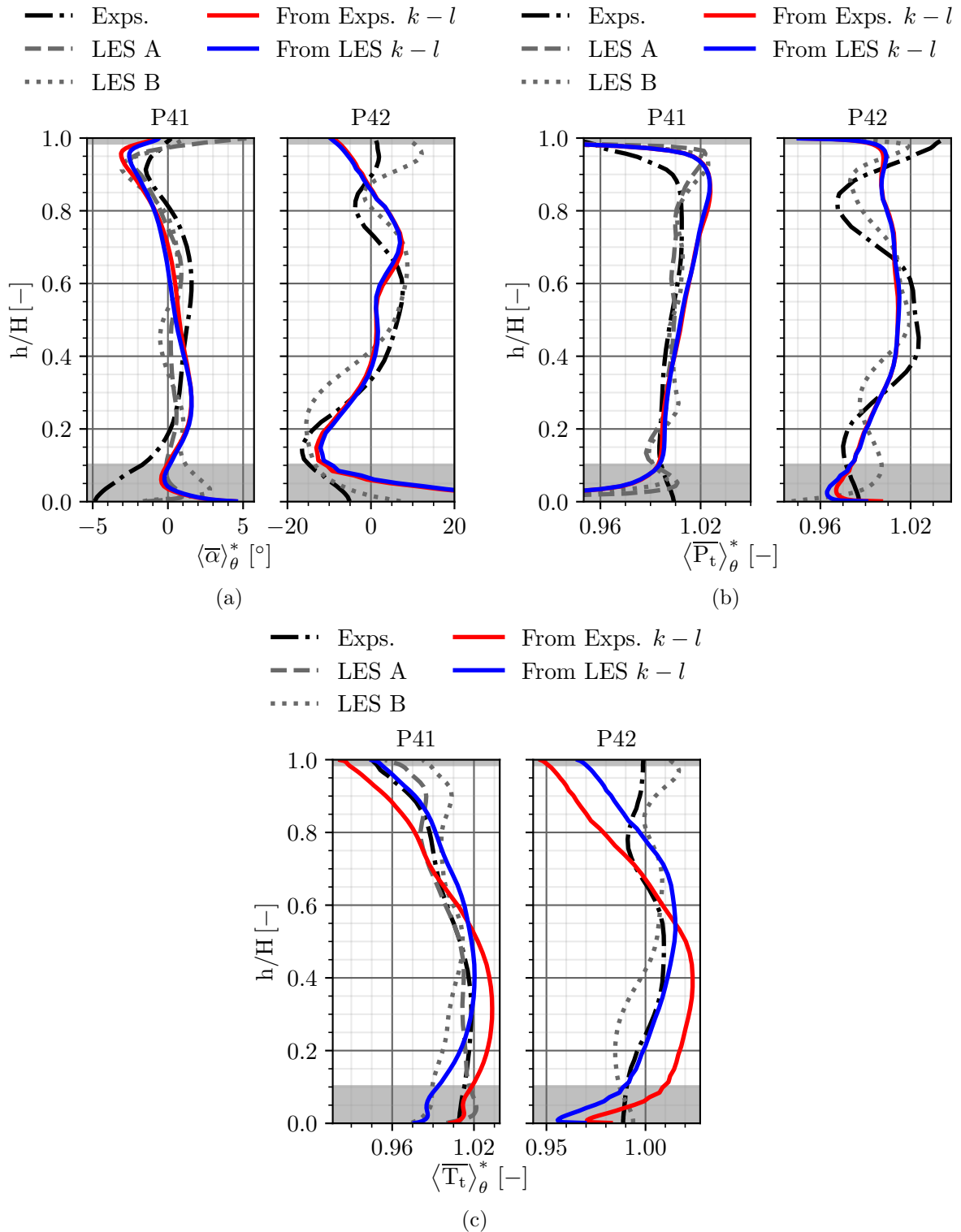


Figure 6.34 – Radial distributions of $\bar{\alpha}$ (a), \bar{P}_t (b) and \bar{T}_t (c) when using the steady inlet map from the LES. Plots in terms of distortions.

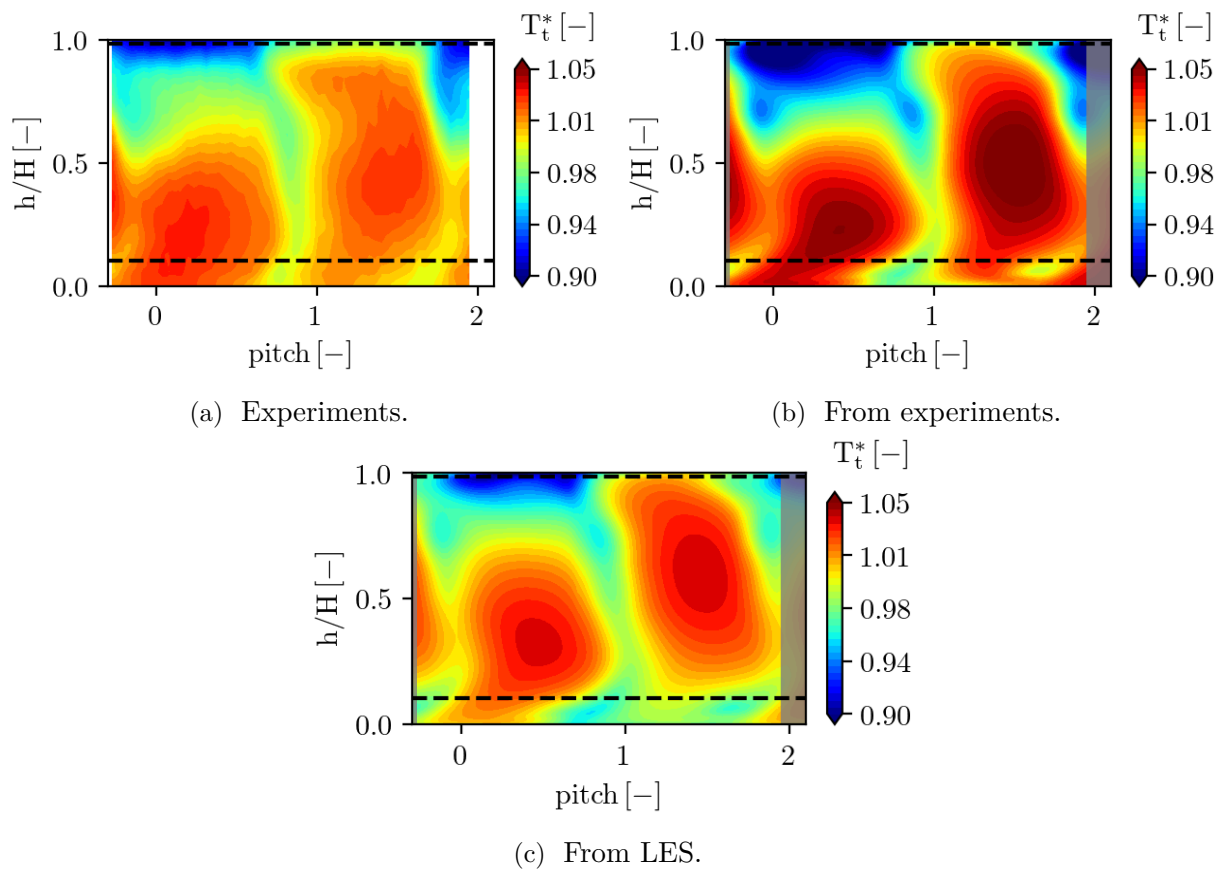


Figure 6.35 – Comparison of \overline{T}_t fields at P41 between the experiments and the simulations.

6.6.2 Isentropic Mach number distribution on the vane surface

Static pressure taps are placed at $h/H = 0.5$: 10 taps are on the PS of NGV1 and 10 others on the SS of NGV2, which enable to obtain the distribution of isentropic Mach number at mid-span of the vane. When extracting the data from the simulations, a unique virtual NGV is created in order to be representative of the two instrumented NGVs. Results are plotted in Figure 6.36. The evolution given in Figure 6.36 shows a relative improvement when using the boundary condition from the LES, especially on the SS. Close to the TE, M_{is} is underestimated, which can be explained by the vane/blade interface that reduces the potential effect of the blade. The effect of the cooling is clearly noticeable, with local increases of M_{is} in the areas circled in black.

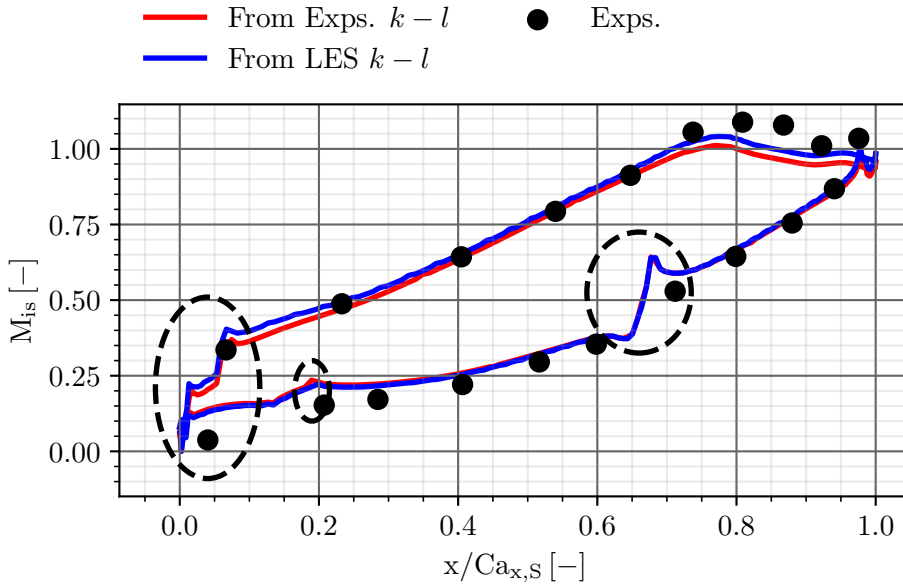


Figure 6.36 – Distribution of isentropic Mach number at $h/H = 0.5$ of the NGVs obtained for different cooled simulations compared to the experiments.

6.6.3 Hub and shroud static pressure taps

Static pressure taps placed over two vane pitches close to P41 (4 mm upstream P41) enable to monitor the evolution of P_s . Results of the simulations are positioned against these measurements and are represented in Figure 6.37. Static pressure evolutions are not influenced by the type of inlet map. At the shroud, the widths of static pressure deficit are well captured, but not the amplitudes. At the hub, neither the widths not the amplitudes are representative of the experiments, which could be explained by a more complex physics occurring close to the hub to the presence of the complete cooling, fillets, and potential effect of the purge.

Comparisons of the results of numerical simulations with the steady experimental data revealed all the difficulties of having representative simulations on several metrics. The transport of temperature being of first importance, temperature evolutions inside the high-pressure turbine showed a good agreement with the experiments when using the inlet boundary condition from the LES. The distribution of isentropic Mach number of

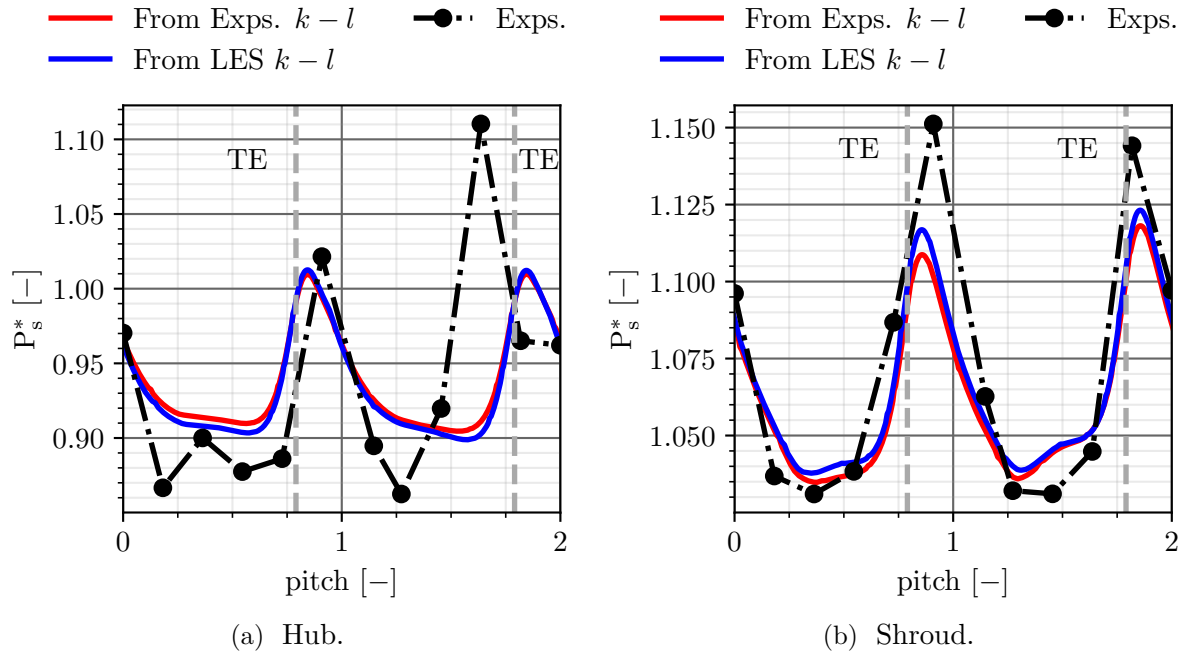


Figure 6.37 – Comparison of static pressure evolutions over the pitch with the experiments.

mid-span of the vane, *i.e.* the vane loading, is well predicted by the RANS simulation, except close to the TE where the potential effect of the blade may play an important role. Finally, it is difficult to predict the static pressure evolution at the endwalls. Only the tendency is given.

6.7 Unsteady pressure measurements

In the scope of FACTOR’s project, unsteady pressure measurements using Fast Response Aerodynamic Probe (FRAP) have been performed by the VKI at P40 and P42. Through this PhD thesis, and with the unsteady simulation F10 taking into account the PVC, some post-processing have been performed to compare these experiments to the numerical simulation in order to exhibit the flow features related both to the PVC and the BPF. They include:

- 2D time-averaged pressure field at P40 to compare to the DLR;
- 2D PSD pressure amplitude at P40 at the f_{PVC} and at the BPF;
- Pressure phase-locked average at P42;
- 1D/2D PSD pressure amplitude at P42 at f_{PVC} and at the BPF.

Total pressure signals are recorded during $t = 2$ s at a sampling frequency $f_s = 500$ kHz and filtered at $f_f = 125$ kHz, leading to $1 \cdot 10^6$ temporal samples at each position. The FRAP records a voltage signal which is converted into total pressure with a calibration. At P40, measurements are performed with the $r - \theta$ traverse of the DLR, describing a zigzag at 1718 spatial positions. At P42, radial measurements are performed at 77 positions at a given azimuthal position. Due to the head probe size, 2.5 mm are not measured from the hub. Note that the probes are pre-aligned with a yaw angle taken from the steady measurements of the DLR (Figure 6.38). A sensor is also placed on the blades and on one of the vanes, giving a signal for a whole rotation of the row. The clocking LEC is considered for the measurements.

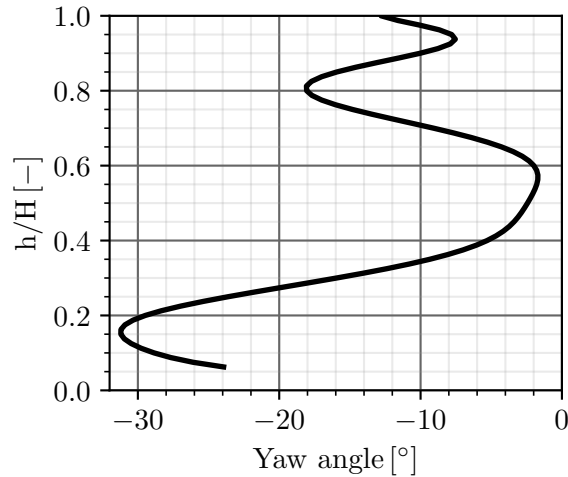


Figure 6.38 – Probe alignment at P42.

6.7.1 Time-averaged pressure field at P40

First of all, the instantaneous signals from the FRAP are time-averaged and compared to the steady measurements from the DLR. Results are depicted in Figure 6.39. The two low total pressure zones induced by the swirling motion generated by the swirlers are clearly evidenced. However, the intensity close to 0 pitch position is smaller for the VKI compared to the DLR. A hysteresis phenomenon could explain the presence of some streaks on the field measured by the VKI.

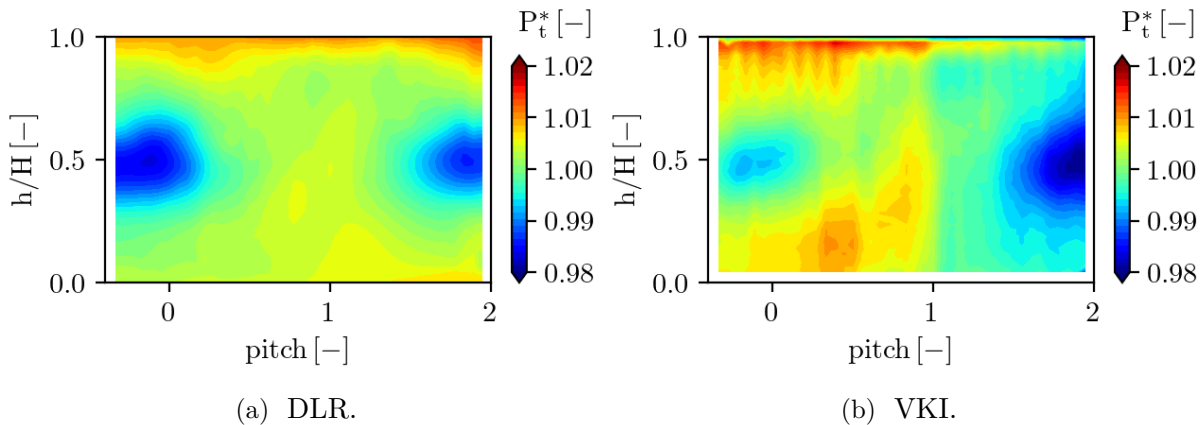


Figure 6.39 – Experimental time-averaged total pressure field at P40.

6.7.2 PSD pressure amplitude at P40

PSDs are used to identify the emergence of characteristic frequencies at P40. PSD computations using Welch's method are performed at each measurement point at P40, where the initial signal is divided into 50 bins with 50% overlap. A Hanning window is used. The characteristic frequency of the PVC at 500 Hz is clearly observable in Figure 6.40, as well as the filtering frequency at 125 kHz. In order to point out the impact of the PVC, the amplitude of the PSD at the frequency of the PVC is collected at each measurement point and a 2D field of amplitudes is built. The resulting map is depicted in Figure 6.41. The amplitudes are normalised by the

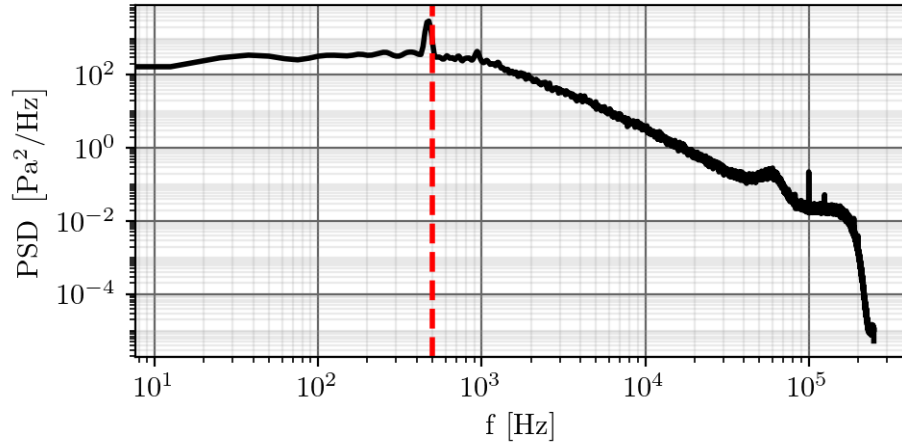


Figure 6.40 – PSD of total pressure in a low total pressure zone at $h/H = 0.5$.

mean value. Two zones of high amplitudes are evidenced and are associated with the two low total pressure zones, as already discussed in Figure 6.39. Pockets of high activity are also visible close to the shroud, because of the presence of the boundary layer. The same post-processing is intended at P40 with case F10 and is represented in Figure 6.42. However, these results are hardly comparable to the experimental ones. The PSD is more active close to the hub and shroud, which could be explained by the swirling motion driving the turbulent boundary layer. The most likely explanation for such discrepancies would be turbulent fluctuations that are not accounted with the numerical simulation, while the swirler would generate very high turbulent activity. In terms of absolute levels, the PSD amplitude is one order of magnitude higher in the experiments compared to the numerical simulations, confirming a possible bias induced by turbulence.

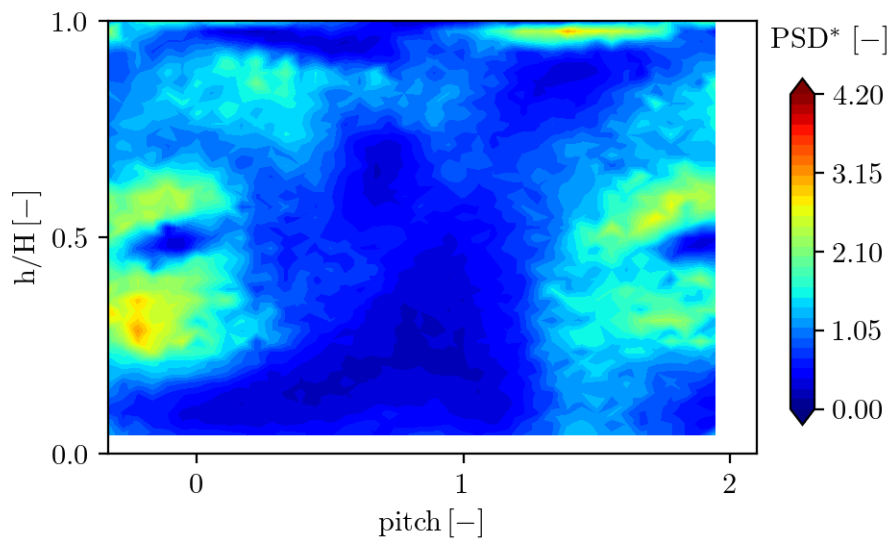


Figure 6.41 – Experimental amplitude of the PSD at the frequency of the PVC at P40.

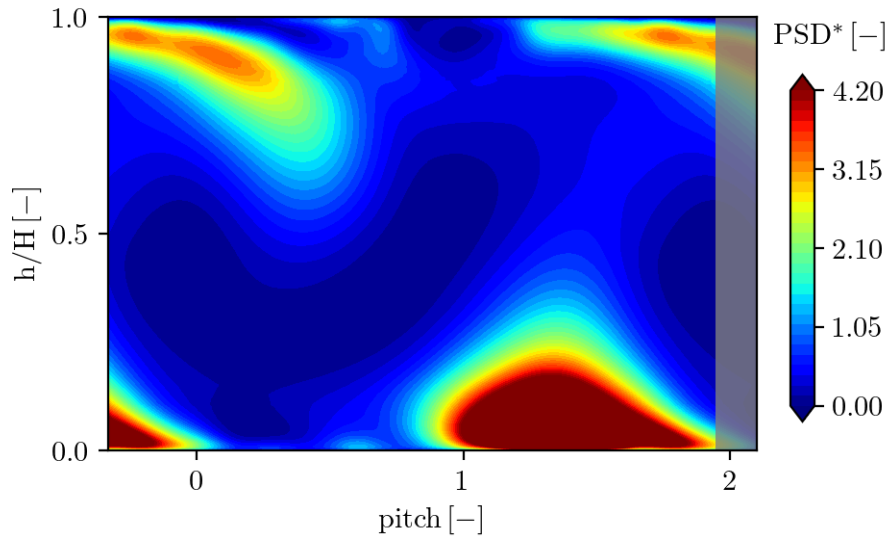


Figure 6.42 – Numerical amplitude of the PSD at the frequency of the PVC at P40.

6.7.3 Phase-locked average at P42

Phase-locked average (PLA) is performed at P42 and is obtained thanks to a top-tour. Each blade passage is divided into several clusters that are averaged afterwards. The knowledge of the top-tour and the number of rotor blades makes it possible to recreate a pitch associated with the rotor row, and thus to obtain a 2D representation from 1D data. Results are depicted in Figure 6.43 and are compared to case F10: it shows 3 patterns that are associated with the rotor blades. The intensity of the distortion is more important in the experiments. Moreover, the position of maximum intensity is shifted upwards in the numerical simulations. The secondary flows are supposed to explain this shift. Moreover, the comparisons are not strictly speaking identical: in the experiments, only the effect of a rotor passage is visible, whereas the field obtained by the numerical simulation covers three rotor passages, two stator passages and one swirler passage.

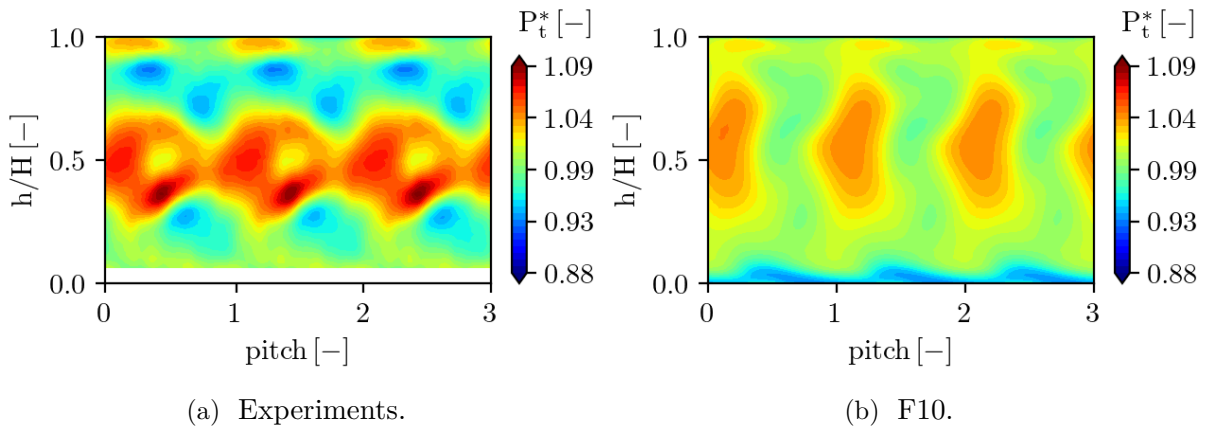


Figure 6.43 – Phase-locked average at P42.

6.7.4 PSD pressure amplitude at P42

Finally, the same post-processing for the PSD pressure amplitude at P40 is performed at P42. For the experiments, the measurements are available at a single azimuthal position (the position is unknown). To account for the effect of the rotor, the amplitudes are plotted both at the frequency of the PVC and at the BPF, and are normalised by the mean value (respectively $\overline{PSD}_{f_{PVC}} = 2238 \text{ Pa}^2 \cdot \text{Hz}^{-1}$ and $\overline{PSD}_{BPF} = 29356 \text{ Pa}^2 \cdot \text{Hz}^{-1}$). Results are shown in Figure 6.44.

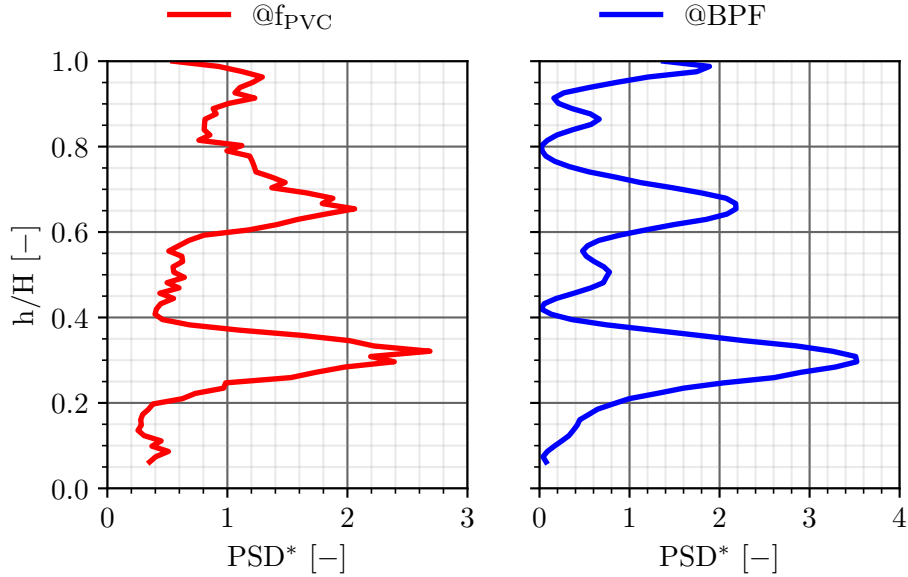


Figure 6.44 – Experimental amplitude of the PSD at the frequency of the PVC and at the BPF at P42.

It shows a very similar radial pattern between both frequencies, except close to the walls. The amplitude in terms of distortions is close but the absolute intensity is different: the dynamics is induced by the rotor with its frequency. For the numerical simulations, it is however possible to have 2D fields, which are represented in Figure 6.45 and Figure 6.46 respectively for f_{PVC} and the BPF. At f_{PVC} , the activity is higher close to the shroud, which may be explained by the strong variations of the flow where a strong mixing happens. At the BPF, the patterns are more organised and follow the shape of the total pressure field depicted in Figure 6.31.

Comparisons of the numerical simulation F10 with the unsteady experiments of the VKI showed numerous differences that make URANS, at this point of the study, unsuitable for the prediction of this low-frequency phenomenon associated with the PVC in the turbine stage. Further studies must be carried out to consolidate the present observations.

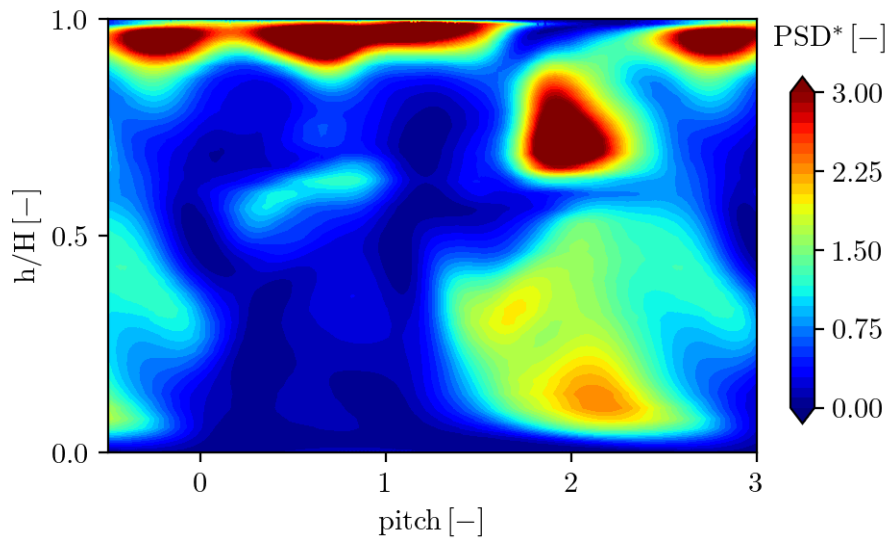


Figure 6.45 – Numerical amplitude of the PSD at the frequency of the PVC at P42.

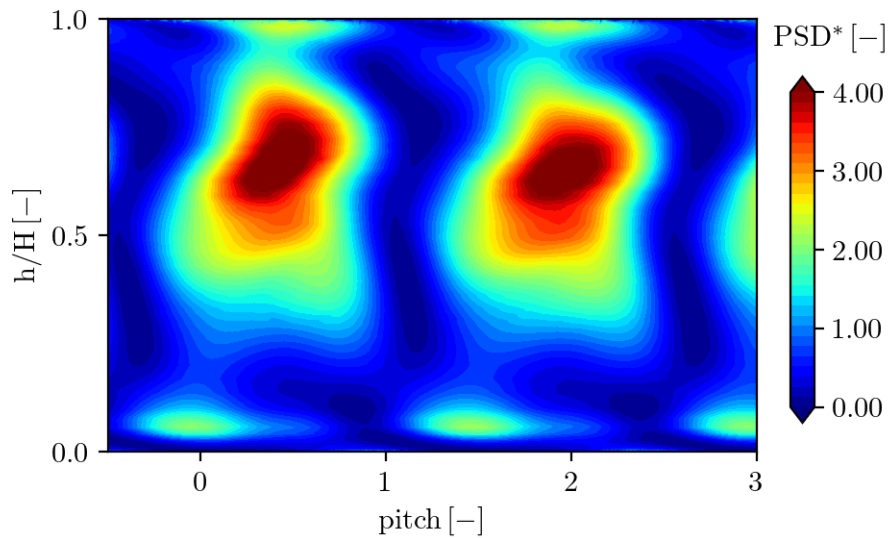


Figure 6.46 – Numerical amplitude of the PSD at the BPF at P42.

6.8 Conclusion

In Chapter 6, the influence of the inlet boundary condition has been tackled. Reviews of the literature revealed strong measurement difficulties at P40, leading to huge blank zones that have been filled up with an extrapolation process. It was decided to use the data from LES as an inlet boundary conditions to evaluate the validity of such a process according to three different aspects. The first one dealt with interpolations

errors in the core of the flow (errors of type 'c'). A parametric study has been performed and revealed the dominant impact of the total temperature map in the transport of temperature inside the high-pressure turbine. Then, the presence of the boundary layers, not measured in the experiments, has been evaluated, by removing from the LES map a portion of the data not measured close to the hub and shroud. Results showed a minor impact of these errors of type 'a' on the dynamics of the mean flow. Finally, because of the presence of an instability at the inlet of the turbine, the PVC, an unsteady boundary condition has been generated based on the SPOD. By selecting the mode and frequency associated with the PVC, it was possible to impose the dynamics of the PVC at the inlet of the high-pressure turbine. Although more representative than the steady boundary condition, the impact is slight on the radial distributions. However, it is clear that in order to study pressure fluctuations (for analyses dedicated to durability), this kind of unsteady boundary condition would be appreciated. The comparisons with the steady measurements lead to relatively good results. Moreover, it should be borne in mind that the generation of the boundary condition as well as the computation and extraction of the snapshots is costly. A preliminary study on the need for such boundary conditions must be performed, since it seems that a better consideration of technological effects and cooling would improve the results. After checking each hypothesis, a first analysis of the unsteady pressure measurements has been carried out. Although of considerable interest, the present results must be consolidated to enable a fair comparison between the experiments and the numerical simulations.

Dans le Chapitre 6, l'influence de la condition limite d'entrée a été abordée. La revue de la littérature a révélé d'importantes lacunes dans les mesures au niveau du P40, conduisant à des zones vides qui ont été comblées par un processus d'extrapolation. Il a été décidé d'utiliser des données de LES comme condition limite d'entrée pour évaluer la validité d'un tel processus selon trois aspects différents. Le premier concerne les erreurs d'interpolation au cœur de l'écoulement (erreurs de type 'c'). Une étude paramétrique a été réalisée et a révélé l'impact dominant de la cartographie de température totale dans le transport de température à l'intérieur de la turbine à haute pression. Ensuite, la présence des couches limites, non mesurées dans les essais, a été évaluée en retirant du champ LES une partie des données non mesurées à proximité du moyeu et du carter. Les résultats ont montré un impact mineur de ces erreurs de type 'a' sur la dynamique de l'écoulement moyen. Enfin, en raison de la présence d'une instabilité en entrée de la turbine, le PVC, une condition limite instationnaire a été générée sur la base de la SPOD. En sélectionnant le mode et la fréquence associés au PVC, il a été possible d'imposer la dynamique du PVC à l'entrée de la turbine haute pression. Bien que plus représentative que la condition aux limites stationnaire, cette condition n'impacte que peu les profils radiaux. Cependant, il est clair que pour étudier les fluctuations de pression (pour des analyses dédiées à la durée de vie), ce type de condition aux limites instationnaire serait apprécié. Les comparaisons avec les mesures stationnaires donnent des résultats relativement bons. De plus, il convient de garder à l'esprit que la génération de la condition aux limites ainsi que le calcul et l'extraction des snapshots sont coûteux. Une étude préliminaire sur la nécessité d'une telle condition aux limites doit être réalisée, car il semble qu'une meilleure prise en compte des effets technologiques

et du refroidissement améliorerait les résultats. Après avoir vérifié chaque hypothèse, une première analyse des mesures instationnaires de pression totale a été effectuée. Bien que d'un intérêt considérable, les résultats actuels doivent être consolidés pour permettre une comparaison plus juste entre les essais et les simulations numériques.

Conclusion

“ *J’ai vu naître l’aviation. J’y ai cru. J’ai voulu y participer. Turbomeca est née de cette volonté voici bientôt un demi-siècle.* ”

Joseph Szydłowski

Reminder of the context and objectives	205
Main findings	206
Perspectives	208

Reminder of the context and objectives

The research work presented in this PhD thesis has been carried out in the context of axial high-pressure turbine flows in turboshaft engines designed by Safran Helicopter Engines. With the development of new combustor technologies which aim at reducing pollutant emissions, the flow at the inlet of the turbine has much more severe thermal stratifications, also known as swirled hot streaks, that can become unstable and oscillate in time. As a consequence, when performing a numerical simulation of an isolated high-pressure turbine, the combustor/turbine interface must be correctly considered. From a practical point of view, the inlet boundary condition issue is not the only one: in the RANS approach, the representativeness of the physical models (*e.g.* cooling) or turbulence modelling have to be assessed in order to represent as accurately as possible the physics associated with this complex component and which have been described in the literature review presented in Chapter 1 (vane/blade interactions, secondary flows, etc.). Therefore, the intent of this thesis was to **investigate the ability of the RANS method, and to check if it can meet the exigent level of accuracy expected, for both aerodynamic and aerothermal behaviours, while applied to cooled turbine stage flows submitted to swirled hot streaks.** Throughout this manuscript, this problematic has been addressed through two topics:

- **RANS turbulence modelling in turbulent swirling flows:** study of the characteristics of turbulence in highly turbulent swirling flows and modelling of anisotropy of turbulence;
- **Validity of the high-pressure turbine inlet boundary condition:** impact of strong velocities and temperature distortions as well as unsteadiness at the inlet on the dynamics of the flow in the turbine.

Main findings

The literature review proposed in Chapter 1 showed that the high-pressure turbine was a very complex component of the gas turbine engine, associated with complicated phenomena which were either due to the coupling between the combustion chamber and the turbine, or which were intrinsic to the component itself. Chapter 2 provided a more accurate definition of the industrial problematic of this PhD thesis, related to the configuration of the FACTOR project. The project itself has been presented, as well as previous numerical simulations performed on the configuration, to assess the difficulties in correctly predicting both the aerodynamic and aerothermal in the turbine stage, especially due to high levels of turbulence, high swirling motions and the presence of instabilities. Even if LES predict the temperature evolution in the turbine stage, RANS and URANS simulations are not able to cope with it. The understanding of this misprediction of temperature evolution has been investigated in the rest of the manuscript. In Chapter 2, an approach allowing to have a clear overview concerning the prediction of the temperature transport inside the high-pressure turbine of FACTOR has been presented: several simulations of different complexity have been performed (effect of the clocking position, unsteady simulations, impact of the operating point and cooling). These simulations did not improve the prediction of temperature transport, except for cooling that must be taken into account since it provides some richer flow physics.

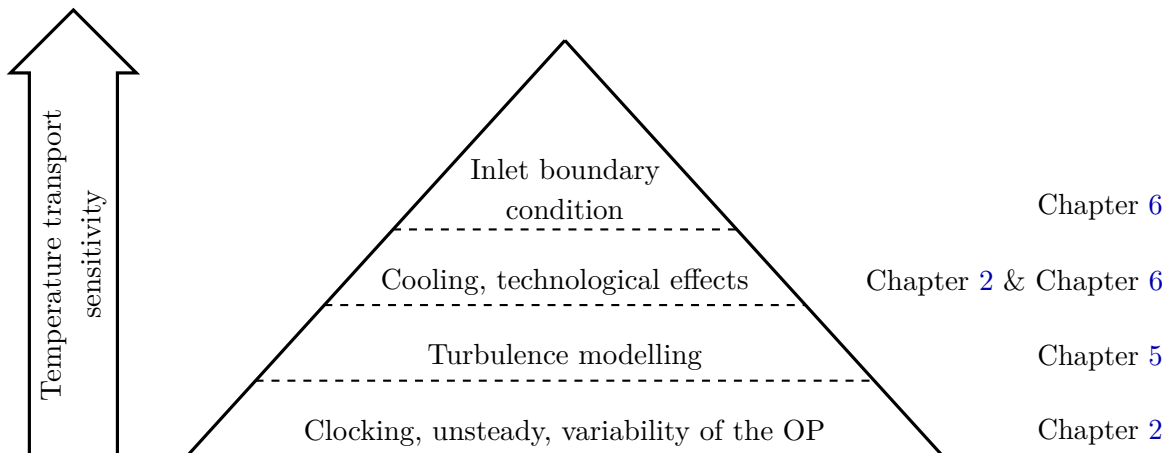
Thus, a lack of complexity was probably not the reason for the bad prediction temperature transport. It was therefore decided to go back to the basics of RANS modelling which deal with turbulence modelling. In Chapter 3 and Chapter 4, a simplified configuration representing a NGV passage has been designed, since the misprediction already appeared in the static part of FACTOR. The redistribution of a highly turbulent swirled hot streak has been studied. LES have been performed to study the topology of the swirled flow. A turbulent kinetic energy budget distinguished two regions where turbulence activity is impacted when the curvature is reached. In that specific zone, production and mean convection terms are dominant, while diffusion and dissipation terms exist, but to a lower extent. The integral scales obtained by autocorrelation showed preferential directions for the global integral length scale, driven by the axial direction in the straight part and by the transverse directions in the curved part. The anisotropy of turbulence analysis based on two metrics highlighted a misalignment of the Reynolds stress tensor and the mean strain-rate tensor (Schmitt's criterion). A strong anisotropy developing inside the bent duct (Lumley's analysis) may cause the failure of the classical RANS turbulence models based on Boussinesq's hypothesis.

On this basis, a sensitivity analysis of RANS to turbulence inlet set-ups and models has been performed to check if RANS was able to predict the correct redistribution of the hot streak inside the channel. Prescribing the turbulent quantities from the LES caused immediate destruction of the swirl components and a too-high total temperature diffusion, which has been clearly evidenced by a turbulent kinetic energy budget. The calibration of the dissipation scale of turbulence, expressed in terms of μ_T/μ , allowed a trade-off between swirl and temperature. This value is a first-order parameter that drives the dynamics of the mean flow. It is based on the physical decrease of the turbulent kinetic energy. Moreover, by covering different values of the dissipation scale of turbulence, different regimes have been identified: dissipation regime (low μ_T/μ), transport regime (moderate μ_T/μ) and diffusion regime (high μ_T/μ). These regimes showed different behaviours when looking at the turbulent kinetic energy budgets. All these

results have been presented in Chapter 3. In Chapter 4, it has been shown that accounting for the anisotropy of turbulence in the RANS modelling with more advanced models (EARSM, RSM) enabled to better match the LES radial distributions by modifying the tensors alignment, but still with a value of μ_T/μ that required the same calibration than Boussinesq’s models. This has been checked by means of turbulent kinetic energy budgets and Lumley’s analysis.

Finally, in the last part of the manuscript, the FACTOR configuration has been tackled again, with the knowledge gained in the present study. Despite promising results in the academic configuration, anisotropic turbulence models did not improve the transport of temperature in the high-pressure turbine configuration, as shown in Chapter 5. This might be attributed to the very complex physics, both in the turbine stage or at the interface between the combustion chamber and the turbine. In that sense, the questioning of the representativeness of the inlet boundary conditions obtained from the experiments and imposed in the numerical simulation was the focus of Chapter 6. Many missing values have been obtained by extrapolation in the experimental campaign. The resulting steady map applied as inlet boundary conditions proved inaccurate, which demonstrates how sensitive this case is. Different hypotheses linked with this extrapolation and which could explain the misprediction of temperature have been put forward: if the presence of the boundary layers did not impact the results, the correct prescription of the temperature field at the inlet partly explained the prediction problems observed on this configuration. A final hypothesis related to the presence of an instability at the inlet of the turbine, the PVC, has been checked. Thanks to the use of a coupled combustion chamber/turbine LES of FACTOR and the SPOD, it was possible to generate an unsteady boundary condition suitable for a URANS simulation fed with the mode and frequency associated with the PVC. In that case, results showed less improvement compared to the correct prescription of the steady field. Finally, both steady and unsteady measurements comparisons have been done, where steady results were in good agreement, while unsteady results were less comparable. Note that this complex flow at the inlet of the high-pressure turbine would be less pronounced (*e.g.* fewer distortions) if a reverse-flow combustion chamber technology was used, which is not the case of FACTOR.

To conclude with the main findings of this PhD thesis, and in an attempt to classify the most predominant factors that impact the temperature transport inside the turbine stage of FACTOR, the following pyramid chart has been produced. The factors at the bottom of the pyramid have the least influence. Then, the higher in the pyramid, the greater the impact on the temperature transport.



Perspectives

Despite covering many aspects, this PhD thesis work also raised other issues which will now be detailed:

- **Complexification of the academic study:** in order to study the coupling between turbulence and hot streak segregation, it would be interesting to mirror the channel and perform a stator/rotor simulation;
- **Enrichment of the simulation of FACTOR with more technological effects:** it seems that technological effects might clearly impact the secondary flows, which, in turn, would promote a different temperature mixing. The idea would be to take correctly into account the fillets and squealer tip. Moreover, the consideration of cooling might be improved in two ways. First of all, with the current method, the patches applied at the NGVs' walls have a greater effective area than if the holes were considered, so a resizing of the patches to correct this could be applied. Moreover, turbulence could be imposed on the patches, instead of the current laminar flow. Finally, pre-swirl could be applied in the upstream and downstream rotor blade cavities. A second way to improve cooling would be to mesh each hole and the secondary air system. The CPU time would be much higher and it would be necessary to switch to unstructured meshes to cope with this kind of configuration;
- **Unsteady simulations of FACTOR with EARSM/RSM turbulence models:** the purpose of Chapter 6 was to focus on the inlet boundary conditions without concern for turbulence modelling. Anisotropic turbulence models might now be tested with the presence of cooling;
- **Comparisons of (U)RANS FACTOR's results with the LES:** in order to understand the difficulties of the (U)RANS approach, it would be interesting to compare in detail with the LES to point out the differences;
- **Deepening of the unsteady analysis:** a final perspective is related to the unsteady analyses that were performed for the first time during this PhD thesis and that deserve to be further studied. For instance, unsteady simulations performed with the use of the SPOD might be used to evaluate unsteady pressure or temperature fluctuations on the NGVs' surfaces. To enrich the simulation, it would also be possible to inject more energy at the inlet and see its impact on the dynamics of the flow. Finally, measurements of heat transfer coefficients on the NGVs' and rotor blade surfaces with infrared thermography might be available soon, which would provide a good comparison from a thermal point of view.

Publications

- **Wingel, C**, Binder, N, Bousquet, Y, Boussuge, J, Buffaz, N, & Le Guyader, S. "Influence of RANS Turbulent Inlet Set-Up on the Swirled Hot Streak Redistribution in a Simplified Nozzle Guide Vane Passage: Comparisons With Large-Eddy Simulations." Proceedings of the ASME Turbo Expo 2022: Turbomachinery Technical Conference and Exposition. Volume 10B: Turbomachinery — Axial Flow Turbine Aerodynamics; Deposition, Erosion, Fouling, and Icing; Radial Turbomachinery Aerodynamics. Rotterdam, Netherlands. June 13–17, 2022. V10BT30A002. ASME. <https://doi.org/10.1115/GT2022-78239> [139].

Part-time teacher

- Lectures and tutorials at ISAE-SUPAERO on compressible fluid mechanics, viscous fluid mechanics and turbulence, aeronautical propulsion and turbomachinery, and aerodynamics of turbomachinery.

Part IV

Appendices

Complementary elements on the academic study

Abstract

In this appendix, complementary studies on the academic case are detailed. Data on the geometry and the numerical set-up have already been presented in the manuscript in Chapter 3.

A.1 Influence of the turbulent Prandtl number	214
A.2 Slight modification of the turbulent Reynolds number	217
A.3 Effect of the mesh	218

A.1 Influence of the turbulent Prandtl number

In first order turbulence closure models, the turbulent heat flux is approximated as follows:

$$q_j^T = -\frac{\mu_T c_p}{Pr_T} \frac{\partial \tilde{T}}{\partial x_j} \quad (\text{A.1})$$

In this equation, Pr_T is the turbulent Prandtl number that is used to compare the eddy kinematic viscosity and the thermal eddy diffusivity:

$$Pr_T = \frac{\nu_T}{\alpha_T} \quad (\text{A.2})$$

Which is essential as it indicates a dissimilarity between turbulent momentum and heat fluxes. Different values of Pr_T can be found in the literature, depending on the nature of the fluid and the ambient conditions. The simplest assumption is based on the Reynolds analogy that leads to a unitary Prandtl number. Pr_T is often taken at a value of 0.9, which is the case in all the simulations presented in this PhD thesis, but its value is higher near solid walls and lower in the freestream, so that it ranges typically from 0.7 to 0.9 for water or air. As the temperature redistribution is studied in the academic case, it is also possible, when the aerodynamics is sufficiently captured, to modify the value of Pr_T . To the initial simulation with $Pr_T = 0.9$, two other simulations are realised and presented in Table A.1. Note that the ratio μ_T/μ is kept at the optimal value, *i.e.* 200.

Case	Turbulence model	T_u	μ_T/μ	P_k	Pr_T
Case 7	Wilcox $k - \omega$	11%	200	from_vorticity	0.9
Case 8	Wilcox $k - \omega$	11%	200	from_vorticity	0.8
Case 9	Wilcox $k - \omega$	11%	200	from_vorticity	0.7

Table A.1 – Test cases for the evaluation of the turbulent Prandtl number.

Profiles of Figure A.1 reveal show that decreasing Pr_T at iso-other parameters implies a higher diminution of the radial total temperature peak, since the eddy diffusivity is increased. However the aerodynamic behaviour is not impacted, which is evidenced by the evolution of the swirl angle not being modified.

The turbulent kinetic energy, resulting in the transport equation of \bar{k} does not vary, which is consistent with the RANS formalism, as evidenced by Figure A.2. Finally the thermal behaviour presented in Figure A.1b is also observable in Figure A.3 where a local evolution of total temperature in the spanwise direction at the position of the maximum total temperature is plotted. Besides presenting the diminution of maximum total temperature when Pr_T decreases, it above all shows that the spreading in the spanwise direction is not affected. We decide to keep the initial value of Pr_T , in order not to have one more parameter to adjust.

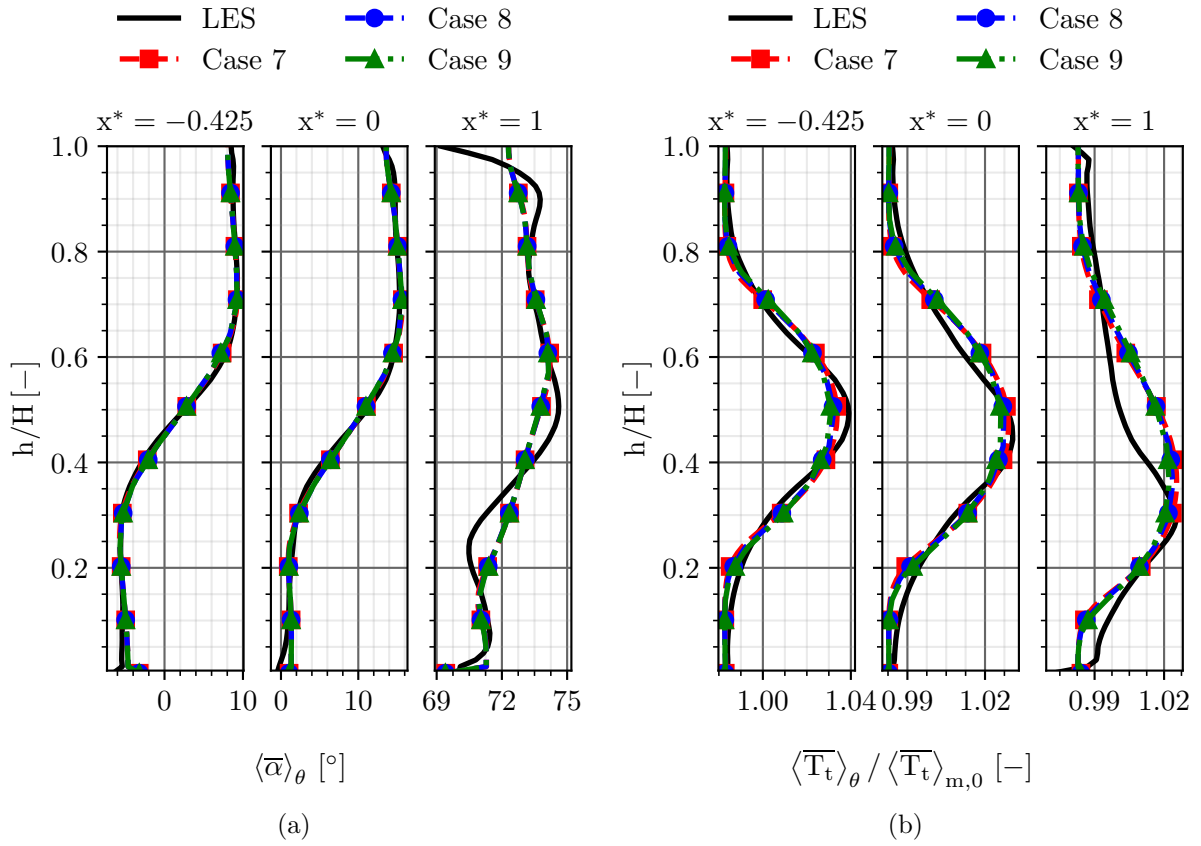


Figure A.1 – Radial profiles of $\bar{\alpha}$ (a) and $\overline{T_t}$ (b) for different turbulent Prandtl numbers.

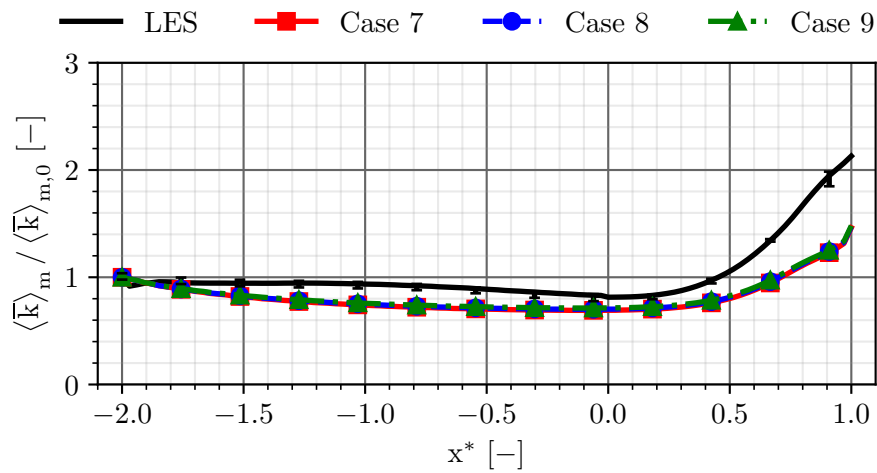


Figure A.2 – Axial evolution of \bar{k} for different turbulent Prandtl numbers.

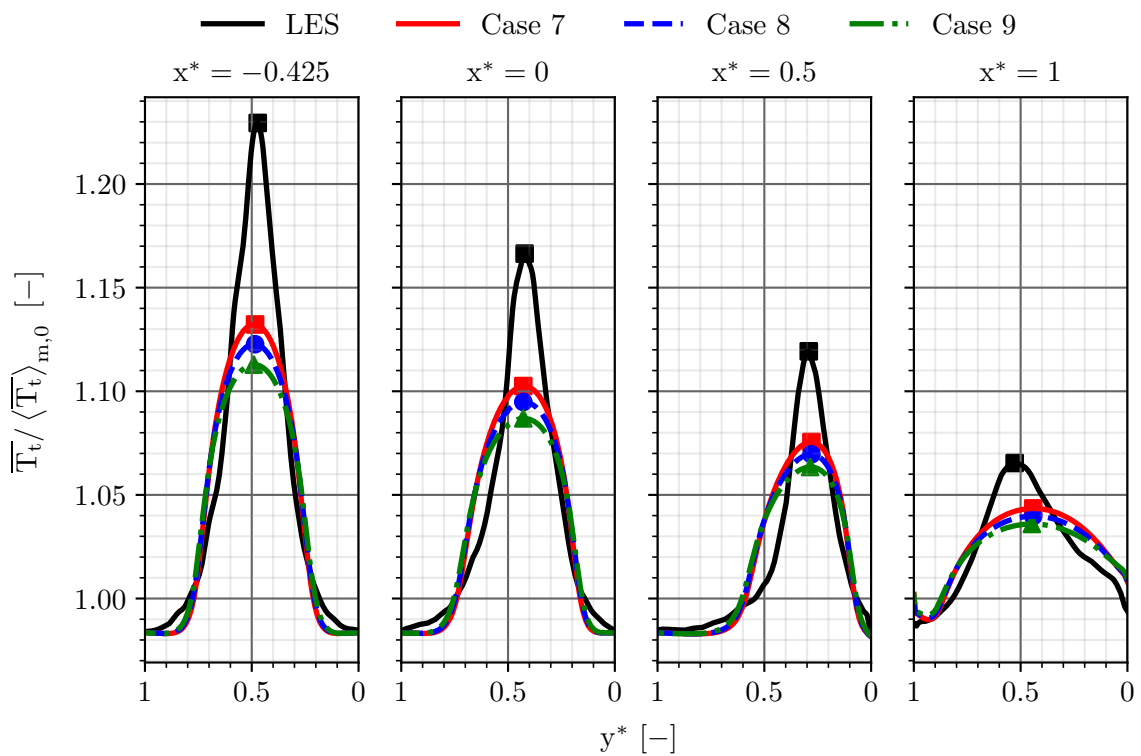


Figure A.3 – Evolution of \overline{T}_t in the spanwise direction at the $z_{T_t, max}^*$ position for different abscissa for different turbulent Prandtl numbers. The position of the maximum total temperature is localised with markers.

A.2 Slight modification of the turbulent Reynolds number

To check the sensitivity of the solution to the value of μ_T/μ , slight modifications around the optimal value are performed and are still compared to the LES and the reference Case 7. The new cases are presented in Table A.2 and Pr_T is set to its initial value of 0.9.

Case	Turbulence model	T_u	μ_T/μ	P_k	Pr_T
Case 7	Wilcox $k - \omega$	11%	200	from_vorticity	0.9
Case 10	Wilcox $k - \omega$	11%	190	from_vorticity	0.9
Case 11	Wilcox $k - \omega$	11%	300	from_vorticity	0.9

Table A.2 – Test cases for the evaluation of the turbulent viscosity.

Results are depicted in Figure A.4, Figure A.5 and Figure A.6. In that case, both the swirl angle and total temperature profiles are affected, provided the modification of the value of μ_T/μ is in the order of 100. This is normal since μ_T appears both in the momentum and energy equations, which was not the case previously with the turbulent Prandtl number. The same comment is done for the evolution of turbulent kinetic energy (Figure A.5). The modification of the spreading of the Gaussian is noticeable in Figure A.6 for $\mu_T/\mu = 300$ at the inlet. A modification in the order of 10 does not impact the results of the simulations. It is well the order of magnitude for the value of μ_T/μ that is looked for.

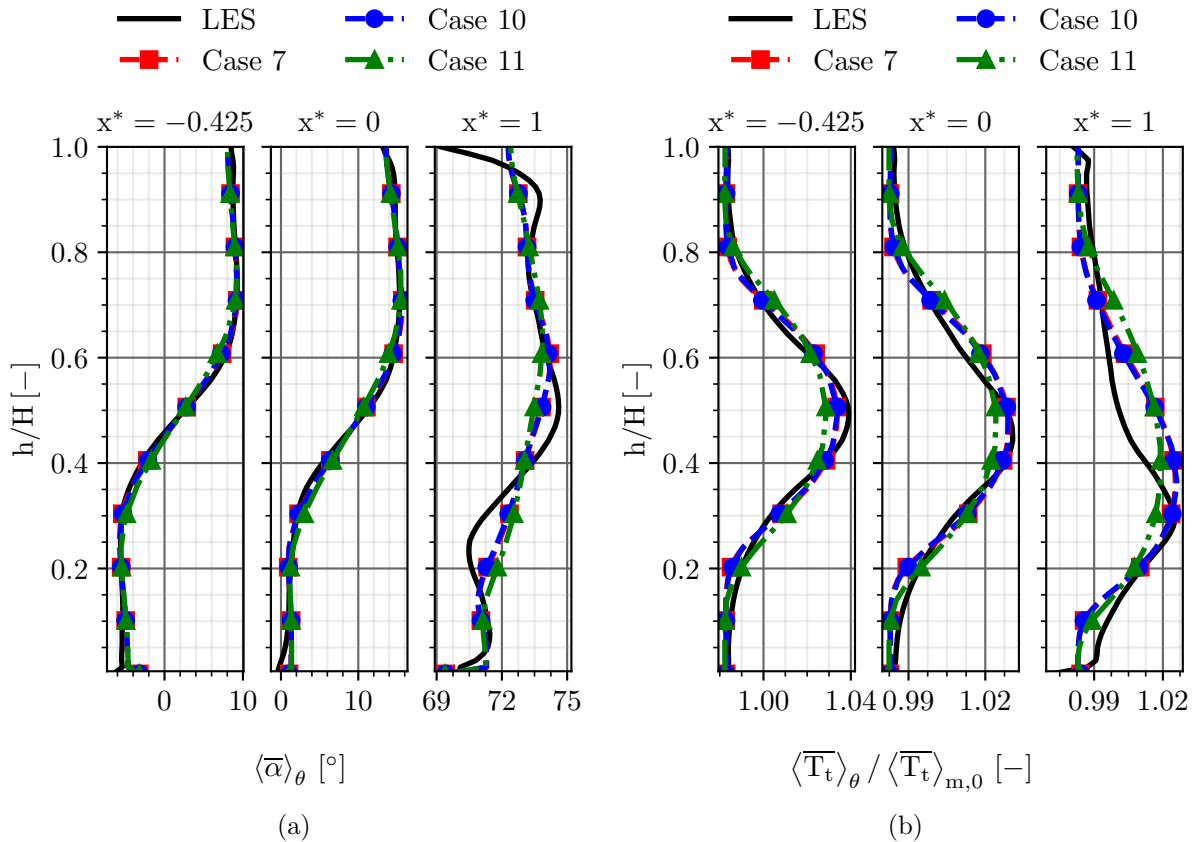


Figure A.4 – Radial profiles of $\bar{\alpha}$ (a) and \bar{T}_t (b) for different turbulent Reynolds numbers.

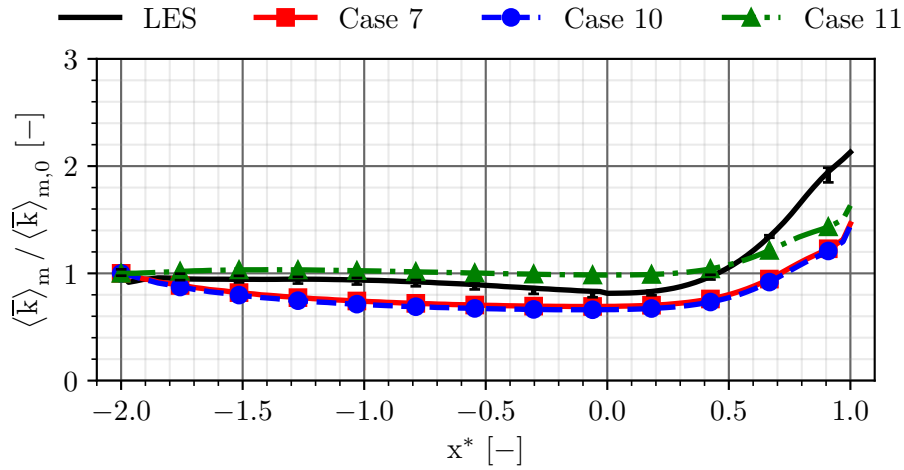


Figure A.5 – Axial evolution of \bar{k} for different turbulent Reynolds numbers.

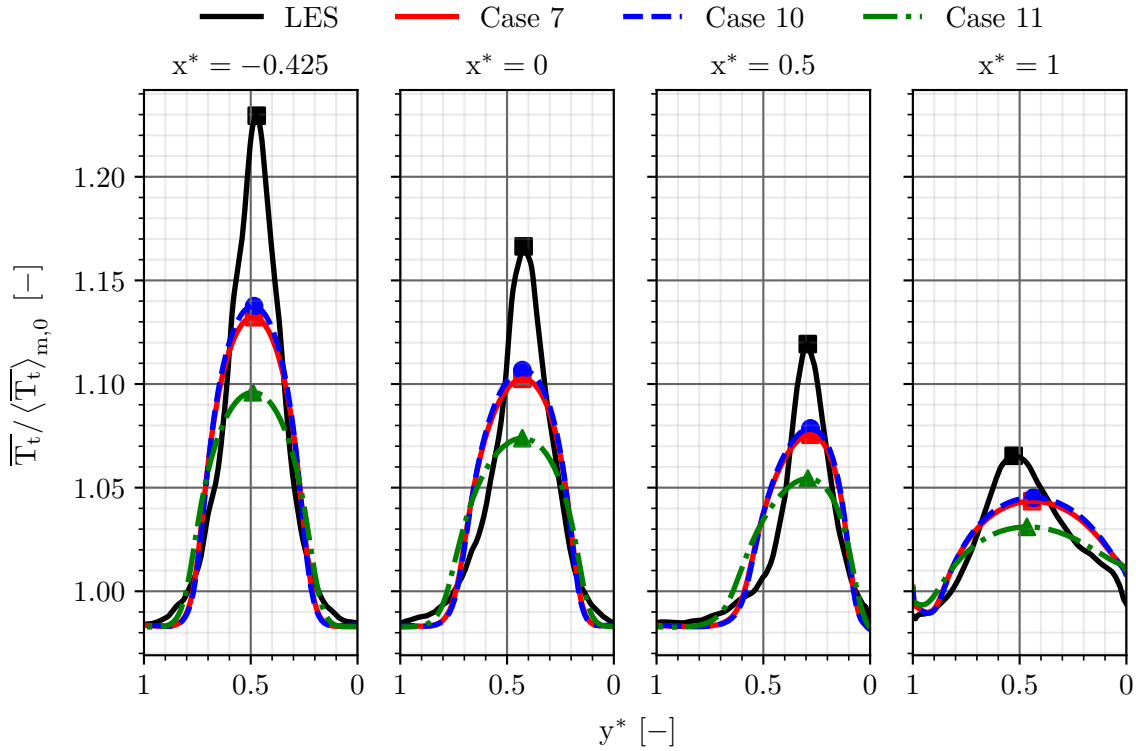


Figure A.6 – Evolution of $\overline{T_t}$ in the spanwise direction at the $z_{\overline{T_t},max}^*$ position for different abscissa for different turbulent Reynolds numbers. The position of the maximum total temperature is localised with markers.

A.3 Effect of the mesh

The mesh is isotropically coarsened to reach a reduction factor of the order of 5.7 ($\approx 7 \cdot 10^5$ cells). The number of points in the radial and spanwise directions are set accordingly to industrial practices in the context of high-pressure turbines. Figure A.7 and Figure A.8 confirm that the results obtained on the LES mesh are reproducible on a RANS mesh: of course, turbulence is slightly modified since it requires fine cells to avoid dissipation. However, swirl angle and total

temperature profiles are nearly not affected (they are modified to a lesser extent than with a modification of the turbulent Prandtl number or the value of μ_T/μ at iso-mesh resolution).

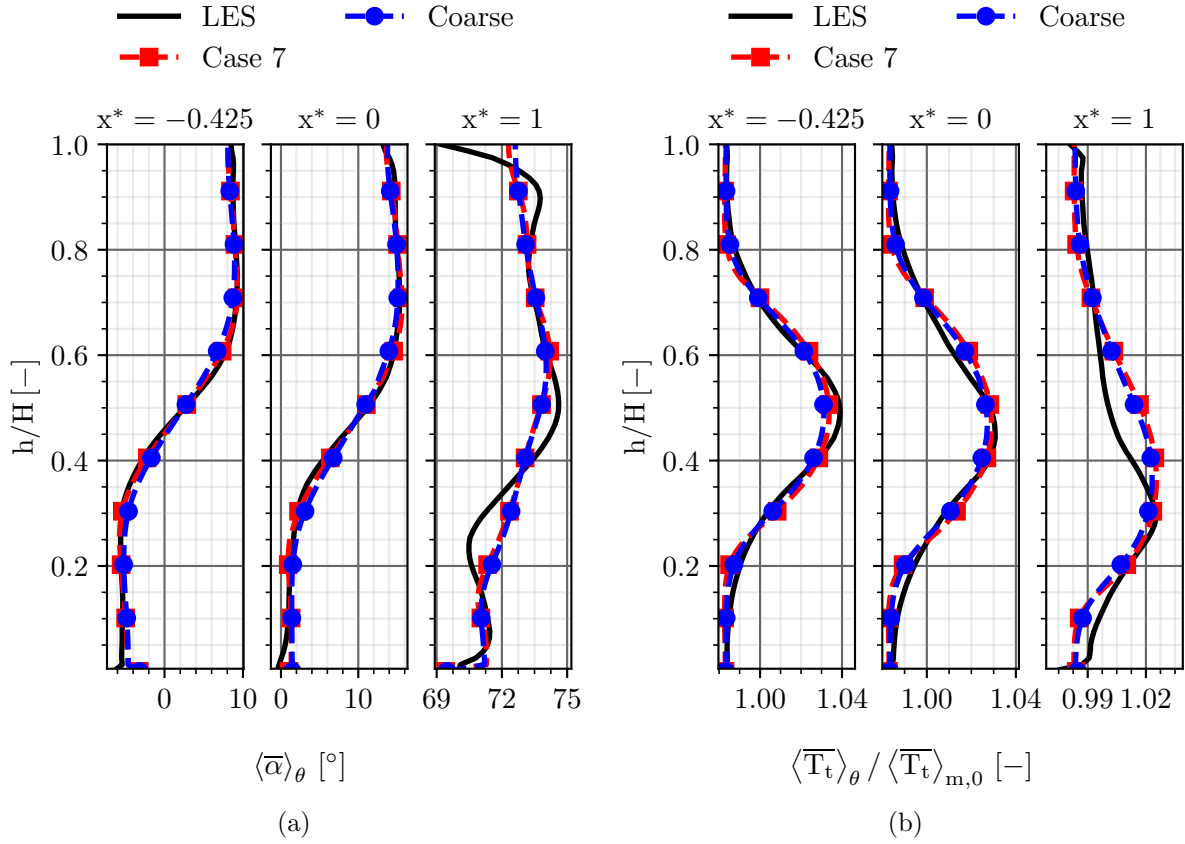


Figure A.7 – Radial profiles of $\bar{\alpha}$ (a) and $\overline{T_t}$ (b) for different meshes.

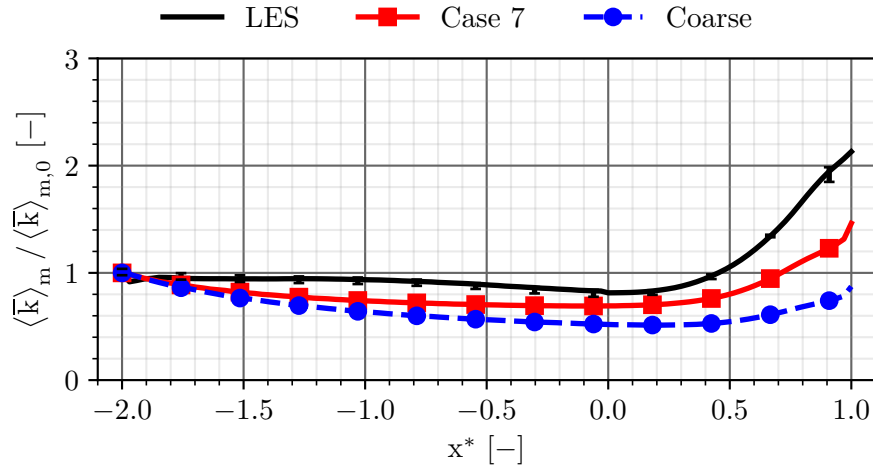


Figure A.8 – Axial evolution of \bar{k} for different meshes.



Complementary analyses of FACTOR's configuration

Abstract

In this appendix, complementary analyses of FACTOR's configuration are detailed. Data on the geometry and the numerical set-up have already been presented in the manuscript in Chapter 2. The results given in this appendix are auxiliary to those presented in Chapter 5 and Chapter 6.

B.1	y^+ distributions on the walls	222
B.2	Mesh refinement effect	223
B.3	Effect of the wall boundary condition for the specific turbulence dissipation rate	224
B.4	Zheng limiter	226
B.5	Influence of the SST correction	227
B.6	Imposition of the turbulent kinetic energy from a LES	229
B.7	Radial distributions of the sensitivity study for errors of type 'c'	230
B.8	Radial distributions with the SST $k - \omega$ turbulence model and the inlet map from the LES	234

B.1 y^+ distributions on the walls

In order to assess the quality of the resolution of the viscous sub-layer for a wall-resolved simulation, the dimensionless wall distance y^+ is represented on the rotor blade surface (Figure B.1), on the endwalls of the static row (Figure B.2) and on the endwalls of the moving row (Figure B.3).

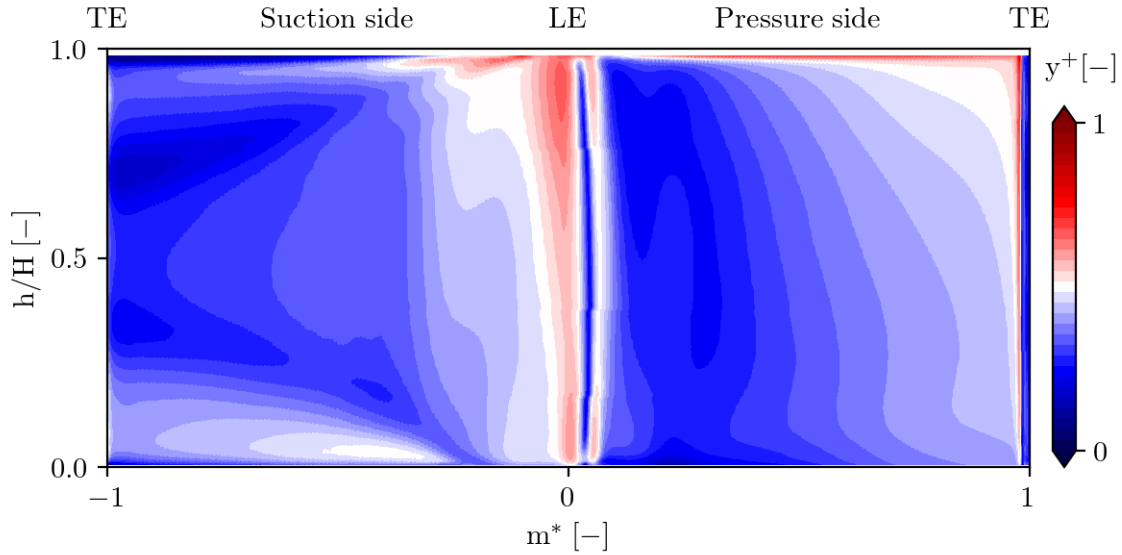


Figure B.1 – y^+ distribution on the unwrapped rotor blade of FACTOR.

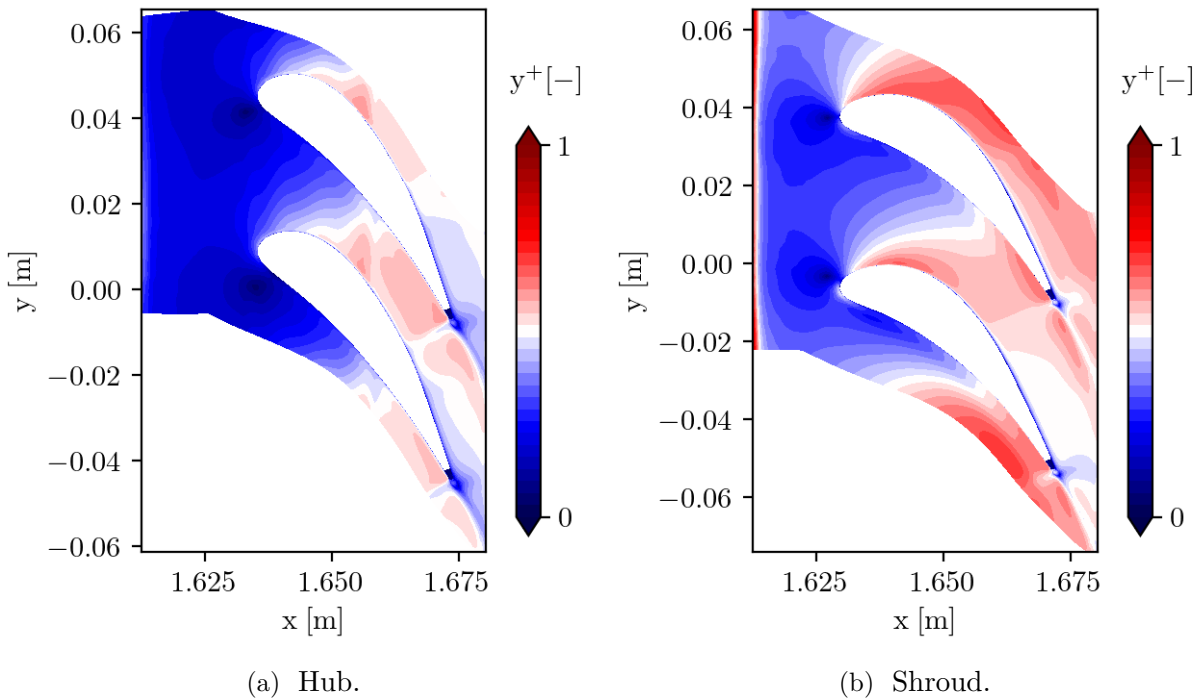


Figure B.2 – y^+ distribution on the hub and shroud walls of the static row.

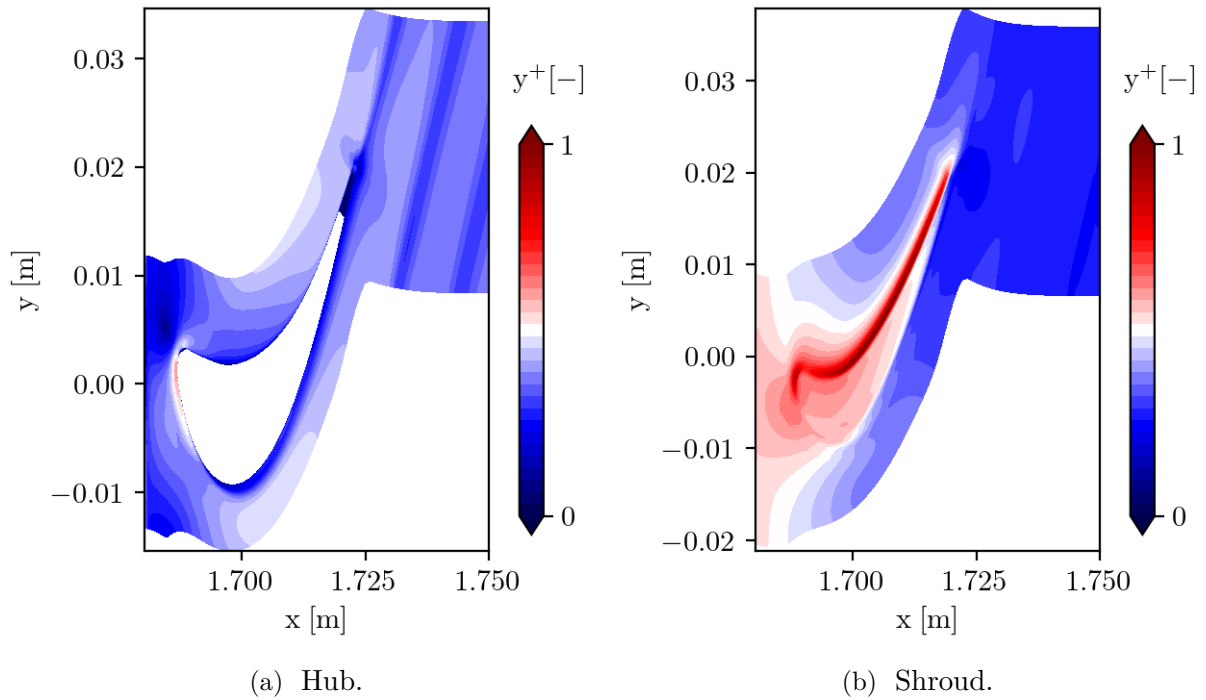


Figure B.3 – y^+ distribution on the hub and shroud walls of the moving row.

B.2 Mesh refinement effect

This mesh convergence study comes from an internal study performed at Safran Helicopter Engines. The nominal mesh is isotropically refined to have twice as many points, and $y^+ = 0.5$ is adopted at the walls. RANS mixing-plane simulations (2 vanes/1 blade configuration) are done. Radial distributions are depicted in Figure B.4 and wall temperature differences in Figure B.5.

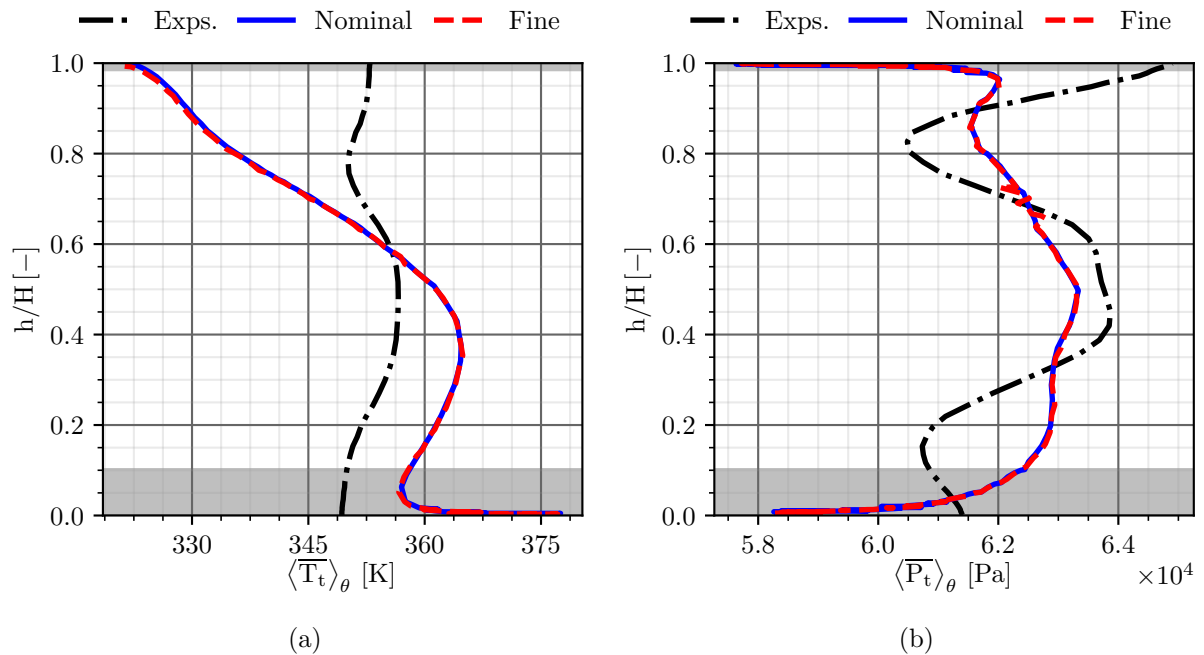


Figure B.4 – Radial profiles of \overline{T}_t (a) and \overline{P}_t (b) for two different meshes at P42.

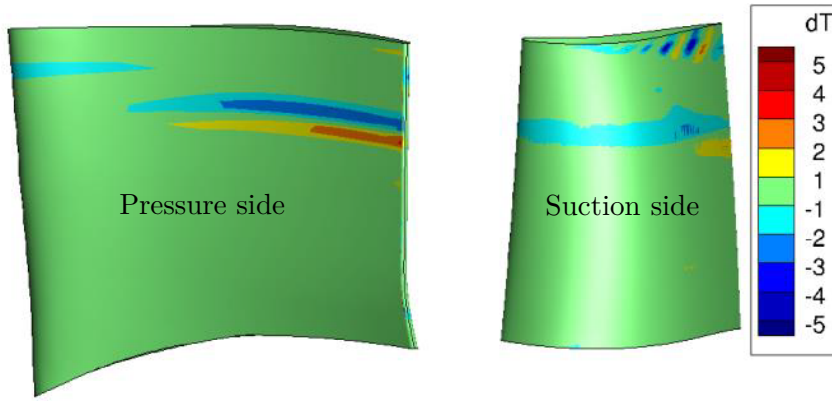


Figure B.5 – $dT = T_{s,fine} - T_{s,nominal}$ on the NGV's walls.

The mesh refinement effect confirms that there is no impact either on the radial profiles or on the static temperature distribution on the walls: the nominal mesh is kept for the rest of the study on FACTOR's configuration.

B.3 Effect of the wall boundary condition for the specific turbulence dissipation rate

Contrary to the $k - l$ or $k - \epsilon$ turbulence models where both l and ϵ are set to 0 on the walls, for the $k - \omega$ turbulence models, ω must be specified with care. If no specific treatment is performed, its value tends to infinity as the inverse of the square of the wall distance η_w :

$$\lim_{\eta_w \rightarrow 0} \omega = \frac{6\nu}{C\eta_w^2} \quad (\text{B.1})$$

Following ONERA's recommendations, a linear extrapolation is used. The value of ω is extrapolated to the wall by using a first-order extrapolation of the slope of ω from Equation B.1. The first-order extrapolation is used to impose the correct value of the gradient of ω which is used to estimate the ω diffusive flux at the wall. This treatment is named '*linear_extrap*' in *elsA*. Other treatments are available and enumerated hereafter using the naming of *elsA*:

- '*pseudo_rough*': a pseudo rough wall condition is used to set ω at the wall. This condition takes into account the effects of wall roughness;
- '*quadratic_extrap*': a second-order extrapolation is applied;
- '*cubic_extrap*': a third-order extrapolation is used.

More details can be found both in the theoretical manual and user manual of *elsA*. The treatments require a refined mesh at the walls *i.e.* $y^+ \leq 1$ in order for the center of the first cell to be at $y^+ \leq 0.5$. All these wall treatments have been tested with the Wilcox $k - \omega$ turbulence model. Results plotted in Figure B.6 and Figure B.7 show an independence of the evolutions with the different wall treatments for ω . Only a slight difference is observable on the evolution of \bar{k} using a pseudo rough wall condition.

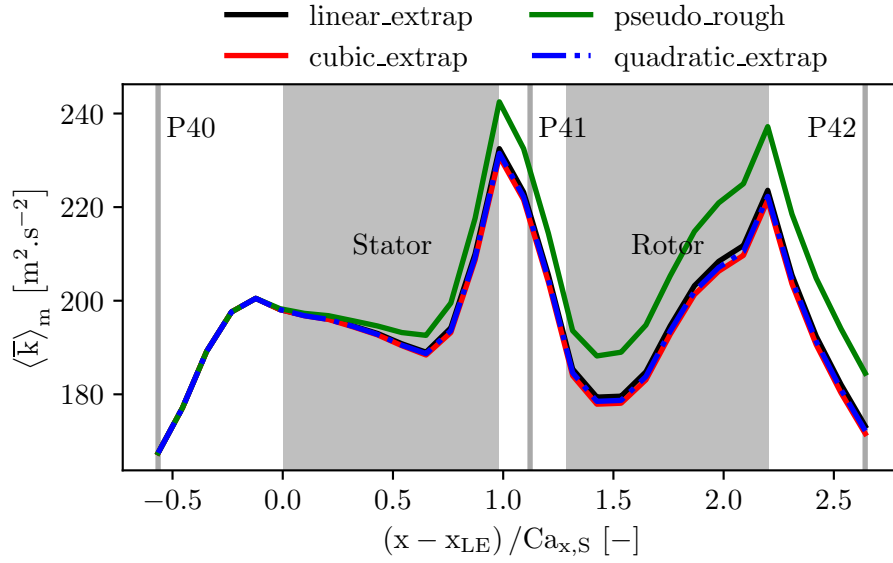


Figure B.6 – Axial evolution of mass-weighted average turbulent kinetic energy for different wall treatments for ω . The position of the stator and rotor is represented with grey zones and the reference planes with grey vertical lines.

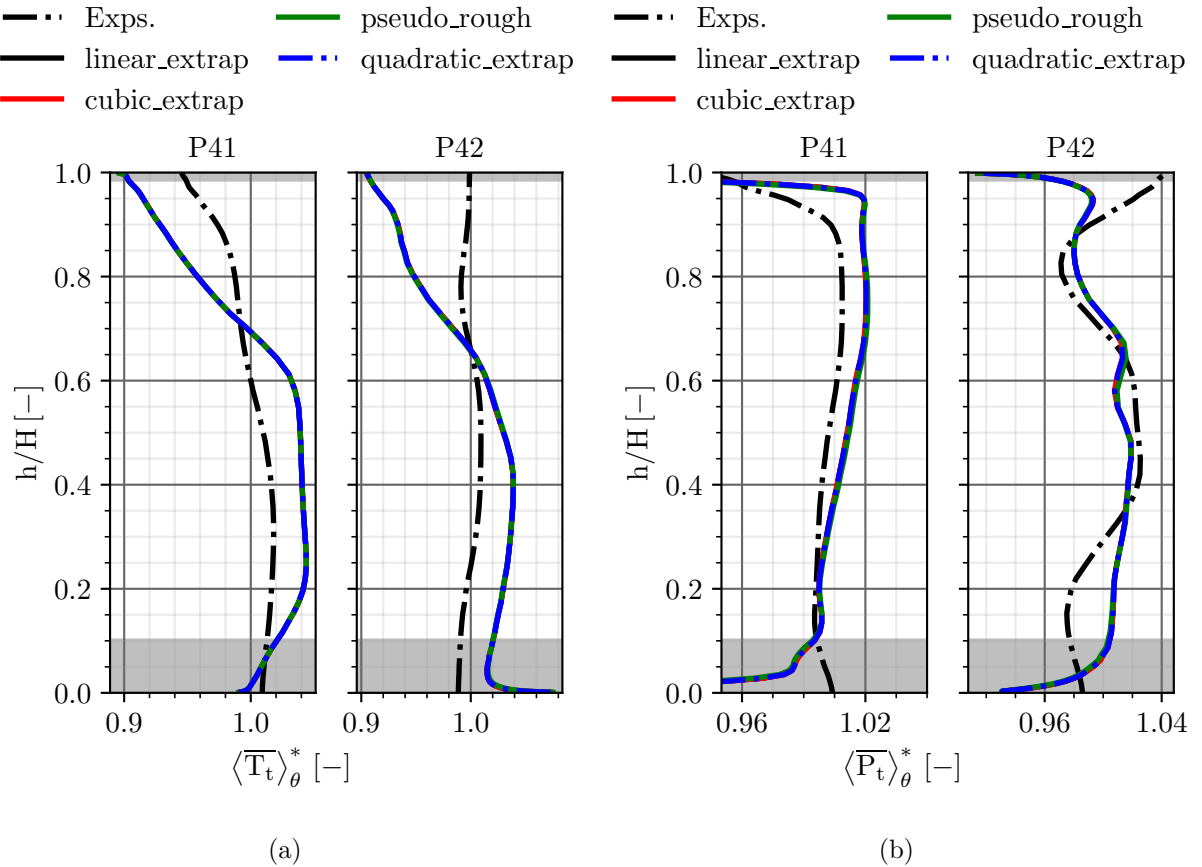


Figure B.7 – Influence of the wall treatment for ω on the radial profiles of \overline{T}_t (a) and \overline{P}_t (b) for steady SV simulations.

B.4 Zheng limiter

The Zheng limiter [143] locally bounds the μ_T/μ level in order to satisfy the Schwarz inequalities for the Reynolds stress tensor components:

$$\overline{\rho v'_i v'_j} \leq \sqrt{\overline{\rho v'_i v'_i} \cdot \overline{\rho v'_j v'_j}} \quad (\text{B.2})$$

Which corresponds for the Reynolds stresses to:

$$\sqrt{\overline{\tau_{ij}^R \tau_{ij}^R}} \leq 2\bar{\rho}k \quad (\text{B.3})$$

Equation B.3 can be rewritten in the following form using Boussinesq's hypothesis:

$$\frac{\mu_T}{\bar{\rho}k} \sqrt{2 \left(\widetilde{S}_{ij} - \frac{1}{3} \frac{\partial \widetilde{v}_k}{\partial x_k} \delta_{ij} \right) \frac{\partial \widetilde{v}_i}{\partial x_j}} \leq \frac{2}{\sqrt{3}} \quad (\text{B.4})$$

Depending on the turbulence model, the maximum value for μ_T gives a lower or upper limit for the second turbulent variable. The limiter is active in all parts of the domain, inside and outside the boundary layer. The Zheng limiter is applied on the Wilcox $k - \omega$ turbulence model, meaning a lower bound for ω is given. The effect of the limiter can be observed in Figure B.8 and Figure B.9, where a very limited impact on the radial profiles is noted. With the Zheng limiter active, the values of \bar{k} are much lower.

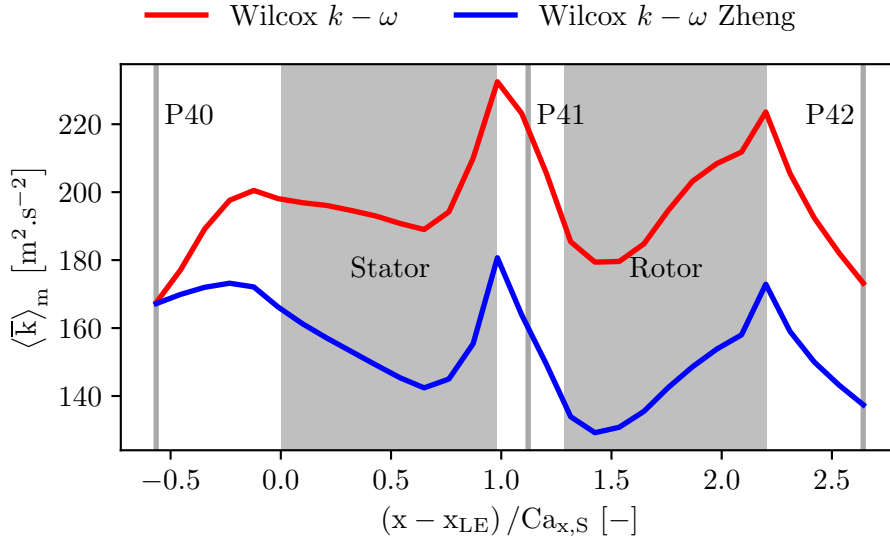


Figure B.8 – Axial evolution of mass-weighted average turbulent kinetic energy using the Zheng limiter. The position of the stator and rotor is represented with grey zones and the reference planes with grey vertical lines.

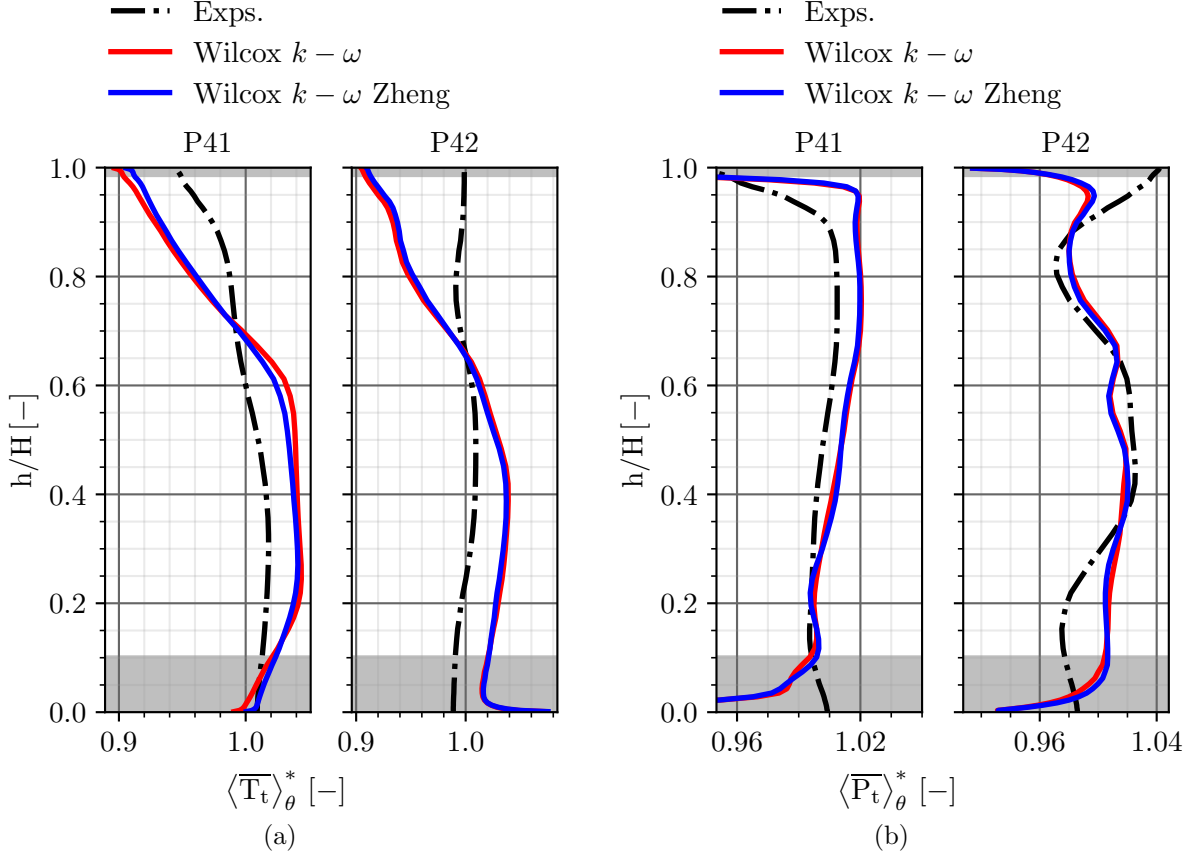


Figure B.9 – Influence of the Zheng limiter on the radial profiles of \overline{T}_t (a) and \overline{P}_t (b) for steady SV simulations.

B.5 Influence of the SST correction

Different types of SST corrections are tested on the Wilcox $k - \omega$ turbulence model, which means that there is no F_1 damping function as for the Menter $k - \omega$ BSL turbulence model [80], for which $F_1 = 1$ leads to the use of the Wilcox $k - \omega$ model [137] and $F_1 = 0$ leads to the use of the modified $k - \epsilon$ Launder-Sharma model [66]. These corrections limit the value of the eddy-viscosity. The SST correction on the Wilcox $k - \omega$ turbulence model presented in Chapter 5 and labelled '*wilcox2006*' does not involve the F_2 damping function, allowing the correction to be active both inside and outside the boundary layer [138]. The damping functions F_1 and F_2 can be found in the original paper of Menter [80]. For the SST corrections presented below, however, the F_2 damping function is present:

- '*standard*': standard SST correction based on the vorticity, as presented by Menter [80];
- '*standard_zheng*': same as the previous one but with the Zheng limiter which is only activated inside the boundary layer with the function F_2 [143];
- '*std_sij*': the limiter is written with the strain-rate tensor;
- '*std_sij_zheng*': the limiter is written with the strain-rate tensor and the Zheng limiter.

The standard SST correction based on the vorticity is written for instance as:

$$\mu_T = \frac{a_1 \bar{\rho} k}{\max(a_1 \omega; \Omega F_2)} \quad (\text{B.5})$$

Where $\Omega = \sqrt{2\Omega_{ij}\Omega_{ij}}$. Despite presenting some differences on the evolution of \bar{k} (Figure B.10), the problem of temperature transport inside the turbine stage is not solved when using different SST corrections (Figure B.11).

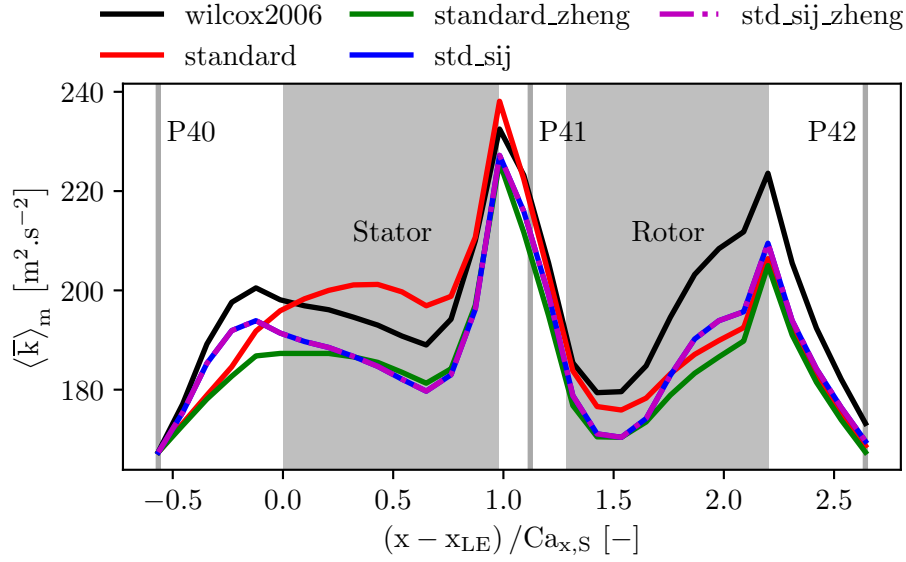


Figure B.10 – Axial evolution of mass-weighted average turbulent kinetic energy for different SST corrections. The position of the stator and rotor is represented with grey zones and the reference planes with grey vertical lines.

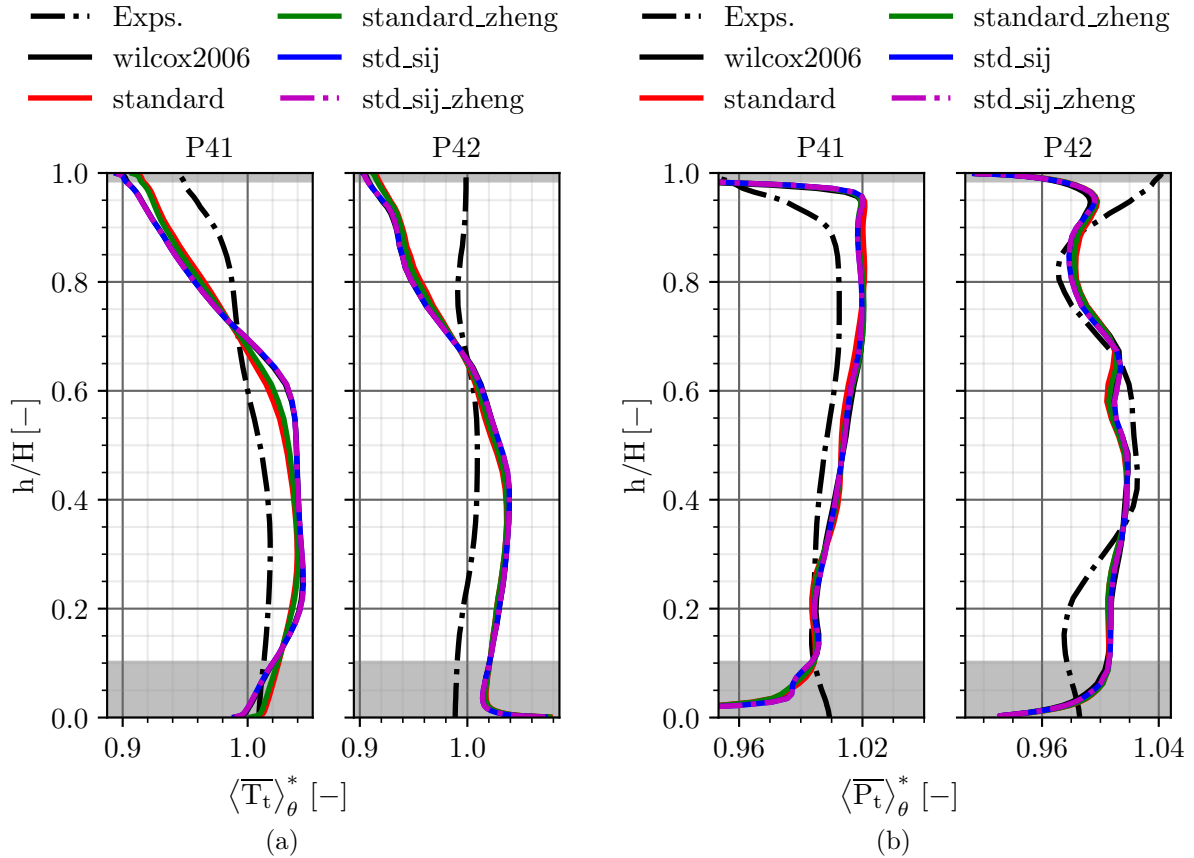


Figure B.11 – Influence of the SST correction on the radial profiles of \bar{T}_t (a) and \bar{P}_t (b) for steady SV simulations.

B.6 Imposition of the turbulent kinetic energy from a LES

Previous LES realised during the project comprising both the combustion chamber and the high-pressure turbine revealed an overestimation of the value of turbulence kinetic energy at P40 compared to the experiments [60, 73]. The average value at P40 from the LES is $328 \text{ m}^2 \cdot \text{s}^{-2}$, while the experiments give a value of $168 \text{ m}^2 \cdot \text{s}^{-2}$. It is proposed here to scale the field of \bar{k} at P40 to match the LES. This new case is compared to the reference case using the value from the experiments.

Results are plotted in Figure B.12 for the turbulence kinetic energy and in Figure B.13 for the radial profiles of total temperature and total pressure. The Smith $k-l$ turbulence model is used without any limiter. Not surprisingly, the evolution of \bar{k} inside the high-pressure turbine stage is impacted by its value at the inlet, as shown in Figure B.12, especially in the stator domain. However, no clear differences are noticeable on the radial profiles: the transport of temperature is not improved when using the turbulence characteristics from a LES.

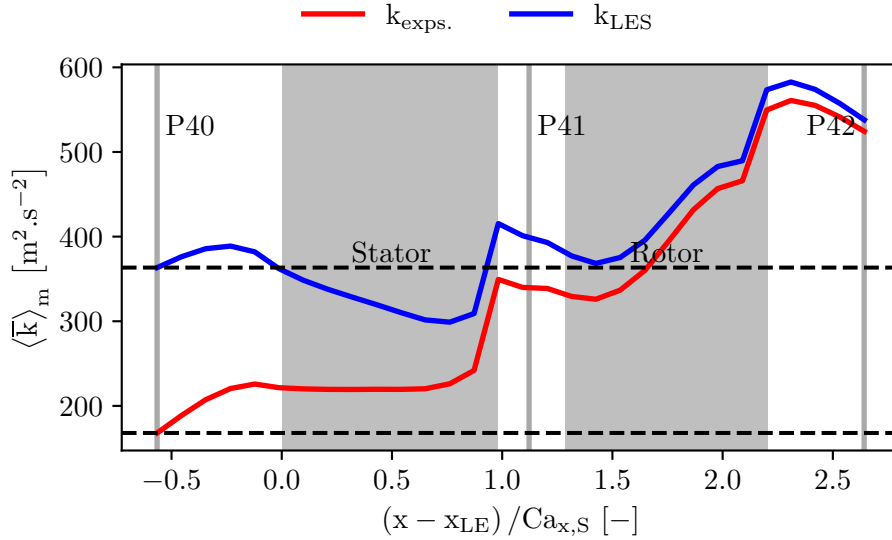


Figure B.12 – Axial evolution of mass-weighted average turbulent kinetic energy for different values of \bar{k} at the inlet. The position of the stator and rotor is represented with grey zones and the reference planes with grey vertical lines.

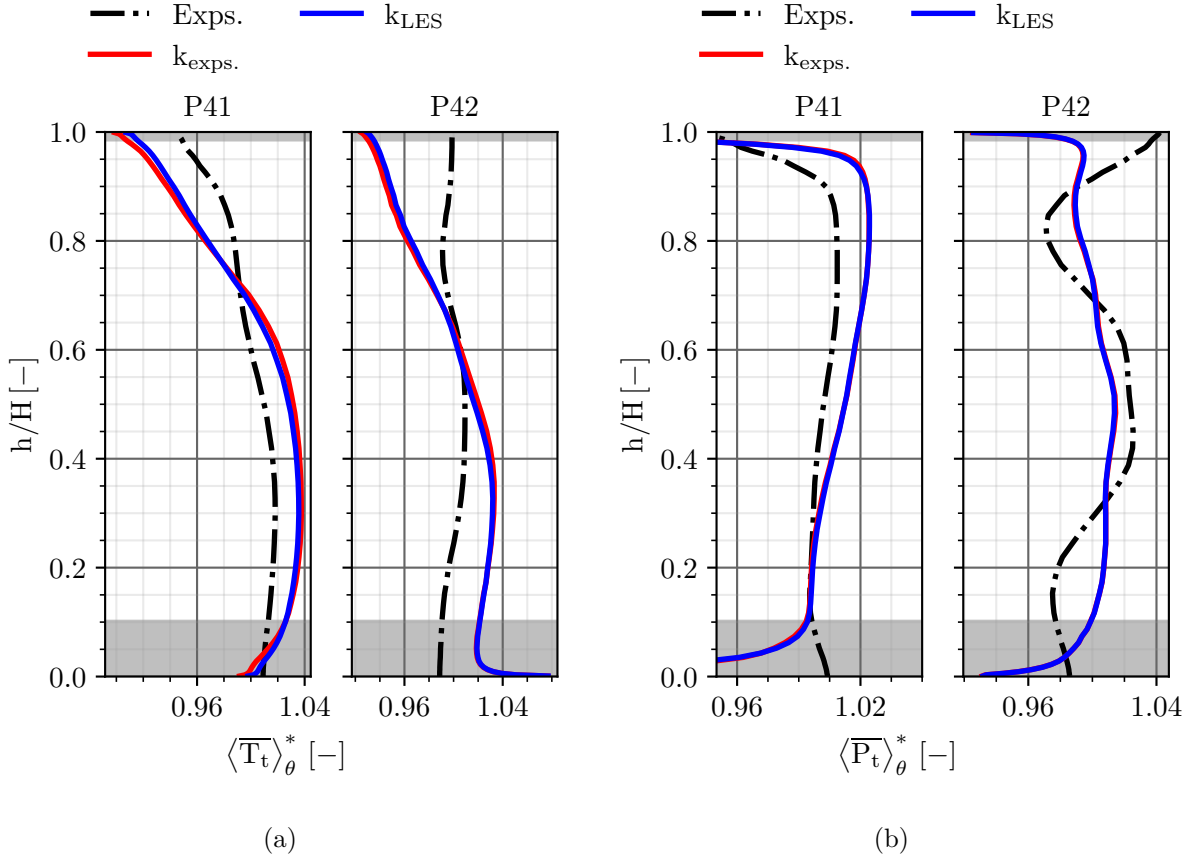


Figure B.13 – Influence of inlet value of \bar{k} on the radial profiles of \overline{T}_t (a) and \overline{P}_t (b) for steady SV simulations.

B.7 Radial distributions of the sensitivity study for errors of type 'c'

Radial distributions of the sensitivity study to the inlet flow variables are presented in the following. As a reminder, the test cases matrix is presented in Table B.1.

First of all, the pitch angle is evaluated and is taken from the LES (Case D). The three remaining quantities are kept from the experiments. Figure B.14 shows that the swirl angle is not affected by this modification. Total temperature is slightly affected. The same comments are made for Case E in Figure B.15 where total pressure is modified. Total temperature is even less affected than previously. The prescription of total temperature from the LES (Case L) dramatically improves the temperature transport, both at P41 and P42, where the distributions are closer to the experiments as depicted in Figure B.16. This observation confirms that errors of type 'c' due to the high flow angles at the inlet have a strong impact on the quality of the results. Finally, combining both the swirl angle and total temperature from the LES does not change significantly the distributions (Case M in Figure B.17) compared to the standalone total temperature, while combining both the pitch angle and total temperature (Case O in Figure B.18) leads to a very satisfactory result. Of course, the best set-up is retrieved when all the quantities are extracted from the LES and imposed at P40.

Case	P_t	T_t	α	ϕ
A	1	1	1	1
B	0	0	1	0
C	0	0	1	1
D	0	0	0	1
E	1	0	0	0
F	1	0	1	0
G	1	0	1	1
H	1	0	0	1
I	1	1	0	0
J	1	1	1	0
K	1	1	0	1
L	0	1	0	0
M	0	1	1	0
N	0	1	1	1
O	0	1	0	1
P	0	0	0	0

Table B.1 – Test cases matrix for the impact of the inlet boundary condition at P40 - '0' comes from the experiments and '1' comes from the LES.

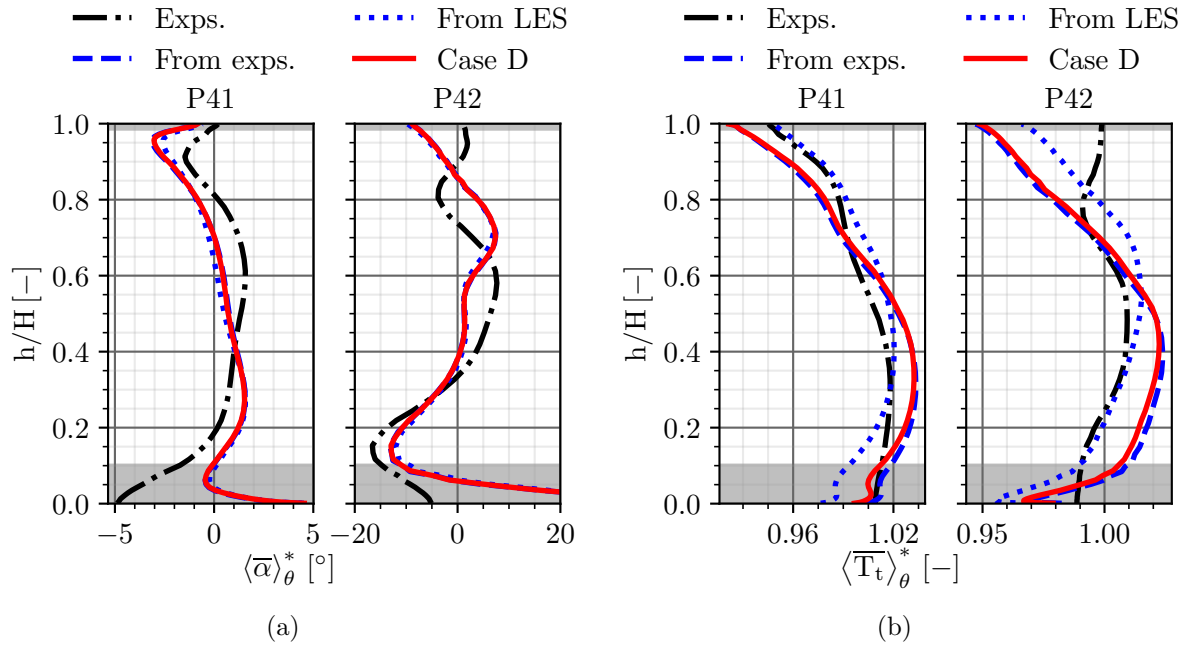


Figure B.14 – Results of Case D for $\bar{\alpha}$ (a) and \bar{T}_t (b) - Exps.: P_t , T_t , α and LES: ϕ .

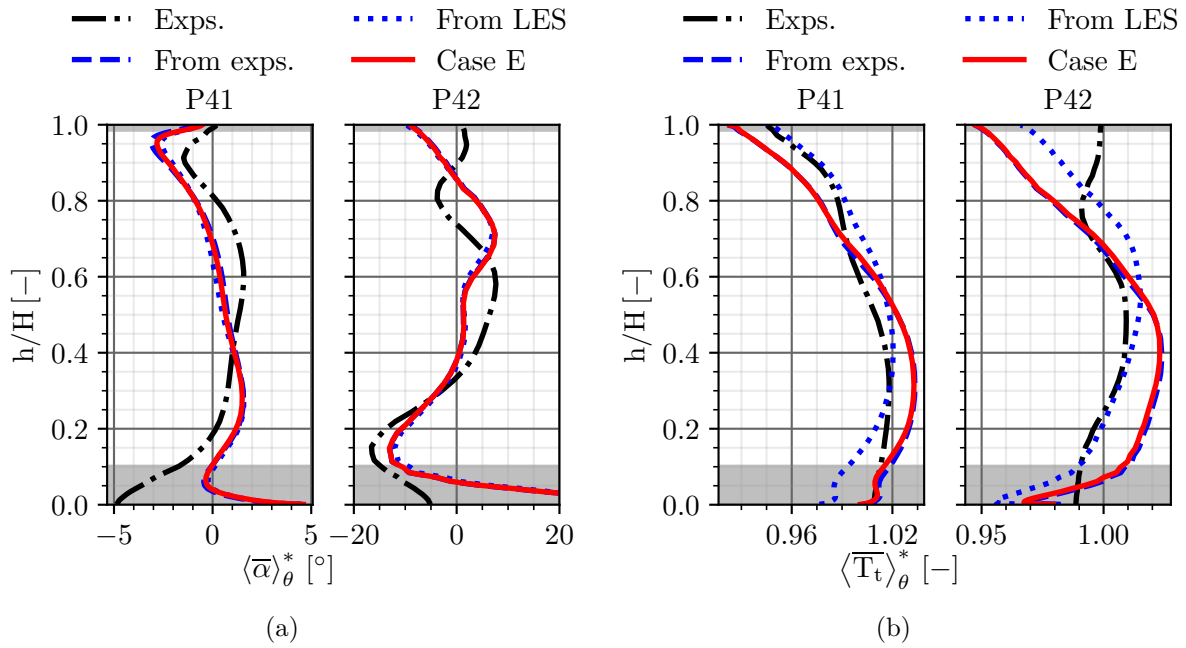


Figure B.15 – Results of Case E for $\bar{\alpha}$ (a) and \bar{T}_t (b) - Exps.: T_t , α , ϕ and LES: P_t .

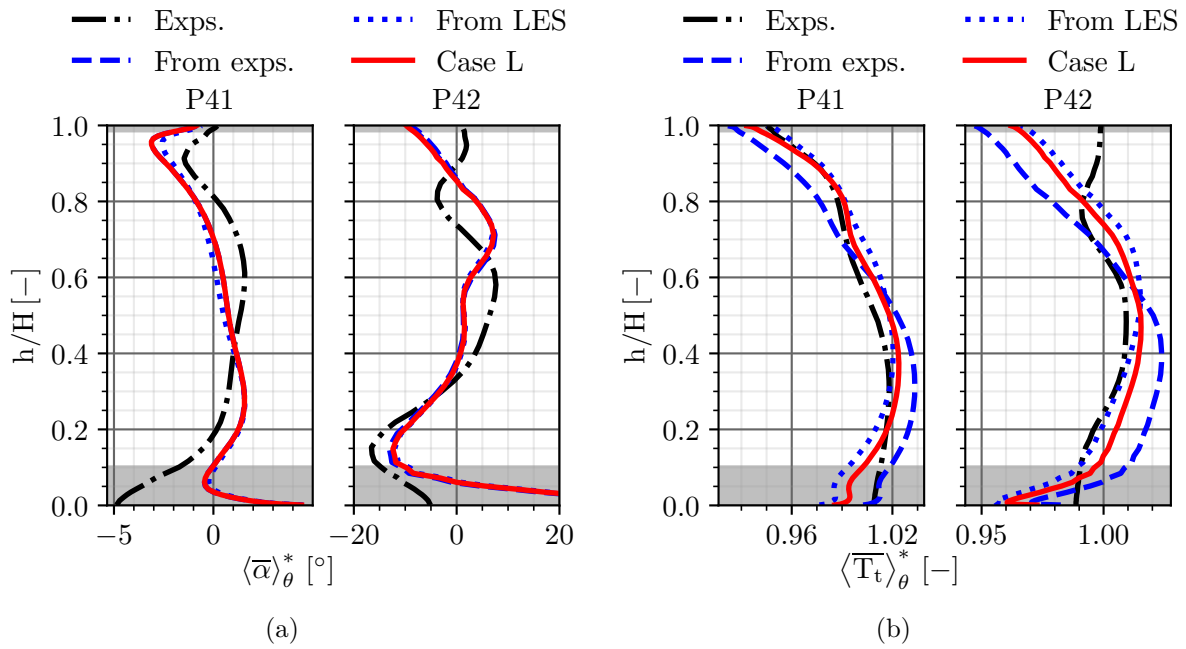


Figure B.16 – Results of Case L for $\bar{\alpha}$ (a) and \bar{T}_t (b) - Exps.: P_t , α , ϕ and LES: T_t .

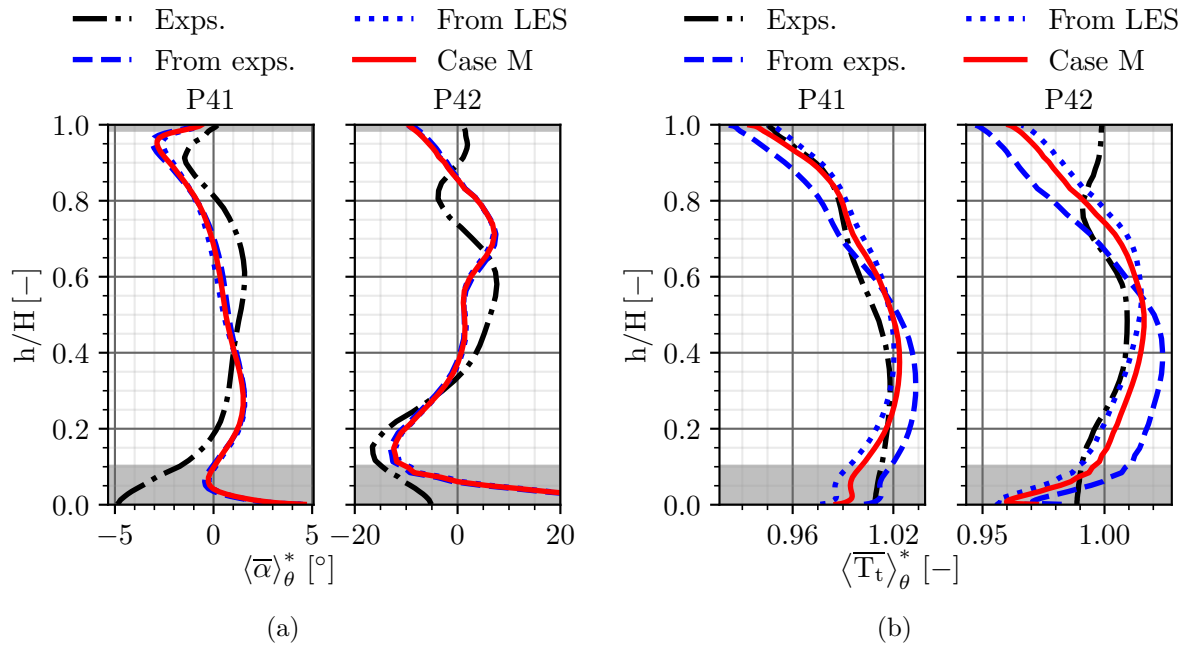


Figure B.17 – Results of Case M for $\bar{\alpha}$ (a) and \bar{T}_t (b) - Exps.: P_t, ϕ and LES: T_t, α .

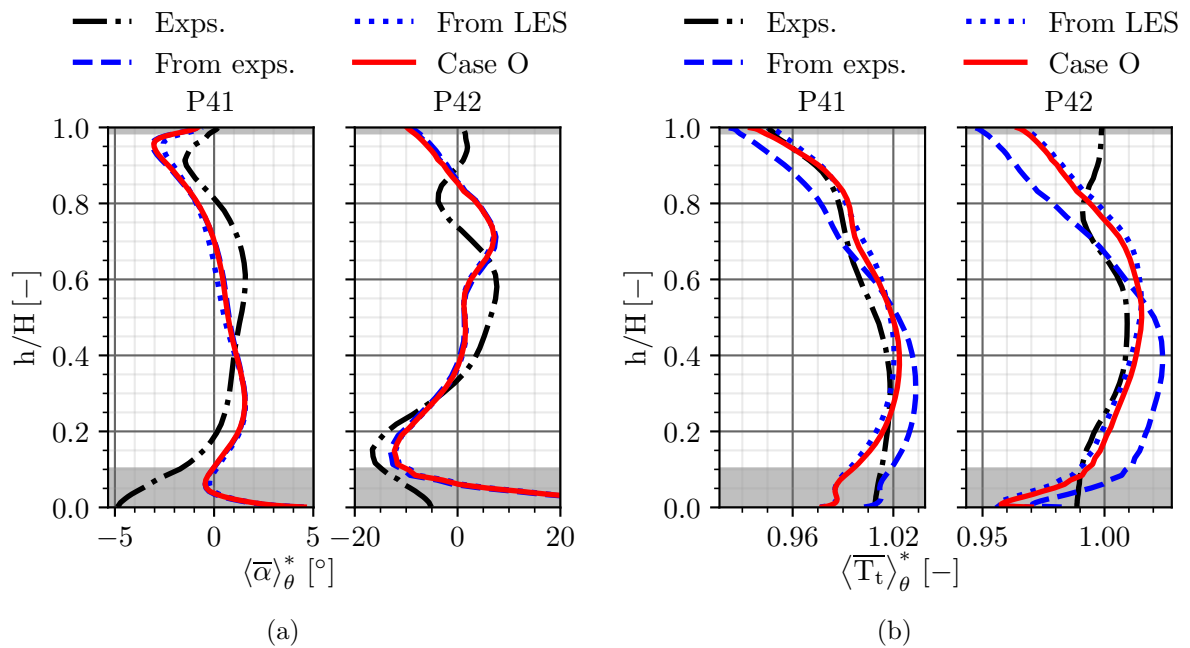


Figure B.18 – Results of Case O for $\bar{\alpha}$ (a) and \bar{T}_t (b) - Exps.: P_t, α and LES: T_t, ϕ .

B.8 Radial distributions with the SST $k - \omega$ turbulence model and the inlet map from the LES

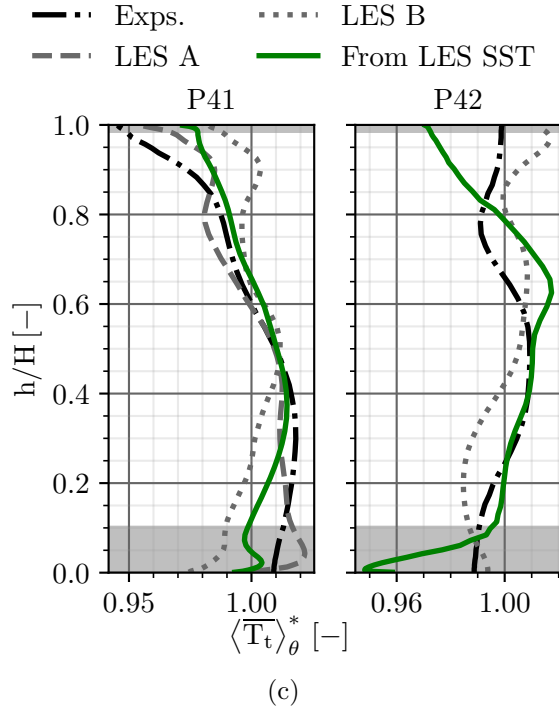
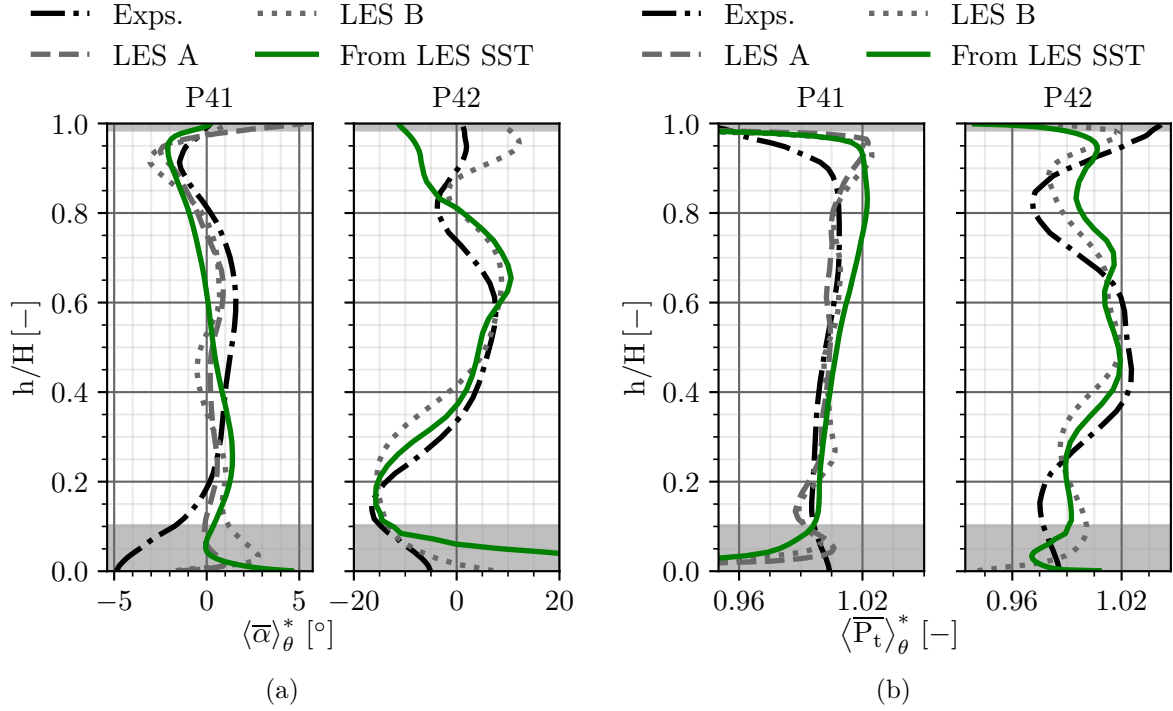


Figure B.19 – Radial distributions of $\bar{\alpha}$ (a), \bar{P}_t (b) and \bar{T}_t (c) when using the steady inlet map from the LES and the SST $k - \omega$ turbulence model. Plots in terms of distortions.

List of Figures

1	Aviation CO ₂ emissions from 1940 to 2018 expressed as a fraction of the total anthropogenic CO ₂ emissions. Adapted from Lee <i>et al.</i> [67].	2
2	Theoretical (black) and real (blue, red) Brayton cycle (a) and evolution of the thermal efficiency with the overall pressure ratio for different values of turbine inlet temperature (b).	3
3	The high-pressure turbine is a component of complex physics.	4
4	Hierarchy of governing equations along the years (left) and CFD contribution of the Airbus A380 (right). From Jameson [53].	5
1.1	Unsteady flow structures with a variation of five or six orders of magnitude in space and time [63].	12
1.2	Unsteady phenomena in turbomachines - Adapted from Callot [17].	13
1.3	Time-averaged surface temperature for a rotor mid-span section - Dorney <i>et al.</i> [27].	14
1.4	Wake transport mechanism in a high-pressure turbine stage evidenced by the entropy field - From Gaetani [39].	15
1.5	Experimental and LES comparisons of swirl (a) and temperature fields (b) - From Koupper [60].	16
1.6	CO ₂ concentration at the inlet (a) and outlet (b) of the NGV passage - From Butler and Sharma [15].	17
1.7	Iso-contour of total temperature at 470 K for two clockings [60].	18
1.8	Typical turbulence field at the inlet of a high-pressure turbine (a) and effect of the turbulence intensity on the temperature peak (b).	19
1.9	Schematic view of the secondary flow structures in axial turbines [44].	20
1.10	Schematic view of a tip leakage vortex (a) and numerical simulation for a tip gap height of 1% of span (b) [10, 134]	20
1.11	Cooling architecture of a high-pressure turbine NGV [46, 118].	21
1.12	Secondary air system in a turbine (a) and rim seal interface (b) - From the <i>Jet Engine</i> [118].	22
1.13	Comparison of the viscosity laws.	24
1.14	Reynolds number evolution in a medium-sized gas turbine engine. Adapted from Mayle [76].	25

1.15	Turbulence energy spectrum and energy cascade together with the different levels of modelling.	26
1.16	Scale separation by the mesh in physical (a) and spectral (b) domains. Adapted from Sagaut [98].	27
1.17	Difference between an unsteady turbulent flow (a) and a steady turbulent flow (b) for a pressure probe signal.	30
1.18	Schematic view of the space-time periodicity of the flow.	37
2.1	NO _x are produced at high temperature close to stoichiometry. Adapted from Foust <i>et al.</i> [38].	43
2.2	Meridional view of the full-annular FACTOR configuration with the positioning of the measurement planes of interest.	44
2.3	Trisector (a) and full-annular (b) test rigs respectively installed at UNIFI and DLR.	45
2.4	Comparison of the normalised temperature distributions at P40 between experiments and standalone combustor simulations [22].	47
2.5	NGVs' adiabatic wall temperature - Comparisons between a full SAS-SST combustor/turbine simulation and an isolated RANS simulation with the inlet boundary condition from a SAS-SST simulation [22].	48
2.6	Visualization of vortex structures in the NGV passage using an isosurface of Q-criterion (10^8) on solutions averaged over 40 ms [121].	48
2.7	Evolution of the turbulent kinetic energy upstream of the NGV of FACTOR for different values of dissipation. Reproduced from Vagnoli <i>et al.</i> [129].	49
2.8	Turbulence intensity on P40 (a) and PSD of turbulent kinetic energy at point 1 (b).	52
2.9	5HP results obtained for the pitch angle (a) and results of INPAINTN interpolation for the total temperature at P40 (b). Yellow lines delineate measured and interpolated zones [62].	53
2.10	Errors on the Mach number and swirl angle for the 5HP [62].	53
2.11	3D view of the numerical domain on the left: blue for mixing-plane and phase-lagged simulations; blue+red for reduced section number simulations - Meridional view of the domain on the right.	55
2.12	Steady aerodynamic maps applied as inlet boundary conditions for the cooled vein simulations for the LEC configuration.	56
2.13	Fourier coefficients of the density field at a fixed position of the rotor azimuthal boundary for a converged chorochronic simulation.	57
2.14	Real cooling holes system with the plenum (a) - View of the patches that replace the cooling holes with unit normal vectors coloured by massflow (b).	57
2.15	Structured multi-blocks O-6H topology of FACTOR's blade. H-blocks in green, O-block in blue and solid body in red. The boundaries of the blocks are displayed in solid black lines.	58
2.16	View from upstream to downstream of the surface mesh on the vanes (a) and blades (b). Shroud walls have been voluntarily removed for sake of clarity.	59
2.17	y^+ distribution on the unwrapped NGV of FACTOR.	59
2.18	Evolution of the massflow rate at the inlet and outlet of the domain for a RANS simulation.	63
2.19	Convergence of continuum, axial momentum, total energy and turbulent residuals for a RANS simulation.	63

2.20	Pressure fluctuation evolution (left column) and FFT of the pressure signal (right column) for different probe locations and time-steps.	64
2.21	Temporal evolution of the moving averaged massflow rates at the inlet and outlet of the domain.	65
2.22	Temporal evolution of the frequency spectrum of the massflow rate signals at the stator outlet (a) and at the rotor inlet (b).	65
2.23	Transport of the HS inside the NGVs evidenced by an iso-contour of total temperature at 450 K for both clocking positions.	67
2.24	Wall static temperature distribution on the two NGVs for LEC and PAC normalised by the inlet total temperature at P40.	68
2.25	Wall static temperature distribution on the rotor blade for LEC and PAC.	68
2.26	Effect of the clocking position on the radial distributions of total temperature inside the high-pressure turbine.	69
2.27	Radial distributions of $\bar{\alpha}$ (a) and \bar{T}_t (b) for different values of \dot{m}_{red}	70
2.28	Radial distributions of normalised $\bar{\alpha}$ (a) and \bar{T}_t (b) for different values of \dot{m}_{red}	71
2.29	Radial distributions of \bar{T}_t (a) and normalised \bar{T}_t (b) for different values of N_{red}	71
2.30	Influence of unsteady simulations on the radial distributions of \bar{T}_t (a) and \bar{P}_t (b) for the SV simulations - RSN: reduced sector number - Choro: chorochronic. Distributions are plotted in distortion.	72
2.31	Influence of the cooling on the radial distributions of $\bar{\alpha}$ (a) and \bar{P}_t (b). Distributions are plotted in distortion.	73
2.32	Influence of the cooling on the radial distributions of \bar{T}_t . Distributions are plotted in distortion.	74
2.33	Comparisons of \bar{T}_t fields at P41 between SV simulation (a), CV simulation (b) and experiments (c).	75
2.34	Wall static temperature distribution on the two NGVs and the rotor blade normalised by the inlet total temperature at P40.	75
2.35	Secondary flows on the suction side of the rotor blade evidenced by iso-surfaces of Q-criterion at $1 \cdot 10^8 \text{ s}^{-2}$ - Comparisons between SV (a) and CV (b).	76
3.1	Geometry of the bent duct with the dimensions normalised by the chord.	86
3.2	Zoom of the mesh in the most curved part (every two points displayed).	88
3.3	Schematic view of the bent duct with the boundary conditions.	88
3.4	Theoretical distributions of the normalised fields obtained from the Vatistas model for $n = 1$	90
3.5	Steady boundary conditions applied at the inlet of the duct for both LES and RANS simulations. Total temperature and total pressure are normalised by the mean value. The vortex is rotating in a clockwise direction looking downstream.	92
3.6	Evolution of Pope's criterion at mid-span of the channel - Contours at 0.2 displayed in black	94
3.7	Spatial PDF of Pope's criterion for the three meshes.	95
3.8	Temporal PDF of Pope's criterion for the baseline mesh.	95
3.9	Radial distributions of $\bar{\alpha}$ (a) and \bar{T}_t (b) for the different meshes.	95
3.10	Axial evolution of k_{RES} for different mesh resolutions.	96
3.11	PSD of fluctuating velocity at probe 5 for different convective times - Top: PSD of v'_x , middle: PSD of v'_y , bottom: PSD of v'_z . Sampling frequency is 45 kHz.	97

3.12	Evolution of the massflow rate at the inlet and outlet of the domain (a) and convergence of the RMS of velocity (b) for the LES.	98
3.13	Iso-contour at 460 K of time-averaged total temperature coloured by pitch angle.	99
3.14	Radial evolution of the transverse static pressure gradient at $x^* = 0.25$	100
3.15	Budget for the turbulent kinetic energy along x^* . Grey zone represents the curved part. Quantities are normalised by $(\rho_\infty v_\infty^3 r_c^2)$	101
3.16	PSD of fluctuating velocity for different axial positions on the mean position of the HS - Top: PSD of v'_x , middle: PSD of v'_y , bottom: PSD of v'_z . Sampling frequency is 45 kHz.	102
3.17	Instantaneous iso-surfaces of Q-criterion at $2.2 \cdot 10^8 \text{ s}^{-2}$ coloured by axial vorticity. The mean position of the HS is represented in grey with an iso-contour at 440 K of time-averaged total temperature.	102
3.18	Normalised fields of turbulent kinetic energy production at two axial positions. Iso-contour of $\text{PTKE}^* = 0$ in black and iso-contour of time-averaged total temperature at 440 K in grey.	103
3.19	Autocorrelation coefficient of the axial velocity for a random probe.	105
3.20	Evolution of the longitudinal integral length scale for different frequency acquisitions along the mean position of the HS. The grey horizontal dashed line represents the turbulence injection scale.	106
3.21	Evolution of different integral length scales along the mean position of the HS. The grey horizontal dashed line represents the targeted turbulence injection scale.	106
3.22	Radial distributions of $\bar{\alpha}$ (a) and \bar{T}_t (b) for the two inlet turbulent length scales.	107
3.23	Axial evolution of \bar{k} for different prescribed inlet integral length scale.	108
3.24	Evolution of \bar{T}_t in the azimuthal direction at the $z_{\bar{T}_t, \max}^*$ position for different abscissa. The position of the maximum total temperature is localised with markers.	109
3.25	Evolution of \bar{T}_t in the radial direction at the $y_{\bar{T}_t, \max}^*$ position for different abscissa. The position of the maximum total temperature is localised with markers.	109
3.26	Axial evolution of $\bar{T}_{t, \max}$ for different prescribed inlet integral length scale.	110
3.27	Positioning of the probes on the mean trajectory of the hot streak.	111
3.28	PSD of axial velocity component at different locations. 20 blocks are used with 50% overlap and a Hann windowing.	112
3.29	Radial distributions of $\bar{\alpha}$ (a) and \bar{T}_t (b) for the laminar/turbulent inlet boundary condition comparisons.	115
3.30	Axial evolution of \bar{l}_T for the laminar/turbulent inlet boundary condition comparisons.	115
3.31	Axial evolution of \bar{k} for the laminar/turbulent inlet boundary condition comparisons.	116
3.32	Radial distributions of $\bar{\alpha}$ (a) and \bar{T}_t (b) for different values of turbulent Reynolds number.	117
3.33	Axial evolution of \bar{k} for different values of turbulent Reynolds number.	117
3.34	Axial evolution of \bar{l}_T for different values of turbulent Reynolds number.	117
3.35	Radial distributions of $\bar{\alpha}$ (a) and \bar{T}_t (b) for different turbulence models.	118
3.36	Axial evolution of \bar{k} for different turbulence models.	118
3.37	Iso-contour at 450 K of total temperature coloured by pitch angle for Case 7. \bar{T}_t fields at the LE and TE are also displayed.	119
3.38	Budget for the turbulent kinetic energy along x^* . Grey zone represents the curved part. Comparisons between LES (—) and Case 7 (---). Quantities are normalised by $(\rho_\infty v_\infty^3 r_c^2)$	119

3.39	Evolution of \overline{T}_t in the azimuthal direction at the $z_{\overline{T}_t, max}^*$ position for different abscissa and different RANS turbulent inlet set-ups. The position of the maximum total temperature is localised with markers.	120
3.40	Comparisons of production (a), diffusion (b), dissipation (c) and convection (d) terms between LES (—), Case 2 (----) and Case 7 (---). Grey zone represents the curved part. Quantities are normalised by $(\rho_\infty v_\infty^3 r_c^2)$	121
4.1	Evolution of turbulent kinetic energy at mid-span of the channel (scaled from the LES values).	128
4.2	Probability density function (a) and cumulative density function (b) of Schmitt's criterion on the domain ranging from $x^* = -2$ to $x^* = 1$ computed from the LES 'SWIRL +' case.	130
4.3	2D field of Schmitt's criterion plotted at different axial positions. Iso-contour of $\rho_{RS} = 0$ and $\rho_{RS} = 0.86$ respectively in grey and black.	131
4.4	2D field of Schmitt's criterion plotted at mid-span of the channel. Iso-contour of $\rho_{RS} = 0$ and $\rho_{RS} = 0.86$ respectively in grey and black.	131
4.5	Lumley's triangle on the plane of the invariants η and ξ of the Reynolds stress anisotropy tensor. Adapted from Pope [91].	133
4.6	Anisotropy invariant map applied close to the walls at $x^* = 0$ (a) and normal components b_{zz} (—) and b_{nn} (—) of the anisotropy tensor at the throat of the channel (b).	133
4.7	Positioning of the probes on the mean trajectory of the hot streak.	134
4.8	Anisotropy invariant map applied to the 'SWIRL +' case.	134
4.9	Deviation of the eigenvectors of the anisotropy tensor with the Cartesian basis.	135
4.10	Anisotropy invariant map applied on an iso-contour at 450 K of time-averaged total temperature at different axial positions. Points are coloured by turbulence kinetic energy.	136
4.11	Radial distributions of $\overline{\alpha}$ (a) and \overline{T}_t (b) using the QCR correction.	138
4.12	Budget for the turbulent kinetic energy along x^* . Grey zone represents the curved part. Comparisons between Case 7 (—) and the QCR correction (---). Quantities are normalised by $(\rho_\infty v_\infty^3 r_c^2)$	138
4.13	Radial distributions of $\overline{\alpha}$ (a) and \overline{T}_t (b) for EARSM/RSM turbulence models.	140
4.14	Axial evolution of $\overline{T}_{t, max}$ for the EARSM/RSM turbulence models.	140
4.15	Budget for the turbulent kinetic energy along x^* . Grey zone represents the curved part. Comparisons between LES (—) and EARSM (---). Quantities are normalised by $(\rho_\infty v_\infty^3 r_c^2)$	141
4.16	Evolution of turbulent kinetic energy at mid-span of the channel using EARSM and Wilcox $k - \omega$ turbulence models compared to the LES (scaled from the LES values).	141
4.17	b_{xz} component of the anisotropy tensor at $x^* = -1$. View from upstream to downstream.	142
4.18	b_{yy} component of the anisotropy tensor at $x^* = -1$. View from upstream to downstream.	143
4.19	Anisotropy invariant map at $x^* = -1$	144
4.20	Anisotropy invariant map at $x^* = 1$	145

4.21	Anisotropy invariant map at $x^* = 0.5$. Highlight of non-realisable turbulence for the Wilcox $k - \omega$ turbulence model.	145
5.1	Influence of the turbulent length scale on the radial distributions of \overline{T}_t (a) and \overline{P}_t (b) for steady SV simulations.	153
5.2	Axial evolution of mass-weighted average turbulent kinetic energy for different values of turbulent length scale at the inlet. The position of the stator and rotor is represented with grey zones and the reference planes with grey vertical lines.	154
5.3	Influence of linear-eddy viscosity turbulence models on the radial distributions of \overline{T}_t (a) and \overline{P}_t (b) for steady SV simulations.	155
5.4	2D maps of relative total pressure plotted in terms of distortions at the TE of the rotor blade for the $k - l$ (a) and SST $k - \omega$ (b) turbulence models simulations.	156
5.5	Axial evolution of mass-weighted average turbulent kinetic energy depending on the turbulence model. The position of the stator and rotor is represented with grey zones and the reference planes with grey vertical lines.	156
5.6	Influence of anisotropic models on the radial distributions of \overline{T}_t (a) and \overline{P}_t (b) for steady SV simulations.	157
5.7	Axial evolution of mass-weighted average turbulent kinetic energy with anisotropic turbulence models. The position of the stator and rotor is represented with grey zones and the reference planes with grey vertical lines.	157
6.1	Radial distributions of total temperature at P41. Comparisons between the experiments, the isolated turbine simulation of Chapter 2 with a steady boundary condition extracted from the experiments and the coupled combustion chamber-/NGVs LES of Martin [73].	164
6.2	5HP results obtained for the pitch angle at P40. From Krumme <i>et al.</i> [62].	165
6.3	Interpolation validation at P41. From Krumme <i>et al.</i> [62].	166
6.4	\overline{T}_t field at P40 between the experiments and the LES.	167
6.5	$\overline{\alpha}$ field at P40 between the experiments and the LES.	167
6.6	$\overline{\phi}$ field at P40 between the experiments and the LES.	167
6.7	\overline{P}_t field at P40 between the experiments and the LES.	168
6.8	Numerical domain of 'LES A'. Courtesy of Martin [73].	169
6.9	Numerical domain of 'LES B'. Courtesy of Martin [73].	169
6.10	Impact of the modification of the geometry on the position of the inlet plane (a) and difference of azimuthal position between LES inlet and RANS inlet (b).	171
6.11	Axial velocity profiles at P40* for different pitch positions.	172
6.12	Velocity boundary layer thickness at the shroud (a) and hub (b) of P40* (—) expressed at a percentage of vein height.	173
6.13	\overline{T}_t field at P40* for the steady LES map (a) and the map obtained with inverse distance weighting (b).	174
6.14	$\overline{\alpha}$ field at P40* for the steady LES map (a) and the map obtained with inverse distance weighting (b).	174
6.15	Radial distributions of $\overline{\alpha}$ (a), \overline{P}_t (b) and \overline{T}_t (c) with and without velocity boundary layer.	175

6.16	Representation of the PVC with an iso-contour of low pressure in black. Turbulent structures are visible with an iso-contour of Q-criterion coloured by static temperature. Courtesy of Martin [73].	177
6.17	Principle of the SPOD method. In this example, each snapshot is composed of $N_v = 1$ variable (P) of length N_p and each block contains $N_f = 4$ snapshots. The overlapping region is composed of $N_o = 1$ snapshot. The flow variable being real, half of the frequencies (positive) are kept ($N_f/2$). The phase is not illustrated but is an output of the treatment.	179
6.18	SPOD mode energy spectrum (a) and pre-multiplied energy spectrum (b).	180
6.19	Cumulated mode energy fraction of the SPOD (a) and zoom close to the frequency of the PVC (b).	181
6.20	Impact of the spatial and temporal interpolations on the time evolution of total temperature at P40* for the F10 reconstruction (a) and zoom on the part delimited by the vertical dashed gray lines (b).	182
6.21	Moving averages of inlet and outlet massflow for F10 (a) and F20 (b).	183
6.22	FFT of instantaneous massflow at P40* for F10 and F20.	183
6.23	Convergence of \overline{T}_t distributions over t_{PVC}	184
6.24	Total temperature signal recorded by a probe in the wake of the rotor blade at mid-span. The lengths of the averages is evidenced by the arrows.	185
6.25	Radial distributions of $\overline{\alpha}$ for case F10 (a) and case F20 (b) compared to the experiments and LES.	185
6.26	Radial distributions of \overline{P}_t for case F10 (a) and case F20 (b) compared to the experiments and LES.	186
6.27	Radial distributions of \overline{T}_t for case F10 (a) and case F20 (b) compared to the experiments and LES.	186
6.28	Comparison of \overline{T}_t fields at P41 between the experiments and the simulation accounting for the PVC.	187
6.29	Comparison of \overline{P}_t fields at P41 between the experiments and the simulations accounting for the PVC.	188
6.30	Comparison of $\overline{\alpha}$ fields at P42 between the experiments and case F10.	189
6.31	Comparison of \overline{P}_t fields at P42 between the experiments and case F10.	189
6.32	Comparison of \overline{T}_t fields at P42 between the experiments and case F10.	189
6.33	Instantaneous total temperature field at P42 over a period of the PVC.	190
6.34	Radial distributions of $\overline{\alpha}$ (a), \overline{P}_t (b) and \overline{T}_t (c) when using the steady inlet map from the LES. Plots in terms of distortions.	192
6.35	Comparison of \overline{T}_t fields at P41 between the experiments and the simulations.	193
6.36	Distribution of isentropic Mach number at $h/H = 0.5$ of the NGVs obtained for different cooled simulations compared to the experiments.	194
6.37	Comparison of static pressure evolutions over the pitch with the experiments.	195
6.38	Probe alignment at P42.	196
6.39	Experimental time-averaged total pressure field at P40.	196
6.40	PSD of total pressure in a low total pressure zone at $h/H = 0.5$	197
6.41	Experimental amplitude of the PSD at the frequency of the PVC at P40.	197
6.42	Numerical amplitude of the PSD at the frequency of the PVC at P40.	198
6.43	Phase-locked average at P42.	198

6.44	Experimental amplitude of the PSD at the frequency of the PVC and at the BPF at P42.	199
6.45	Numerical amplitude of the PSD at the frequency of the PVC at P42.	200
6.46	Numerical amplitude of the PSD at the BPF at P42.	200
A.1	Radial profiles of $\bar{\alpha}$ (a) and \bar{T}_t (b) for different turbulent Prandtl numbers.	215
A.2	Axial evolution of \bar{k} for different turbulent Prandtl numbers.	215
A.3	Evolution of \bar{T}_t in the spanwise direction at the $z_{\bar{T}_t, max}^*$ position for different abscissa for different turbulent Prandtl numbers. The position of the maximum total temperature is localised with markers.	216
A.4	Radial profiles of $\bar{\alpha}$ (a) and \bar{T}_t (b) for different turbulent Reynolds numbers.	217
A.5	Axial evolution of \bar{k} for different turbulent Reynolds numbers.	218
A.6	Evolution of \bar{T}_t in the spanwise direction at the $z_{\bar{T}_t, max}^*$ position for different abscissa for different turbulent Reynolds numbers. The position of the maximum total temperature is localised with markers.	218
A.7	Radial profiles of $\bar{\alpha}$ (a) and \bar{T}_t (b) for different meshes.	219
A.8	Axial evolution of \bar{k} for different meshes.	219
B.1	y^+ distribution on the unwrapped rotor blade of FACTOR.	222
B.2	y^+ distribution on the hub and shroud walls of the static row.	222
B.3	y^+ distribution on the hub and shroud walls of the moving row.	223
B.4	Radial profiles of \bar{T}_t (a) and \bar{P}_t (b) for two different meshes at P42.	223
B.5	$dT = T_{s, fine} - T_{s, nominal}$ on the NGV's walls.	224
B.6	Axial evolution of mass-weighted average turbulent kinetic energy for different wall treatments for ω . The position of the stator and rotor is represented with grey zones and the reference planes with grey vertical lines.	225
B.7	Influence of the wall treatment for ω on the radial profiles of \bar{T}_t (a) and \bar{P}_t (b) for steady SV simulations.	225
B.8	Axial evolution of mass-weighted average turbulent kinetic energy using the Zheng limiter. The position of the stator and rotor is represented with grey zones and the reference planes with grey vertical lines.	226
B.9	Influence of the Zheng limiter on the radial profiles of \bar{T}_t (a) and \bar{P}_t (b) for steady SV simulations.	227
B.10	Axial evolution of mass-weighted average turbulent kinetic energy for different SST corrections. The position of the stator and rotor is represented with grey zones and the reference planes with grey vertical lines.	228
B.11	Influence of the SST correction on the radial profiles of \bar{T}_t (a) and \bar{P}_t (b) for steady SV simulations.	228
B.12	Axial evolution of mass-weighted average turbulent kinetic energy for different values of \bar{k} at the inlet. The position of the stator and rotor is represented with grey zones and the reference planes with grey vertical lines.	229
B.13	Influence of inlet value of \bar{k} on the radial profiles of \bar{T}_t (a) and \bar{P}_t (b) for steady SV simulations.	230
B.14	Results of Case D for $\bar{\alpha}$ (a) and \bar{T}_t (b) - Exps.: P_t , T_t , α and LES: ϕ	231
B.15	Results of Case E for $\bar{\alpha}$ (a) and \bar{T}_t (b) - Exps.: T_t , α , ϕ and LES: P_t	232
B.16	Results of Case L for $\bar{\alpha}$ (a) and \bar{T}_t (b) - Exps.: P_t , α , ϕ and LES: T_t	232

LIST OF FIGURES

B.17 Results of Case M for $\bar{\alpha}$ (a) and \bar{T}_t (b) - Exps.: P_t , ϕ and LES: T_t , α 233

B.18 Results of Case O for $\bar{\alpha}$ (a) and \bar{T}_t (b) - Exps.: P_t , α and LES: T_t , ϕ 233

B.19 Radial distributions of $\bar{\alpha}$ (a), \bar{P}_t (b) and \bar{T}_t (c) when using the steady inlet map
from the LES and the SST $k - \omega$ turbulence model. Plots in terms of distortions. 234

List of Tables

2.1	Operating point for the full-annular test rig at DLR (LEC).	46
2.2	Main numerical simulations realised in the scope of the FACTOR project - CC and NGV respectively stands for combustion chamber and nozzle guide vane.	50
2.3	Coverage of the measurements with the traverse system at P40, P41 and P42 for LEC and PAC.	51
2.4	Summary of the use of available experimental data in the manuscript.	54
2.5	Averaged values at the inlet boundary conditions for the smooth vein and cooled vein simulations.	55
2.6	Main features of the meshes used for both steady and unsteady simulations.	59
2.7	Numerical set-up for the steady simulations of FACTOR.	61
2.8	Numerical set-up for the unsteady simulations of FACTOR.	61
2.9	Comparison of CPU time for different FACTOR simulations.	66
3.1	Targeted values of the flow at plane 40.	86
3.2	Reynolds numbers and flow characteristic scales.	87
3.3	Characteristics of the vortex.	91
3.4	Numerical set-up for the Navier-Stokes numerical approaches.	93
3.5	Meshes characteristics for the mesh convergence. The CPU time is normalised with respect the baseline mesh time necessary for the convergence of the statistics.	94
3.6	Evaluation of the computational cost on the channel's configuration.	97
3.7	RANS test cases matrix for the sensitivity study. T_u and μ_T/μ are averaged values on the inlet plane.	113
6.1	Geometrical differences between the simulations of this PhD thesis and the simulations of Martin.	169
6.2	Test cases matrix for the impact of the inlet boundary condition at P40.	170
6.3	Parameters of the database and of the SPOD analysis.	180
6.4	Comparisons of CPU time for different FACTOR simulations with both steady and unsteady boundary condition from the LES.	190
A.1	Test cases for the evaluation of the turbulent Prandtl number.	214
A.2	Test cases for the evaluation of the turbulent viscosity.	217

B.1 Test cases matrix for the impact of the inlet boundary condition at P40 - '0' comes from the experiments and '1' comes from the LES. 231

Bibliography

- [1] U. Ahmed, D. Apsley, T. Stallard, P. Stansby, and I. Afgan. Turbulent length scales and budgets of reynolds stress-transport for open-channel flows. *Journal of Hydraulic Research*, 59(1):36–50, apr 2020. (Cited on page [105](#).)
- [2] A. Andreini, B. Facchini, M. Insinna, L. Mazzei, and S. Salvadori. Hybrid RANS-LES Modeling of a Hot Streak Generator Oriented to the Study of Combustor-Turbine Interaction. In *Volume 5C: Heat Transfer*. American Society of Mechanical Engineers, jun 2015. (Cited on pages [47](#) and [50](#).)
- [3] antares Development Team. Antares Documentation Release 1.19.0, 2022. (Cited on pages [52](#) and [60](#).)
- [4] T. Bacci. *Experimental Investigation on a High Pressure NGV Cascade in the Presence of a Representative Lean Burn Aero-Engine Combustor Outflow*. PhD thesis, University of Florence, 2017. (Cited on pages [45](#), [51](#), and [176](#).)
- [5] B. Baldwin and H. Lomax. Thin-layer approximation and algebraic model for separated turbulentflows. In *16th Aerospace Sciences Meeting*. American Institute of Aeronautics and Astronautics, jan 1978. (Cited on page [31](#).)
- [6] D. G. Barhaghi and L. Hedlund. Numerical Investigation of Fluid Flow Parameters in a Combustor Simulator. In *Volume 5C: Heat Transfer*. American Society of Mechanical Engineers, jun 2018. (Cited on page [50](#).)
- [7] J. A. Benek, J. L. Steger, F. C. Dougherty, and P. Buning. Chimera. a grid-embedding technique. 1986. (Cited on page [54](#).)
- [8] Bhagwat, J. Mahendra, Leishman, and J. Gordon. Generalized viscous vortex model for application to free-vortex wake and aeroacoustic calculations. 2002. (Cited on page [89](#).)
- [9] K. Bhide and S. Abdallah. Anisotropic turbulent kinetic energy budgets in compressible rectangular jets. *Aerospace*, 9(9):484, aug 2022. (Cited on page [100](#).)
- [10] J. P. Bindon. The Measurement and Formation of Tip Clearance Loss. *Journal of Turbomachinery*, 111(3):257–263, jul 1989. (Cited on pages [19](#), [20](#), and [237](#).)

-
- [11] R. Bizzari, D. Lahbib, A. Dauplain, F. Duchaine, L. Y. M. Gicquel, and F. Nicoud. A thickened-hole model for large eddy simulations over multiperforated liners. *Flow, Turbulence and Combustion*, 101(3):705–717, apr 2018. (Cited on page 168.)
- [12] J. Bodart and J. Larsson. Sensor-based Computation of a Transitional Flows Using Wall-modeled Large Eddy Simulation. *Annual Research Briefs, Center for Turbulence Research*, 2012. (Cited on page 92.)
- [13] C. Bode, T. Aufderheide, D. Kožulović, and J. Friedrichs. The effects of turbulence length scale on turbulence and transition prediction in turbomachinery flows. In *Volume 2B: Turbomachinery*. American Society of Mechanical Engineers, jun 2014. (Cited on page 85.)
- [14] C. Bogey and C. Bailly. Turbulence and energy budget in a self-preserving round jet: direct evaluation using large eddy simulation. *Journal of Fluid Mechanics*, 627:129–160, may 2009. (Cited on page 100.)
- [15] T. Butler, O. Sharma, H. Joslyn, and R. Dring. Redistribution of an Inlet Temperature Distortion in an Axial Flow Turbine Stage. In *22nd Joint Propulsion Conference*. American Institute of Aeronautics and Astronautics, jun 1986. (Cited on pages 13, 16, 17, and 237.)
- [16] L. Caldas, C. Kissner, M. Behn, U. Tapken, and R. Meyer. Comparison of techniques for the estimation of flow parameters of fan inflow turbulence from noisy hot-wire data. *Fluids*, 6(11):372, oct 2021. (Cited on page 105.)
- [17] S. Callot. *Analyse des mécanismes macroscopiques produits par les interactions rotor/stator dans les turbomachines*. PhD thesis, Ecole Centrale de Lyon, 2002. (Cited on pages 13 and 237.)
- [18] L. Cambier, S. Heib, and S. Plot. The OneraelsACFD software: input from research and feedback from industry. *Mechanics & Industry*, 14(3):159–174, 2013. (Cited on page 60.)
- [19] R.-D. Cecora, R. Radespiel, B. Einfeld, and A. Probst. Differential reynolds-stress modeling for aeronautics. *AIAA Journal*, 53(3):739–755, mar 2015. (Cited on pages 33, 34, and 137.)
- [20] D. Cherrared. Numerical Simulation of Film Cooling a Turbine Blade Through a Row of Holes. *Journal of Thermal Engineering*, 3(2):1110–1110, apr 2017. (Cited on page 21.)
- [21] F. Cottier, P. Pinchaud, and G. Dumas. Aerothermal Predictions of Combustor/Turbine Interactions Using Advanced Turbulence Modeling. In *13th European Conference on Turbomachinery Fluid Dynamics and Thermodynamics*. European Turbomachinery Society, 2019. (Cited on pages 47, 49, 50, 163, and 188.)
- [22] S. Cubeda, L. Mazzei, and A. Andreini. External Heat Transfer on Nozzle Guide Vanes Under Highly Swirled Combustor Outlet Flow. In *13th European Conference on Turbomachinery Fluid Dynamics and Thermodynamics*. European Turbomachinery Society, 2019. (Cited on pages 47, 48, 50, and 238.)
- [23] S. Cubeda, L. Mazzei, T. Bacci, and A. Andreini. Impact of Predicted Combustor Outlet Conditions on the Aerothermal Performance of Film-Cooled High Pressure Turbine Vanes. *Journal of Engineering for Gas Turbines and Power*, 141(5), dec 2018. (Cited on pages 47 and 50.)
-

- [24] S. Delbecq, J. Fontane, N. Gourdain, H. Mugnier, T. Planès, and F. Simatos. Isae-superaero aviation and climate: a literature review. 2022. (Cited on page 1.)
- [25] J. D. Denton. The calculation of three-dimensional viscous flow through multistage turbomachines. *Journal of Turbomachinery*, 114(1):18–26, jan 1992. (Cited on page 36.)
- [26] N. S. Dhamankar, G. A. Blaisdell, and A. S. Lyrintzis. Overview of turbulent inflow boundary conditions for large-eddy simulations. *AIAA Journal*, 56(4):1317–1334, apr 2018. (Cited on page 29.)
- [27] D. Dorney, R. Davis, D. Edwards, and N. Madavan. Unsteady analysis of hot streak migration in a turbine stage. In *26th Joint Propulsion Conference*. American Institute of Aeronautics and Astronautics, jul 1990. (Cited on pages 13, 14, 16, and 237.)
- [28] D. J. Dorney and K. Gundy-Burlet. Hot Streak Clocking Effects in a 1-1/2 Stage Turbine. In *Volume 1: Turbomachinery*. American Society of Mechanical Engineers, jun 1995. (Cited on page 17.)
- [29] F. Duchaine, J. Dombard, L. Gicquel, and C. Koupper. Integrated Large Eddy Simulation of Combustor and Turbine Interactions: Effect of Turbine Stage Inlet Condition. In *Volume 2B: Turbomachinery*. American Society of Mechanical Engineers, jun 2017. (Cited on page 50.)
- [30] P. Durbin. On the k-3 stagnation point anomaly. *International Journal of Heat and Fluid Flow*, 17(1):89–90, feb 1996. (Cited on pages 35 and 115.)
- [31] J. Erdos and E. Alzner. Computation of unsteady transonic flows through rotating and stationary cascades. Technical report, 1977. (Cited on pages 37 and 38.)
- [32] J. Fang, Z. Li, and L. Lu. An Optimized Low-Dissipation Monotonicity-Preserving Scheme for Numerical Simulations of High-Speed Turbulent Flows. *Journal of Scientific Computing*, 56(1):67–95, nov 2012. (Cited on page 93.)
- [33] A. J. A. Favre. Formulation of the statistical equations of turbulent flows with variable density. In *Studies in Turbulence*, pages 324–341. Springer New York, 1992. (Cited on page 29.)
- [34] M. Fiore. *Influence of Cavity Flow on Turbine Aerodynamics*. PhD thesis, ISAE Supaero, 2019. (Cited on page 21.)
- [35] A.-L. Fiquet. *Analyse et modélisation de phénomènes aéroélastiques non-synchrones dans un compresseur axial multi-étages*. PhD thesis, Ecole Centrale de Lyon, 2021. (Cited on page 60.)
- [36] A. Firrito, Y. Bousquet, N. Binder, and L. Pintat. Influences of Turbulence Boundary Conditions on RANS and URANS Simulations for an Inter-Turbine Duct. In *Volume 2D: Turbomachinery*. American Society of Mechanical Engineers, sep 2020. (Cited on pages 113 and 153.)
- [37] G. J. V. Fossen and C. Y. Ching. Measurements of the influence of integral length scale on stagnation region heat transfer. *International Journal of Rotating Machinery*, 3(2):117–132, 1997. (Cited on page 105.)

-
- [38] M. Foust, D. Thomsen, R. Stickles, C. Cooper, and W. Dodds. Development of the GE aviation low emissions TAPS combustor for next generation aircraft engines. In *50th AIAA Aerospace Sciences Meeting including the New Horizons Forum and Aerospace Exposition*. American Institute of Aeronautics and Astronautics, jan 2012. (Cited on pages 4, 43, and 238.)
- [39] P. Gaetani. Stator-rotor interaction in axial turbine: Flow physics and design perspective. In *Aircraft Technology*. InTech, sep 2018. (Cited on pages 15 and 237.)
- [40] D. Garcia. Robust smoothing of gridded data in one and higher dimensions with missing values. *Computational Statistics:Data Analysis*, 54(4):1167–1178, apr 2010. (Cited on pages 51 and 165.)
- [41] E. Garnier, N. Adams, and P. Sagaut. *Large Eddy Simulation for Compressible Flows*. SPRINGER NATURE, Aug. 2009. (Cited on page 27.)
- [42] M. Germano, U. Piomelli, P. Moin, and W. H. Cabot. A Dynamic Subgrid-Scale Eddy Viscosity Model. *Physics of Fluids A: Fluid Dynamics*, 3(7):1760–1765, jul 1991. (Cited on page 28.)
- [43] G. A. Gerolymos, G. J. Michon, and J. Neubauer. Analysis and application of chorochronic periodicity in turbomachinery rotor/stator interaction computations. *Journal of Propulsion and Power*, 18(6):1139–1152, nov 2002. (Cited on page 37.)
- [44] R. J. Goldstein and R. A. Spores. Turbulent Transport on the Endwall in the Region Between Adjacent Turbine Blades. *Journal of Heat Transfer*, 110(4a):862–869, nov 1988. (Cited on pages 18, 19, 20, and 237.)
- [45] S. Gövert, F. Ferraro, A. Krumme, C. Buske, M. Tegeler, F. Kocian, and F. di Mare. Investigation of Combustor-Turbine-Interaction in a Rotating Cooled Transonic High-Pressure Turbine Test Rig: Part 2 — Numerical Modelling and Simulation. In *Volume 2B: Turbomachinery*. American Society of Mechanical Engineers, jun 2019. (Cited on pages 50 and 163.)
- [46] J.-C. Han and A. Rallabandi. Turbine Blade Film Cooling Using PSP Technique. *Frontiers in Heat and Mass Transfer*, 1(1), jun 2010. (Cited on pages 21 and 237.)
- [47] L. He. Method of simulating unsteady turbomachinery flows with multiple perturbations. *AIAA Journal*, 30(11):2730–2735, nov 1992. (Cited on page 38.)
- [48] A. Hellsten. New advanced k-w turbulence model for high-lift aerodynamics. 43(9):1857–1869, sep 2005. (Cited on page 33.)
- [49] J. Hilgert, M. Bruschewski, H. Werschnik, and H.-P. Schiffer. Numerical Studies on Combustor-Turbine Interaction at the Large Scale Turbine Rig (LSTR). In *Volume 2A: Turbomachinery*. American Society of Mechanical Engineers, jun 2017. (Cited on page 47.)
- [50] J.-C. Hoarau, P. Cinnella, and X. Gloerfelt. Large eddy simulation of turbomachinery flows using a high-order implicit residual smoothing scheme. *Computers & Fluids*, 198:104395, feb 2020. (Cited on page 28.)
-

- [51] C. A. Horowitz. Paris agreement. *International Legal Materials*, 55(4):740–755, aug 2016. (Cited on page 1.)
- [52] Y. Huang and V. Yang. Dynamics and stability of lean-premixed swirl-stabilized combustion. *Progress in Energy and Combustion Science*, 35(4):293–364, aug 2009. (Cited on page 110.)
- [53] A. Jameson. Computational fluid dynamics: Past, present and future, 2012. (Cited on pages 5 and 237.)
- [54] S. Jenkins, K. Varadarajan, and D. G. Bogard. The effects of high mainstream turbulence and turbine vane film cooling on the dispersion of a simulated hot streak. *Journal of Turbomachinery*, 126(1):203–211, jan 2004. (Cited on page 21.)
- [55] P. Jenny, C. Lenherr, R. S. Abhari, and A. Kalfas. Effect of Hot Streak Migration on Unsteady Blade Row Interaction in an Axial Turbine. *Journal of Turbomachinery*, 134(5), may 2012. (Cited on page 16.)
- [56] J. Jiménez, S. Hoyas, M. Siemens, and Y. Mizuno. Turbulent boundary layers and channels at moderate Reynolds numbers. *Journal of Fluid Mechanics*, 657:335–360, jun 2010. (Cited on page 100.)
- [57] Y. Khalighi, F. Ham, J. Nichols, S. Lele, and P. Moin. Unstructured Large Eddy Simulation for Prediction of Noise Issued from Turbulent Jets in Various Configurations. In *17th AIAA/CEAS Aeroacoustics Conference (32nd AIAA Aeroacoustics Conference)*. American Institute of Aeronautics and Astronautics, jun 2011. (Cited on page 93.)
- [58] M. Klein, A. Sadiki, and J. Janicka. A digital filter based generation of inflow data for spatially developing direct numerical or large eddy simulations. *Journal of Computational Physics*, 186(2):652–665, apr 2003. (Cited on pages 28 and 91.)
- [59] N. Kolmogorov. The local structure of turbulence in incompressible viscous fluid for very large reynolds numbers. *Proceedings of the Royal Society of London. Series A: Mathematical and Physical Sciences*, 434(1890):9–13, jul 1991. (Cited on page 24.)
- [60] C. Koupper. *Unsteady Multi-Component Simulations Dedicated to the Impact of the Combustion Chamber on the Turbine of Aeronautical Gas Turbines*. PhD thesis, Toulouse INP, 05 2015. (Cited on pages 16, 17, 18, 43, 45, 50, 51, 176, 229, and 237.)
- [61] C. Koupper, G. Bonneau, L. Gicquel, and F. Duchaine. Large Eddy Simulations of the Combustor Turbine Interface: Study of the Potential and Clocking Effects. In *Volume 5B: Heat Transfer*. American Society of Mechanical Engineers, jun 2016. (Cited on pages 14, 45, 50, and 163.)
- [62] A. Krumme, C. Buske, J. R. Bachner, J. Dähnert, M. Tegeler, F. Ferraro, S. Gövert, F. Kocian, F. di Mare, and A. Pahs. Investigation of Combustor-Turbine-Interaction in a Rotating Cooled Transonic High-Pressure Turbine Test Rig: Part 1 — Experimental Results. In *Volume 2B: Turbomachinery*. American Society of Mechanical Engineers, jun 2019. (Cited on pages 45, 51, 52, 53, 163, 165, 166, 168, 238, and 242.)
- [63] J. E. Lagraff, D. E. Asphis, M. L. G. Oldfield, and J. P. Gostelow. Unsteady Flows in Turbomachinery. Technical report, NASA, 2006. (Cited on pages 12 and 237.)

-
- [64] B. Lakshminarayana. *Fluid Dynamics and Heat Transfer of Turbomachinery*. John Wiley & Sons, Inc., dec 1995. (Cited on pages [20](#) and [21](#).)
- [65] L. S. Langston. Secondary flows in axial turbines—a review. *Annals of the New York Academy of Sciences*, 934(1):11–26, 2001. (Cited on page [18](#).)
- [66] B. Launder and B. Sharma. Application of the energy-dissipation model of turbulence to the calculation of flow near a spinning disc. *Letters in Heat and Mass Transfer*, 1(2):131–137, nov 1974. (Cited on pages [31](#) and [227](#).)
- [67] D. Lee, D. Fahey, A. Skowron, M. Allen, U. Burkhardt, Q. Chen, S. Doherty, S. Freeman, P. Forster, J. Fuglestedt, A. Gettelman, R. D. León, L. Lim, M. Lund, R. Millar, B. Owen, J. Penner, G. Pitari, M. Prather, R. Sausen, and L. Wilcox. The contribution of global aviation to anthropogenic climate forcing for 2000 to 2018. *Atmospheric Environment*, 244:117834, jan 2021. (Cited on pages [2](#) and [237](#).)
- [68] J. L. Lumley. The structure of inhomogeneous turbulent flows. *Yaglom, A.M. and Tartarsky, V.I., Eds., Atmospheric Turbulence and Radio Wave Propagation, 166-177*, 1967. (Cited on page [176](#).)
- [69] J. L. Lumley and G. R. Newman. The return to isotropy of homogeneous turbulence. *Journal of Fluid Mechanics*, 82(1):161–178, aug 1977. (Cited on pages [131](#) and [136](#).)
- [70] K. H. Luo and N. D. Sandham. Direct Numerical Simulation of Supersonic Jet Flow. *Journal of Engineering Mathematics*, 32(2/3):121–142, 1997. (Cited on page [93](#).)
- [71] D. Luquet, F. Julienne, A. Arntz, and E. Lippinois. Evaluation of the Numerical Modelling of a High Pressure Turbine Test Rig. In *Volume 2C: Turbomachinery*. American Society of Mechanical Engineers, jun 2019. (Cited on pages [50](#) and [163](#).)
- [72] R. M. Manglik and A. E. Bergles. Swirl flow heat transfer and pressure drop with twisted-tape inserts. In *Advances in Heat Transfer*, pages 183–266. Elsevier, 2003. (Cited on page [110](#).)
- [73] B. Martin. *Méthodes numériques et conditions limites pour la simulation aux grandes échelles du couplage entre plusieurs composants d’une turbomachine*. PhD thesis, 2021. (Cited on pages [50](#), [163](#), [164](#), [166](#), [168](#), [169](#), [176](#), [177](#), [178](#), [180](#), [181](#), [183](#), [229](#), [242](#), and [243](#).)
- [74] B. Martin, F. Duchaine, L. Gicquel, and N. Odier. Generation of realistic boundary conditions at the combustion chamber/turbine interface using large-eddy simulation. *Energies*, 14(24):8206, dec 2021. (Cited on pages [168](#) and [178](#).)
- [75] B. Martin, F. Duchaine, L. Gicquel, N. Odier, and J. Dombard. Accurate inlet boundary conditions to capture combustion chamber and turbine coupling with large-eddy simulation. In *Volume 2D: Turbomachinery - Multidisciplinary Design Approaches, Optimization, and Uncertainty Quantification, Radial Turbomachinery Aerodynamics, Unsteady Flows in Turbomachinery*. American Society of Mechanical Engineers, jun 2021. (Cited on pages [45](#), [47](#), [48](#), [168](#), and [178](#).)
- [76] R. E. Mayle. The role of laminar-turbulent transition in gas turbine engines. In *Volume 5: Manufacturing Materials and Metallurgy; Ceramics; Structures and Dynamics; Controls*,
-

- Diagnostics and Instrumentation; Education; IGTI Scholar Award; General.* American Society of Mechanical Engineers, jun 1991. (Cited on pages 25 and 237.)
- [77] A. A. McCarter, X. Xiao, and B. Lakshminarayana. Tip Clearance Effects in a Turbine Rotor: Part II—Velocity Field and Flow Physics. *Journal of Turbomachinery*, 123(2):305–313, feb 2000. (Cited on page 19.)
- [78] G. McLelland, D. di Cugno, D. G. MacManus, and V. Pachidis. Boundary Conditions for Vortex CFD Simulations. In *Volume 8: Turbomachinery, Parts A, B, and C*. American Society of Mechanical Engineers, jun 2012. (Cited on page 89.)
- [79] C. L. Memory, J. P. Chen, and J. P. Bons. Implicit large eddy simulation of a stalled low-pressure turbine airfoil. *Journal of Turbomachinery*, 138(7), feb 2016. (Cited on page 28.)
- [80] F. R. Menter. Two-equation eddy-viscosity turbulence models for engineering applications. *AIAA Journal*, 32(8):1598–1605, aug 1994. (Cited on pages 154 and 227.)
- [81] J.-F. Monier. *Analyse de la modélisation turbulente en écoulements tourbillonnaires*. PhD thesis, Ecole Centrale de Lyon, 2018. (Cited on pages 100 and 129.)
- [82] M. Munk and R. Prim. On the Multiplicity of Steady Gas Flows Having the Same Streamline Pattern. *Proceedings of the National Academy of Sciences*, 33(5):137–141, may 1947. (Cited on page 16.)
- [83] W. Munters, C. Meneveau, and J. Meyers. Turbulent inflow precursor method with time-varying direction for large-eddy simulations and applications to wind farms. *Boundary-Layer Meteorology*, 159(2):305–328, jan 2016. (Cited on page 28.)
- [84] N. V. Nikitin, N. V. Popelenskaya, and A. Stroh. Prandtl’s secondary flows of the second kind. problems of description, prediction, and simulation. *Fluid Dynamics*, 56(4):513–538, jun 2021. (Cited on page 141.)
- [85] J. Ong and R. J. Miller. Hot Streak and Vane Coolant Migration in a Downstream Rotor. In *Volume 6: Turbomachinery, Parts A, B, and C*. ASMEDC, jan 2008. (Cited on pages 16 and 18.)
- [86] J. Ong, R. J. Miller, and J. D. Denton. The Prediction of Hot Streak Migration in a High-Pressure Turbine. *Proceedings of the Institution of Mechanical Engineers, Part A: Journal of Power and Energy*, 224(1):119–128, aug 2009. (Cited on page 16.)
- [87] P. P. Palies, R. Acharya, and A. Hoffie. Design and challenges of lean fully premixed injectors for gas turbine engines. In *AIAA Propulsion and Energy 2019 Forum*. American Institute of Aeronautics and Astronautics, aug 2019. (Cited on pages 4 and 43.)
- [88] R. Parker and J. F. Watson. Interaction effects between blade rows in turbomachines. *Proceedings of the Institution of Mechanical Engineers*, 186(1):331–340, jun 1972. (Cited on pages 14 and 15.)
- [89] U. Piomelli and E. Balaras. Wall-Layer Models for Large-Eddy Simulations. *Annual Review of Fluid Mechanics*, 2002. (Cited on page 86.)

-
- [90] S. Plot. The High Level of Maturity of the elsA CFD Software for Aerodynamics Applications. 2019. (Cited on page 60.)
- [91] S. B. Pope. *Turbulent Flows*. Cambridge University Press, aug 2000. (Cited on pages 24, 30, 86, 87, 103, 104, 128, 129, 132, 133, and 241.)
- [92] T. J. Praisner, J. W. Magowan, and J. P. Clark. Predictions of Temperature Redistribution in a Turning Duct and in High-Pressure Turbines. In *Volume 5: Turbo Expo 2003, Parts A and B*. ASMEDC, jan 2003. (Cited on page 16.)
- [93] L. Prandtl. Uber flussigkeitsbewegung bei sehr kleiner reibung. *Verhandlungen des dritten internationalen Mathematiker-Kongresses*, 1904. (Cited on page 171.)
- [94] D. Prasad and G. J. Hendricks. A Numerical Study of Secondary Flow in a Axial Turbines with Application to Radial Transport of Hot Streaks. *Journal of Turbomachinery*, 122(4):667–673, feb 2000. (Cited on pages 13 and 16.)
- [95] R. W. Radomsky and K. A. Thole. Flowfield Measurements for a Highly Turbulent Flow in a Stator Vane Passage. In *Volume 3: Heat Transfer, Electric Power, Industrial and Cogeneration*. American Society of Mechanical Engineers, jun 1999. (Cited on page 18.)
- [96] O. Reynolds. IV. on the dynamical theory of incompressible viscous fluids and the determination of the criterion. *Philosophical Transactions of the Royal Society of London. (A.)*, 186:123–164, dec 1895. (Cited on page 29.)
- [97] L. F. Richardson and P. Lynch. *Weather Prediction by Numerical Process*. Cambridge University Press, 2007. (Cited on page 24.)
- [98] P. Sagaut. *Large Eddy Simulation for Incompressible Flows*. Springer-Verlag GmbH, 2005. (Cited on pages 27, 28, 86, 104, and 238.)
- [99] C. Scalo, S. K. Lele, and L. Hesselink. Numerical Investigation of a Traveling-Wave Thermoacoustic Stirling Heat Engine. *Annual Research Briefs, Center for Turbulence Research*, 2013. (Cited on page 92.)
- [100] J. Schenderlein and T. Clayton. Comparison of Helicopter Turboshaft Engines. *AIAA*, 2014. (Cited on page 16.)
- [101] P. J. Schmid. Dynamic mode decomposition of numerical and experimental data. *Journal of Fluid Mechanics*, 656:5–28, jul 2010. (Cited on page 176.)
- [102] O. T. Schmidt and T. Colonius. Guide to spectral proper orthogonal decomposition. *AIAA Journal*, 58(3):1023–1033, mar 2020. (Cited on page 177.)
- [103] F. G. Schmitt. About boussinesq’s turbulent viscosity hypothesis: historical remarks and a direct evaluation of its validity. *Comptes Rendus Mécanique*, 335(9-10):617–627, sep 2007. (Cited on pages 129 and 130.)
- [104] O. P. Sharma and T. L. Butler. Predictions of Endwall Losses and Secondary Flows in Axial Flow Turbine Cascades. In *Volume 1: Turbomachinery*. American Society of Mechanical Engineers, jun 1986. (Cited on page 19.)
-

- [105] D. Shepard. A two-dimensional interpolation function for irregularly-spaced data. In *Proceedings of the 1968 23rd ACM national conference on -*. ACM Press, 1968. (Cited on page [173](#).)
- [106] Shift. Shift project. pouvoir voler en 2050 : quelle aviation dans un monde contraint ? Technical report, 2021. (Cited on page [2](#).)
- [107] A. J. Simonsen and P.-Å. Krogstad. Turbulent stress invariant analysis: Clarification of existing terminology. *Physics of Fluids*, 17(8):088103, aug 2005. (Cited on pages [131](#) and [132](#).)
- [108] L. Sirovich. Turbulence and the dynamics of coherent structures part i: Coherent structures. *Quarterly of Applied Mathematics*, 45(3):561–571, 1987. (Cited on pages [176](#) and [178](#).)
- [109] J. Smagorinsky. General circulation experiments with the primitive equations. *Monthly Weather Review*, 91(3):99–164, mar 1963. (Cited on page [28](#).)
- [110] B. Smith. A near wall model for the k - l two equation turbulence model. In *Fluid Dynamics Conference*. American Institute of Aeronautics and Astronautics, jun 1994. (Cited on pages [32](#) and [113](#).)
- [111] P. Spalart. Strategies for turbulence modelling and simulations. *International Journal of Heat and Fluid Flow*, 21(3):252–263, jun 2000. (Cited on page [137](#).)
- [112] P. Spalart and S. Allmaras. A one-equation turbulence model for aerodynamic flows. In *30th Aerospace Sciences Meeting and Exhibit*. American Institute of Aeronautics and Astronautics, jan 1992. (Cited on page [31](#).)
- [113] B. Stankovic, S. Belosevic, N. Crnomarkovic, A. Stojanovic, I. Tomanovic, and A. Milicevic. Specific aspects of turbulent flow in rectangular ducts. *Thermal Science*, 21(suppl. 3):663–678, 2017. (Cited on page [141](#).)
- [114] N. Syred. A review of oscillation mechanisms and the role of the precessing vortex core (PVC) in swirl combustion systems. *Progress in Energy and Combustion Science*10.1115/1.4049103, 32(2):93–161, jan 2006. (Cited on pages [110](#), [111](#), and [176](#).)
- [115] G. Sáez Mischlich. *High-order numerical methods for unstructured grids and sliding mesh*. PhD thesis, Toulouse INP, 2021. (Cited on page [93](#).)
- [116] R. Takahashi and R. Ni. Unsteady Hot Streak Simulation Through a 1-1/2 Stage Turbine Engine. In *27th Joint Propulsion Conference*. American Institute of Aeronautics and Astronautics, jun 1991. (Cited on pages [13](#) and [16](#).)
- [117] G. I. Taylor. The spectrum of turbulence. *Proceedings of the Royal Society of London. Series A - Mathematical and Physical Sciences*, 164(919):476–490, feb 1938. (Cited on page [104](#).)
- [118] The Jet Engine. *The Jet Engine*. Rolls-Royce, London, 2005. (Cited on pages [21](#), [22](#), and [237](#).)
- [119] M. Thomas. *Combustor-turbine interactions : Hot spot migration and thermal environment prediction for a better understanding and design of helicopter engines*. PhD thesis, Toulouse INP, 2021. (Cited on page [43](#).)

-
- [120] M. Thomas, J. Dombard, F. Duchaine, L. Gicquel, and C. Koupper. Large eddy simulation of combustor and complete single-stage high-pressure turbine of the FACTOR test rig. In *Volume 2A: Turbomachinery*. American Society of Mechanical Engineers, jun 2019. (Cited on pages 46 and 50.)
- [121] M. Thomas, L. Gicquel, F. Duchaine, and C. Koupper. Impact of realistic inlet condition on LES predictions of isolated high pressure vanes. In *12th International ERCOFTAC Symposium on Engineering Turbulence Modelling and Measurements*, 2018. (Cited on pages 45, 47, 48, 50, and 238.)
- [122] E. F. Toro, M. Spruce, and W. Speares. Restoration of the Contact Surface in the HLL-Riemann Solver. *Shock Waves*, 4(1):25–34, jul 1994. (Cited on page 93.)
- [123] E. Touber and N. D. Sandham. Large-Eddy Simulation of Low-Frequency Unsteadiness in a Turbulent Shock-Induced Separation Bubble. *Theoretical and Computational Fluid Dynamics*, 23(2):79–107, may 2009. (Cited on page 91.)
- [124] A. Towne, O. T. Schmidt, and T. Colonius. Spectral proper orthogonal decomposition and its relationship to dynamic mode decomposition and resolvent analysis. *Journal of Fluid Mechanics*, 847:821–867, may 2018. (Cited on page 177.)
- [125] C. Tropea, A. L. Yarin, and J. F. Foss, editors. *Springer Handbook of Experimental Fluid Mechanics*. Springer Berlin Heidelberg, 2007. (Cited on page 96.)
- [126] P. Tucker. Computation of unsteady turbomachinery flows: Part 1—progress and challenges. *Progress in Aerospace Sciences*, 47(7):522–545, oct 2011. (Cited on page 13.)
- [127] P. Tucker. Computation of unsteady turbomachinery flows: Part 2—LES and hybrids. *Progress in Aerospace Sciences*, 47(7):546–569, oct 2011. (Cited on page 29.)
- [128] P. Tucker. Trends in turbomachinery turbulence treatments. *Progress in Aerospace Sciences*, 63:1–32, nov 2013. (Cited on pages 24 and 29.)
- [129] S. Vagnoli, T. Verstraete, C. Koupper, and G. Bonneau. Assessment of RANS Against LES for the Aero-Thermal Behavior of High Pressure Turbine Stages Under Realistic Inlet Conditions. In *Volume 2C: Turbomachinery*. American Society of Mechanical Engineers, jun 2016. (Cited on pages 48, 49, 50, 107, 116, 121, 156, 163, and 238.)
- [130] G. H. Vatistas, V. Kozel, and W. C. Mih. A simpler model for concentrated vortices. *Experiments in Fluids*, 11(1):73–76, apr 1991. (Cited on page 89.)
- [131] A. W. Vreman. An eddy-viscosity subgrid-scale model for turbulent shear flow: Algebraic theory and applications. *Physics of Fluids*, 16(10):3670–3681, oct 2004. (Cited on pages 28 and 93.)
- [132] S. Wallin and A. V. Johansson. An explicit algebraic reynolds stress model for incompressible and compressible turbulent flows. 403:89–132, jan 2000. (Cited on page 33.)
- [133] Z. Wang, Z. Liu, and Z. Feng. Influence of Mainstream Turbulence Intensity on Heat Transfer Characteristics of a High Pressure Turbine Stage with Inlet Hot Streak. *Journal of Turbomachinery*, 138(4), dec 2015. (Cited on pages 18 and 107.)
-

- [134] Z. Wei, G. Ren, X. Gan, M. Ni, and W. Chen. Influence of shock wave on loss and breakdown of tip-leakage vortex in turbine rotor with varying backpressure. *Applied Sciences*, 11(11):4991, may 2021. (Cited on pages 20 and 237.)
- [135] R. C. Wilcock, J. B. Young, and J. H. Horlock. The effect of turbine blade cooling on the cycle efficiency of gas turbine power cycles. *Journal of Engineering for Gas Turbines and Power*, 127(1):109–120, jan 2005. (Cited on page 21.)
- [136] D. Wilcox. *Turbulence modeling for CFD*. DCW Industries, La Canada, Calif, 2006. (Cited on pages 24, 35, 100, 113, and 116.)
- [137] D. C. Wilcox. Reassessment of the scale-determining equation for advanced turbulence models. *AIAA Journal*, 26(11):1299–1310, nov 1988. (Cited on pages 32, 113, and 227.)
- [138] D. C. Wilcox. Formulation of the k-w turbulence model revisited. *AIAA Journal*, 46(11):2823–2838, nov 2008. (Cited on pages 154 and 227.)
- [139] C. Wingel, N. Binder, Y. Bousquet, J.-F. Boussuge, N. Buffaz, and S. L. Guyader. Influence of RANS turbulent inlet set-up on the swirled hot streak redistribution in a simplified nozzle guide vane passage: Comparisons with large-eddy simulations. In *Volume 10B: Turbomachinery — Axial Flow Turbine Aerodynamics ; Deposition, Erosion, Fouling, and Icing; Radial Turbomachinery Aerodynamics*. American Society of Mechanical Engineers, June 2022. (Cited on page 208.)
- [140] F. Xiao, M. Dianat, and J. J. McGuirk. An LES turbulent inflow generator using a recycling and rescaling method. *Flow, Turbulence and Combustion*, 98(3):663–695, oct 2016. (Cited on page 28.)
- [141] Z.-T. Xie and I. P. Castro. Efficient Generation of Inflow Conditions for Large Eddy Simulation of Street-Scale Flows. *Flow, Turbulence and Combustion*, 81(3):449–470, apr 2008. (Cited on page 91.)
- [142] S. Yoon and A. Jameson. An LU-SSOR scheme for the euler and navier-stokes equations. In *25th AIAA Aerospace Sciences Meeting*. American Institute of Aeronautics and Astronautics, mar 1987. (Cited on page 60.)
- [143] X. Zheng and F. Liu. Staggered upwind method for solving navier-stokes and k-omega turbulence model equations. *AIAA Journal*, 33(6):991–998, jun 1995. (Cited on pages 116, 226, and 227.)
- [144] Y. Zhiyin. Large-eddy simulation: Past, present and the future. *Chinese Journal of Aeronautics*, 28(1):11–24, feb 2015. (Cited on page 29.)

THÈSE

DOCTORAT DE L'UNIVERSITÉ DE TOULOUSE

Délivré par : *l'Institut Supérieur de l'Aéronautique et de l'Espace (ISAE-SUPAERO)*

École doctorale/spécialité : *MEGEP : Dynamique des fluides*

Unité de recherche : *ISAE-ONERA EDyF*

Présentée et soutenue le *08/09/2023* par : **Christopher WINGEL**

Titre : Évaluation de l'approche RANS pour l'étude des écoulements avec points chauds dans les turbines refroidies

L'écoulement en entrée de turbine haute-pression est caractérisé par des forts niveaux de turbulence et des points chauds swirlés qui impactent l'aérodynamique et l'aérothermique de l'étage de turbine. La prédiction fiable de cet écoulement de point chaud swirlé doit donc se faire en amont avec des simulations numériques. Dans ce travail de thèse, l'approche RANS est évaluée sur la configuration du projet FACTOR, où des données LES et expérimentales sont disponibles. Un premier état des lieux sur cette turbine confirme un écoulement complexe à prédire. Une configuration simplifiée est déclinée, afin de réaliser une étude phénoménologique d'un point chaud swirlé, en se focalisant sur la turbulence, grâce à des LES. La modélisation RANS sur cette configuration conduit à l'utilisation de modèles anisotropes. Suite à cette étude académique, la configuration FACTOR est de nouveau traitée. Les modèles anisotropes sont évalués, mais les résultats manquent de prédictibilité quand ils sont comparés aux essais. Deux problèmes sont mis en avant : des erreurs de mesure au P40 en raison des forts niveaux de giration, et une nature instationnaire du P40 à cause de la présence d'une instabilité. Les analyses montrent que le premier point est d'une importance capitale, alors que le second améliore les résultats dans une moindre mesure.

Mots-clefs : RANS, LES, turbulence, turbine haute-pression, point chaud.

Title: Investigation of the RANS approach for the prediction of cooled turbine stage flows submitted to swirled hot streaks

The flow at the inlet of the high-pressure turbine is characterised by high levels of turbulence, swirling motion and hot streaks which impact the aerodynamics and aerothermal of the high-pressure turbine, and the reliable prediction of this type of flow must be performed with numerical simulations. In this work, the RANS method is evaluated on the FACTOR project, where LES and experimental results are available. A first inventory on this turbine confirms a complex flow to predict. A simplified configuration is therefore studied for the analysis of a highly turbulent swirled hot streak with LES, especially in terms of turbulence. The RANS modelling on this configuration leads to the use of anisotropic turbulence models. Following the experience gained from this academic study, the FACTOR configuration is tackled again. Anisotropic turbulence models are applied, but still suffer from a lack of predictability when looking at temperature profiles. Two problems are put forward: measurement errors at P40 because of the high levels of swirl, and an unsteady nature of P40 due to the presence of an instability. Investigations show that the first point is of major importance, while the second improves the results to a lesser extent.

Keywords: RANS, LES, turbulence, high-pressure turbine, hot streak.
